STRUCTURAL SYSTEMS
RESEARCH PROJECT

Report No.
SSRP - 97/11

RESPONSE OF THE CORONADO BAY BRIDGE PILE-TO-PILE CAP CONNECTIONS UNDER SIMULATED SEISMIC LOADS

by

Pedro Silva
Frieder Seible
Nigel Priestley

Report on a Research Project funded by Caltrans under Contract No. 59V374

December 1997

Division of Structural Engineering
University of California, San Diego
La Jolla, California 92093-0085

Structural Systems Research Project

Report No. SSRP-97/11

RESPONSE OF THE CORONADO BAY BRIDGE PILE-TO-PILE CAP CONNECTIONS UNDER SIMULATED SEISMIC LOADS

by

Pedro Silva

Graduate Student Researcher

Frieder Seible

Professor of Structural Engineering

M.J. Nigel Priestley

Professor of Structural Engineering

Report on a Research Project funded by

Caltrans under Contract No. 59V374

December 1997

Technical Report Documentation Page

1. Report No.	2. Government Accession No.	3. Recipient's Catalog No.
SSRP-97/11		

4. Title and Subtitle	5. Report Date
RESPONSE OF THE CORONADO BAY BRIDGE PILE-TO-PILE CAP CONNECTIONS UNDER SIMULATED SEISMIC LOADS	December 1997
	6. Performing Organization Code
7. Author(s) Pedro F. Silva, Frieder Seible, M. J. Nigel Priestley	8. Performing Organization Report No.
9. Performing Organization Name and Address Division of Structural Engineering School of Engineering University of California, San Diego La Jolla, California 92093-0085	10. Work Unit No. (TRAIS)
	11. Contract or Grant No. 59V374 Area #2
12. Sponsoring Agency Name and Address California Department of Transportation Engineering Service Center 1801 30th Street Sacramento, California 95807	13. Type of Report and Period Covered 2 of 2
	14. Sponsoring Agency Code

15. Supplementary Notes

16. Abstract

This research project was developed to better predict the complete response and the vulnerability of the San Diego Coronado Bay Bridge to seismic events. The analytical prediction of the response of this bridge to seismic loads is influenced significantly by the structural response of the foundation system at the connections of the piles to the pile cap. Since the mud line profile varies considerably along the length of this bridge it was decided to test two piles with different lengths to obtain the structural response range of the piles and their connections to the pile cap. In addition, a third pile was tested with imposed initial damage to model the current damage state of the piles reported from underwater surveys.

The first test was defined as test unit *COR1* and consisted of a long pile with an aspect ratio of 5 and with expected flexural response characteristics. The test specimen performed in a very ductile manner in both loading directions.

The second test was similar to the first test and was defined as *COR2* and consisted of short pile with an aspect ratio of approximately 2.5. Unlike test unit *COR1*, test unit *COR2* displayed a more predominant flexural-shear response while achieving the theoretical flexural strength of the pile section.

The third test was defined as *COR3* and was identical to test unit *COR1* with imposed damage of the precast concrete shell and reinforcement. Test results suggest that the imposed cracks and cutting of the spiral and prestressing reinforcement did not have great influence in the overall response of the structure. In comparison with the test results for test unit *COR1*, test unit *COR3* achieved approximately the same flexural strength under axial compressive loads, and even exceeded the flexural strength of test unit *COR1* pile under axial tensile loads. Test results from the three test units significantly exceeded design assumptions used at the time for the Coronado Bay Bridge retrofit design.

17. Key Words	18. Distribution Statement
Pile, Pile Connections, Seismic Response	

19. Security Classification (of this report)	20. Security Classification (of this page)	21. No. of Pages	22. Price
Unclassified	Unclassified	~350	

Form DOT F 1700.7 (8-72) Reproduction of completed page authorized

Disclaimer

Any opinions, findings, conclusions and recommendations expressed in this final test report are those of the authors and do not necessarily reflect views of Caltrans or the Federal Highway Administration.

Acknowledgments

The research project described in this preliminary report was funded by the California Department of Transportation (Caltrans) under contract No. 59V374.

As in any other experimental project there are several people that made this work possible. We would like to thank Dr. Charles Sikorsky and Mr. Bob Jones of Caltrans, Mr. Joe Tognoli and Mr. Thomas Kompfner of McDaniel Engineering / J. Muller International Joint Venture for their technical participation during the preliminary design of the test unit.

In addition, we would like to thank Cliff Ohlwiler and all the technicians and engineers from Utility Vault and Michael Baumann and Andrew Scott from UCSD for their invaluable help during the construction of the precast prestressed concrete shells while at Utility Vault.

We would also like to thank Dr. Chris Latham at the UCSD Powell Structural Research Laboratories for all the recommendations and the extra work that he put in programming the control loading program for the simulation of the seismic loads. Moreover, the help of Larry Berman, Charles Stearns, Alex Sherman and Andrew Scott during construction and set up of the test specimen is greatly appreciated.

Response of the San Diego Coronado Bay Bridge Pile-to-Pile-Cap Connections Under Simulated Seismic Loading

List of Symbols

A_b	Cross sectional area of a bar.
A_g	Gross section area.
$A_{g,shell}$	Concrete shell section area.
$A_{g,core}$	Inner core section area.
A_{gl}	Effective area.
A_{sl}	Total longitudinal steel area.
A_{psl}	Total prestressing steel area.
A_{ps}	Prestressing steel area.
A_{sh}	Transverse steel area.
AXL	Axial Load Ratio.
b_{je}	Effective joint width assuming a 45° spread in all directions.
c	Distance between laterally supported longitudinal bars.
C_c	Concrete compression force.
C_s'	Reinforcing steel compression force.
D	Pile diameter or width.
D^*	Nominal pile diameter.
d_b	Diameter of reinforcement bar.
d_{bp}	Diameter of prestressing strand.
d_s	Circular spirals center to center diameter.
E_c	Young's modulus of concrete or tangent modulus of elasticity of concrete.
E_{ci}	Young's modulus of concrete at transfer.
E_{ps}	Young's modulus of prestressing strands.
E_s	Young's modulus of reinforcing steel.
E_{sec}	Secant modulus of elasticity of concrete.
E_{shell}	Young's modulus of steel shell.
F_T	Prestressing force at transfer.
F_J	Prestressing force at jacking.
F_{DT}	Prestressing force at day of test.
f_{eq}	Equivalent transformed section stress.

f_c	Concrete stress (compressive or tensile).
f_{ci}	Concrete compressive strength at transfer of prestressing strands.
f_c'	Concrete compressive strength.
$f_{c,shell}'$	Concrete compressive strength of concrete shell.
$f_{c,core}'$	Concrete compressive strength of inner core.
f_{co}'	Unconfined concrete compressive strength.
f_{cc}'	Confined concrete compression strength.
f_{cu}	Confined concrete compressive strength at ultimate concrete strain.
f_l'	Effective lateral confining pressure.
f_l	Lateral confining pressure from transverse reinforcement.
f_{to}	Modulus of rupture of concrete.
f_h	Horizontal axial stress in the joint region.
f_{pe}	Effective prestressing stress after transfer and after losses.
f_{ps}	Prestressing stress.
f_v	Vertical axial stress in the joint region.
f_s	Reinforcement tensile stress.
f_{se}	Initial prestressing stress.
f_s'	Reinforcement compressive stress.
f_{sl}	Reinforcement stress (compressive or tensile).
f_y	Yield strength of steel reinforcement.
f^o_y	Reinforcement yield strength at overstrength.
H_{cap}	Depth of pile cap.
H_{pile}	Length of pile section above pile cap interface.
H_{eff}	Effective length of the pile section for deflection calculations.
H_i	Experimental lateral load at each cyclic response.
H_o	Experimental initial lateral load due to the imposed initial axial load.
I_x	Area moment of inertia.
I_{eff}	Effective section moment of inertia.
KB_p	Bending stiffness of a single pile.
KA_p	Axial stiffness of a single pile.
K_s	Equivalent spring stiffness.
k_e	Confinement effectiveness coefficient.
K_g	Section geometry factor.
k_h	Coefficient of horizontal subgrade reaction modulus.
h_{cur}	Height of curvature cell.
h^*_{cur}	Revised height of curvature cell to include strain penetrations at the pile cap interface.

L_{BED} Distance between casting bed strong-end bulkheads.
L_a Strain penetration length.
l_a Anchorage length.
l_d Development length of reinforcing steel.
l_{dp} Development length of prestressing steel.
l_f Prestressing flexural bond length.
l_p Plastic hinge length.
l_t Prestressing transfer length.
M_C Column moment.
M_{cr} Cracking moment.
M_{UP} Pile ultimate moment.
NA Section neutral axis.
n_p Number of piles in a pile group.
OTM_c Column overturning moment.
P Axial load.
P_C Column axial load.
P_{IC} Axial load computed from loading path equations.
P^*_C Allowable compression design axial load in piles.
P_h Horizontal axial force on the joint.
P_i Experimental axial load at each cyclic response.
P_o Initial axial load on a single pile due to gravity loads.
P_P Pile axial load.
P^*_T Allowable tension design axial load in piles.
P_v Vertical axial force on the joint.
s' Vertical clear distance between spirals.
s Sample variance.
T_s Reinforcing steel tension force.
T_{ps} Prestressing steel tension force.
V_C Column shear force.
V_{cr} Lateral load at section cracking moment.
V_P Pile shear force.
V'_y Lateral load at first section yielding.
V'_{yC} Lateral load at first section yielding - *Compression loading branch.*
V'_{yT} Lateral load at first section yielding - *Tension loading branch.*
V_y Lateral load at ideal flexural strength.
V_{yC} Lateral load at ideal flexural strength - *Compression loading branch.*

V_{yT} Lateral load at ideal flexural strength - *Tension loading branch.*
V_{jv} Vertical joint shear force.
v_{jv} Vertical joint shear stress.
W_{cur} Length of curvature cell.
X Distance to end of section or member.
Z_x Elastic section modulus.
Z Depth soil stratum.

α_{ps} Parameter relating position of segment to end of prestressing steel.
α_s Parameter relating position of segment to end of reinforcing steel.
α_{av} Average bond strength constant.
Δ Pile lateral deflection.
Δ_{cap} Prototype pile cap lateral translation.
Δ_i Experimental residual displacements.
Δ_{max} Maximum achieved experimental lateral displacement.
Δ_N Displacement measured by a linear potentiometer within a curvature cell.
Δ_S Displacement measured by a linear potentiometer within a curvature cell.
Δ_{shear} Shear deformation.
Δ_x Segment length.
Δ_y' First section yield displacement.
Δ_{yC}' First section yield displacement - *Compression loading branch.*
Δ_{yT}' First section yield displacement - *Tension loading branch.*
Δ_y Yield displacement.
Δ_{yC} Yield displacement - *Compression loading branch.*
Δ_{yT} Yield displacement - *Tension loading branch.*
Δ_Z Spacing of soil springs.
δ_L Chuck seating at live end.
δ_D Chuck seating at dead end.
ϵ Section strain.
ϵ_c Concrete compressive strain.
ϵ_{cc} Concrete strain at peak confined compression stress.
ϵ_{co} Concrete strain at peak unconfined compression stress.
ϵ_{cu} Ultimate concrete compressive strain.
ϵ'_s Steel reinforcement compressive strain.
ϵ_s Steel reinforcement tensile strain.
ϵ_{ps} Prestressing reinforcement tensile strain.

η_{pi} Moduli ratio at time of transfer = E_{ps}/E_{ci}.

θ_{cap} Prototype pile cap rotation.

μ_{Δ} Displacement ductility.

$\langle \mu_{1-\alpha} \rangle$ Confidence interval.

ρ_t Joint principal tensile stress.

ρ_{ps} Reinforcement ratio of longitudinal prestressing strands.

ϕ Section curvature.

ϕ_{ave} Experimentally determined average curvature.

ϕ_i Pile section curvature a position i.

ϕ_{i-1} Pile section curvature a position i-1.

ψ_{cap} Rotation of pile cap.

Response of the San Diego Coronado Bay Bridge Pile-to-Pile-Cap Connections Under Simulated Seismic Loading

Table of Contents

Disclaimer i

Acknowledgments ii

List of Symbols iii

Table of Contents viii

List of Figures xii

List of Tables xxi

Abstract xxi

1. Introduction 1

2. Geometry and Design of the Test Units 3

2.1 Prototype Reinforcement Layout 3

2.2 Overall Test Setup and Geometry 11

2.2.1 Test Units *COR1* and *COR3* - General Test Configuration 11

2.2.2 Test Unit *COR2* - General Test Configuration 17

2.3 Test Units *COR1*, *COR2* and *COR3* - Pile Cap Design and Capacity 20

2.4 Test Units *COR1* and *COR3* - Pile Design and Capacity 25

2.4.1 Test Units *COR1* and *COR3* - Pre-Test Analysis 28

2.4.2 Test Units *COR1* and *COR3* - Effective Cantilever Length 44

2.5 Test Unit *COR2* - Pile Design and Capacity 48

2.5.1 Test Unit *COR2* - Pre-Test Analysis 50

2.5.2 Test Unit COR2 - Effective Cantilever Length 55

3. Construction, Instrumentation and Testing Procedure 57
3.1 Construction of the Test Specimens 57
3.1.1 Construction of Test Units *COR1* and *COR3* 57
3.1.2 Construction of Test Unit *COR2* 70
3.2 Test Units *COR1*, *COR2* and *COR3* - Material Properties 74
3.3 Instrumentation of the Test Specimens 81
3.3.1 Instrumentation of Test Unit *COR1* and *COR3* 81
3.3.2 Instrumentation of Test Unit *COR2* 95
3.4 Testing Procedure 105
3.4.1 Test Unit *COR1* and *COR3* - Loading Path and Control Program 113
3.4.2 Test Unit *COR1* - Loading History 118
3.4.3 Test Unit *COR3* - Loading History 118
3.4.4 Test Unit *COR2* - Loading Path and Control Program 121
3.4.5 Test Unit *COR2* - Loading History 126

4. Development Length of Prestressing Strands 128
4.1 Fabrication of the Precast Prestressed Concrete Shells 130
4.1.1 Prestressing Losses 130
4.1.1.1 Elastic Shortening of Concrete 130
4.1.1.2 Shrinkage of Concrete 131
4.1.1.3 Relaxation of Strand 131
4.1.1.4 Chuck Seating 132
4.1.1.5 Bed Shortening 132
4.1.2 Prestressing Schedule 134
4.2 Transfer Bond Length 135
4.2.1 Regression Analysis 136
4.3 Flexural Bond Length 143
4.3.1 Evaluation of Code Provisions for the Development Length of Prestressing Strands 143
4.3.2 Proposed Code Provisions for the Development Length of Prestressing Strands 143

5. **Test Unit *COR1* Experimental Test Results** 146
5.1 General Test Observations 146
5.2 Load Deformation Characteristics 157
5.3 Pile Curvature Profiles 164
5.4 Pile Inner Core Longitudinal Reinforcement Strain Profiles 167
5.4.1 Pile Longitudinal Reinforcement - Vertical Strain Profiles 167
5.4.2 Pile Longitudinal Reinforcement - Circumferential Strain Profiles 172
5.5 Prestressing Strands Vertical Strain Profiles 177
5.6 Pile Transverse Reinforcement Strain Profiles 182
5.6.1 Pile Transverse Reinforcement - Vertical Strain Profiles 182
5.6.2 Pile Transverse Reinforcement - Circumferential Strain Profiles 187
5.7 Pile Cap Reinforcement Strain Profiles 191
5.8 Pile Cap Rotation 193

6. **Test Unit *COR2* Experimental Test Results** 195
6.1 General Test Observations 195
6.2 Load Deformation Characteristics 208
6.3 Pile Curvature Profiles 215
6.4 Flexural and Shear Components of Deformation 217
6.5 Pile Inner Core Longitudinal Reinforcement Strain Profiles 220
6.5.1 Pile Longitudinal Reinforcement - Vertical Strain Profiles 220
6.5.2 Pile Longitudinal Reinforcement - Circumferential Strain Profiles 225
6.6 Prestressing Strands Vertical Strain Profiles 230
6.7 Pile Transverse Reinforcement Strain Profiles 235
6.7.1 Pile Transverse Reinforcement - Vertical Strain Profiles 235
6.7.2 Pile Transverse Reinforcement - Circumferential Strain Profiles 240
6.8 Pile Cap Reinforcement Strain Profiles 244
6.9 Pile Cap Rotation 246

7. Test Unit *COR3* Experimental Test Results 247
7.1 General Test Observations 247
7.2 Load Deformation Characteristics 260
7.3 Pile Curvature Profiles 267
7.4 Vertical Profiles of Artificial Cracks Opening 269
7.5 Pile Inner Core Longitudinal Reinforcement Strain Profiles 272
7.5.1 Pile Longitudinal Reinforcement - Vertical Strain Profiles 272
7.5.2 Pile Longitudinal Reinforcement - Circumferential Strain Profiles 277
7.6 Prestressing Strands Vertical Strain Profiles 282
7.7 Pile Transverse Reinforcement Strain Profiles 287
7.7.1 Pile Transverse Reinforcement - Vertical Strain Profiles 287
7.8 Pile Cap Reinforcement Strain Profiles 292
7.9 Pile Cap Rotation 294

8. Discussion of Experimental Test Results 295
8.1 Test Units *COR1, COR2* and *COR3* 295
8.1.1 Test Unit *COR1* and *COR2* - Post-Test Analysis Concrete Models 296
8.1.1.1 Mander Model 297
8.1.1.2 Modified Bjerkeli Model 298
8.1.2 Test Units *COR1, COR2* and *COR3*- Post-Test Analysis Tensile Strain Penetration Contribution to Pile Lateral Deflection . . . 302
8.2 Comparison of Test Results 303
8.2.1 Test Units *COR1* and *COR3* 303
8.2.2 Test Units *COR1, COR2* and *COR3* 313

9. Conclusions 315

References 318

Appendix A - Test Unit *COR3* - Concrete Core Data 322

Appendix B - Control Program Loading Path 328
B.1 Test Units *COR1* and *COR3* - Flowchart 330
B.2 Test Unit *COR2* - Flowchart 335

Response of the San Diego Coronado Bay Bridge Pile-to-Pile-Cap Connections Under Simulated Seismic Loading

List of Figures

Fig. 2-1 Pier 2 - Pile Cap Prototype Drawings 5
Fig. 2-2 Pier 2 - Pile Cap Prototype Drawings 6
Fig. 2-3 Pier 5 - Pile Cap Prototype Drawings 7
Fig. 2-4 Pier 5 - Pile Cap Prototype Drawings 8
Fig. 2-5 Pier 2 and Pier 5 - Pile Cap Precast Soffit Slab 9
Fig. 2-6 Pier 2 and Pier 5 - Prototype Type I Pile Drawings 10
Fig. 2-7 Test Units *COR1*, *COR2* and *COR3* - General Layout Plan View 14
Fig. 2-8 Test Units *COR1* and *COR3* - General Layout Front View 15
Fig. 2-9 Test Units *COR1* and *COR3* - General Layout Side View 16
Fig. 2-10 Test Unit *COR2* - General Layout Front View 18
Fig. 2-11 Test Unit *COR2* - General Layout Side View 19
Fig. 2-12 Pile Cap Bending Moment Diagram 20
Fig. 2-13 Test Units *COR1*, *COR2* and *COR3* - Pile Cap Reinforcement Layout 22
Fig. 2-14 Test Units *COR1*, *COR2* and *COR3* - Modeled Precast soffit Slab 23
Fig. 2-15 Test Units *COR1*, *COR2* and *COR3*
Pile Cap Moment and Shear Demands and Capacities 24
Fig. 2-16 Test Unit *COR1* and *COR3* - Pile Reinforcement Layout 27
Fig. 2-17 Test Unit *COR1* and *COR3* - Stress Block Design Parameters 29
Fig. 2-18 Test Units *COR1* and *COR3* - Bending Moment Demand and 30
Fig. 2-19 Tension Shift Effect in a Diagonally
Cracked Reinforced Concrete Section 34
Fig. 2-20 Moment Profiles - Axial Compression Load P = +2793kN 36
Fig. 2-21 Moment Profiles - Axial Tension Load P = -302kN 36
Fig. 2-22 Curvature Distribution 37
Fig. 2-23 Test Unit *COR1*- Pre-Test Analysis 41
Fig. 2-24 Test Unit *COR3* - Pre-Test Analysis 41
Fig. 2-25 Test Unit *COR1* - Predicted Shear Capacity and Flexural Response 42

Fig. 2-26 Test Unit *COR3* - Predicted Shear Capacity and Flexural Response 42
Fig. 2-27 Test Units *COR1* and *COR3* -
Joint Region Principal Tensile Stresses Pre-Test Analysis 43
Fig. 2-28 Test Unit *COR1* and *COR3* Soil-Structure 44
Fig. 2-29 Test Units *COR1* and *COR3* - Pile Bending Moment Profile and
Lateral Deflection for a Fixed Head Single Pile 47
Fig. 2-30 Test Unit *COR2* - Pile Reinforcement Layout 49
Fig. 2-31 Moment Profiles - Axial Compression Load P = +2793kN 52
Fig. 2-32 Moment Profile - Axial Tension Load P = -302kN 52
Fig. 2-33 Test Unit *COR2* - Pre-Test Analysis 54
Fig. 2-34 Test Unit *COR2* Predicted Shear Capacity and Flexural Response 54
Fig. 2-35 Test Unit *COR2* Soil-Structure 55
Fig. 2-36 Test Unit *COR2* - Pile Bending Moment Profile and
Lateral Deflection for a Fixed Head Single Pile 56

Fig. 3-1 Self-Reacting Casting Bed Components 58
Fig. 3-2 Installing Inner Core Form Before Casting of Concrete Shell 60
Fig. 3-3 Installing Inner Core Form Before Casting of Concrete Shell 60
Fig. 3-4 Inner Core Tube Mechanism 61
Fig. 3-5 Top Form Aperture 61
Fig. 3-6 Casting of the Concrete Shell at *Utility Vault* 62
Fig. 3-7 Fully Assembled Self Reacting Casting Bed 62
Fig. 3-8 Pile Cap Reinforcement Cage 63
Fig. 3-9 Pile Cap Reinforcement Cage Before Installing Precast Concrete Shell 63
Fig. 3-10 Installing Concrete Shell Thru Inner Core Reinforcement Cage 64
Fig. 3-11 Installing Concrete Shell Thru Inner Core Reinforcement Cage 64
Fig. 3-12 Concrete Shell in Place Before Casting of Pile Cap 65
Fig. 3-13 Casting of Pile Cap 65
Fig. 3-14 Soffit Slab Reinforcement Cage Before Casting 66
Fig. 3-15 Soffit Slab Reinforcement Cage Before Casting 66
Fig. 3-16 Test Unit *COR3* Longitudinal Saw Cut Lines 67
Fig. 3-17 Test Unit *COR3* Longitudinal Saw Cut Lines 67
Fig. 3-18 Test Setup Unit *COR1* 68
Fig. 3-19 Test Setup Unit *COR3* 69
Fig. 3-20 First Stages of Preparation for Construction of Concrete Shell For *COR2* . . 71

Fig. 3-21 Positioning of Strands Through Wooden Piece Separator Before Prestressing 71
Fig. 3-22 *wedge-chuck* **VSL S5N** Anchorage System 72
Fig. 3-23 Finished Precast Concrete Shell Before Separation at Wooden Piece for *COR2* 72
Fig. 3-24 Test Setup Unit *COR2* 73
Fig. 3-25 Test Setup Unit *COR2* 73
Fig. 3-26 Stress-Strain Curve of Prestressing Steel 77
Fig. 3-27 Test Unit *COR1* Pile Layout - Concrete Material Properties 78
Fig. 3-28 Test Unit *COR2* Pile Layout - Concrete Material Properties 79
Fig. 3-29 Test Unit *COR3* Pile Layout - Concrete Material Properties 80
Fig. 3-30 Curvature Measurement 81
Fig. 3-31 Test Units *COR1* and *COR3* - Instrumentation Setup Front View 85
Fig. 3-32 Test Units *COR1* and *COR3* - Instrumentation Setup Side View 86
Fig. 3-33 Test Unit *COR3* - Instrumentation Setup Front View 87
Fig. 3-34 Test Units *COR1* and *COR3* - Pile Inner Core Reinforcement Strain Gages 88
Fig. 3-35 Test Units *COR1* and *COR3* - Pile Prestressing Reinforcement Strain Gages 89
Fig. 3-36 Test Units *COR1* and *COR3* - Pile Transverse Reinforcement Strain Gages 90
Fig. 3-37 Test Units *COR1* and *COR3* - Pile Cap Reinforcement Strain Gages 91
Fig. 3-38 Test Units *COR1* and *COR3* - Pile Cap Reinforcement Strain Gages 92
Fig. 3-39 Test Units *COR1* and *COR3* - Pile Cap Reinforcement Strain Gages 93
Fig. 3-40 Test Units *COR1* and *COR3* - Concrete Surface Strain Gages Applied During Manufacturing of Precast Concrete Shells 94
Fig. 3-41 Test Unit *COR2* - Instrumentation Setup Front View 97
Fig. 3-42 Test Unit *COR2* - Instrumentation Setup Side View 98
Fig. 3-43 Test Unit *COR2* - Shear Panel Deformation Instrumentation Layout 99
Fig. 3-44 Test Unit *COR2* - Estimation of Shear Deformation 100
Fig. 3-45 Test Unit *COR2* - Pile Inner Core Reinforcement Strain Gages 101
Fig. 3-46 Test Unit *COR2* - Pile Prestressing Reinforcement Strain Gages 102
Fig. 3-47 Test Unit *COR2* - Pile Transverse Reinforcement Strain Gages 103

Fig. 3-48 Test Unit *COR2* - Concrete Surface Strain Gages Applied During Manufacturing of Precast Concrete Shells 104
Fig. 3-49 Prototype Structure Deformed Shape 107
Fig. 3-50 Pier 2 - Prototype Structure Finite Element Model 110
Fig. 3-51 Pier 5 - Prototype Structure Finite Element Model 111
Fig. 3-52 Pier 5 Piles - Loading Path 114
Fig. 3-53 Test Units *COR1* and *COR3*- Control Program Loading Path 114
Fig. 3-54 Test Unit *COR1* - Loading History 119
Fig. 3-55 Test Unit *COR3* - Loading History 120
Fig. 3-56 Pier 2 Piles - Loading Path 122
Fig. 3-57 Test Unit *COR2* - Control Program Loading Path 122
Fig. 3-58 Test Unit *COR2* - Loading History 127

Fig. 4-1 Strand Jacking and Cut Sequence 134
Fig. 4-2 Test Unit *COR1* - Strand Strain versus Time at 152mm from the Pile Head 136
Fig. 4-3 Test Unit *COR1* - Strand Strain versus Time at 914mm from the Pile Head 137
Fig. 4-4 Test Unit *COR1* - Strand Strain versus Time at 2337mm from the Pile Head 138
Fig. 4-5 Test Unit *COR2* - Strand Strain versus Time at 610mm from the Pile Head 139
Fig. 4-6 Transfer Bond Length Regression Analysis 142
Fig. 4-7 Stress Profiles versus Distance to Pile Ends 145

Fig. 5-1 Bilinear approximation 148
Fig. 5-2 Onset of Flexural Cracking at Lateral Deflection +25.65mm 151
Fig. 5-3 Cracking Pattern at -20.57mm 152
Fig. 5-4 Cracking Pattern at +51.05mm 152
Fig. 5-5 Onset of Plastic Hinge Relocation at +68.07mm 153
Fig. 5-6 Cracking Pattern at -109.73mm 153
Fig. 5-7 Extent of Spalling at +85.09mm 154
Fig. 5-8 Unwinding of Prestressing Strands at Lateral Deflection +85.09mm 155
Fig. 5-9 Wide Open Crack Above Inner Core Bar 155
Fig. 5-10 Plastic Hinge Relocation at -137.16mm 156

Fig. 5-11 Complete Test Setup After Testing 156
Fig. 5-12 Lateral Load versus Lateral Deflection Characteristics 158
Fig. 5-13 Lateral Load versus Base Curvature Characteristics 160
Fig. 5-14 Axial Load versus Lateral Deflection Characteristics 162
Fig. 5-15 Axial Load versus Lateral Load Characteristics 163
Fig. 5-16 Curvature Vertical Profiles 166
Fig. 5-17 Vertical Strain Profiles Inner Core Bar ***A*** 168
Fig. 5-18 Vertical Strain Profiles Inner Core Bar ***B*** 169
Fig. 5-19 Vertical Strain Profiles Inner Core Bar ***C*** 170
Fig. 5-20 Vertical Strain Profiles Inner Core Bar ***D*** 171
Fig. 5-21 Inner Core Reinforcement Strain Profiles Along Horizontal Line ***1*** and ***2*** . 173
Fig. 5-22 Inner Core Reinforcement Strain Profiles Along Horizontal Line ***3*** and ***4*** . 174
Fig. 5-23 Inner Core Reinforcement Strain Profiles Along Horizontal Line ***5*** and ***6*** . 175
Fig. 5-24 Inner Core Reinforcement Strain Profiles Along Horizontal Line ***7*** and ***8*** . 176
Fig. 5-25 Vertical Strain Profiles Along Strand ***A*** 178
Fig. 5-26 Vertical Strain Profiles Along Strand ***B*** 179
Fig. 5-27 Vertical Strain Profiles Along Strand ***C*** 180
Fig. 5-28 Vertical Strain Profiles Along Strand ***D*** 181
Fig. 5-29 Pile Transverse Reinforcement Strain Profiles Along Line ***A*** 183
Fig. 5-30 Pile Transverse Reinforcement Strain Profiles Along Line ***B*** 184
Fig. 5-31 Pile Transverse Reinforcement Strain Profiles Along Line ***C*** 185
Fig. 5-32 Pile Transverse Reinforcement Strain Profiles Along Line ***D*** 186
Fig. 5-33 Pile Transverse Reinforcement Strain Profiles
Along Horizontal Line ***1*** and ***2*** 188
Fig. 5-34 Pile Transverse Reinforcement Strain Profiles
Along Horizontal Line ***3*** and ***4*** 189
Fig. 5-35 Pile Transverse Reinforcement Strain Profiles
Along Horizontal Line ***5*** and ***6*** 190
Fig. 5-36 Lateral Deflection versus Strain
Strain Gage Pile Cap Bottom Reinforcement ***Bottom 3-B*** 191
Fig. 5-37 Lateral Deflection versus Strain
Strain Gage Pile Cap Vertical Reinforcement ***3-B*** 192
Fig. 5-38 Lateral Deflection versus Pile Cap Uplift 194

Fig. 6-1 Bilinear approximation 196
Fig. 6-2 Onset of Flexural and Vertical Splitting Cracking 200
Fig. 6-3 Cracking Pattern at -8.63mm 200
Fig. 6-4 Onset of Inclined Shear Cracking at -12.95mm 201
Fig. 6-5 Onset of Inclined Shear Cracking at -12.95mm 201
Fig. 6-6 Cracking Pattern at +17.78mm 202
Fig. 6-7 Cracking Pattern at −17.27mm 202
Fig. 6-8 Cracking Pattern at −21.59mm 203
Fig. 6-9 Cracking Pattern at +26.67mm 203
Fig. 6-10 Cracking Pattern at +35.56mm 204
Fig. 6-11 Cracking Pattern at -43.18mm 204
Fig. 6-12 Onset of Concrete Crushing at +44.45mm 205
Fig. 6-13 Post Test Damage State 205
Fig. 6-14 Post Test Damage State 206
Fig. 6-15 Spiral Fracture Along Inclined Shear Crack 206
Fig. 6-16 Spiral Fracture at Prestressing Strand 207
Fig. 6-17 Extent of Spalling of the Cover Concrete at Pile Cap Interface 207
Fig. 6-18 Lateral Load versus Lateral Deflection Characteristics 210
Fig. 6-19 Lateral Load versus Base Curvature Characteristics 211
Fig. 6-20 Axial Load versus Lateral Deflection Characteristics 213
Fig. 6-21 Axial Load versus Lateral Load Characteristics 214
Fig. 6-22 Curvature Vertical Profiles 216
Fig. 6-23 Displacement Components versus Pile Lateral Deflection 218
Fig. 6-24 Displacement Components versus Lateral Load 219
Fig. 6-25 Vertical Strain Profiles Inner Core Bar ***A*** 221
Fig. 6-26 Vertical Strain Profiles Inner Core Bar ***B*** 222
Fig. 6-27 Vertical Strain Profiles Inner Core Bar ***C*** 223
Fig. 6-28 Vertical Strain Profiles Inner Core Bar ***D*** 224
Fig. 6-29 Inner Core Reinforcement Strain Profiles Along Horizontal Line ***1*** and ***2*** . . 226
Fig. 6-30 Inner Core Reinforcement Strain Profiles Along Horizontal Line ***3*** and ***4*** . . 227
Fig. 6-31 Inner Core Reinforcement Strain Profiles Along Horizontal Line ***5*** and ***6*** . . 228
Fig. 6-32 Inner Core Reinforcement Strain Profiles Along Horizontal Line ***7*** and ***8*** . . 229
Fig. 6-33 Vertical Strain Profiles Along Strand ***A*** 231
Fig. 6-34 Vertical Strain Profiles Along Strand ***B*** 232
Fig. 6-35 Vertical Strain Profiles Along Strand ***C*** 233

Fig. 6-36 Vertical Strain Profiles Along Strand ***D*** 234
Fig. 6-37 Pile Transverse Reinforcement Strain Profiles Along Line ***A*** 236
Fig. 6-38 Pile Transverse Reinforcement Strain Profiles Along Line ***B*** 237
Fig. 6-39 Pile Transverse Reinforcement Strain Profiles Along Line ***C*** 238
Fig. 6-40 Pile Transverse Reinforcement Strain Profiles Along Line ***D*** 239
Fig. 6-41 Pile Transverse Reinforcement Strain Profiles
Along Horizontal Line ***1*** and ***2*** 241
Fig. 6-42 Pile Transverse Reinforcement Strain Profiles
Along Horizontal Line ***3*** and ***4*** 242
Fig. 6-43 Pile Transverse Reinforcement Strain Profiles
Along Horizontal Line ***5*** and ***6*** 243
Fig. 6-44 Lateral Deflection versus Strain
Strain Gage Pile Cap Bottom Reinforcement ***Bottom 2-B*** 244
Fig. 6-45 Lateral Deflection versus Strain
Strain Gage Pile Cap Vertical Reinforcement ***3-B*** 245
Fig. 6-46 Lateral Deflection versus Pile Cap Uplift 246

Fig. 7-1 Bilinear approximation 248
Fig. 7-2 Onset of Flexure Cracking at V=+317kN 252
Fig. 7-3 Cracking Pattern at +26.42mm 252
Fig. 7-4 Cracking Pattern at +26.42mm 253
Fig. 7-5 Cracking Pattern at +26.42mm 253
Fig. 7-6 Cracking Pattern at +26.42mm 254
Fig. 7-7 Cracking Pattern at -11.68mm 254
Fig. 7-8 Cracking Pattern at +39.62mm 255
Fig. 7-9 Cracking Pattern at +39.62mm 255
Fig. 7-10 Cracking Pattern at -17.53mm 256
Fig. 7-11 Cracking Pattern at -17.53mm 256
Fig. 7-12 Cracking Pattern at Lateral Deflection of +78.74mm 257
Fig. 7-13 Cracking Pattern at Lateral Deflection of -52.07mm 257
Fig. 7-14 Cracking Pattern at Lateral Deflection of -52.07mm 258
Fig. 7-15 Extent of Spalling of Cover Concrete at
Lateral Deflection of +105.92mm 258
Fig. 7-16 Plastic Hinge Relocation 259
Fig. 7-17 Wide Open Crack 259

Fig. 7-18 Lateral Load versus Lateral Deflection Characteristics 262
Fig. 7-19 Lateral Load versus Base Curvature Characteristics 263
Fig. 7-20 Axial Load versus Lateral Deflection Characteristics 265
Fig. 7-21 Axial Load versus Lateral Load Characteristics 266
Fig. 7-22 Curvature Vertical Profiles 268
Fig. 7-23 Crack Width Opening Vertical Profiles Along Line ***A*** 270
Fig. 7-24 Crack Width Opening Along Vertical Line ***D*** 271
Fig. 7-25 Vertical Strain Profiles Inner Core Bar ***A*** 273
Fig. 7-26 Vertical Strain Profiles Inner Core Bar ***B*** 274
Fig. 7-27 Vertical Strain Profiles Inner Core Bar ***C*** 275
Fig. 7-28 Vertical Strain Profiles Inner Core Bar ***D*** 276
Fig. 7-29 Inner Core Reinforcement Strain Profiles Along Horizontal Line ***1*** and ***2*** . 278
Fig. 7-30 Inner Core Reinforcement Strain Profiles Along Horizontal Line ***3*** and ***4*** . 279
Fig. 7-31 Inner Core Reinforcement Strain Profiles Along Horizontal Line ***5*** and ***6*** . 280
Fig. 7-32 Inner Core Reinforcement Strain Profiles Along Horizontal Line ***7*** and ***8*** . 281
Fig. 7-33 Vertical Strain Profiles Along Strand ***A*** 283
Fig. 7-34 Vertical Strain Profiles Along Strand ***B*** 284
Fig. 7-35 Vertical Strain Profiles Along Strand ***C*** 285
Fig. 7-36 Vertical Strain Profiles Along Strand ***D*** 286
Fig. 7-37 Pile Transverse Reinforcement Strain Profiles Along Line ***A*** 288
Fig. 7-38 Pile Transverse Reinforcement Strain Profiles Along Line ***B*** 289
Fig. 7-39 Pile Transverse Reinforcement Strain Profiles Along Line ***C*** 290
Fig. 7-40 Pile Transverse Reinforcement Strain Profiles Along Line ***D*** 291
Fig. 7-41 Lateral Deflection versus Strain
Strain Gage Pile Cap Bottom Reinforcement ***Bottom 3-C*** 292
Fig. 7-42 Lateral Deflection versus Strain
Strain Gage Pile Cap Vertical Reinforcement ***3-B*** 293
Fig. 7-43 Lateral Deflection versus Pile Cap Uplift 294

Fig. 8-1 Stress-Strain Curve for Confined and Unconfined Concrete -
Mander Model 300
Fig. 8-2 Stress-Strain Curve for Confined and Unconfined Concrete -
Modified Bjerkeli Model 300
Fig. 8-3 Concrete Models Stress-Strain Characteristics 301
Fig. 8-4 Curvature Profiles 302

Fig. 8-5 Test Units *COR1* and *COR3* - Lateral Load versus Lateral Deflection Envelope 305
Fig. 8-6 Onset of Flexural Cracking at μ_Δ 1.5x3 - Test Unit *COR1* 306
Fig. 8-7 Onset of Flexural Cracking at First Section Yielding - Test Unit *COR3* . . 306
Fig. 8-8 Vertical Strain Profiles Inner Core Bar ***A*** 307
Fig. 8-9 Vertical Strain Profiles Inner Core Bar ***B*** 308
Fig. 8-10 Vertical Strain Profiles Inner Core Bar ***C*** 309
Fig. 8-11 Vertical Strain Profiles Inner Core Bar ***D*** 310
Fig. 8-12 Test Units *COR1* and *COR3* - Curvature Vertical Profiles 311
Fig. 8-13 Extent of Spalling of Cover Concrete - Test Unit *COR1* 312
Fig. 8-14 Extent of Spalling of Cover Concrete - Test Unit *COR3* 312
Fig. 8-15 Test Units *COR1, COR2* and *COR3* - Moment versus Curvature Envelopes 314

Fig. A-1 Plan View Pier 19 - Surveyed Pile Cap 323
Fig. A-2 Pier 19 - Surveyed Pile Number ***4*** 324
Fig. A-3 Pier 19 - Surveyed Pile Number ***12*** 325
Fig. A-4 Pier 19 -Surveyed Pile Number ***16*** 326
Fig. A-5 Pier 19 -Surveyed Pile Number ***33*** 327

Fig. B-1 Test Units *COR1* and *COR3* - Flowchart **Region 1** 329
Fig. B-2 Test Units *COR1* and *COR3* - Flowchart **Region 2** 330
Fig. B-3 Test Units *COR1* and *COR3* - Flowchart **Region 3** 331
Fig. B-4 Test Units *COR1* and *COR3* - Flowchart **Region 4** 332
Fig. B-5 Test Unit *COR2* - Flowchart **Region 1** 334
Fig. B-6 Test Unit *COR2* - Flowchart **Region 2** 335
Fig. B-7 Test Unit *COR2* - Flowchart **Region 3** 336
Fig. B-8 Test Unit *COR2* - Flowchart **Region 4** 337

Response of Standard Caltrans Pile-to-Pile-Cap Connections Under Simulated Seismic Loading

List of Tables

Table 2-1 Test Units *COR1, COR2* and *COR3* - Prototype Scaling Parameters 13

Table 3-1 Concrete Material Properties - High Strength Concrete 74
Table 3-2 Concrete Material Properties - Normal Strength Concrete 75
Table 3-3 Test Units *COR1, COR2* and *COR3* Steel Material Properties 76
Table 3-4 Test Unit *COR1* and *COR3*-
Casting Operation Summary of Instrumentation 83
Table 3-5 Test Unit *COR1* and *COR3*-
Testing Procedure Summary of Instrumentation 84
Table 3-6 Test Unit *COR2* - Summary of Instrumentation 96

Table 4-1 Summary of Prestress Losses 133

Table 9-1 Test Unit *COR1* - Experimental Test Results 316
Table 9-2 Test Unit *COR2* - Experimental Test Results 317
Table 9-3 Test Unit *COR3* - Experimental Test Results 317

Abstract

This research project was developed to better predict the complete response and the vulnerability of the San Diego Coronado Bay Bridge to seismic events. The analytical prediction of the response of this bridge to seismic loads is influenced significantly by the structural response of the foundation system at the connections of the piles to the pile cap. Since the mud line profile varies considerably along the length of this bridge, it was decided to test two piles with different lengths to obtain the structural response range of the piles and their connections to the pile cap. In addition, a third pile was tested with imposed initial damage to model the current damage state of the piles reported from underwater surveys.

The first test was defined as test unit *COR1* and consisted of a long pile with an aspect ratio of 5 and with an expected flexural response characteristics. The test specimen performed in a very ductile manner in both loading directions .

The second test was similar to the first test and was defined as *COR2* and consisted of short pile with an aspect ratio of approximately 2.5. Unlike test unit *COR1*, test unit *COR2* displayed a more predominant flexural-shear response, while achieving the theoretical flexural strength of the pile section.

The third test was defined as test unit *COR3* and was identical to Test unit *COR1* with imposed damage of the precast concrete shell and reinforcement. Test results suggests that the imposed cracks and cutting of the spiral and prestressing reinforcement did not have great influence in the overall response of the structure. In comparison with the test results for test unit *COR1*, test unit *COR3* achieved approximately the same flexural strength under axial compressive loads and even exceeded the flexural strength of test unit *COR1* pile under axial tensile loads. Test results from the three test units significantly exceeded design assumptions currently used for the Coronado Bay Bridge retrofit design.

1. Introduction

The complete structural response of the San Diego Coronado Bay Bridge to seismic loading was analyzed by the consulting engineering firm ANATECH of San Diego by employing a global model time-history analysis to this bridge. In 1995, ANATECH completed a single pile cap capacity analysis of a typical Coronado pile at Pier 6 [1] and concluded that at a displacement ductility 3 a collapse condition is likely, and the design criteria for the piles should not exceed a displacement ductility of 2. Underwater surveying of the existing piles indicates cracking of the precast concrete shell and corrosion of the prestressing strands and spiral reinforcement. Based on this information, the design team proposed a more conservative criteria than a ductility of 2 criteria.

Engineers from McDaniel Engineering / J. Muller International Joint Venture established a criteria such that deformation demands be limited to levels that cause a concrete compressive strain of 0.005. In 1996, ANATECH, from a pile group pushover analyses developed deformation versus rotation (i.e. Δ_{cap} vs. θ_{cap}) capacity envelope curves based on this 0.005 concrete strain criteria. Pushover analyses results indicate that the controlling case for design has been the case in which rotation of the pile cap is restrained and the pile cap lateral translation is the primary mode of deformation. In this case, the concrete compressive strain of 0.005 was first achieved at the pile head at a displacement ductility between 1 and 2, depending on the height and geometry of the pile group [1]. Thus, the main objective of this experimental research is to verify these design constraints and to validate the design criteria recommended by the design team for the seismic retrofit of the Coronado Bay Bridge.

In this research project, three models of the as-built Type I pile of the San Diego Coronado Bay Bridge were investigated at UCSD. These test units were designed as 2/3 scale models of the prototype piles and are composed of a precast prestressed concrete shell with cast-in-place reinforced concrete at the connection region and unreinforced concrete away from the pile cap. The experimental test setup for each test unit consists of a single cantilevered pile and part of the scaled prototype pile cap. The pile of test unit *COR1* has an aspect ratio of approximately 5 and was designed to capture the boundary conditions for a pile embedded in a saturated soil stratum with a deep mud line elevation. Test results indicate this test unit displayed a ductile flexural response without shear failure.

To account for shallower mud line elevations at bents close to the ends of the bridge, the cantilever length of test unit *COR2* was designed with an aspect ratio of approximately 2.5. Unlike test unit *COR1*, test results indicate test unit *COR2* displayed a more predominant flexural-shear response, while achieving the theoretical flexural strength of the pile section due to its considerably lower aspect ratio. Fracture of the transverse reinforcement along inclined cracks, at later stages of the testing procedure, illustrates flexural-shear response of test unit *COR2.*

Finally, test unit *COR3* was identical to test unit *COR1* and was constructed with imposed initial cracking of the precast concrete shell in the form of vertical cracks and by cutting the prestressing strands and spiral reinforcement along the simulated vertical cracks to model corrosion of this reinforcement, as reported from underwater condition survey of the Coronado Bay Bridge piles **[2]**. The experimental test results of test unit *COR3* were compared with test unit *COR1* results and showed that both units displayed a ductile flexural response under the simulated seismic loads. In addition, based on maximum loads and achieved displacement ductility levels, it can be concluded that cracking and corrosion of the reinforcement in the precast concrete shell did not considerably affect the response of test unit *COR3,* since the section achieved the same maximum lateral deflection and lateral load as in test unit *COR1.*

Based on the experimental test results, ANATECH performed a calibration of the finite element model used in developing the pile capacity deformation versus rotation envelope curves. The final retrofit design scheme was then based on the deformation which leads to 80% of the maximum lateral force in the post-peak lateral force drop-off, and a displacement ductility of 4 was set as the maximum limiting ductility capacity.

2. Geometry and Design of the Test Units

Test configuration and design of the proposed test units was based on the San Diego Coronado Bay Bridge piles. Design of the test units was developed in close collaboration with engineers from Caltrans, McDaniel Engineering Company, Inc., J. Muller International and researchers from the University of California at San Diego. Design of test unit *COR1* and test unit *COR3* was based on the Type I pile at Pier 5 and test unit *COR2* to that at Pier 2.

2.1 Prototype Reinforcement Layout

Pier 2 prototype drawings are shown in **Fig. 2-1** and **Fig. 2-2**. The pile cap longitudinal reinforcement layout consists of 19-#11 bars at 339 mm on centers at bottom and bundled 22-#11 bars at 345 mm on centers at top, and the pile cap transverse reinforcement consists of 44-#11 bars at 241 mm on center bottom. For additional reinforcement layout details (see **Fig. 2-2**).

Pier 5 prototype drawings are shown in **Fig. 2-3** and **Fig. 2-4**. The pile cap longitudinal reinforcement layout consists of 29-#11 bars at 305 mm on centers at bottom and bundled 42-#11 bars at 241 mm on centers at top, and the pile cap transverse reinforcement consists of 68-#11 bars at 241 mm on center bottom. For additional reinforcement layout details (see **Fig. 2-4**).

Precast soffit slabs were used as a working platform for alignment and cleaning of the pile heads and then used as a form work for construction of the pile cap. Typical design drawings of the soffit slabs are presented in **Fig. 2-5**.

Fig. 2-6 shows typical design drawings of Type I piles at pier 2 and pier 5. The piles are composed of a precast prestressed concrete shell 127 mm thick with cast in place reinforced concrete at the connection region and unreinforced concrete away from the pile cap. Prestressing of the concrete shell consists of 34 seven-wire prestressing steel strands 13 mm in diameter of low relaxation type, arranged around the inner circumference of the spiral steel with a concrete cover of 50.80 mm, resulting in a prestressing reinforcement ratio of 0.23%. The total required design prestressing force after losses for the Type I pile was 3425 kN.

For the transverse reinforcement changes along the length of the pile (see **Fig. 2-6**). In the first 1,219 mm length of the pile closest to the pile cap, the transverse reinforcement consists of deformed #4 bars on a spiral pitch of 102 mm, resulting in a horizontal volumetric reinforcement ratio of 0.40%. After this level, and for the next 1,524 mm, the transverse reinforcement ratio consists of undeformed wire W4 on a spiral pitch of 50.80 mm, resulting in a horizontal volumetric reinforcement ratio of 0.16%. In the remaining length of the pile, the transverse reinforcement ratio consists of undeformed wire W4 on a spiral pitch of 102 mm, resulting in a horizontal volumetric reinforcement ratio of 0.08%.

Starter bars into the pile cap consist of 24-#11 bars arranged in an inner circle with a diameter of 940 mm, resulting in a reinforcement ratio of 1.64%. The length of these bars into the pile cap is 1,219 mm and into the pile is 2,438 mm. This inner cage was tied together with hoop reinforcement #4 bars at 305 mm on centers (see **Fig. 2-6**).

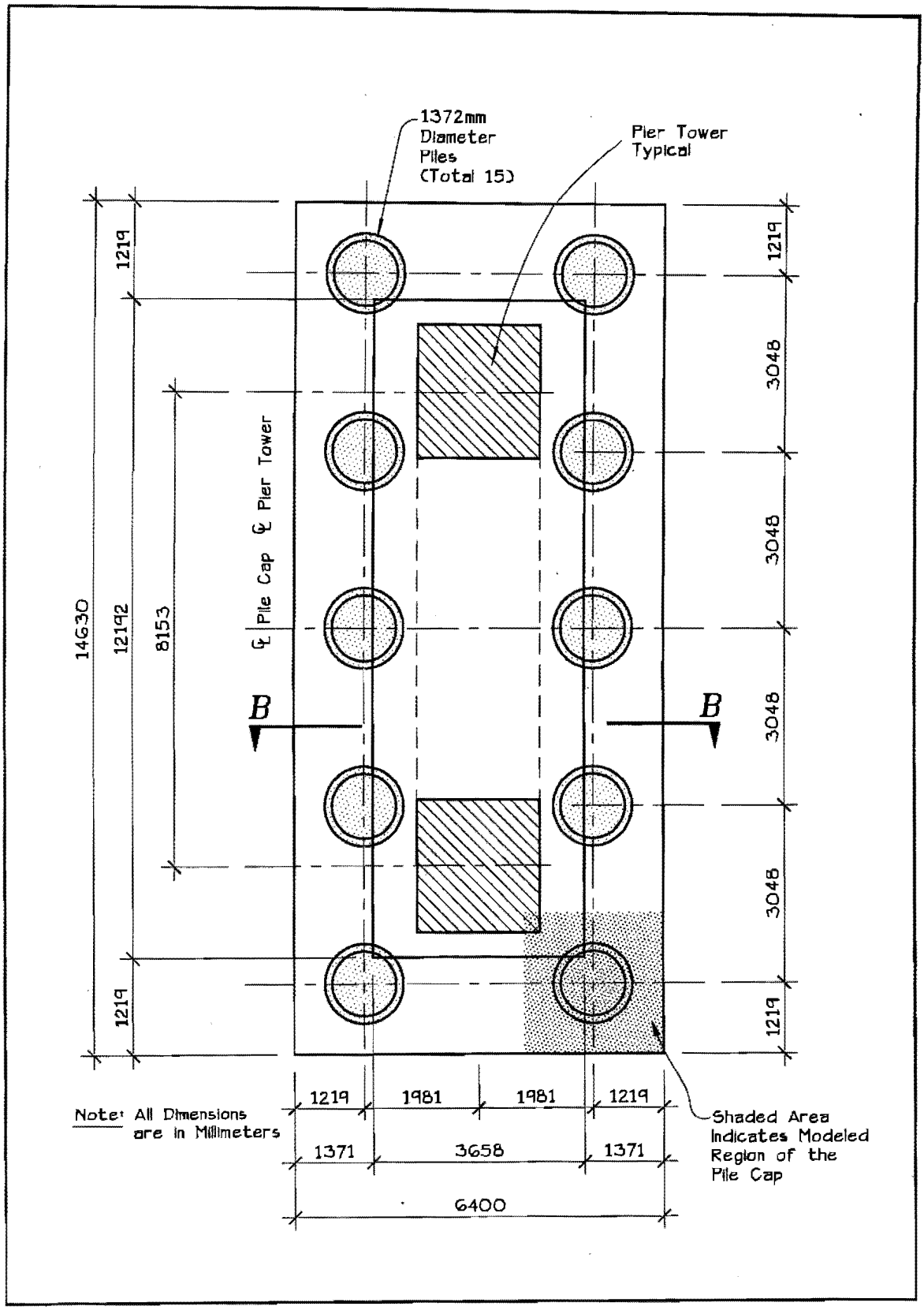

Fig. 2-1 Pier 2 - Pile Cap Prototype Drawings

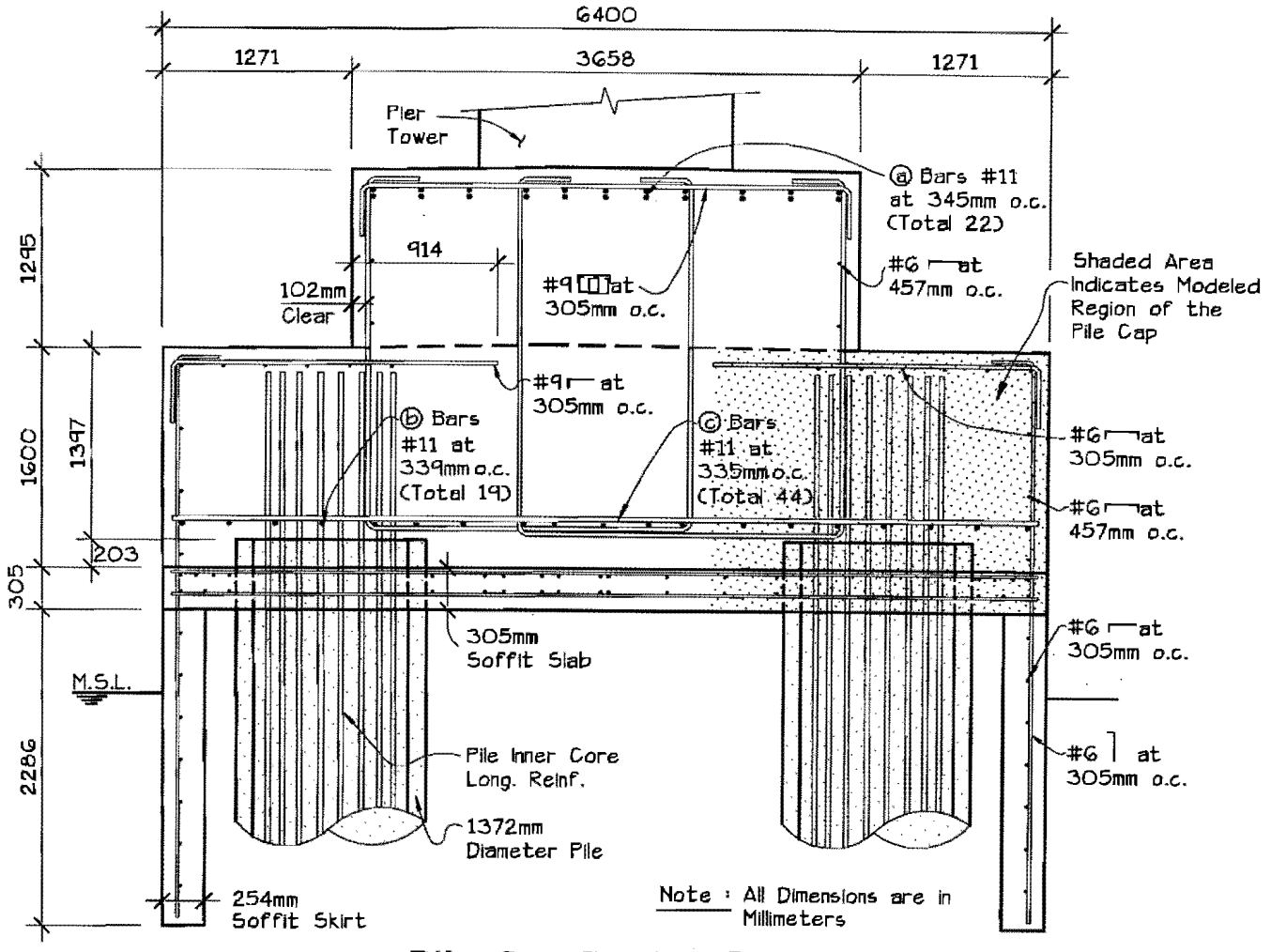

Pile Cap Section B–B

Fig. 2–2 Pier 2 - Pile Cap Prototype Drawings

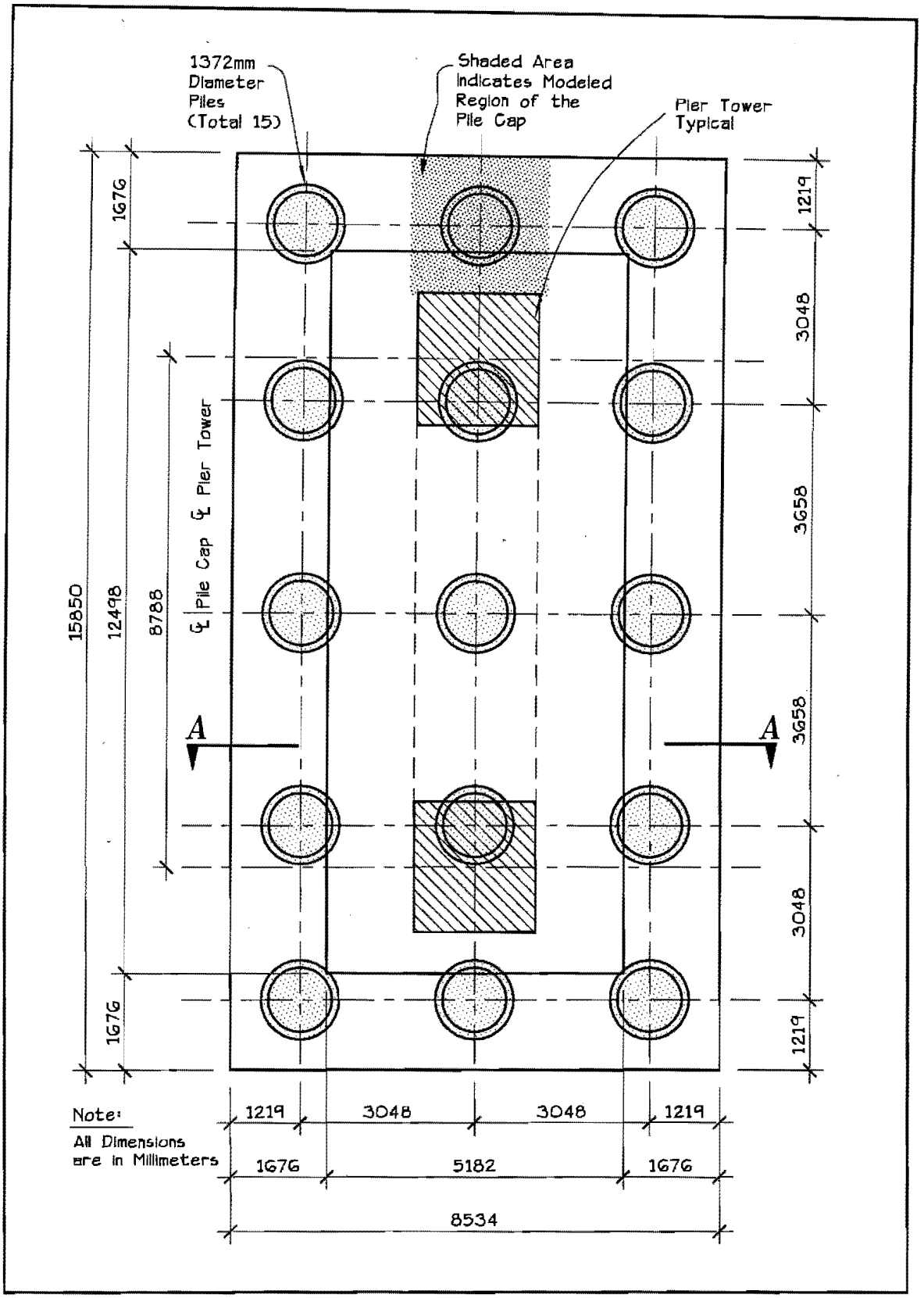

Fig. 2-3 Pier 5 - Pile Cap Prototype Drawings

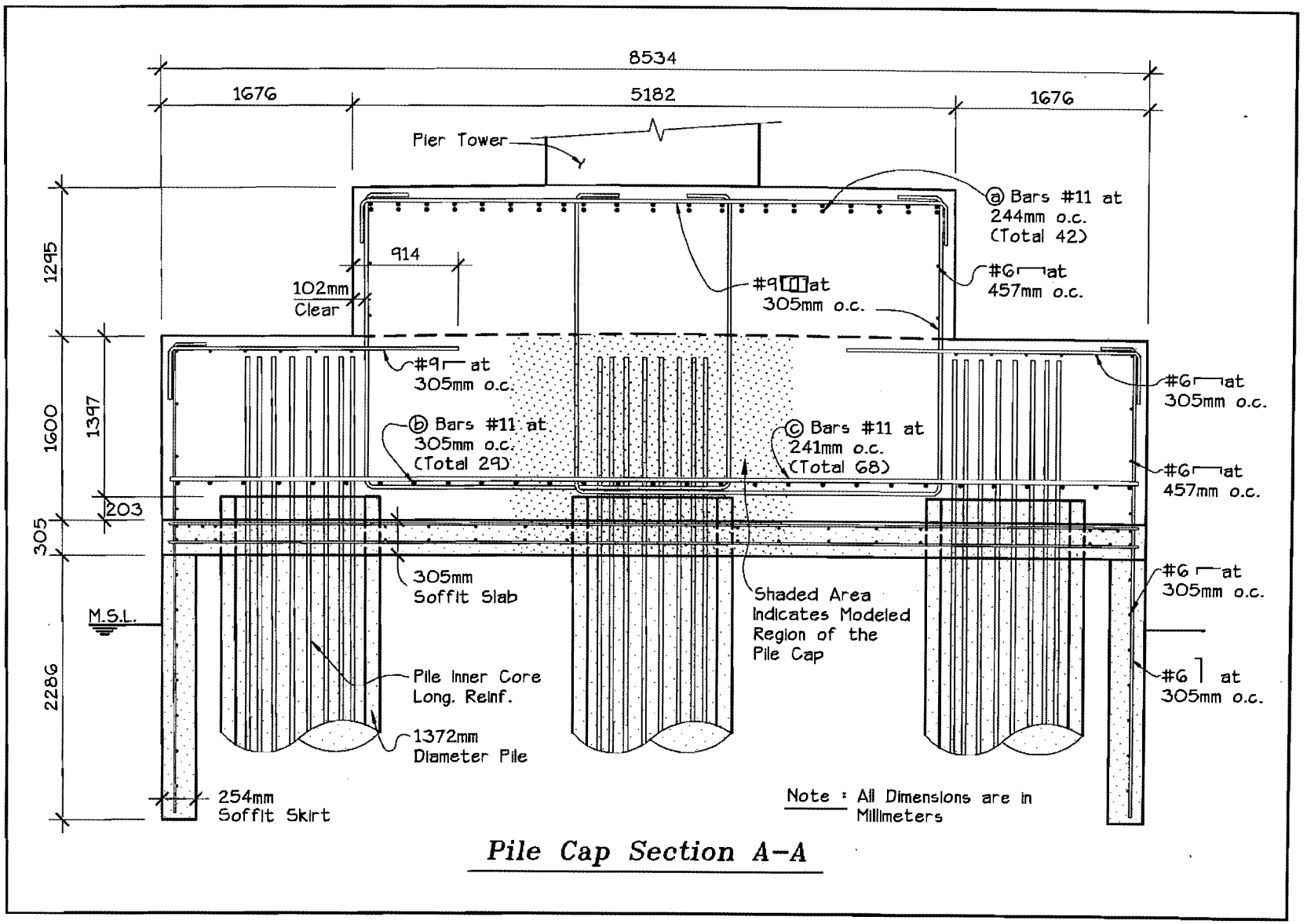

Fig. 2-4 Pier 5 - Pile Cap Prototype Drawings

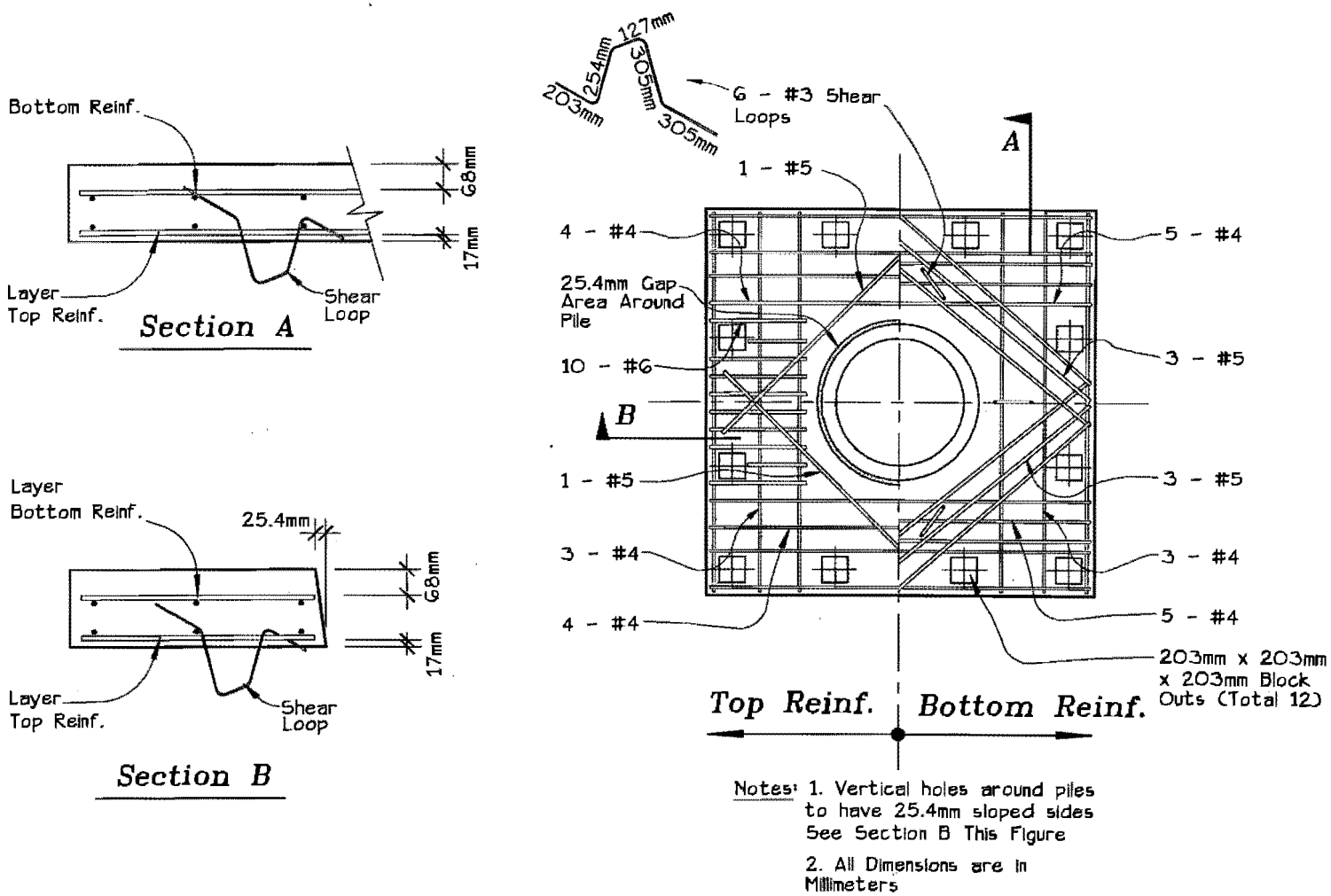

Notes: 1. Vertical holes around piles to have 25.4mm sloped sides See Section B This Figure

2. All Dimensions are in Millimeters

Fig. 2-5 Pier 2 and Pier 5 - Pile Cap Precast Soffit Slab

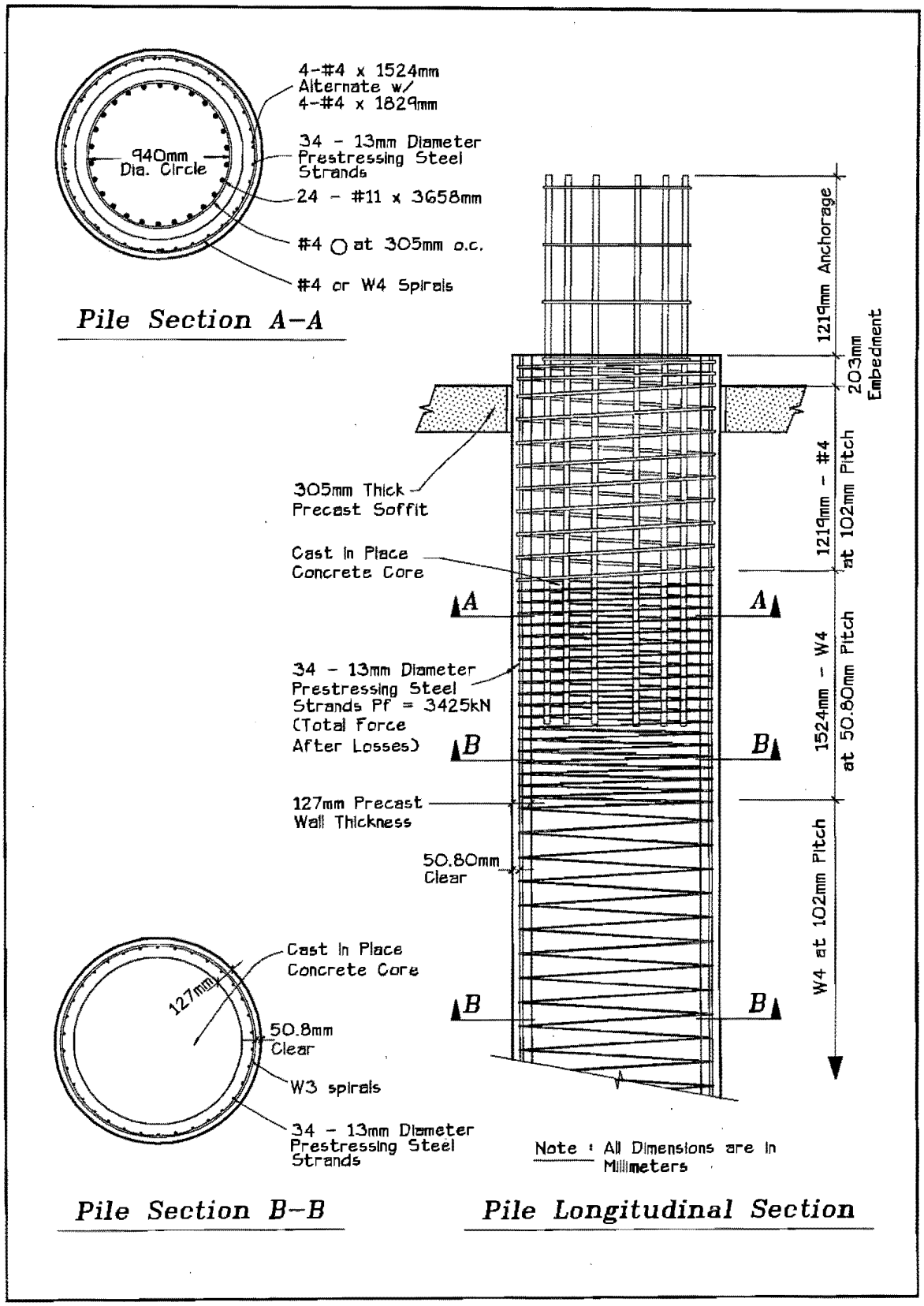

Fig. 2-6 Pier 2 and Pier 5 - Prototype Type I Pile Drawings

2.2 Overall Test Setup and Geometry

The overall geometry and reinforcement layout for the test units were taken directly from the prototype drawings described in the previous section and will be presented in this section. In this section, a brief description of the complete test setup, geometry and pile reinforcement layout are presented for test units *COR1*, *COR2* and *COR3*.

2.2.1 Test Units *COR1* and *COR3* - General Test Configuration

Test units *COR1* and *COR3* are 2/3 scale models of the as-built Type I pile at Pier 5 of the San Diego Coronado Bay Bridge. A summary of the scaling parameters is presented in **Table 2-1**.

The pile cap test unit was designed to model the behavior of an interior pile of the prototype pile cap at the joint region, and the pile of test units *COR1* and *COR3* was designed to capture the boundary conditions for a pile embedded in a saturated soil stratum with a deep mud line elevation. In addition, test unit *COR3* specimen was constructed to provide a direct means of comparison between the structural response of a pile with no initial cracks and a pile with imposed damage that models the worst current state of damage of the existing in situ piles of the Coronado Bay Bridge.

Referring to **Fig. 2-8** and **Fig. 2-9**, the test units were built in an inverted position as they occur in the prototype structure to ease installation and loading of the test specimen. However, in the next sections, all parts of the test units are referred to as they occur in the prototype structure.

During a seismic event, the forces transmitted from the bridge superstructure into the foundation system produces rotation and translation of the pile cap. As the rotation of the pile cap increases, those piles in front of the axis of rotation experience an increase in the axial compressive load and, if the rotation of the pile cap is significant, those piles at the back of the axis of rotation will most likely be subjected to axial tensile loads. On the other hand, for piles embedded in a saturated soil with a deep mud line elevation, as the in situ conditions at Pier 5, the soil stiffness is not adequate in preventing lateral translations, and lateral translation of the pile cap imposes resisting moments to develop at the pile heads. Thus, under a seismic event, the individual piles of a pile group experience reversed cyclic loading in both axial and lateral load.

Variations in the axial load to the specimen were applied by means of two hydraulic actuators installed on the sides of the pile cap on support blocks and attached to a steel loading beam, which was mounted on the load stub, as shown in **Fig. 2-8**. Variations in the horizontal lateral load were also applied by means of a hydraulic actuator connected to the strong wall and the load stub (see **Fig. 2-9**). Because of the changes in the axial and lateral load, it was necessary to label the direction of the applied loads according to their loading direction. Thus, for testing purposes, when in compression the axial force was designated as positive and when in tension the axial force was designated as negative. In addition, when in the compression loading branch, the lateral force was defined as positive and in the tension loading branch the lateral force was defined as negative. A complete scheme of the applied loads will be presented in later sections when describing the testing procedure.

Concrete core data from a condition survey of the Coronado Bay Bridge piles **[2]** indicates that where cracks of 1.60 mm or wider occur, corroded spirals or prestressing reinforcement can be encountered. In Appendix A of this report, a brief summary of the concrete core data is presented. In addition, from all the piles surveyed, no cracks where reported in the plug region where the inner core reinforcement is present. Outside this plug region, the inner core cast in place concrete is composed of sandy veins and other low quality materials that lower the concrete strength of the tremie concrete.

Based on the data provided from the condition survey **[2]**, the imposed damage to test unit *COR3* pile consisted of saw cutting two lines of cracks along lines A and D through the precast prestressed concrete shell and extending it above the termination of the inner core reinforcement, for a length of approximately 1,575 mm, as indicated in **Fig. 2-7** through **Fig. 2-9**. Along these artificial cracks, all the spiral reinforcement was cut, and adjacent to these longitudinal cracks at the top and bottom, 25.4 mm diameter holes where core drilled through the prestressing strands, as indicated in **Fig. 2-8** and **Fig. 2-9**. In addition, to model the low quality of concrete in the core region above the longitudinal reinforcement, the inner core was cast with a low concrete strength, which will be discussed in Chapter 3 when describing the concrete material properties.

Table 2-1 Test Units *COR1, COR2* and *COR3* - Prototype Scaling Parameters

	PROTOTYPE	MODEL*
Pile Height	7,010 mm - Pier 5 3,353 mm - Pier 2	4,673 mm - *COR1* and *COR3* 2,235 mm - *COR2*
Pile Diameter (O.D.)	1,372 mm Outside Diameter	914 mm Outside Diameter
Precast Wall Thickness	127 mm	86 mm
Clearance To Prestress	50.8 mm Clearance	35 mm Clearance
Core Dia. To Long. Reinf.	940 mm Diameter Circle	628 mm Diameter Circle
Pile Embedment Length	203 mm	137 mm
Prestress Reinforcing	34 -12.7 mm ⌀ Strand $\rho_l = 0.00227$	27 - 9.53 mm ⌀ Strand $\rho_l = 0.00225$
Prestress Force	3,425 kN	1,521 kN
CIP Section Longitudinal Reinforcement	24-#11 x 3,658 mm $\rho_l = 0.01635$	28 - #7 x 2,438 mm $\rho_l = 0.01650$
Longitudinal Reinforc. Embedment Length	1,219 mm	813 mm
Precast Section Long. Reinforcement	8 - #4 $\rho_l = 0.000699$	6 - #3 $\rho_l = 0.000648$
Spirals (Pile Head) Section A-A, see **Fig. 2-16** and **Fig. 2-30**	#4 @ 102 mm Pitch $\rho_h = 0.004$ L = 1,219 mm	#3 @ 84 mm Pitch $\rho_h = 0.004$ L = 948 mm
Spirals (Middle Layer) Section B-B, see **Fig. 2-16** and **Fig. 2-30**	W4 @ 51 mm Pitch $\rho_h = 0.0016$ L = 1,524 mm	W3 @ 57 mm Pitch $\rho_h = 0.0016$ L = 1,016 mm
Spirals (Bottom Layer) Section C-C, see **Fig. 2-16**	W4 @ 102 mm Pitch $\rho_h = 0.0008$	W3 @ 114 mm Pitch $\rho_h = 0.0008$
Axial Compression Force	+6,761 kN [3]	+3,007 kN
Axial Tension Force	-681 kN [3]	-302 kN

* scale factor $f = 2/3$

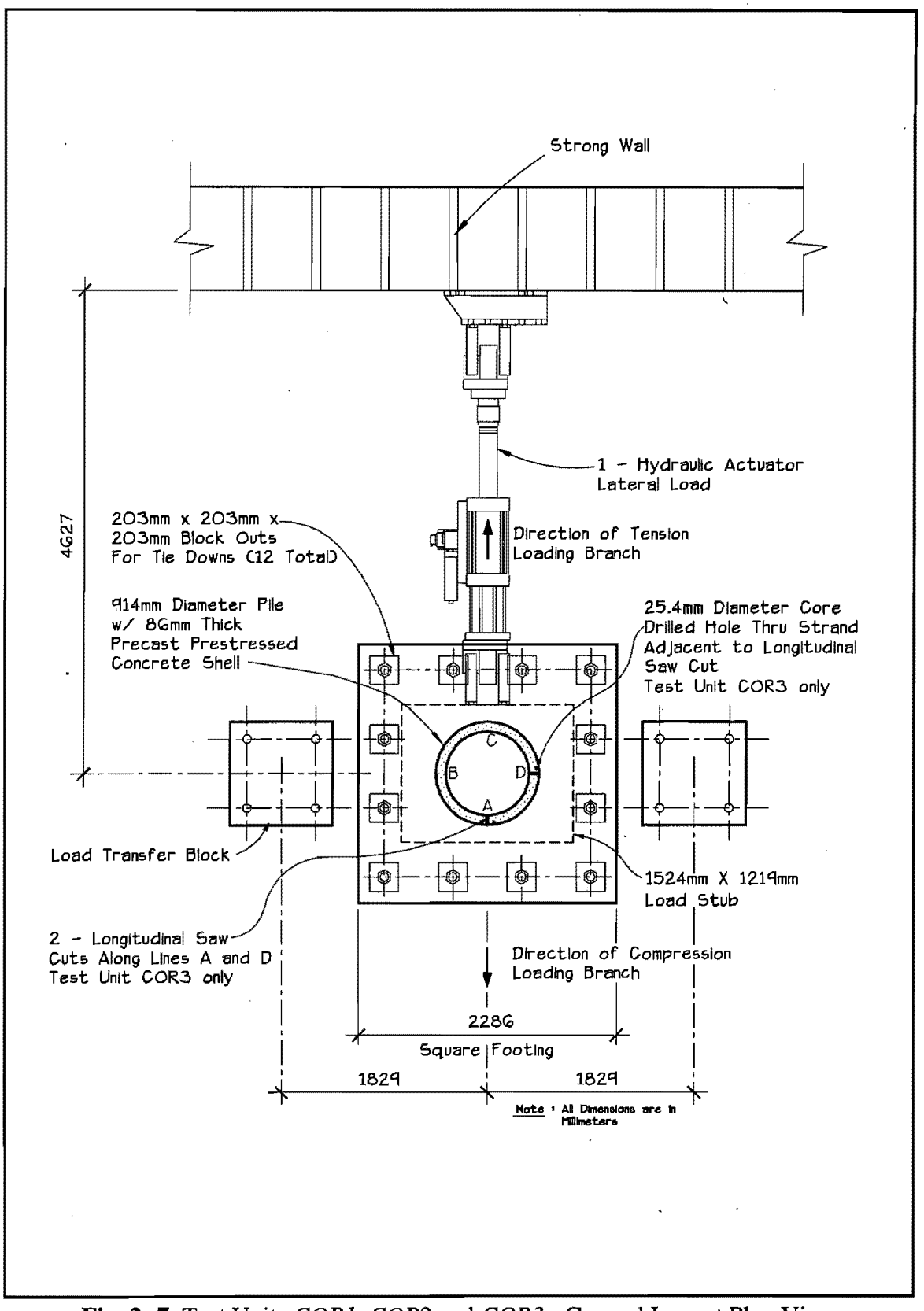

Fig. 2-7 Test Units *COR1*, *COR2* and *COR3* - General Layout Plan View

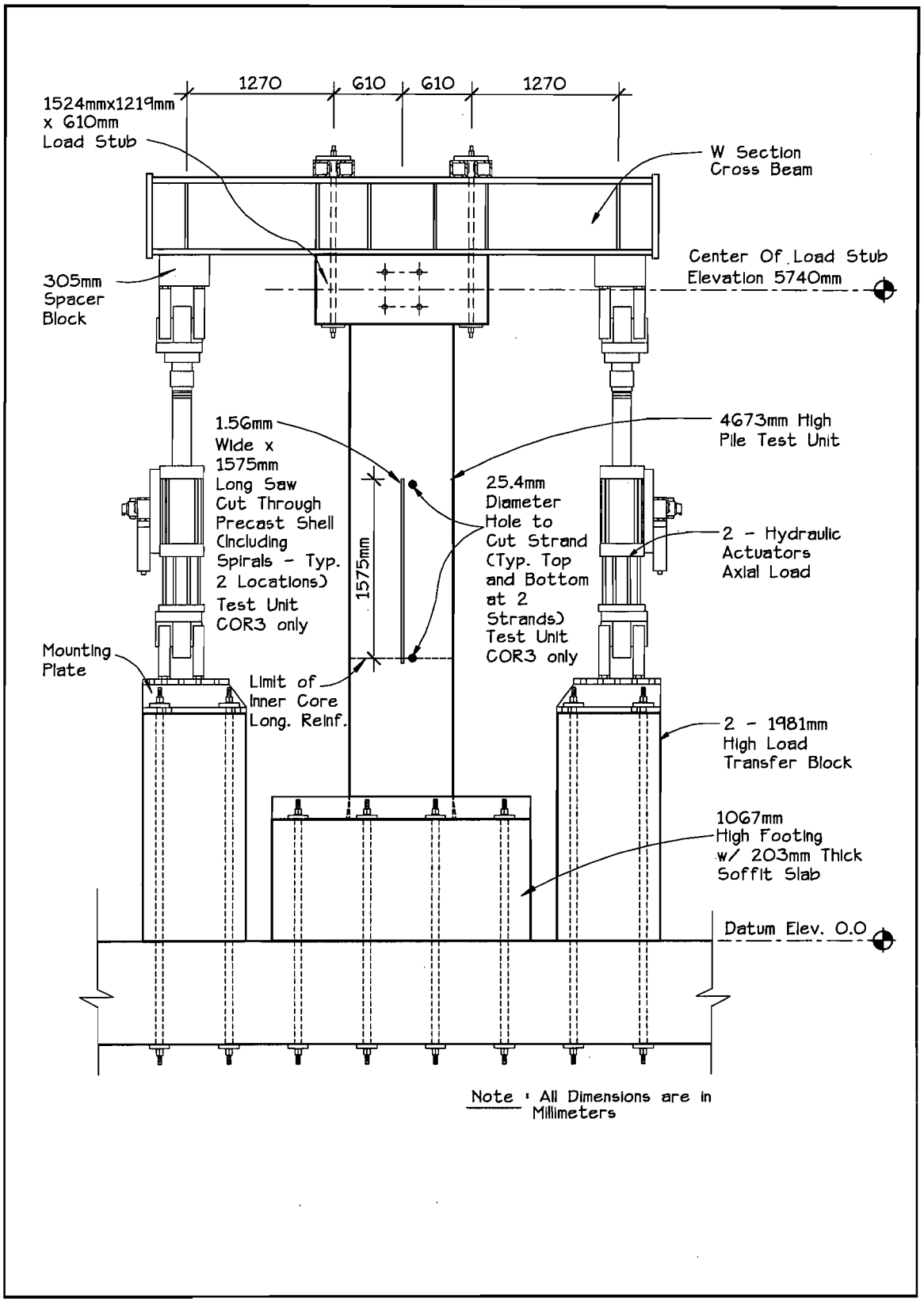

Fig. 2-8 Test Units *COR1* and *COR3* - General Layout Front View

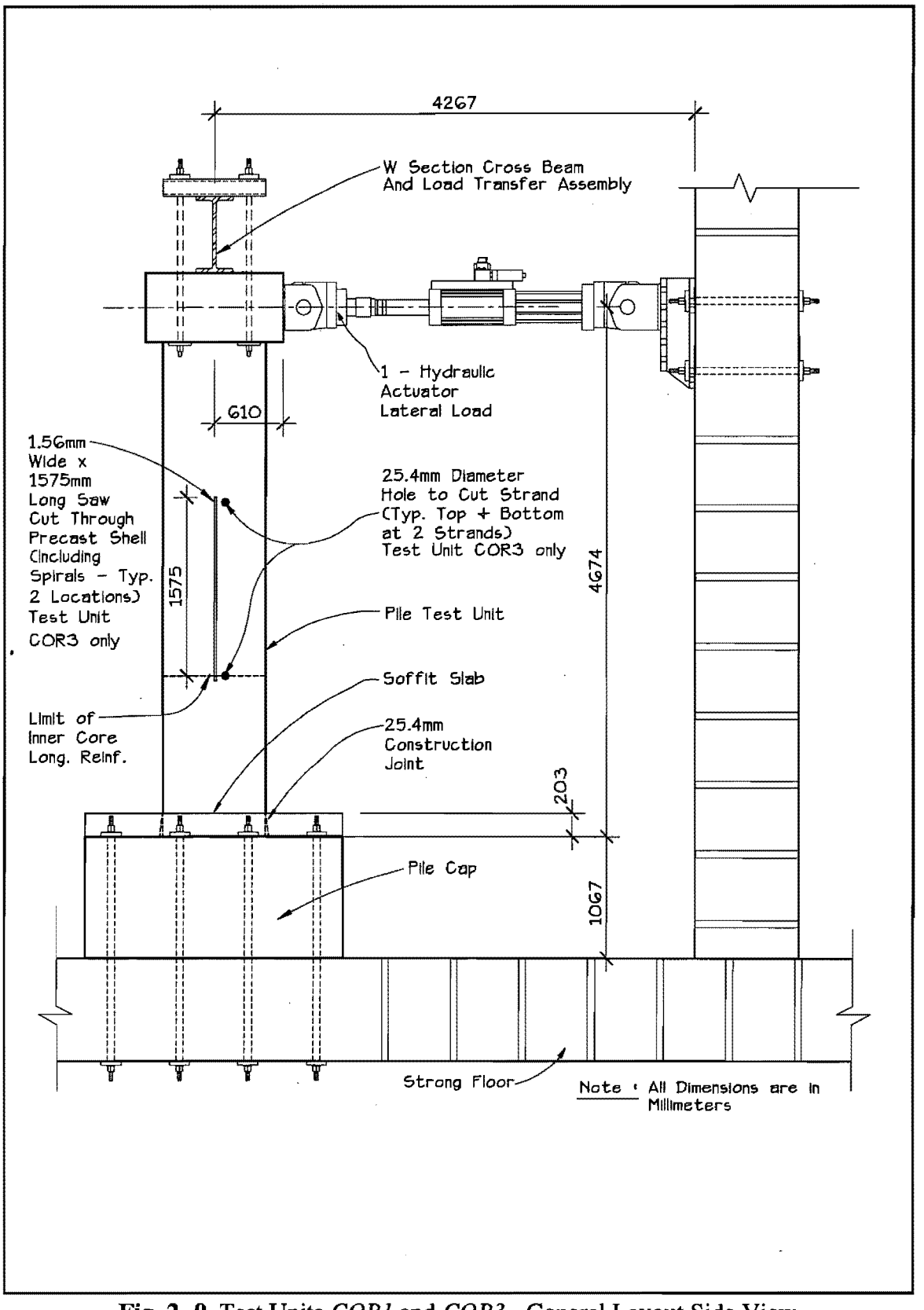

Fig. 2-9 Test Units *COR1* and *COR3* - General Layout Side View

2.2.2 Test Unit *COR2* - General Test Configuration

Fig. 2-10 and **Fig. 2-11** depict the general layout of test unit *COR2*. Test unit *COR2* is a 2/3 scale model of the as-built Type I pile of Pier 2 of the San Diego Coronado Bay Bridge. A summary of the scaling parameters for this test unit was presented in **Table 2-1**.

Similar to test units *COR1* and *COR3*, the pile cap test unit was also designed to model the behavior of an interior pile of the prototype pile cap at the joint region and, unlike test unit *COR1* and *COR3*, the pile of test unit *COR2* was designed to capture the boundary conditions for a pile embedded in a saturated soil stratum with a shallow mud line elevation.

Application of the simulated seismic loading in test unit *COR2* was similar to that procedure described for test units *COR1* and *COR3*. The axial load was applied by means of two vertical actuators positioned on the sides of the test specimen, as illustrated in **Fig. 2-10** and the lateral load by a single actuator connected to the load stub, as illustrated in **Fig. 2-11**.

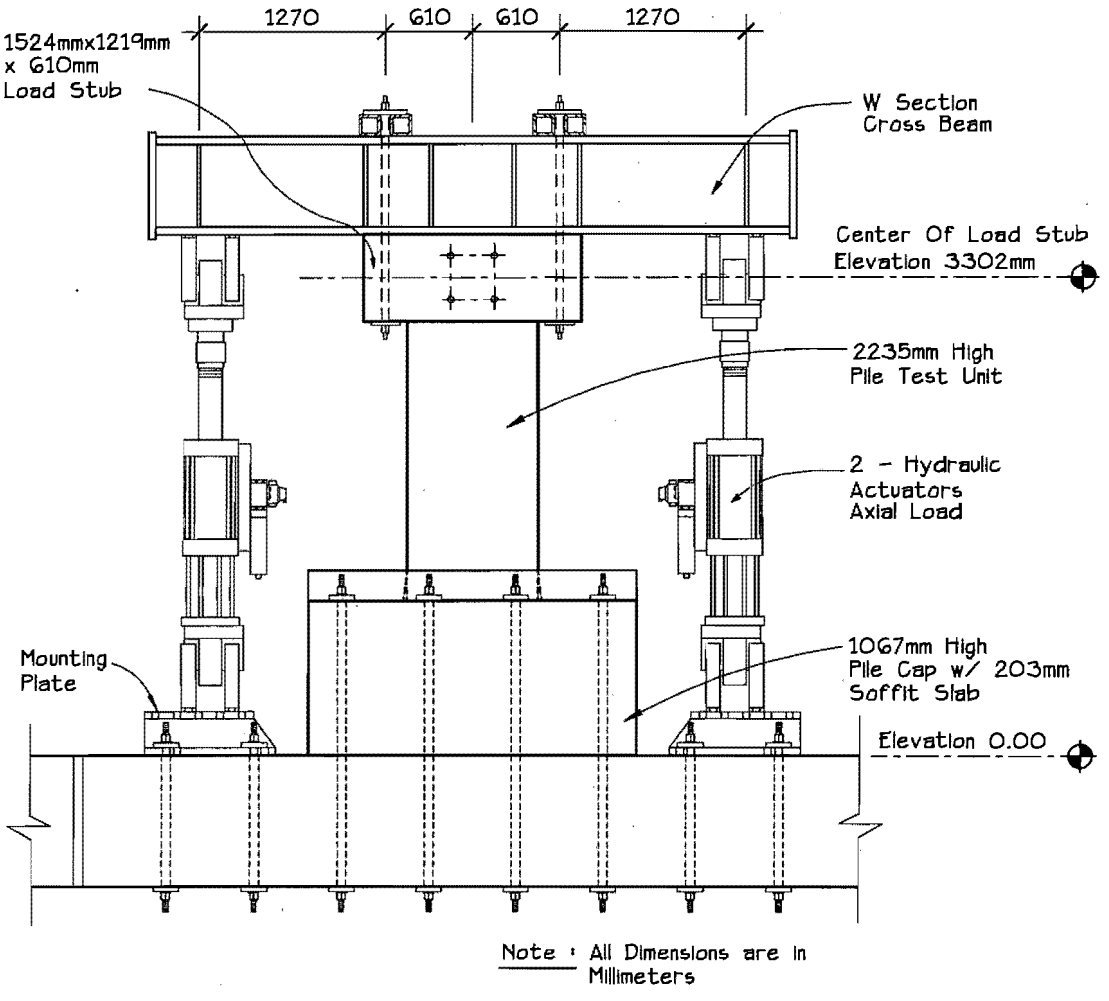

Fig. 2-10 Test Unit *COR2* - General Layout Front View

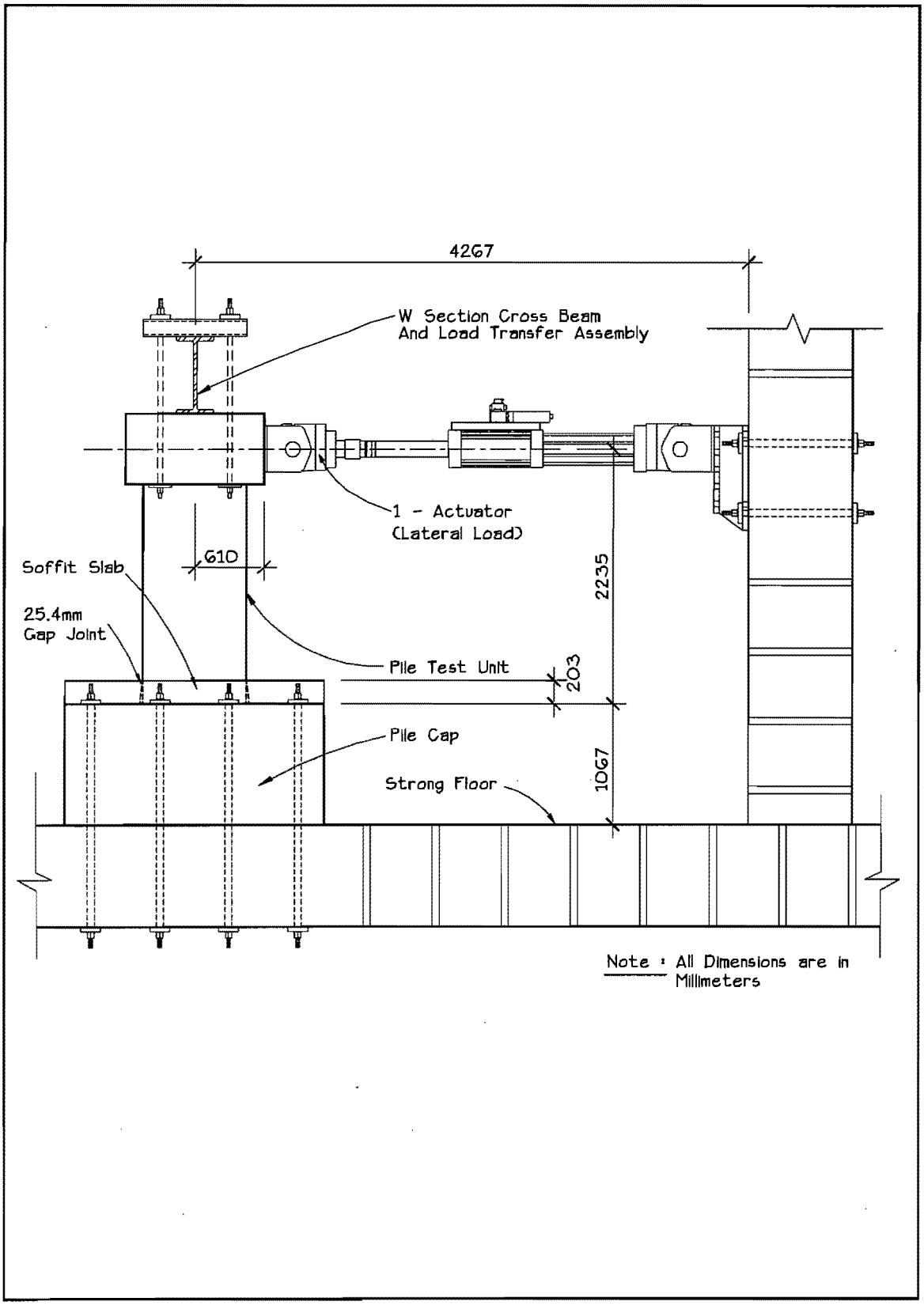

Fig. 2-11 Test Unit *COR2* - General Layout Side View

2.3 Test Units *COR1*, *COR2* and *COR3* - Pile Cap Design and Capacity

The pile cap dimensions and reinforcement layout were chosen to match that of the prototype pile cap as closely as possible and were identical for all the test units *COR1*, *COR2* and *COR3*. Preliminary analysis reveals that the pile cap of the prototype structure has reserve capacity to transmit loads into the piles. Since no damage was expected in the pile cap, and to reduce weight of the test specimen, the pile cap depth of the test specimen was based on the shortest prototype depth of 1,600 mm and not the overall depth of 2,895 mm, as illustrated in **Fig. 2-2** and **Fig. 2-4**. Thus, employing the 2/3 scale factor the scaled depth of the test specimen was 1,067 mm, as shown in **Fig. 2-8** and **Fig. 2-10**. To account for this decrease in the pile cap depth, the vertical stirrup reinforcement ratio was increased to obtain equivalent shear capacity and to avoid large deterioration of the pile cap at the joint region. The vertical stirrup reinforcement in the models consisted of #6 bars at 178 mm on centers.

Design of the pile cap modeled as closely as possible the behavior of the prototype pile cap in the vicinity of an interior pile at the joint region. Thus, to model the continuity of the transverse reinforcement across the piles in the prototype pile cap, the transverse reinforcement in the specimen pile cap was hooked at the ends, as illustrated in **Fig. 2-13**. The amount of reinforcement provided in the pile cap region was identical to the prototype section design. As previously discussed, the pile cap for the test units was setup in an inverted position. However, in this section, all parts of the test units are named as they occur in the prototype structure. A total of 13-#7 bars top and bottom with a reinforcement ratio of 0.24% were provided in the longitudinal and transverse directions (see **Fig. 2-13**).

The modeled precast soffit slab dimensions and reinforcement layout are presented in **Fig. 2-14**. During construction of the soffit slab, block-outs were positioned at 12 locations over the finished surface of the pile cap, as illustrated in **Fig. 2-13** and **Fig. 2-14**. The block outs were provided to tie-

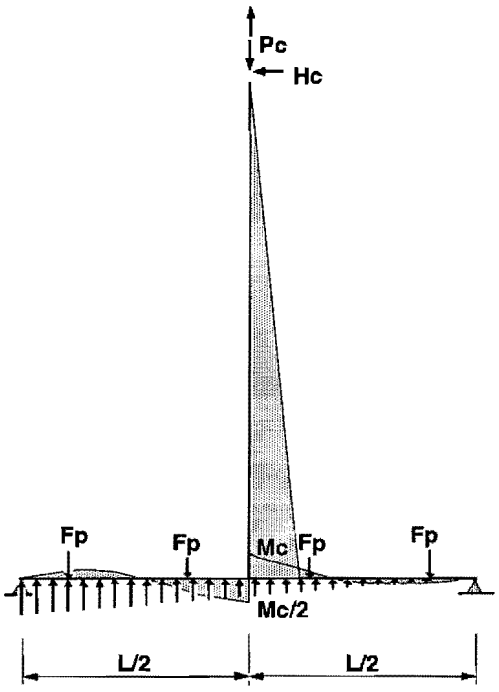

Fig. 2-12 Pile Cap Bending Moment Diagram

down the specimen to the strong floor only at the pile cap level and to allow for any relative motion between the soffit slab and the pile cap as it might occur in the prototype structure.

Based on the pile cap section properties, moment and shear demand and capacity diagrams were prepared for the pile cap of these test units. Approximated bending moment and shear demand diagrams were constructed for the test units, based on the applied loads presented in **Fig. 2-12**, for a direct comparison with the capacity diagrams to determine the expected damage state of the pile caps. Referring to **Fig. 2-15(a)**, the moment demand imposed on the test unit pile caps was always considerably lower than the first section yielding, and **Fig. 2-15(b)** indicates the shear capacity of the pile cap section was significantly higher than the shear demand.

Two shear capacity curves are presented in **Fig. 2-15(b)**. The shear capacity curve indicated as H_{cap}=1,067 mm was obtained for a pile cap with a depth of 1,067 mm and the vertical reinforcement described previously, which is the test specimen pile cap. On the other hand, the curve indicated as H_{cap}=1,931 mm relates to the scaled prototype structure at its maximum depth, and the vertical reinforcement matches the scaled prototype reinforcement, which is #6 bars at 178 mm on centers. Referring to this figure, it is clear that the capacity obtained for these two cases is approximately the same as previously stipulated, and reduction of the pile cap depth should not considerably affect the strength of the pile cap.

The pile cap moment curvature and shear capacity analysis presented in **Fig. 2-15(a)** and **Fig. 2-15(b)** were performed using average material properties obtained from test unit *COR1* material properties. Concrete material properties used for the pile cap pre-test analysis were obtained from three concrete cylinder tests at 28 days, and the steel material properties from three reinforcement tensile tests. Concrete compression strength at 28 days was f'_c=32 MPa, as indicated in **Table 3-2**, for batch No. 1 of test unit *COR1*, the pile cap top and bottom reinforcement yield strength was f_y=465 MPa, and the pile cap vertical reinforcement yield strength was f_y=472 MPa (see **Table 3-3**).

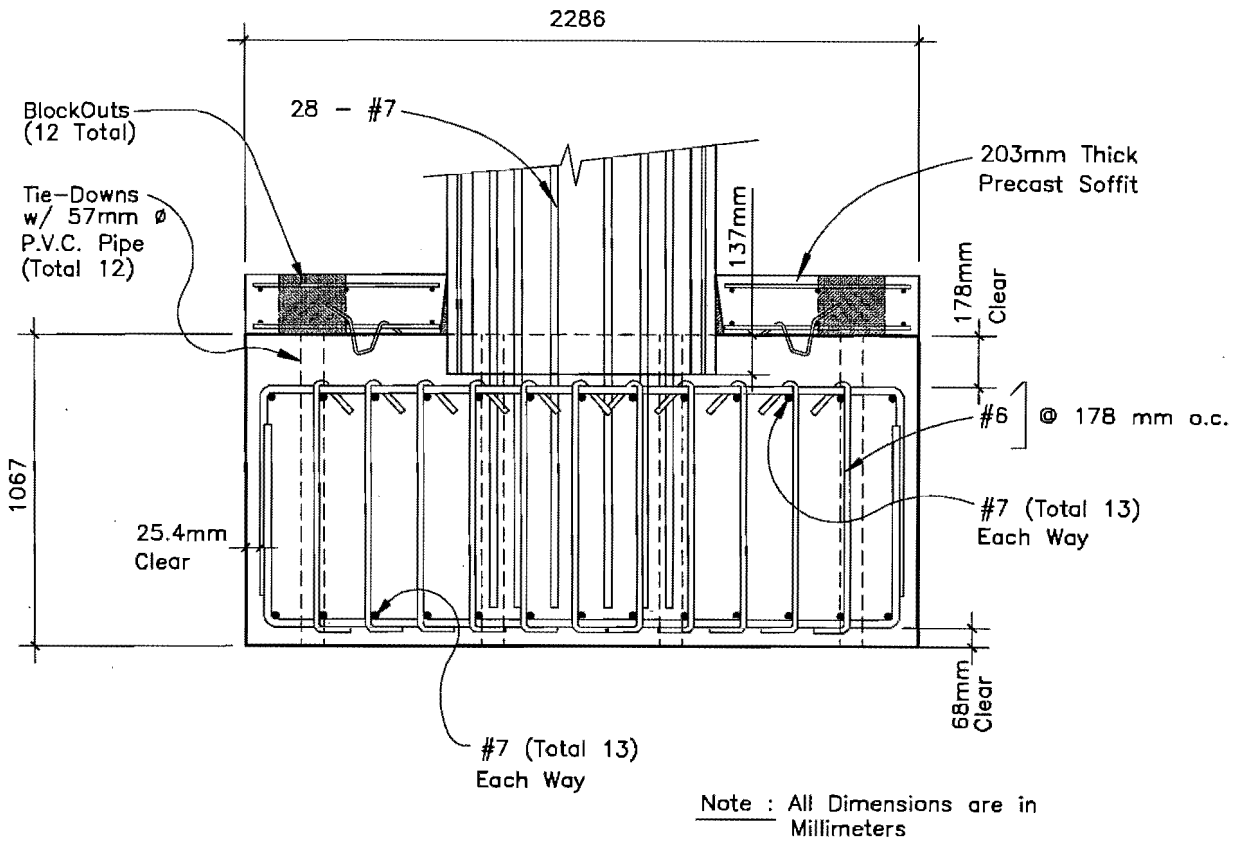

Pile Cap Cross Section

Fig. 2–13 Test Units *COR1*, *COR2* and *COR3* - Pile Cap Reinforcement Layout

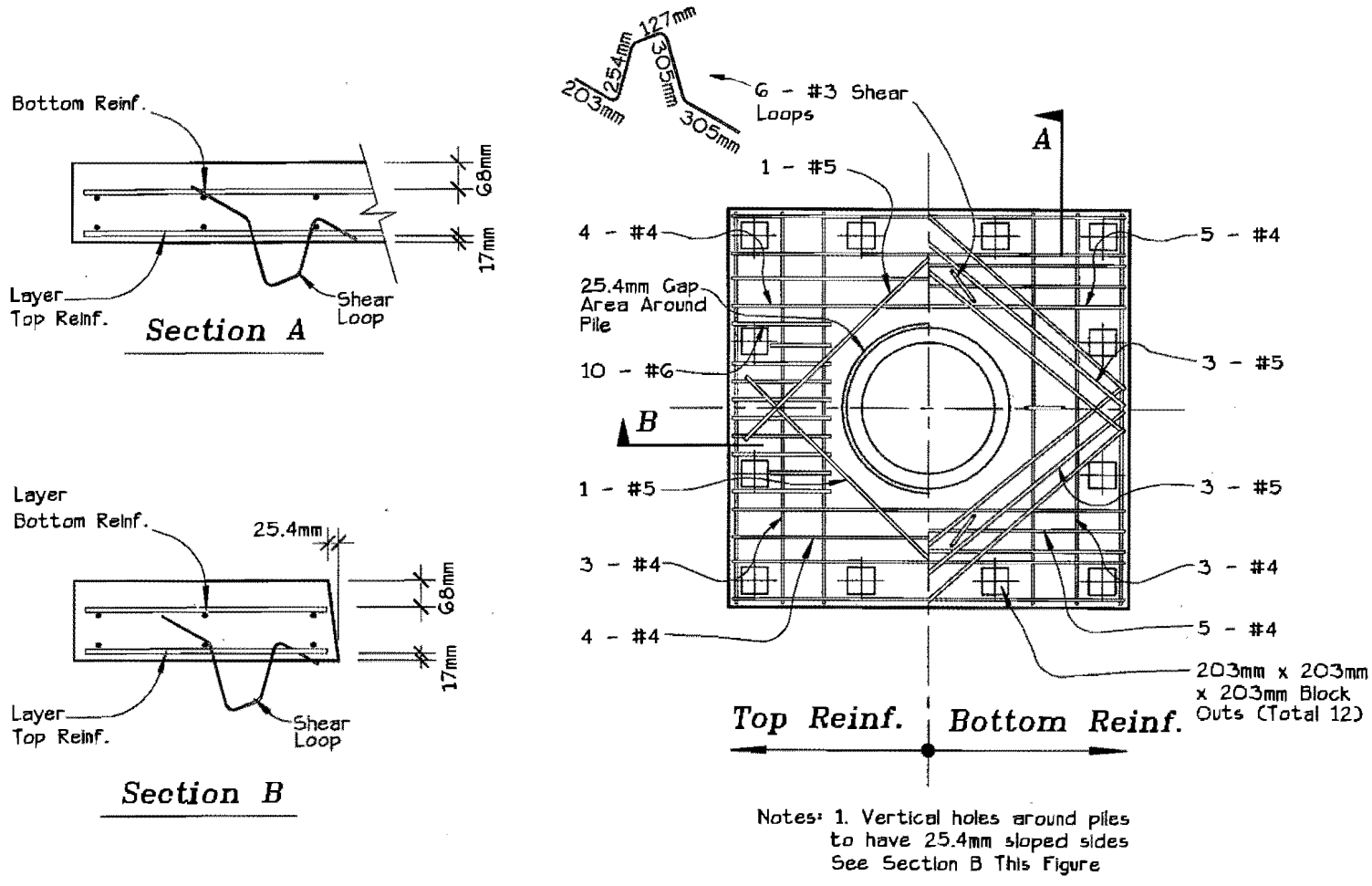

Fig. 2–14 Test Units *COR1*, *COR2* and *COR3* - Modeled Precast soffit Slab

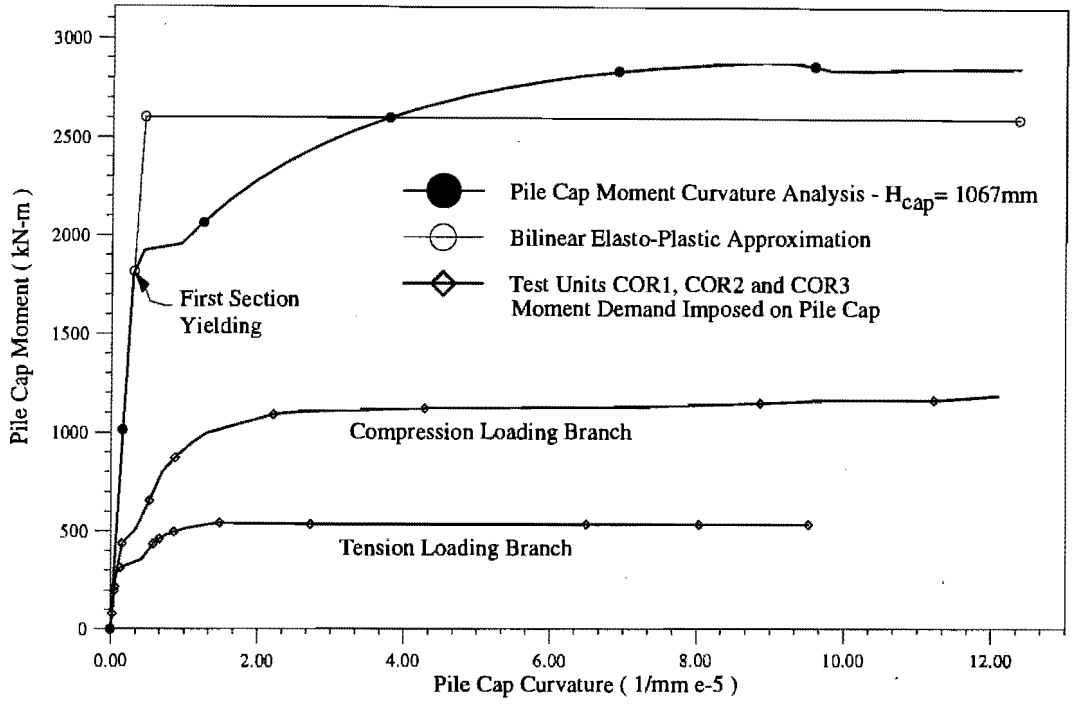

(a) Pile Cap Test Units COR1, COR2 and COR3 - Moment Curvature Analysis Diagram

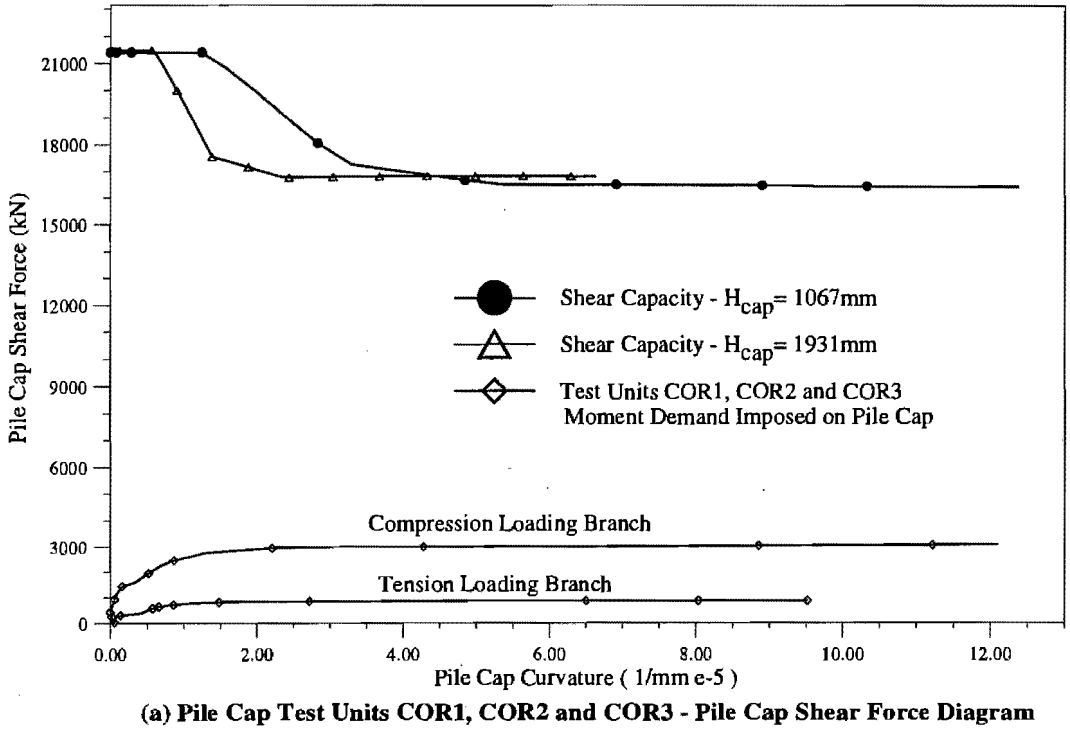

(a) Pile Cap Test Units COR1, COR2 and COR3 - Pile Cap Shear Force Diagram

Fig. 2-15 Test Units *COR1*, *COR2* and *COR3*
Pile Cap Moment and Shear Demands and Capacities

2.4 Test Units *COR1* and *COR3* - Pile Design and Capacity

Test units *COR1* and *COR3* pile geometry and reinforcement layout were scaled from the prototype structure based on a 2/3 scaling factor and were designed in order to obtain similar reinforcement ratios as in the prototype piles indicated in **Table 2-1**. The scaled model test specimen for test units *COR1* and *COR3* is presented in **Fig. 2-16**.

Scaling of the prototype pile resulted in a shell 86 mm thick. Prestressing of the concrete shell consists of 27 seven-wire strand low relaxation type prestressing steel 9.53 mm in diameter placed around the circumference with a concrete cover of 35 mm, resulting in a reinforcement ratio of 0.23%.The total required prestressing force after losses for each test unit was 1522 kN.

As in the prototype, the transverse reinforcement was also changed along the length of the pile. Referring to **Fig. 2-16**, closest to the pile cap and up to a length of 948 mm, the transverse reinforcement consists of deformed #3 bars on a spiral pitch of 84 mm, resulting in a horizontal volumetric reinforcement ratio of approximately 0.40%. After this level, and for the next 1,016 mm, the transverse reinforcement ratio was changed to undeformed reinforcement W3 wires on a spiral pitch of 57 mm, resulting in a horizontal volumetric reinforcement ratio of 0.16%. In the remaining length of the pile, the transverse reinforcement ratio consists also of undeformed W3 wire, but with a spiral pitch of 114 mm, resulting in a horizontal volumetric reinforcement ratio of 0.08%.

The inner cage starter bars to the pile cap consist of 28 - #7 bars arranged in an inner circle with a diameter of 628 mm. The length of these bars is 2,438 mm with an anchorage length into the pile cap of 813 mm. This inner cage was tied together with hoop reinforcement #3 bars at 254 mm on centers.

As previously described, test unit *COR3* was constructed to provide a direct means of comparison between the structural response of a pile with no initial cracks and a pile with imposed damage that models the worst current state of damage of the existing in situ piles of the Coronado Bay Bridge. Based on the data provided from the condition survey **[2]**, the imposed damage to test unit *COR3* pile consisted of saw cutting two lines of longitudinal cuts through the precast prestressed concrete shell and extending it above the termination of the inner core reinforcement for a length of approximately 1,575 mm, as depicted in **Fig. 2-16**. Along these lines, all of the spiral reinforcement was cut, and adjacent to these longitudinal

cuts at the top and bottom, 25.4 mm diameter holes were core drilled through the prestressing strands. To model the low quality of concrete in the core region above the longitudinal reinforcement, the inner core was cast with a low concrete strength of 16 MPa.

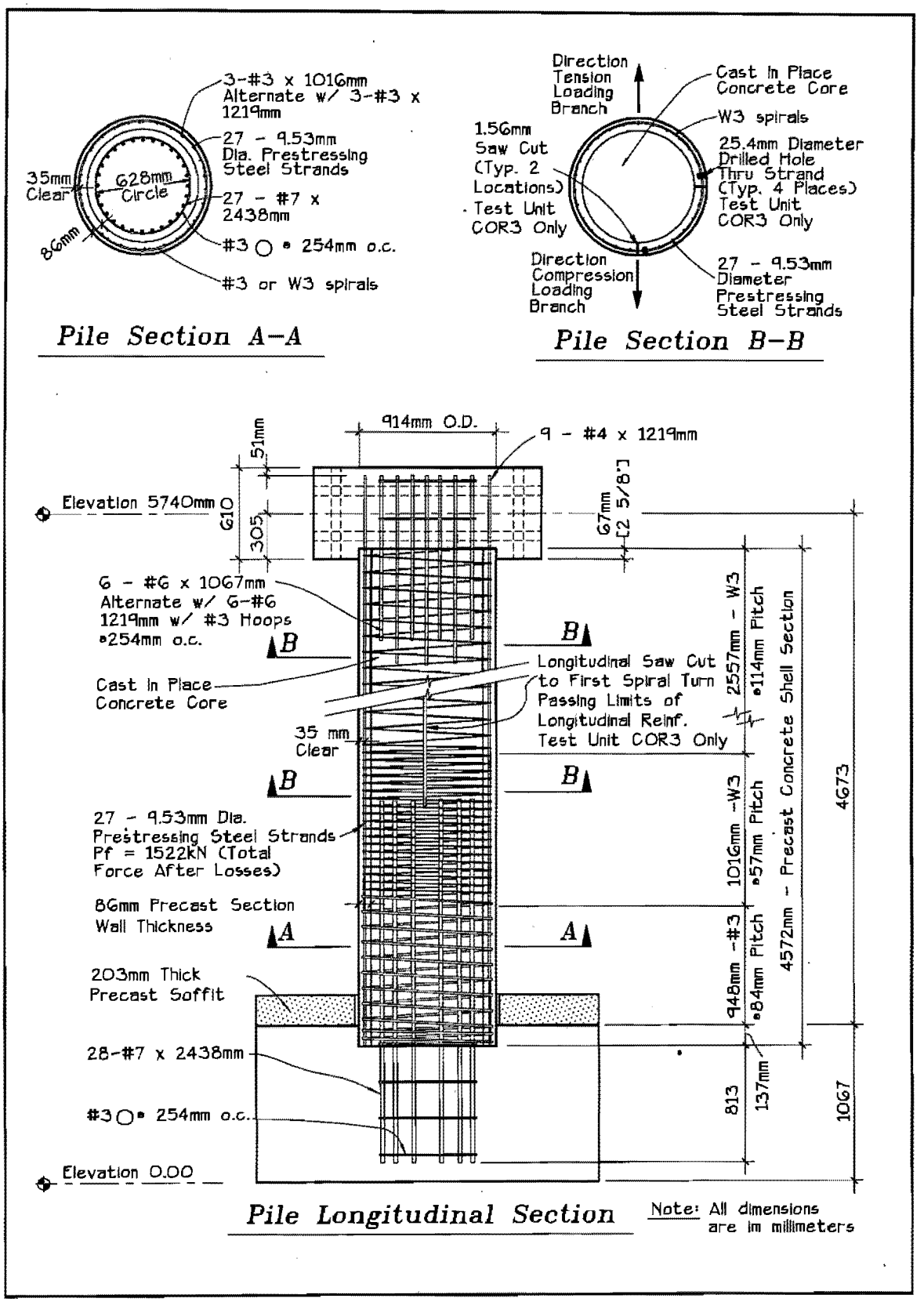

Fig. 2-16 Test Unit *COR1* and *COR3* - Pile Reinforcement Layout

2.4.1 Test Units *COR1* and *COR3* - Pre-Test Analysis

Because of the changes in the pile longitudinal and transverse reinforcement layout, it is expected that the pile flexural capacity will not be constant along the length of the pile, as illustrated in **Fig. 2-18(e)**. Thus, it was necessary to perform a detailed analysis of the flexural capacity along the pile length to investigate regions where section flexural capacity might be lower than demand, which would result in plastic hinge formation to occur at this level and not at the pile cap interface.

Referring to **Fig. 2-18**, a few key issues had to be addressed to perform the flexural capacity analysis along the length of the pile. First, the termination of the longitudinal reinforcement, 1,489 mm away from the pile cap interface indicated in **Fig. 2-18(c)**, which corresponds approximately to 32% of the pile overall length, causes drastic changes in the moment capacity for which the moment demand gradient might intersect the moment capacity curve. Secondly, at the pile cap interface, the prestressing strands do not provide moment resistance capacity to the section, and the required development length of the prestressing strands is crucial in determining the correct moment capacity profile, as illustrated in **Fig. 2-18(e)**.

Detailed analysis of the pile section revealed the development length of the prestressing strands considerably influences the pile flexural capacity profile along the pile height, in particular at the location where the inner core longitudinal reinforcement terminates. Thus, during construction of the precast prestressed concrete shell, data was recorded from strain gage devices applied along the length of the prestressing strands to estimate transfer length of the prestressing strands. In addition, 24 hours after casting of the concrete shell, strain gages were applied on the exterior surface of the concrete shell to obtain data about the strain change in the concrete due to the transfer of the prestressing steel forces into the concrete. In Chapter 4, a detailed discussion of strain gage data recorded during precasting of the concrete shells is presented.

Development length for the deformed longitudinal reinforcement was based on an average bond strength of $0.66\sqrt{f_c'}, [MPa]$, which based on the expression:

$$l_d = \frac{d_b f_y}{2.64\sqrt{f_c'}} \tag{2.1}$$

results in a development length for a #7 of 415 mm. Where d_b is the pile inner core main bar diameter, f_y is the Grade40 yield strength and f'_c is the concrete strength of the inner core

tested at 28 days. The stresses in the longitudinal reinforcement were linearly interpolated in this region from zero to its maximum value at the end of the development region.

Prestressing strand transfer length for these test units was obtained from a regression analysis taking into account strains in the steel and in the concrete, as illustrated in Chapter 4. Based on transfer lengths obtained from the regression analysis, three different runs were performed with transfer lengths that varied between 1,219 mm and 1,727 mm, corresponding approximately to $128d_b$ and $181d_b$, which imply a bond strength of 2.7 MPa and 1.9 MPa for an effective prestressing stress of 1,370 MPa. The ACI code equation **[4]** implies a bond strength of 5.2 MPa to obtain the effective prestress in the strand. The forces in the prestressing strands in this region were then interpolated linearly from the free end of the strand to the effective prestressing stress, f_{pe}, at the end of the transfer length, l_t.

In addition, in order to develop prestressing stresses, f_{ps}, above f_{pe} as required by flexural analysis, a flexural bond length was added to the transfer length according to the expression **[4]**:

$$l_{dp} = l_t + 0.145\,(f_{ps} - f_{pe})\,d_{bp} \qquad \textbf{(2.2)}$$

where the second term estimates the development length required to develop f_{ps} above f_{pe} based on an average bond strength of 1.7 MPa **[5]**.

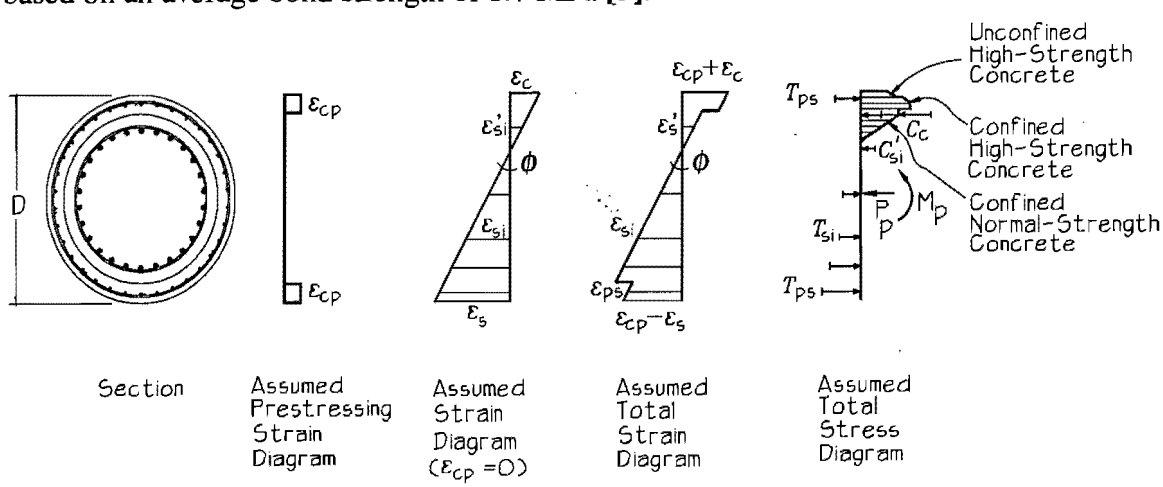

Fig. 2-17 Test Unit *COR1* and *COR3* - Stress Block Design Parameters

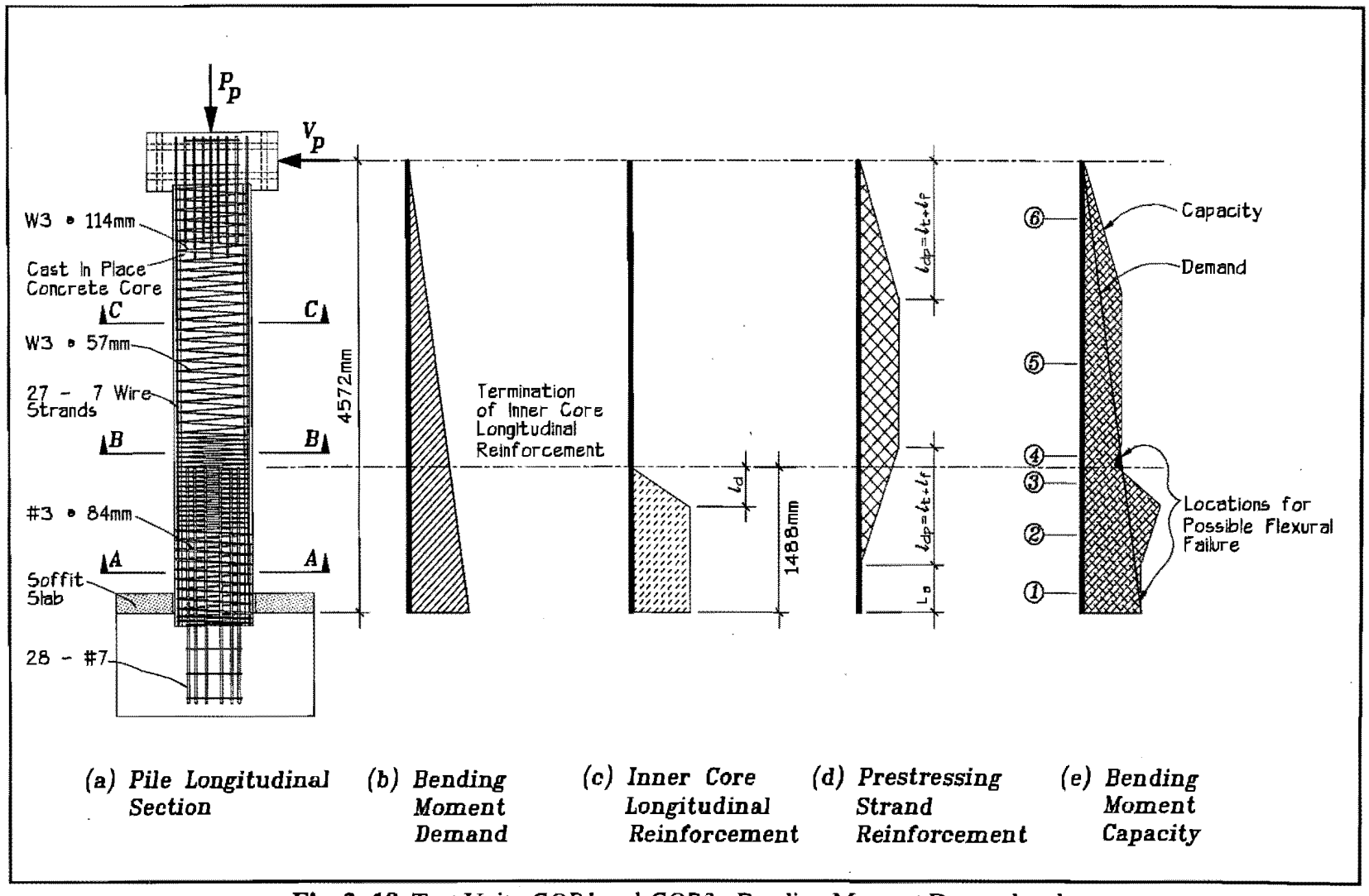

Fig. 2–18 Test Units *COR1* and *COR3* - Bending Moment Demand and Capacity Profiles Along Pile Longitudinal Section

Referring to **Fig. 2-18(e)**, six regions were defined according to the development length of the inner core longitudinal reinforcement and prestressing strands. In region ①, along length, L_a, the effective prestressing strain, ε_{cp}, is assumed equal to zero, and the force equilibrium equations were written by equating only the total compressive forces present in the concrete and reinforcing steel to the total tensile forces present in the reinforcing steel and applied axial load according to the expression :

$$\sum C_c + \sum C'_{si} = \sum T_{si} + P_p \tag{2.3}$$

where due to the applied curvature, φ, depicted in **Fig. 2-17**, $\sum C_c$ is the compression force present in the concrete, $\sum C'_{si}$ is the compression force present in the reinforcing steel, $\sum T_{si}$ is the tension force present in the reinforcing steel and P_p is the applied axial load on the pile section. Length, L_a, corresponds to the tensile strain penetration, obtained from the expression:

$$L_a = 0.022\, d_b f_s \tag{2.4}$$

where f_s is the steel strain at the current curvature. In this region, the prestressing strands are assumed to provide no moment capacity because when the cover concrete begins to spall, bond strength is assumed negligible and slippage of the prestressing strands occurs along an assumed length L_a.

In region ②, along length l_{dp} and up to length l_d, the prestressing strands make an increasingly higher contribution to the flexural capacity of the pile section, and the force equilibrium equation may be written by equating the total compressive forces present in the concrete and reinforcing steel to the total tensile forces present in the reinforcing and prestressing steel. Thus:

$$\sum C_c + \sum C'_{si} = \sum T_{si} + \alpha_{ps} \sum T_{psi} + P_p \tag{2.5}$$

where due to the applied curvature, φ (see **Fig. 2-17**) $\sum C_c$ is the compression force in the concrete, $\sum C'_{si}$ is the compression force present in the reinforcing steel, $\sum T_s$ is the tension force present in the reinforcing steel, $\alpha_{ps} \sum T_{psi}$ is the resultant tension force in the prestressing steel, and α_{ps} is a parameter described by a function which relates the position of the segment given by equation **(2.5)** to the transfer length of the prestressing strands. Thus, α_{ps} is equal to one in regions outside the prestressing transfer length and varies linearly along l_{dp} according to X/l_{dp}, where X is the distance from the free end of the prestressing strand to the section where the moment curvature is being analyzed, and l_{dp} is the development length for the prestressing steel.

In region ③, along length, l_d, the force present in the reinforcing steel begins to decrease according to the development length, l_d, and the force equilibrium equations were written by equating the total compressive forces present in the concrete and reinforcing steel to the total tensile forces present in the reinforcing and prestressing steel. Thus:

$$\sum C_c + \alpha_s \sum C'_{si} = \alpha_s \sum T_{si} + \alpha_{ps} \sum T_{psi} + P_p \qquad \textbf{(2.6)}$$

where similar to α_{ps}, α_s is a parameter described by a function which relates the position of the segment given by equation **(2.6)** to the development length of the inner core reinforcing steel. Thus, α_s is equal to one in regions X is the distance from the free end of the reinforcing steel to the section where the moment curvature is being analyzed, and l_d is the development length of the reinforcing steel.

Region ④ corresponds to the remaining length l_{dp}. This region no longer carries reinforcing steel, and the moment capacity is only developed in terms of forces present in the concrete and prestreessing strands according to the expression:

$$\sum C_c = \alpha_{ps} \sum T_{psi} + P_p \qquad \textbf{(2.7)}$$

Region ⑤ is very similar to region ④, but the prestressing strands are fully developed and the force equilibrium equation is described in terms of the expression:

$$\sum C_c = \sum T_{psi} + P_p \qquad \textbf{(2.8)}$$

Finally, region ⑥ is identical to region ④, but the prestressing force decreases in this region rather than increasing as the height increases. Subregions were also defined along these six regions to model different levels of confinement provided by the different types of transverse reinforcement along the pile height, as indicated in **Fig. 2-18(a)** .

In all of these six regions, different concrete material properties were used to model the concrete shell and the inner core. High-strength and normal-strength concrete material properties used for the pile section pre-test analysis were obtained from three concrete cylinder tests at 28 days for each batch. For test unit *COR1*, the pile concrete shell compression strength at 28 days was f'_c=69 MPa, as indicated in **Table 3-1**, and the inner core concrete compression strength at 28 days was f'_c=33 MPa, as indicated in **Table 3-2**.

For test unit *COR3*, the pile concrete shell compression strength at 28 days was f'_c=68 MPa, and the inner core concrete compression strength was f'_c=36 MPa, up to the level where the inner core longitudinal terminates. A different concrete strength was used for the analysis

in the region above the termination of the inner core longitudinal reinforcement, as illustrated in **Fig. 3-29**. The concrete compression strength in this region was f'_c=18 MPa, which is considerably lower then the concrete compression strength in the lower region.

Per ASTM current standards **[5]**, the prestressing strands yield strength was determined at a total strain of one percent based on stress-strain curves obtained from three sample tensile tests. At one percent of strain, the stress was f_{py}=1,830 MPa, which corresponds to 90% of the maximum stress f_{pu}=2,008 MPa, as illustrated in **Table 3-3**.

Steel material properties were obtained from three reinforcement tensile tests. The inner core longitudinal reinforcement yield strength was f_y=283 MPa, and the transverse reinforcement yield strength was f_y=448 MPa for the #3 bars and f_y=599 MPa for the wire W3 (see **Table 3-3**). All of the test units were built with reinforcing steel from the same batch and the same steel properties were used in the analysis of the three test units.

A moment curvature analysis was then developed with curvatures obtained along the height of the pile according to the equilibrium equations previously described. **Fig. 2-20** and **Fig. 2-21** present results for different levels of axial load. The prestressing transfer length used to develop the moment capacity curve for *Runs A* and *D* was 1,219 mm, for *Runs B* and *E* the prestressing transfer length was 1,473 mm, and for *Runs C* and *F* the prestressing transfer length was 1,727 mm. These transfer length values were obtained from a regression analysis of strain measurements recorded from the prestressing strands during manufacturing of the precast concrete shell, and this regression analysis is presented in Chapter 4.

An axial compression load of +2,793 kN was used in developing the capacity curves for *Runs A*, *B* and *C*, and demand curves at peak response are presented in **Fig. 2-20**. In this figure, *Run A* results indicate that regions of inelastic deformation are likely to develop at the pile cap interface and potentially where the inner core longitudinal reinforcement terminates. However, at later stages of the testing procedure the moment capacity at the region where the inner core longitudinal reinforcement terminates is considerably lower than the moment demand and inelastic deformations will most likely be concentrated in this region. *Run B* moment capacity curve barely intersects the moment demand curve where the longitudinal reinforcement terminates, which shows that if inelastic deformations develop in this location, they are likely to be concentrated over a very small region, as illustrated in **Fig. 2-20**. Finally, based on *Run C* results, the moment capacity is always higher than the moment demand at any

position along the height of the pile section and inelastic deformations will only occur at the pile cap interface.

The capacity curves for *Runs D*, *E* and *F*, and demand curves at peak response are presented in **Fig. 2-21** and were developed with an axial tension load of -302 kN. *Runs D*, *E* and *F* results indicate that in all cases a second region of inelastic deformation is likely to occur where the longitudinal reinforcement terminates. *Run D* results indicate that a larger region of inelastic deformation is likely to occur than for *Runs E* and *F*, where the longitudinal terminates because the moment capacity curve intersects the moment demand over a larger region. Smaller regions of inelastic deformation are likely to form for *Runs E* and *F*. Analytical results indicate that flexural response of the pile section is directly dependent on the transfer length. Employing different transfer length values results show that the extent of potential inelastic deformation at the location where the longitudinal reinforcement terminates is rather large for larger transfer lengths and for axial tension loads. Test results presented in Chapter 5 through Chapter 7 indicate that extensive spalling of the cover concrete was observed in the region near the termination of the inner core longitudinal reinforcement and two regions of plastic deformations occurred, which corroborate pre-test analysis results.

Amplification of the moment demand along the pile length, due to inclined cracks according to tension shift effects **[6]**, were also considered in the analysis and are presented in **Fig. 2-20** as a dashed line entitled *Tension Shift Effect at Peak Response*. **Fig. 2-19** indicates that the longitudinal tension force at level **1** is not proportional to the moment demand at this level but is proportional to a moment below this level, as a result of the inclined cracks that form along the pile. Increase in the longitudinal tension force may be readily computed by

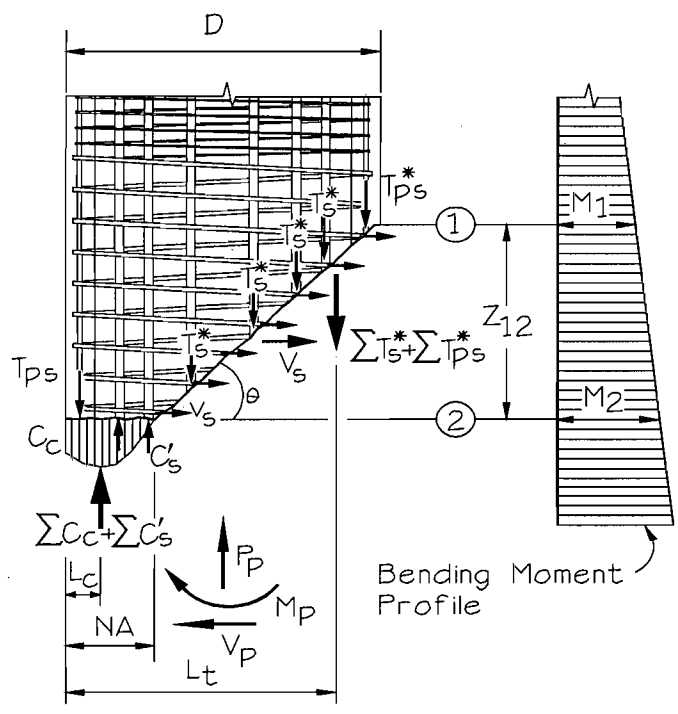

Fig. 2-19 Tension Shift Effect in a Diagonally Cracked Reinforced Concrete Section

considering the internal forces that develop, as a result of the applied forces in conjunction with the geometry of a diagonally crack section as illustrated in **Fig. 2-19**.

The moment demand at level **2** may be computed according to the following expressions:

$$M_2 = M_1 + V_p Z_{12} \tag{2.9}$$

and

$$M_2 = \left(\sum T_s^* + \sum T_{ps}^*\right)\left(L_t - L_c\right) + V_s \frac{Z_{12}}{2} + P_p \left(D/2 - L_c\right) \tag{2.10}$$

where L_t is the position of the resultant internal tension forces, which include both the reinforcing steel forces, $\sum T^*_s$, and the prestressing forces, $\sum T^*_{ps}$, and L_c is the position of the resultant internal compression forces which includes both the compression forces that are present in the concrete, $\sum C_c$, and in the reinforcing steel, $\sum C'_s$. Position of the resultant forces L_t and L_c were computed based on the moment curvature analysis using the equilibrium equations previously described. The internal forces $\sum T^*_s$ and $\sum T^*_{ps}$ represent the exact internal forces present in the reinforcement that is :

$$\sum T_s^* + \sum T_{ps}^* = \left(\sum T_s + \sum T_{ps}\right) + \Delta T^* \tag{2.11}$$

where ΔT^* is the increase in the longitudinal tension forces due to tension shift effects, and $\sum T_s$ and $\sum T_{ps}$ are internal forces determined solely based on a moment curvature analysis.

Moment curvature analysis at level **1** gives:

$$M_1 = \left(\sum T_s + \sum T_{ps}\right) + P_p \left(D/2 - L_c\right) \tag{2.12}$$

Based on the expressions **(2.9)**, **(2.10)** and **(2.12)**, increase in the moment demand at level **1** may then be computed according to the expression:

$$\Delta M_1 = \left(V_p - V_s/2\right) Z_{12} \tag{2.13}$$

where Vs is the tension force generated in the stirrups given by equation **(2.16)**, and Z_{12} is the vertical distance between levels **1** and **2**, determined based on the inclination of the diagonal crack θ given by $Z_{12} = (D - NA) \cot \theta$.

Thus, amplification of the moment demand along the pile length due to inclined cracks tends to magnify the possibility for plastic deformations to develop where the longitudinal reinforcement terminates.

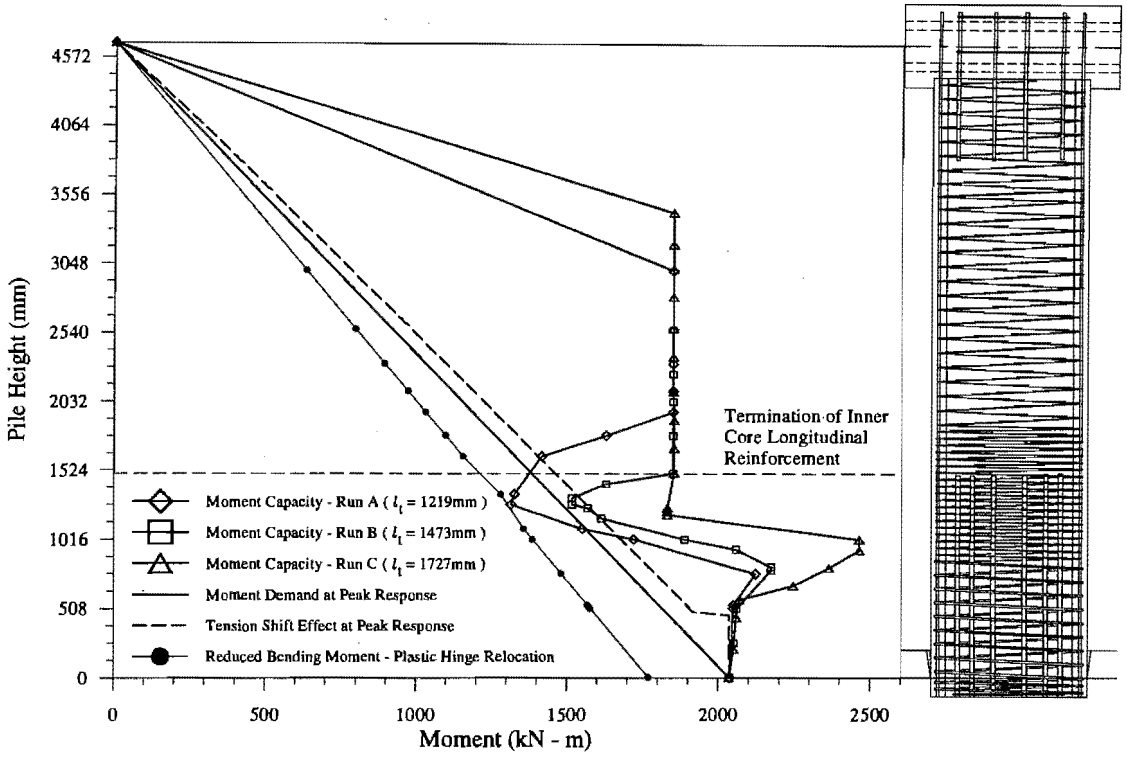

Fig. 2-20 Moment Profiles - Axial Compression Load P = +2793kN

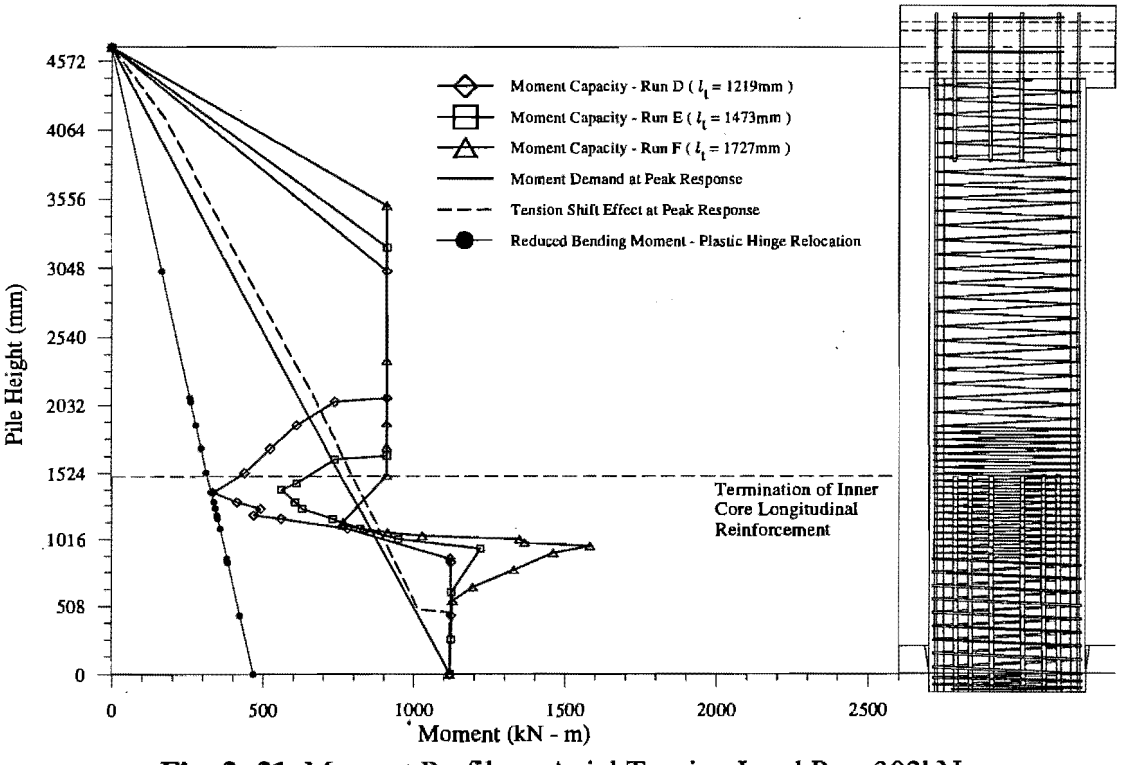

Fig. 2-21 Moment Profiles - Axial Tension Load P = -302kN

Lateral deflections due to flexural effects were then computed with the second moment area theorem according to the expression:

$$\Delta = \sum_{X=0}^{H_{pile}} \left((\varphi_i + \varphi_{i-1}) \frac{\Delta_x}{2} X \right) \tag{2.14}$$

in which φ_i and φ_{i-1} are the curvatures in the pile section within the segment Δ_x, and X is the distance from the center of the respective segment to the center of the applied lateral load, as indicated in **Fig. 2-22**. Up to peak lateral load, the vertical curvature profiles were obtained based on the moment curvature analysis and are presented in **Fig. 2-22(a)**, corresponding to peak lateral load. However, when the lateral load decreases as curvature increases, theoretical plastic hinge length must be introduced in order to compute fixed base deflections with curvature profiles, depicted in **Fig. 2-22(b)**.

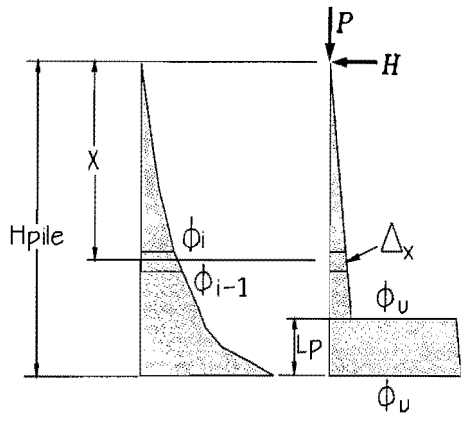

(a) Peak Load Curvature Profile *(b) Ultimate Curvature Profile*

Fig. 2-22 Curvature Distribution

Test unit *COR1* pre-test analysis lateral load versus lateral deflection response is presented in **Fig. 2-23**. The loading curve described in terms of axial load versus lateral load used to construct the pre-test analysis is presented in Chapter 3.

Test unit *COR3* pre-test analysis was similar to test unit *COR1*, but a few modifications to the analytical models were performed after testing of test units *COR1* and *COR2*. Tensile strain penetration and a different concrete model were used to develop the pre-test analysis for test unit *COR3*. Discussion of these modifications in the analysis are presented in Chapter 8. Lateral load versus lateral deflection response is presented in **Fig. 2-24** for test unit *COR3*. The loading curve described in terms of axial load versus lateral load used to construct the pre-test analysis was identical to test unit *COR1* and is presented in Chapter 3.

The shear strength of test units *COR1* and *COR3* was computed according to the predictive shear strength model developed at UCSD by Priestley et al. [7], which consists of three components described as follows :

(1) Concrete component :

$$V_c = 0.8\, A_g\, K \sqrt{f_c'} \tag{2.15}$$

where K depends on the curvature ductility, μ_φ, as presented in reference [8].

(2) Steel truss component for circular columns:

$$V_s = \frac{\pi}{2} \frac{A_{sp} f_y (D' - NA)}{s} \cot \theta \tag{2.16}$$

where NA is the section neutral axis, D' is the confined core diameter, A_{sp} is the cross sectional area of the spiral transverse reinforcement, and θ is the crack angle taken as 30° degrees.

(3) Axial load component :

$$V_p = P_{axial} \frac{D/2 - NA/2}{H_{pile}} \tag{2.17}$$

The shear strength of the test units was computed according to the expression [7]:

$$V = V_c + V_s + V_p \tag{2.18}$$

Fig. 2-25 indicates that according to UCSD predictive shear strength model, shear capacity of the section exceeds approximately 100% the shear demand at ultimate response in both loading directions. In addition, test unit *COR1* displays a well defined ductile flexural response without indication of a shear failure.

Test unit *COR3* transverse reinforcement above the inner core longitudinal reinforcement was cut according to **Fig. 2-16** and, in computing the shear strength for this test unit, the steel truss component was not used. Thus, according to **Fig. 2-26**, shear failure of test unit *COR3* may be expected by extensive opening of the imposed longitudinal cracks, as indicated in **Fig. 2-16**, at a displacement of approximately +76.20 mm in the compression loading branch and -101.60 mm in the tension loading branch, while no shear failure was expected in test unit *COR1*.

Based on an average bond stress of approximately $1.17\sqrt{f_c'}$ *[MPa]*, and with a reinforcement overstrength of $f_y^o = 1.4 f_y$, a required anchorage length for the longitudinal pile section of approximately 324 mm was calculated from the following expression **[8]**:

$$l_d = \frac{0.3\, d_b f_y}{\sqrt{f_c'}} \quad (mm)\ [MPa] \tag{2.19}$$

Referring to **Fig. 2-16**, the development length of the pile longitudinal reinforcement is 813 mm and thus, no bond failure of the pile inner core longitudinal reinforcement was expected.

Diagonal cracking in the joint region can be expected when the principal tensile stresses exceed $0.29\sqrt{f_c'}$ *[MPa]*, and failure of the joint region is likely to occur when the principal tensile stresses exceed $0.42\sqrt{f_c'}$ *[MPa]*, **[8]**. A simple Mohr's circle analysis for stress shows principal tensile stresses are given by:

$$p_t = \left(\frac{f_h + f_v}{2}\right) - \sqrt{\left(\frac{f_h - f_v}{2}\right)^2 + v_{jv}^2} \tag{2.20}$$

where f_t is the principal tension stress, f_x is the axial stress on the joint in the x-direction, f_y is the axial stress on the joint in the y-direction and v_{jv} is the joint shear stress. Joint axial stresses and joint shear stress are calculated according to the following relations:

(1) Joint Axial Stress:

$$f_x = \frac{P_h}{b_{je}\, l_a} \quad ; \quad f_y = \frac{P_v}{(D + 0.5\, H_{cap})\, b_{je}} \tag{2.21}$$

(2) Vertical Joint Shear Stress :

$$v_{jv} = \frac{V_{jv}}{l_d b_j} \tag{2.22}$$

where P_h is the axial force in the horizontal direction, b_{je} is the effective joint width assuming a 45° spread in all directions **[8]**, l_d is the depth of the longitudinal reinforcement, D is the pile section width and H_{cap} is the pile cap section depth. V_{jv} is the vertical joint shear force computed according to the following expression **[9]**:

$$V_{jv} = \frac{M_u - 0.4\, D\, P_c}{0.7\, D} \tag{2.23}$$

where M_U, is the pile section ultimate moment capacity and P_p is the pile section axial force.

V_{jv} may be computed at load levels below ultimate response using the resultant tension force extracted from the moment curvature analysis. Based on these expressions, maximum principal tensile stress in the compression loading branch was $0.16\sqrt{f_c'} < 0.29\sqrt{f_c'}$ *[MPa]* and, in the tensile loading branch $0.27\sqrt{f_c'} < 0.29\sqrt{f_c'}$ *[MPa]*, which are below cracking levels. Principal tensile stresses presented in **Fig. 2-27** indicate that cracking in the joint region will not occur at any stage of the loading procedure.

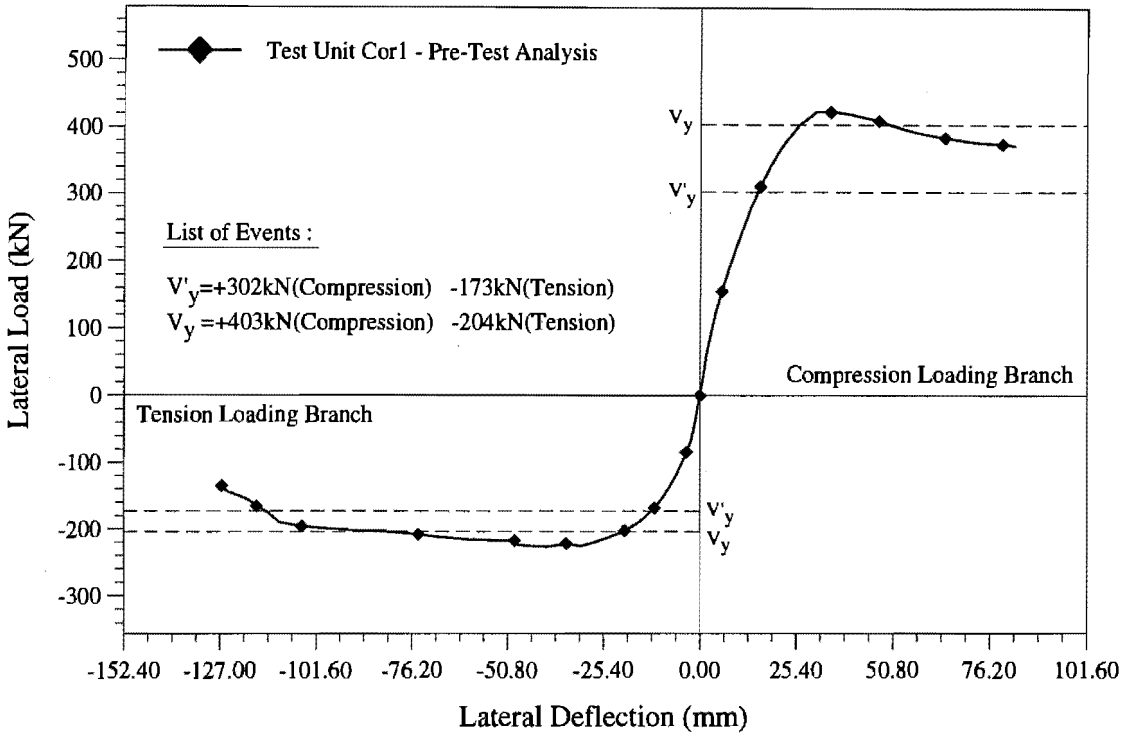

Fig. 2-23 Test Unit *COR1*- Pre-Test Analysis

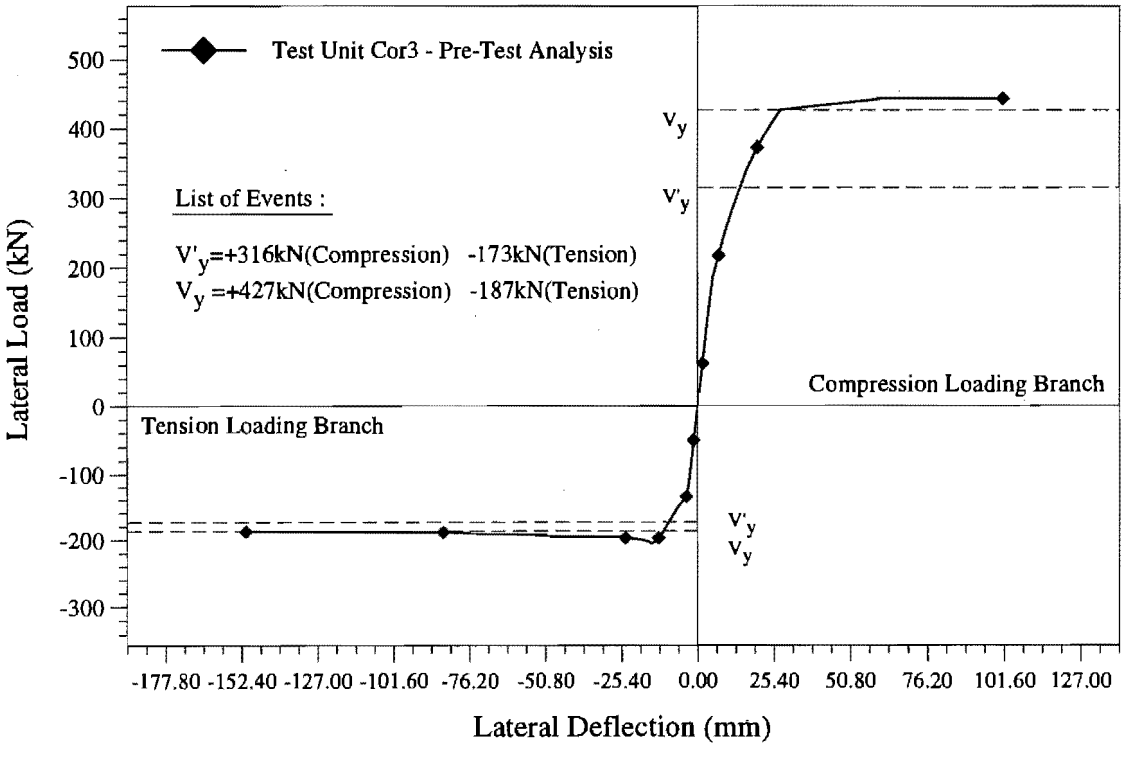

Fig. 2-24 Test Unit *COR3* - Pre-Test Analysis

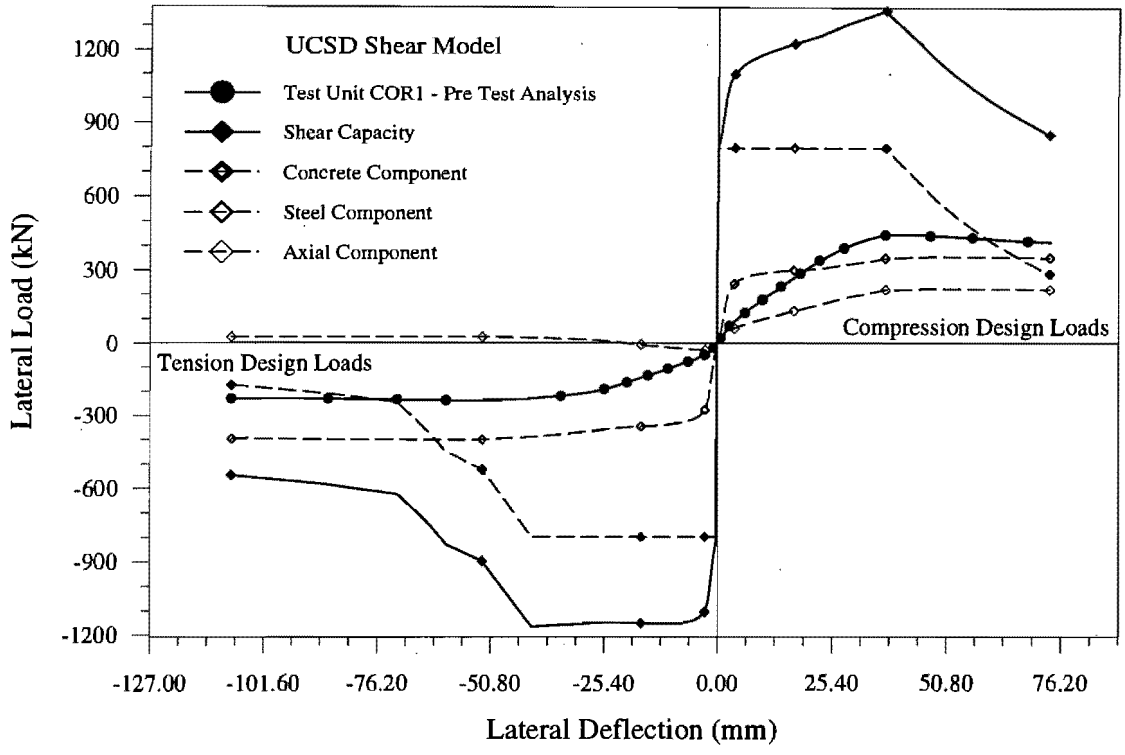

Fig. 2-25 Test Unit *COR1* - Predicted Shear Capacity and Flexural Response

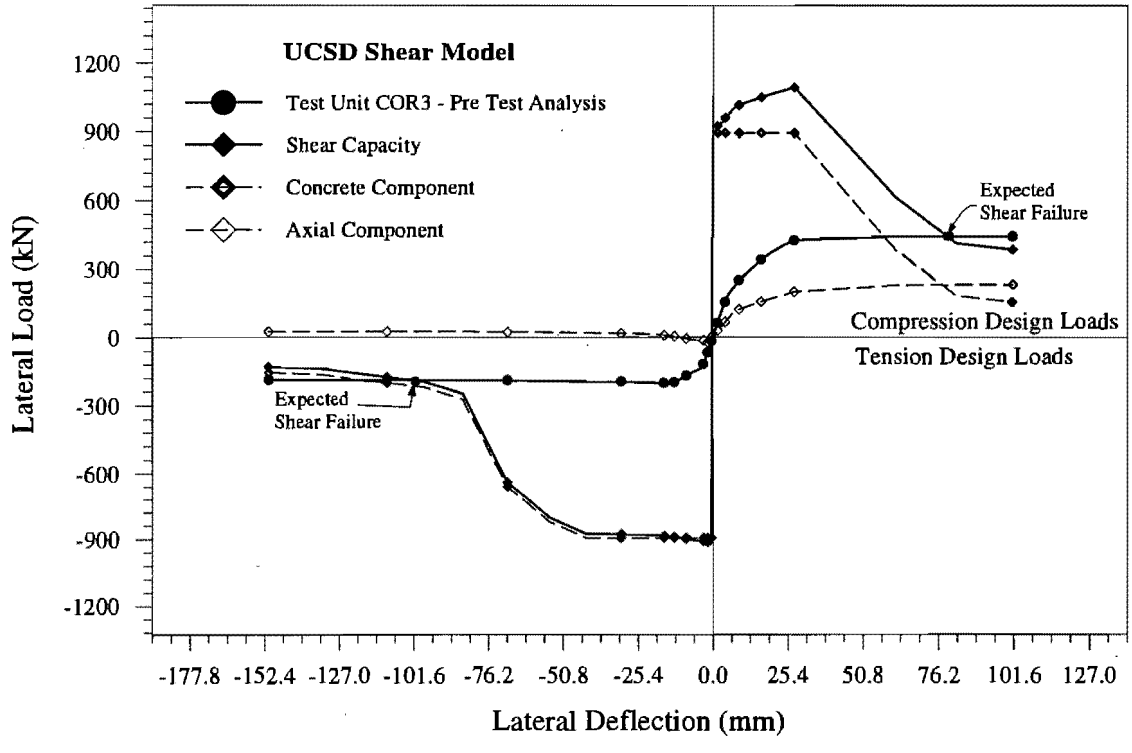

Fig. 2-26 Test Unit *COR3* - Predicted Shear Capacity and Flexural Response

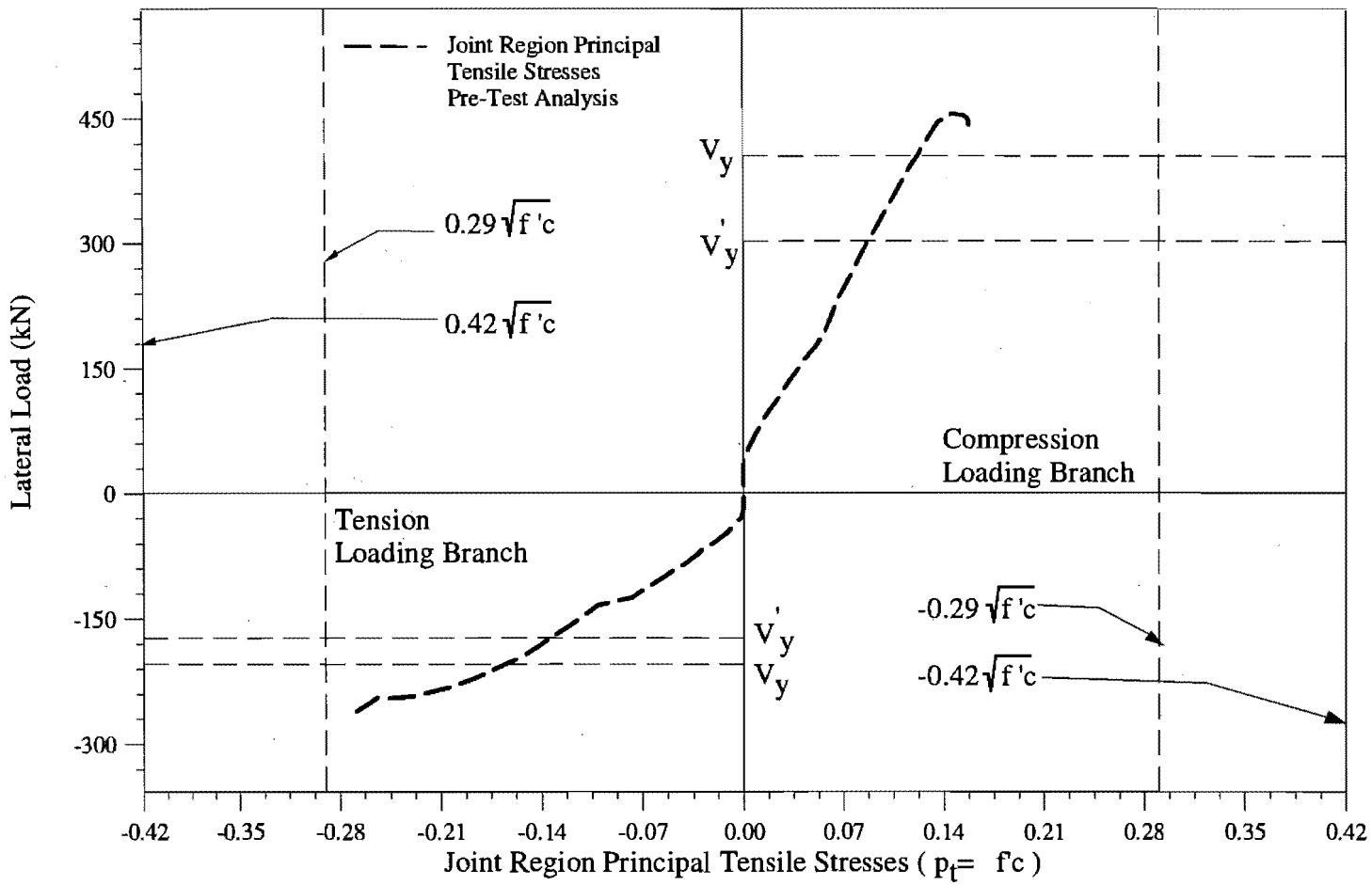

Fig. 2-27 Test Units *COR1* and *COR3* - Joint Region Principal Tensile Stresses Pre-Test Analysis

2.4.2 Test Units *COR1* and *COR3* - Effective Cantilever Length

Preliminary analysis indicated that in the prototype structure, damage is most likely to occur in regions adjacent to the pile cap and/or at the termination of the longitudinal reinforcement for a single pile. Thus, the design team opted to test the piles in single bending to model the region of the pile connection to the pile cap, as in the as-built structure neglecting other regions of maximum moment demand below the mud line elevation. The cantilever length of the test specimen was designed to produce shear force demands similar to the prototype pile in the connection region, neglecting reduction of shear forces below the mud line elevation as a result of pressures that develop in the surrounding soil due to lateral deformations of the pile.

Selection of the cantilever length of the pile specimen was obtained from a detailed 2-D finite element analysis of a single prototype pile embedded in a soil stratum. The finite element model includes the effects of soil-structure interaction, as shown in the model presented in **Fig. 2-28**. The finite element package used to carry out the soil-structure interaction analysis was a finite element developed at UCSD by Seible et al. **[10]** entitled CALSD.

Design of test units *COR1* and *COR3* was established to study the response of a pile section with predominant flexural characteristics. As a result, the axial load used in the analysis of a single pile had to reflect a section with the highest possible cantilever length. For test units *COR1* and *COR3*, the finite element model depicted in **Fig. 2-28** was analyzed

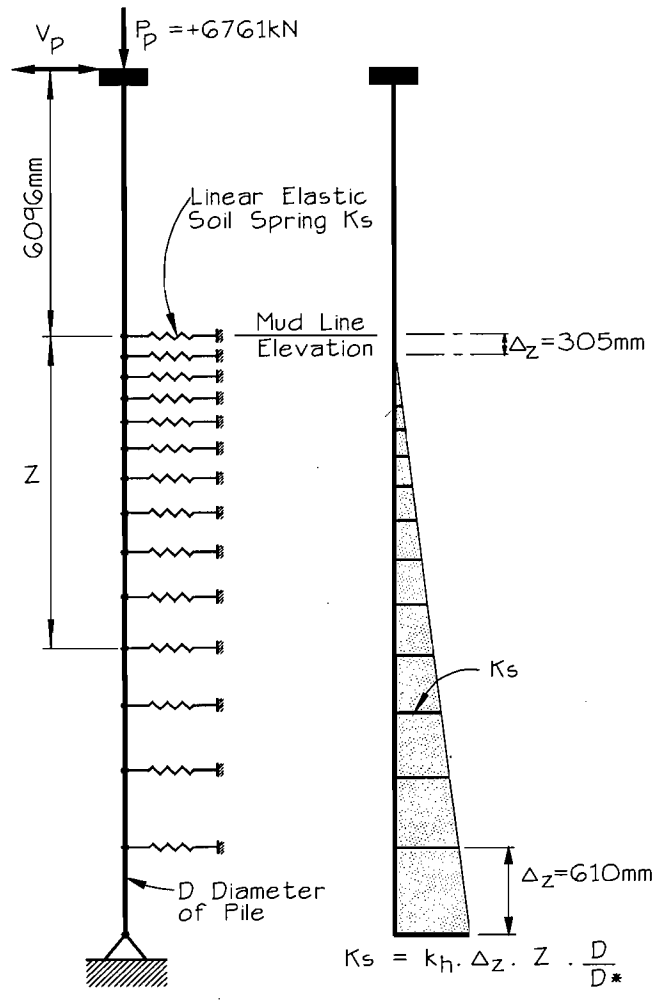

Fig. 2-28 Test Unit *COR1* and *COR3* Soil-Structure Interaction FEM

with an axial compression load of +6761 kN. This axial load level corresponds to the maximum compressive axial load presented in reference **[3]**, and it was used in the analysis of a single pile because it represents the load case which lead to the highest cantilever length than compared with lower levels of axial load.

Multiple runs were performed to obtain an average cantilever length for a pile embedded in different soil stiffness that approximately match the properties of in situ geotechnical test results **[11]**. The coefficient of horizontal subgrade reaction modulus used in the analysis varied between 785 kN/m^3 and 3200 kN/m^3. These numbers reflect estimated soil properties presented in reference **[11]**. The idealized cantilever length of the test units was found from the top of the pile to the first point of contra-flexure obtained from the finite element analysis.

In the finite element model, the soil was modeled as an array of uncoupled linear elastic springs, according to the Winkler soil idealization **[12]**, and positioned along the length of the pile, as shown in **Fig. 2-28**. Springs were only positioned beyond the first 6,096 mm of the pile length, which corresponds to the measured mud line elevation from data obtained in 1995 **[13]**. Calculations of the linear elastic springs were performed according to the expression:

$$K_s = k_h \, \Delta_z \, z \tag{2.24}$$

where K_s is the equivalent spring stiffness, k_h is the coefficient of horizontal subgrade reaction modulus and Δ_z is the spacing between springs at the depth of the soil stratum z. Assuming the coefficient of horizontal subgrade reaction modulus can be normalized in terms of a nominal pile diameter of 1,829 mm, as presented in **[12]** and **[14]**, then k_h may be expressed in terms of the nominal pile diameter, D^*, and the pile section diameter, D, thus:

$$k_h = k_h^* \left(\frac{D}{D^*} \right) \tag{2.25}$$

where k_h^* is the nominal coefficient of horizontal subgrade reaction.

To provide a closer spacing for the soil springs in the regions of maximum bending moment, the distance between the soil springs varied along the length of the pile according to a quadratic progression from 305 mm *(D/4.5)* at the mud line elevation to 610 mm *(D/2.25)* at the pile lower end. The piles were modeled with beam elements positioned between the soil springs nodes, and the pile head was assumed constrained against rotation, as illustrated in **Fig. 2-28**.

To calculate the stiffness of each beam element, a linear iterating analysis was performed where at each iteration, element stiffness were updated based on the tangent stiffness approach, according to the relation; $EI_{eff}=M_p/\varphi$, obtained from moment curvature analysis. For this test unit, a moment curvature program using Mander's model for confined concrete **[15]** was developed to study the correct behavior of each pile and implemented in the previously described finite element model. When analyzing test units *COR1* and *COR3*, it was necessary to allow for the changes in the longitudinal reinforcement according to the six regions previously described and presented in **Fig. 2-18**. The axial load used to compute the element stiffness properties corresponds to the maximum compression design load +6761 kN presented in **Table 2-1**.

In the first iteration all of the elements stiffness were based on the uncracked section properties, and the initial imposed lateral load was calculated such that the section was below the cracking limit state. Then, the element properties were updated based on the previous iteration and the applied lateral load was slightly increased. At each iteration, while maintaining the imposed lateral load constant, intermediate steps were performed and equilibrium was achieved when the element properties remained constant along the length of the pile. This procedure was carried out until the maximum bending moment was achieved.

The effective cantilever length of test units *COR1* and *COR3* was 7,010 mm, computed from the average of the obtained results. Employing the 2/3 scale factor, the scaled effective cantilever length for test units *COR1* and *COR3* was 4,673 mm. **Fig. 2-29** presents the moment profile along the pile length and the selected pile height for test units *COR1* and *COR3*.

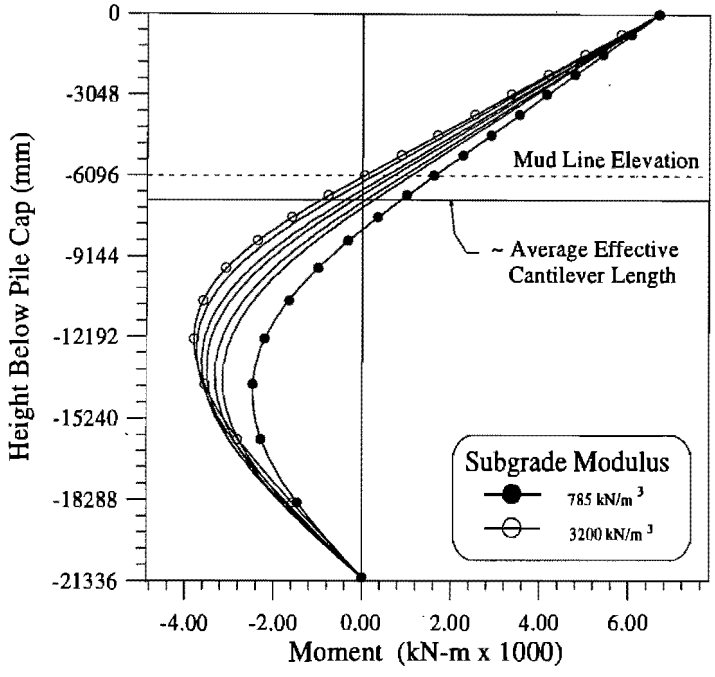

(a) Bending Moment Profile - Test Units COR1 and COR3

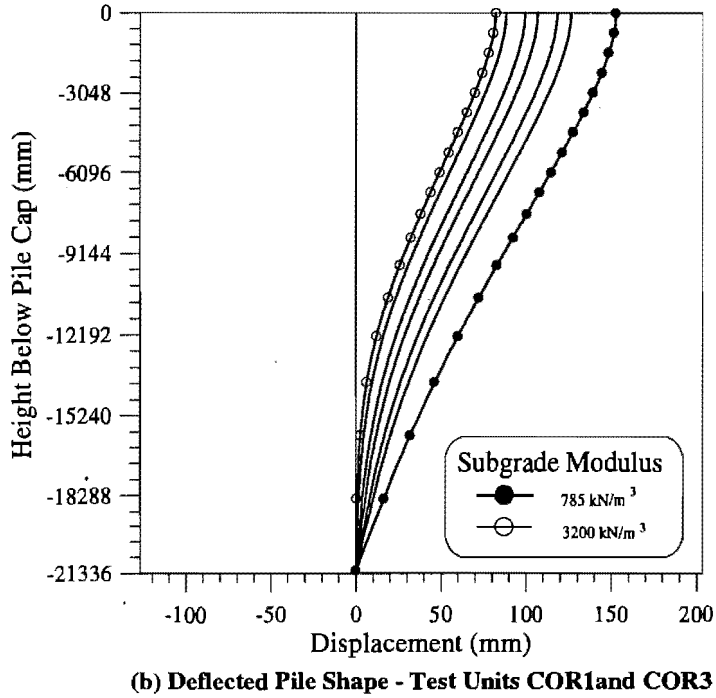

(b) Deflected Pile Shape - Test Units COR1and COR3

Fig. 2-29 Test Units *COR1* and *COR3* - Pile Bending Moment Profile and Lateral Deflection for a Fixed Head Single Pile

2.5 Test Unit *COR2* - Pile Design and Capacity

Similar to test units *COR1* and *COR3,* test unit *COR2* pile geometry and reinforcement layout were scaled from the prototype structure based on a 2/3 scaling factor and were designed in order to obtain similar reinforcement ratios as computed for the prototype piles indicated in **Table 2-1**. The scaled model test specimen is presented in **Fig. 2-30**.

As in test units *COR1* and *COR3*, scaling of the prototype pile resulted in a shell 86 mm thick. Prestressing of the concrete shell consists of 27 seven-wire strands of low relaxation type. The strands are 9.53 mm in diameter and were placed around the circumference of the concrete shell with a concrete cover of 35 mm, resulting in a reinforcement ratio of 0.23%. The total required prestressing force after losses was 1522 kN, which is the same for test units *COR1* and *COR3*. The prestressing strands were anchored with *wedge-chuck* **VSL S5N** at the end opposite to the pile head for clamping to the concrete shell in order to reduce prestressing losses from this pile end. Chapter 3 presents the construction sequence for this pile section.

The transverse reinforcement was also changed along the length of the pile. However, because test unit *COR2* was designed based on a shallower mud line elevation, the effective cantilever length for this test unit led to a height in which only two zones of transverse reinforcement were considered. Referring to **Fig. 2-30**, closest to the pile cap up to a length of 948 mm, the transverse reinforcement consists of deformed #3 bars on a spiral pitch of 84 mm, resulting in a horizontal volumetric reinforcement ratio of approximately 0.40%. In the remaining length of the pile, the transverse reinforcement ratio consists of W3 wires on a spiral pitch of 57 mm, resulting in a horizontal volumetric reinforcement ratio of 0.16%.

The inner cage starter bars to the pile cap consists of 28 - #7 arranged in an inner circle with a diameter of 628 mm. The length of these bars is 2,438 mm with an anchorage length into the pile cap of 813 mm. This inner cage was tied together with hoop reinforcement #3 at 254 mm on centers.

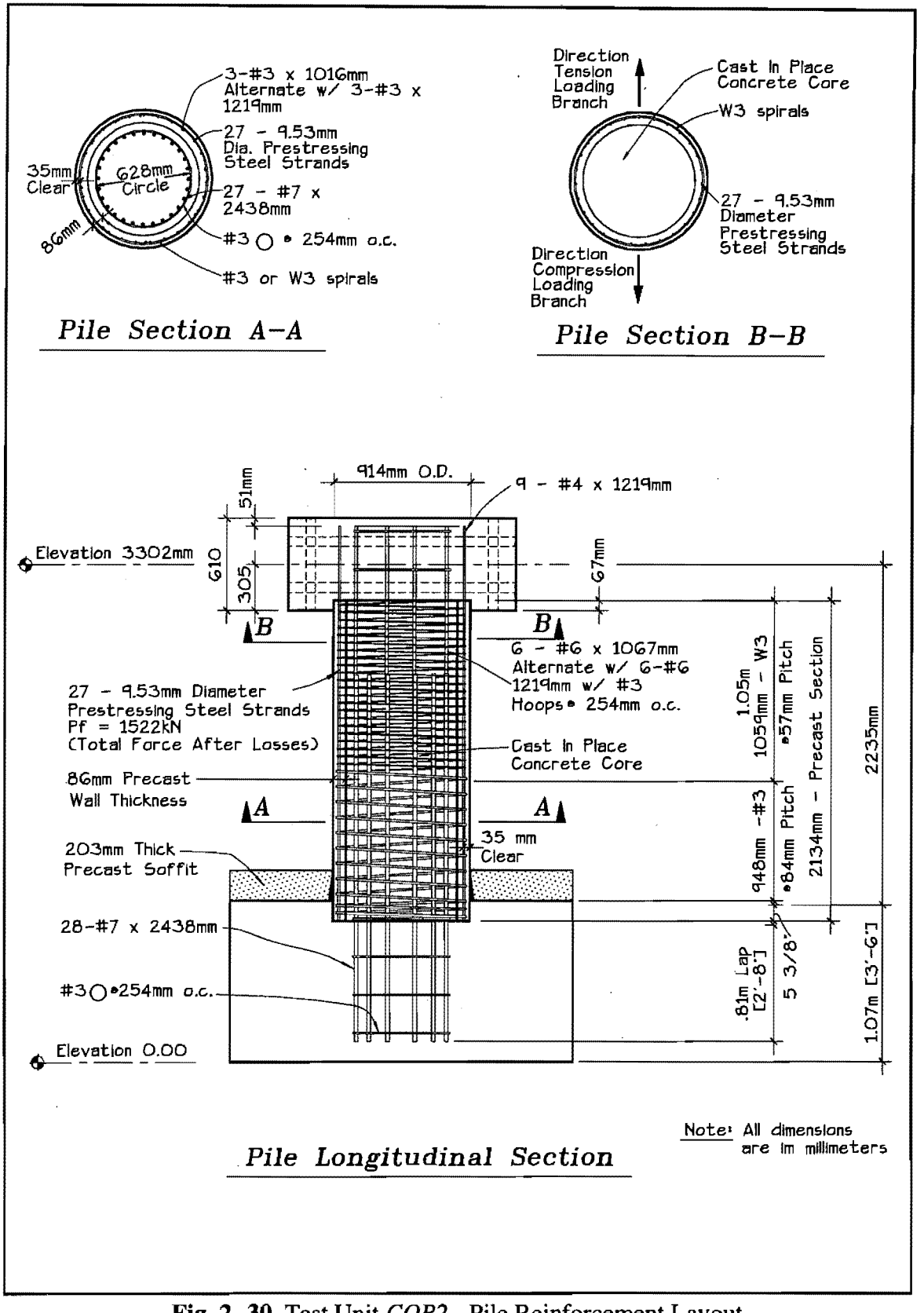

Fig. 2-30 Test Unit *COR2* - Pile Reinforcement Layout

2.5.1 Test Unit *COR2* - Pre-Test Analysis

Similar to test units *COR1* and *COR3*, a detailed analysis of the pile capacity along the pile length was performed in order to investigate regions where flexural capacity might be lower than the moment demand, which could result in a secondary plastic hinge forming at this level.

In test unit *COR2*, the inner core longitudinal reinforcement terminates at 1,489 mm away from the pile cap interface, as indicated in **Fig. 2-30**, which corresponds approximately to 67% of the pile overall length. As before, at the pile cap interface the prestressing strands do not provide moment resistance capacity to the section, and the required development length of the prestressing strands is crucial in determining the correct moment capacity profile, as illustrated in **Fig. 2-18(e)**, and presented earlier while describing test units *COR1* and *COR3* pre-test analysis. The same equilibrium equations used to develop the analysis for test units *COR1* and *COR3* were also used in developing the analysis for test unit *COR2*.

High-strength and normal-strength concrete material properties used for the pile section pre-test analysis were obtained from three concrete cylinder tests at 28 days for each batch. For test unit *COR2*, the pile concrete shell compression strength at 28 days was f'_c=58 MPa, as indicated in **Table 3-1**, and the inner core concrete compression strength at 28 days was f'_c=32 MPa, as indicated in **Table 3-2**.

As before, a moment curvature analysis was performed for different levels of axial load and transfer length for the prestressing strands, and a study was conducted to determine regions where inelastic deformation are most likely to originate along the length of the pile. In **Fig. 2-31** and **Fig. 2-32**, the moment capacity curve obtained for *Runs G* and *J* was developed based on a transfer length of 1,219 mm, in *Runs H* and *K* the transfer length was 1,473 mm, and for *Runs I* and *L* the transfer length was 1,727 mm, which are identical values to those used in the analysis of test units *COR1* and *COR3*.

Analytical results presented in **Fig. 2-31** were developed with an axial compression load of +2793 kN and indicate that for *Runs G*, *H* and *I*, inelastic deformations will only form at the pile cap interface, and amplification of the moment demand due to tension shift effects is also below the presented moment capacity analysis.

Results based on an axial load tension of -302 kN are presented in **Fig. 2-32**. *Run J* results presented in this figure indicate that a second region of inelastic deformations is likely to occur where the longitudinal reinforcement terminates. *Run K* moment capacity curve indicate that only minor inelastic deformations are likely to develop in this region as a result of tension shift effects **[8]**. Finally, *Run L* results indicate that plastic deformations will only occur at the pile cap interface. Thus, similar to test units *COR1* and *COR3*, results employing different values for transfer length of the prestressing strands and different levels of applied axial load indicate that location of potential inelastic activity are likely to form where the longitudinal reinforcement terminates.

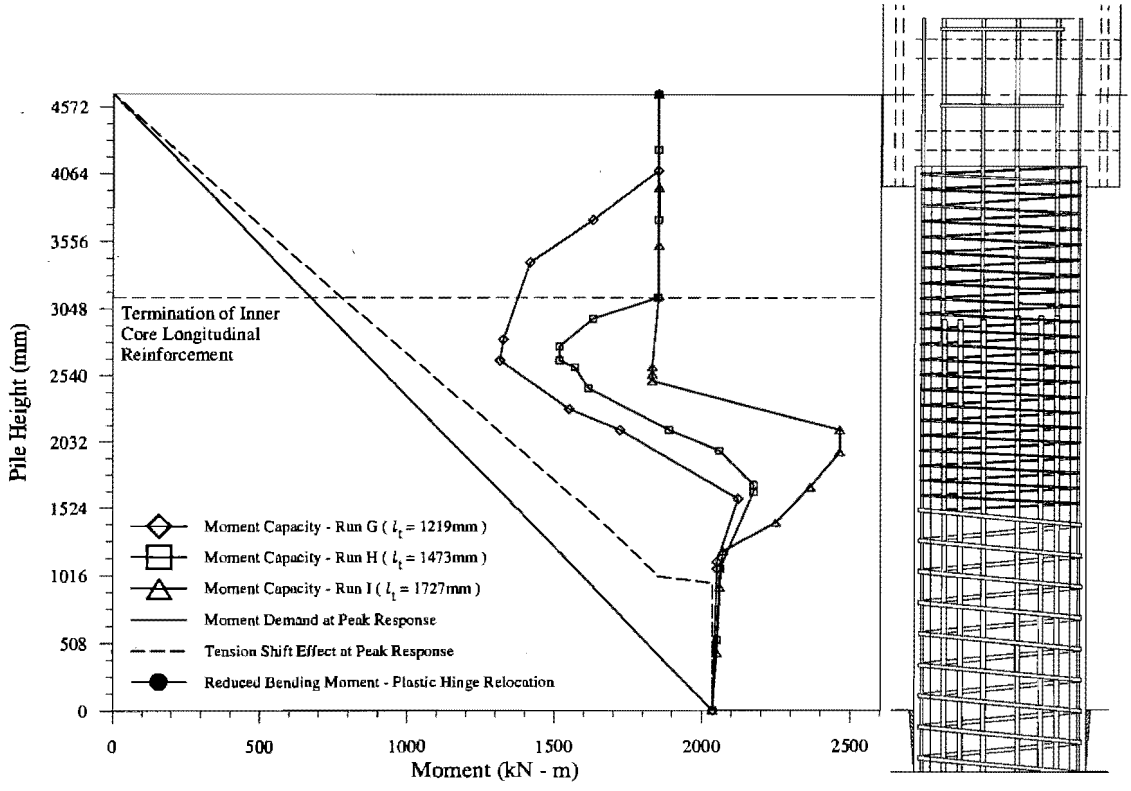

Fig. 2-31 Moment Profiles - Axial Compression Load P = +2793 kN

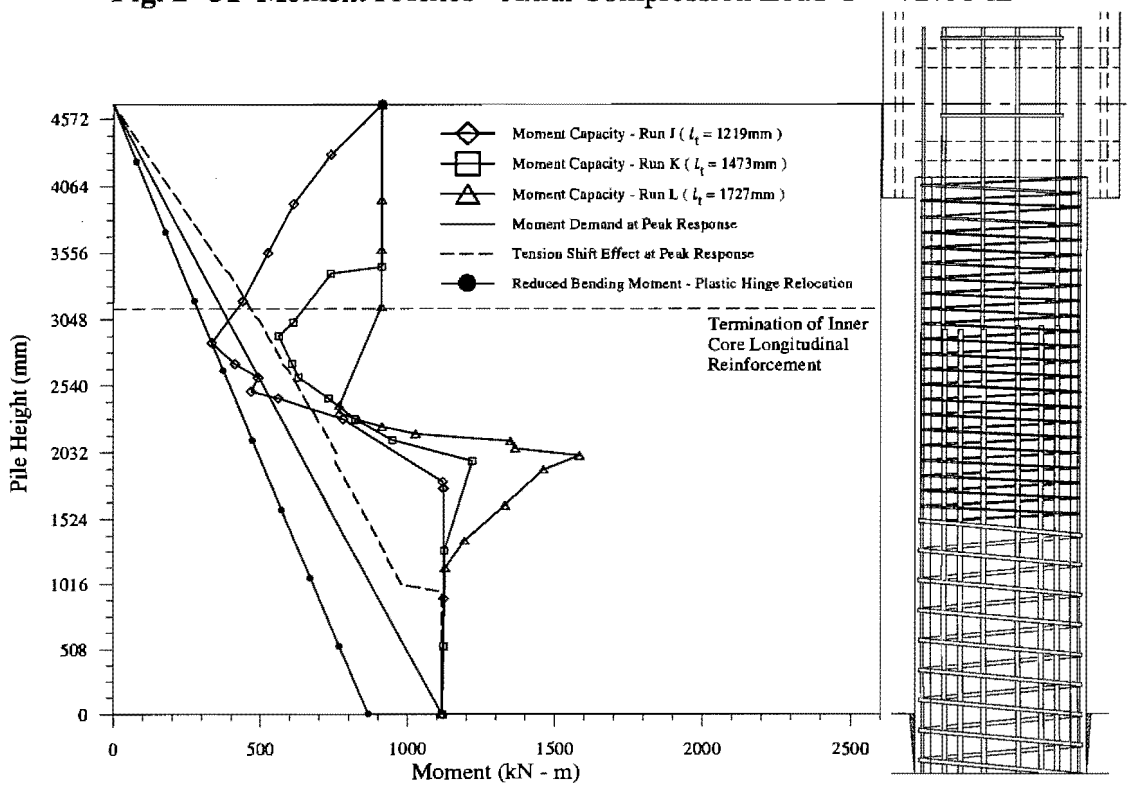

Fig. 2-32 Moment Profile - Axial Tension Load P = -302 kN

The lateral deflections due to flexural effects for test unit *COR2* were computed according to the second moment area theorem given by equation **(2.14)** and curvature profiles, described in **Fig. 2-22**. However, for test unit *COR2*, shear deformations were also considered because of the small aspect ratio according to the expression:

$$\Delta_{shear} = V_p \sum_{X=0}^{H_{pile}} \left(\frac{\Delta_x}{0.9\ A_g\ 0.4\ E_c} \right) \tag{2.26}$$

In equation **(2.26)** E_c may now be replaced by the relation $V_P H_{pile} /(I_x\ \varphi_i)$ to evaluate the shear deformations according to the following expression:

$$\Delta_{shear} = \sum_{X=0}^{H_{pile}} \left(\frac{\Delta_x\ \varphi_i\ I_x}{0.9\ A_g\ 0.4\ H_{pile}} \right) \tag{2.27}$$

Test unit *COR2* pre-test analysis total lateral deflection consists of flexural and shear components of deformations, as presented in **Fig. 2-33**. The loading curve described in terms of axial load versus lateral load used to construct the pre-test analysis is presented in Chapter 3. At ultimate response in the compression and tension loading branch, the shear deformation component is approximately 16% of the total lateral deflection.

Shear strength analysis of test unit *COR2* was developed similar to the analysis presented for test units *COR1* and *COR3*. Referring to **Fig. 2-34**, predictive shear analysis may be conducted by comparing the lateral load versus lateral deformation envelope with the shear strength envelope obtained from the UCSD three component model previously described. In **Fig. 2-34**, the UCSD three component shear strength envelopes, shear capacity and demand are presented. A rapid study of this plot suggests that in the compression loading branch, the shear capacity of the pile section is considerably higher than the shear demand. However, in the tension loading branch, analysis suggests that the section may be susceptible to a ductile flexural-shear failure at a lateral displacement of -25.40 mm, because the shear capacity curve approaches and parallels the shear demand curve indicated by test unit *COR2* pre-test analysis curve.

Test unit *COR2* maximum principal tensile stress in the compression loading branch and in the tension loading branch are identical to those computed for test units *COR1* and *COR3*, which were $0.16\sqrt{f_c'} < 0.29\sqrt{f_c'}$ *[MPa]* and $0.27\sqrt{f_c'} < 0.29\sqrt{f_c'}$ *[MPa]*, respectively, and are below cracking levels. Principal tensile stresses presented in **Fig. 2-27** indicate that cracking in the joint region will not occur at any stage in the loading procedure.

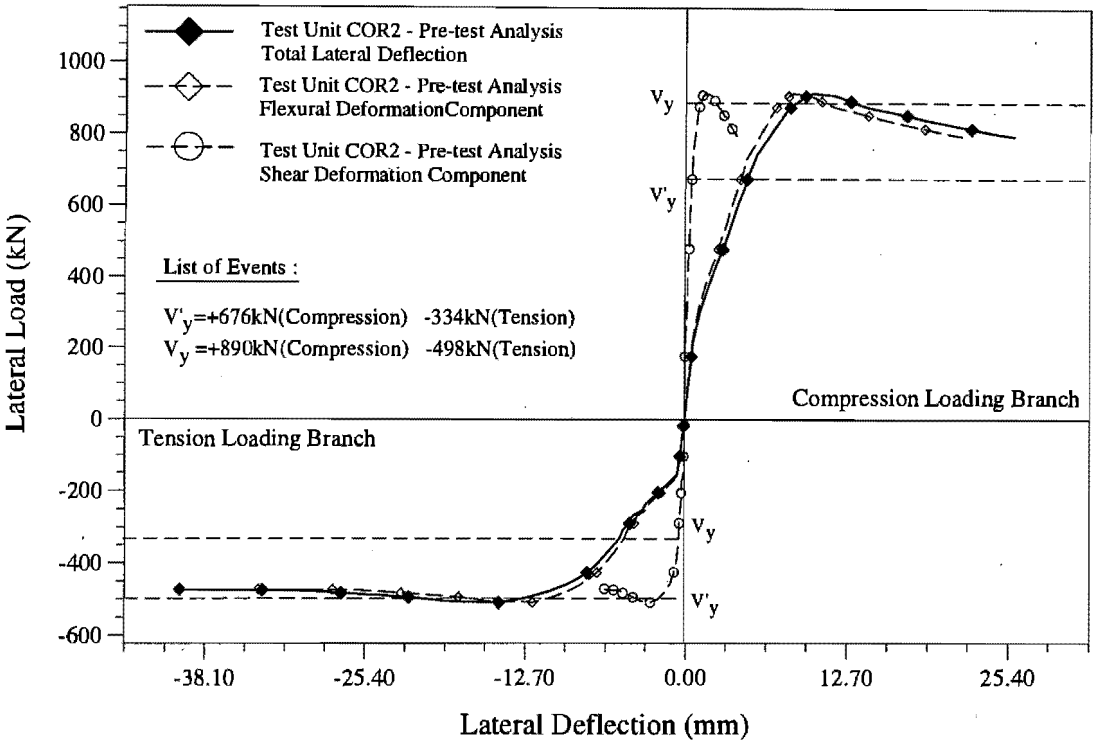

Fig. 2-33 Test Unit *COR2* - Pre-Test Analysis

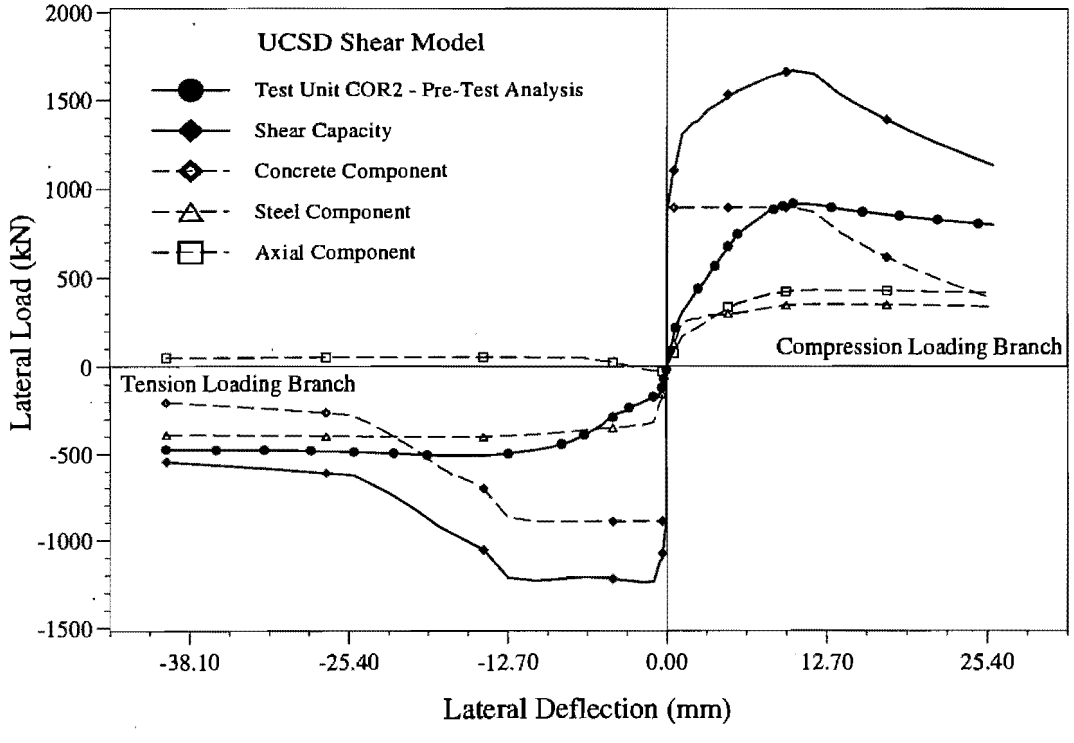

Fig. 2-34 Test Unit *COR2* Predicted Shear Capacity and Flexural Response

2.5.2 Test Unit COR2 - Effective Cantilever Length

As in test units *COR1* and *COR3*, in test unit *COR2* the cantilever length of the pile was obtained according to the cantilever idealization of a single pile to produce shear force demands similar to the prototype pile at the connection region, neglecting reduction of shear forces down the pile as a result of soil confinement.

Selection of the cantilever length of the pile specimen was obtained from a detailed 2-D finite element analysis of a single prototype pile embedded in a soil stratum, depicting the effects of soil-structure interaction with a shallow mud line elevation of 1,676 mm, as shown in **Fig. 2-35**. As in test units *COR1* and *COR3*, the finite element model was analyzed with an axial compression load of +6,761 kN **[3]**, with multiple runs depicting different soil properties. The idealized cantilever length of this test unit was computed from the top of the pile to the first point of contra-flexure obtained from the finite element analysis. Development of the soil-structure interaction analysis was identical to test unit *COR1* and *COR3* analysis.

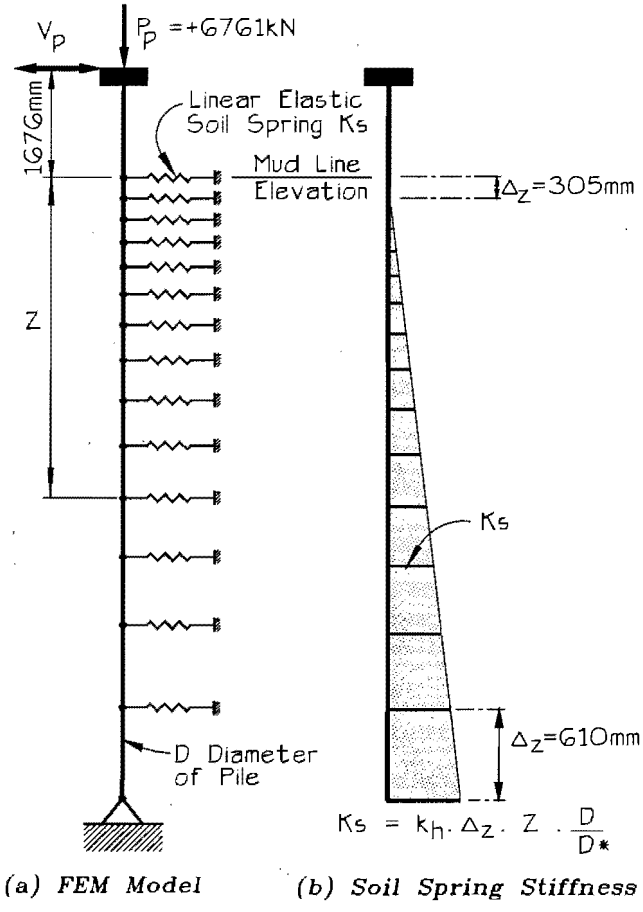

Fig. 2-35 Test Unit *COR2* Soil-Structure Interaction FEM

Similar to test unit *COR1* and *COR3*, the finite element model was analyzed for each pile with different coefficients of horizontal subgrade reaction, which varied between 785 kN/m^3 and 3,200 kN/m^3 **[11]**. The effective cantilever length of test unit *COR2* was 3,353 mm, computed from the average of the obtained results. Employing the 2/3 scale factor, the scaled effective cantilever length for test unit *COR2* was 2,235 mm. **Fig. 2-36** presents the moment profile along the pile length and the selected pile height for test unit *COR2*.

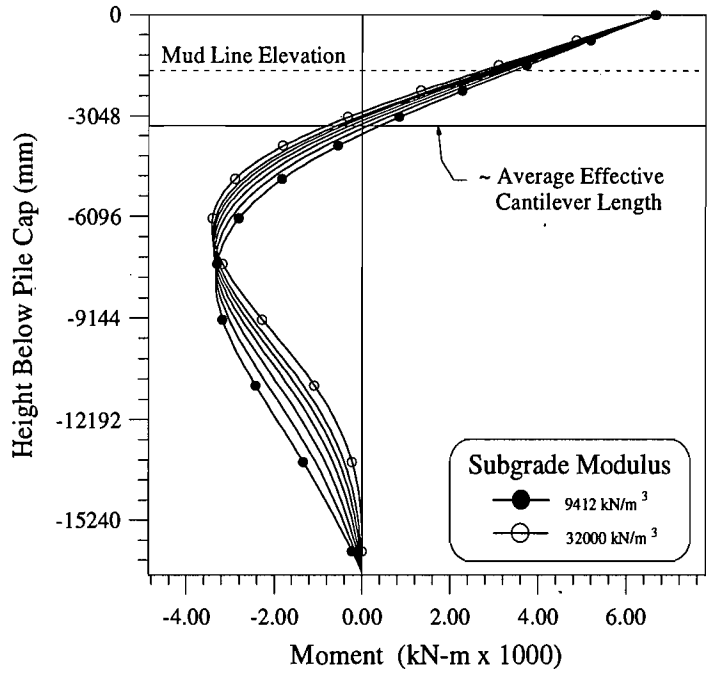

(a) Bending Moment Profile - Test Unit 2

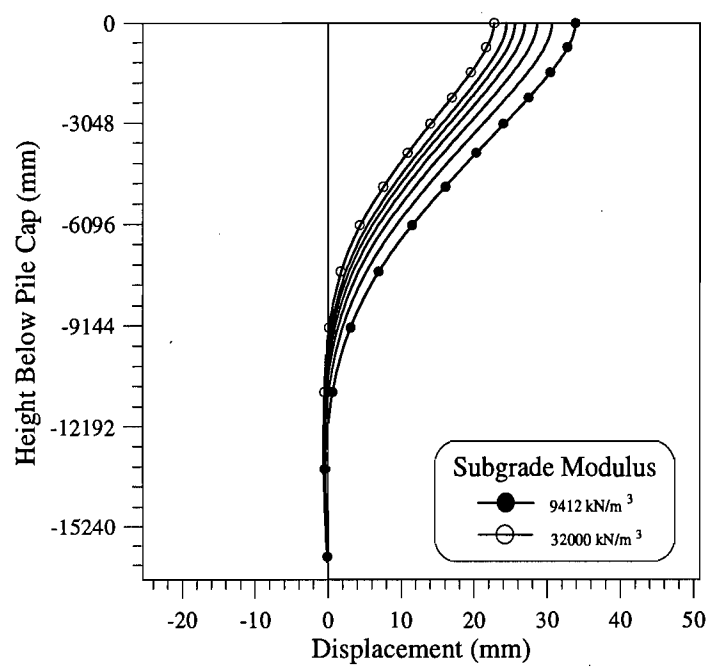

(b) Deflected Pile Shape - Test Unit 2

Fig. 2–36 Test Unit *COR2* - Pile Bending Moment Profile and Lateral Deflection for a Fixed Head Single Pile

3. Construction, Instrumentation and Testing Procedure

In this chapter, a detailed description of the construction, instrumentation, and reinforcement material properties of the different bar sizes used for the construction of the test specimens, as well as concrete material properties and testing procedure for the three test specimens are presented.

3.1 Construction of the Test Specimens

Construction of the test specimens was conducted in phases to produce a similar construction sequence as that during the construction of the prototype structure. As previously indicated, the test specimens were constructed in an inverted position for ease of installation and loading. As a result, the construction sequence was adjusted as necessary in order to facilitate construction without considerably affecting the response of the test units under the simulated seismic loading. In this section, a brief description of the construction sequence are presented for the three test units.

3.1.1 Construction of Test Units *COR1* and *COR3*

The first step in the construction phase consisted of manufacturing the precast concrete shells in the construction facilities of *Utililty Vault* in Fontana, California. Manufacturing of the precast concrete shells involved two stages. First, the fabrication of the spiral cages and instrumentation of the prestressing strands with electric resistance strain gages was conducted in the laboratory facilities of UCSD. Detailed description of the instrumentation setup is presented in this chapter.

The next stage was conducted at *Utility Vault* and involved assembling the self reacting casting bed, followed by stressing the strands and casting of the concrete shells. The precast prestressed concrete shells were cast in a self reacting casting bed with the different assembly components illustrated in **Fig. 3-1**. Because the casting bed was self reacting,the casting bed components were assembled before stressing and disassembled for removal of the concrete shells. First, the spiral cages were positioned in the bottom form without the top form in place. Next, he top form was placed over the bottom form and the strong-end bulkheads were aligned with the continuous reaction rods. The prestressing strands were then passed through the strong-end bulkheads, and wedges were placed on the outside face of the bulkheads.

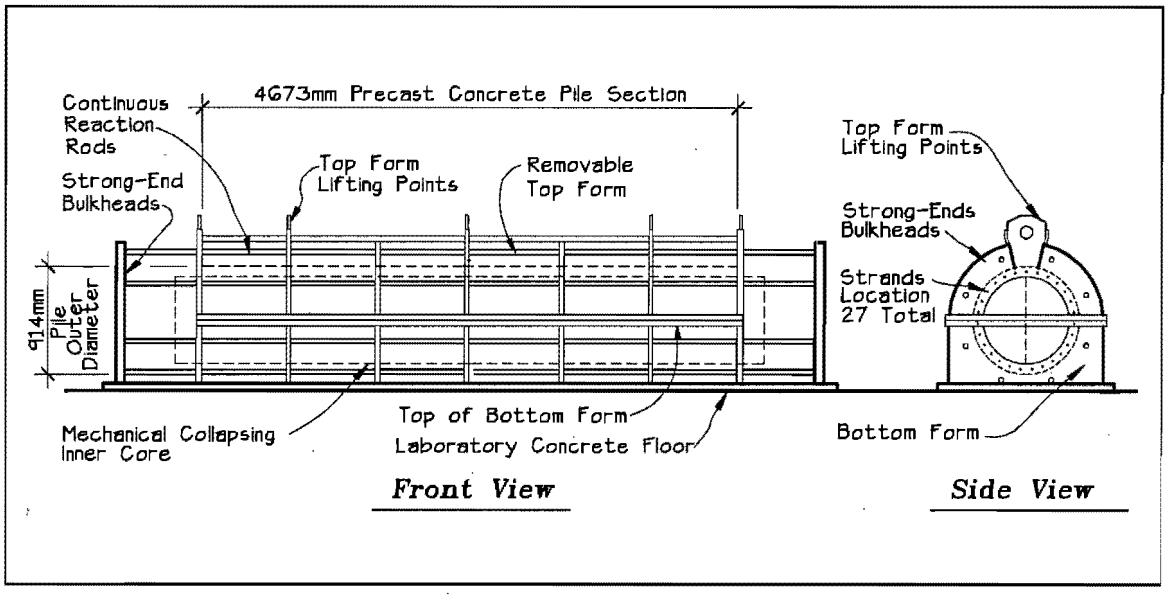

Fig. 3-1 Self-Reacting Casting Bed Components

After all of the strands were in place, the strands were initially stressed to 14% of the total jacking force to remove slack in the strands. The spirals were realigned to the desired pitch and the strands were then stressed to the final jacking force. In both of these stressing stages, the electric cables from the strain gages were connected to a rapid data acquisition system to record strain gage readings during the precasting phase. Strain gage readings obtained during precasting of the concrete shells are presented in Chapter 4.

Next, the concrete shell inner diameter was obtained by inserting a mechanical collapsing inner core tube through the inside of the casting bed, as illustrated in **Fig. 3-2** and **Fig. 3-3**, before casting. **Fig. 3-4** shows turnbuckles positioned along the inside of the inner core tube for expansion or contraction of the inner core tube. The top form was constructed with an aperture over the top for casting of the concrete shells, as illustrated in **Fig. 3-5**. After the inner core tube was placed, casting of the concrete shells was accomplished as depicted in **Fig. 3-6**. The fully assembled casting bed is shown in **Fig. 3-7**

After casting, the prestressing bed was covered by a plastic sheet and curing was obtained at 70°F by steam tubes placed inside the inner core form. Concrete cylinders of 76 mm and 152 mm in diameter were obtained for each unit to obtain concrete compressive strength at different time intervals, and they were placed inside the inner core during curing. Strain gages were then installed 24 hours after casting on the concrete shell top surface through the aperture in the top form to monitor transfer of forces after the strands are cut in order to predict the transfer length of the prestressing strands.

In all units, prestressing transfer was performed by flame cutting the strands when the concrete compressive strength was approximately 28 MPa, which was determined by concrete compression tests of 76 mm in diameter cylinders performed at *Utility Vault,* and 152 mm cylinders tested at UCSD.

Completion of the test units was then carried out at UCSD in three phases. In the first phase, the pile cap reinforcement cage was assembled followed by placement of the concrete shell through the inner core longitudinal reinforcement, and casting of the pile cap was accomplished. **Fig. 3-8** through **Fig. 3-13** illustrate steps described in the first construction phase.

During the second phase, the soffit slab reinforcement cage was assembled and casting of the soffit slab and pile, up to the termination of the inner longitudinal reinforcement, was accomplished. **Fig. 3-14** and **Fig. 3-15** show soffit slab reinforcement cage with block outs for tie downs to pile cap before casting. Finally, the load stub reinforcement cage was assembled, and casting of the remainder of the inner core of the pile and load stub was accomplished.

In addition, for test unit *COR3* two lines of cracks were imposed on the sides of the concrete shell, as previously discussed and illustrated in **Fig. 3-16** and **Fig. 3-17**. Completed test units *COR1* and *COR3* are presented in **Fig. 3-18** and **Fig. 3-19**, respectively.

Fig. 3-2 Installing Inner Core Form Before Casting of Concrete Shell

Fig. 3-3 Installing Inner Core Form Before Casting of Concrete Shell

Fig. 3-4 Inner Core Tube Mechanism

Fig. 3-5 Top Form Aperture

Fig. 3-6 Casting of the Concrete Shell at *Utility Vault*

Fig. 3-7 Fully Assembled Self Reacting Casting Bed

Fig. 3-8 Pile Cap Reinforcement Cage

Fig. 3-9 Pile Cap Reinforcement Cage Before Installing Precast Concrete Shell

Fig. 3-10 Installing Concrete Shell Thru Inner Core Reinforcement Cage

Fig. 3-11 Installing Concrete Shell Thru Inner Core Reinforcement Cage

Fig. 3-12 Concrete Shell in Place Before Casting of Pile Cap

Fig. 3-13 Casting of Pile Cap

Fig. 3-14 Soffit Slab Reinforcement Cage Before Casting

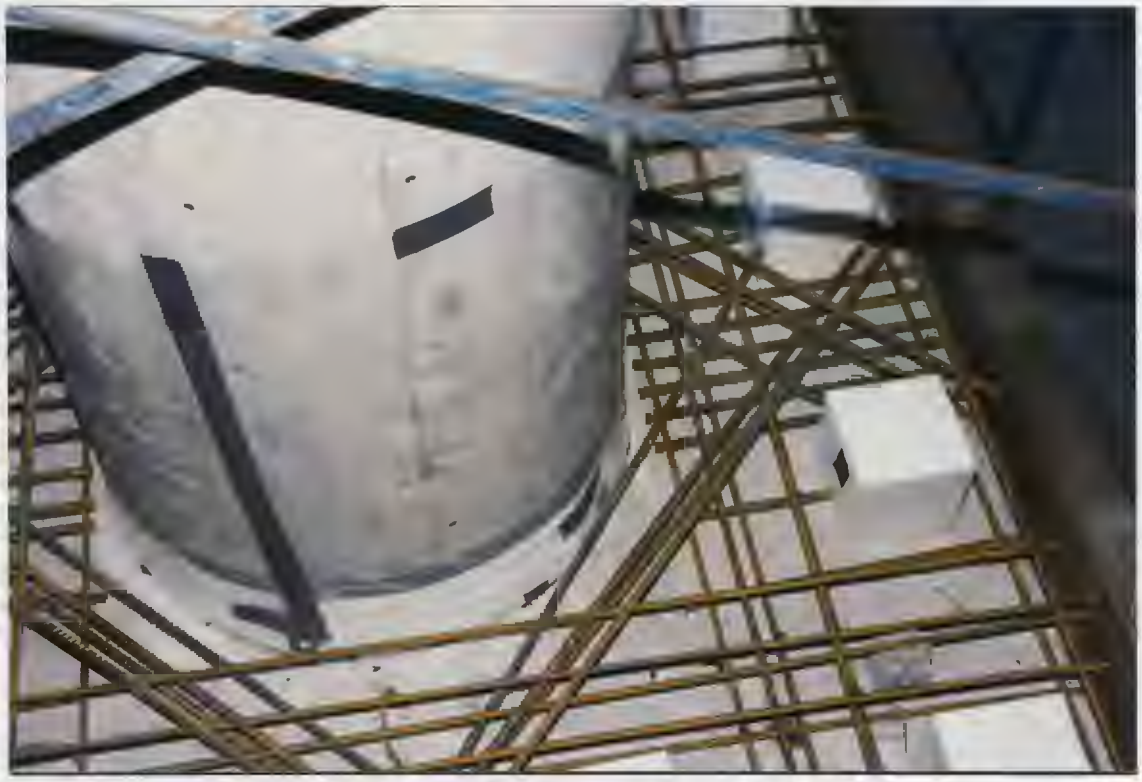

Fig. 3-15 Soffit Slab Reinforcement Cage Before Casting

Fig. 3-17 Test Unit *COR3* Longitudinal Saw Cut Lines

Fig. 3-16 Test Unit *COR3* Longitudinal Saw Cut Lines

Fig. 3-18 Test Setup Unit *COR1*

Fig. 3-19 Test Setup Unit *COR3*

3.1.2 Construction of Test Unit *COR2*

A few extra steps were attained while manufacturing test unit *COR2* concrete shell because of its shorter length. Test unit *COR2* concrete shell was manufactured in the same casting bed as test units *COR1* and *COR3* concrete shell. As illustrated in **Fig. 3-20**, the spiral cage reinforcement was positioned only on one side of the casting bed with the desired length of the concrete shell, and the remaining part of the casting bed was cast without spiral reinforcement. A circular wooden piece was placed in the casting bed for easier separation of the two casting parts. **Fig. 3-21** illustrates positioning of the prestressing strands through this circular wooden piece.

After the strands were stressed to the jacking force, this wooden piece was moved into the desired position and the inner core tube was installed in place as previously described in **Fig. 3-2**. In addition, to reduce the effects of prestress losses in the pile end near the load stub, the prestressing strands were anchored with *wedge-chuck* VSL S5N Anchorage System, as illustrated in **Fig. 3-22**. **Fig. 3-23** shows the concrete shell before separation at wooden piece. A chain saw was then used to cut the section in two parts at the wooden piece. During separation of the concrete shell, the strain gages cables were maintained connected to the data acquisition system to monitor strand strain losses at the anchorage system.

By casting the full bed, two objectives were achieved; (1) reduced length of exposed strands minimized wave propagation of the strands during cutting of the strands away from the region where the wedges were positioned, thus reducing mechanical bond losses in this region. (2) strain gage readings were also used after transfer of the prestressing strands to calculate transfer length in the pile head region.

Completion of test unit *COR2* was then carried out at UCSD with similar construction phases as in test units *COR1* and *COR3*. Completed test unit *COR2* before testing is presented in **Fig. 3-24** and **Fig. 3-25**.

Fig. 3-20 First Stages of Preparation for Construction of Concrete Shell For *COR2*

Fig. 3-21 Positioning of Strands Through Wooden Piece Separator Before Prestressing

Fig. 3-22 *wedge-chuck* **VSL S5N** Anchorage System

Fig. 3-23 Finished Precast Concrete Shell Before Separation at Wooden Piece for *COR2*

Fig. 3-24 Test Setup Unit *COR2*

Fig. 3-25 Test Setup Unit *COR2*

3.2 Test Units *COR1*, *COR2* and *COR3* - Material Properties

Casting of the three test units concrete shells was performed with high strength concrete, designed to reach a concrete compressive strength of 28 MPa at 24 hours for transfer and 62 MPa at 28 days with a mix design number *UV-161*, designed by *Utility Vault* engineers. The mix design used contained 10 bags of Type V - LA portland cement per cubic yard with 1/2 in. rock and special admixtures such as WRDA-79, WRDA-19A, DCI and Force 1000. Concrete cylinder test results for the high strength concrete utilized in casting of the concrete shells are presented in **Table 3-1**.

A higher water content was used in the concrete mix design of test unit *COR2* to ensure that the concrete mix filled all the tight spaces in the vicinity of the anchorage system which is illustrated in **Fig. 3-22**. This accounts for the lower compression strength of test unit *COR2* concrete, as shown in **Table 3-1**. Thus, prestressing transfer for test unit *COR2* was accomplished approximately 4 days after casting, while prestressing transfer for test units *COR1* and *COR3* was executed approximately 24 hours after casting. This ensures that estimation of transfer length for the three test units was carried out at approximately the same concrete compression strength.

Table 3-1 Concrete Material Properties - High Strength Concrete

Cylinder Test Date Days	Unit *COR1* [MPa]	Unit *COR2* [MPa]	Unit *COR3* [MPa]
1	26[1]	15	26[1]
4	43	25[1]	44
14	63	54	64
28	69	58	68
Day of Test	77[2]	68[3]	75[4]

[1] Prestress transfer.
[2] Test unit *COR1* day of test 110 days after casting of concrete shell.
[3] Test unit *COR2* day of test 126 days after casting of concrete shell.
[4] Test unit *COR3* day of test 151 days after casting of concrete shell.

Casting of the test units was performed according to the pour sequence described in **Fig. 3-27** and **Fig. 3-29**. Concrete cylinders 152 mm in diameter for normal strength concrete utilized in the casting of the three test units were tested in Satec® materials testing machine at UCSD in time intervals indicated in **Table 3-2**

Table 3-2 Concrete Material Properties - Normal Strength Concrete

Cylinder Test Date	Unit *COR1*[1] [MPa]		Unit *COR2*[2] [MPa]		Unit *COR3*[3] [MPa]	
	28 Days	Test Day 110 Days	28 Days	Test Day 126 Days	28 Days	Test Day 151 Days
Batch No. 1[4,5]	32	35	35	38	39	40
Batch No. 2[4,6]	33	34	32	34	36	39
Batch No. 3[4]	32[7]	34	-	-	18[8]	20
Batch No. 4[4,9]	-	-	-	-	36	39

[1] For concrete material properties layout see **Fig. 3-27**.
[2] For concrete material properties layout see **Fig. 3-28**.
[3] For concrete material properties layout see **Fig. 3-29**.
[4] Maximum aggregate is specified as 25.40 mm
[5] Concrete strength was specified at $f'_c = 35$ MPa.
[6] Concrete strength was specified at $f'_c = 35$ MPa.
[7] Concrete strength was specified at $f'_c = 35$ MPa.
[8] Concrete strength was specified at $f'_c = 16$ MPa.
[9] Concrete strength was specified at $f'_c = 35$ MPa.

Three samples of each reinforcement type were tested to determine the stress-strain curve characteristics for each bar size. The different types of reinforcement are shown in **Table 3-3** with their properties. These properties were obtained by testing three 914 mm long reinforcement test samples on the Satec® materials testing machine at UCSD.

Table 3-3 Test Units *COR1, COR2* and *COR3* Steel Material Properties

	Bar Size	Location	Yield Strength f_y (Mpa)	Ultimate Strength f_u (Mpa)
Reinforcement[1] (Grade 40)	#7	Pile Section Inner Core Longitudinal Reinforcement	283	414
Reinforcement[1] (Grade 60)	#7	Pile Cap Top and Bottom Layer Reinforcement	465	757
	#6	Pile Cap J-Hooks	472	745
	#3	Pile Section Transverse Reinforcement	448	689
Smooth Wire Reinforcement[1]	W3	Pile Transverse Reinforcement	599	717
Prestressing Strands[1,2,3] (Grade 270)	9.53 mm ⌀	Concrete Prestressing Strands	1723	1998

[1] Average yield stress determined from 3 bar test specimens.

[2] 9.53 mm ⌀ 7-Wire Strand

[3] Grade 270 is specified at 1860 MPa ultimate strength

Yielding of high-strength steel used in the manufacturing of prestressing strands can not be readily determined, as in the case of normal strength, and the yield strength of the prestressing strands was determined based on a strain criterion according to ASTM current standards **[5]**. The prestressing strands yield strength was determined at a total strain of one percent based on stress-strain curves obtained from three sample tensile tests. At one percent of strain, the stress was f_{py}=1,830 MPa, which corresponds to 90% of the maximum stess f_{pu}=2,008 MPa, as illustrated in **Table 3-3** and presented in **Fig. 3-26**.

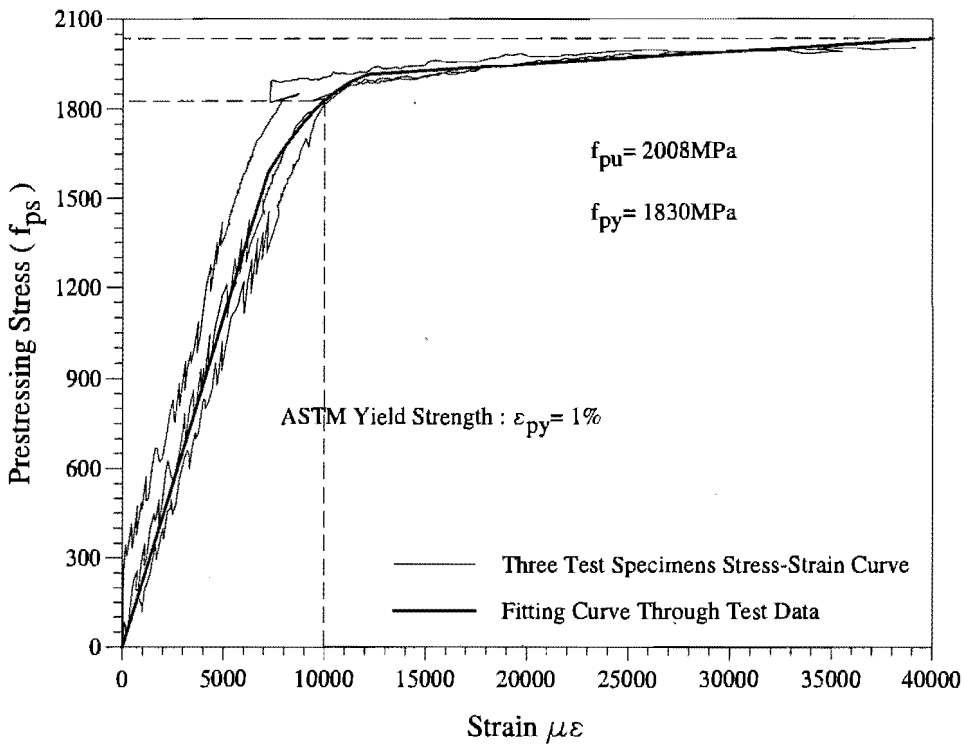

Fig. 3-26 Stress-Strain Curve of Prestressing Steel

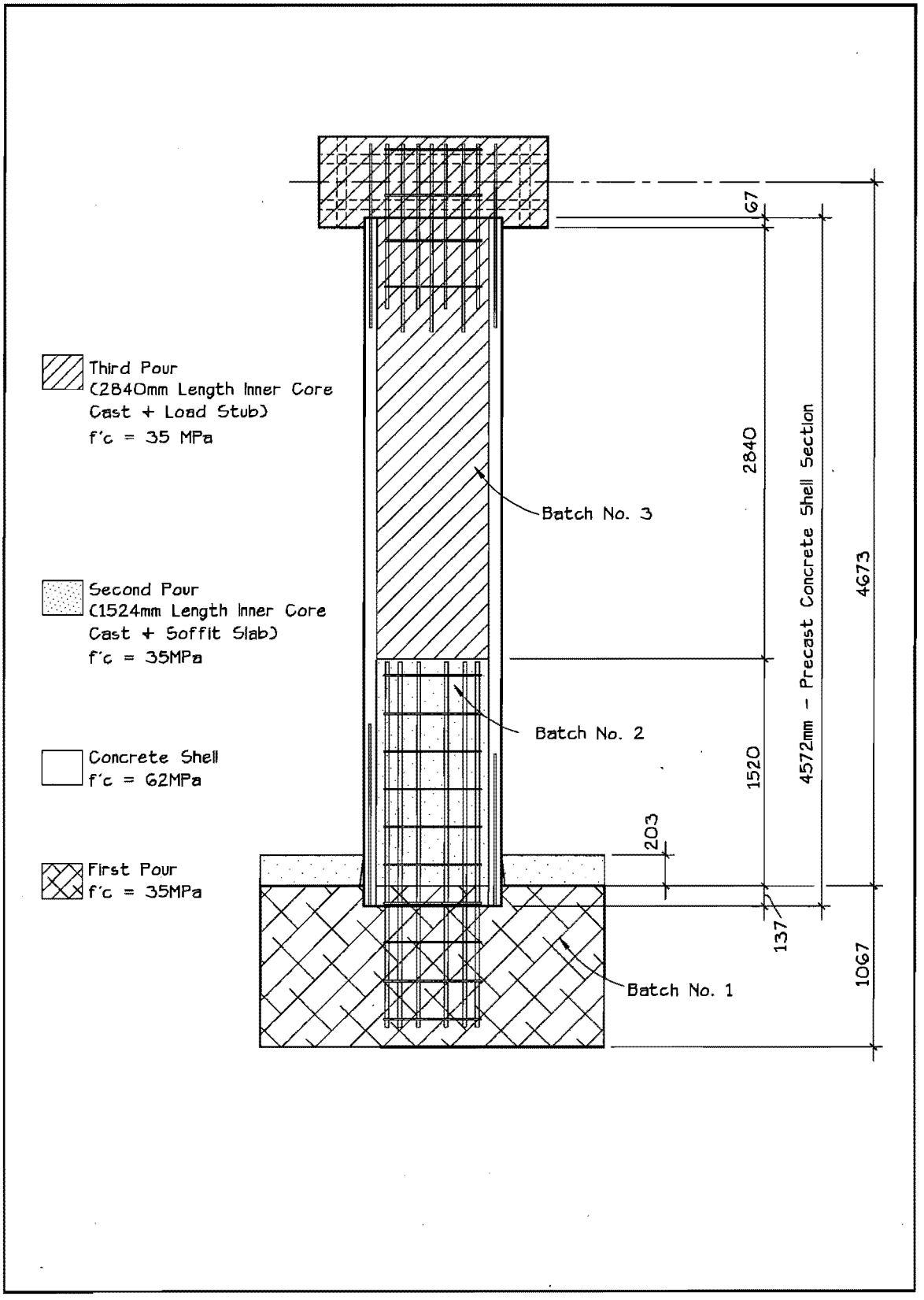

Fig. 3-27 Test Unit *COR1* Pile Layout - Concrete Material Properties

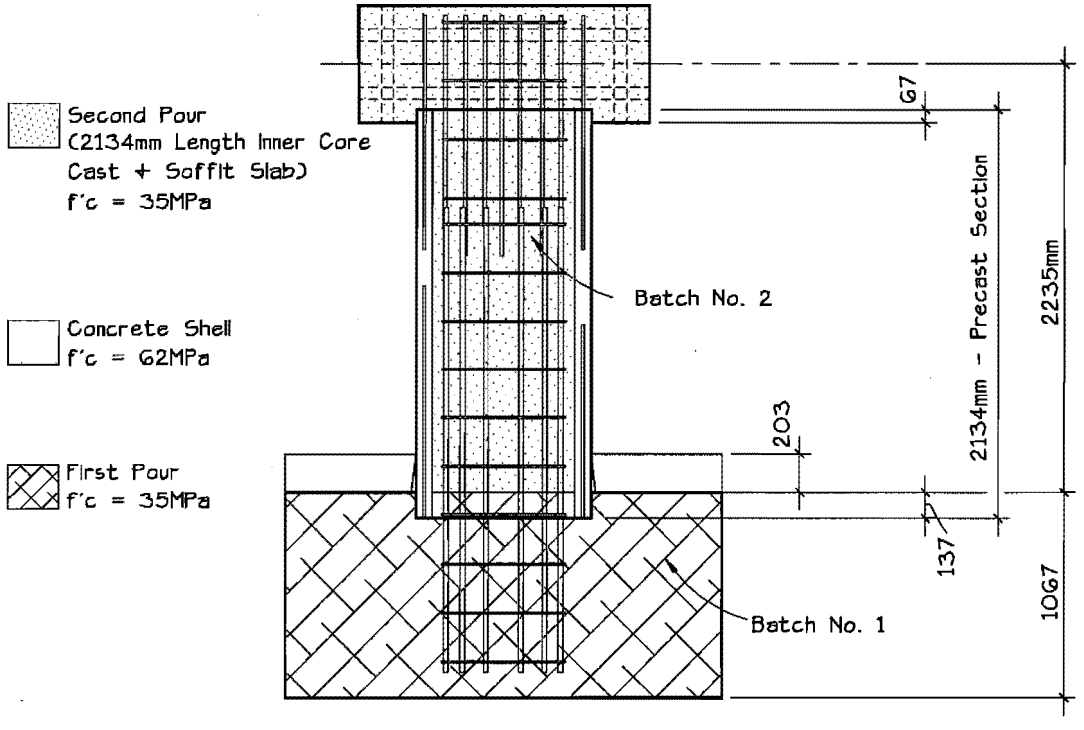

Fig. 3-28 Test Unit *COR2* Pile Layout - Concrete Material Properties

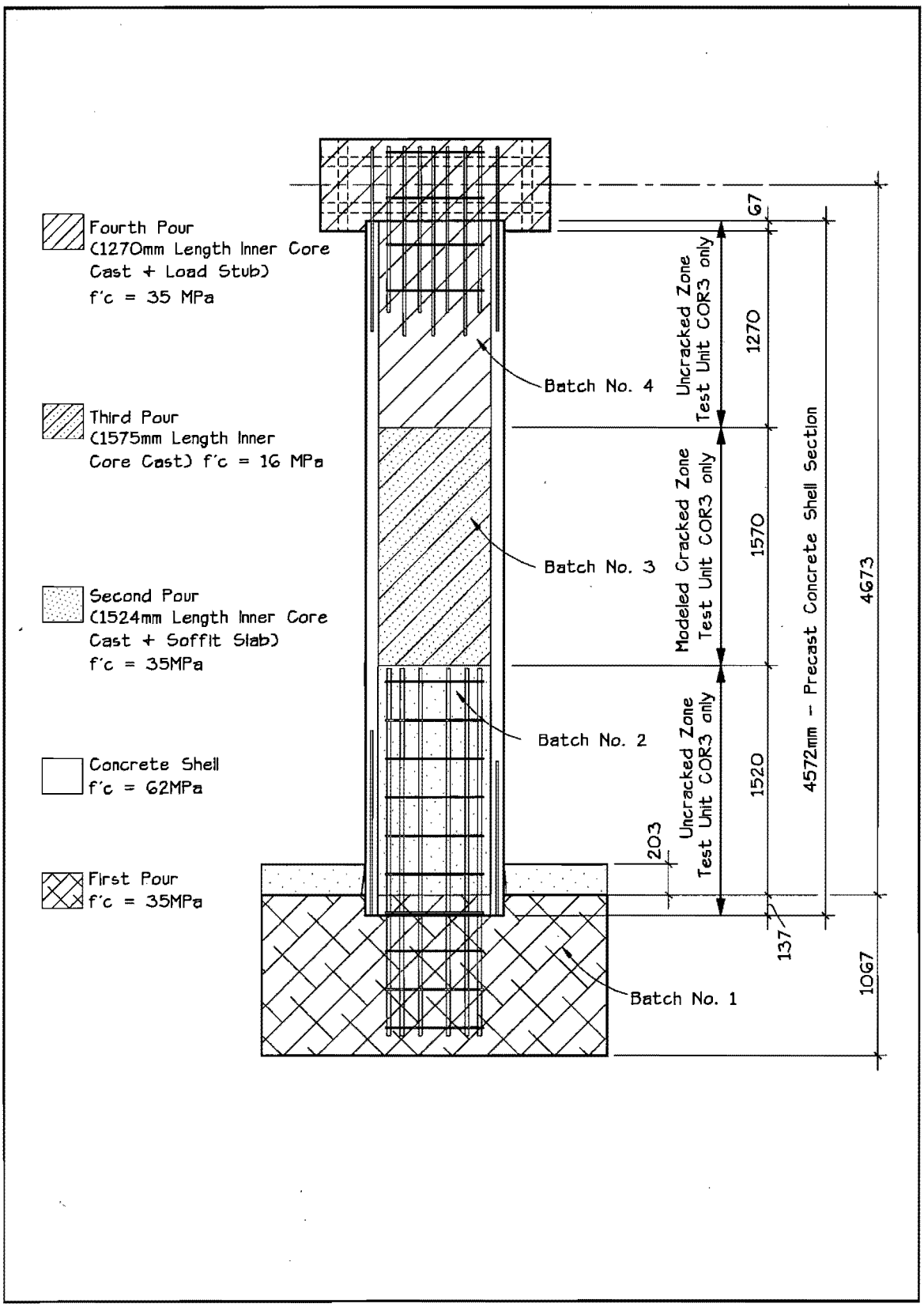

Fig. 3-29 Test Unit *COR3* Pile Layout - Concrete Material Properties

3.3 Instrumentation of the Test Specimens

In this research project each test unit was instrumented with different types of measuring devices. All instruments were connected to a high-speed data acquisition system controlled by software developed at UCSD. The data acquisition system was used to record data triggered by a predetermined force or displacement interval, whichever occurred first. Instrumentation of the test specimens consisted of linear potentiometers, rotation devices and electric resistance strain gages. In this section, a brief description of the instrumentation provided in the test specimens is provided.

3.3.1 Instrumentation of Test Unit *COR1* and *COR3*

In test Unit *COR1* and *COR3*, a total of 9 channels of electronically monitored instrumentation devices were installed in the specimen to measure deflection of the pile section and rotation of the pile cap, according to the summary presented in **Table 3-5**. The lateral deflection at the level of application of the lateral force, which corresponds to the center of the load stub, was recorded by a linear potentiometer, as shown in **Fig. 3-31** and **Fig. 3-32**. This linear potentiometer had a stroke of ±152.40 mm and was used to control the testing procedure according to a control program which will be discussed in later sections for each test unit.

Other instrumentation consisted of two linear potentiometers installed on the side of the load stub, according to **Fig. 3-32**. These linear potentiometers were used to monitor twisting and out-of-plane deformation of the pile section. During the testing procedure, these linear potentiometers were connected to the controller, which is the computer system used to control the application of loading into the specimen. When the recorded displacement difference between these two devices exceeded 25.40 mm, or the out-of-plane deflection of the load stub exceeded 25.40 mm, the controller would shut-off the hydraulic service manifold which feeds high-pressure hydraulic fluid to the actuators.

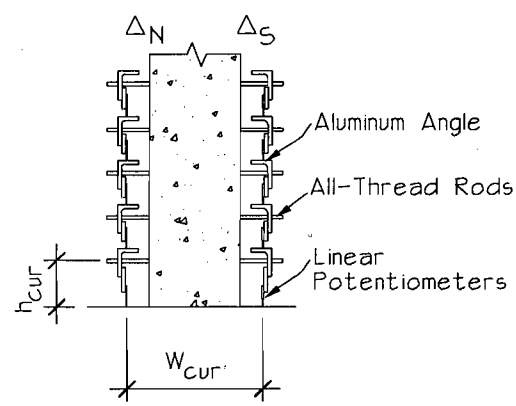

Fig. 3-30 Curvature Measurement

Curvatures along the pile height were experimentally determined from linear potentiometers positioned on both sides of the

pile section, as shown in **Fig. 3-31** and **Fig. 3-32**. Pairs of 9.53 mm all-thread rods were cast in the pile concrete shells during precasting at *Utility Vault* to support aluminum angles to which the linear potentiometers were attached. The linear potentiometers were placed on the extreme faces of the pile and were estimated according to the following expression:

$$\varphi_{ave} = \frac{\Delta_N - \Delta_S}{W_{cur}\ h_{cur}} \tag{3.1}$$

where φ_{ave} represent average computed curvature, Δ_N and Δ_S, are the relative vertical displacements between adjacent curvature rods in the extreme faces on opposite sides of the pile section, W_{cur} is the length of the curvature cell or horizontal distance between the pair of linear potentiometers and h_{cur} is the height of the curvature cell or vertical distance between the adjacent linear potentiometers.

One rotational device or inclinometer was installed on the load stub face opposite to the two linear potentiometers used to measure load stub deformations, as illustrated in **Fig. 3-31**. In addition, two rotational devices were installed on the pile cap faces, as shown in **Fig. 3-31**.

A total of three load cells were used during each test to measure application of vertical and lateral forces to the test specimen. Each of the three actuators, previously defined in Chapter 2, used to apply loading to the test specimen contained a calibrated load-cell.

In addition, in test unit *COR3,* 8 linear potentiometers were positioned along the saw cuts, as illustrated in **Fig. 3-33**, to measure the width opening of these cuts during the testing procedure. Moreover, at the base of the pile section of test unit *COR3,* 16 electric resistance strain gages, produced by Tokyo Sokki Kenkyujo Co., Ltd, were installed over the concrete surface as illustrated in **Fig. 3-33**. These strain gages had a gage length of 5 mm and a gage resistance of 120±0.3Ω with a scale factor of 2.13.

A summary of the instrumentation applied on the reinforcement of test units *COR1* and *COR3* is presented in **Table 3-5**. Instrumentation of the reinforcement consisted of electric resistance strain gages produced by Tokyo Sokki Kenkyujo Co., Ltd. These strain gages had a gage length of 5 mm and a gage resistance of 120±0.3Ω with a scale factor of 2.13. A total of 32 strain gages were applied on the pile inner core longitudinal reinforcement according to **Fig. 3-34**. The prestressing strands were instrumented with 32 strain gages, according to the layout presented in **Fig. 3-35**. In addition, the concrete shells spiral cages

were instrumented also with 32 strain gages, as illustrated in **Fig. 3-36**. Moreover, 26 strain gages were applied on the top and bottom pile cap reinforcement, according to **Fig. 3-37** and **Fig. 3-38**, and 8 strain gages were applied on the pile cap vertical reinforcement, according to **Fig. 3-39**.

During the precasting operation while at *Utility Vault*, 16 strain gages were applied on the exposed surface of the concrete shells while inside the casting bed, as illustrated in **Fig. 3-40** to record transfer of forces from the prestressing strands to the concrete section after transfer during a time interval of approximately 48 hours.

A total of 64 data channels were used in the instrumentation of test units *COR1* and *COR3* during manufacturing of the precast concrete shells, according to **Table 3-4**. During the testing procedure, 163 data channels were used in the instrumentation of test unit *COR1*, and 187 data channels were used in the instrumentation of test unit *COR3*, as indicated in **Table 3-5**.

Table 3-4 Test Unit *COR1* and *COR3*- Casting Operation Summary of Instrumentation

Strain Gages	Concrete Shell Prestressing Strands	24	
	Concrete Shell Transverse Reinforcement	24	
	Concrete Surface Gages - Precasting Only	16	
	Total		64
	TOTAL INSTRUMENTATION		64

Table 3-5 Test Unit *COR1* and *COR3*- Testing Procedure Summary of Instrumentation

Displacement Gages	Pile Lateral Deflection Pile Cap Uplift Soffit Slab Load Stub - Control Program Saw Cuts - Test Unit *COR3* only	1 4 2 2 8	
	Test Unit *COR1* - Total **Test Unit *COR3* - Total**		9 17
Curvature Gages	Pile		18
Rotation Gages	Load Stub Pile Cap	1 2	
	Total		3
Strain Gages	Pile Inner Core Longitudinal Reinforcement Concrete Shell Prestressing Strands Concrete Shell Transverse Reinforcement Pile Cap Longitudinal Reinforcement Pile Cap Transverse Reinforcement Pile Cap Vertical Reinforcement Base pile section Concrete Surface Gages - Test Unit *COR3* only	32 32 32 18 8 8 16	
	Test Unit *COR1* - Total **Test Unit *COR3* - Total**		130 146
Load Cells	Actuators **Total**		3
	TEST UNIT *COR1* - TOTAL INSTRUMENTATION **TEST UNIT *COR3* - TOTAL INSTRUMENTATION**		163 187

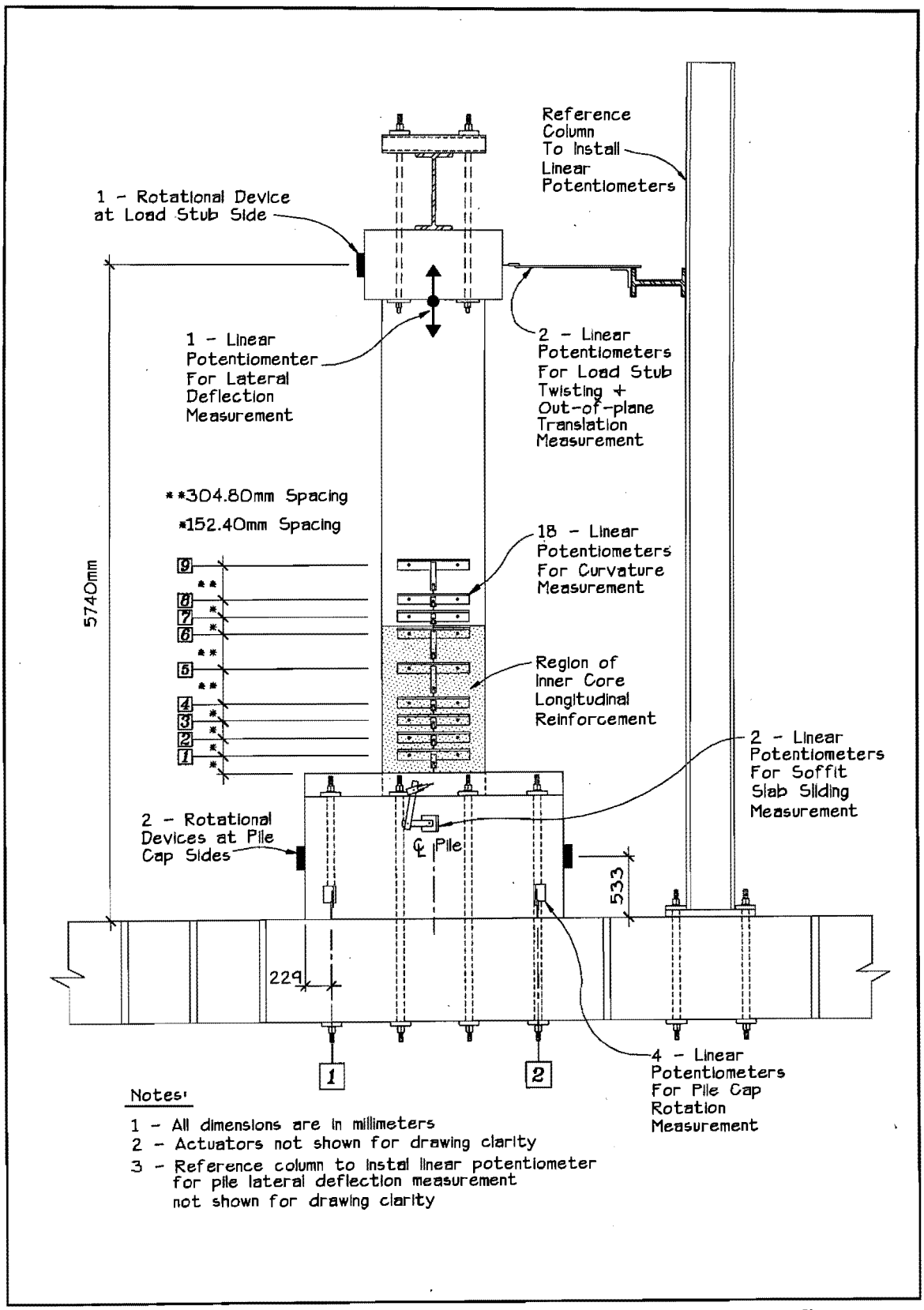

Fig. 3-31 Test Units *COR1* and *COR3* - Instrumentation Setup Front View

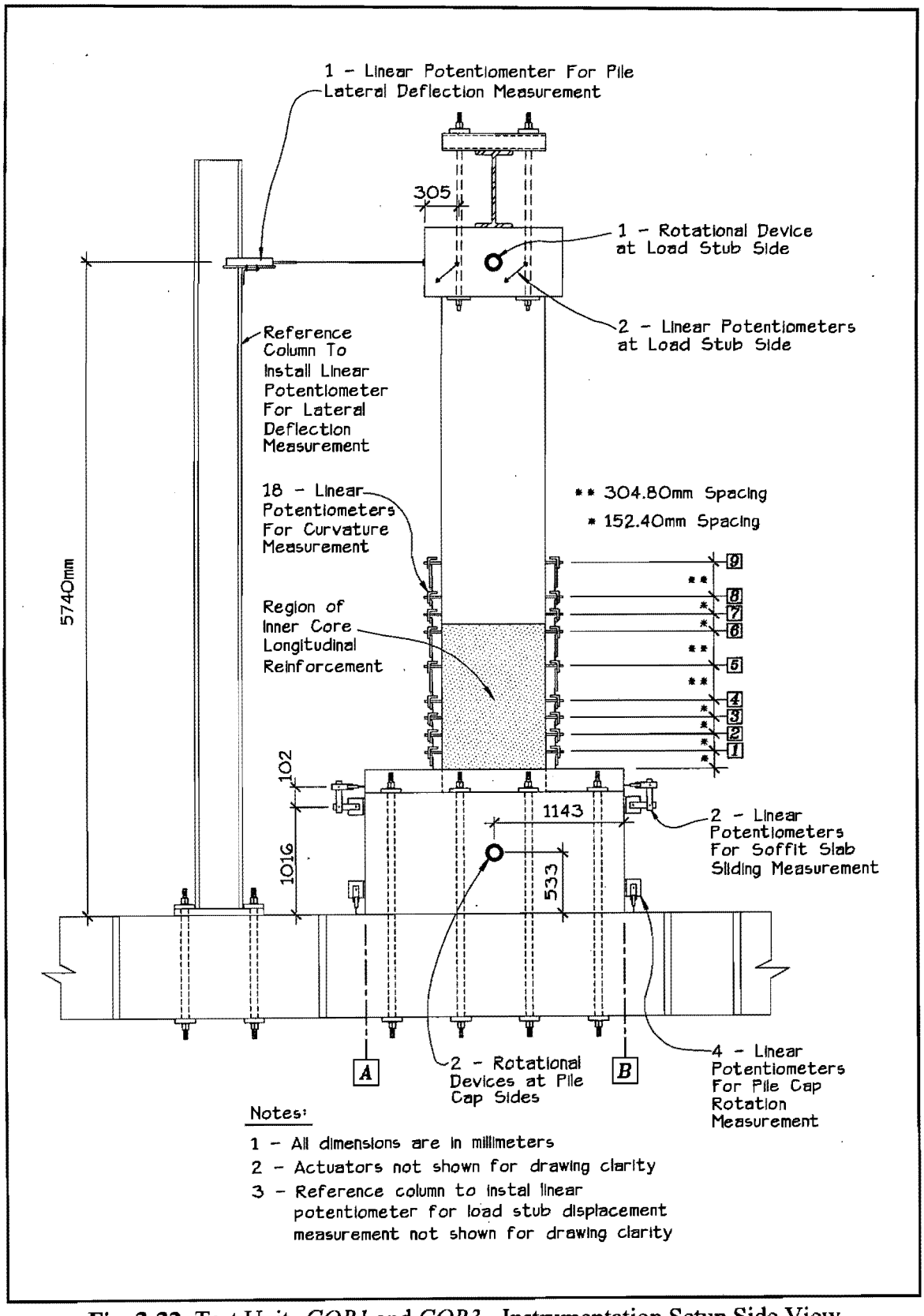

Fig. 3-32 Test Units *COR1* and *COR3* - Instrumentation Setup Side View

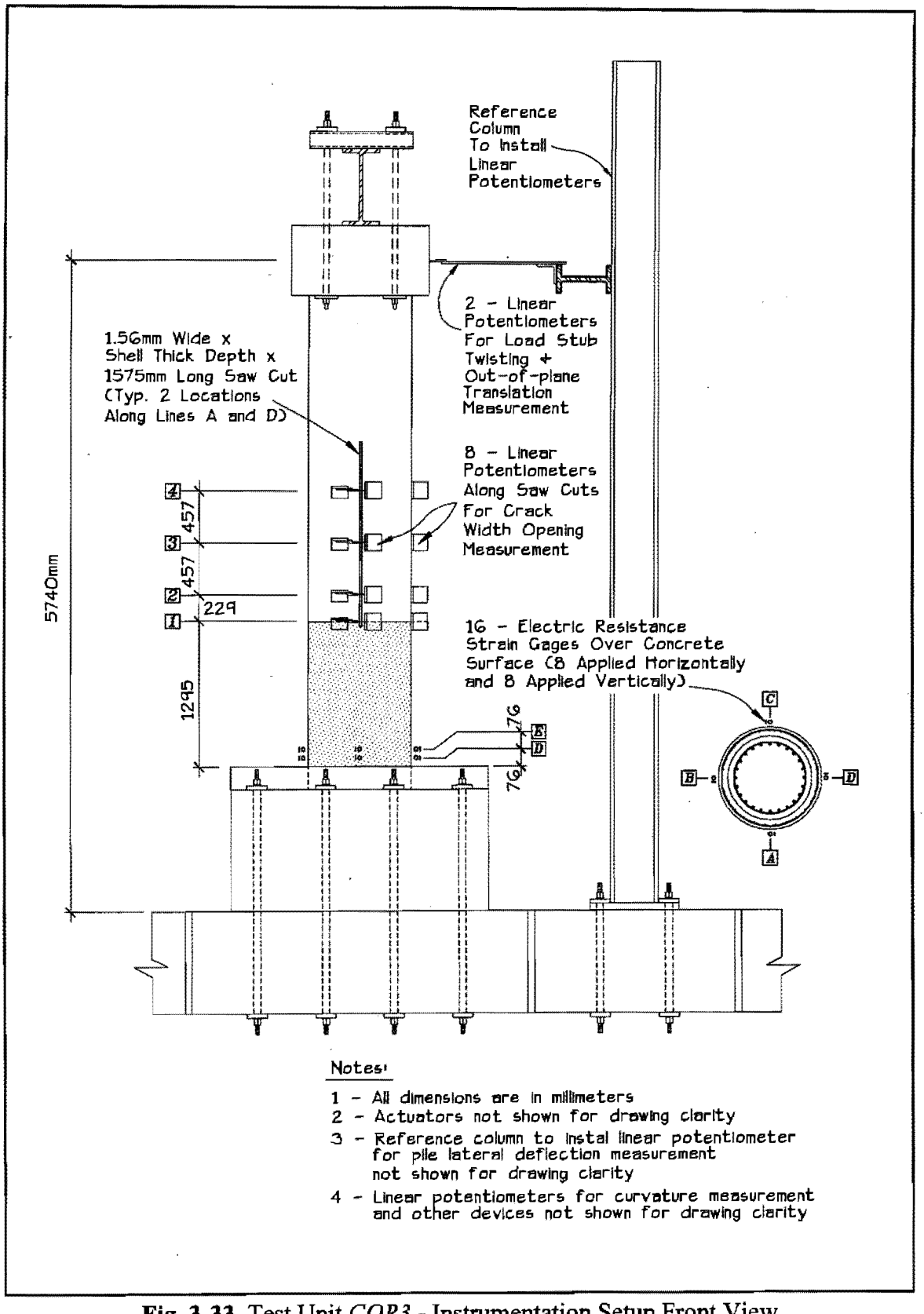

Fig. 3-33 Test Unit *COR3* - Instrumentation Setup Front View

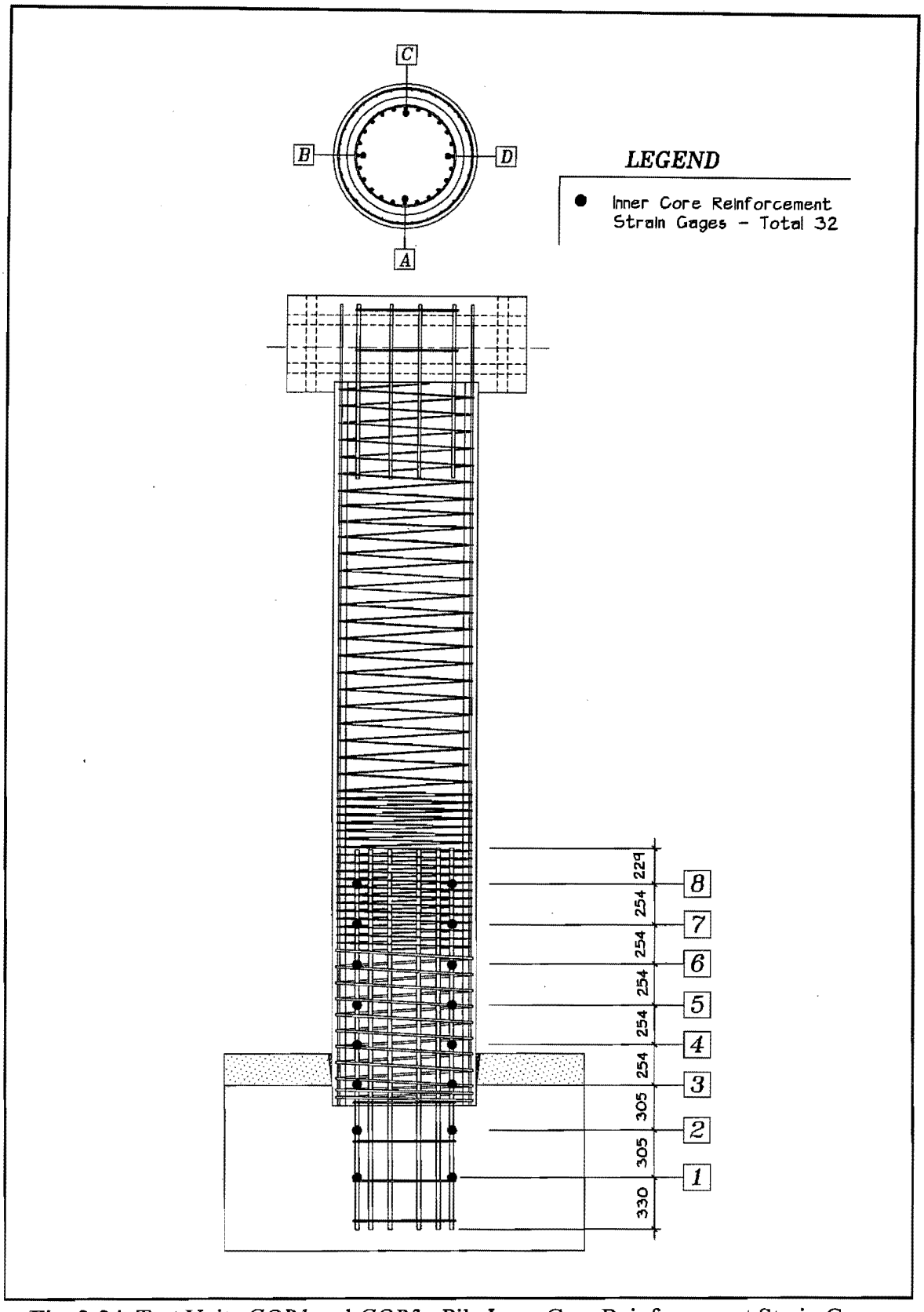

Fig. 3-34 Test Units *COR1* and *COR3* - Pile Inner Core Reinforcement Strain Gages

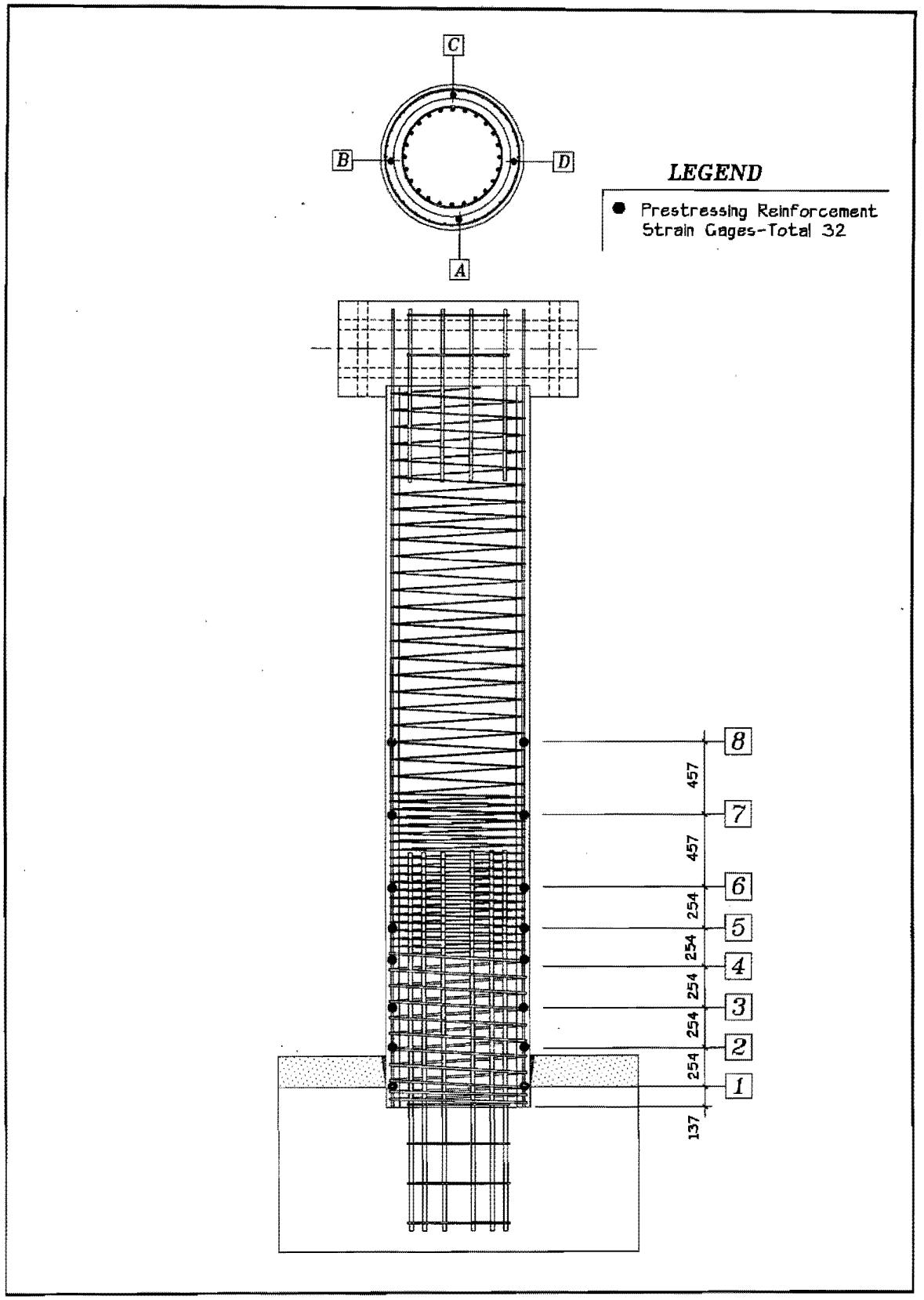

Fig. 3-35 Test Units *COR1* and *COR3* - Pile Prestressing Reinforcement Strain Gages

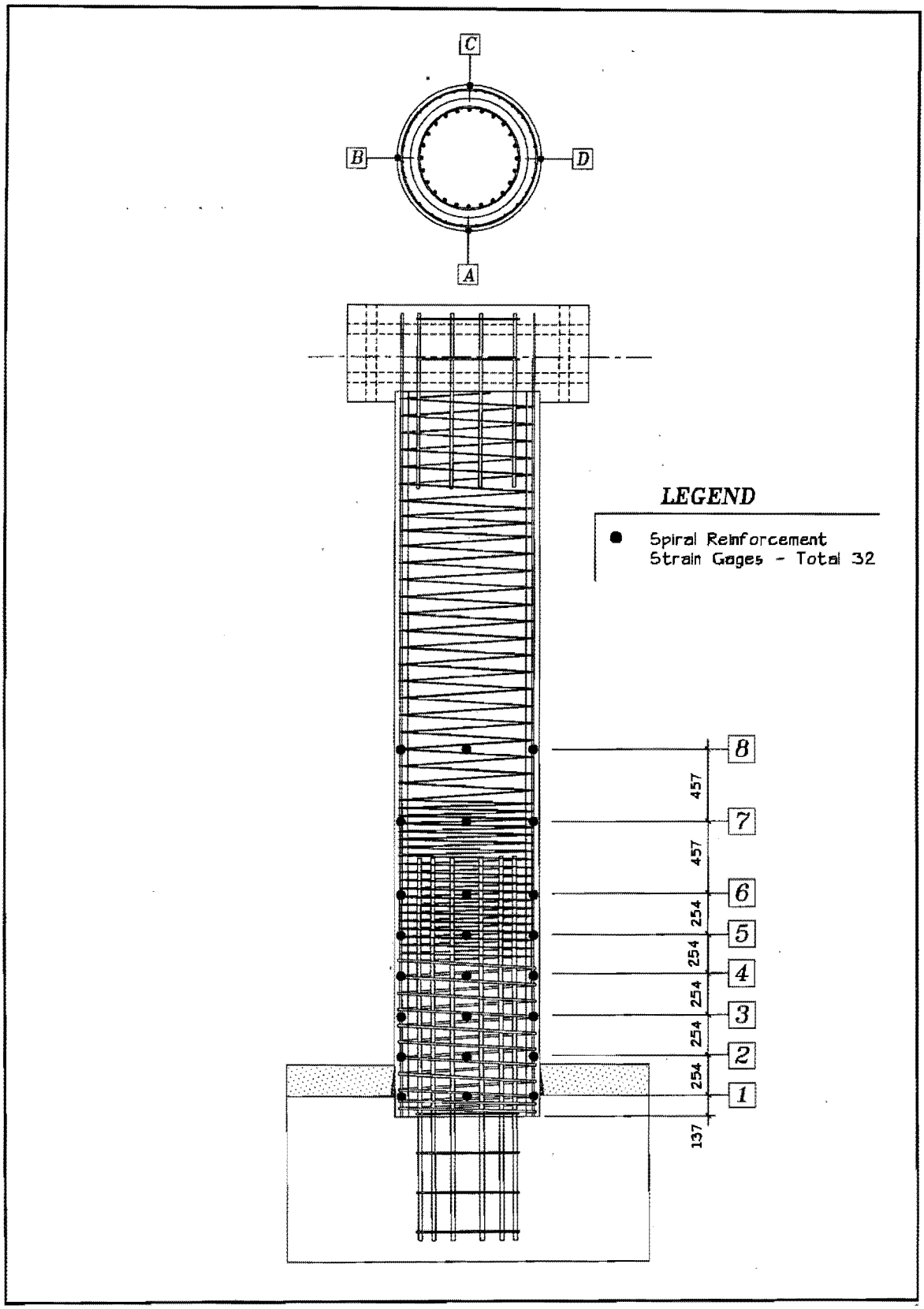

Fig. 3-36 Test Units *COR1* and *COR3* - Pile Transverse Reinforcement Strain Gages

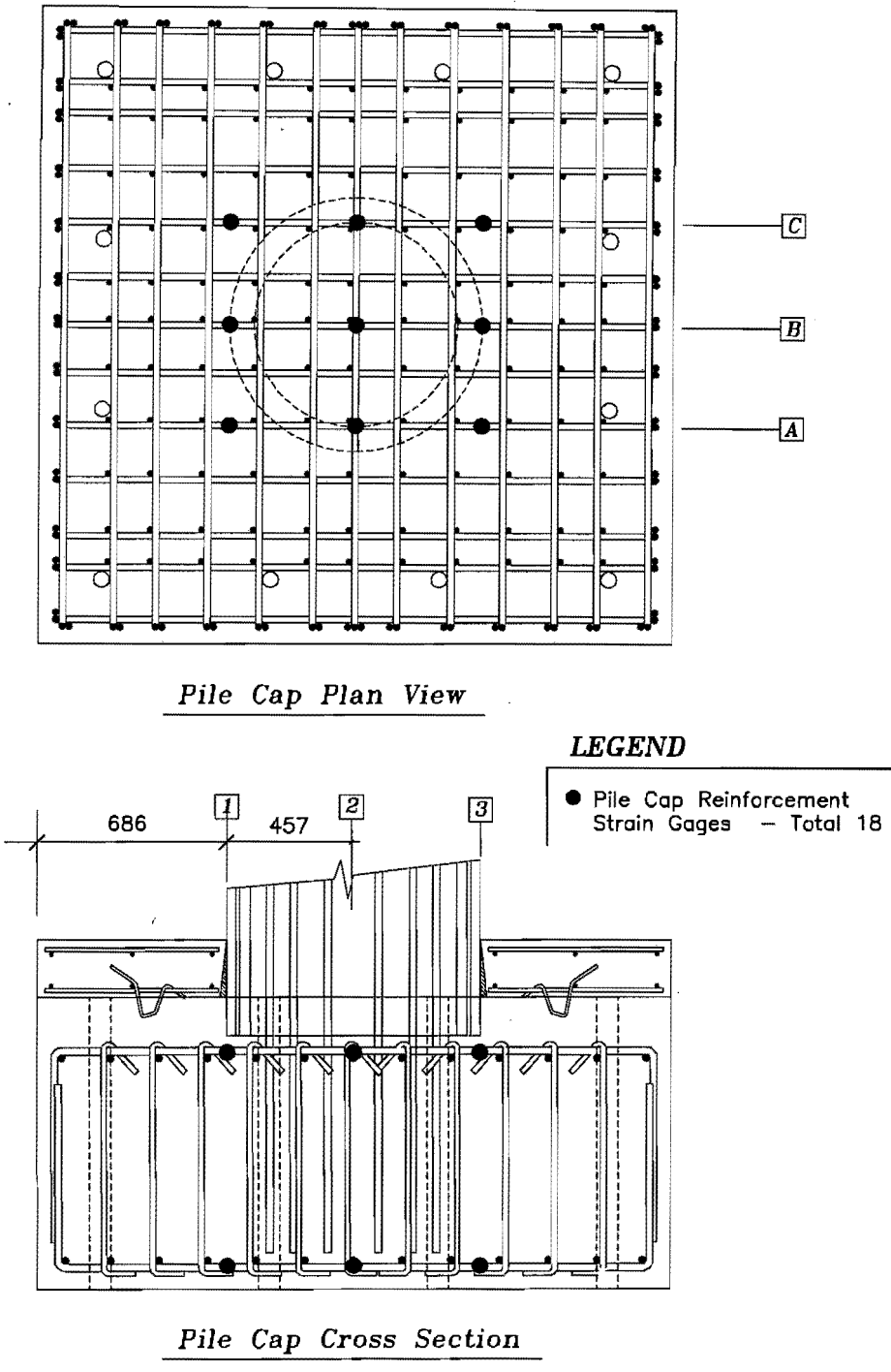

Fig. 3-37 Test Units *COR1* and *COR3* - Pile Cap Reinforcement Strain Gages

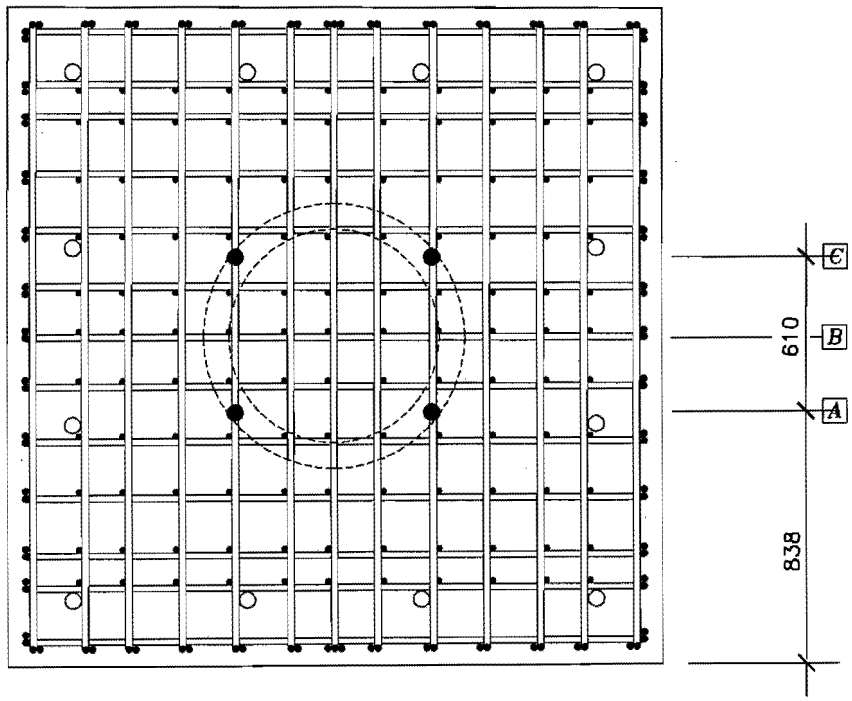

Pile Cap Plan View

LEGEND

● Pile Cap Reinforcement Strain Gages – Total 8

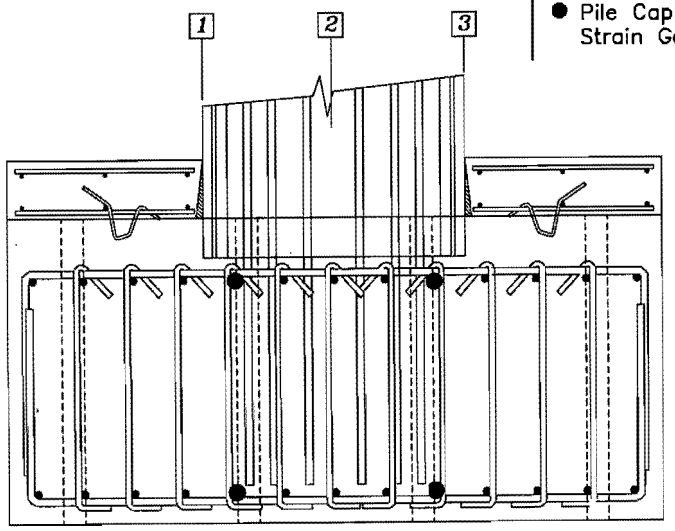

Pile Cap Cross Section

Fig. 3-38 Test Units *COR1* and *COR3* - Pile Cap Reinforcement Strain Gages

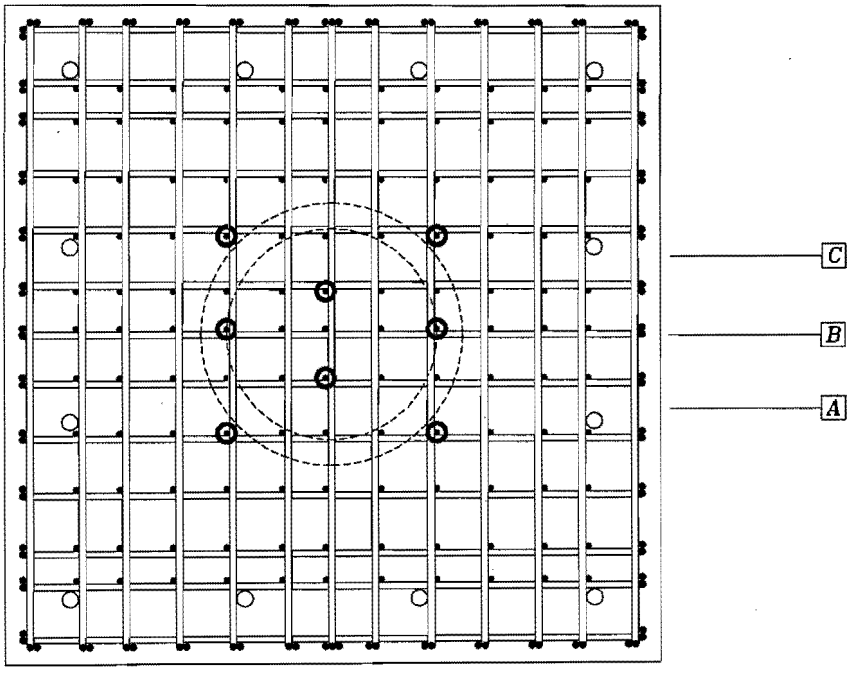

Pile Cap Plan View

LEGEND

● Pile Cap Stirrups Strain Gages – Total 8

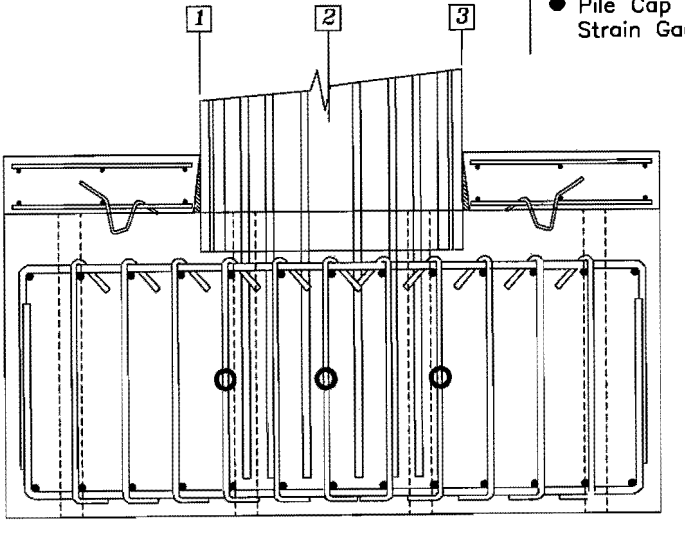

Pile Cap Cross Section

Fig. 3-39 Test Units *COR1* and *COR3* - Pile Cap Reinforcement Strain Gages

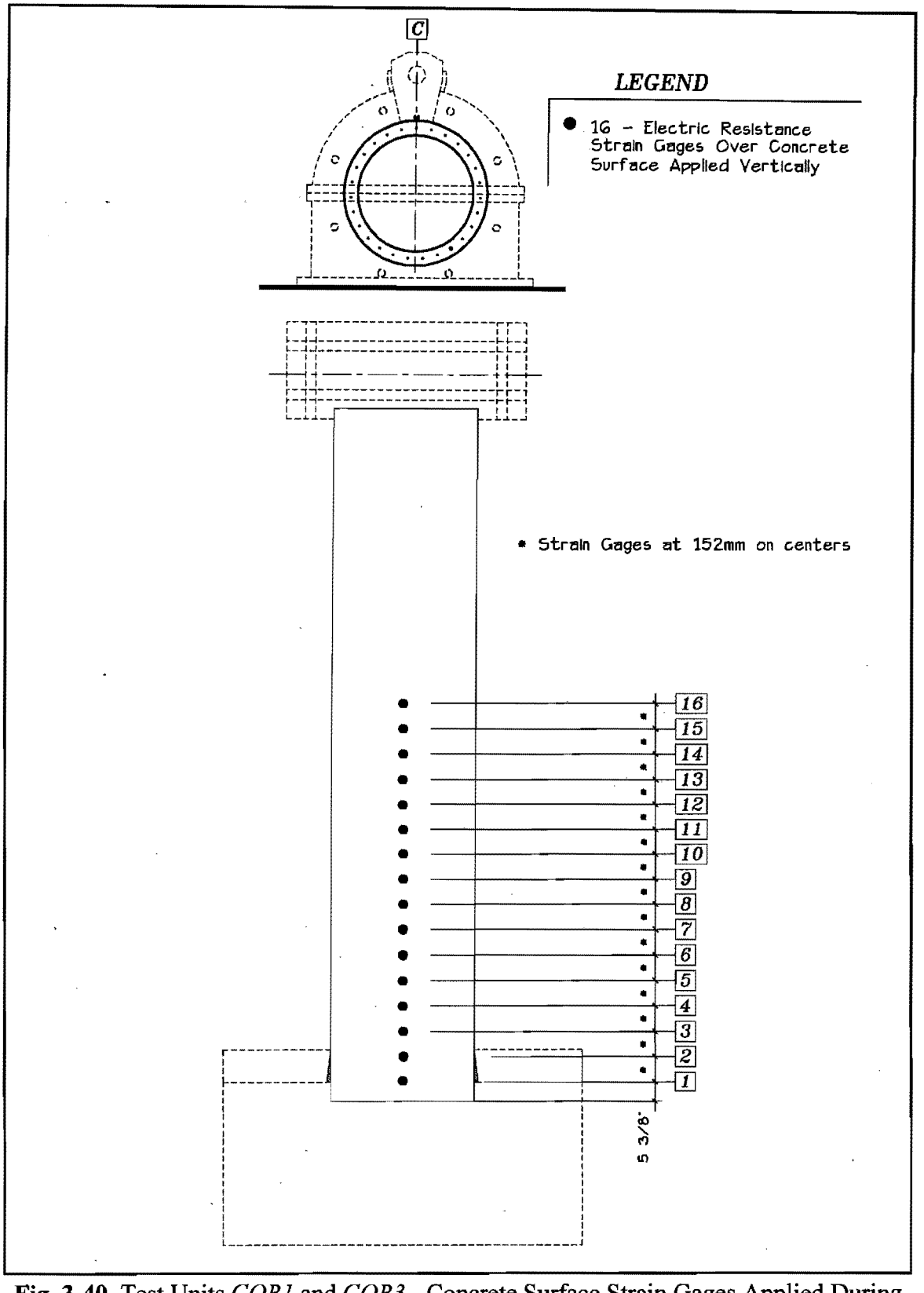

Fig. 3-40 Test Units *COR1* and *COR3* - Concrete Surface Strain Gages Applied During Manufacturing of Precast Concrete Shells

3.3.2 Instrumentation of Test Unit *COR2*

Similar to test units *COR1* and *COR3*, in test unit *COR2* the same amount of linear potentiometers were installed in the test specimen according to the summary presented in **Table 3-6**. In test unit *COR2*, a total of 9 channels of electronically monitored instrumentation were installed in the specimen to measure the horizontal displacement of the pile section and uplift of the pile cap, as shown in **Fig. 3-41** and **Fig. 3-42**. As before, one of these linear potentiometers was used to measure the pile section lateral deflection. Other instrumentation consisted of four linear potentiometers to measure uplift of the pile cap as a result of the imposed overturning moment. Moreover, two linear potentiometers were installed on the sides of the load stub to monitored twisting and out of plane deformation of the pile section, as illustrated in **Fig. 3-41** and **Fig. 3-42**. During the testing procedure, these two linear potentiometers were connected to the controller to monitor twisting and out of plane deformation of the pile section. In case the relative difference between these two devices exceeded 25.40 mm, or the total out of plane deflection exceeded also 25.40 mm, the controller would cause dumping of the hydraulic fluid to the actuators, as established earlier, while discussing test unit *COR1* and *COR3* instrumentation layout.

In addition, 14 linear potentiometers were installed on the sides of the pile section according to **Fig. 3-43**, to estimate the shear component of deformation according to the equations presented in **Fig. 3-44**.

A summary of strain gages applied on the reinforcement of test unit *COR2* is presented in **Table 3-6**. A total of 32 strain gages were applied to test unit *COR1* pile inner core longitudinal reinforcement, according to the setup illustrated in **Fig. 3-45**. In addition, 32 gages were applied on the concrete shell prestressing strands, shown in **Fig. 3-46**, and the concrete shell spiral cage was instrumented with 32 gages, according to **Fig. 3-47**. Moreover, 16 strain gages were applied on the concrete shell, as indicated in **Fig. 3-48**, to monitor transfer of forces from the prestressing strands to the concrete shell during cutting of the strands.

Similar to test unit *COR1* and *COR3*, in test unit *COR2* the top and bottom pile cap longitudinal and vertical reinforcement was instrumented with 34 strain gages with the layout shown in **Fig. 3-37** through **Fig. 3-39**.

As before, a total of 64 data channels were used in the instrumentation of test unit *COR2* during manufacturing of the precast concrete shells, according to **Table 3-4**. During the testing procedure 175 data channels were used in the instrumentation of test unit *COR2* as indicated in **Table 3-6**.

Table 3-6 Test Unit *COR2* - Summary of Instrumentation

Displacement Gages	Pile Lateral Deflection Pile Cap Uplift Soffit Slab Load Stub - Control Program	1 4 2 2	
	Total		9
Shear Panel Deformation	Vertical Horizontal Diagonal	8 2 4	
	Total		14
Curvature Gages	Pile		16
Rotation Gages	Load Stub Pile Cap	1 2	
	Total		3
Strain Gages	Pile Inner Longitudinal Reinforcement Concrete Shell Prestressing Strands Concrete Shell Transverse Reinforcement Pile Cap Longitudinal Reinforcement Pile Cap Transverse Reinforcement Pile Cap Vertical Reinforcement	32 32 32 18 8 8	
	Total		130
Load Cells	Actuators **Total**		3
		TOTAL INSTRUMENTATION	175

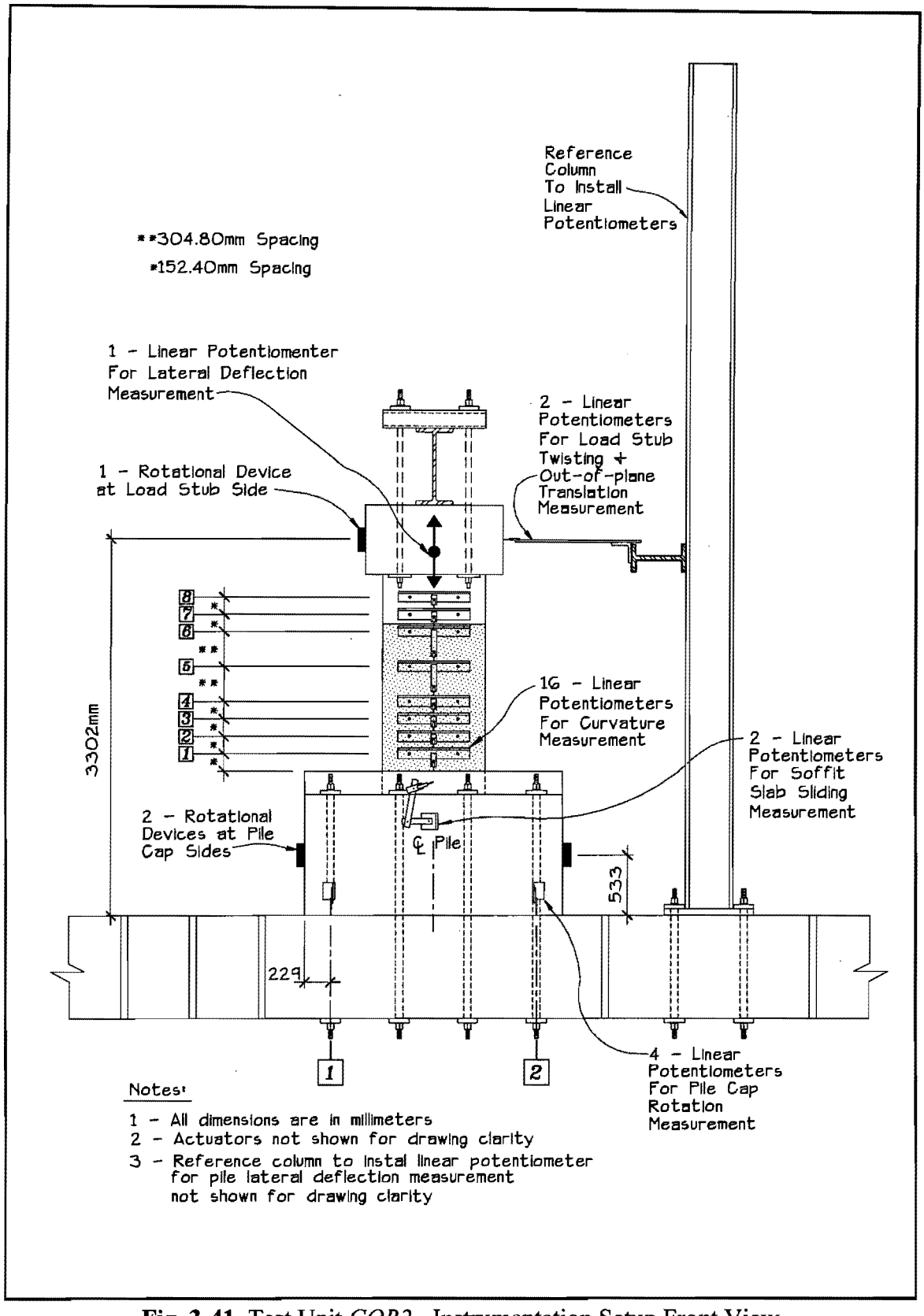

Fig. 3-41 Test Unit *COR2* - Instrumentation Setup Front View

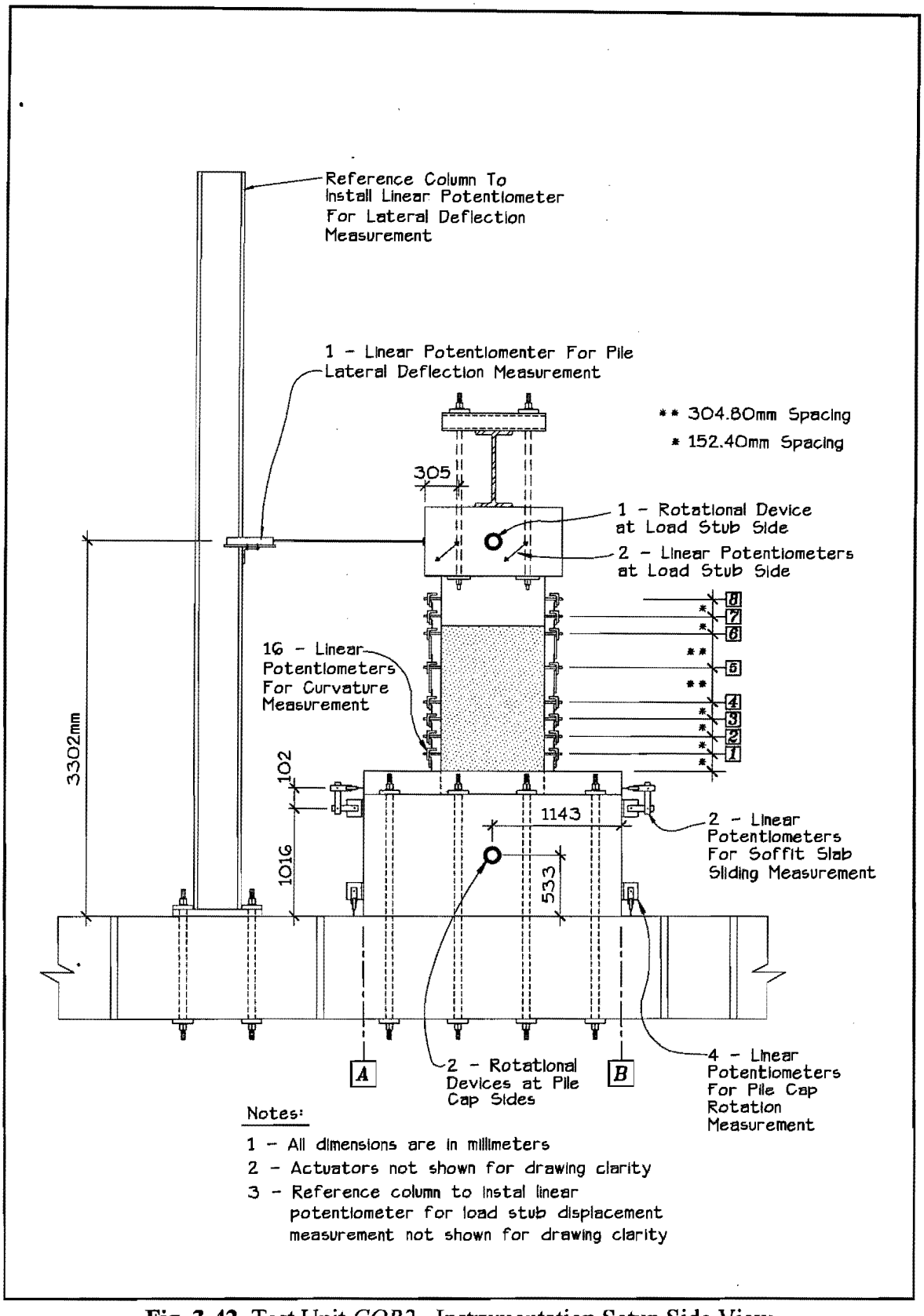

Fig. 3-42 Test Unit *COR2* - Instrumentation Setup Side View

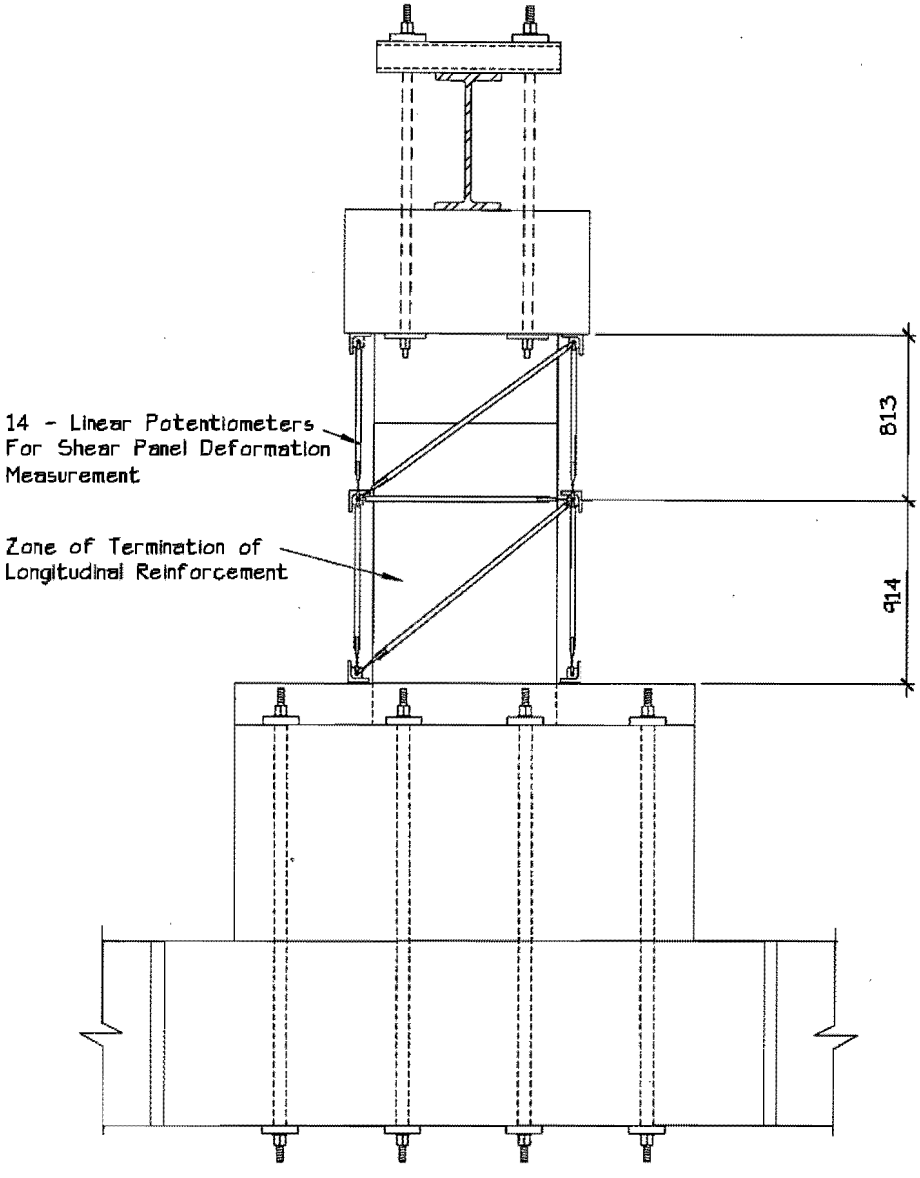

Notes:

1 - All dimensions are in millimeters
2 - Actuators not shown for drawing clarity
3 - Reference column to instal linear potentiometer for pile lateral deflection measurement not shown for drawing clarity
4 - Linear potentiometers for curvature measurement and other devices not shown for drawing clarity

Fig. 3-43 Test Unit *COR2* - Shear Panel Deformation Instrumentation Layout

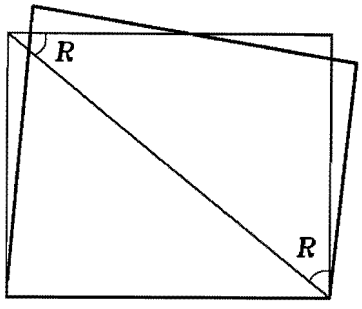

(a) Overall Deformation

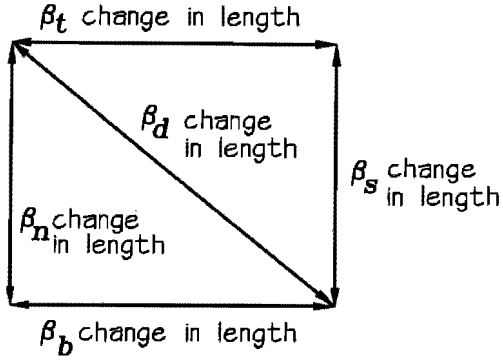

(b) Measured Deformations

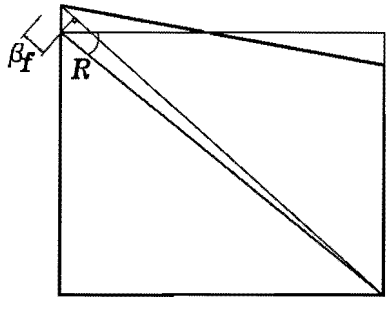

(c) Flexural Deformation

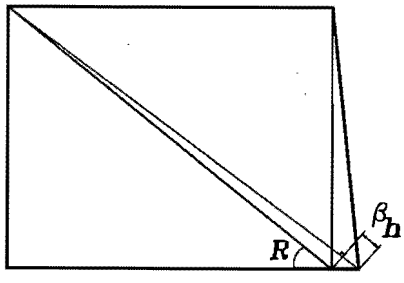

(b) Horizontal Deformation Due to Cracks

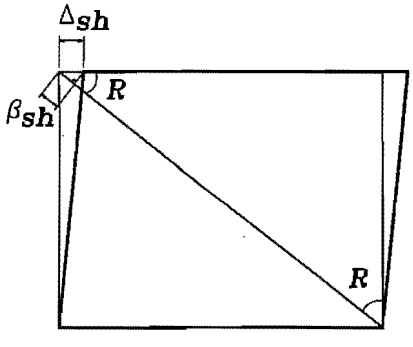

(e) Shear Deformation

$\beta_{sh} = \beta_d - \beta_f - \beta_h$

and hence : $\Delta_{sh} = \beta_{sh} / \cos R$

where : $\beta_f = \{(\beta_n + \beta_s)/2\} \sin R$

and : $\beta_h = \{(\beta_t + \beta_b)/2\} \cos R$

Fig. 3-44 Test Unit *COR2* - Estimation of Shear Deformation

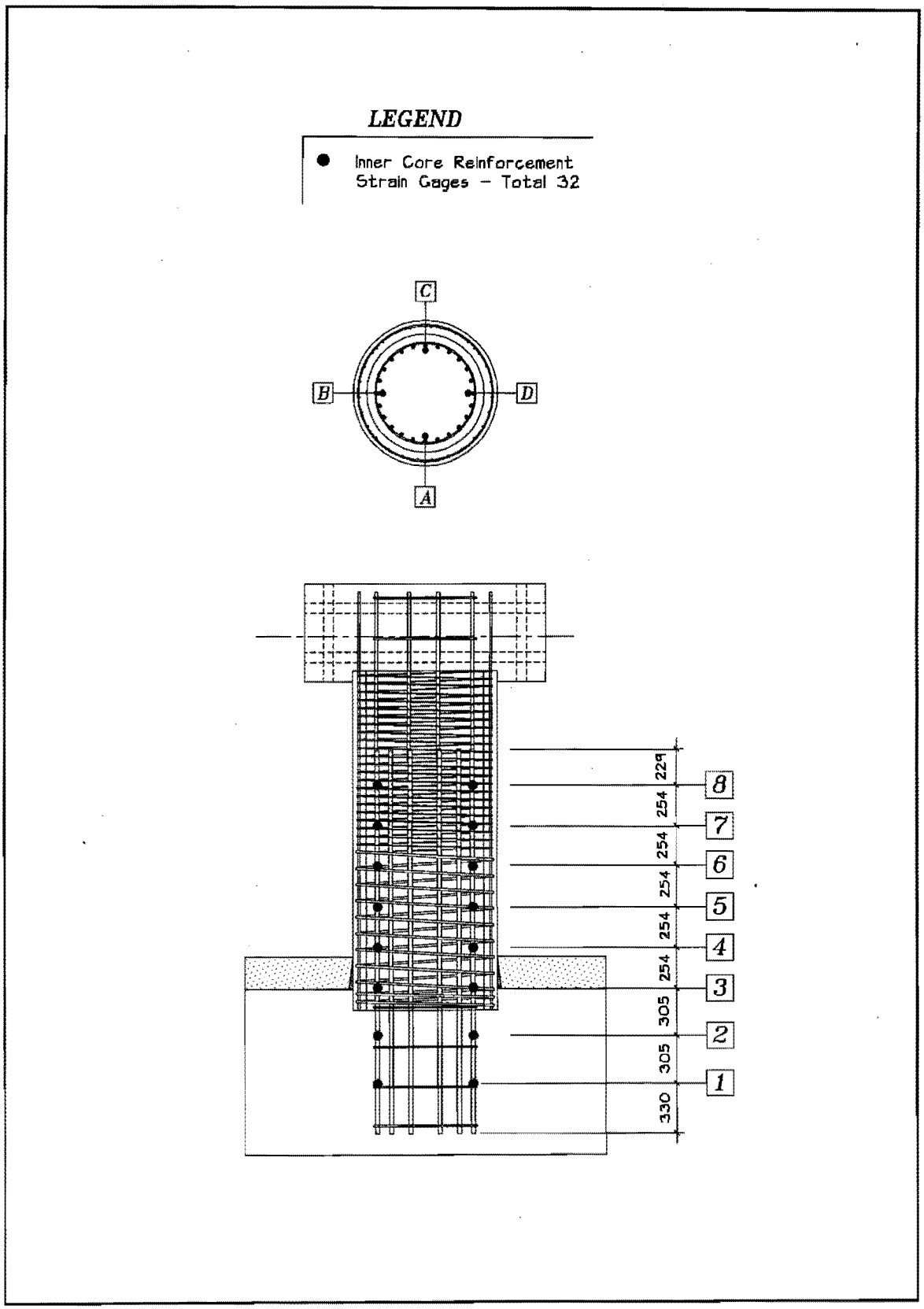

Fig. 3-45 Test Unit *COR2* - Pile Inner Core Reinforcement Strain Gages

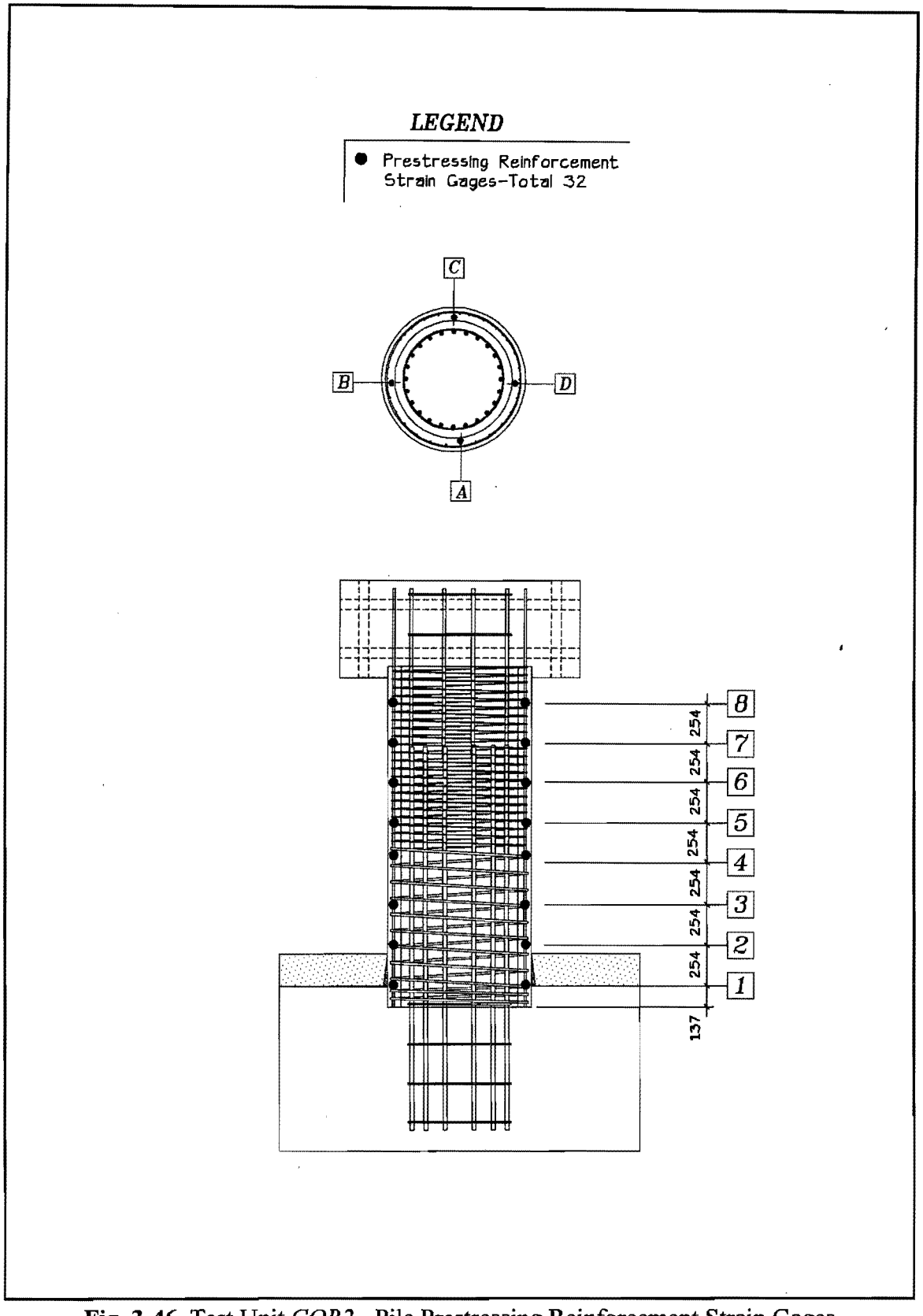

Fig. 3-46 Test Unit *COR2* - Pile Prestressing Reinforcement Strain Gages

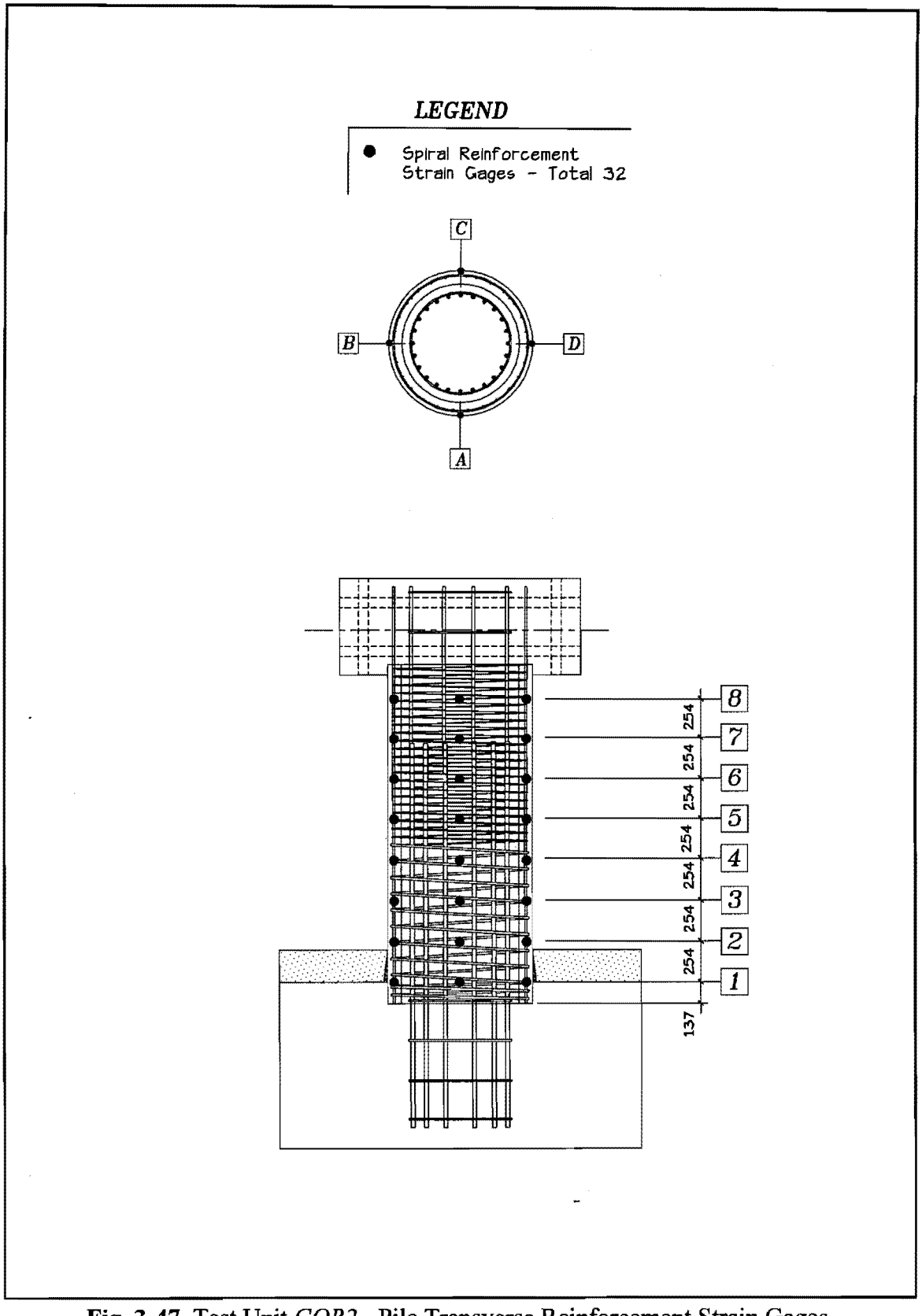

Fig. 3-47 Test Unit *COR2* - Pile Transverse Reinforcement Strain Gages

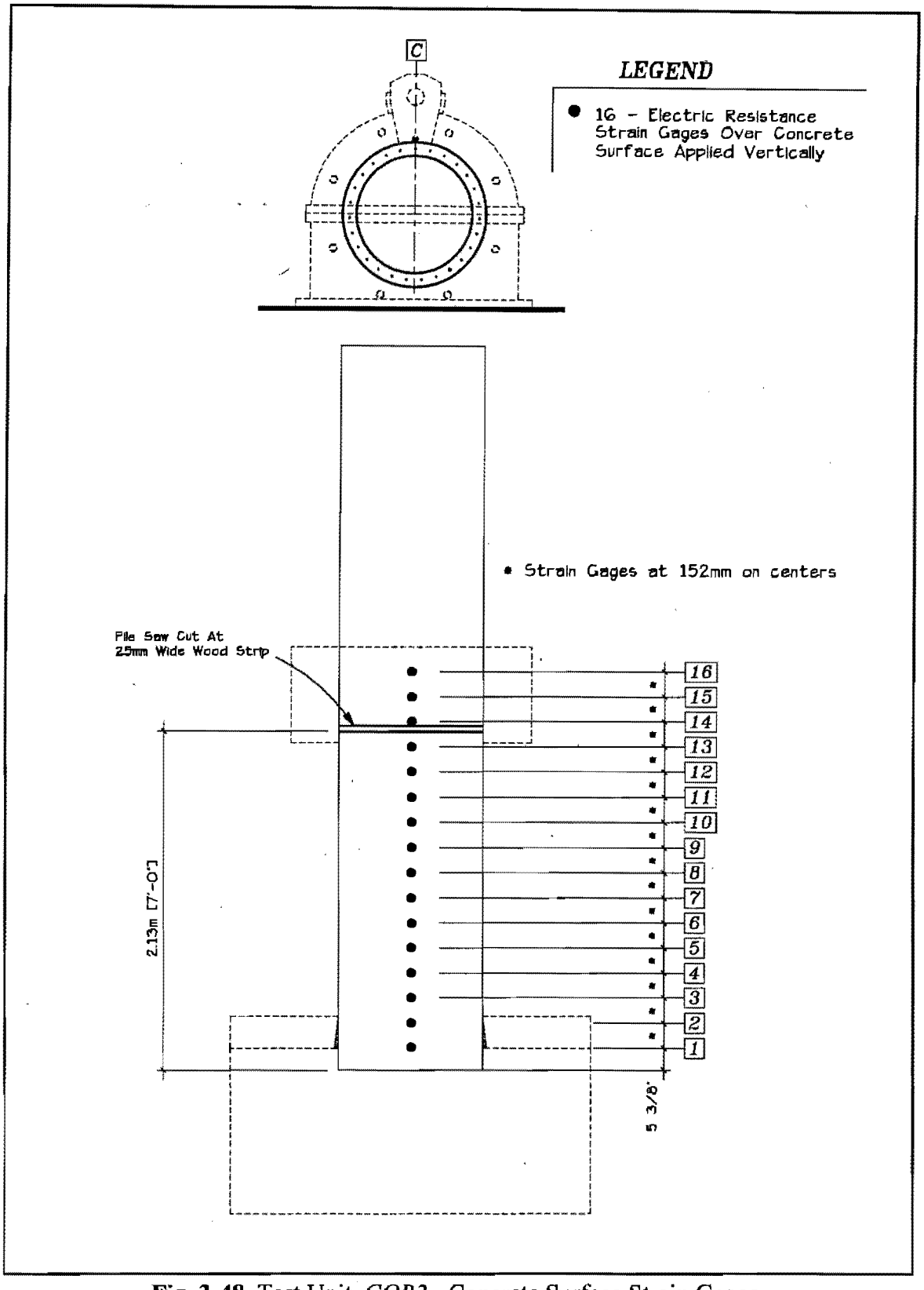

Fig. 3-48 Test Unit *COR2* - Concrete Surface Strain Gages Applied During Manufacturing of Precast Concrete Shells

3.4 Testing Procedure

Analysis of the prototype foundation system to seismic loading was conducted to develop the loading scheme to be implemented in the testing procedure. During a seismic event, individual piles of a pile group experience reversed cyclic loading in both axial and lateral loads as a result of deformations of the pile cap. The cyclic axial and lateral loads imposed on the pile section depend on the loads transferred from the bridge superstructure and column into the pile cap and, subsequently, into the pile group. Thus, a correlation between the axial and the lateral loads imposed on an extreme pile of a pile group, as shown in **Fig. 2-1** and **Fig. 2-3**, under seismic loading, was obtained from a 3-D nonlinear finite element analysis of the prototype structure.

Correlation between the axial and lateral load depends directly on soil properties such as soil stiffness and mud line elevation, number of piles in the pile group, spacing of piles in the direction of seismic loading, pile material properties and transferred column shear and axial loads. The response of pile groups to seismic loading is directly related to the soil properties. Under the imposed lateral and axial loads transferred from the bridge superstructure, the pile cap translates and/or rotates in the direction of the applied lateral load according to the stiffness of the underlying soil stratum. In the presence of a considerably dense soil, the pile cap is inhibited from translating and to provide the necessary resisting moment to the imposed overturning moment (see **Fig. 3-49**) the pile cap tries to rotate in order to develop resisting forces at the pile heads. As the pile cap rotates, piles at the edges of the pile group will be loaded in tension or compression depending on their position relative to the axis of rotation. On the other hand, in the presence of a considerably soft soil, lateral translation is the pile cap primary mode of deformation and minimum resistive axial forces are developed in the piles and the resisting moment is primarily in terms of moments developed at the pile heads.

Lateral loads imposed on the piles may be expressed in terms of the following expression:

$$\Delta_{cap} = \frac{V_C - V_{fr}}{\sum_{i=1}^{n_p} \left(f(KB_p)_i + f(K_s)_i \right)} \tag{3.2}$$

Where V_{fr} is the force which develops due to the pile cap overcoming the passive pressure along the side of the pile cap and/or friction along the bottom of the cap in contact with the soil

Development of equation **(3.2)** assumes that the lateral translation, Δ_{cap}, is the same in all the piles and the summation of stiffness is c mputed for all the piles in the pile group where n_p is the number of piles in a pile group. Functions $f(KB_{pile})$ and $f(K_{sh})$ identify the pile section bending stiffness and soil stiffness, respectively, recognizing that pile and soil stiffness change along the pile length. Based on this expression, it can be recognized that as the soil stiffness decreases, an increase in the pile cap lateral translation occurs, and in the presence of a soil stratum with zero stiffness in the proximity of the pile cap, expression **(3.2)** converts to that of a section with an applied point load and no support from the soil stratum.

An expression to determine the pile cap rotation may be expressed in terms of the overall column overturning forces and resisting moments developed at the pile heads given by the expression:

$$\theta_{cap} = \frac{OTM_c - \sum_{i=1}^{n_p} \left(V_{P_i} f(l_{eff}, \frac{1}{f(K_s)})_i \right)}{\sum_{i=1}^{n_p} \left(f(KA_p)_i L_i^2 \right)} \tag{3.3}$$

Development of equation **(3.3)** assumes the pile cap rotates as a rigid body and rotation of the pile cap, θ_{cap}, produces equal rotations in all pile heads. The contribution of the bending moment present in the pile heads to the overall resisting moment is approximately given by the summation for all piles of the respective shear force, V_p, times the pile effective cantilever length, l_{eff}, which is related to a function inversely proportional to the soil stiffness, $1/f(K_s)$. This expression also describes that the pile cap rotation is inversely proportional to the axial stiffness of the pile section given by the function $f(KA_p)$ and the distance square L_i of the pile section to the center of the pile cap. Based on this expression, it can be recognized that as the soil stiffness decreases or the mud line elevation increases, the effective cantilever length increases and, as a result, a decrease in the pile cap rotation is expected, as previously noted. On the other hand, as the soil stiffness increases, the effective cantilever length decreases and an increase in the pile cap rotation is expected. This analysis of the pile cap indicates that the loading path which correlates the axial load and moment on the corner piles is closely related to the stiffness of the soil stratum and mud line elevation.

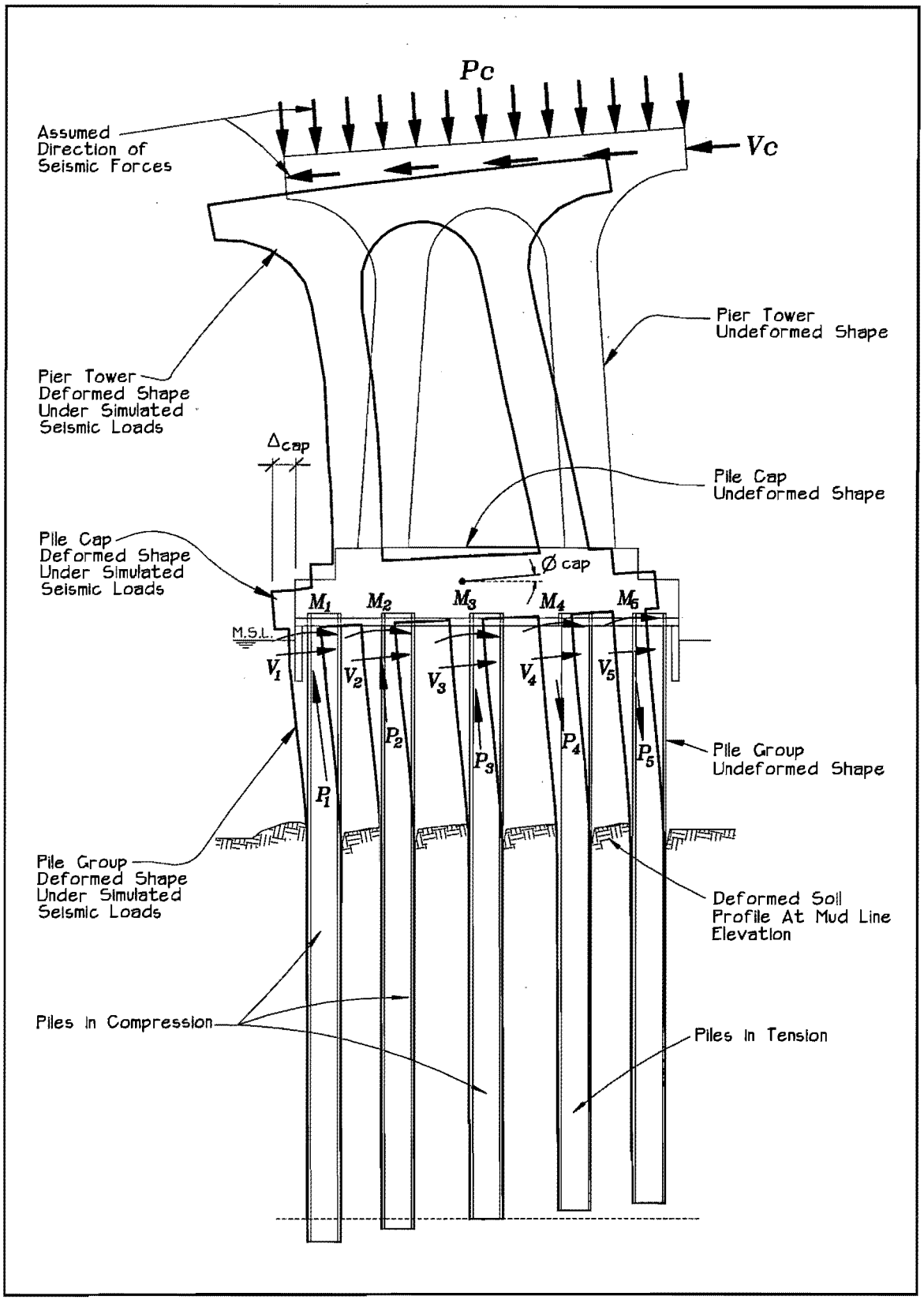

Fig. 3-49 Prototype Structure Deformed Shape

The finite element analysis program *COSMOS/M* **[16]** was used to implement the prototype structure finite element model to study the behavior of a pile group under lateral and axial load. **Fig. 3-50** and **Fig. 3-51** presents the finite element model that was used to analyze the prototype structure at Pier 2 and Pier 5, respectively, and were based on the prototype structure dimensions presented in **Fig. 2-1** through **Fig. 2-6**.

The finite element model used to study the response of the prototype structure under simulated seismic loading was set up by using approximate transformed section nonlinear piecewise elastic material model properties for modeling the column, the pile cap, and the piles of the prototype structure. Four-node quadrilateral thick shell elements with membrane and bending capabilities were used to model the pile cap and bridge column. This element type is defined with the element name *SHELL4T* in the users guide for *COSMOS/M*. The piles were modeled using two-node uniaxial element for three dimensional structural models with axial and bending capabilities. This element type is defined with the element name *BEAM3D* in the users guide for *COSMOS/M*. Finally, the soil was modeled with linear elastic springs elements in the form of a Winkler idealization of soil properties, described previously in Chapter 2. Modeling of the soil elements was performed by employing a two-node uniaxial element with only axial capabilities. This element type is defined with the element name *SPRING* in the users guide for *COSMOS/M*.

The nonlinear material properties of concrete for the pile cap, bridge column and piles were set up using the equations based on Mander **[15]** model for confined concrete. The steel properties were added to those of concrete based on a transformed area approach.

The nonlinear material properties necessary to model each bridge component were approximated by imposing axial compressive and tensile strains on a given section. Next, by equating the computed axial forces in a section composed of a homogeneous material and in the composite reinforced concrete section, the stress-strain curve for the different components was obtained. In the compression zone, along the path of the confined concrete stress-strain diagram, the new transformed section material property was set up such that the strength of this new section equaled that of the two materials, concrete and steel, behaving independently. On the tension side, up to cracking, the concrete tensile strength was used in conjunction with the steel strength, according to the approach described previously, and after cracking, only the steel material properties were used.

To illustrate this procedure, consider a section with area A_g , concrete stress-strain

curve, $f_c(\varepsilon)$, steel area, A_{sl}, and steel stress-strain curve, $f_{sl}(\varepsilon)$. Then, the stress-strain curve of the equivalent transformed section, $f_{eq}(\varepsilon)$, may be defined according to the following expression:

$$f_{eq}(\varepsilon) = \frac{(A_g - A_{sl}) f_c(\varepsilon) + A_{sl} f_{sl}(\varepsilon)}{A_g} \tag{3.4}$$

Boundary conditions used in the finite element model used fixed end conditions at the soil spring elements nodes opposite to the beam element connection and, at the base of the piles, pin conditions were employed to allow for any possible rotations at this location.

In order to avoid a singular or negative stiffness matrix after peak response, the numerical procedure introduced in the finite element model was the constant stiffness method. The finite element model was run by employing a displacement control iterative technique in order to obtain the response of the structure beyond peak response of the column section. In this technique, the pattern of applied loading is proportionally incremented to achieve equilibrium of the structure under the specified displacement of the controlled degree of freedom. For this model, the controlled degree of freedom was that of the central node at the top of column in the direction of the applied lateral loading.

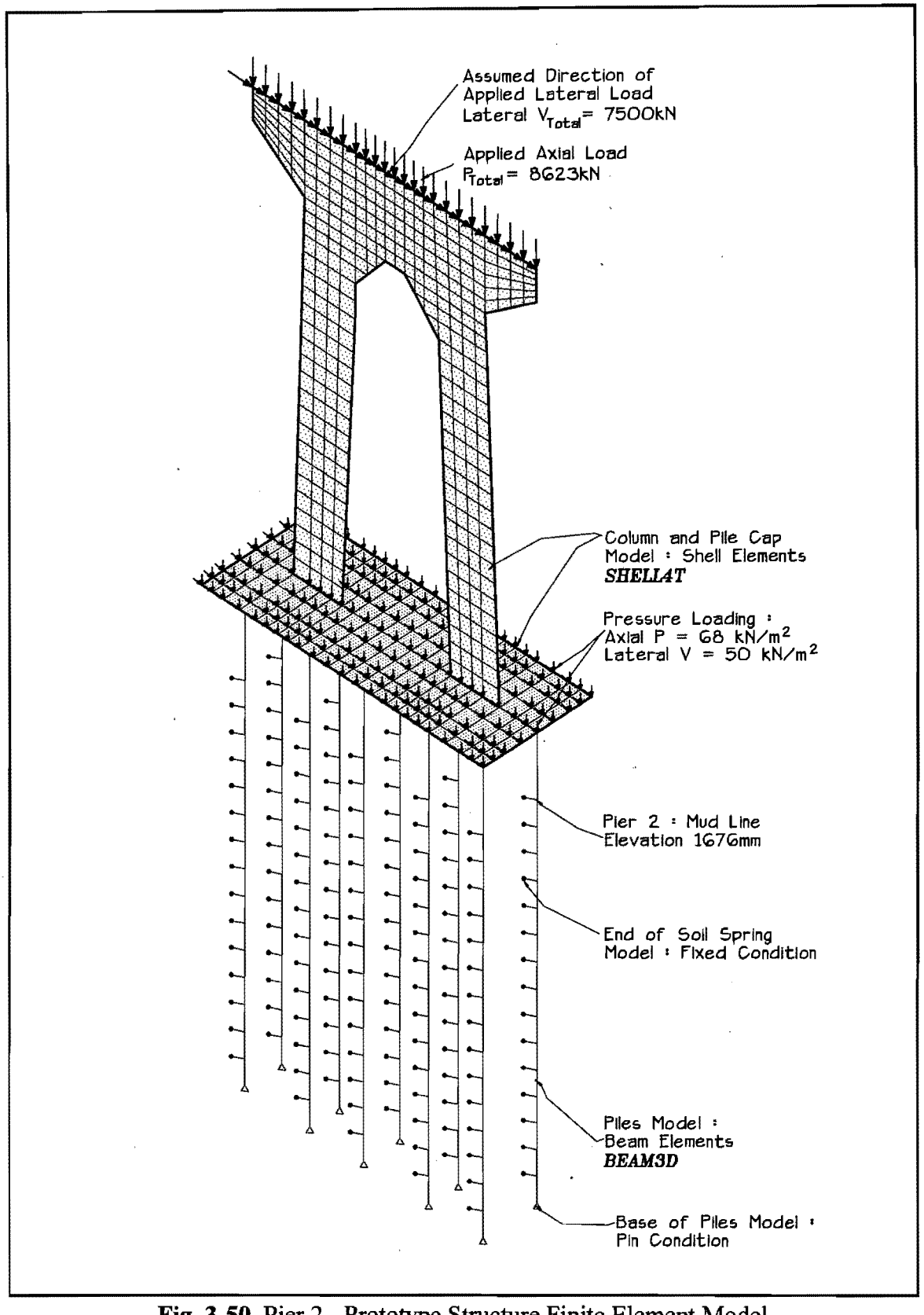

Fig. 3-50 Pier 2 - Prototype Structure Finite Element Model

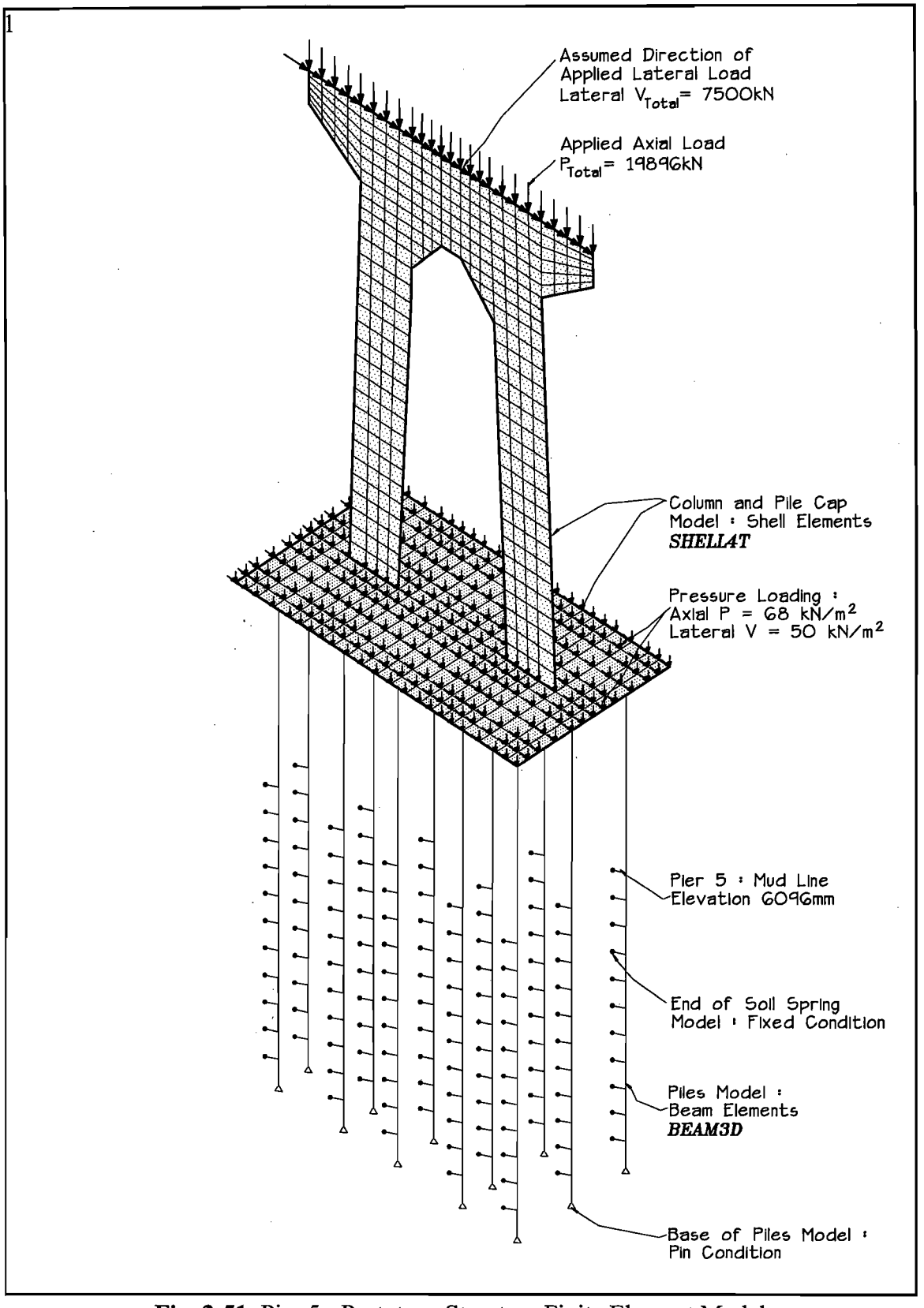

Fig. 3-51 Pier 5 - Prototype Structure Finite Element Model

Superstructure and column gravity loads were applied at the top of the column. Pile cap gravity load was defined by considering surface loads along the pile cap, as depicted in **Fig. 3-50** and **Fig. 3-51**. At Pier 2, the maximum applied gravity load applied was 8,623 kN and, at Pier 5, was 19,896 kN, which includes tributary area load from superstructure and pier towers self-weight. Pressure loading on the pile cap to model self-weight of the pile cap was 68 kN/m^2, which includes pile cap self-weight for a total load of approximately 6,389 kN and 9,229 kN for Pier 2 and Pier 5, respectively.

Lateral loading of the prototype structure was applied at the top of the column and on the pile cap to model the simulated seismic loading of the prototype structure. Maximum specified lateral load at the top of the column was 7500 kN at Pier 2 and Pier 5. Because the pile cap has a large mass, it was also necessary to apply additional lateral loading to model the pile cap inertia. This loading was applied as a surface load along the pile cap elements with a magnitude of 50 kN/m^2 obtained for a PGA of 1.45g and a force reduction factor of Z=2.0, corresponding to a total load of 1457 kN and 6691 kN for Pier 2 and Pier 5, respectively.

3.4.1 Test Unit *COR1* and *COR3* - Loading Path and Control Program

In order to set up the loading paths for each test unit, output results for two corner piles in compression and tension were extracted from the finite element analysis previously described. The loading path obtained from the nonlinear finite element analysis expressed in terms of moment versus axial load is presented in **Fig. 3-52**. This nonlinear loading path was then converted to a piecewise linear curve to develop the control program to simulate the seismic loading of test units *COR1* and *COR3*. This curve is indicated as the Pre-Test Analysis Control Loading Path curve in **Fig. 3-52**.

The axial load upper and lower bounds were set to the design loads defined in Chapter 2 and presented in reference **[3]**, which are +6,761 kN in compression and -681 kN in tension, which corresponds to the prototype structure loads transmitted into the piles. For analysis of the test units pile section, these values were +3,007 kN and -302 kN, which corresponds to the scaled values based on the 2/3 scale factor previously described. The compression design axial load corresponds to an axial load ratio *AXL* of 10%, determined by the expression:

$$AXL = \frac{P_C^*}{\left(f'_{c,shell} \left(A_{g,shell} - A_{psl} \right) + f'_{c,core} \left(A_{g,core} - A_{sl} \right) + A_{sl} f_y \right)} \tag{3.5}$$

And the tension design axial load corresponds to an axial load ratio *AXL* of 10% determined by the expression:

$$AXL = \frac{P_T^*}{A_{sl} f_y} \tag{3.6}$$

Thus, both compression and tension design axial loads are considerably below the capacity of the pile section.

The linearized loading path was then used to set up the program to control the application of the experimental axial and lateral loads. In order to develop the control program loading path, regions were defined according to the loading status of the test unit.

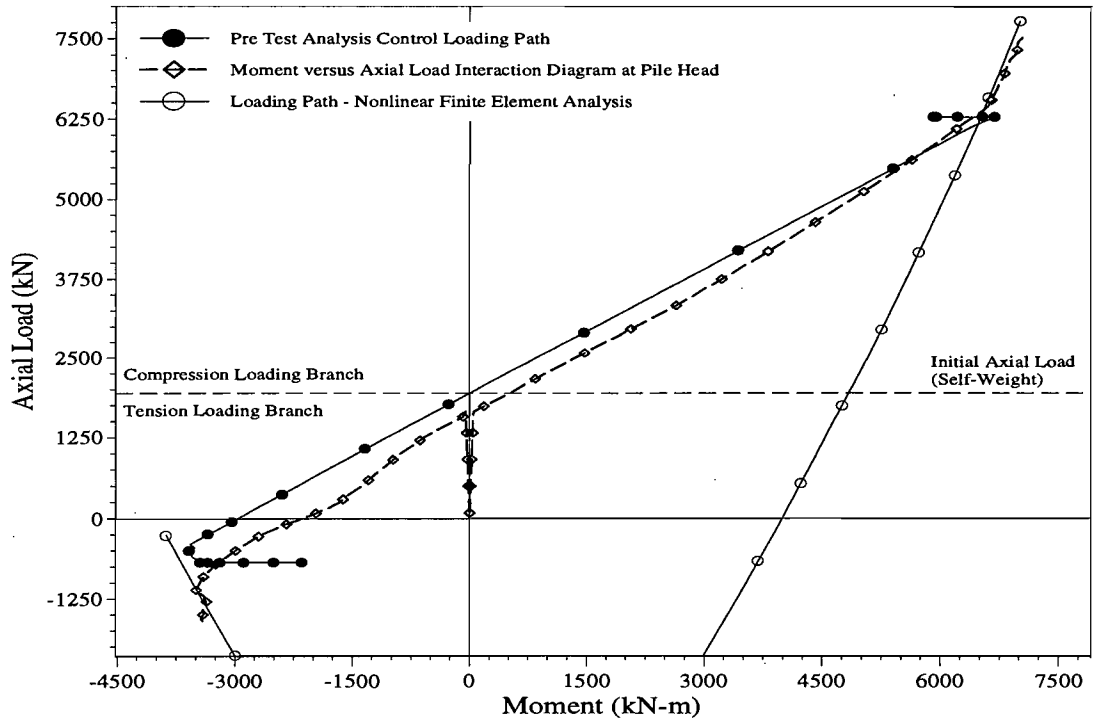

Fig. 3-52 Pier 5 Piles - Loading Path

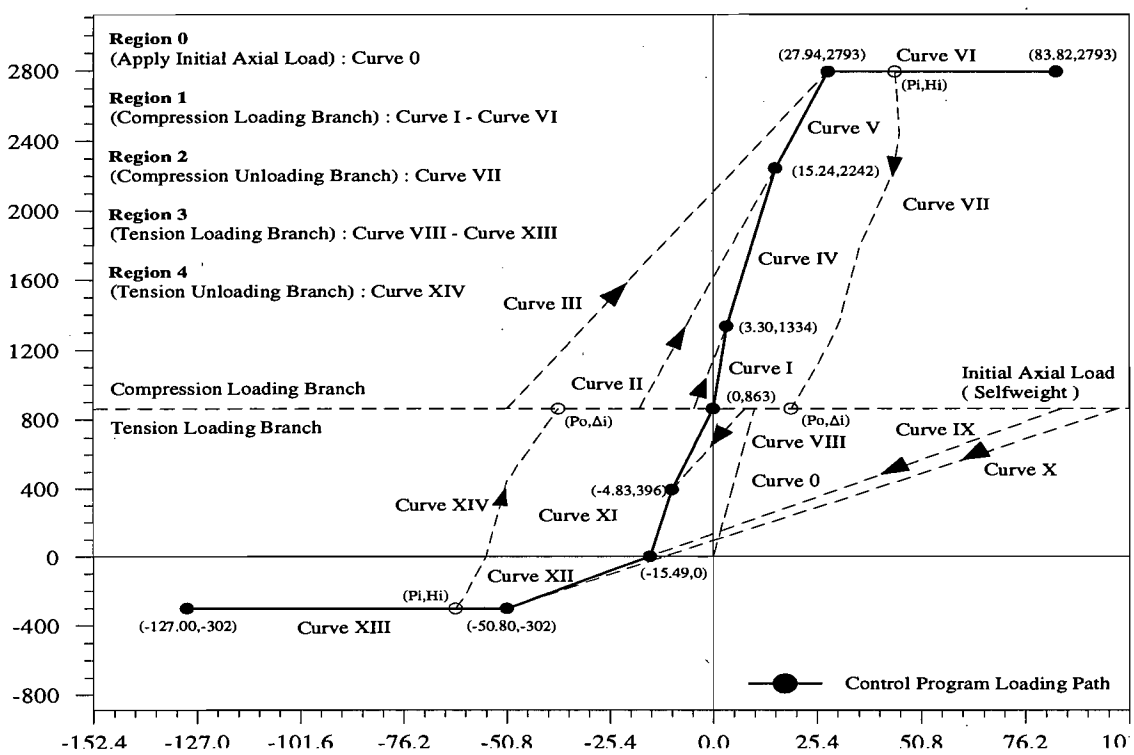

Fig. 3-53 Test Units *COR1* and *COR3*- Control Program Loading Path

Referring to **Fig. 3-53**, five loading regions were defined to fully describe the complete loading sequence of test units *COR1* and *COR3* and were as follows:

Region 0 describes the application of the initial load, while the pile top lateral deflection is maintained at zero according to Curve 0. When the initial axial load P_o=863 kN is reached, the lateral load, H_o, is recorded for input to establish Curve VII and Curve XIV.

Region 1 was defined as the *Compression Loading Branch* when loading of the structure occurs under increasing axial load and pile lateral deflection. In this region, the axial load is always in compression and in this branch the structure was loaded according to loading Curve I through Curve VI. In this region, when the residual displacement $\Delta_i \geq -2.90$ mm, loading is accomplished according to Curve I. However, if $\Delta_i \geq -16.51$ mm then Curve II controls the application of the axial and lateral load. Finally, in the compression loading branch, if $\Delta_i < -16.51$ mm, then loading of the test specimen is controlled by Curve III. Thus, in this region, Curve I through Curve III utilizes the residual displacements, Δ_i, recorded from Region 0 or Region 4 to redirect the loading path towards the original curve. Residual displacements refer to the lateral deflection of the pile section when the recorded axial load is equal to the initial axial load of 863 kN. A flowchart describing this loading path is presented in Appendix B.

Region 2 was defined as the *Compression Unloading Branch* when unloading of the structure occurs after Region I. In this branch, the structure was unloaded according to loading Curve VII. In this Region, when either the target load or displacement are reached, the axial load, P_i, and lateral load, H_i, are recorded to define Curve VII, which unloads the structure back to the initial conditions, P_o, and lateral load, H_o. In the passage from Region 2 to Region 3, residual displacements, Δ_i, are recorded as input to define settings for Curve VIII through Curve X.

Region 3 was defined as the *Tension Loading Branch* when loading of the structure occurs with decreasing axial load and pile lateral deflection. In this region, the axial load may be in compression or tension because of the initial axial load, which simulates the selfweight of the prototype structure and was described according to loading Curve VIII through Curve XIII. In this region, when the residual displacement $\Delta_i \leq +7.76$ mm, loading is accomplished according to Curve VIII. However, if $\Delta_i \leq +85.23$ mm, then loading is controlled in terms of Curve IX. Finally, in the tension loading branch, if $\Delta_i > +85.23$ mm, then loading of the test specimen is controlled by Curve X. Thus, in this region, Curve VIII through Curve X utilizes

the residual displacements, Δ_i, recorded from Region 2 to redirect the loading path towards the original curve.

Region 4 was defined as the *Tension Unloading Branch* when unloading of the structure occurs after Region III and is defined according to the loading Curve IX. In this region, when the load or displacement target are reached, the axial load, P_i, and lateral load, H_i, are recorded to define Curve IX, which unloads structure back to initial conditions P_o and lateral load, H_o. In the passage from Region 4 to Region 1, residual displacements, Δ_i, are recorded as input to define the settings of Curve I through Curve III.

The equations that were developed to describe the loading curves depicted in **Fig. 3-53** are the following:

Curve 0 - *Initial Axial Load Simulation* - Region 0 :

$$\Delta = 0 \; ; \quad P \leq 863kN \tag{3.7}$$

Curve I : *Compression Loading* - Region 1 (*if* $\Delta_i \geq -2.90$ *mm*) :

$$P_{1C} = 863 + \frac{1334 - 863}{3.30 - \Delta_i} (\Delta - \Delta_i) \; ; \quad P \leq 1334\,kN \tag{3.8}$$

Curve II : *Compression Loading* - Region 1 (*if* $\Delta_i \geq -16.51$ *mm*) :

$$P_{2C} = 863 + \frac{2242 - 863}{15.24 - \Delta_i} (\Delta - \Delta_i) \; ; \quad P \leq 2242\,kN \tag{3.9}$$

Curve III : *Compression Loading* - Region 1 (*if* $\Delta_i < -16.51$ *mm*) :

$$P_{3C} = 863 + \frac{2793 - 863}{27.94 - \Delta_i} (\Delta - \Delta_i) \; ; \quad P \leq 2793\,kN \tag{3.10}$$

Curve IV : *Compression Loading* - Region 1:

$$P_{4C} = 1334 + \frac{2242 - 1334}{15.24 - 3.30} (\Delta - 3.30) \; ; \quad P \leq 2242\,kN \tag{3.11}$$

Curve V : *Compression Loading* - Region 1:

$$P_{5C} = 2242 + \frac{2793 - 2242}{27.94 - 15.24} (\Delta - 15.24) \; ; \quad P \leq 2793\,kN \tag{3.12}$$

Curve VI : *Compression Loading* - Region 1:

$$P_{6C} = 2793 \; ; \quad \Delta \geq +27.94mm \tag{3.13}$$

Curve VII : *Compression Unloading* - Region 2:

$$P_{7C} = P_i + \frac{863 - P_i}{H_o - H_i}(H - H_i) \;;\; P \geq 863\,kN,\; H \geq H_o \tag{3.14}$$

Curve VIII : *Tension Loading* - Region 3 (*if* $\Delta_i \leq +7.76\,mm$) :

$$P_{8C} = 863 + \frac{396 - 863}{-4.83 - \Delta_i}(\Delta - \Delta_i) \;;\; P \geq 396\,kN \tag{3.15}$$

Curve IX : *Tension Loading* - Region 3 (*if* $\Delta_i \leq +85.23\,mm$) :

$$P_{9C} = 863 + \frac{0 - 863}{-15.49 - \Delta_i}(\Delta - \Delta_i) \;;\; P \geq 0\,kN \tag{3.16}$$

Curve X : *Tension Loading* - Region 3 (*if* $\Delta_i > +85.23\,mm$) :

$$P_{10C} = 863 + \frac{-302 - 863}{-50.80 - \Delta_i}(\Delta - \Delta_i) \;;\; P \geq -302\,kN \tag{3.17}$$

Curve XI : *Tension Loading* - Region 3:

$$P_{11C} = 396 + \frac{0 - 396}{-15.49 + 4.83}(\Delta + 4.83) \;;\; P \geq 0\,kN \tag{3.18}$$

Curve XII : *Tension Loading* - Region 3:

$$P_{12C} = 0 + \frac{-302 - 0}{-50.80 + 15.49}(\Delta + 15.49) \;;\; P \geq -302\,kN \tag{3.19}$$

Curve XIII : *Tension Loading* - Region 3:

$$P_{13C} = -302 \;;\; \Delta \leq -50.80mm \tag{3.20}$$

Curve XIV : *Tension Unloading* - Region 4:

$$P_{14C} = P_i + \frac{863 - P_i}{H_o - H_i}(H - H_i) \;;\; P \leq 863\,kN \quad H \leq H_o kN \tag{3.21}$$

Based on the expressions presented above, Curve 0 is used to apply the initial axial load, while maintaining the pile lateral deflection at zero. At this stage, the lateral load was recorded and its value was assigned to the variable, H_o, used to describe Curve V and Curve IX.

In Region 1 and Region 3, the control program was expressed in terms of axial load versus pile top lateral deflection, as indicated in the curves to describe these regions. When the target displacement and/or lateral load were reached, the structure was unloaded to the

initial axial load of +863 kN, and the lateral load, H_o, in terms of axial load versus lateral load, because during unloading the target must be the initial condition, which is the pair (H_o , P_o=+863). At this stage the residual displacement, Δ_i, was recorded and its value used to describe loading Curve I through Curve III and Curve VIII through Curve X.

3.4.2 Test Unit *COR1* - Loading History

The loading history to simulate the seismic loading of test unit *COR1* is presented in **Fig. 3-54**. Observation of **Fig. 3-54** indicates that the first step in the testing procedure consisted of loading the specimen to an initial axial load of +863 kN, which corresponds to the prototype structure tributary initial axial load. In the next four cycles, the specimen was loaded to ±25%, ±50%, ±75% and ±100% of theoretical first section yielding in force control.

Next, incremental displacement ductility levels were obtained based on lateral deflections and lateral loads recorded at ±100% of experimental first section yielding and lateral loads at theoretical yielding. The structure was than loaded solely in displacement control with three cycles at each specified lateral deflection, according to the deflections presented in **Fig. 3-54**.

3.4.3 Test Unit *COR3* - Loading History

The loading history to simulate the seismic loading of test unit *COR3* is presented in **Fig. 3-55**. Similar to test unit *COR1,* observation of **Fig. 3-55** indicates that the first step in the testing procedure consisted of loading the specimen to the initial axial load of +863 kN, which corresponds to the prototype structure tributary initial axial load. In the next four cycles, the specimen was loaded to ±25%, ±50%, ±75% and ±100% of theoretical first section yielding in force control.

Next, incremental displacement ductility levels were obtained based on lateral deflections and lateral loads recorded at ±100% of experimental first section yielding and lateral loads at theoretical yielding. The structure was than loaded solely in displacement control with three cycles at each specified lateral deflection according to the deflections presented in **Fig. 3-55**.

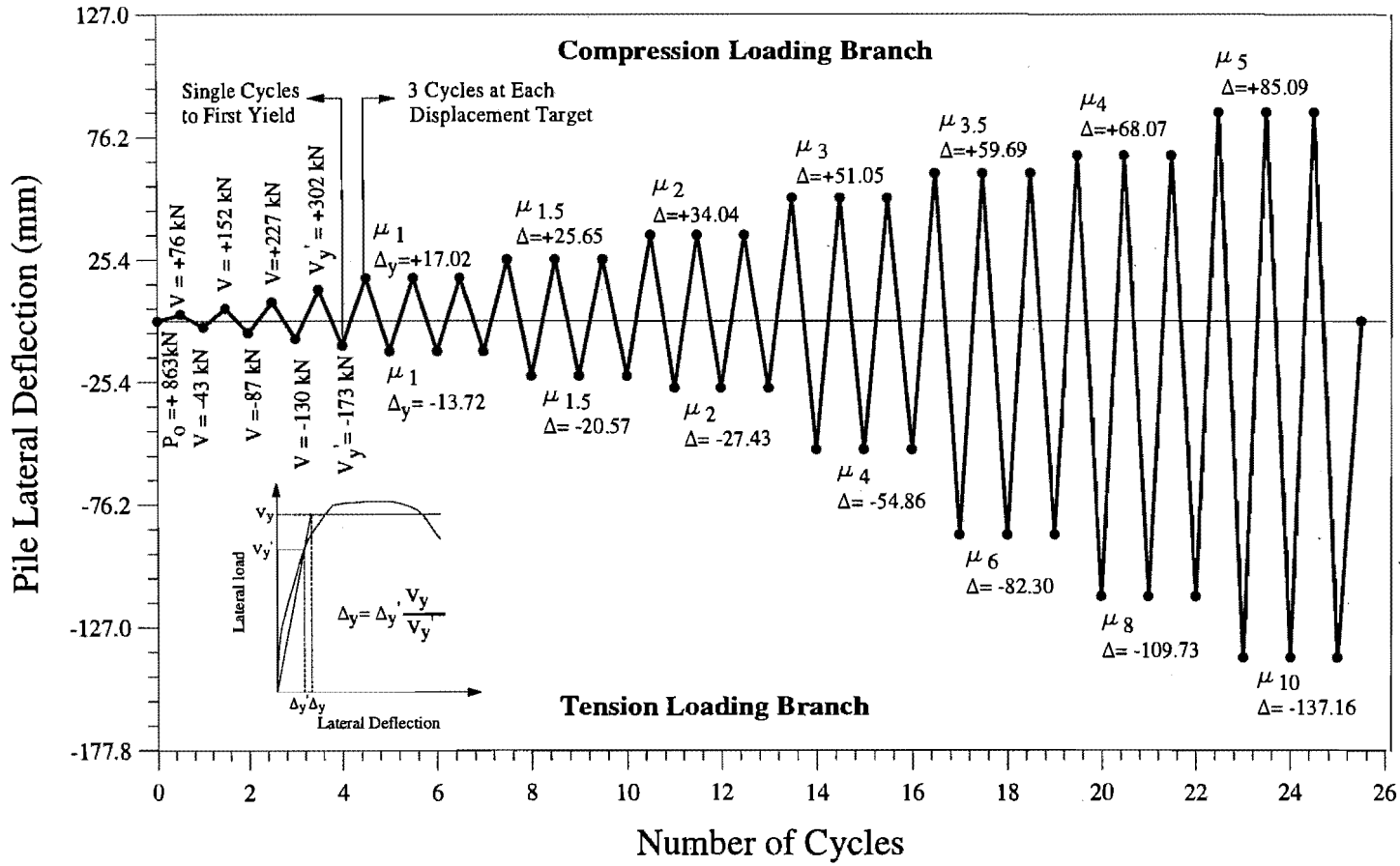

Fig. 3-54 Test Unit *COR1* - Loading History

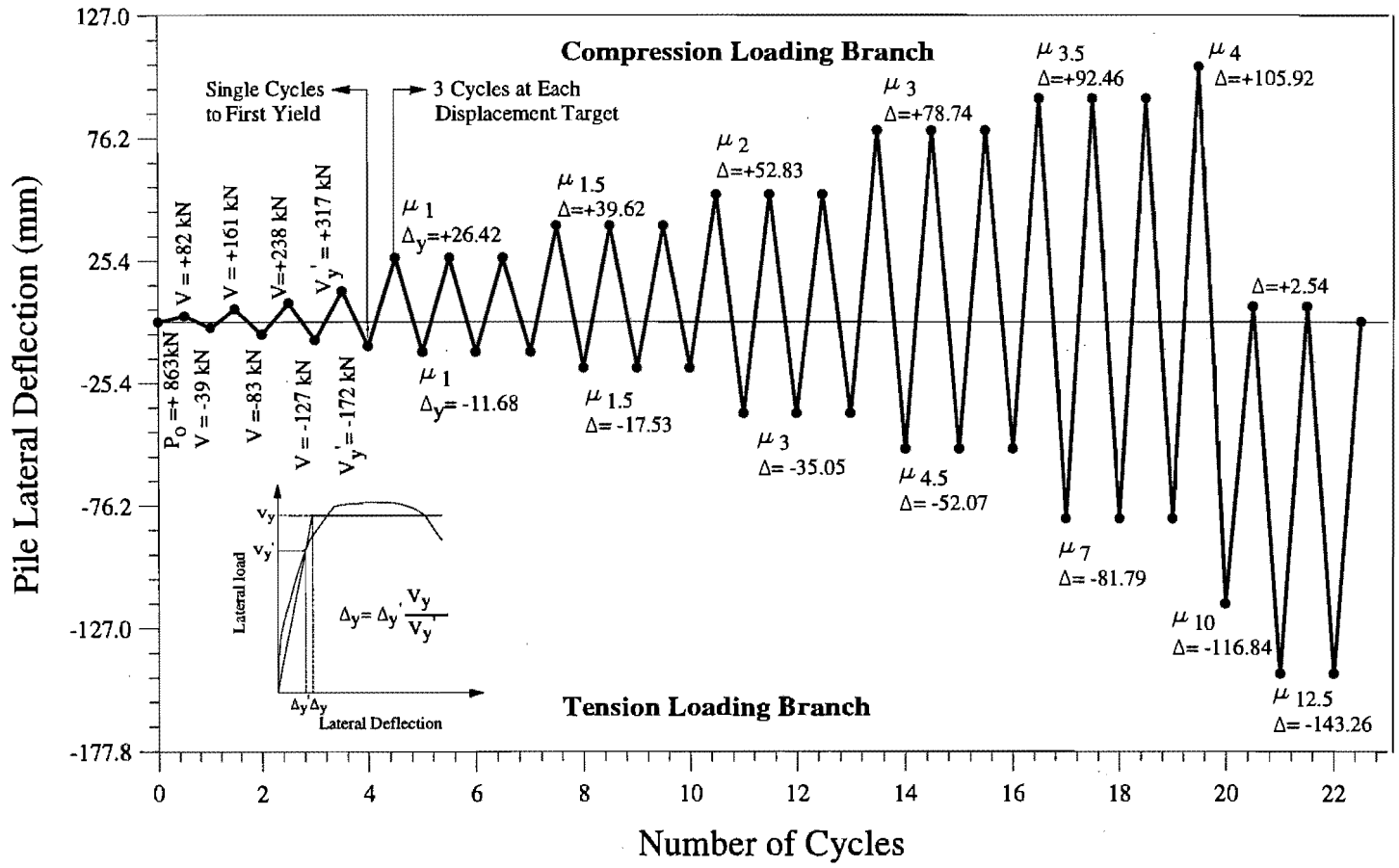

Fig. 3-55 Test Unit *COR3* - Loading History

3.4.4 Test Unit *COR2* - Loading Path and Control Program

Similar to the test units *COR1*and *COR3,* the pile section material properties implemented into the nonlinear finite element analysis to analyze the prototype structure using the pile material properties of test unit *COR2* were obtained according to the procedure described by equation **(3.4)**.

The loading path, expressed in terms of moment versus axial load, and obtained from the nonlinear finite element model analysis, is presented in **Fig. 3-56**. This loading path was then linearized to develop the control program to simulate the seismic loading of this test unit and is shown as the Pre Test Analysis Control Loading Path curve.

The axial load upper and lower bounds were set to the design loads defined in Chapter 2 and presented in reference **[3]** which are +6,761 kN in compression and -681 kN in tension, which corresponds to the prototype structure loads transmitted into the piles. For analysis of the test units pile section, these values were +3,007 kN and -302 kN, which corresponds to the scaled values based on the 2/3 scale factor previously described. These values are identical to those presented for test units *COR1* and *COR3.* The compression and tension design axial load corresponds to an axial load ratio *AXL* of 10% as for test units *COR1* and *COR3.*

The linearized loading path was then used to set up the program to control the application of the experimental axial and lateral loads. In order to develop the control program loading path, loading regions were defined according to the loading status of the test unit.

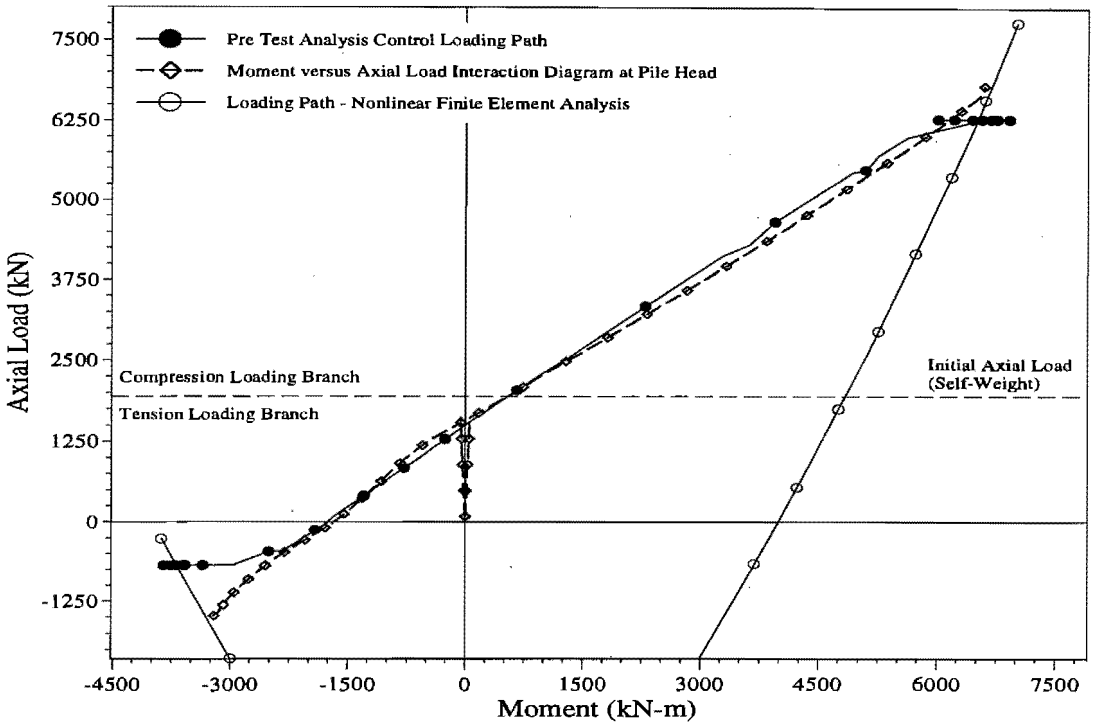

Fig. 3-56 Pier 2 Piles - Loading Path

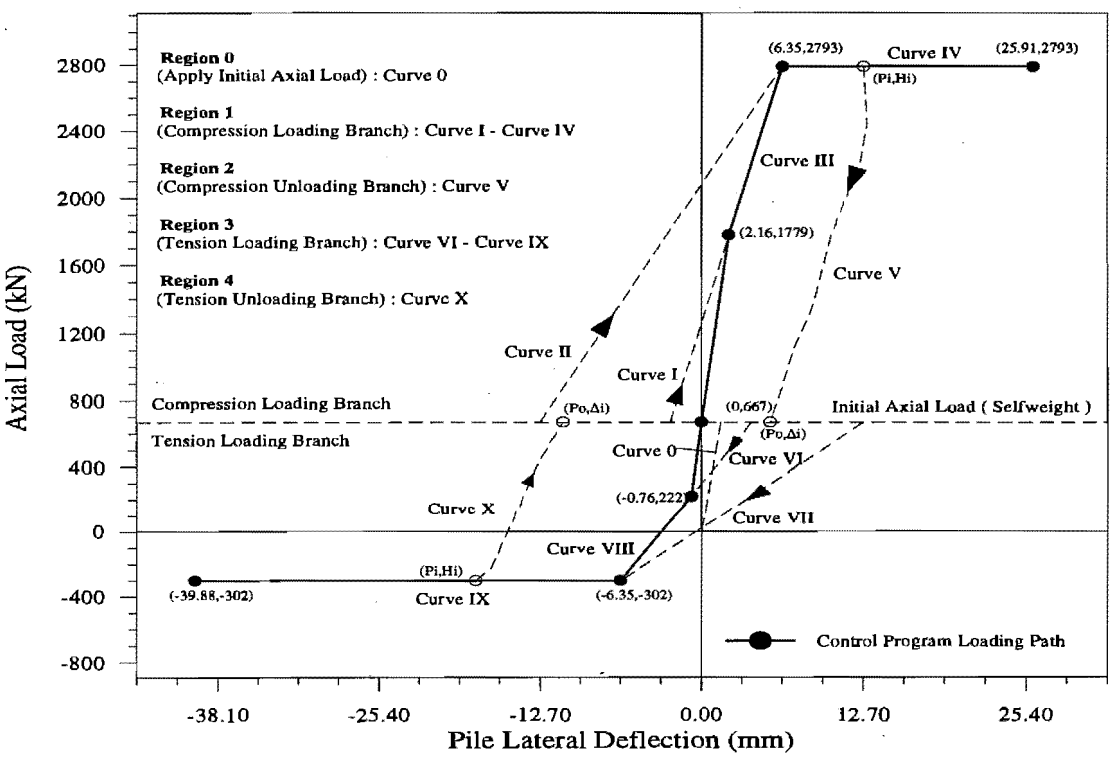

Fig. 3-57 Test Unit *COR2* - Control Program Loading Path

Similar to test units *COR1* and *COR3*, referring to **Fig. 3-57**, five loading regions were defined to fully describe the complete loading sequence of the test unit and were as follows:

Region 0 describes the application of the initial load according to Curve 0.

Region 1 was defined as the *Compression Loading Branch* when loading of the structure occurs under increasing axial load and pile lateral deflection. In this region, the axial load is always in compression and, in this branch, the structure was loaded according to loading Curve I through Curve IV. In this region, when the residual displacement $\Delta_i \geq -2.44$ mm, loading is accomplished according to Curve I. However, if $\Delta_i > -2.44$ mm, then Curve II controls the application of the axial and lateral load. Thus, in this region, Curve I and Curve II utilizes the residual displacements, Δ_i, recorded from Region 0 or Region 4 to redirect the loading path towards the original curve. A flowchart describing this loading path is presented in Appendix B.

Region 2 was defined as the *Compression Unloading Branch* when unloading of the structure occurs after Region I. In this branch, the structure was unloaded according to loading Curve V. In this Region, when either the target load or displacement are reached, the axial load, P_i, and lateral load, H_i, are recorded to define Curve V, which unloads the structure back to the initial conditions, P_o, and lateral load, H_o. In the passage from Region 2 to Region 3, residual displacements, Δ_i, are recorded as input to define settings for Curve VI and Curve VII.

Region 3 was defined as the *Tension Loading Branch* when loading of the structure occurs with decreasing axial load and pile lateral deflection. In this region, the axial load may be in compression or tension because of the initial axial load, and was described according to loading Curve VI through Curve IX. In this region,when the residual displacement $\Delta_i \leq +3.97$ mm, loading is accomplished according to Curve VI. However, if $\Delta_i > 3.97$ mm, then loading is controlled in terms of Curve VII. Thus, in this region, Curve VI and Curve VII utilizes the residual displacements, Δ_i, recorded from Region 2 to redirect the loading path towards the original curve.

Region 4 was defined as the *Tension Unloading Branch* when unloading of the structure occurs after Region III and is defined according to the loading Curve X. In this region, when the load or displacement target are reached the axial load, P_i, and lateral load,

H_i, are recorded to define Curve X, which unloads structure back to initial conditions, P_o, and lateral load, H_o. In the passage from Region 4 to Region 1, residual displacements, Δ_i, are recorded as input to define the settings of Curve I and Curve II.

Curve 0 - *Initial Axial Load Simulation* - Region 0 :

$$\Delta = 0 \; ; \quad P \leq 667kN \tag{3.22}$$

Curve I : *Compression Loading* - Region 1 (*if* $\Delta_i \geq -2.44$ *mm*) :

$$P_{1C} = 667 + \frac{1779 - 667}{2.16 - \Delta_i} (\Delta - \Delta_i) \; ; \quad P \leq 1779\,kN \tag{3.23}$$

Curve II : *Compression Loading* - Region 1 (*if* $\Delta_i < -2.44$ *mm*) :

$$P_{2C} = 667 + \frac{2793 - 667}{6.35 - \Delta_i} (\Delta - \Delta_i) \; ; \quad P \leq 2793\,kN \tag{3.24}$$

Curve III : *Compression Loading* - Region 1:

$$P_{3C} = 1779 + \frac{2793 - 1779}{6.35 - 2.16} (\Delta - 2.16) \; ; \quad P \leq 2793\,kN \tag{3.25}$$

Curve IV : *Compression Loading* - Region 1:

$$P_{4C} = 2793 \; ; \quad \Delta \geq +6.35mm \tag{3.26}$$

Curve V : *Compression Unloading* - Region 2:

$$P_{5C} = P_i + \frac{667 - P_i}{H_o - H_i} (H - H_i) \; ; \quad P \geq 667\,kN \, , \; H \geq H_o \tag{3.27}$$

Curve VI : *Tension Loading* - Region 3 (*if* $\Delta_i \leq +3.97$ *mm*) :

$$P_{6C} = 667 + \frac{222 - 667}{-0.76 - \Delta_i} (\Delta - \Delta_i) \; ; \quad P \geq 222\,kN \tag{3.28}$$

Curve VII : *Tension Loading* - Region 3 (*if* $\Delta_i > +3.97\ mm$) :

$$P_{7C} = 667 + \frac{-302 - 667}{-6.35 - \Delta_i} (\Delta - \Delta_i) \ ; \quad P \geq -302\ kN \tag{3.29}$$

Curve VIII : *Tension Loading* - Region 3:

$$P_{8C} = 222 + \frac{-302 - 222}{-6.35 + 0.76} (\Delta + 0.76) \ ; \quad P \geq -302\ kN \tag{3.30}$$

Curve IX : *Tension Loading* - Region 3:

$$P_{9C} = -302 \ ; \quad \Delta \leq -6.35mm \tag{3.31}$$

Curve X : *Tension Unloading* - Region 4:

$$P_{10C} = P_i + \frac{667 - P_i}{H_o - H_i} (H - H_i) \ ; \quad P \leq 667\ kN \quad H \leq H_o kN \tag{3.32}$$

Based on the expressions presented above, Curve 0 is used to apply the initial axial load. When the initial axial load is reached, the lateral load was recorded and its value was assigned to the variable H_o, used to describe Curve V and Curve X.

In Region 1 and Region 3, the control program was expressed in terms of axial load versus pile top lateral deflection, as indicated in the curves to describe these regions. When the target displacement and/or lateral load were reached, the structure was unloaded to the initial axial load of +667 kN and lateral load, H_o, in terms of axial load versus lateral load because during unloading the target must be the initial conditions, which is the pair (H_o,+667). At this stage, the residual displacement, Δ_i, was recorded and its value was used to describe the loading Curve I and Curve II in Region 1 and Curve VI and Curve VII in Region 3.

3.4.5 Test Unit *COR2* - Loading History

The loading history to simulate the seismic loading of test unit *COR2* is presented in **Fig. 3-58**. The first step in the testing procedure consisted of loading the specimen to an initial axial load of +667kN, which corresponds to the prototype structure tributary initial axial load. Similar to test units *COR1* and *COR3,* in the next four cycles the specimen was loaded to ±25%, ±50%, ±75% and ±100% of theoretical first section yielding in force control. Next, incremental displacement ductility levels were obtained based on lateral deflections and lateral loads recorded at ±100% of experimental first section yielding and lateral loads at theoretical yielding. The structure was than loaded solely in displacement control with three cycles at each specified lateral deflection according to the deflections presented in **Fig. 3-58**.

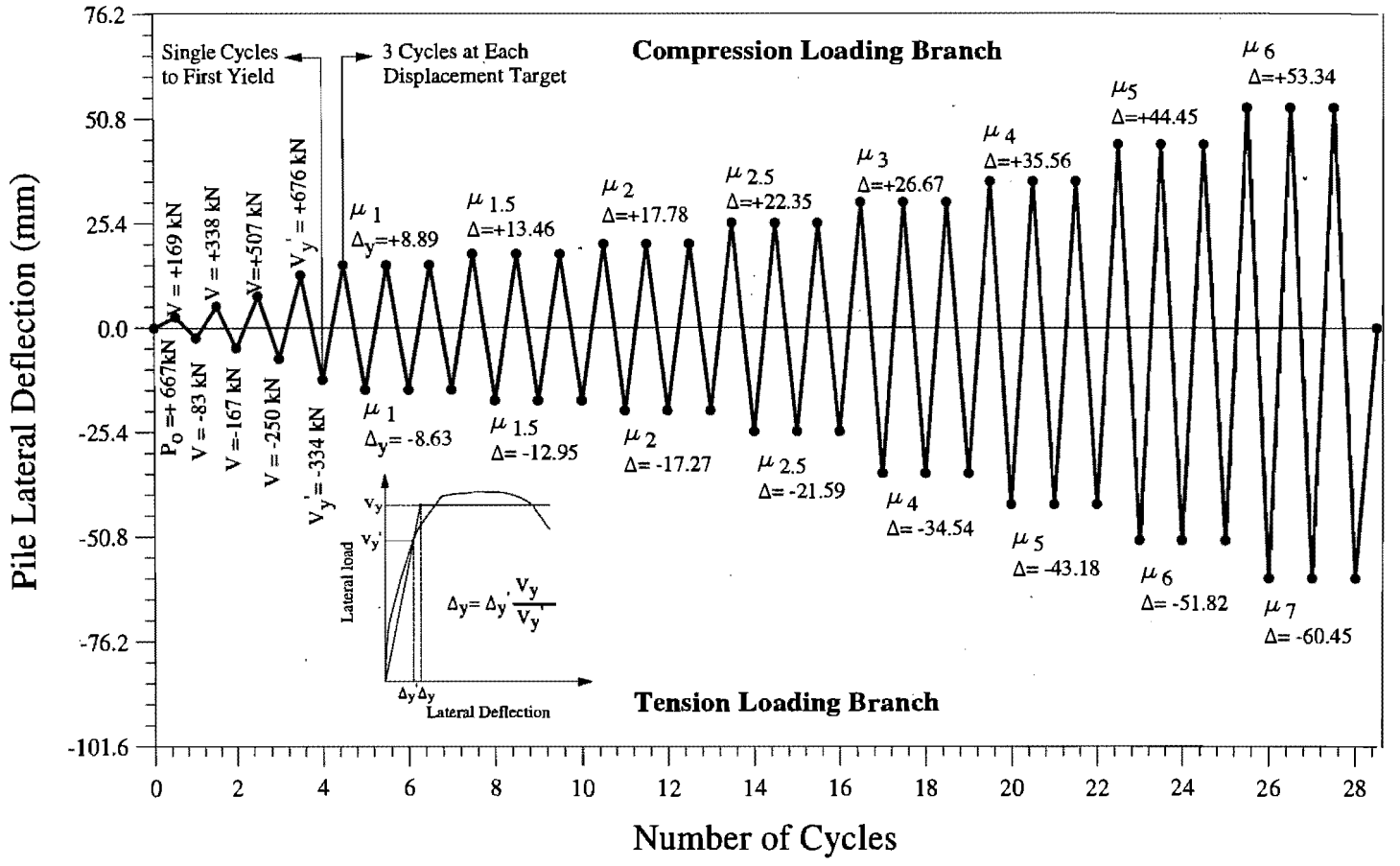

Fig. 3-58 Test Unit *COR2* - Loading History

4. Development Length of Prestressing Strands

Experimental investigation to predict the behavior of precast prestressed concrete shell piles of the San Diego Coronado Bay Bridge under simulated seismic loads has led to an experimental study to estimate the development length of 9.53 mm diameter prestressing strands. Moment curvature analysis of these piles at the pile head revealed that a more precise knowledge of the development length of the prestressing reinforcement in these piles was required to better predict the failure mode of test units *COR1*, *COR2* and *COR3*.

Development length of prestressing strands is commonly defined in terms of two expressions which consider the aspects of bond between prestressing steel and concrete at different stages of loading **[17]**. The first stage that may be considered in the loading of prestressing members is the sudden or slow release of the prestressing strands. In this stage, the initial prestressing force is transferred to the concrete by anchorage and bond of the steel over a distance at the ends of the precast member. Anchorage of the prestressing steel to the concrete is due to the mechanical interlock of the strands, and bond is developed as a result of friction between the two materials. These two mechanisms of force transfer are known as transfer bond and must be developed over a length, commonly defined as the *transfer bond length*, to transfer the initial prestressing force to the surrounding concrete.

Another expression considers the additional length at the ends of the precast member required to transfer the prestressing force through bonding due to the imposed external forces and is termed *flexural bond length*. Thus, as forces increase in the prestressing strands at different loading stages, the required length of strand to transfer these forces is termed *development length* and is composed of the *transfer bond length* and *flexural bond length*.

Recorded data during the precasting of the concrete shells and during the experimental testing procedure of test units *COR1, COR2* and *COR3* was used to estimate the required *development length* of the prestressing strands used in the construction of the test units. Regression analysis of the obtained experimental test data during manufacturing of the concrete shells revealed that the estimated transfer length is significantly higher than outlined in recent code provisions. Code provisions show that common values for the transfer length of prestressing reinforcement is in the range of $50d_b$ to $80d_b$, while based on this experimental investigation, values in the range of $120d_b$ to $190d_b$ can be expected.

Experimental test data presented in this chapter was obtained during the precasting operation while at *Utility Vault*. A total of 64 data channels were used in the instrumentation of test units *COR1, COR2* and *COR3* during manufacturing of the precast concrete shells, according to the outline presented in **Table 3-4**. These strain gages were connected to a rapid data acquisition system to record strains in the prestressing strands from stressing to removal of the shells from the casting bed, and strains in the concrete section after transfer for a time interval of approximately 48 hours. Strain gage readings from the time of jacking to transfer were recorded from the prestressing strands in 8 locations for strands ***B***, ***C*** and ***D***, according to the installation layout presented in **Fig. 3-35** and **Fig. 3-46**, and for test units *COR1* and *COR3* and test unit *COR2,* respectively. In addition, before transfer, 16 more strain gages were installed on the top surface of the concrete shell to monitored strain accumulations in the concrete and predict elastic strain losses due to concrete shortening and estimate the *transfer bond length.* These strain gages were installed as presented in **Fig. 3-40** and **Fig. 3-48**.

4.1 Fabrication of the Precast Prestressed Concrete Shells

Manufacturing of the precast concrete shells took place in the construction facilities of *Utililty Vault* in Fontana, California with the construction outline presented in Chapter 3.

4.1.1 Prestressing Losses

The total required jacking force was obtained by considering prestress losses due to: (1) Elastic Shortening of Concrete - Δf_{ES}, (2) Shrinkage of Concrete - Δf_S, (3) Relaxation of Strand - Δf_R, (4) Chuck Seating - Δf_{CS}, and (5) Bed Shortening -Δf_{BS}.

Evaluation of prestress losses was performed in two phases according to the casting operation sequence. The final prestress force after prestress losses was obtained from the construction specifications of the prototype structure. The total final prestress force for the 2/3 scale models was 1521 kN, which was determined by scaling of the prototype prestress force of 3425 kN. For each strand, the required final prestress force after losses was 56 kN.

4.1.1.1 Elastic Shortening of Concrete

The elastic shortening of concrete was computed at transfer of the prestressing strands. Prestress losses due to elastic shortening of concrete were computed based on the following equation **[18]**:

$$\Delta f_{ES} = \left[\frac{1}{1 - \eta_{pi}\, \rho_{ps}} \right] \frac{F_{DT}}{A_{ps}} \tag{4.1}$$

Where η_{pi} is the moduli ratio given by E_{ps}/E_{ci}, ρ_{ps} is the reinforcement ratio of the prestressing strands and A_{ps} is the cross sectional area of a single strand. F_{DT} is the required final force in each strand before testing. Based on equation **(4.1)**, prestress losses due to elastic shortening of concrete between transfer and day of test were estimated at 55 MPa.

4.1.1.2 *Shrinkage of Concrete*

Shrinkage of concrete between transfer and day of test was also considered in estimating prestressing losses. Prestress losses due to shrinkage were computed based on the following expression [18]:

$$\Delta f_S\,(t_i, t_j) = E_{ps}\ \varepsilon_{SU}\ K_{SH}\ K_{SS}\ 0.157\ Ln\left(\frac{t_j}{t_i}\right) \tag{4.2}$$

Where K_{SH} is the humidity correction factor given by $K_{SH} = 1.40 - 0.01\ H$ where H was estimated at 0.60 humidity, K_{SS} is the shape factor, which for a volume-to-surface ratio of 1.70, leads to $K_{SS} = 0.98$ presented in reference [18], and t_j is the time in days between day of test and transfer, t_i, which was estimated at 90 days for all test units, and ε_{SU} was computed based on :

$$\varepsilon_{SU} = \left[2 + \frac{11}{1337}\,(w - 1279)\right] 10^{-4} \tag{4.3}$$

Where w is the concrete mix design water content in newtons per cubic meter. Based on equation **(4.2)**, prestress losses due to shrinkage of concrete between transfer and day of test were estimated at 68 MPa.

4.1.1.3 *Relaxation of Strand*

Relaxation of the strands was computed in two time intervals between transfer and day of test, and between transfer and jacking. Prestress losses due to strand relaxation were computed based on the following expression [18]:

$$\Delta f_R\,(t_i, t_j) = \frac{f_{ps}\,(t_i)}{45}\left(\frac{f_{ps}\,(t_i) - 0.55}{f_{py}}\right) log\left(\frac{t_j}{t_i}\right) \tag{4.4}$$

Where $f_{ps}(t_i)$ is the stress present in the strand at the beginning of the time interval, f_{py}=1,830 MPa, as presented in **Table 3-3** and **Fig. 3-26**, and t_j was estimated at 90 days between transfer and day of test and 4 days between jacking and transfer for all three test units, and t_i must be equal to one. Between transfer and day of test, $f_{ps}(t_{i=5})$ was estimated by adding prestress losses due $\Delta f_{ES} + \Delta f_S + \Delta f_R$ to $f_{ps}(t_{j=90})$ to estimate $f_{ps}(t_{i=5})$, and between jacking and transfer, $f_{ps}(t_i=1)$, was estimated by adding prestress losses due $\Delta f_{CS} + \Delta f_{BS} + \Delta f_R$ to $f_{ps}(t_{j=5})$ to estimate $f_{ps}(t_{i=1})$, where $f_{ps}(t_{=1})$, $f_{ps}(t_{=5})$ and $f_{ps}(t_{=90})$ corresponds to the time at jacking, transfer and day of test, respectively. Based on equation **(4.4)**, prestress losses due to strand relaxation between transfer and day of test, and between jacking and transfer, were estimated at 34 MPa and 62 MPa, respectively.

4.1.1.4 Chuck Seating

Another source of prestress losses that was considered was slippage of the strands in the anchorage device, which is defined in this section as chuck seating. Prestress losses due to chuck seating was obtained based on the following expression :

$$\Delta f_{CS} = E_{ps} \Delta \varepsilon \tag{4.5}$$

Where $\Delta\varepsilon$ is the estimated strain loss due to chuck seating. At the live end, which corresponds to the pulled end of the strand, the chuck seating was estimated at $\delta_L=9.53\ mm$ and at the dead end, which corresponds to the side of the strand that was bearing against the strong-end bulkhead during stressing of the strands, the chuck seating was estimated at $\delta_D=3.18\ mm$. These values were provided by *Utility Vault.* Thus, the total strain loss may be computed as $\Delta\varepsilon= (\delta_L+\delta_D)/L_{BED}$, where $L_{BED} = 6{,}096\ mm$ is the distance between the casting bed strong-end bulkheads. Based on equation **(4.5)**, prestress losses due to chuck seating were estimated at 409 MPa.

4.1.1.5 Bed Shortening

Prestress loss due to shortening of the casting bed was obtained based on the following expression:

$$\Delta f_{BS} = E_{ps} \Delta \varepsilon \tag{4.6}$$

Where $\Delta\varepsilon$ is the estimated strain loss due to bed shortening. Bed shortening was estimated at $\delta_{BED}=5.10\ mm$ provided by *Utility Vault.* Thus, the total strain loss may be computed as $\Delta\varepsilon= \delta_{BED}/L_{BED}$. Based on equation **(4.6)**, prestress losses due to chuck seating were estimated at 164 MPa. **Table 4-1** presents a summary for the different sources of prestress loss.

Table 4-1 Summary of Prestress Losses

Sources of Prestress Loss	Time Interval *Jacking - Transfer* [MPa]	Time Interval *Transfer - Test Date* [MPa]
Elastic Shortening of Concrete - Δf_{ES}	-	55
Shrinkage of Concrete - Δf_S	-	68
Relaxation of Strand - Δf_R	34	62
Chuck Seating - Δf_{CS}	409	-
Bed Shortening -Δf_{BS}	164	-

Computation of prestress losses was based on the final prestressing force of 56 kN, and to the expected sources of prestress losses during the time intervals of transfer to test date and jacking to transfer as indicated in**Table 4-1**. Based on the values presented in **Table 4-1**, the total prestress loss is then $\Delta f = \Delta f_{ES} + \Delta f_R + \Delta f_S + \Delta f_{CS} + \Delta f_{BS} = 792$ MPa which leads to the total jacking force of 93 kN per strand. This value will impose a concrete compressive stress of 11 MPa in the concrete shell, which is approximately 40% of the estimated concrete compressive strength at time of transfer f_{ci}.

4.1.2 Prestressing Schedule

The strands were stretched between two strong-end bulkheads depicted in **Fig. 3-1**. Each strand was stressed using a center-hole ram, and the tension in the strand was monitored by a pressure meter. Each strand was initially stressed to 14% of the total jacking force to remove slack in the strands. After all the strands were pulled to the initial prestressing force of 13 kN, the concrete shell spiral cage was realigned to the desired pitch and the strands were then stressed to the final jacking force of 93 kN. In both of these stressing stages, the electric cables from the strain gages were connected to a rapid data acquisition system to record strain gage readings during the precasting phase.

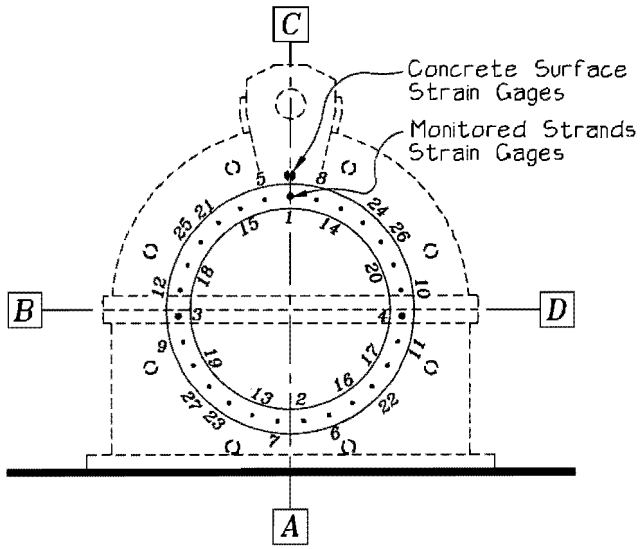

Fig. 4-1 Strand Jacking and Cut Sequence

To minimize unbalanced load of the casting bed, the strands were pulled and flamed cut according to the sequence presented in **Fig. 4-1**. Strands ***B***, ***C*** and ***D*** strain gages were monitored during the manufacturing of the concrete shells.

4.2 Transfer Bond Length

Estimated transfer length for test units *COR1*, *COR2* and *COR3,* used in pre-test and post-test analysis, was obtained from a regression analysis. Strain gage readings obtained for each strand and at the concrete surface allowed the evaluation of strain at different locations along the concrete shells.

Strain gage readings recorded during manufacturing of test unit *COR1*, at a distance of 152 mm, 914 mm and 2,337 mm from the pile head, are presented in **Fig. 4-2**, **Fig. 4-3** and **Fig. 4-4**. Total pile length is 4,572 mm. Referring to **Fig. 4-2**, it is clear that strain losses at the section ends are mostly due to loss of mechanical bond. Strains obtained from the concrete surface gage indicate minimum strain losses due to elastic shortening of the concrete shell. Away from the section ends, at a distance of 914 mm, there is a reduction in mechanical bond losses and an apparent increase in losses due to elastic shortening, as illustrated in **Fig. 4-3**. Finally, at approximately the center of the pile section, prestress losses are only due to elastic shortening of concrete, as shown in **Fig. 4-4**, because strain in the strand, $\varepsilon_{ps}(t_f)$, at a time, t_f, equals the strain in the strand, $\varepsilon_{transfer}$, obtained at transfer plus strain in the concrete shell ε_{conc} at time, t_f (i.e.$\varepsilon_{ps}(t_f) = \varepsilon_{transfer} + \varepsilon_{conc}$).

In test unit *COR2,* the strands were anchored with a *wedge-chuck* VSL S5N Anchorage System, as illustrated in **Fig. 3-22**, in order to reduce the effects of prestress losses in the pile end near the load stub. Vertical strain profiles for the prestressing strands of test unit *COR2,* presented in Chapter 6, suggest that the anchorage system was adequate in clamping the strands near the load stub interface. Moreover, strand strain gage readings taken during manufacturing of the precast concrete shell indicate small amount of slippage in the region near the anchorage system.

Referring to **Fig. 4-5**, the concrete shell was separated in two parts at approximately 86 hours. Oscillations in the strand strain gage readings indicate wave propagation during cutting of the strands. It is clear that before and after cutting of the strands, strain gage readings were approximately the same, which indicates small amounts of strain losses while cutting the pile section at the wood strip.

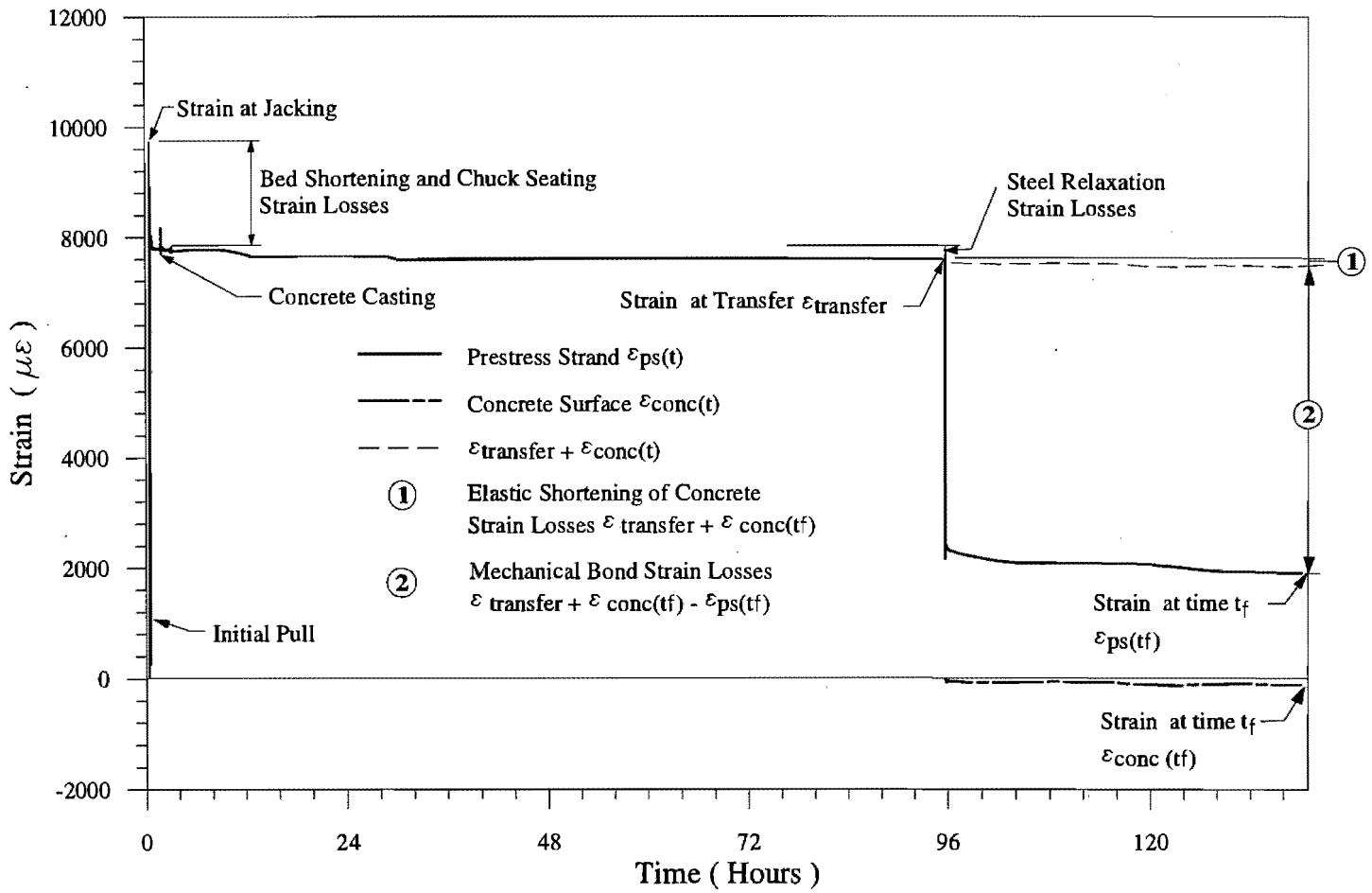

Fig. 4-2 Test Unit *COR1* - Strand Strain versus Time at 152mm from the Pile Head

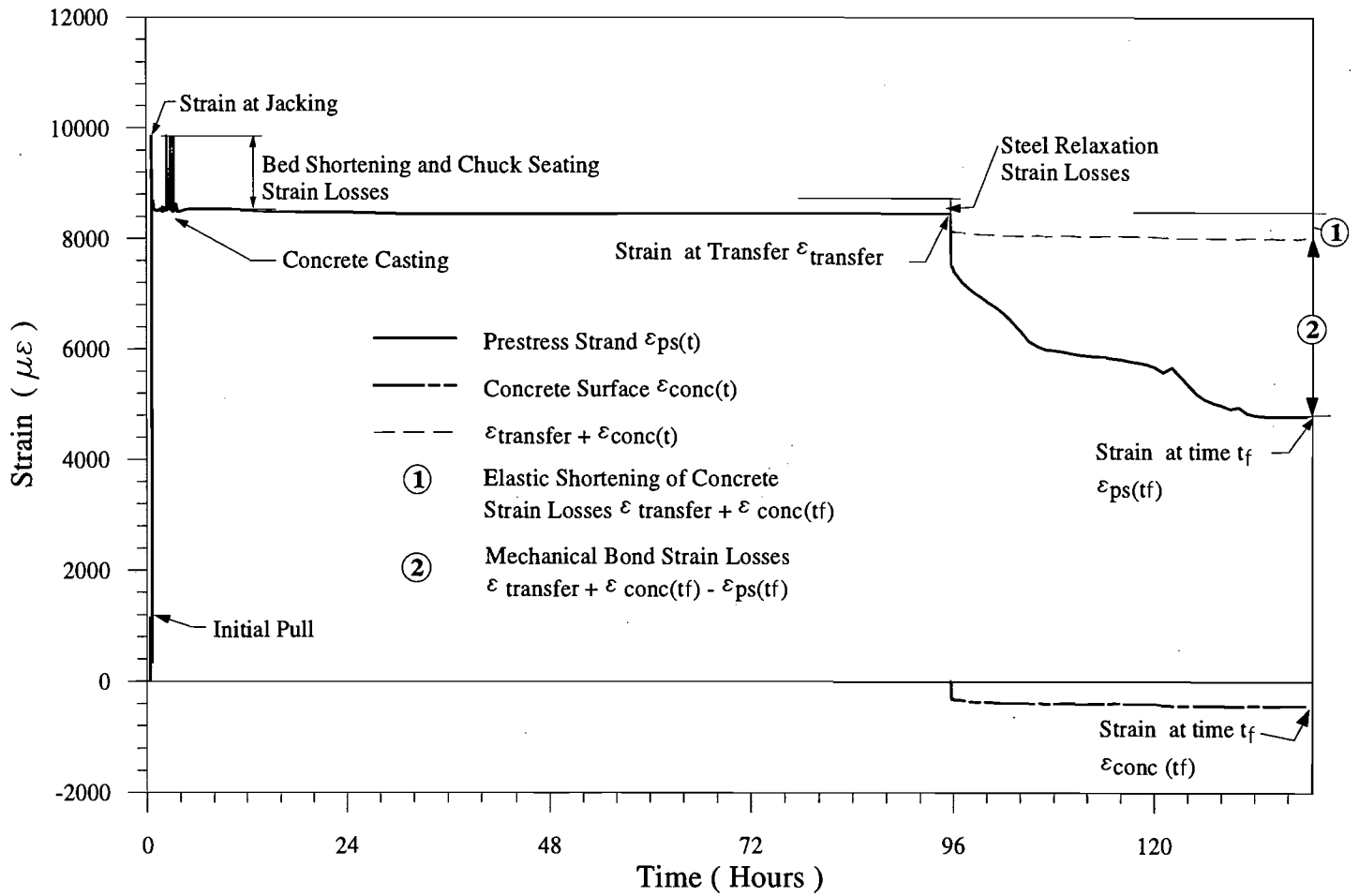

Fig. 4-3 Test Unit *COR1* - Strand Strain versus Time at 914mm from the Pile Head

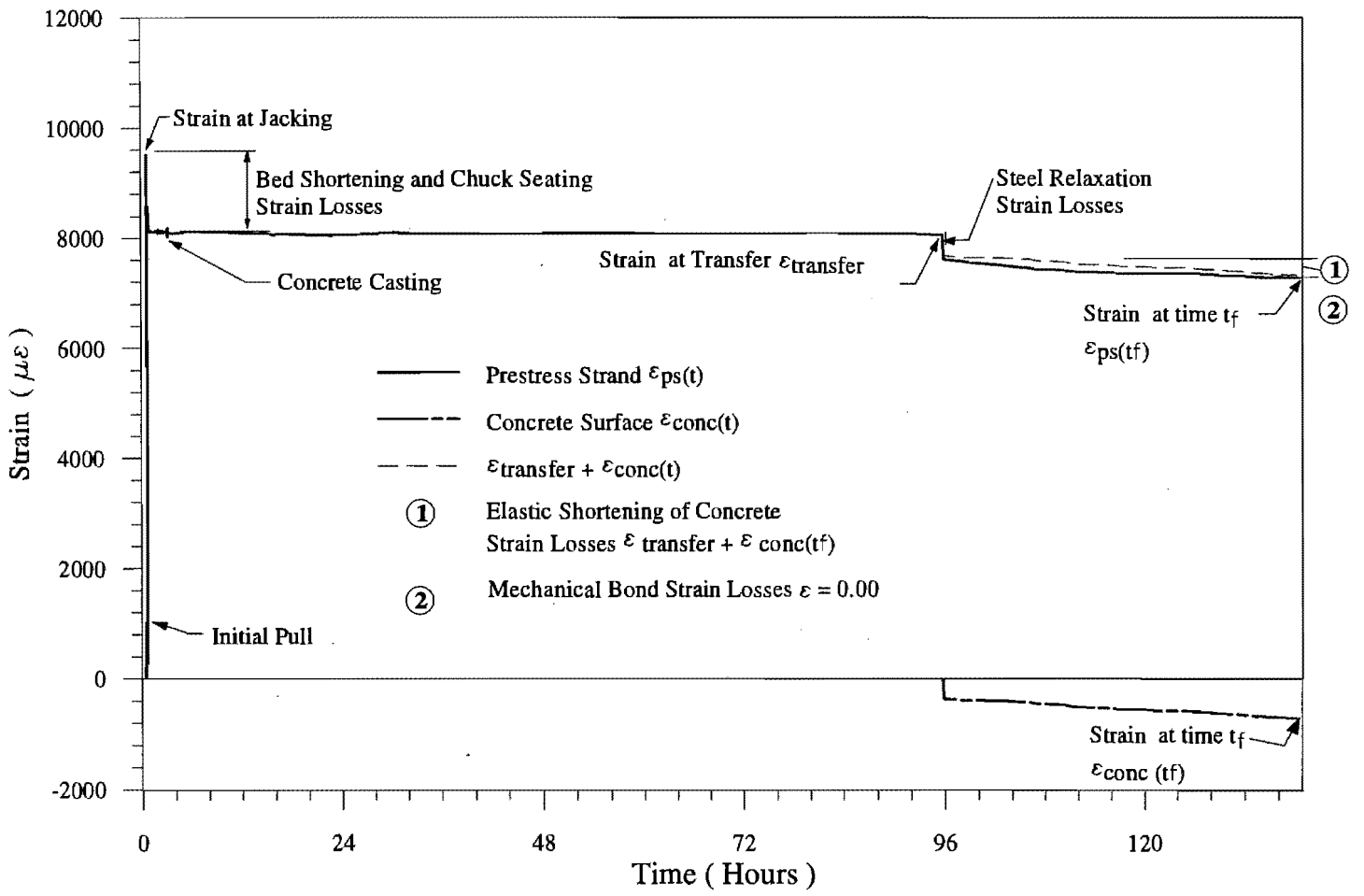

Fig. 4-4 Test Unit *COR1* - Strand Strain versus Time at 2337mm from the Pile Head

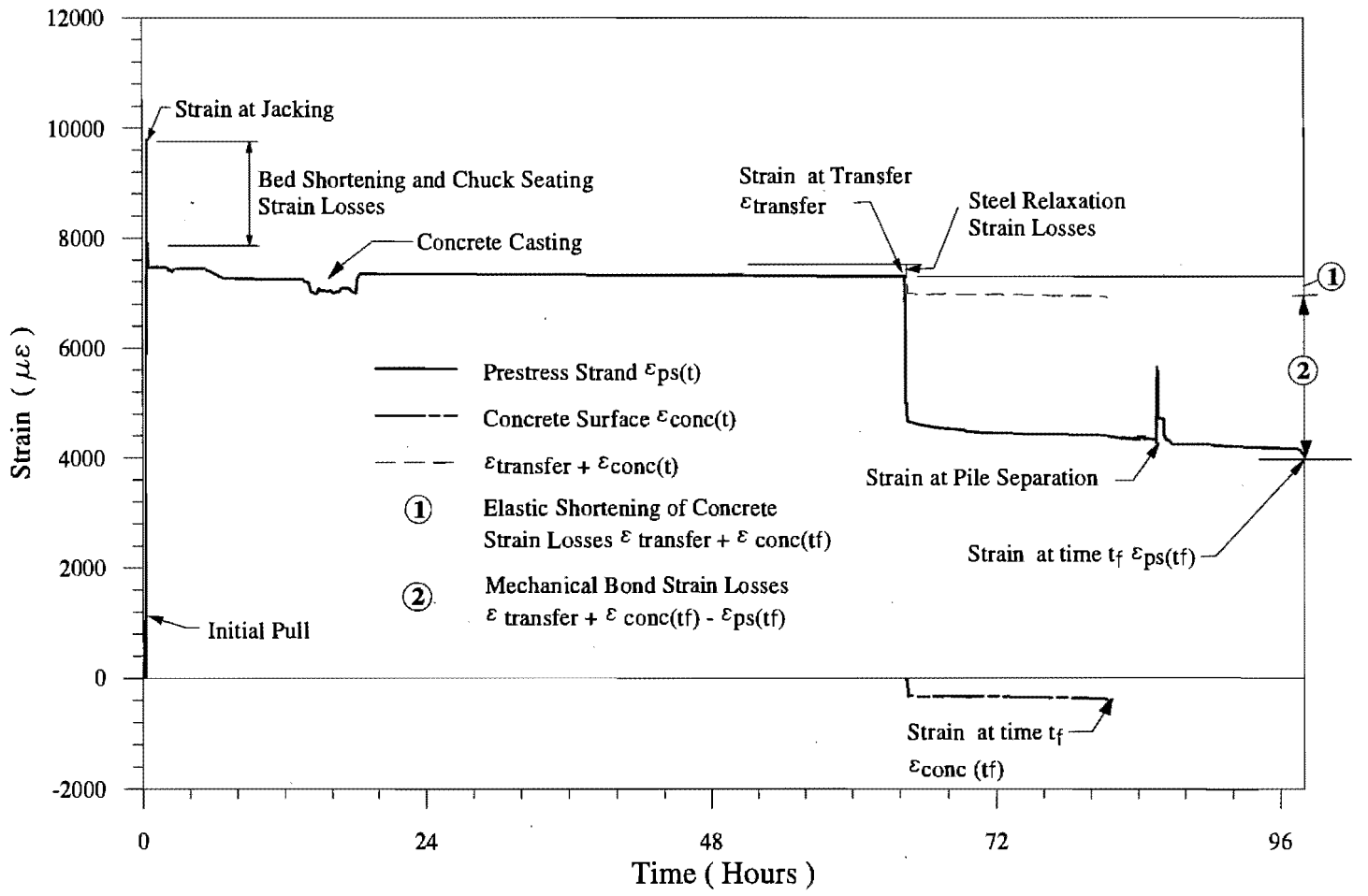

Fig. 4-5 Test Unit *COR2* - Strand Strain versus Time at 610mm from the Pile Head

4.2.1 Regression Analysis

Based on all the strain gage readings obtained during manufacturing of the three concrete shells, a regression analysis was performed in order to estimate the transfer bond length for the prestressing strands. Regression analysis of the obtained data was performed by minimizing the sum of the squared errors for different degrees of polynomials between order one and order four. The best curve fit for the prestressing strands strain gage reading was a quadratic curve, and for the concrete shell surface strain gage readings, the best curve fit was a straight line.

The best curve fit was obtained for the curve with the minimum squared error according to the following expression **[19]**:

$$\Delta^2 = \sum_{i=1}^{n} (y_i - \overline{y_i})^2 \tag{4.7}$$

Where y_i represents the different normalized strain gage readings and $\overline{y_i}$ represents values obtained from the regression curve evaluated at the position of the strain gages. **Fig. 4-6** presents the regression analysis final results.

The strain gage readings were normalized in terms of the following expressions:

$$\varepsilon_{ps} (t_f) / \varepsilon_{transfer} \tag{4.8}$$

for the strand strain gage readings, and:

$$1 - \varepsilon_{conc} (t_f) / \varepsilon_{transfer} \tag{4.9}$$

for the concrete surface strain gage readings. In addition, a 95% confidence interval was established to obtain different ranges of transfer length for pre-test and post-test analysis to study sensitivity of analysis of the pile section under simulated seismic response, as discussed in Chapter 2.

Confidence interval in the estimation of the mean values at different positions corresponding to location of the strain gages was obtained based on the following expression **[20]** :

$$\langle \mu_{1-\alpha} \rangle = \left[\overline{y} \pm t_{\frac{\alpha}{2}, n-1} \frac{s}{\sqrt{n}} \right] \tag{4.10}$$

Where $\langle \mu_{1-\alpha} \rangle$ represents the interval with a confidence of α=95%, $\overline{y}$ is the mean for the normalized strain gage readings as defined earlier, $t_{\frac{\alpha}{2}, n}$ is the t distribution value estimated

at $\alpha/2$ with $n-1$ degrees of freedom, n is the number of data points at each gage position, and s is the unbiased sample variance obtained according to the expression **[20]**:

$$s = \frac{1}{n-1}\left[\sum_{i=1}^{n} y_i^2 - n\,\overline{y^2}\right] \tag{4.12}$$

Regression analysis to estimate the transfer bond length is presented in **Fig. 4-6**. In this figure, data from all of the three test units was used in developing the regression analysis. This analysis takes into account the strain transfer from the prestressing strands into the concrete shell, as a result of the mechanical interlock and bond friction between the strands and the concrete. Assuming that elastic shortening of the concrete shell did not occur, the transfer length would be the distance from the free end of the strand to a point in which no strain losses are observed in the prestressing steel. However, losses due to elastic shortening of the concrete are present and, as expected, losses in the prestressing steel always occur as it is suggested in the plots shown in **Fig. 4-2** through **Fig. 4-4**, obtained from the recorded strain gage data. These plots show the strain versus time history for three different locations along the pile length for test unit *COR1*. Similar plots may be developed for the other test units as illustrated in **Fig. 4-5**.

The prestressing transfer length limit corresponds to that point in which no strain losses occur due to a mechanical bond slip mechanism. In the regression analysis, the transfer bond length was defined as the intersection point between the quadratic regression analysis curve for the strands strain gage data profile and the concrete surface strain gage data profile shown in **Fig. 4-6**. Based on this regression analysis, the transfer bond length was estimated at 1,473 mm, with a 95%confidence interval upper bound of 1,727 mm and lower bound of 1,219 mm. These three values were used in the pre-test and post-test analysis of test units *COR1, COR2* and *COR3,* as discussed in Chapter 2.

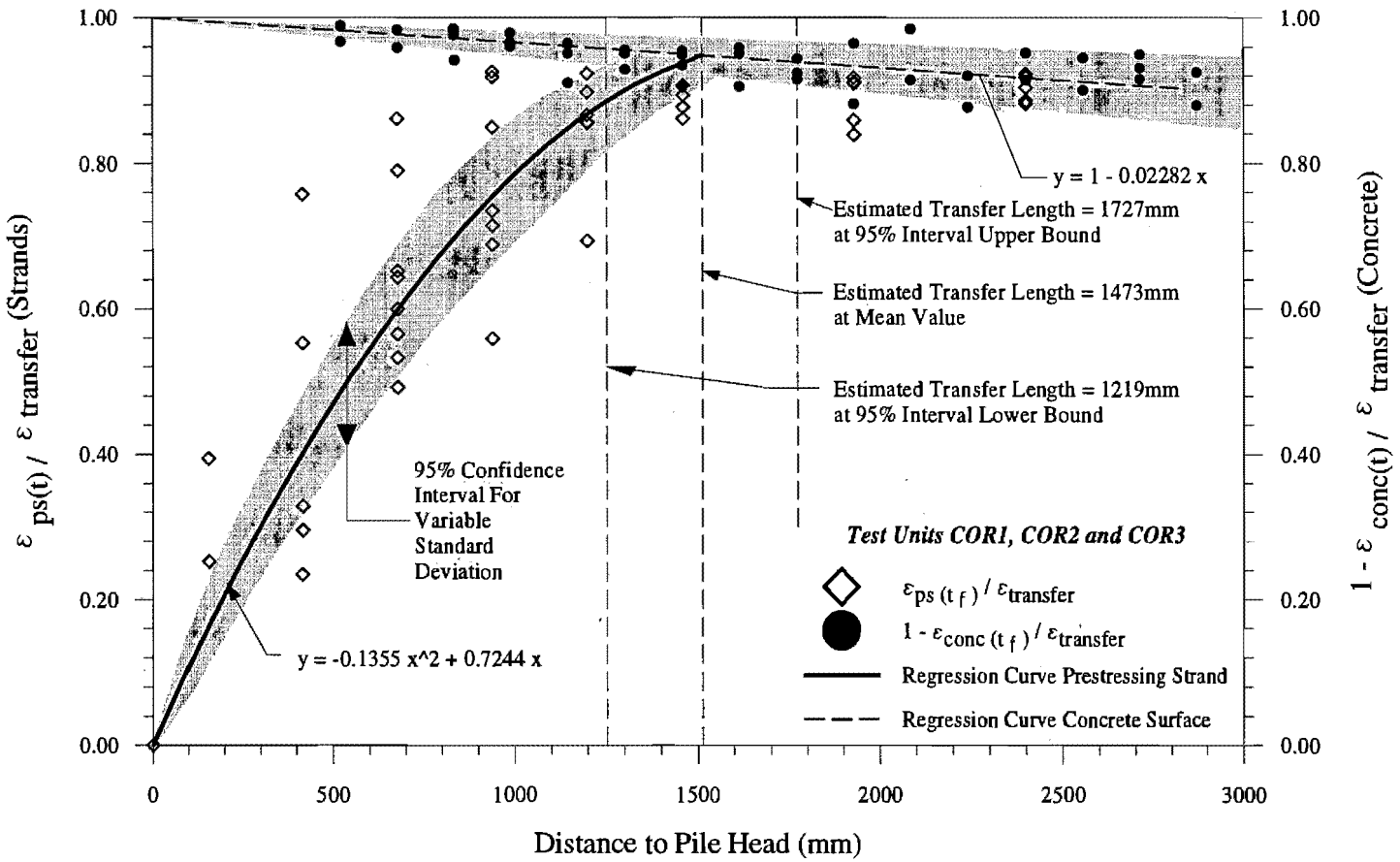

Fig. 4-6 Transfer Bond Length Regression Analysis

4.3 Flexural Bond Length

Flexural bond length for pre-test analysis was based on an average bond strength of 1.72 MPa, which corresponds to the current ACI [4] average bond strength.

4.3.1 Evaluation of Code Provisions for the Development Length of Prestressing Strands

Current ACI code provisions specify that three or seven wire strands shall be bonded within a development length according to the expression [4]:

$$l_{dp} = 0.048 f_{se} d_{bp} + 0.145 (f_{ps} - f_{se}) d_{bp} \quad (SI\ units) \tag{4.13}$$

where the first and second terms represent the transfer and flexural bond length, respectively. Thus, ACI current code provisions specify an average bond strength of 5.21 MPa and 1.72 MPa for transfer and flexural bond, respectively. Based on equation **(4.13)** and assuming an initial prestress of 1,400 MPa, the transfer bond length and flexural bond length are $70d_{bp}$ and $90d_{bp}$, respectively. Thus, the development length for a 9.53 mm diameter prestressing strand with an initial prestressing stress of 1,400 MPa is $160d_{bp}$.

4.3.2 Proposed Code Provisions for the Development Length of Prestressing Strands

Martin et al. **[21]** introduces a different development length requirement for prestressing strands, based on reevaluation of Hanson et al. **[22]** research data. Martin has proposed different equations than the ACI current code provisions for estimation of prestressing development length by fitting a bilinear curve to the curves, calculated by Hanson. Martin recommends the following equations to estimate the prestressing stress at a distance of l_x from the section end of a 9.53 mm diameter prestressing strand **[21]** :

$$f_{ps} = 1.72\, l_x \quad ; \quad l_x \le 80\, d_{bp} \ \text{and}\ d_{bp} = 9.53\ mm \quad (a)$$

$$f_{ps} = 1096 + 0.28\, l_x \quad ; \quad l_x > 80\, d_{bp} \ \text{and}\ d_{bp} = 9.53\ mm \quad (b) \tag{4.14}$$

$$(SI\ units)$$

As before, assuming an initial prestress of 1,400 MPa, the transfer bond length and flexural bond length are $113d_{bp}$ and $229d_{bp}$, respectively. Thus, based on Martin's equations, the development length for a 9.53 mm diameter prestressing strand with an initial prestressing stress of 1400 MPa is $342d_{bp}$, which is approximately 2 times greater than the development length proposed by current ACI code provisions.

Russel et al. more recently developed the following transfer length equation **[23]**:

$$l_t = 0.0725\, f_{se}\, d_{bp} \quad (SI\ units) \tag{4.15}$$

which, yields the transfer length for a 9.53 mm diameter prestressing strand with an initial prestress 1400 MPa of $106d_{bp}$. Russel proposes the flexural bond length be computed according to the average bond length of 1.72 MPa.

Fig. 4-7 presents the normalized prestressing stresses in terms of f_{se} away from the pile ends for the experimental test results, the regression analysis and the different equations presented earlier. In this figure, the experimental test results consist of the final prestressing force recorded in the strands after testing of the three test units in single bending, and the transfer stresses, f_{se}, recorded during manufacturing of the concrete shells. Vertical strain profiles for the prestressing strands for the three test units are presented in Chapters 5, 6 and 7.

In **Fig. 4-7**, the stresses indicated by the experimental test results increase from the pile head to approximately 1,000 mm, and there is a reduction of stresses beyond a distance of approximately 1,600 mm. This reduction in stress can be explained in terms of reduced moment demand along the height of the pile. At the base of the pile, the moment demand is highest, which is in the region of development of the prestress, as illustrated in **Fig. 2-18**. Thus, it is not possible to quantify the flexural bond length for these test units based on the experimental test results because of the reduction in stresses outside of the transfer length zone.

The top linear part of the regression analysis curve presented in **Fig. 4-7** was obtained by assuming an average flexural bond strength of 1.72 MPa. Referring to this figure, it is clear that in regions near the pile ends, the regression analysis curve approximates the curves proposed by Martin and Russel and the proposed code provision curve presents a lower bound. In conclusion, test results in comparison with the pre-test analysis presented in Chapter 2 suggests a higher transfer length than the one estimated based on ACI 318 requirements.

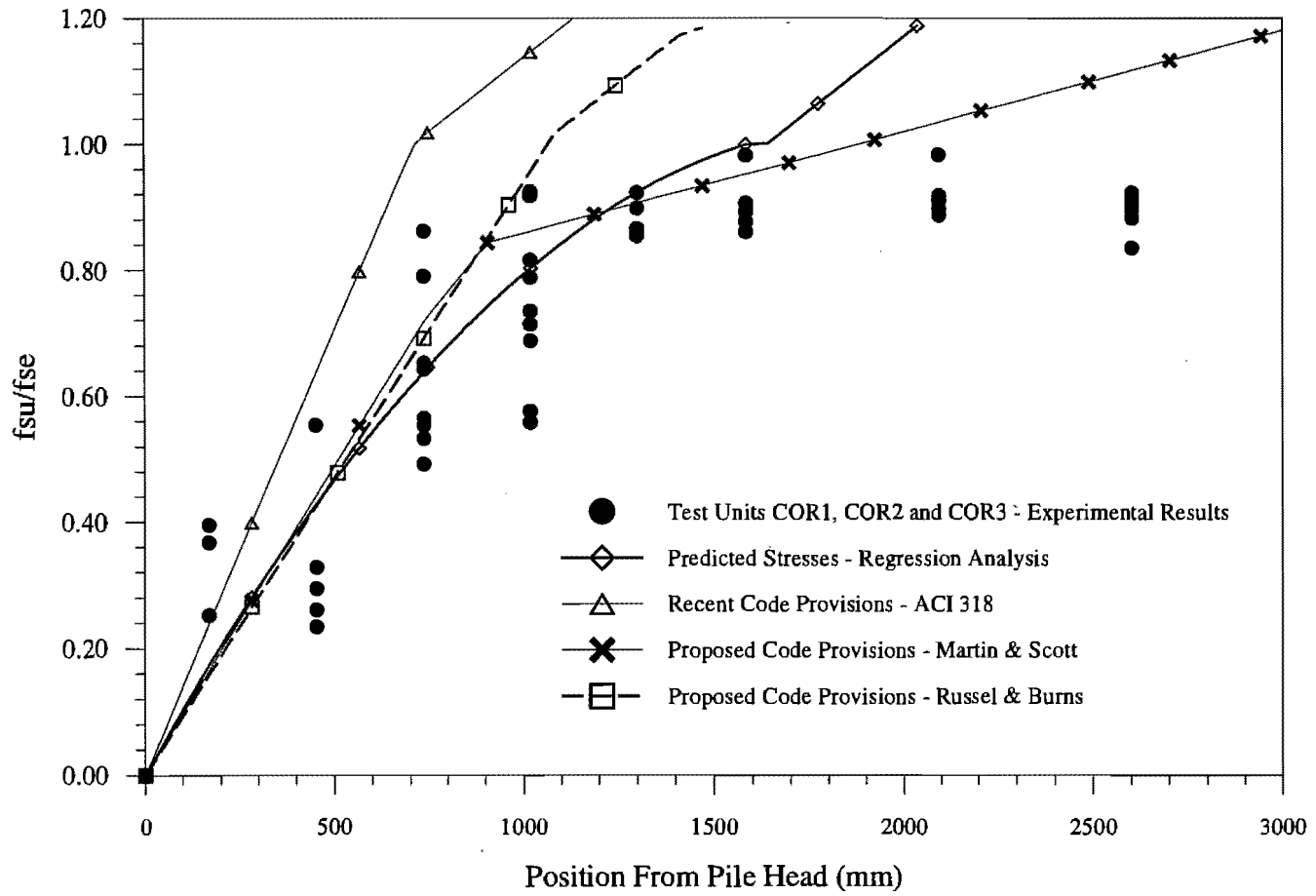

Fig. 4-7 Stress Profiles versus Distance to Pile Ends

5. Test Unit *COR1* Experimental Test Results

This chapter includes a brief discussion of the general test description, load deformation characteristics, control loading program performance, axial load versus lateral load characteristics, vertical strain profiles longitudinal reinforcement and curvature profiles.

5.1 General Test Observations

Seismic load simulation of the pile specimen required application of fully reversed cycles in both the vertical and lateral actuators. In this section, when in compression, the axial force is designated as positive and, when in tension, the axial force is designated as negative. In addition, when in the compression loading branch, the lateral force is positive and in the tension loading branch, the lateral force is designated as negative. The complete test setup for unit *COR1* is shown in **Fig. 3-18**. Indicated on the test unit, 1,295 mm above the pile cap is a horizontal line that marks the end of the inner core longitudinal reinforcement.

General observations recorded during the testing procedure are summarized as follows:

Initial Axial Force Simulation : The first loading stage in the testing procedure consisted of loading the specimen axially to +863 kN while controlling the top lateral displacement to +0.00 mm. At the end of this loading stage, the lateral force was registered at approximately +4 kN. This lateral force was then used as H_o to define Curve VII and Curve XIV for unloading, as described in Chapter 3, while describing test unit *COR1* control program outline.

At +76 kN in the compression loading branch: This loading stage corresponds to the specified +25% yielding force level. In this cycle, the registered lateral deflection was +1.47 mm and the axial load was +1,029 kN.

At -43 kN in the tension loading branch: This loading stage corresponds to the prescribed -25% yielding force level. The lateral deflection and the axial load were respectively -1.49 mm and +738 kN.

At +152 kN in the compression loading branch: At the prescribed +50% yielding force level, the lateral deflection was +4.09 mm and the axial load was+1320 kN. At this loading stage, the structure displayed no signs of physical distress, as no cracks were observed in the test specimen.

At -87 kN in the tension loading branch: At -50% yielding, the lateral deflection and axial load were, respectively, -3.22 mm and +578 kN.

At +227 kN in the compression loading branch: In this cycle the structure was loaded to +75% yielding in which the lateral deflection was registered at +7.37 mm and the axial load was+1596 kN.

At -130 kN in the tension loading branch: At -75% yielding the lateral deflection was -5.92 mm and the axial was +393 kN.

At +302 kN in the compression loading branch: This loading stage corresponds to the theoretical first section yielding (+100% yielding), at which stage the lateral deflection and axial load were, respectively, +12.75 mm and +1948 kN. During loading of the specimen a noise was heard, followed by a slight drop in the lateral load. However, inspection of the structure revealed no signs of physical distress.

At -173 kN in the tension loading branch: This loading stage corresponds to the theoretical first section yielding while in the tension loading branch (-100%yielding). At this stage the lateral deflection and the axial load were registered at approximately -11.64 mm and +190 kN, respectively.

After this cycle the loading pattern was changed from single cycles to three cycles, according to the prescribed displacement ductility levels. The experimental yield displacements, Δ'_y, and the loads corresponding to theoretical first section yield, V'_y, and yield, V_y, that were used in the bilinear approximation calculations are as follows:

1. Lateral deflections at theoretical first section yielding:

   Compression : Δ'_{yC} = +12.75 mm Tension : Δ'_{yT} = -11.64 mm

2. Lateral load at theoretical first section yielding:

   Compression : V'_{yC} = +302 kN Tension : V'_{yT} = -173 kN

3. Lateral load at theoretical section yielding:

Compression : V_{yC}=+ 403 kN

Tension : V_{yT}= -204 kN

4. Calculation of displacement ductility μ_Δ = +,-1:

$$Compression : \frac{V_{yC}}{V'_{yC}} \Delta'_{yC} = +17.02mm$$

$$Tension : \frac{V_{yT}}{V'_{yT}} \Delta'_{yT} = -13.72mm$$

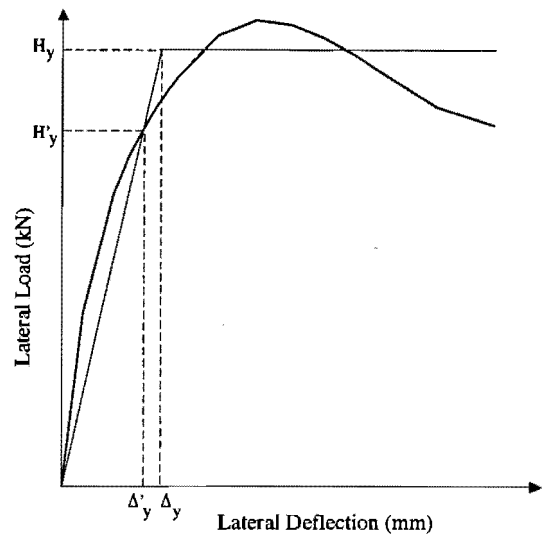

Fig. 5-1 Bilinear approximation

At Δ = +17.02 mm in the compression loading branch (μ_Δ = +1): In this cycle the structure was displaced to the theoretical section yielding computed above. No damaged was yet observed in this stage. The peak lateral load was recorded at +347 kN and the axial load at +2304 kN.

At Δ = -13.72 mm in the tension loading branch (μ_Δ = -1): In this cycle the structure was displaced to the theoretical section yielding computed above. At this displacement ductility level, the lateral load was -178 kN and the axial load was +66 kN.

At Δ = +25.65 mm in the compression loading branch (μ_Δ = +1.5): Onset of cracking began with a single horizontal flexural crack registered at approximately 457 mm from the soffit slab and a vertical splitting crack 1,092 mm long, starting at 584 mm from the soffit slab, providing first visual evidence of slipping of the prestressing strands (see **Fig. 5-2**). Peak lateral and axial loads at this displacement ductility level were +415 kN and +2,630 kN, respectively.

At Δ = -20.57 mm in the tension loading branch (μ_Δ = -1.5): In the tension loading branch, onset of cracking began also at this level, with similar observations described earlier. A horizontal flexural crack was first observed at a height of 1,219 mm, and a vertical splitting crack started at 76 mm from the soffit slab and extended 1,956 mm centered about the line, marking the end of the longitudinal reinforcement (see **Fig. 5-3**). Peak lateral and axial loads at this displacement ductility level were -194 kN and -28 kN, respectively. At this cycle the axial load was for the first time in tension.

At Δ = +34.04 mm in the compression loading branch (μ_Δ = +2): Lateral load and axial load at this displacement level were +456 kN and +2,758 kN, respectively. At this cycle, the prescribed maximum axial compressive load that the prototype structure might experience in a seismic event was achieved.

At Δ = -27.43 mm in the compression loading branch (μ_Δ = -2): At this displacement ductility level, the lateral load was -191 kN and the axial load was -38 kN.

At +51.05 mm in the compression loading branch (μ_Δ = +3): Minor crushing and spalling of the cover concrete at the base of the pile indicate first signs of formation of plastic hinge in this region. More extensive vertical splitting cracks appeared in the region where the longitudinal reinforcement terminates. One additional horizontal flexural crack was observed at approximately 1,270 mm above the soffit slab. In addition, on the sides of the pile, the previous marked flexural cracks are beginning to incline towards the opposite side of the compression toe, as indicated in **Fig. 5-4**. This occurrence is opposite to the formation of the flexural-shear cracking pattern that might be expected in any flexural-shear test. At this displacement ductility level, the lateral load was +520 kN and the axial load was +2,758 kN. At this stage, the maximum flexural strength was achieved under axial compressive loading.

At -54.86 mm in the tension loading branch (μ_Δ = -4): The structure is expected to display an increased displacement ductility capacity in the tension loading branch, compared to the ductility levels obtained for the compression loading branch. As a result, the loading procedure was effected such that the ratio in increase of the current ductility level to the expected ultimate ductility level was approximately the same in both loading branches to avoid early failure in any one of the loading branches. Registered lateral load and axial load were -229 kN and -298 kN, respectively. Concurrently with the compression loading branch in the tension loading branch, the maximum flexural strength of the structure was achieved at this stage.

At +59.69 mm in the compression loading branch (μ_Δ = +3.5): A few minor cracks were recorded in this stage which emanated from previous cracks. Peaks loads at this displacement ductility level were +494 kN and +2,758 kN, respectively.

At -82.30 mm in the tension loading branch (μ_Δ = -6): Peaks loads at this displacement ductility level were -215 kN and -302 kN, respectively. At this cycle the prescribed maximum axial tensile load that the prototype structure might experience in a seismic event was achieved.

At +68.07 mm in the compression loading branch (μ_Δ = +4): No significant increase in the number of flexural, vertical or inclined cracks was recorded. However, present cracks are wide open, which corroborates the section negative stiffness while in the transition from the compression to the tension loading branch, or vice versa, until cracks begin to close at the compression toe. Peak loads were lateral load +495 kN and axial load +2758 kN. Slight drop in the lateral load from peak load was observed. During the third cycle at this displacement level, crushing and spalling of the cover concrete at the region where the longitudinal reinforcement terminates is observed, which indicates plastic hinge formation in this region (see **Fig. 5-5**).

At -109.73 mm in the tension loading branch (μ_Δ = -8): Wide open horizontal flexural crack at the termination of the inner core reinforcement was observed. Concentration of inclined flexural cracks is more visible when in the tension loading branch than in the compression loading branch and inclination of flexural-shear cracks are towards the opposite side of the compression toe as previously documented (see **Fig. 5-6**). At this displacement ductility level, the lateral load was -211 kN and the axial load was -302 kN.

At +85.09 mm cycle in the compression loading branch (μ_Δ = +5): Significant crushing and spalling of the cover concrete in the region where the longitudinal reinforcement terminates indicates considerable loss in the moment carrying capacity of the section in this region (see **Fig. 5-7**). At this displacement ductility level, the lateral load was +457 kN and the axial load was +2758 kN. Lateral load continued to drop from peak load by approximately 10%. At the third cycle, increased crushing and spalling of the cover concrete was observed, and fracture of the spiral bars, due to buckling of the prestressing strands, occurred at the termination of the longitudinal reinforcement. This event was followed by unwinding and buckling of the exposed prestressing strands, with increasing propagation of the plastic hinge at this level (see **Fig. 5-8** and **Fig. 5-9**).

At -137.16 mm in the tension loading branch (μ_Δ = -10): At this displacement ductility level, the lateral load and axial load were –192 kN and -302 kN, respectively. The lateral capacity of the pile specimen was approximately 84% of the registered maximum lateral capacity. The testing procedure was stopped at this stage because rapid lateral load degradation occurred during the last cycles of the testing procedure. However, the axial load was still being supported by the specimen. **Fig. 5-10** indicates formation of second region of plastic deformations above soffit slab where inner core longitudinal reinforcement terminates.

Post test investigation of the specimen revealed that a total of 5 fractures occurred in the spiral cage and that the inner core bars were exposed. In addition, at the termination of the inner core longitudinal reinforcement, a crack approximately 25.4 mm wide was visible. **Fig. 5-11** shows the final damage state of the test unit.

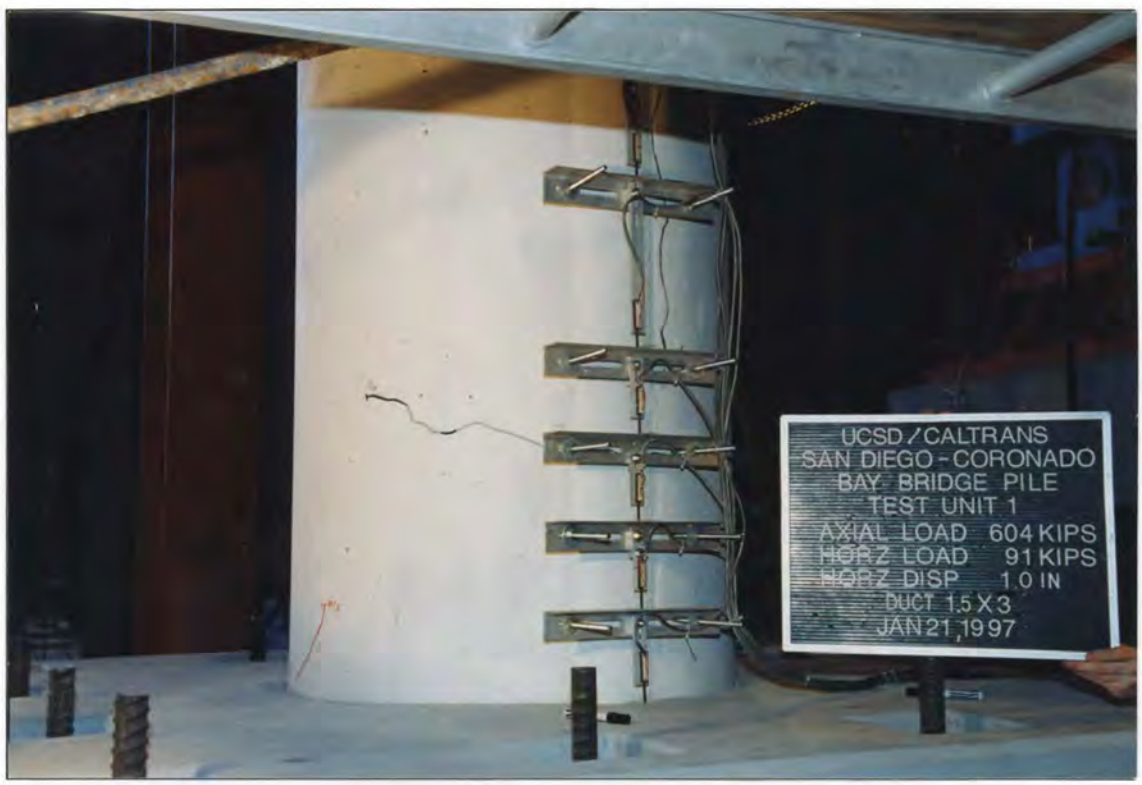

Fig. 5-2 Onset of Flexural Cracking at Lateral Deflection +25.65 mm

Fig. 5-4 Cracking Pattern at +51.05mm

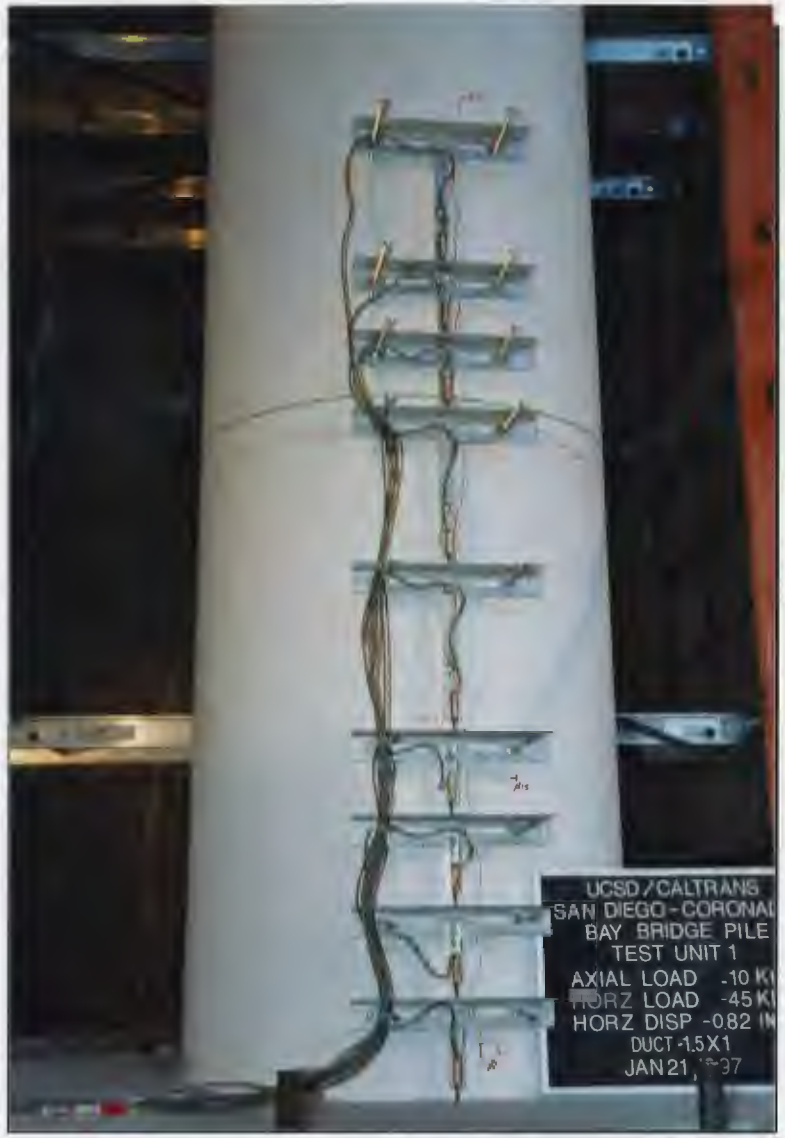

Fig. 5-3 Cracking Pattern at -20.57mm

Fig. 5-6 Cracking Pattern at -109.73mm

Fig. 5-5 Onset of Plastic Hinge Relocation at +68.07mm

Fig. 5-7 Extent of Spalling at +85.09mm

Fig. 5-8 Unwinding of Prestressing Strands at Lateral Deflection +85.09mm

Fig. 5-9 Wide Open Crack Above Inner Core Bars

Fig. 5-11 Complete Test Setup After Testing

Fig. 5-10 Plastic Hinge Relocation at -137.16mm

5.2 Load Deformation Characteristics

Fig. 5-12 shows the measured lateral force versus lateral deflection response of test unit *COR1*. The initial response of the pile section indicates a slightly higher stiffness than originally predicted in both the compression and tension loading branch. At peak load in the compression loading branch, the predicted maximum load was approximately 20% lower than the measured maximum load. However, in the tension loading branch, the predicted value matches closely the observed test results.

In the compression loading branch, a maximum lateral force of +520 kN was recorded at approximately μ_Δ=3x1. At this level, 5% degradation of lateral strength between successive cycles was recorded, and between μ_Δ=3x1 and μ_Δ=4x1, only a minor reduction was observed, which coincides with the first stages of crushing and spalling of the cover concrete in the region where the longitudinal reinforcement terminates. At μ_Δ=5x1 there was a significant drop in the lateral strength of the section and, at successive cycles, the lateral load decreased rapidly as a consequence of loss of the cover concrete around the termination of the longitudinal reinforcement and slipping of the prestressing strands.

A maximum lateral force of -229 kN was recorded in the tension loading branch during cycle μ_Δ=-4x1. At successive cycles μ_Δ=-8x1 and μ_Δ=-10x1, approximately 3% of loss in the lateral strength was recorded. The testing procedure was stopped at μ_Δ=-10x3 because of rapid degradation in the lateral strength of the section.

Post test investigation of the test data indicates that the maximum displacement ductility of μ_Δ=+5 was achieved in the compression loading branch and μ_Δ=−10 was achieved in the tension loading branch. However, excessive degradation at these levels is significant. In the compression loading branch, lateral deflections at maximum displacement and yield were, respectively, Δ_{max}= +85.09 mm and Δ_y = +17.02 mm, while in the tension loading branch these values were Δ_{max}= -137.16 mm and Δ_y= -13.72 mm, respectively.

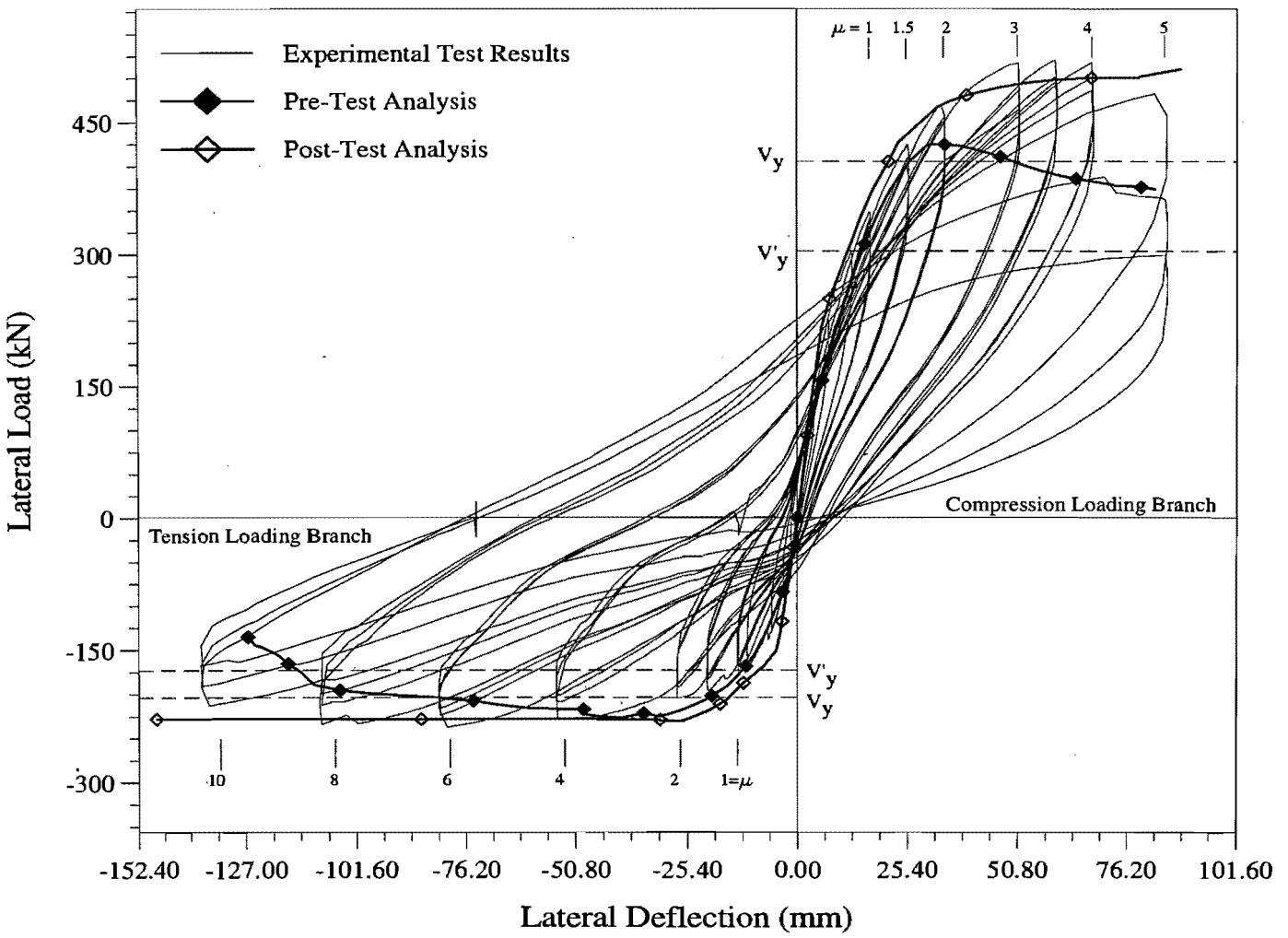

Fig. 5-12 Lateral Load versus Lateral Deflection Characteristics

Fig. 5-13 shows the measured lateral force versus curvatures computed at the pile cap interface. The diagram depicted in this figure indicates a good correlation between the post test analysis and the experimental test results, in particularly at peak forces. The main characteristics visible in this figure are very similar to those indicated earlier for the pile lateral deflection, mainly negative stiffness at the transition from the compression to the tension loading branch and vice versa and lower stiffness in the compression loading branch.

Post test investigation of the test data indicates that a maximum curvature ductility of μ_φ=+11 was achieved in the compression loading branch and μ_φ=-17 in the tension loading branch. In the compression loading branch, maximum and yield curvatures are, respectively, φ_{max}=+0.00006 mm^{-1} and φ_y=+0.0000055 mm^{-1}, and φ_{max}=-0.000085 mm^{-1} and φ_y=-0.000005 mm^{-1} in the tension loading branch. As expected, curvature ductility levels are slightly higher than displacement ductility levels.

Curvatures presented in **Fig. 5-13** represent average values and were computed according to the expression:

$$\varphi_{ave} = \frac{\Delta_N - \Delta_S}{W_{cur}\, h_{cur}} \tag{5.1}$$

where Δ_N and Δ_S are the relative vertical displacements between adjacent curvature rods in the extreme faces on opposite sides of the pile section, W_{cur} is the horizontal distance between the pair of linear potentiometers and h_{cur} is the vertical distance between the adjacent linear potentiometers.

During computations of curvatures at the pile cap interface, the height of the linear potentiometer cell h_{cur} include an additional term to account for tensile strain penetration into the pile cap by including the strain penetration length into the curvature cell height, h_{cur}, according to the expression:

$$h_{Total} = h_{cur} + 0.022\, d_b\, f_s \tag{5.2}$$

where d_b is the main pile bar diameter and f_s is the pile main bar stress obtained from the pile inner core reinforcement strains. In the early stages of the testing procedure, strain levels in the inner core reinforcement are minimum and f_s should be used instead of f_y because tensile strain penetrations are negligible.

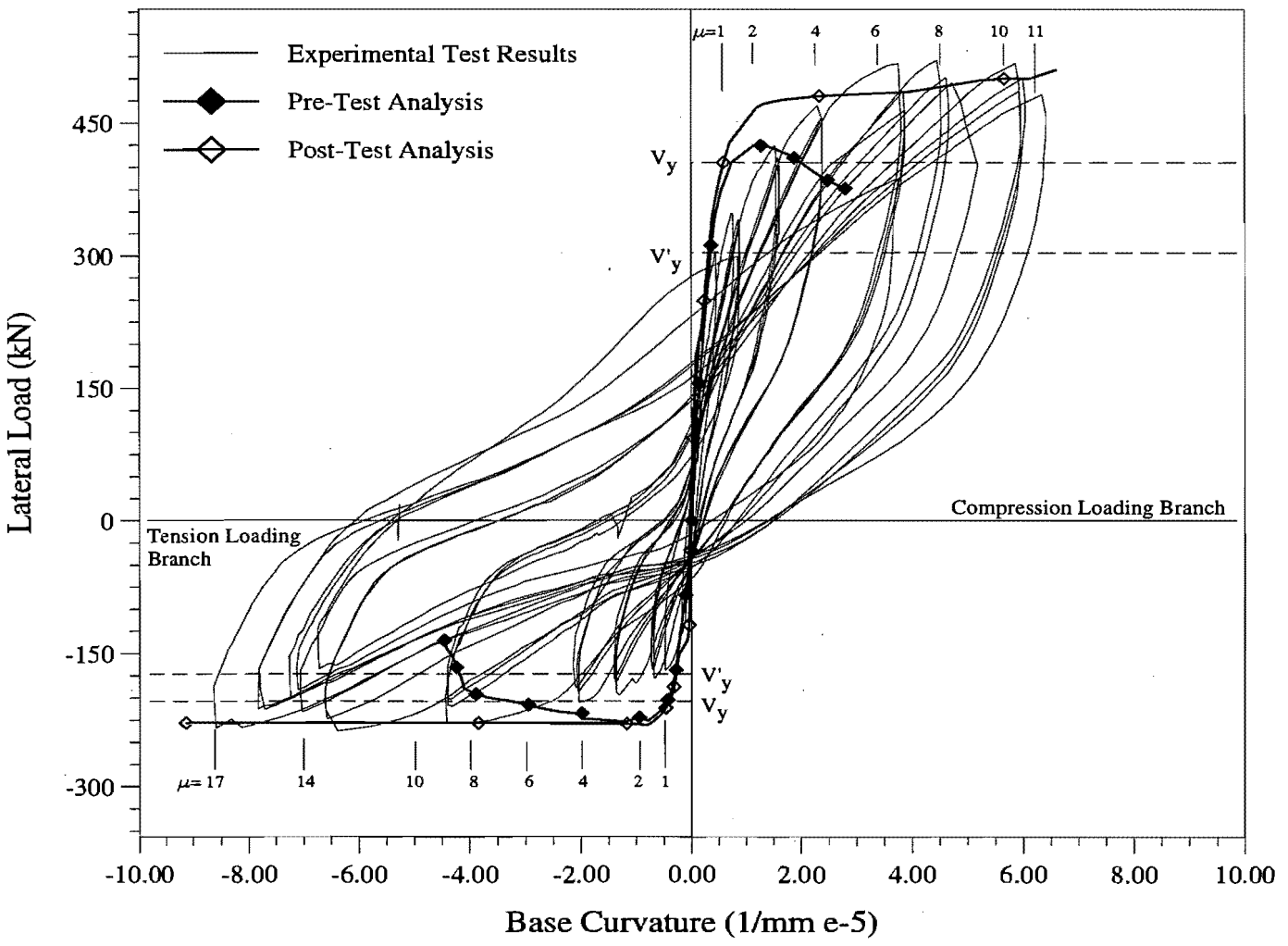

Fig. 5-13 Lateral Load versus Base Curvature Characteristics

Axial load versus lateral deflection characteristics are presented in **Fig. 5-14**. This figure also shows the profile of the loading path that was employed to control the application of the simulated seismic forces. The maximum and minimum axial loads were predefined at +2793 kN in the compression loading branch and -302 kN in the tension loading branch, respectively.

Loading curves defined in Chapter 3 for test unit *COR1* are also presented in **Fig. 5-14**. In addition, indicated in this figure are the location at which the residual displacements Δ_i were obtained when Curve VII and Curve XIV crossed the initial axial load axis and used to define Curve I, Curve II and/or Curve III in **Region 1** and Curve VIII, Curve IX and/or Curve X in **Region 3**, which redirect the loading path towards the control program loading path. In **Fig. 5-14** not all curves are presented for clarity. Refer to **Fig. 3-53** for additional curves not shown here. As expected, these curves are straight lines which emanate from the residual displacements, Δ_i, and point towards the end points of these curves.

Fig. 5-15 presents the axial load versus the lateral load characteristics for test unit *COR1*. In this figure is also shown the pre-test analysis loading path which was used to develop the control program loading path depicted in **Fig. 5-14**. Pinching in the hysteresis loops at the initial axial load are due to the fact that the control program loading path in the unloading branches is described by a straight line initiating at the peak deformation to the initial load state.

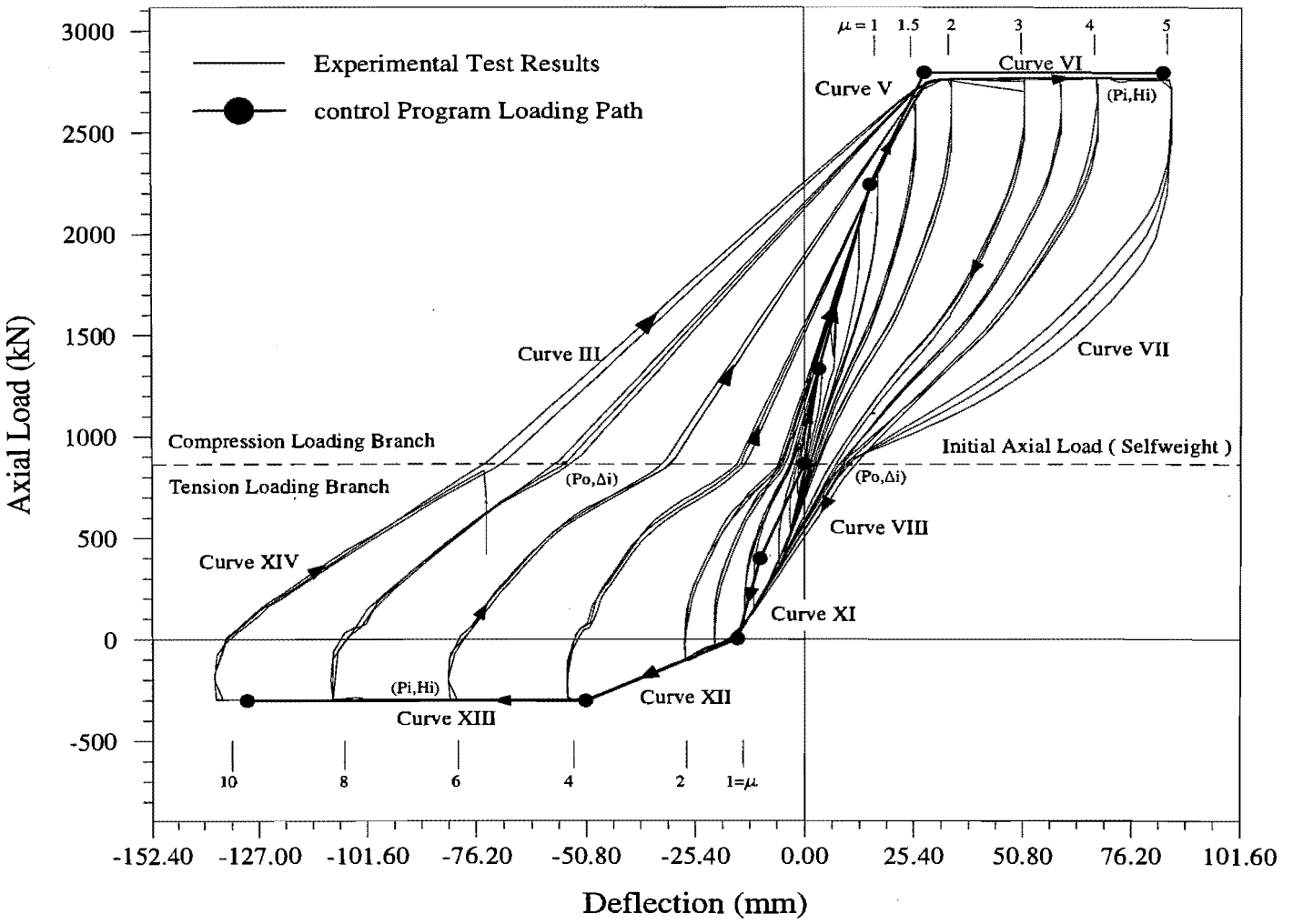

Fig. 5-14 Axial Load versus Lateral Deflection Characteristics

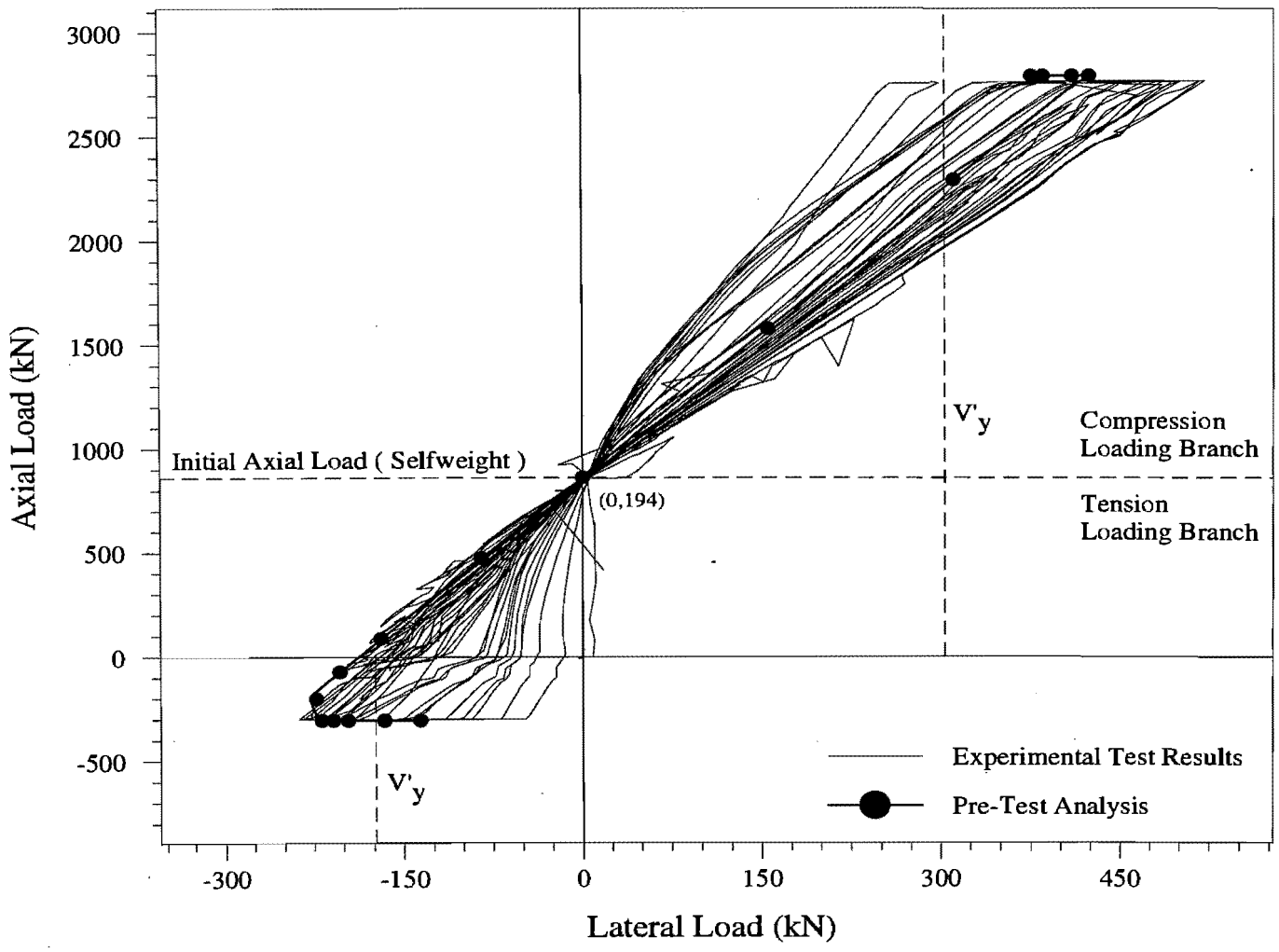

Fig. 5-15 Axial Load versus Lateral Load Characteristics

5.3 Pile Curvature Profiles

In this section and future sections, the plotted values are the first cycle peak values for each cyclic response. Curvature vertical profiles along the height of the pile are presented in **Fig. 5-16(a)** and **Fig. 5-16(b)** for initial and final stages of the testing procedure, respectively.

The curvature profiles depicted in **Fig. 5-16(a)** show that in the initial stages of the testing procedure region of plastic deformations form at the bottom of the pile section illustrated by a significant increase in curvature a position ***1***. A second region of plastic deformations is well illustrated in **Fig. 5-16(a)**, depicted by a significant increase in the curvature near the region where the inner core longitudinal reinforcement terminates. This second region of plastic deformations began to form when the lateral deflection was approximately Δ=-54.86 mm as a result of wide open cracks at this location, as it was previously described.

The curvature profiles along the height of the pile, illustrated in **Fig. 5-16(b)**, indicate the length of the plastic hinge reached a maximum height of approximately 356 mm above the pile cap interface. Referring to **Fig. 5-16(b),** in the tension loading branch, maximum curvatures at the soffit slab were recorded when the lateral deflection was approximately Δ=−109.27 mm, and a decrease in curvature is observed at increasing lateral deflections which indicates relocation of plastic hinge. At the same displacement levels, curvatures at the termination of the inner longitudinal reinforcement increase with increasing lateral deflection.

Indicated in these figures are the yield curvature levels obtained from **Fig. 5-16(a)**, which provides a visual indication of regions of plastic deformations achieved in the different loading stages. The length of the plastic hinge reached a maximum height of approximately 356 mm near the soffit slab, which is considerably less than the theoretical effective plastic hinge length, l_p, of 522 mm, obtained from the expression **[8]**:

$$l_p = 0.08\, H_{pile} + 0.022\, d_b\, f_y \qquad \textbf{(5.3)}$$

This difference between experimental and theoretical results can be attributed to minimum crushing of cover concrete at the base of the pile section. If plastic deformations at the base of the pile section are sought to occur only in terms of yielding of the longitudinal reinforcement, then one obtains from the tensile strain penetration term presented above the

plastic hinge length of approximately 148 mm. Thus, a smaller value than the experimental test results can be explained in terms of some crushing of the cover concrete. Note inner core reinforcement is Grade40 steel.

At the location where the longitudinal reinforcement terminates, it is not readily perceived what is the exact length of plastic deformations; however, region of plastic deformations are more concentrated between positions ***8*** and ***5***, which leads to a plastic hinge length of approximately 609 mm.

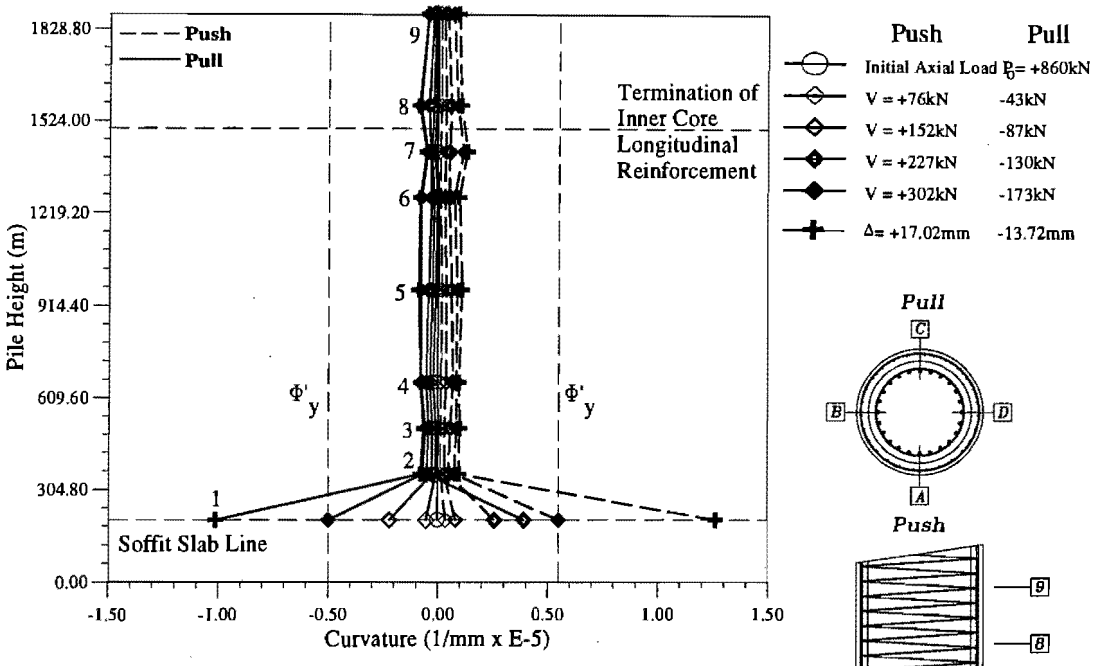

(a) Curvature Vertical Profiles - Initial Stages of Testing

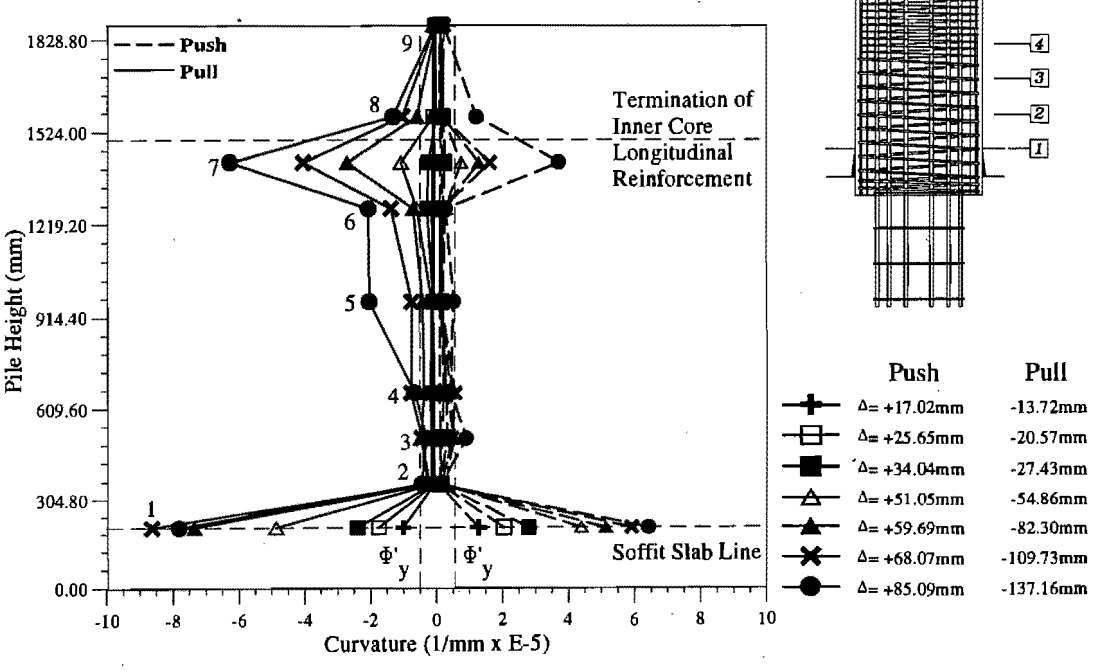

(b) Curvature Vertical Profiles - Final Stages of Testing

Fig. 5-16 Curvature Vertical Profiles

5.4 Pile Inner Core Longitudinal Reinforcement Strain Profiles

The inner core reinforcement consists of #7 Grade40 (f_y=276 MPa) steel with a yield strain of approximately 1500$\mu\varepsilon$.

5.4.1 Pile Longitudinal Reinforcement - Vertical Strain Profiles

Vertical strain profiles for the inner core longitudinal reinforcement are presented in **Fig. 5-17** through **Fig. 5-20**.

Strain profiles along inner core bar ***A*** reveal that yielding of this bar in compression occurred at approximately 304 mm above the pile cap line at μ_Δ=+2, and yield in tension at the same location at μ_Δ=-1.5. Yield strain penetrations were recorded in this bar to a depth of approximately -304 mm, which indicates a strain penetration of approximately $0.045 d_b f_y$. In addition, strain profiles indicate an approximate linear variation of strains from the top of the bar to approximately position ***6***, which suggests a development length of approximately 533 mm. For this level of development length, an average bond stress of approximately $\mu_{ave} = 223\sqrt{f_c'}\ [Mpa]$ is required according to the expression $\mu_{ave} = (d_b f_y)/(4 l_d)$. Basic development length of a #7 bar, as required by the ACI318 [4], implies a bond strength of $\mu_{ave} = 128\sqrt{f_c'}\ [MPa]$.

The profiles for bars ***B*** and ***D***, which are positioned on the sides of the pile, revealed that these bars where always in tension and reached yielding only at later stages of the testing procedure.

Strain profiles along inner core bar ***C*** reveal this bar yielded in tension at approximately μ_Δ=+2 and, in compression, the recorded strains were always below yielding. Furthermore, yield strain penetration into the pile cap did not occur until later stages of the testing procedure. Yield strain levels for this bar were not recorded below a depth of approximately -304 mm, which matches the results for bar ***A***.

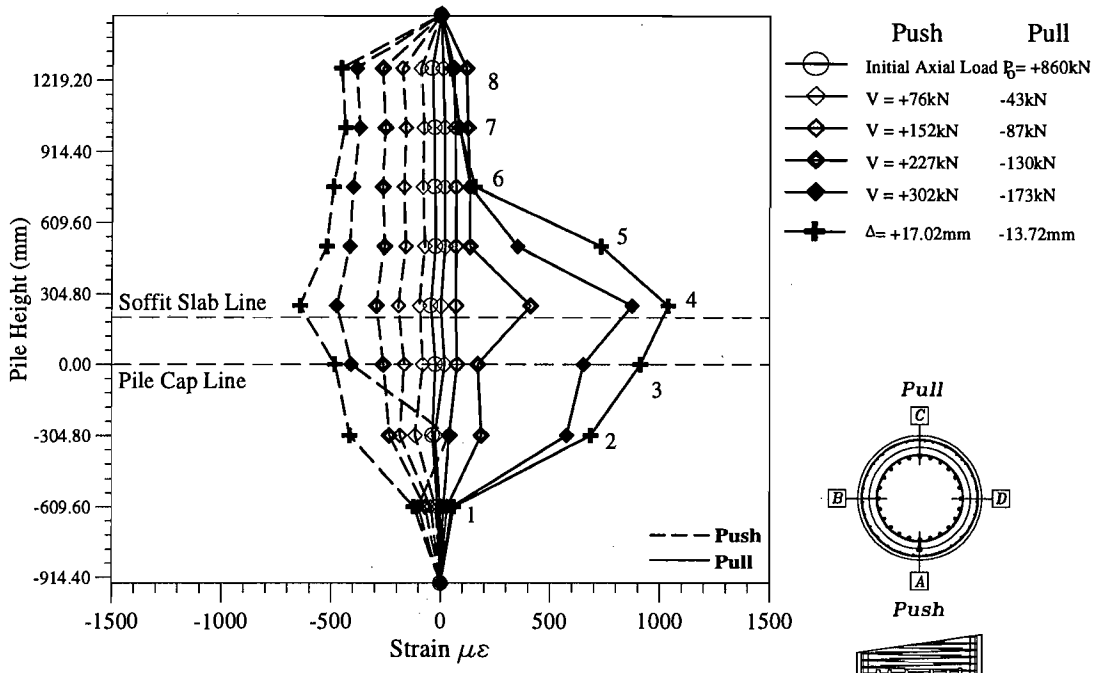

(a) Vertical Strain Profiles - Initial Stages of Testing

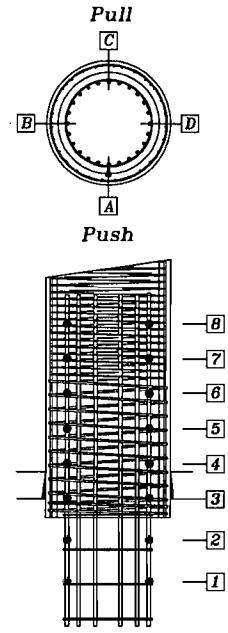

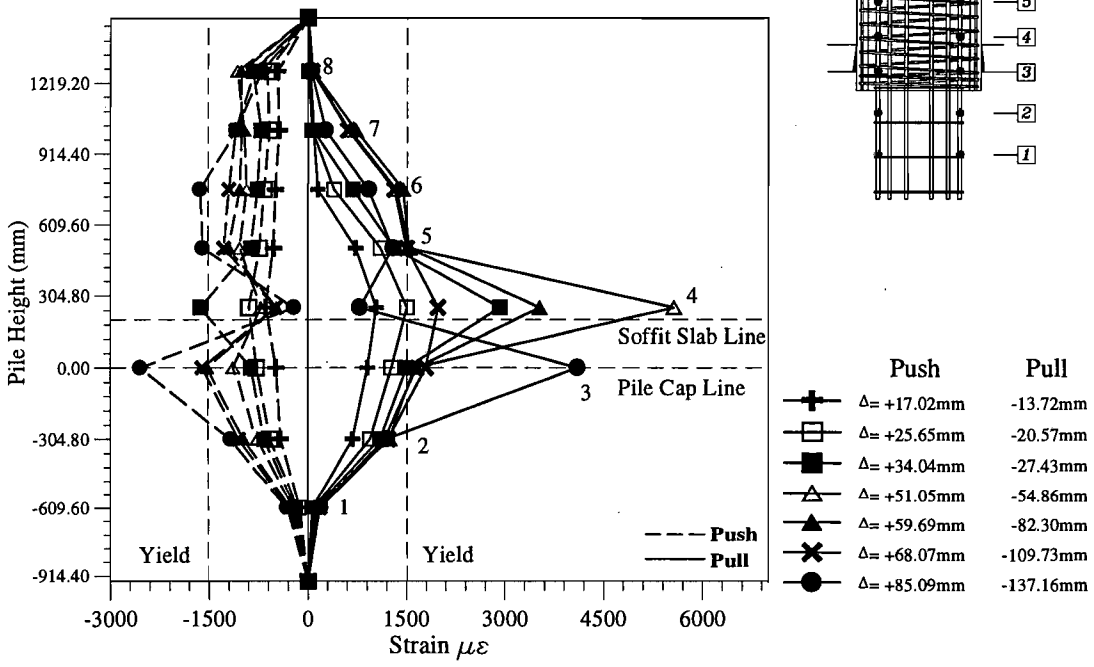

(b) Vertical Strain Profiles - Final Stages of Testing

Fig. 5-17 Vertical Strain Profiles Inner Core Bar *A*

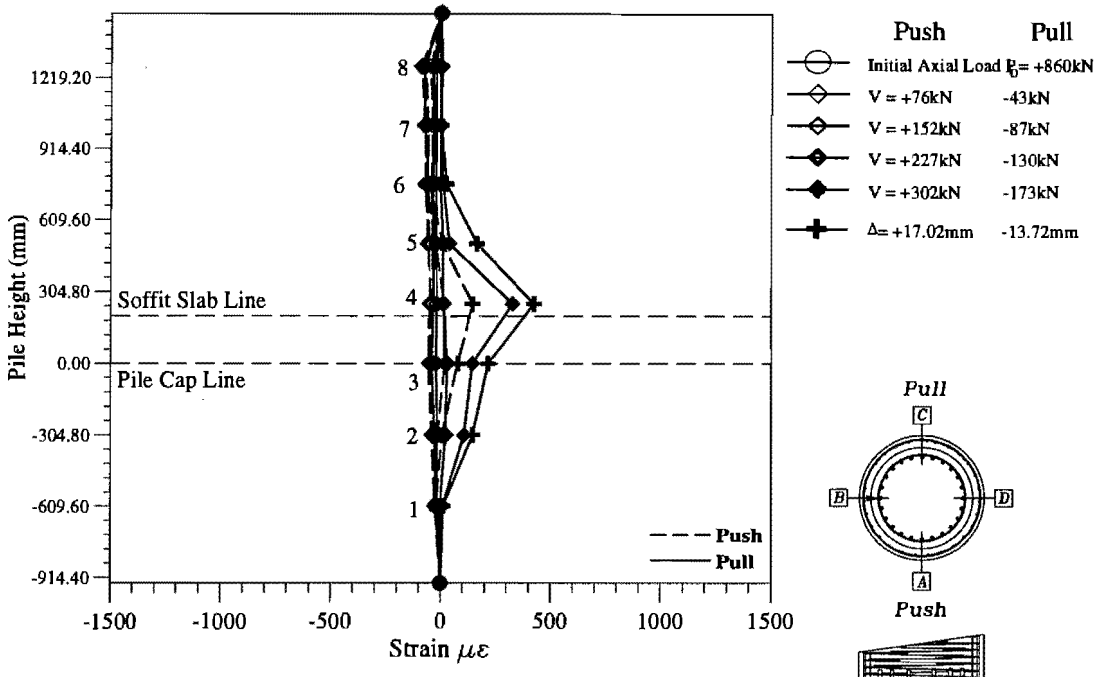

(a) Vertical Strain Profiles - Initial Stages of Testing

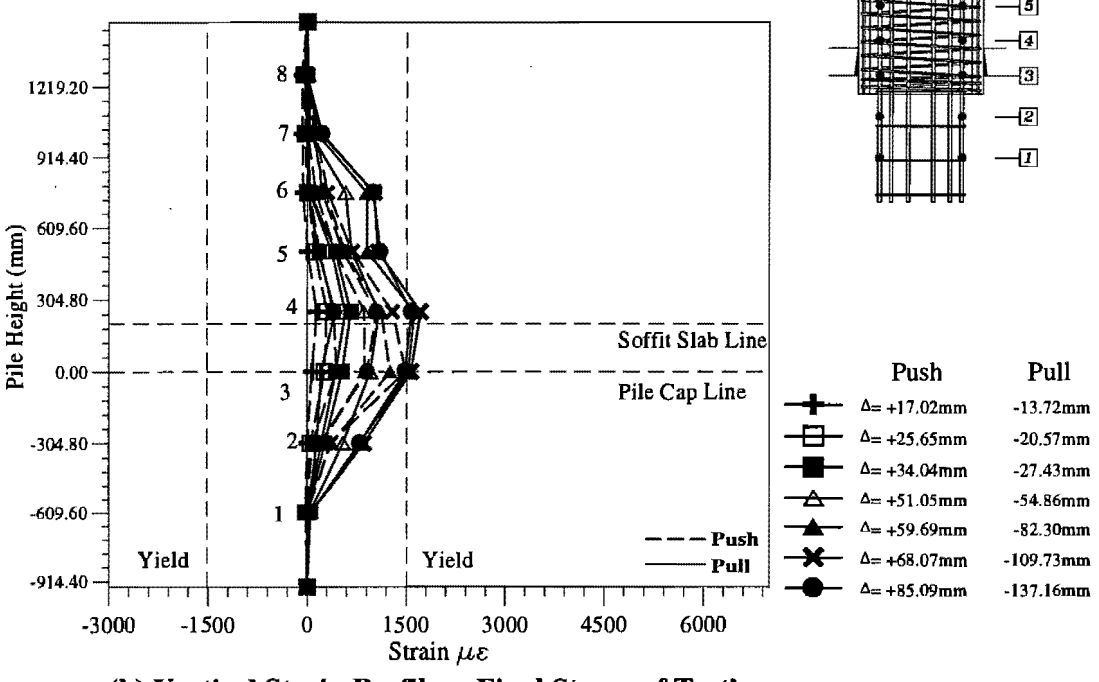

(b) Vertical Strain Profiles - Final Stages of Testing

Fig. 5-18 Vertical Strain Profiles Inner Core Bar ***B***

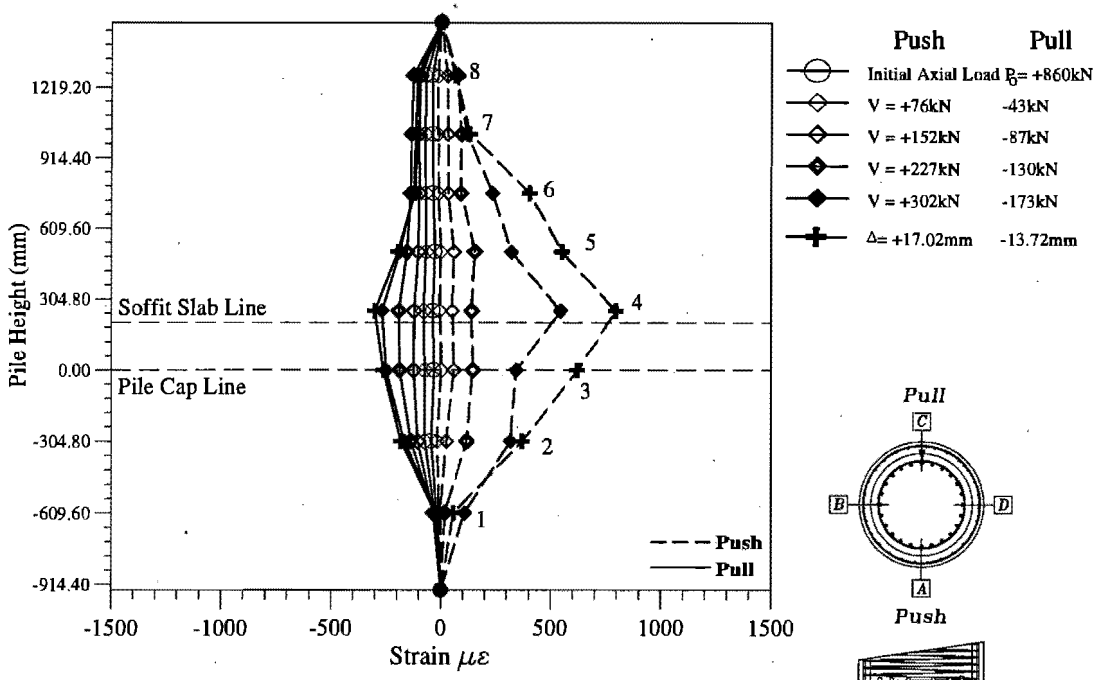

(a) Vertical Strain Profiles - Initial Stages of Testing

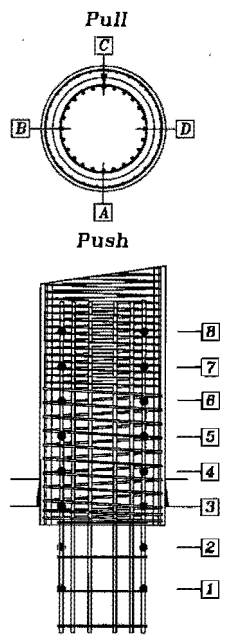

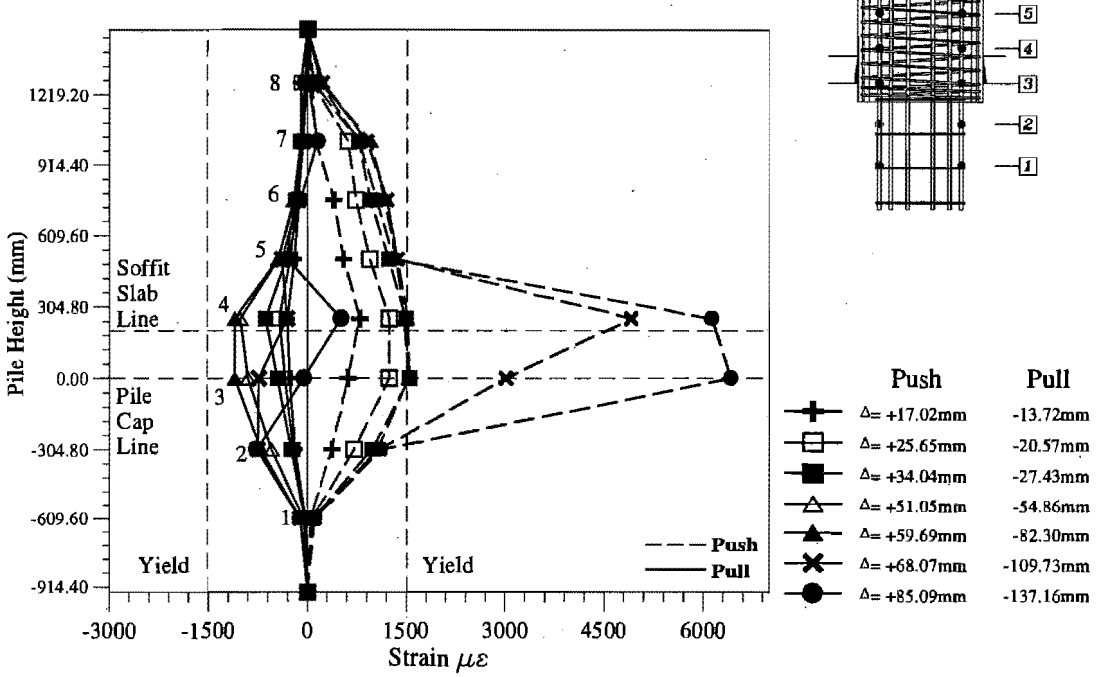

(b) Vertical Strain Profiles - Final Stages of Testing

Fig. 5-19 Vertical Strain Profiles Inner Core Bar *C*

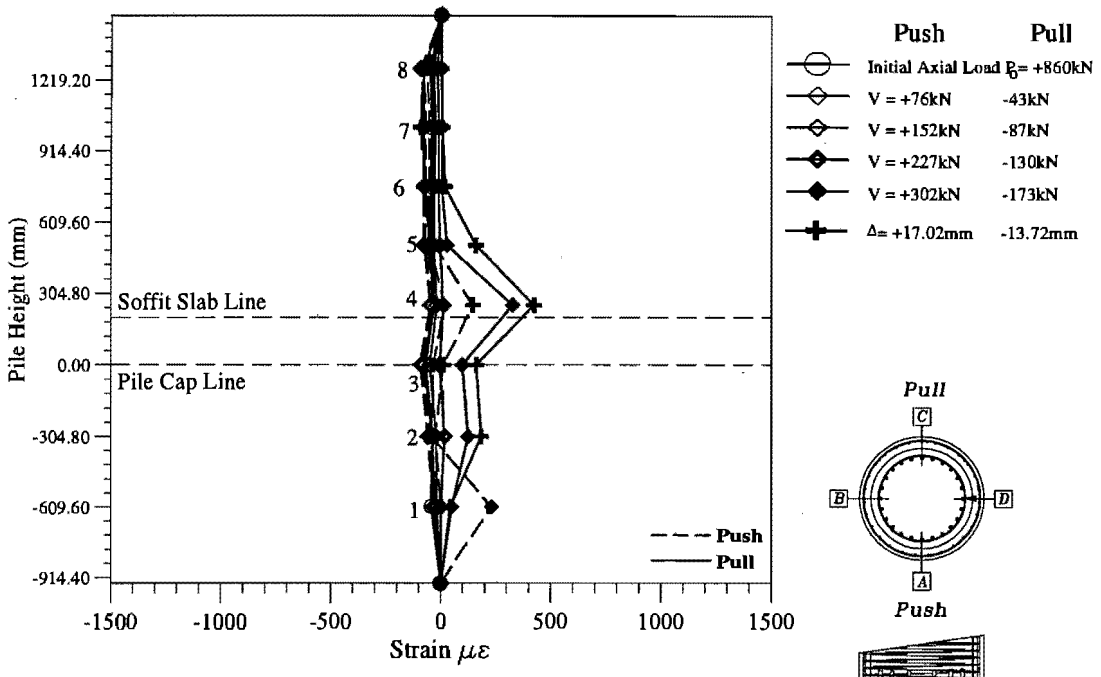

(a) Vertical Strain Profiles - Initial Stages of Testing

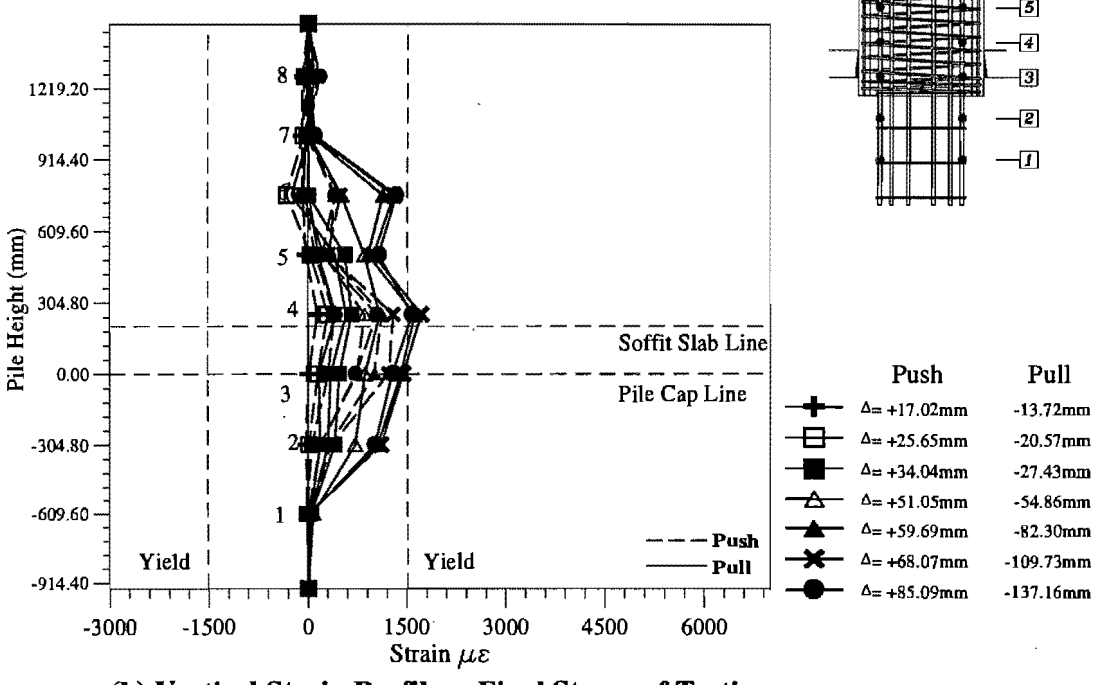

(b) Vertical Strain Profiles - Final Stages of Testing

Fig. 5-20 Vertical Strain Profiles Inner Core Bar ***D***

5.4.2 Pile Longitudinal Reinforcement - Circumferential Strain Profiles

Circumferential strain profiles for the pile inner core longitudinal reinforcement are presented in **Fig. 5-21** through **Fig. 5-24**. The circumferential profiles depicted in these figures indicate, in the initial and final stages of testing, a linear variation of strain between the longitudinal bars, which indicate small excursions into yielding strain. Yielding occurred mainly between horizontal lines *2* and *7* with strains higher than yielding only between levels *3* and *4*.

Strain profiles at level *8* indicate minimum strains in the pull direction; however, in the push direction, strains approximate yielding which indicates a much smaller development length under compressive strains.

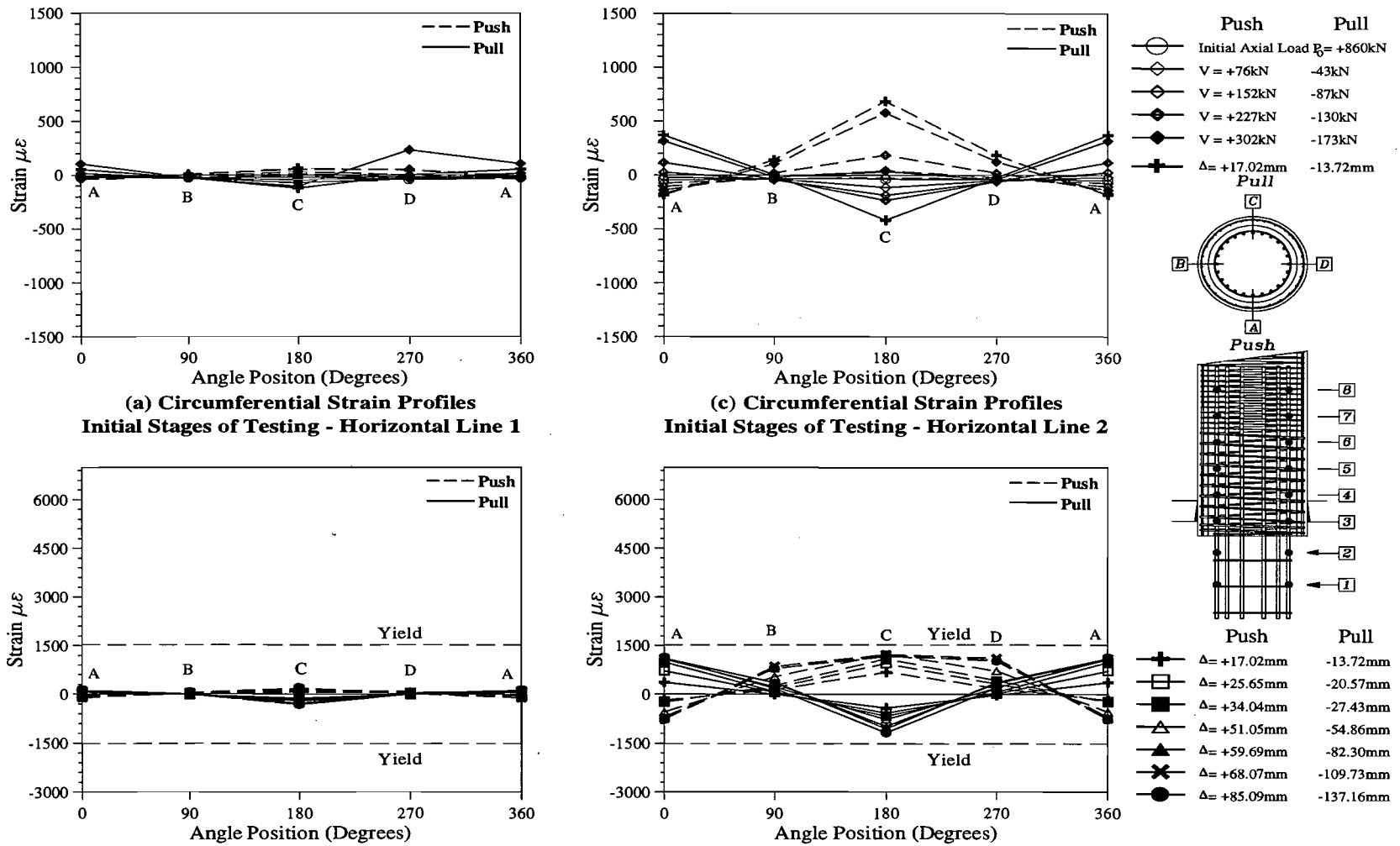

(a) Circumferential Strain Profiles
Initial Stages of Testing - Horizontal Line 1

(c) Circumferential Strain Profiles
Initial Stages of Testing - Horizontal Line 2

(b) Circumferential Strain Profiles
Final Stages of Testing - Horizontal Line 1

(d) Circumferential Strain Profiles
Final Stages of Testing - Horizontal Line 2

Fig. 5-21 Inner Core Reinforcement Strain Profiles Along Horizontal Line *1* and *2*

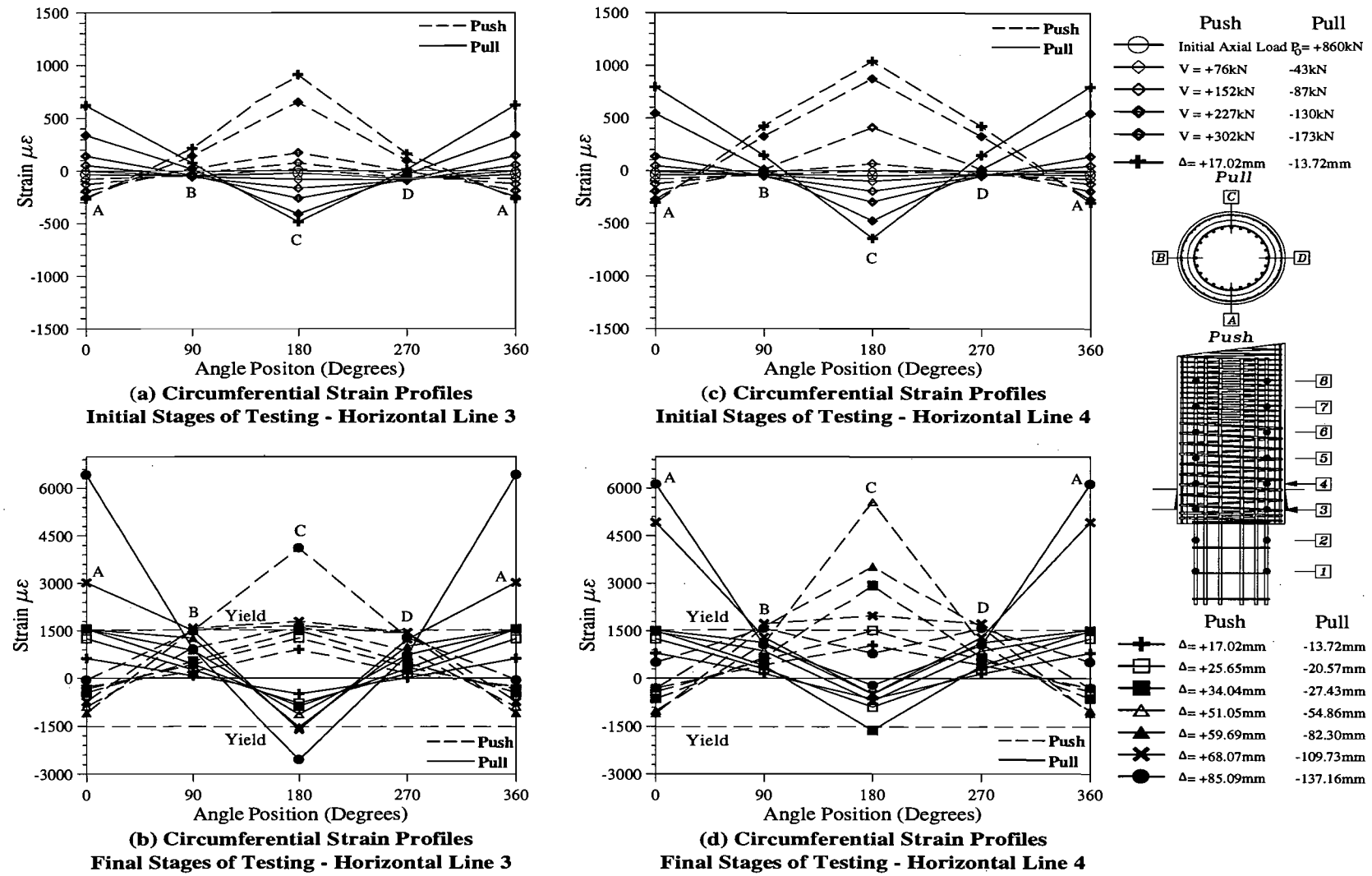

(a) Circumferential Strain Profiles
Initial Stages of Testing - Horizontal Line 3

(c) Circumferential Strain Profiles
Initial Stages of Testing - Horizontal Line 4

(b) Circumferential Strain Profiles
Final Stages of Testing - Horizontal Line 3

(d) Circumferential Strain Profiles
Final Stages of Testing - Horizontal Line 4

Fig. 5-22 Inner Core Reinforcement Strain Profiles Along Horizontal Line *3* and *4*

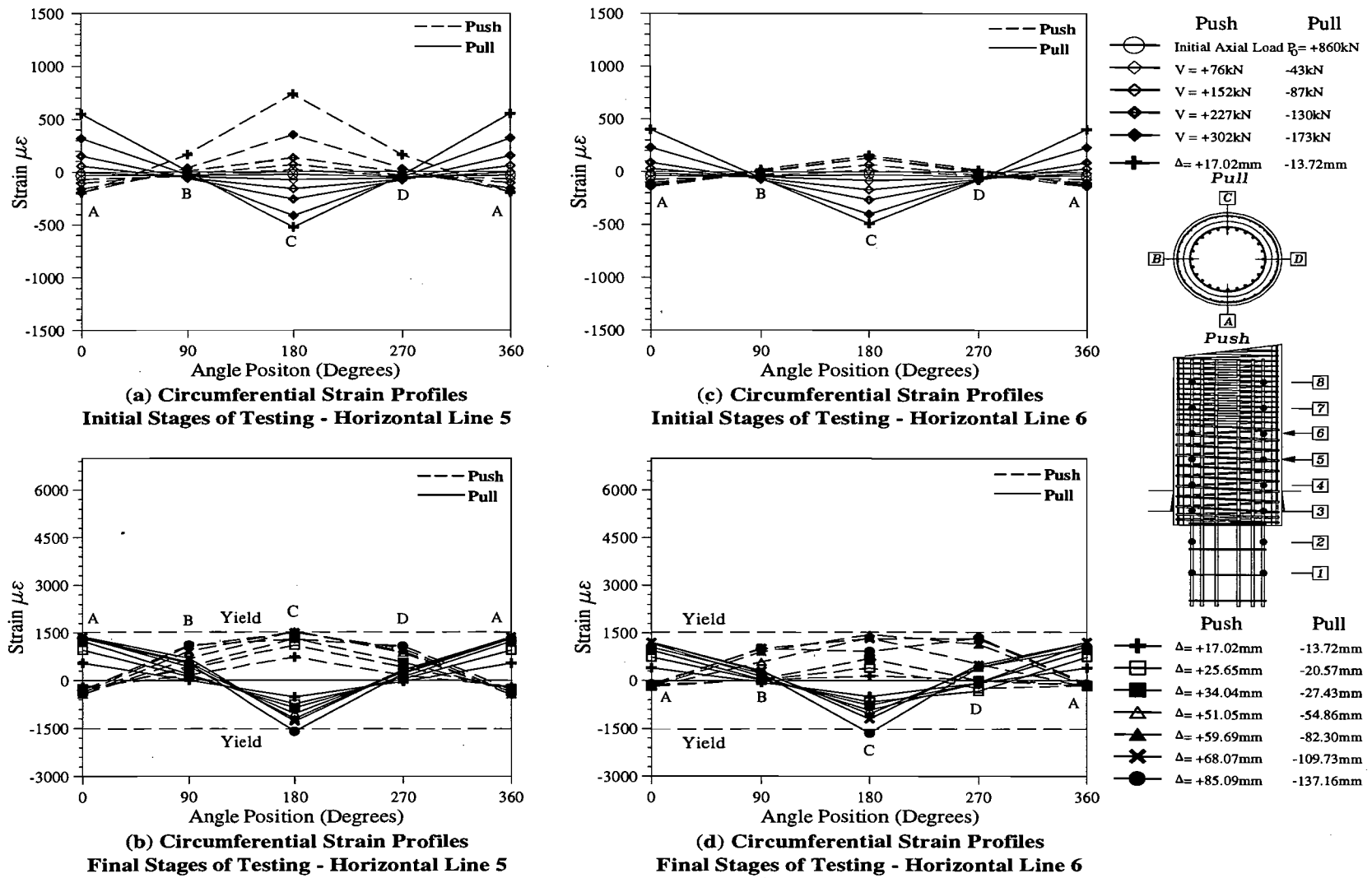

(a) Circumferential Strain Profiles
Initial Stages of Testing - Horizontal Line 5

(c) Circumferential Strain Profiles
Initial Stages of Testing - Horizontal Line 6

(b) Circumferential Strain Profiles
Final Stages of Testing - Horizontal Line 5

(d) Circumferential Strain Profiles
Final Stages of Testing - Horizontal Line 6

Fig. 5-23 Inner Core Reinforcement Strain Profiles Along Horizontal Line *5* and *6*

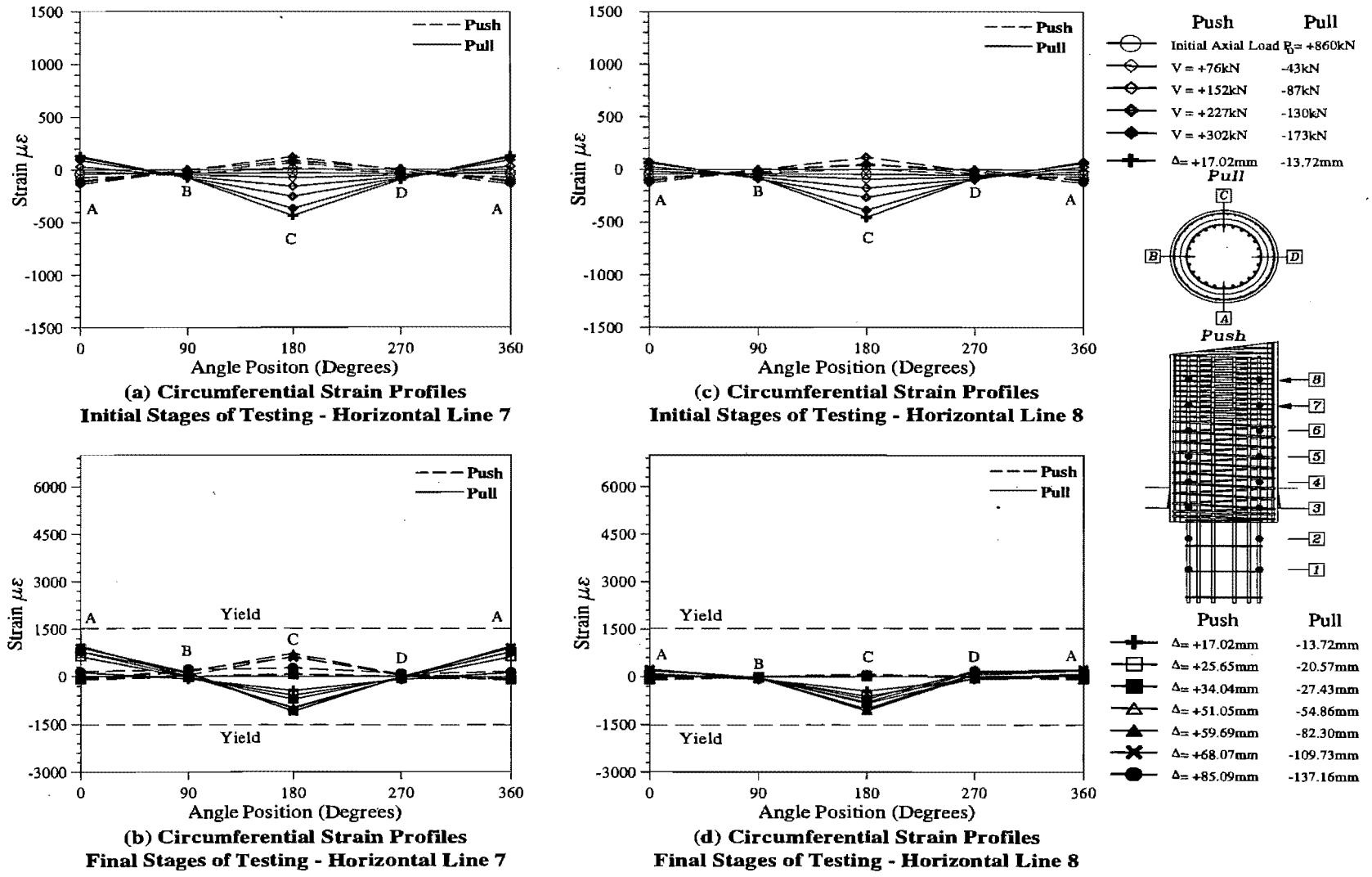

(a) Circumferential Strain Profiles
Initial Stages of Testing - Horizontal Line 7

(c) Circumferential Strain Profiles
Initial Stages of Testing - Horizontal Line 8

(b) Circumferential Strain Profiles
Final Stages of Testing - Horizontal Line 7

(d) Circumferential Strain Profiles
Final Stages of Testing - Horizontal Line 8

Fig. 5-24 Inner Core Reinforcement Strain Profiles Along Horizontal Line *7* and *8*

5.5 Prestressing Strands Vertical Strain Profiles

Strain profiles for the prestressing strands are presented in **Fig. 5-25** through **Fig. 5-28**. Strain readings were obtained during fabrication of the precast prestressed concrete shell while at *Utility Vault* and the gages were disconnected between fabrication and testing at UCSD. Then, before testing, these same gages were reconnected to the data acquisition system and balanced to zero. Then, the final strains recorded during the fabrication process were added to the strains obtained during testing.

In the final stages of the testing procedure, strain profiles presented in these figures indicate that maximum strains were achieved between positions *5* and *6*, which is approximately where the inner core longitudinal reinforcement terminates. This indicates that a total development length of approximately 1,524 mm is expected. The code required development length is computed based on the following equation **[18]**:

$$l_d = \frac{f_{se}}{3} d_b + (f_{ps} - f_{se}) d_b \tag{5.4}$$

where the first and second terms represent the transfer and flexural bond length, respectively. Based on an initial prestressing force of approximately 1378 MPa and a prestressing diameter of 9.53 mm, one obtains the required development length of 1,302 mm, which is slightly less than extrapolated from experimental test results.

Difficulties associated with obtaining the prestressing development length, with a good degree of confidence for this test setup, arise because regions of transfer forces are associated with regions where moment demand is the highest. In addition, at the pile cap interface, flexure cracking is significant and reduces bond strength, which in term increases required development length. Development length extrapolated from test results match with those values used in the pre-test analysis and are corroborated by test results in which plastic deformations occurred where longitudinal reinforcement terminates.

Strain profiles presented in **Fig. 5-25** through **Fig. 5-28** indicate that prestressing forces are always in tension with minimum decrease under compressive loads and increase under tension loads, depending on the position of the strand relative to section compression toe. For example, along strand *A*, maximum strains are observed in the pull direction because in this direction this strand is in tension, and along strand *C*, maximum strains are observed in the push direction when this strand is in tension.

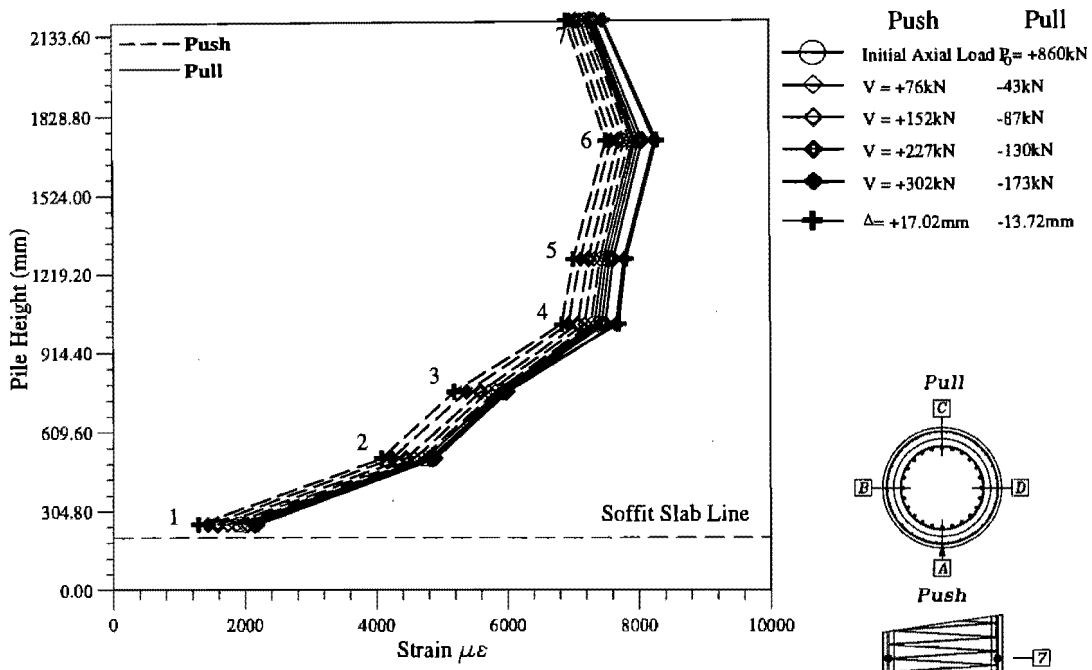

(a) Vertical Strain Profiles - Initial Stages of Testing

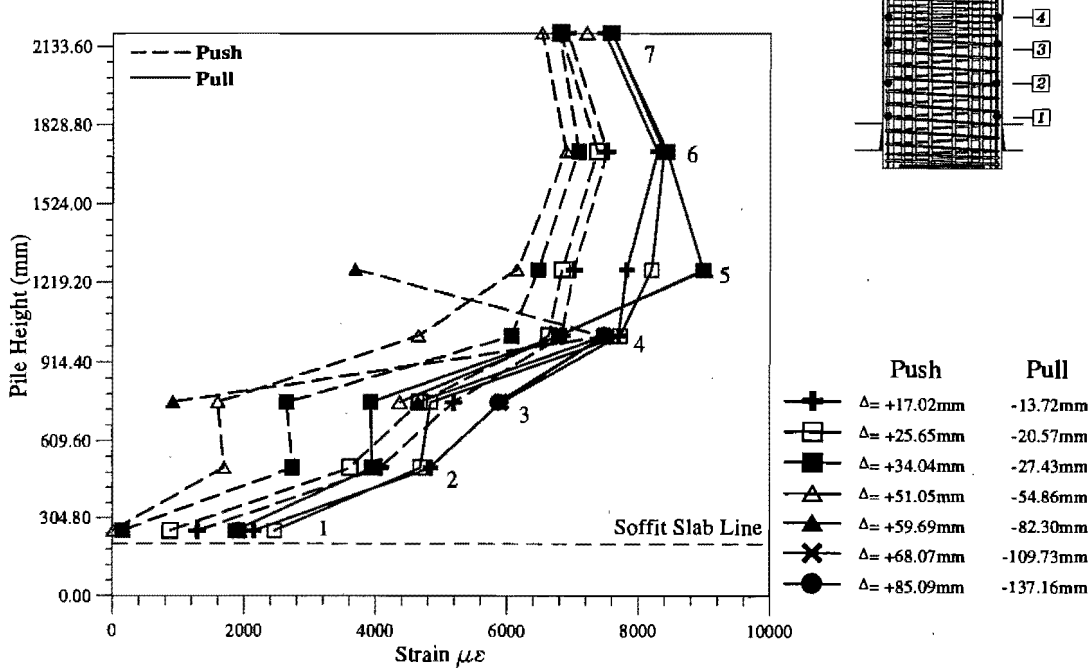

(b) Vertical Strain Profiles - Final Stages of Testing

Fig. 5-25 Vertical Strain Profiles Along Strand *A*

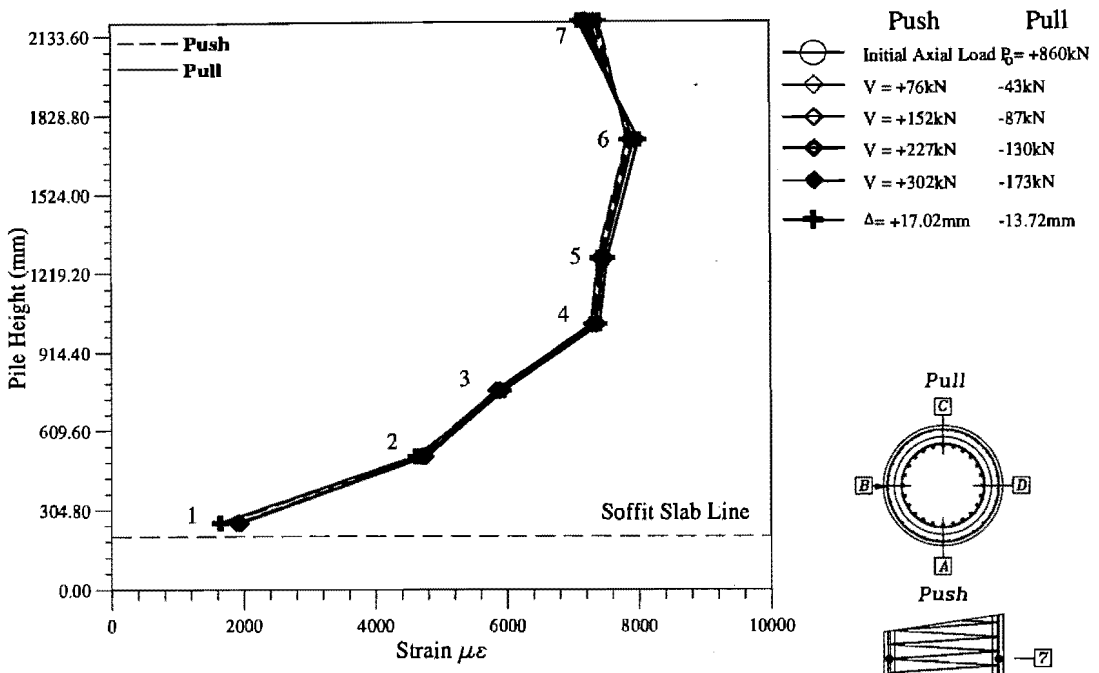

(a) Vertical Strain Profiles - Initial Stages of Testing

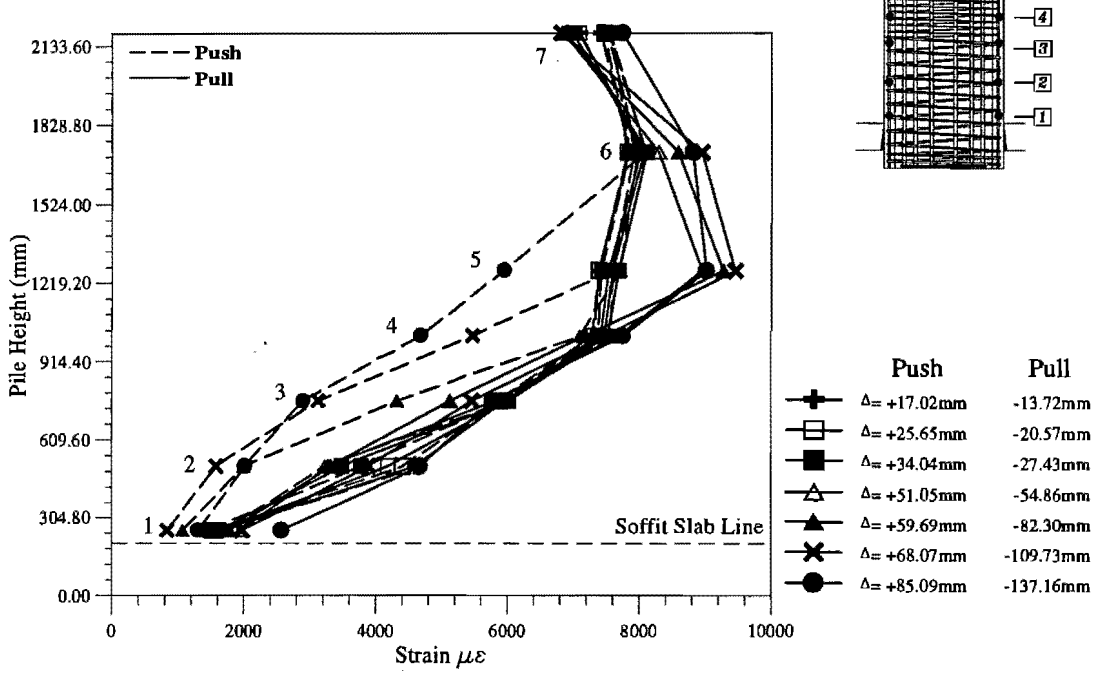

(b) Vertical Strain Profiles - Final Stages of Testing

Fig. 5-26 Vertical Strain Profiles Along Strand ***B***

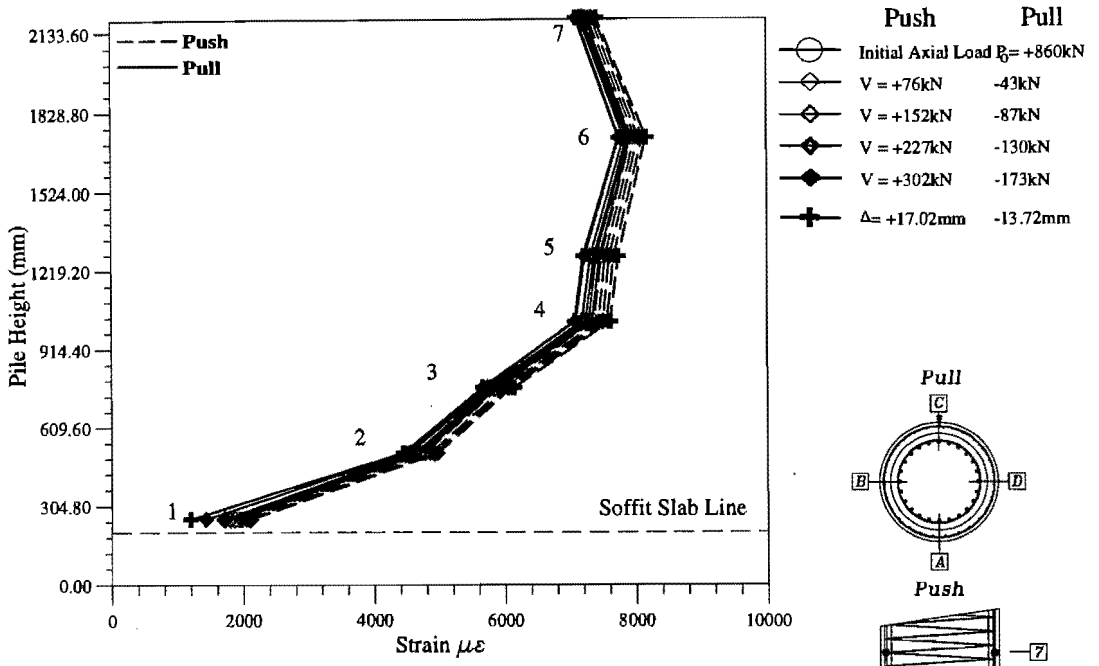

(a) Vertical Strain Profiles - Initial Stages of Testing

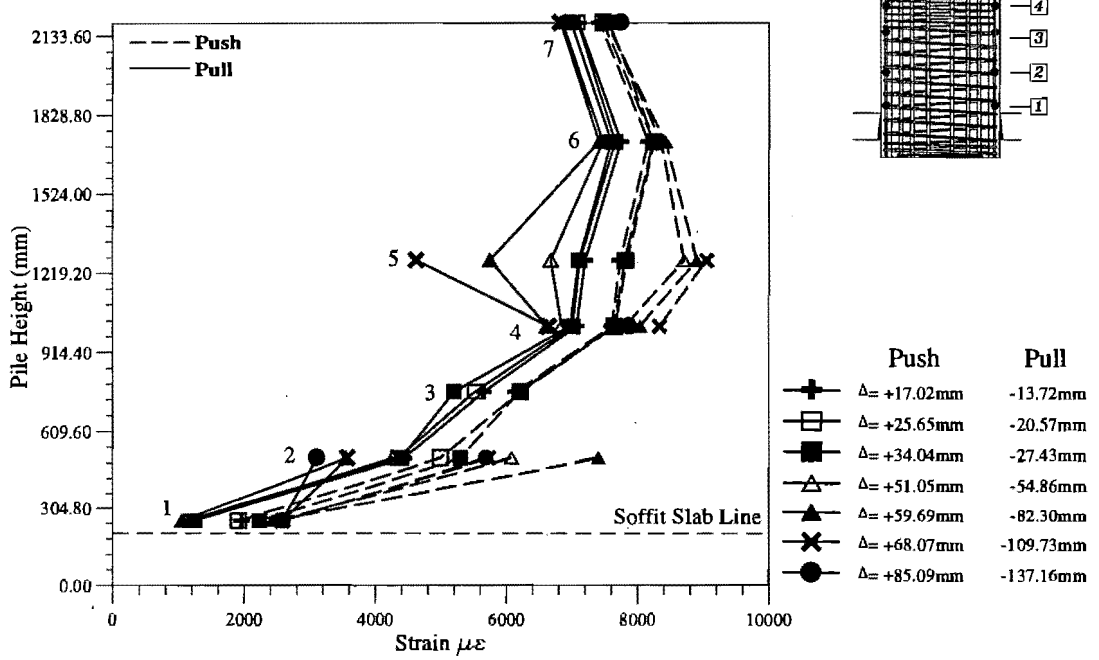

(b) Vertical Strain Profiles - Final Stages of Testing

Fig. 5-27 Vertical Strain Profiles Along Strand *C*

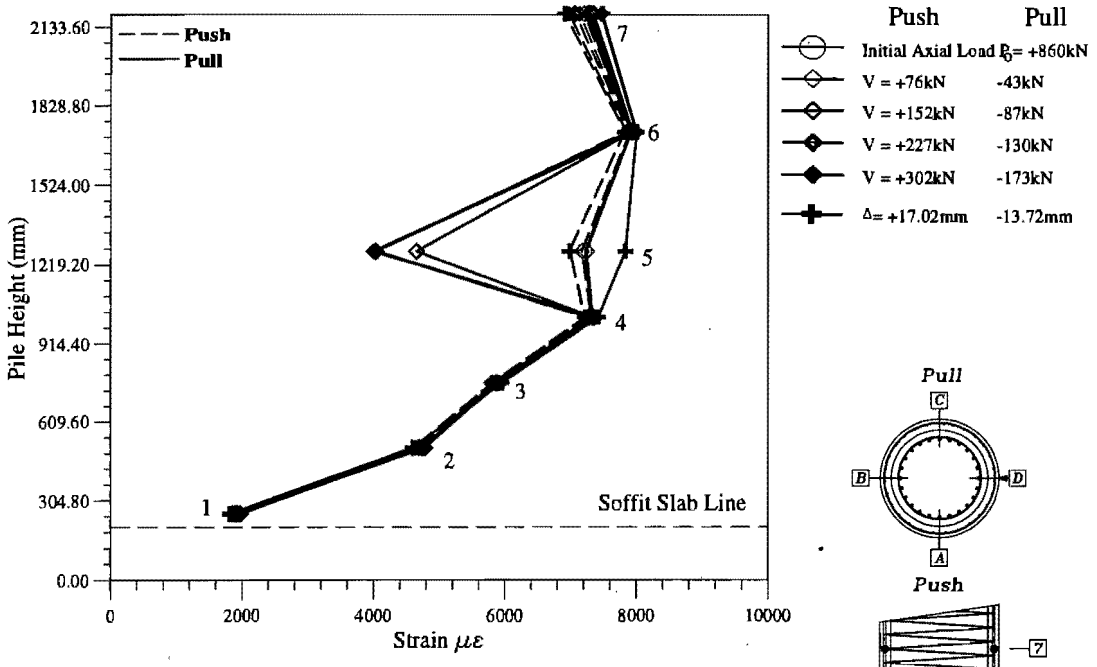

(a) Vertical Strain Profiles - Initial Stages of Testing

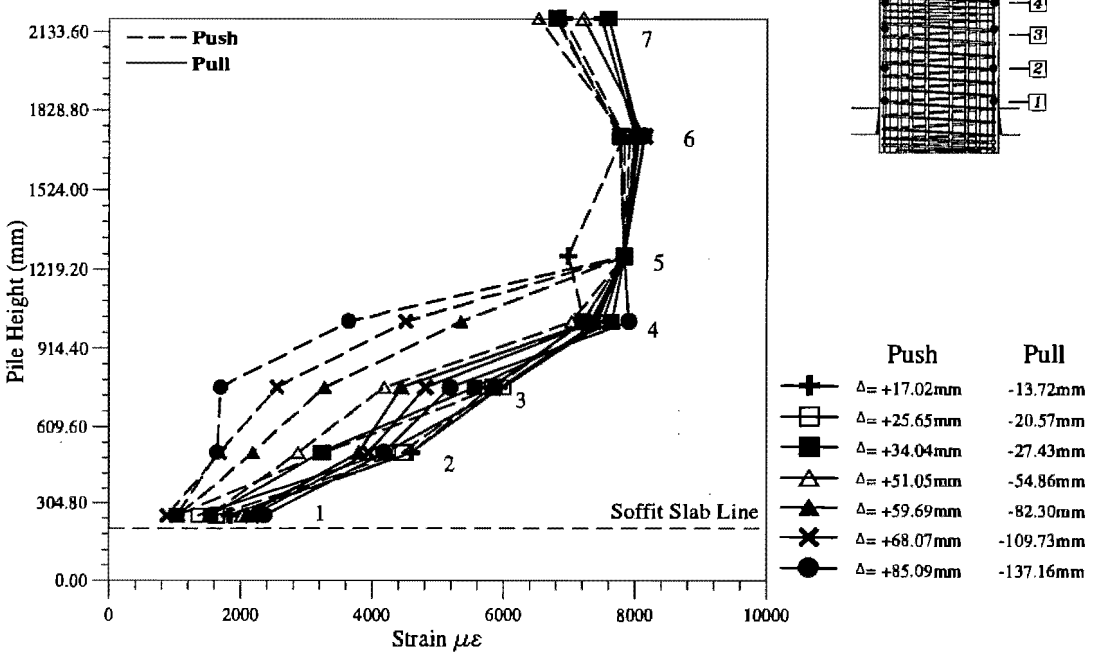

(b) Vertical Strain Profiles - Final Stages of Testing

Fig. 5-28 Vertical Strain Profiles Along Strand ***D***

5.6 Pile Transverse Reinforcement Strain Profiles

The spiral reinforcement used in this test unit varied between #3 on a 84 mm spiral pitch at the pile cap interface to a W3 on a 114 mm spiral pitch above the inner cage longitudinal reinforcement.

5.6.1 Pile Transverse Reinforcement - Vertical Strain Profiles

Vertical strain profiles for the pile transverse reinforcement are presented in **Fig. 5-29** through **Fig. 5-32**. The strain profiles along longitudinal line ***A*** (see **Fig. 5-29**) and along longitudinal line ***C*** (see **Fig. 5-31**) indicate the level of confinement strain developed in the pile section as a result of the applied axial load and deformations. Strains in the spiral cage recorded along these lines in the early stages of the testing procedure indicate higher strains along line ***A*** than along line ***C*** because of higher axial compressive forces that develop in the push direction, which results in higher confinement demands. Along line ***A*** in the final stages of the testing procedure, vertical strain profiles are slightly higher between positions ***4*** and ***6*** because extensive spalling of the cover concrete and unwinding of strands occurred in these locations, as previously noted, which also indicates higher confinement demands in this region. Along longitudinal ***C***, it is also visible high confinement demands in this region.

The strain profiles along longitudinal line ***B*** (see **Fig. 5-30**) and along longitudinal line ***D*** (see **Fig. 5-32**) indicate the level of shear-induced strain as a result of the applied lateral load. High strains below position ***3*** indicate higher shear demands in this region, which matches extensive cracking of the pile section below termination of longitudinal reinforcement with two cracks at 45° cracks marked on the sides of the pile section.

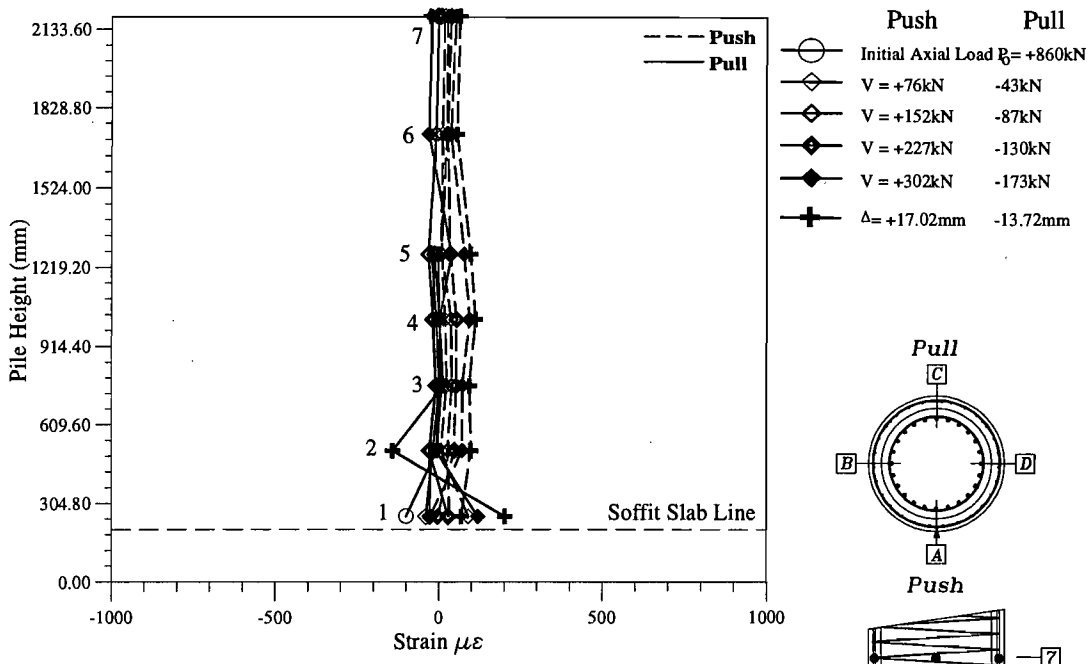

(a) Vertical Strain Profiles - Initial Stages of Testing

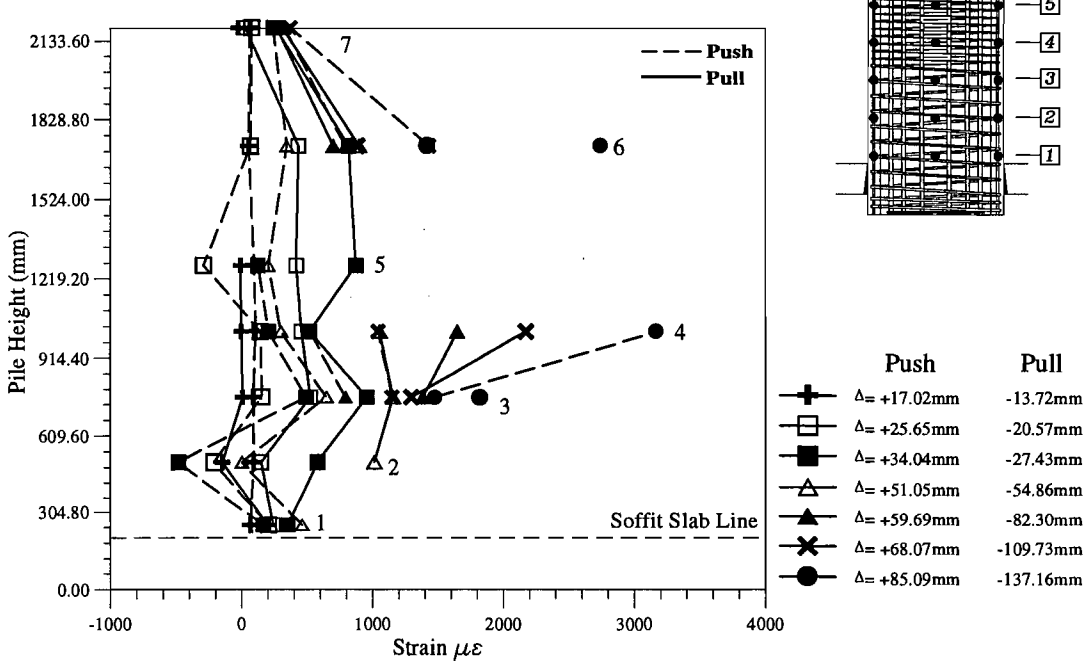

(b) Vertical Strain Profiles - Final Stages of Testing

Fig. 5-29 Pile Transverse Reinforcement Strain Profiles Along Line *A*

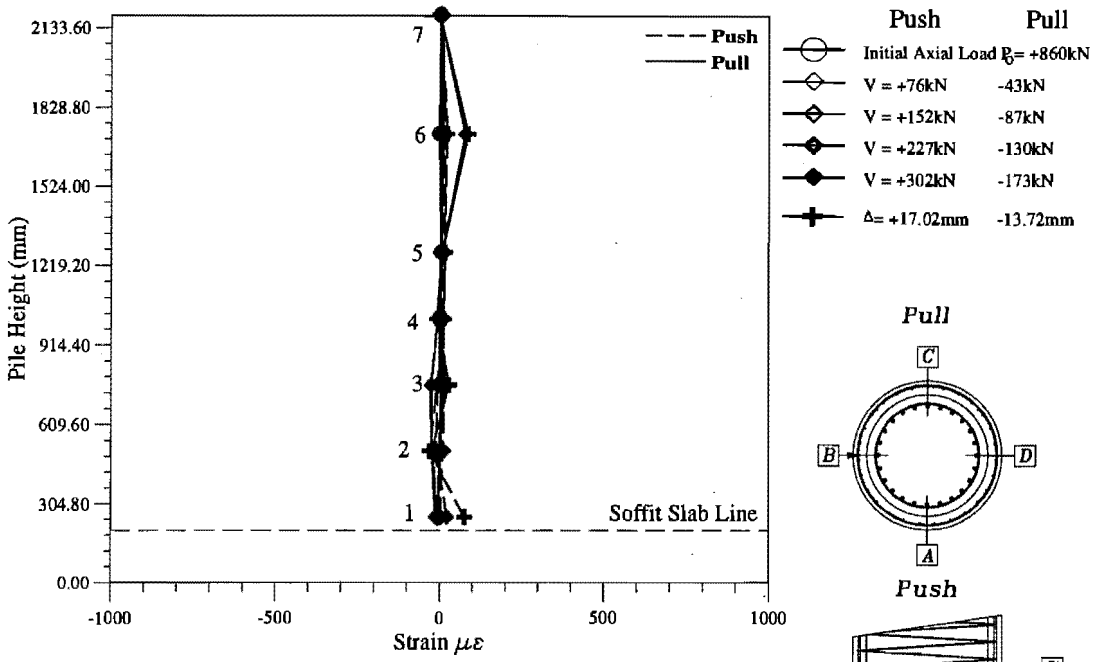

(a) Vertical Strain Profiles - Initial Stages of Testing

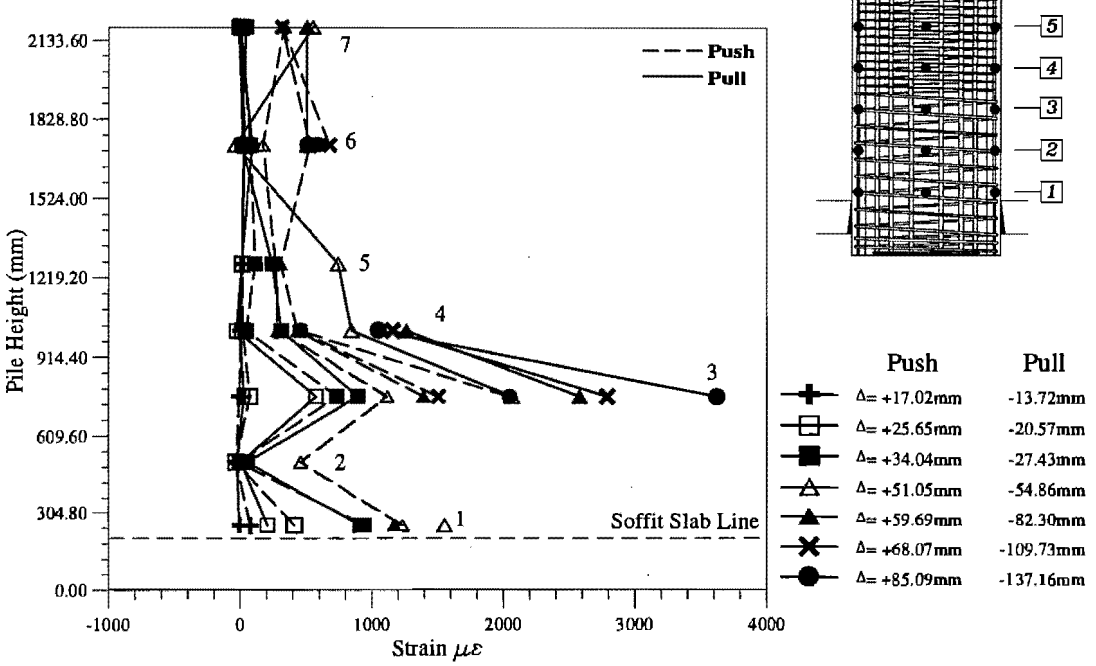

(b) Vertical Strain Profiles - Final Stages of Testing

Fig. 5-30 Pile Transverse Reinforcement Strain Profiles Along Line ***B***

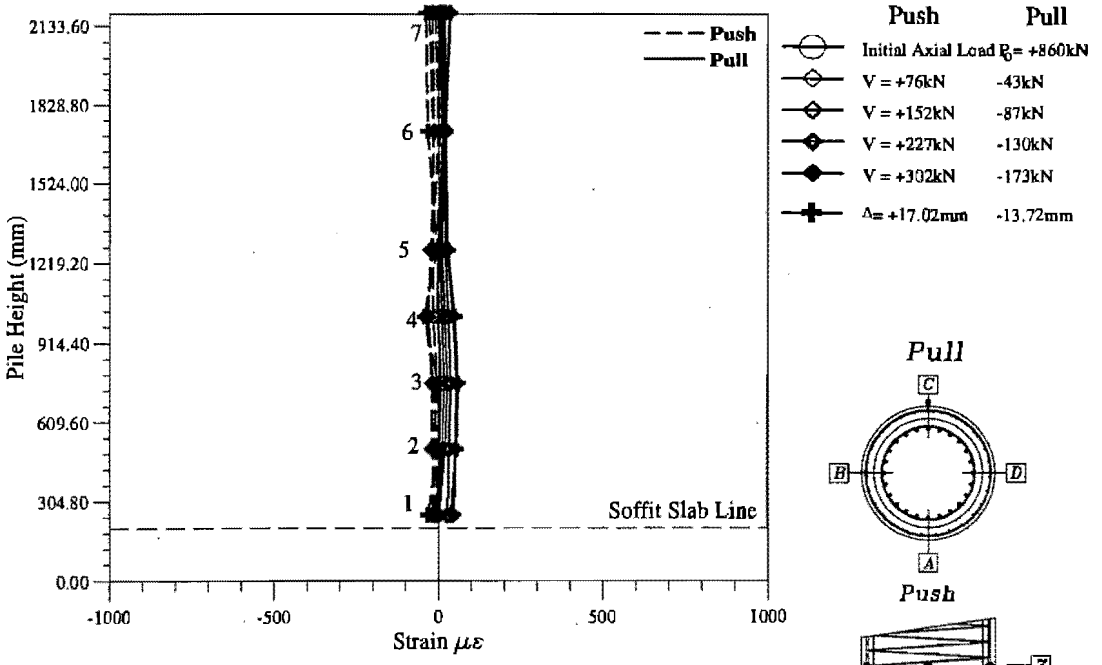

(a) Vertical Strain Profiles - Initial Stages of Testing

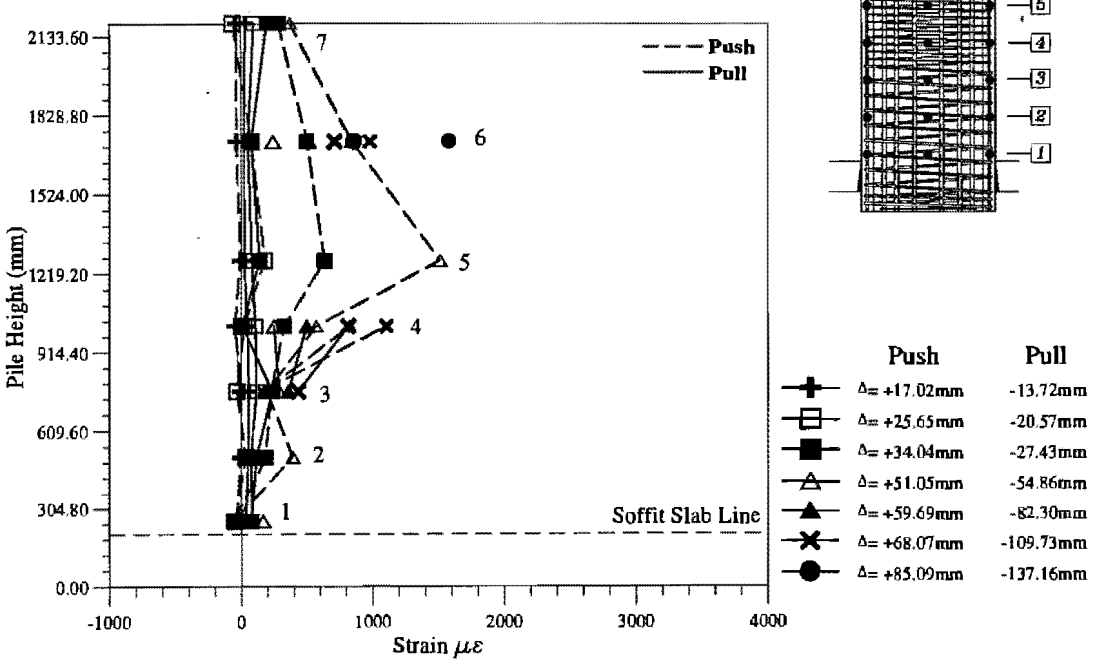

(b) Vertical Strain Profiles - Final Stages of Testing

Fig. 5-31 Pile Transverse Reinforcement Strain Profiles Along Line *C*

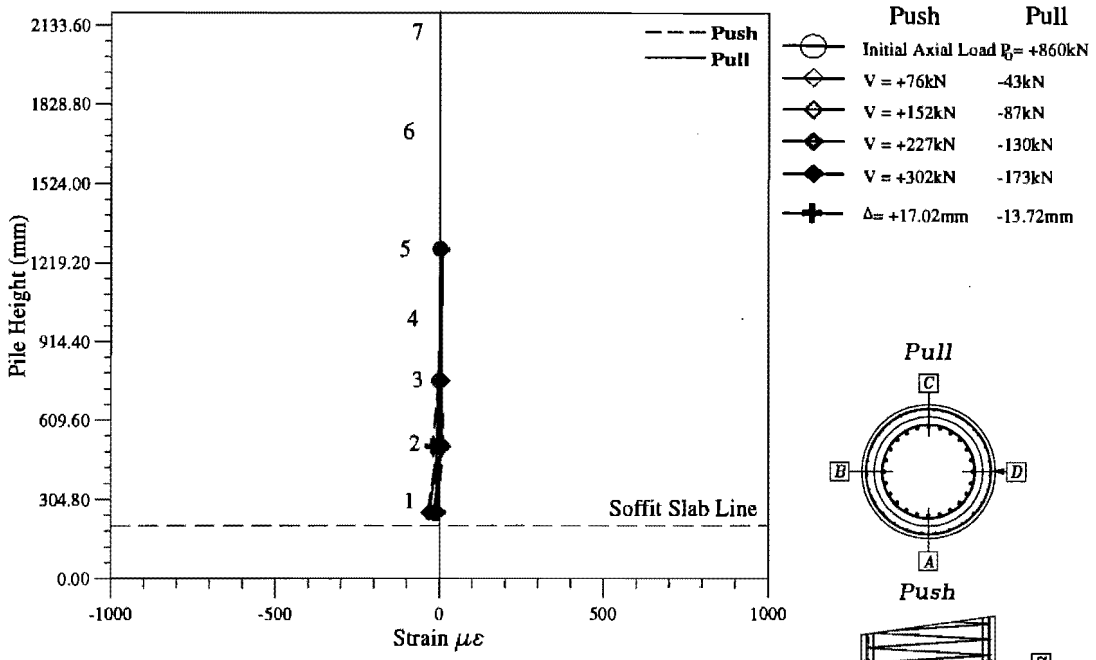

(a) Vertical Strain Profiles - Initial Stages of Testing

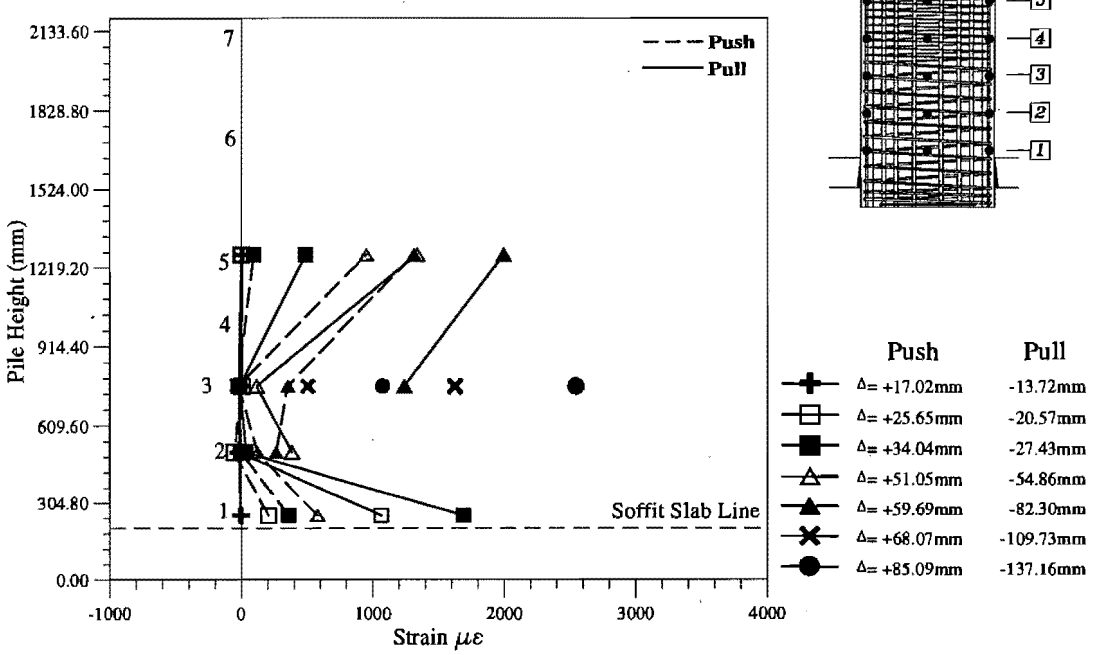

(b) Vertical Strain Profiles - Final Stages of Testing

Fig. 5-32 Pile Transverse Reinforcement Strain Profiles Along Line ***D***

5.6.2 Pile Transverse Reinforcement - Circumferential Strain Profiles

Circumferential strain profiles for the pile transverse reinforcement are presented in **Fig. 5-33** through **Fig. 5-35**. Circumferential strain profiles indicate higher strains are always registered at position ***A*** rather than at position ***C*** as a result of confinement induced strains in the early stages of the testing procedure. At later stages of the testing procedure, this increase in strains at position ***A*** are more a result of prevention of strands buckling due to spalling of the cover concrete where longitudinal reinforcement terminates.

Maximum strains are recorded at positions ***B*** and ***D*** at later stages of the testing procedure, which illustrates increase in shear demand in regions where shear-induced inclined cracks were registered.

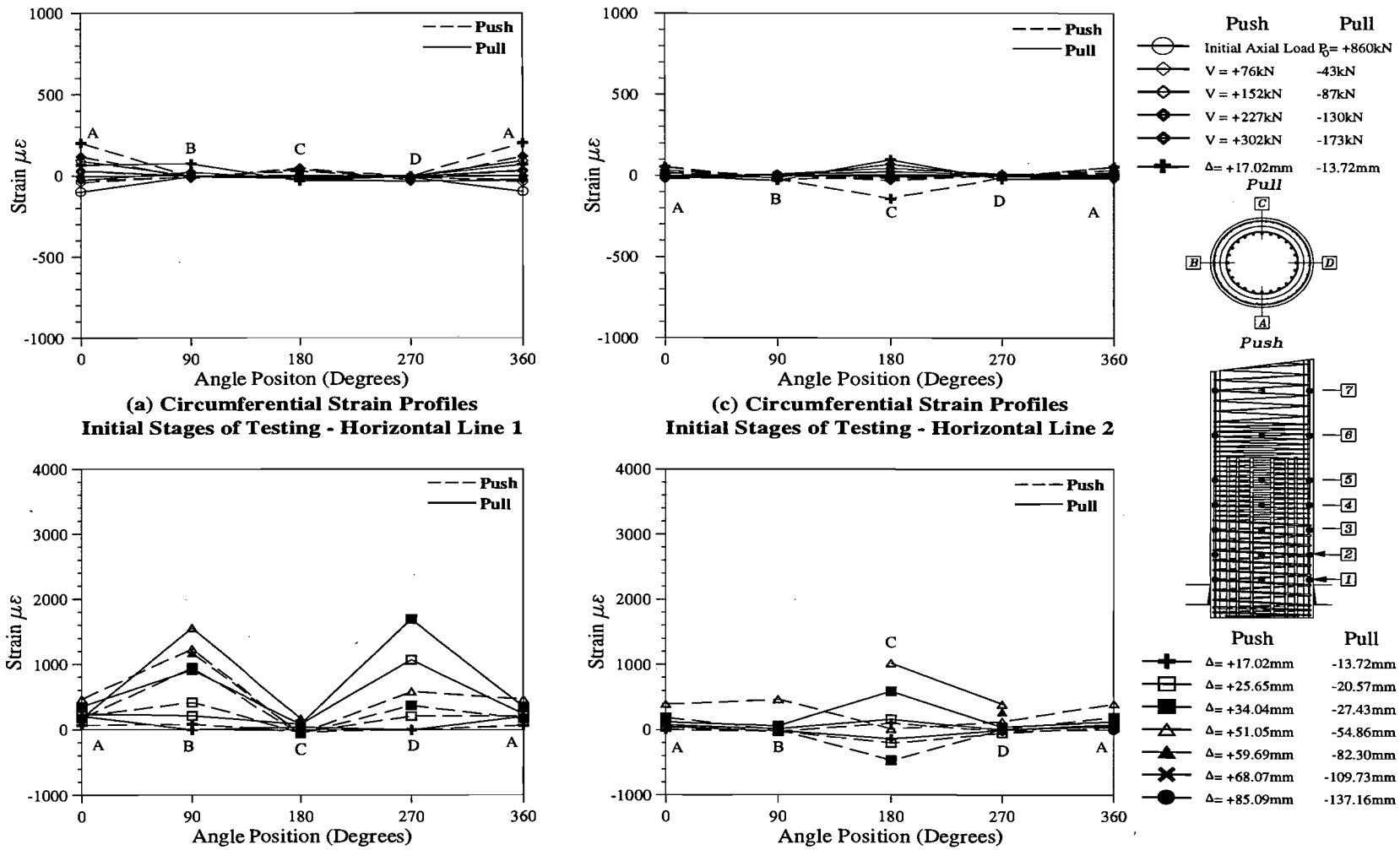

(a) Circumferential Strain Profiles
Initial Stages of Testing - Horizontal Line 1

(c) Circumferential Strain Profiles
Initial Stages of Testing - Horizontal Line 2

(b) Circumferential Strain Profiles
Final Stages of Testing - Horizontal Line 1

(d) Circumferential Strain Profiles
Final Stages of Testing - Horizontal Line 2

Fig. 5-33 Pile Transverse Reinforcement Strain Profiles Along Horizontal Line *1* and *2*

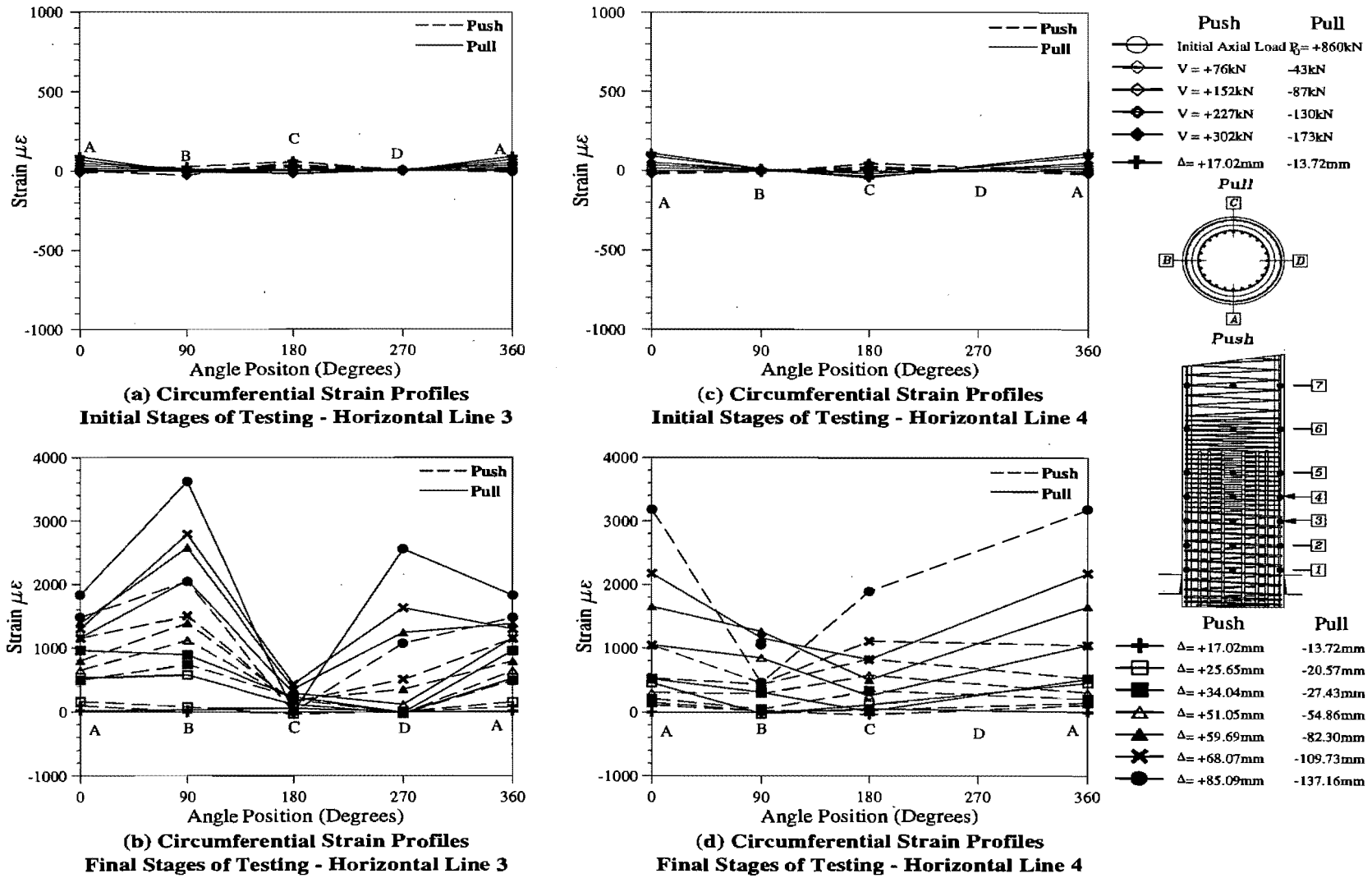

Fig. 5-34 Pile Transverse Reinforcement Strain Profiles Along Horizontal Line *3* and *4*

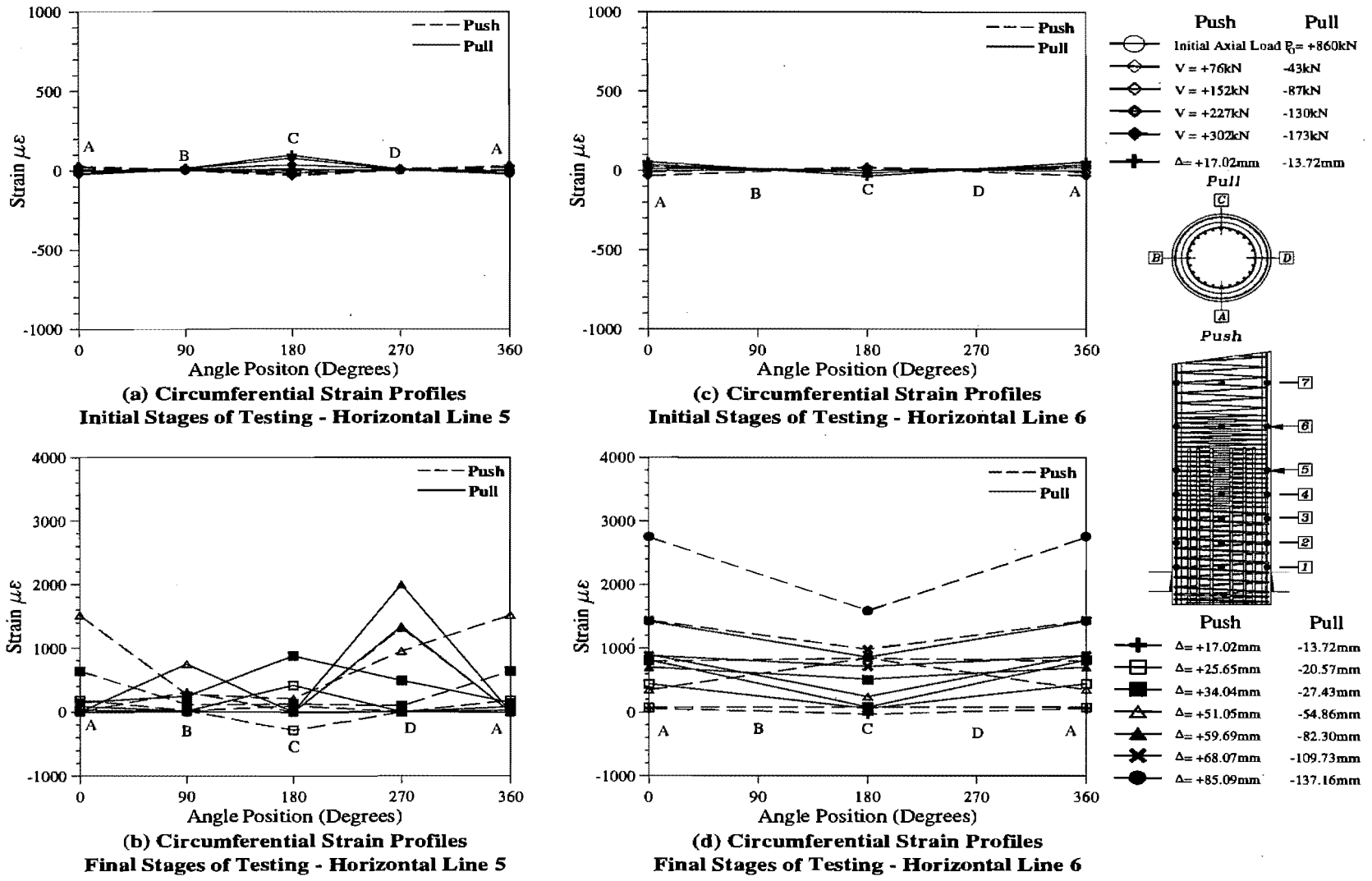

Fig. 5-35 Pile Transverse Reinforcement Strain Profiles Along Horizontal Line *5* and *6*

5.7 Pile Cap Reinforcement Strain Profiles

Maximum strains in the pile cap top and bottom reinforcement, positioned in the direction of applied lateral load, were registered in the pile cap bottom reinforcement at strain gage ***Bottom 3-B***. Note that bottom reinforcement refers to position of reinforcement as it occurs in the prototype structure. For strain gage location, refer to **Fig. 3-37**. Strain readings illustrated in **Fig. 5-36** indicate minimum strains recorded in this reinforcement. Thus, strain profiles for the pile cap top and bottom reinforcement are not shown since strain levels were always considerably below yielding.

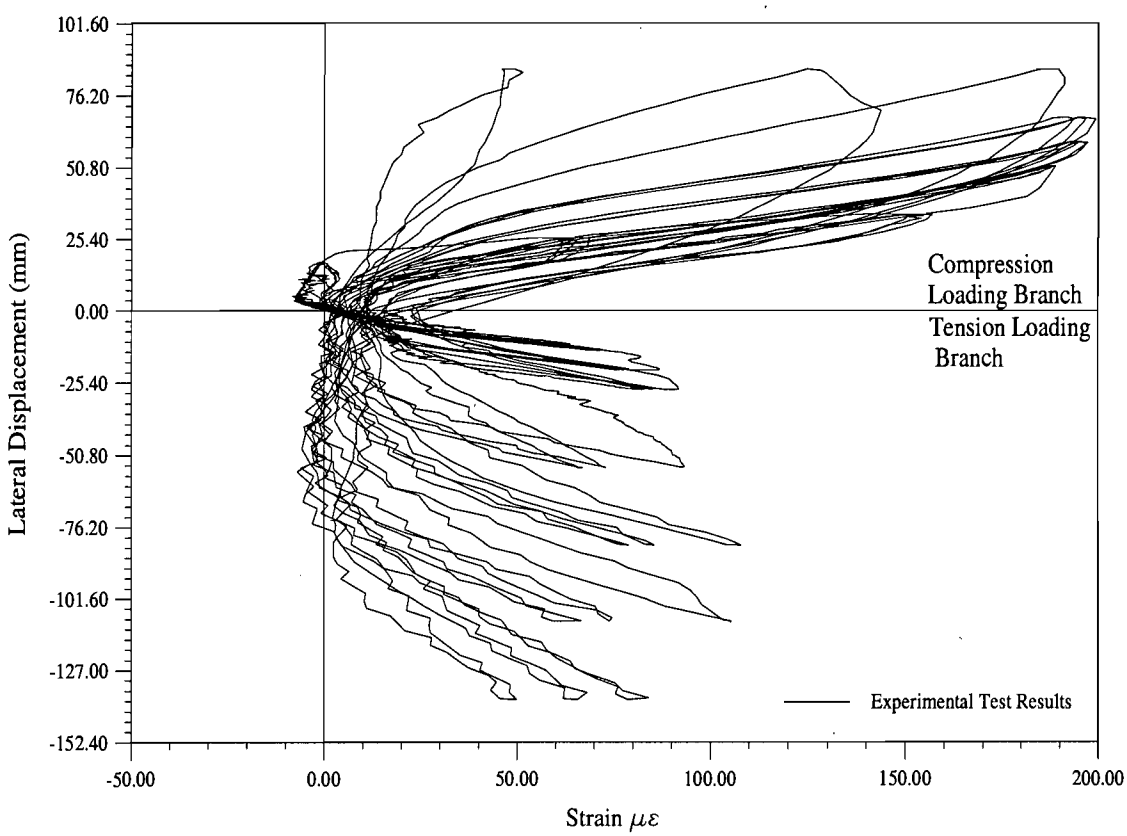

Fig. 5-36 Lateral Deflection versus Strain
Strain Gage Pile Cap Bottom Reinforcement ***Bottom 3-B***

Maximum strains in the pile cap vertical reinforcement were registered at strain gage ***3-B***. For strain gage location, refer to **Fig. 3-39**. Strain readings illustrated in **Fig. 5-37** indicate minimum strains recorded in this reinforcement. Thus, strain profiles for the pile vertical reinforcement are not shown since strain levels were always considerably below yielding. Strain levels recorded in this reinforcement can be taken as an indication of joint performance. Levels of principal tensile stress computed in Chapter 2 and presented in **Fig. 2-27** indicate that no joint shear failure was expected as a result of minimum level of expected stress in the joint region, which were $0.16\sqrt{f_c'} < 0.29\sqrt{f_c'}$ *[MPa]* and $0.27\sqrt{f_c'} < 0.29\sqrt{f_c'}$ *[MPa]*. These values corroborate observed test results in which negligible strains were recorded in the pile cap vertical reinforcement indicating that no joint cracking occurred.

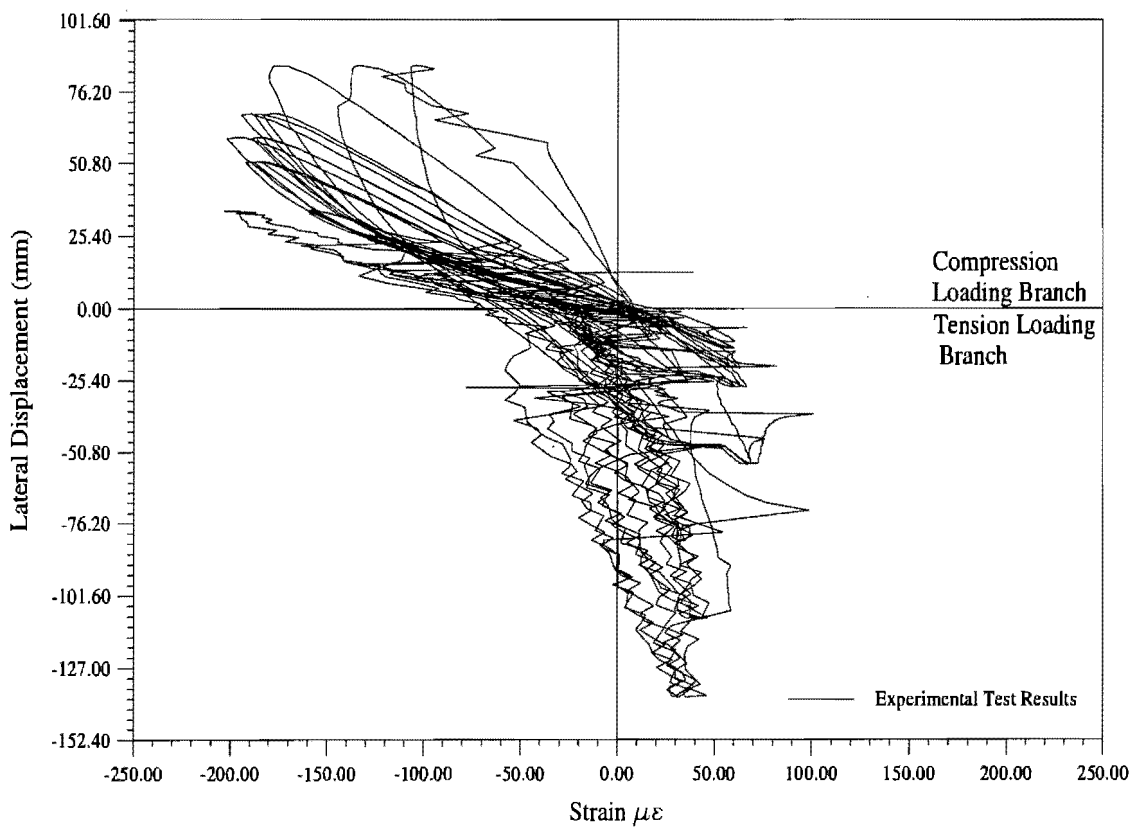

Fig. 5-37 Lateral Deflection versus Strain
Strain Gage Pile Cap Vertical Reinforcement ***3-B***

5.8 Pile Cap Rotation

Uplift of the pile cap from the strong floor was monitored by linear potentiometers positioned at the base of the pile cap, as illustrated in **Fig. 3-31** and **Fig. 3-32**. Rotation of the pile cap was then computed based on the expression :

$$\psi_{cap} = \frac{UP_A - UP_B}{L_{AB}} \tag{5.5}$$

where ψ_{cap} is the pile cap rotation $UP_A = (UP_1 + UP_2) / 2$, $UP_B = (UP_3 + UP_4) / 2$, UP_1 through UP_4 are the measurement readings taken from the linear potentiometers positioned at the base of the pile cap, and L_{AB} is the distance between the linear potentiometers positioned along lines ***A*** and ***B***. Contribution of pile cap rotation to pile lateral deflection may then be estimated according to the expression :

$$\Delta_\Delta = \psi_{cap} (H_{pile} + H_{cap}) \tag{5.6}$$

Based on the values presented in **Fig. 5-38**, the maximum pile cap rotation, ψ_{cap}, was 0.000020/rad and it was computed when the lateral deflection was +51.69 mm, which coincides with the cycle at which the lateral load began to drop. This rotation of the pile cap will contribute 0.11 mm to the pile lateral deflection at peak response, which is rather small and, as a result, no correction to the pile lateral deflection was computed.

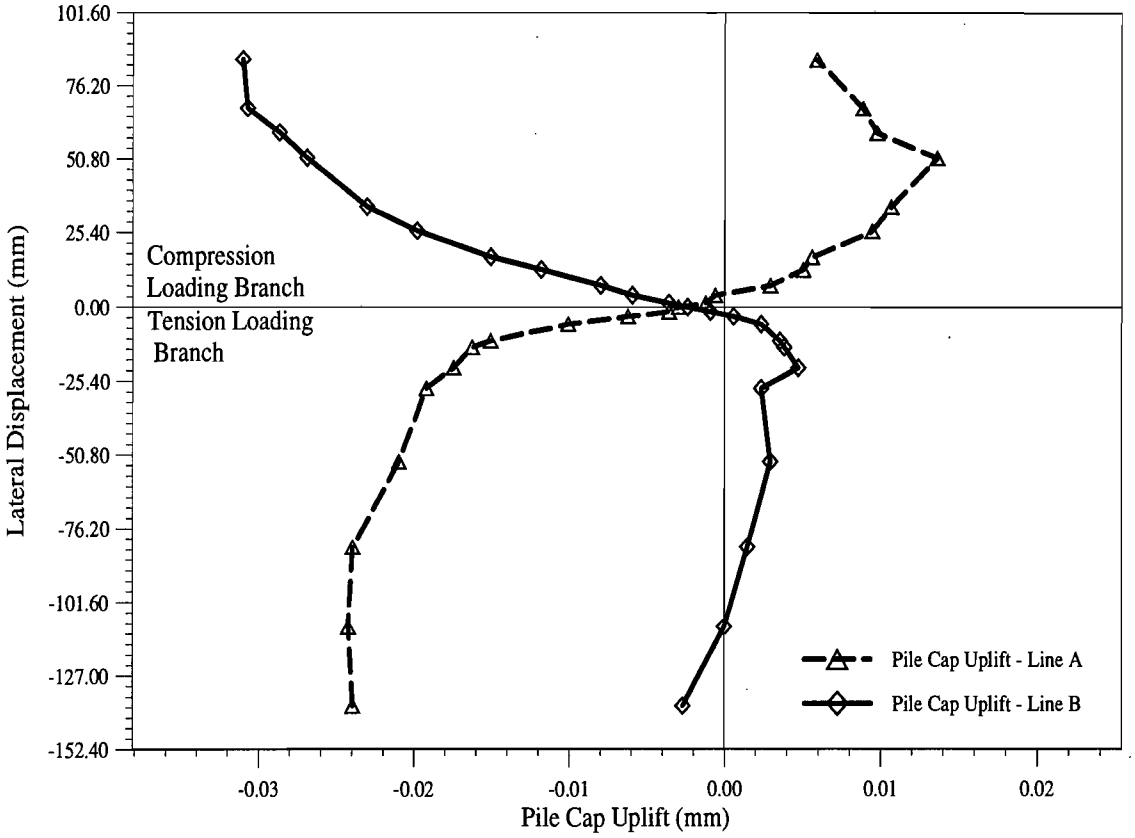

Fig. 5-38 Lateral Deflection versus Pile Cap Uplift

6. Test Unit *COR2* Experimental Test Results

This chapter includes a brief discussion of the general test description, load deformation characteristics, control loading program performance, axial load versus lateral load characteristics, vertical strain profiles longitudinal reinforcement and curvature profiles.

6.1 General Test Observations

Seismic load simulation of the pile specimen required application of fully reversed cycles in both the vertical and lateral actuators. In this section, when in compression, the axial force is designated as positive and when in tension, the axial force is designated as negative. In addition, when in the compression loading branch the lateral force is positive and in the tension loading branch the lateral force is designated as negative. The complete test setup for unit *COR2* is shown in **Fig. 3-24** and **Fig. 3-25**. Indicated on the test unit, 1,295 mm above the pile cap is a horizontal line that marks the end of the inner core longitudinal reinforcement.

General observations recorded during the testing procedure are summarized as follows:

Initial Axial Force Simulation : The first loading stage in the testing procedure consisted of loading the specimen axially to +667 kN while controlling the top lateral displacement to +0.00 mm. At the end of this loading stage, the lateral load was negligible.

At +169 kN in the compression loading branch: This loading stage corresponds to the specified +25% yielding force level. In this cycle, the registered deflection was +1.19 mm and the axial load was +1,189 kN.

At -83 kN in the tension loading branch: This loading stage corresponds to the prescribed -25% yielding force level. The lateral deflection and the axial load were -0.57 mm and +399 kN, respectively.

At +338 kN in the compression loading branch: At the prescribed +50% yielding force level, the lateral deflection was +2.63 mm and the axial load was+1,856 kN. During loading of the specimen at this cycle, onset of horizontal and vertical splitting cracks began, as illustrated in **Fig. 6-2**. Formation of vertical splitting cracks provides first visual evidence of slipping of the prestressing strands.

At -167 kN in the tension loading branch: At -50% yielding the lateral deflection and axial load were -1.34 mm and +205 kN, respectively.

At +507 kN in the compression loading branch: In this cycle the structure was loaded to +75% yielding, in which the lateral deflection was registered at +4.28 mm and the axial load was +2,249 kN.

At -250 kN in the tension loading branch: At -75% yielding the lateral deflection was -2.75 mm and the axial was +75 kN.

At +676 kN in the compression loading branch: This loading stage corresponds to the theoretical first section yielding (+100% yielding), at which stage the lateral deflection and axial load were +6.68 mm and +2718 kN, respectively.

At -334 kN in the tension loading branch: This loading stage corresponds to the theoretical first section yielding while in the tension loading branch (-100%yielding). At this stage, the lateral deflection and the axial load were -5.63 mm and -216 kN, respectively. At this cycle the axial load was for the first time in tension.

After this cycle the loading pattern was changed from single cycles to three cycles, according to the prescribed displacement ductility levels. The experimental yield displacements, Δ'_y, and the loads corresponding to theoretical first section yield, V'_y, and yield, V_y, that were used in the bilinear approximation calculations are as follows:

1. Lateral deflections at theoretical first section yielding:

   Compression : Δ'_{yC} = +6.68 mm

   Tension : Δ'_{yT} = -5.63 mm

2. Lateral load at theoretical first section yielding:

   Compression : V'_{yC} = +676 kN

   Tension : V'_{yT} = -334 kN

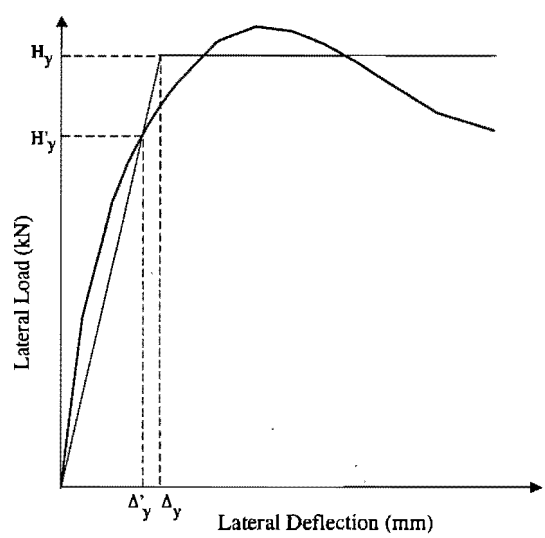

Fig. 6-1 Bilinear approximation

3. Lateral load at theoretical section yielding:

Compression : V_{yC}=+ 899 kN Tension : V_{yT}= -511 kN

4. Calculation of displacement ductility μ_Δ = +,-1:

$$Compression : \frac{V_{yC}}{V'_{yC}} \Delta'_{yC} = +8.89mm \quad Tension : \frac{V_{yT}}{V'_{yT}} \Delta'_{yT} = -8.63mm$$

At Δ = +8.89 mm in the compression loading branch (μ_Δ = +1): This loading stage corresponds to the displacement ductility level of μ_Δ= +1 based on the values computed above. The peak lateral load was recorded at +785 kN and the axial load at +2718 kN.

At Δ = -8.63 mm in the tension loading branch (μ_Δ = -1): In the tension loading branch at the displacement ductility of μ_Δ= -1, the lateral load was -422 kN and the axial load was -269 kN. In the tension loading branch onset of vertical splitting crack was registered in this cycle, as illustrated in **Fig. 6-3**.

At Δ = +13.46 mm in the compression loading branch (μ_Δ = +1.5): Peak lateral and axial loads at this displacement ductility level were +924 kN and +2739 kN, respectively.

At Δ = -12.95 mm in the tension loading branch (μ_Δ = -1.5): Peak lateral and axial loads at this displacement ductility level were -480 kN and -302 kN, respectively. Onset of inclined cracking was recorded at this stage with two cracks emanating from the load stub, as illustrated in **Fig. 6-4** and **Fig. 6-5**. At the load stub interface, the cracks are almost horizontal but begin to inclined towards the compression toe along the pile length, which provides first evidence of shear induced cracking. However, on the sides of the pile and closer to the soffit slab, these cracks are almost vertical as a result of the forces present in the prestressing strands which incline the compression field near these cracks. In addition, at this cycle the prescribed maximum axial tensile load as defined in reference **[3]** that the prototype structure might experience in a seismic event was achieved.

At Δ = +17.78 mm in the compression loading branch (μ_Δ = +2): Lateral load and axial load at this displacement level were +981 kN and +2754 kN, respectively. At this cycle the prescribed maximum axial compressive load as defined in reference **[3]** that the prototype structure might experience in a seismic event was achieved. Cracking pattern registered at this stage is illustrated in **Fig. 6-6**.

At Δ = -17.27 mm in the compression loading branch (μ_Δ = -2): At this displacement ductility level the lateral load was -455 kN and the axial load was -302 kN. Increase in horizontal and inclined cracks is visible in **Fig. 6-7**.

At +22.35 mm in the compression loading branch (μ_Δ = +2.5): At this displacement ductility level the lateral load was +1,009 kN and the axial load was +2,754 kN. At this stage, the specimen achieved its maximum flexural strength under axial compressive loading.

At -21.59 mm in the tension loading branch (μ_Δ = -2.5): Registered lateral load and axial load were -450 kN and -302 kN, respectively. Horizontal cracks wrap around the column near the soffit slab as indicated in **Fig. 6-8**.

At +26.67 mm in the compression loading branch (μ_Δ = +3): Peaks loads at this displacement ductility level were +1,030 kN and +2,754 kN, respectively. In the compression loading branch, onset of vertical cracking was first registered in this cycle. **Fig. 6-9** indicates the cracking pattern recorded in this stage.

At -34.54 mm in the tension loading branch (μ_Δ = -4): Peaks loads at this displacement ductility level were -506 kN and -302 kN, respectively. At this stage, the specimen achieved its maximum flexural strength under axial tensile loading.

At +35.56 mm in the compression loading branch (μ_Δ = +4): Peak loads were lateral load +1,039 kN and axial load +2,754 kN. Cracking pattern registered in this cycle is presented in **Fig. 6-10**.

At -43.18 mm in the tension loading branch (μ_Δ = -5): At this displacement ductility level, the lateral load was -487 kN and the axial load was -302 kN. Horizontal cracks near the termination of the inner core longitudinal reinforcement were wide open (see **Fig. 6-11**), which suggests that the flexural capacity/demand ratio at this level is lower than the flexural capacity/demand ratio at the base of the pile under tensile loads, which corroborates with analysis along the pile length discussed in Chapter 2 and presented in **Fig. 2-31** and **Fig. 2-32**.

At +44.45 mm cycle in the compression loading branch (μ_Δ = +5): At this displacement ductility level, the lateral load was +1,043 kN and the axial load was +2,754 kN. Onset of spalling of the cover concrete in the region of termination of the inner core longitudinal reinforcement was observed at this stage, as illustrated in **Fig. 6-12**, which

indicates formation of a second region of plastic deformations at this location.

At -51.82 mm in the tension loading branch (μ_Δ = -6): At this displacement ductility level, the lateral load and axial load were –482 kN and -302 kN, respectively.

At +53.34 mm cycle in the compression loading branch (μ_Δ = +6): At this displacement ductility level the lateral load was +1055 kN and the axial load was +2754 kN.

At -60.45 mm in the tension loading branch (μ_Δ = -7): At this displacement ductility level, the lateral load and axial load were –473 kN and -302 kN, respectively.

Final stages of the testing procedure clearly shows the extent of spalling of the cover concrete and unwinding of the prestressing strands in the region of termination of the inner core longitudinal reinforcement (see **Fig. 6-13**). Post test inspection of the test unit revealed that a total of 2 fractures occurred in the spiral cage along an inclined crack, as illustrated in **Fig. 6-14** and **Fig. 6-15**, which indicates onset of shear failure. Notes taken during the testing procedure indicate that these spirals fractured during the last cycle. In addition, necking of a third spiral was observed along this same line. This spiral did not fracture at the necking, however, fracture of this same spiral level was observed two strand spacings to the side of the exposed concrete core as a result of a strand bearing on this spiral, which is shown in **Fig. 6-16**.

After completion of the testing procedure, the soffit slab concrete around the pile section was removed, as indicated in **Fig. 6-17**. Removal of this concrete shows spalling of the cover concrete occurred at the base of the pile section, which indicates that plastic deformations were also observed at the pile cap interface, as discussed in Chapter 2.

The testing procedure was stopped due to a large difference between the vertical displacements of the two vertical actuators; however, no reduction of the pile section lateral load carrying capacity was observed and the axial load was still being supported by the specimen.

Fig. 6-3 Cracking Pattern at -8.63mm

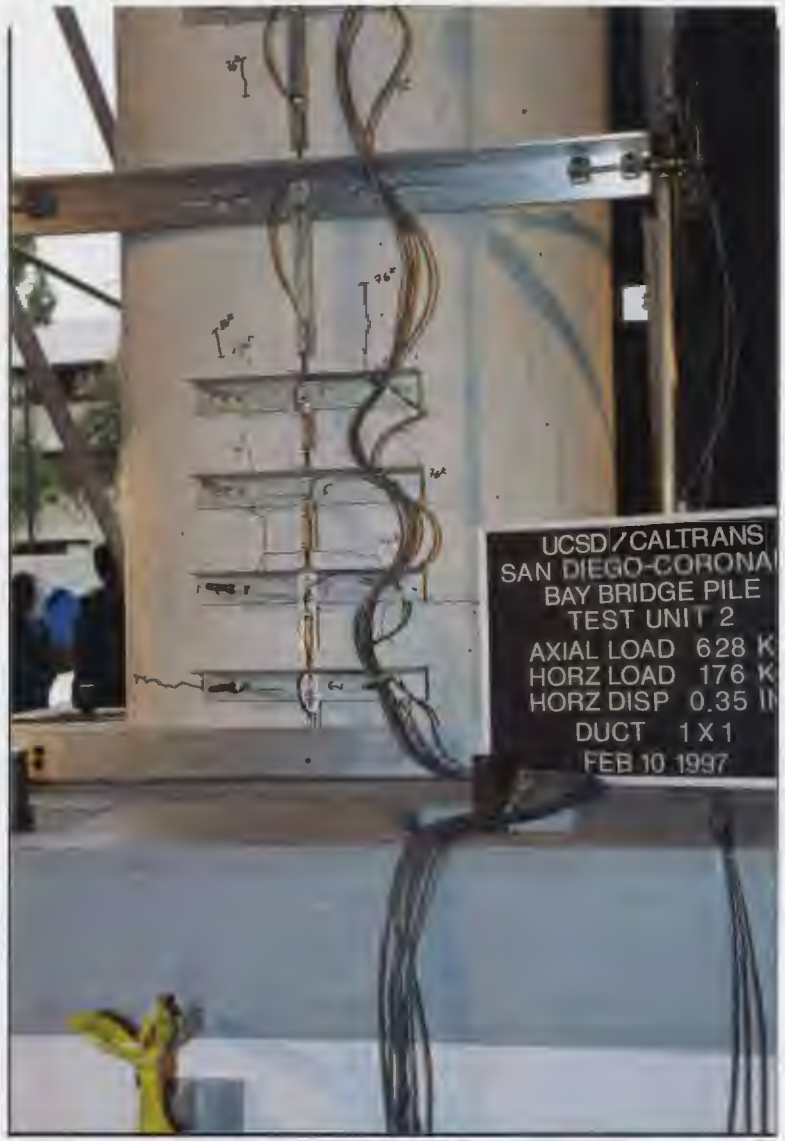

Fig. 6-2 Onset of Flexural and Vertical Splitting Cracking

Fig. 6-5 Onset of Inclined Shear Cracking at -12.95mm

Fig. 6-4 Onset of Inclined Shear Cracking at -12.95mm

Fig. 6-7 Cracking Pattern at −17.27mm

Fig. 6-6 Cracking Pattern at +17.78mm

Fig. 6-9 Cracking Pattern at +26.67mm

Fig. 6-8 Cracking Pattern at −21.59mm

Fig. 6-11 Cracking Pattern at -43.18mm

Fig. 6-10 Cracking Pattern at +35.56mm

Fig. 6-13 Post Test Damage State

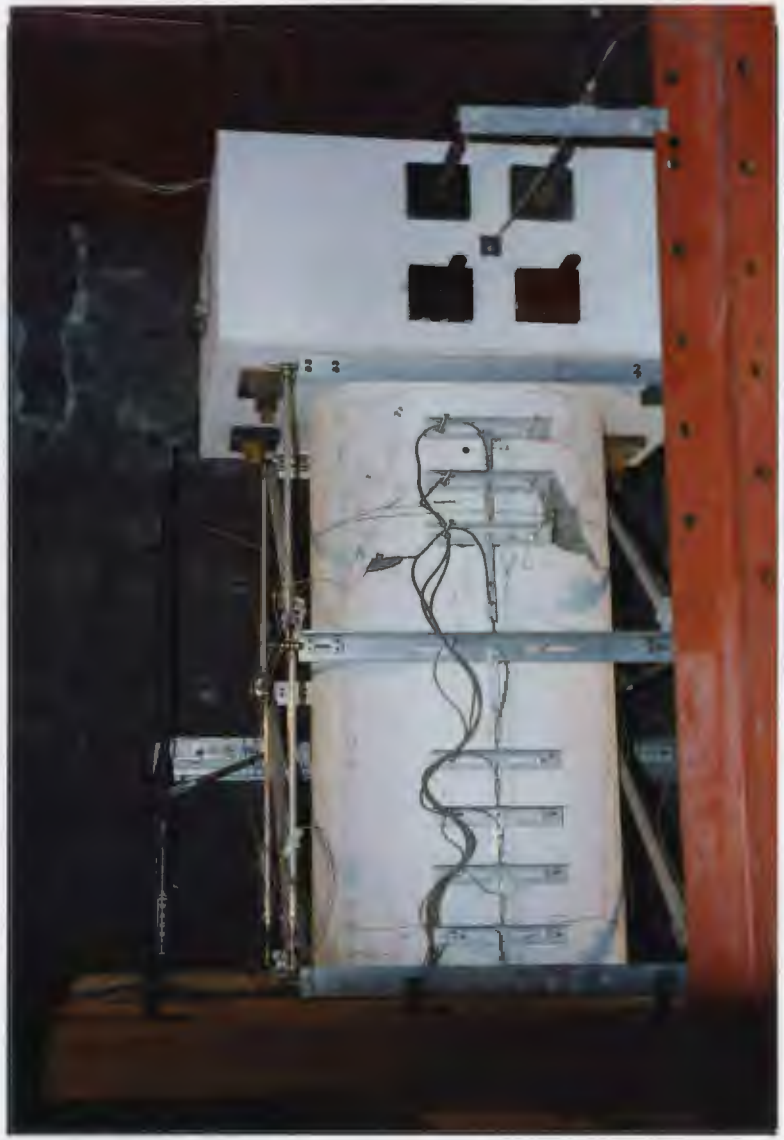

Fig. 6-12 Onset of Concrete Crushing at +44.45mm

Fig. 6-14 Post Test Damage State

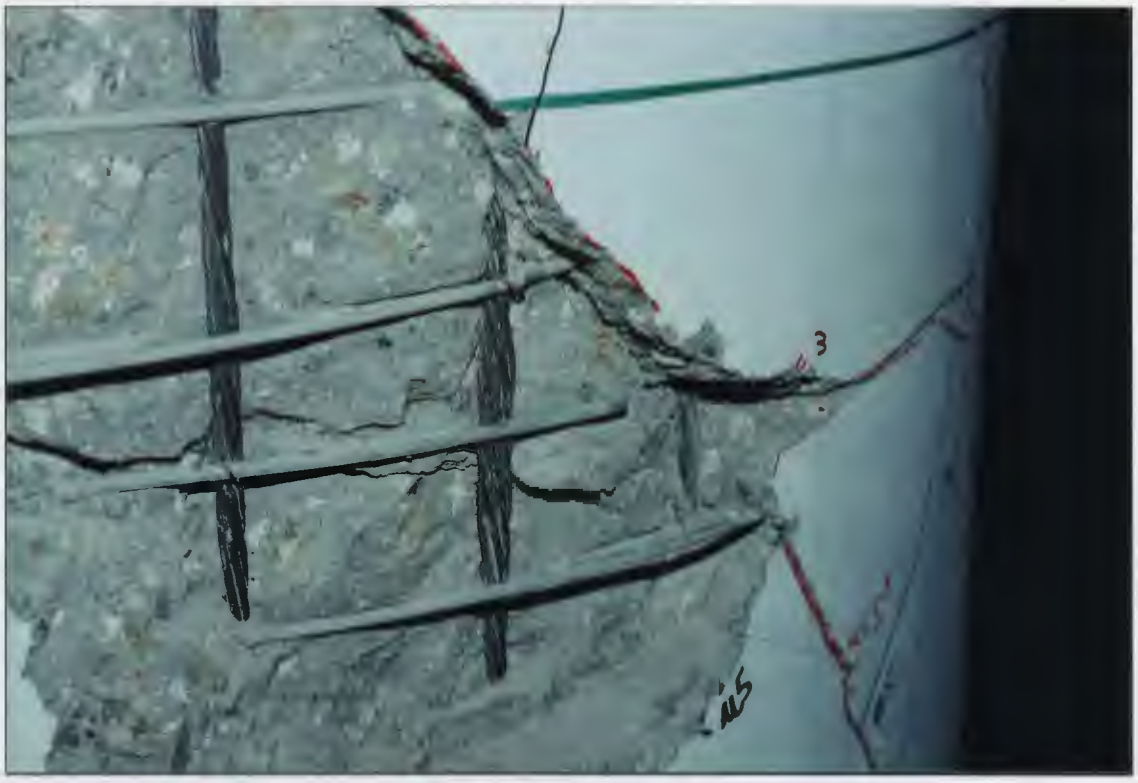

Fig. 6-15 Spiral Fracture Along Inclined Shear Crack

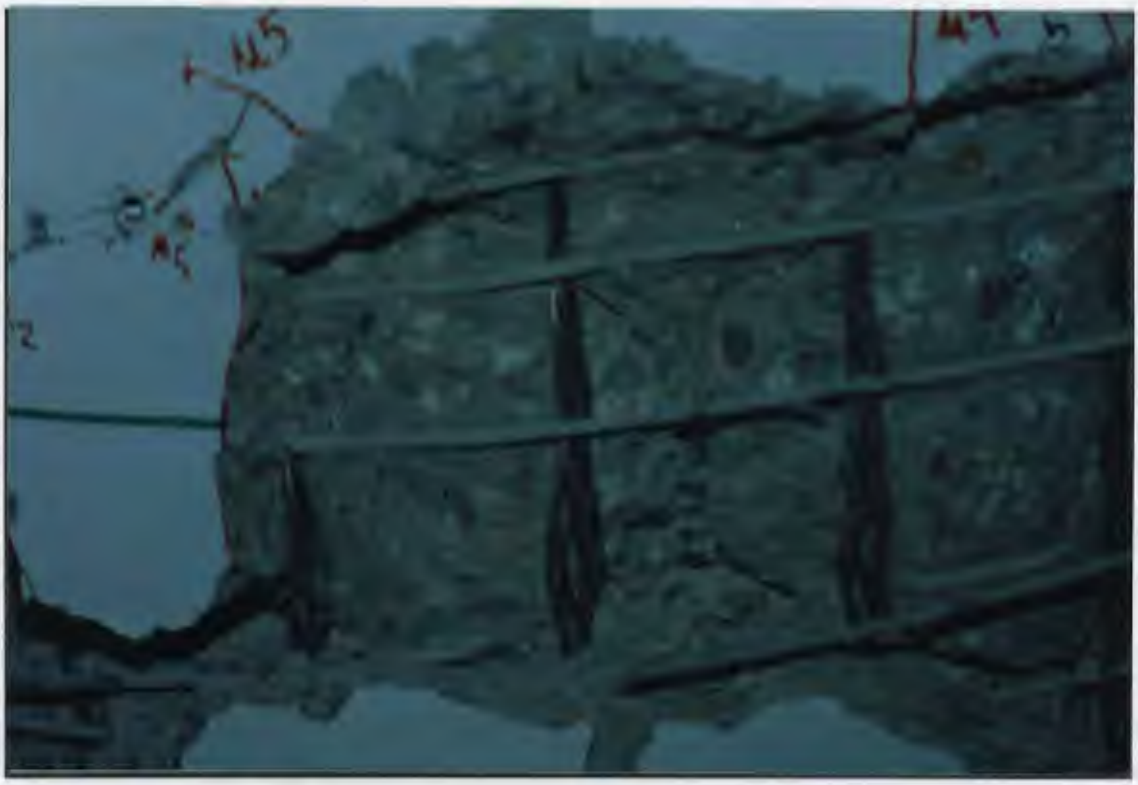

Fig. 6-16 Spiral Fracture at Prestressing Strand

Fig. 6-17 Extent of Spalling of the Cover Concrete at Pile Cap Interface

6.2 Load Deformation Characteristics

Fig. 6-18 shows the measured lateral force versus lateral deflection response of test unit *COR2*. The initial response of the pile section indicates a slightly higher stiffness than originally predicted in both the compression and tension loading branch. In the post-test analysis, presented in Chapter 8, this finding is attributed in part to the concrete model that was employed during development of the post-test analysis. Also, in the transition of the loading procedure from compression to the tension, and vice-versa, there is a significant pinching of the hysteresis loops, because in this transition region, the axial force is not effective in closing the open cracks.

At peak load in the compression loading branch, the predicted maximum load was approximately 15% lower than the measured maximum load. However, in the tension loading branch, the predicted value matches closely the observed test results, which suggests that the concrete used to develop the pre-test analysis underestimates the confined compressive strength of the high-strength concrete. This is so because, in the compression loading branch, the contribution of the concrete component to the flexural capacity of the section is significantly higher than for axial tension loads.

In the compression loading branch, a maximum lateral force of +1009 kN was recorded at approximately μ_Δ=2.5. At this level, 5% degradation of lateral strength between successive cycles was recorded, and between μ_Δ=2.5x1 and μ_Δ=5x1, no significant reduction was observed in the lateral load.

A maximum lateral force of -506 kN was recorded in the tension loading branch during cycle μ_Δ=-4x1. At successive cycles between μ_Δ=-4x1 and μ_Δ=-7x1, minimum loss in the lateral strength was recorded. The testing procedure was stopped at μ_Δ=-7x3 because the section was maintaining constant lateral load and maximum achieved lateral deflection and it was considerably higher than those estimated during analysis. Moreover, a large difference between the vertical displacements of the two vertical actuators was observed and, to safeguard integrity of the equipment, the testing procedure was stopped at this stage.

Post test investigation of the test data indicates that a maximum displacement ductility of μ_Δ=+5 was achieved in the compression loading branch and μ_Δ=−7 was achieved in the tension loading branch, with minimum degradation in the lateral strength of the section. In the compression loading branch lateral deflections at maximum displacement and yield were,

respectively, Δ_{max}= +53.34 mm and Δ_y= +8.89 mm, while in the tension loading branch these values were Δ_{max} = -60.45 mm and Δ_y = -8.63 mm, respectively.

In **Fig. 6-18** the curve labeled *Corrected Deformations* was obtained by integrating the vertical curvature profiles along the length of the pile based on the experimental test results and neglecting the increase in curvature at the region of termination of the inner core longitudinal reinforcement. Curvature vertical profiles are described in later sections. An immediate observation of this curve reveals that there is no significant decrease in the compression loading branch maximum lateral deflection, and approximately one ductility level drop is observed in the tension loading branch.

Fig. 6-19 shows the measured lateral force versus curvatures computed at the pile cap interface. The main characteristics visible in this figure are very similar to those indicated earlier for the pile lateral deflection, mainly pinching of the hysteresis loops at the transition from the compression to the tension loading branch and vice versa.

Post test investigation of the test data indicates that a maximum curvature ductility of μ_φ=+7.5 was achieved in the compression loading branch and μ_φ=-9 in the tension loading branch. In the compression loading branch, maximum and yield curvatures are, respectively, φ_{max}=+0.000061 mm^{-1} and φ_y=+0.0000071 mm^{-1}, and φ_{max}=-0.000047 mm^{-1} and φ_y=−0.0000052 mm^{-1} in the tension loading branch. As expected, curvature ductility levels are slightly higher than displacement ductility levels.

Curvatures presented in **Fig. 6-19** represent average values and were computed according to equation 82, 159. Also, during computations of curvatures at the pile cap interface, the height of the linear potentiometer cell, h_{cur}, includes an additional term to account for tensile strain penetration into the pile cap by including the strain penetration length into the curvature cell height, h_{cur}, according to equation **(5.2)**.

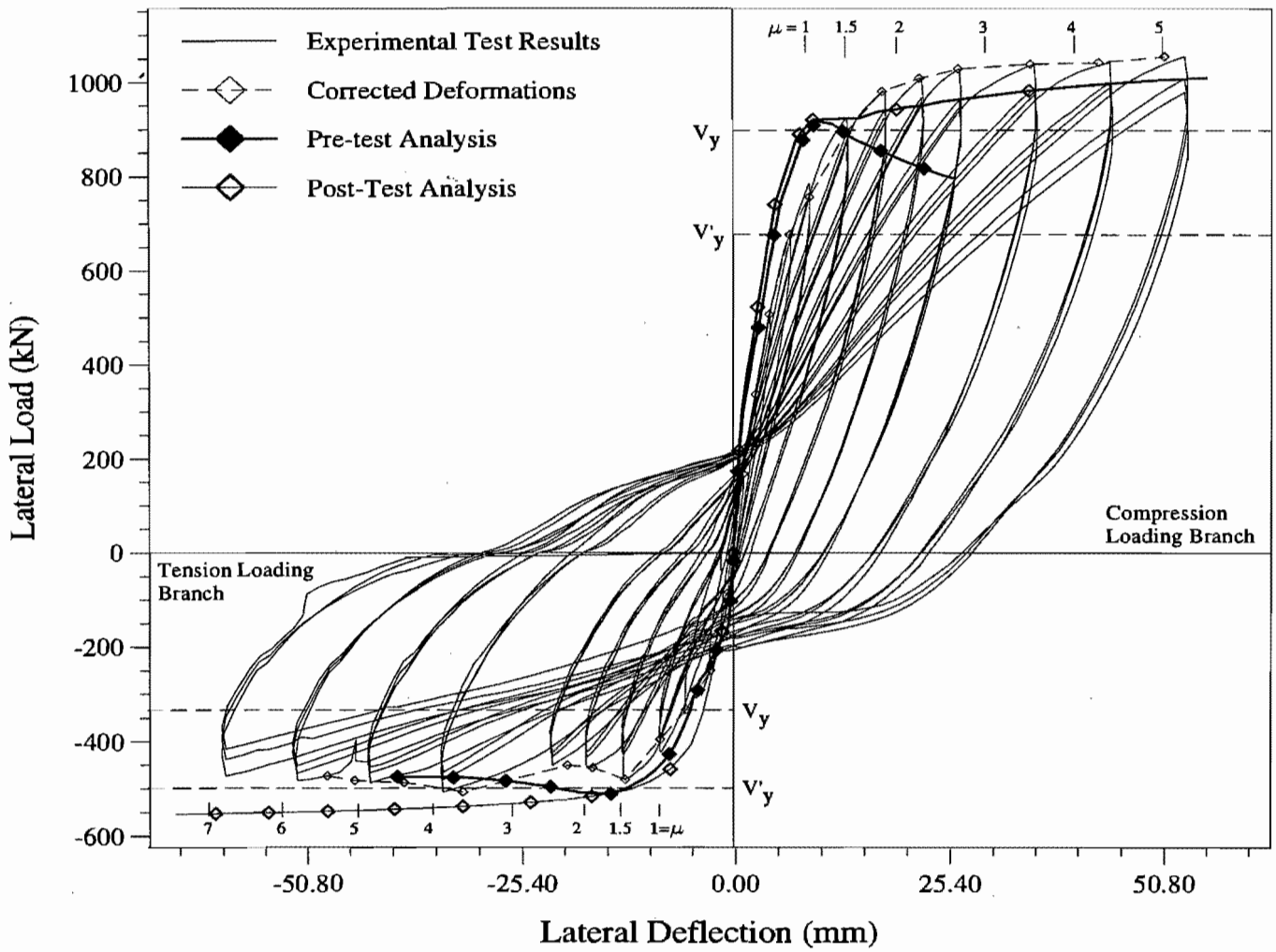

Fig. 6-18 Lateral Load versus Lateral Deflection Characteristics

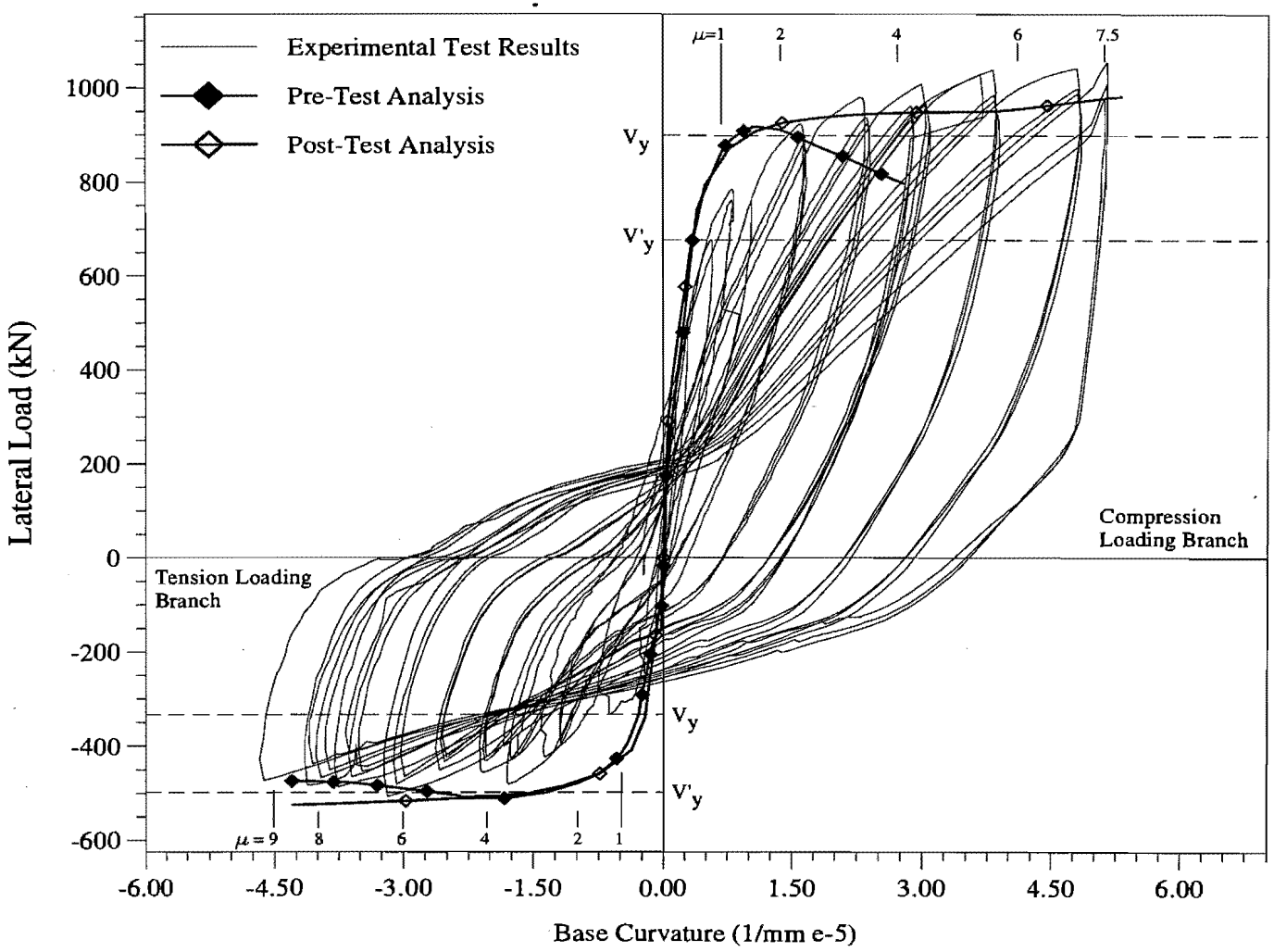

Fig. 6-19 Lateral Load versus Base Curvature Characteristics

Axial load versus lateral deflection characteristics are presented in **Fig. 6-20**. This figure also shows the profile of the loading path that was employed to control the application of the simulated seismic forces. The maximum and minimum axial loads were predefined at +2793 kN in the compression loading branch and -302 kN in the tension loading branch, respectively.

Loading curves defined in Chapter 3 for test unit *COR2* are also presented in **Fig. 6-20**. In addition, indicated in this figure are the location at which the residual displacements, Δ_i, were obtained when Curve V and Curve X crossed the initial axial load axis and used to define Curve I and/or Curve II in **Region 1** and Curve VI and/or Curve VII in **Region 3**, which redirect the loading path towards the control program loading path. In **Fig. 6-20** not all curves are presented for clarity. Refer to **Fig. 3-57** for additional curves not shown here. As expected, these curves are straight lines which emanate from the residual displacements, Δ_i, and point towards the end points of these curves.

Fig. 6-21 presents the axial load versus the lateral load characteristics for test unit *COR2*. In this figure is also shown the pre-test analysis loading path which was used to develop the control program loading path depicted in **Fig. 6-20**. Pinching in the hysteresis loops at the initial axial load are due to the fact that the control program loading path in the unloading branches is described by a straight line initiating at the peak deformation to the initial load state.

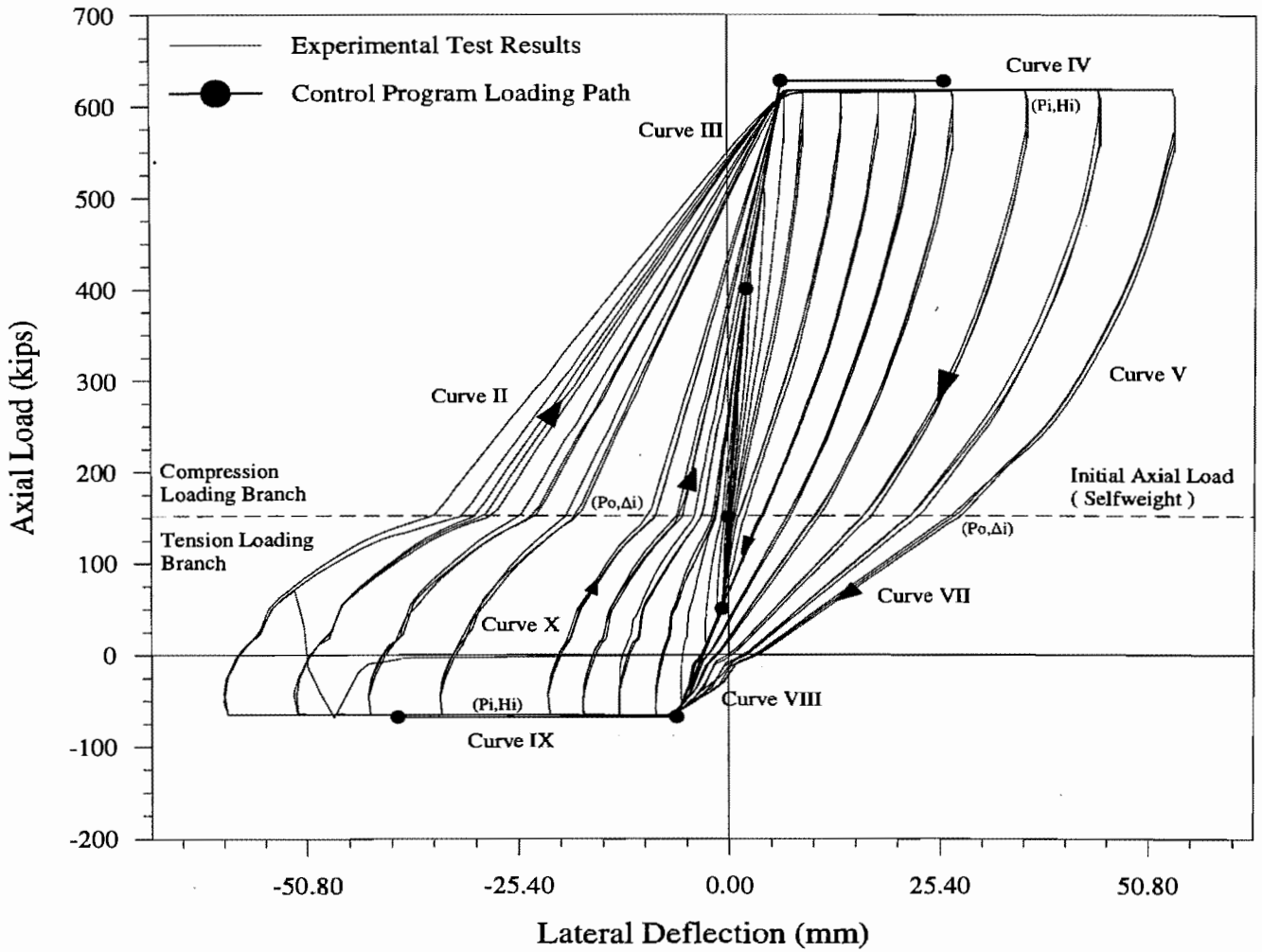

Fig. 6-20 Axial Load versus Lateral Deflection Characteristics

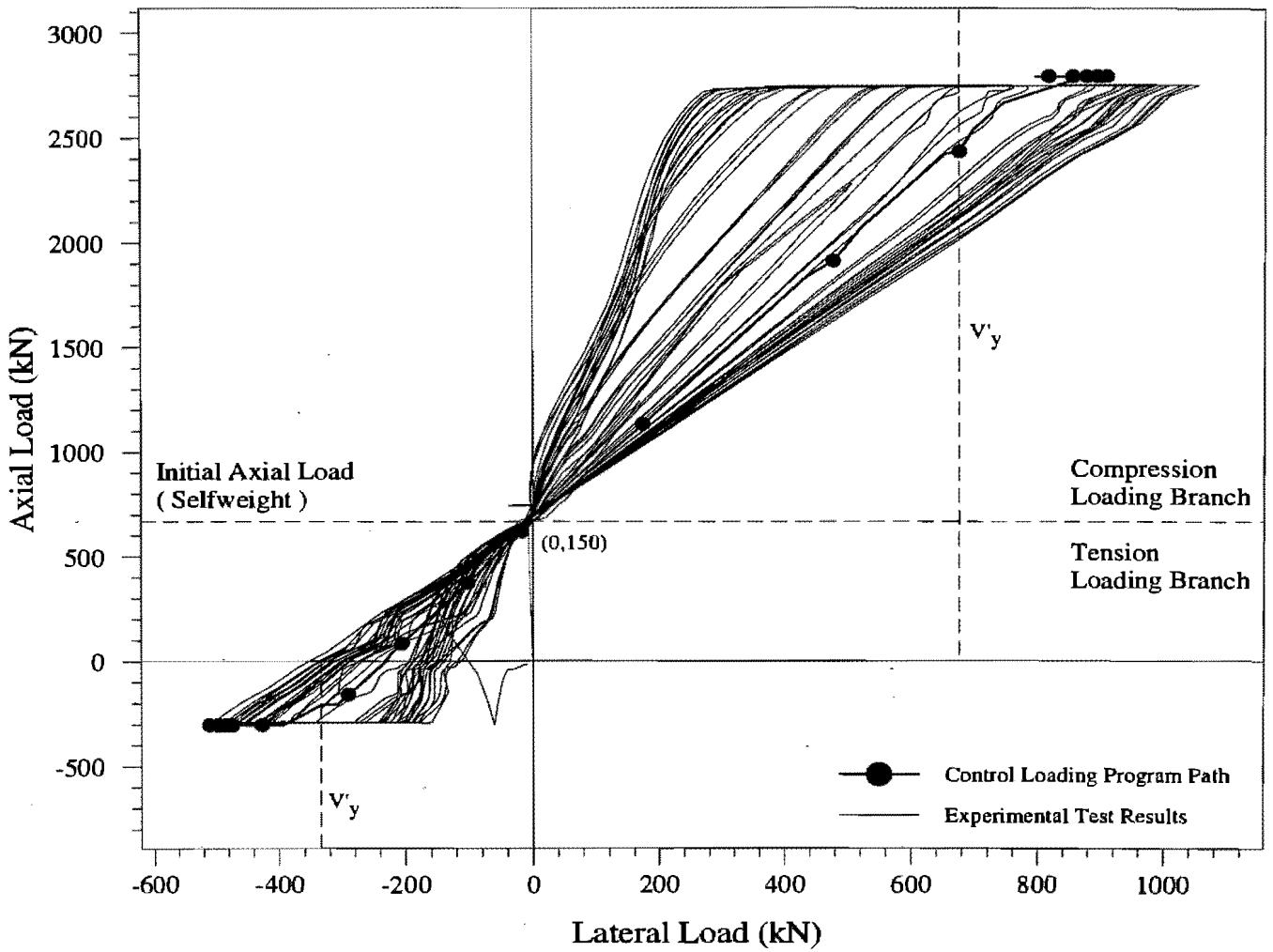

Fig. 6-21 Axial Load versus Lateral Load Characteristics

6.3 Pile Curvature Profiles

In this section and future sections, the plotted v lues are the first cycle peak values for each cyclic response. Curvature vertical profiles along the height of the pile are presented in **Fig. 6-22(a)** and **Fig. 6-22(b)** for initial and final stages of the testing procedure, respectively.

The curvature profiles depicted in **Fig. 6-22(a)** show that in the initial stages of the testing procedure, region of plastic deformations form at the bottom of the pile section, illustrated by a significant increase in curvature a position ***1***. A second region of plastic deformations is well illustrated in **Fig. 6-22(a)**, depicted by a significant increase in the curvature near the region where the inner core longitudinal reinforcement terminates. Increase in curvature in this region is more accentuated in the tension loading branch. This second region of plastic deformations began to form when the lateral deflection was $\Delta = -21.59$ mm, as a result of wide open cracks at this location previously described.

Indicated in these figures are the yield curvature levels obtained from **Fig. 6-22(a)** which provides a visual indication of regions of plastic deformations achieved in the different loading stages. The length of the plastic hinge reached a maximum height of approximately 423 mm near the soffit slab, which is sightly higher than the theoretical effective plastic hinge length, l_p, of 326 mm, obtained from equation **(5.3)**.

At the location where the longitudinal reinforcement terminates, it is not readily perceived what is the exact length of plastic deformations; however, region of plastic deformations are more concentrated between positions ***8*** and ***5***, which leads to a plastic hinge length of approximately 609 mm.

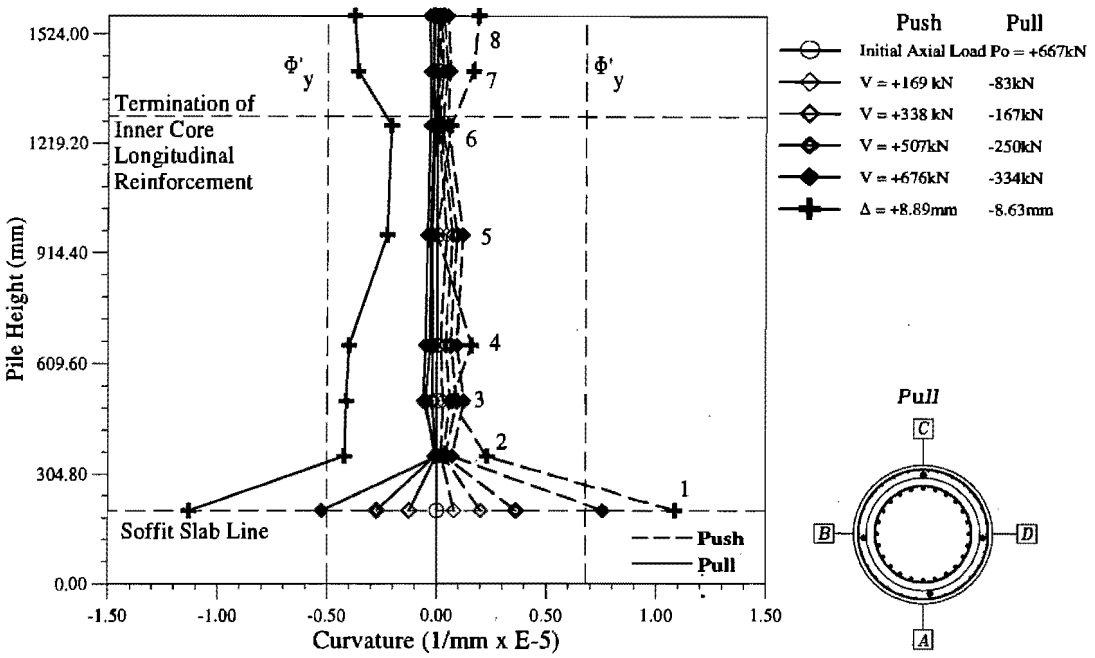

(a) Vertical Strain Profiles - Initial Stages of Testing

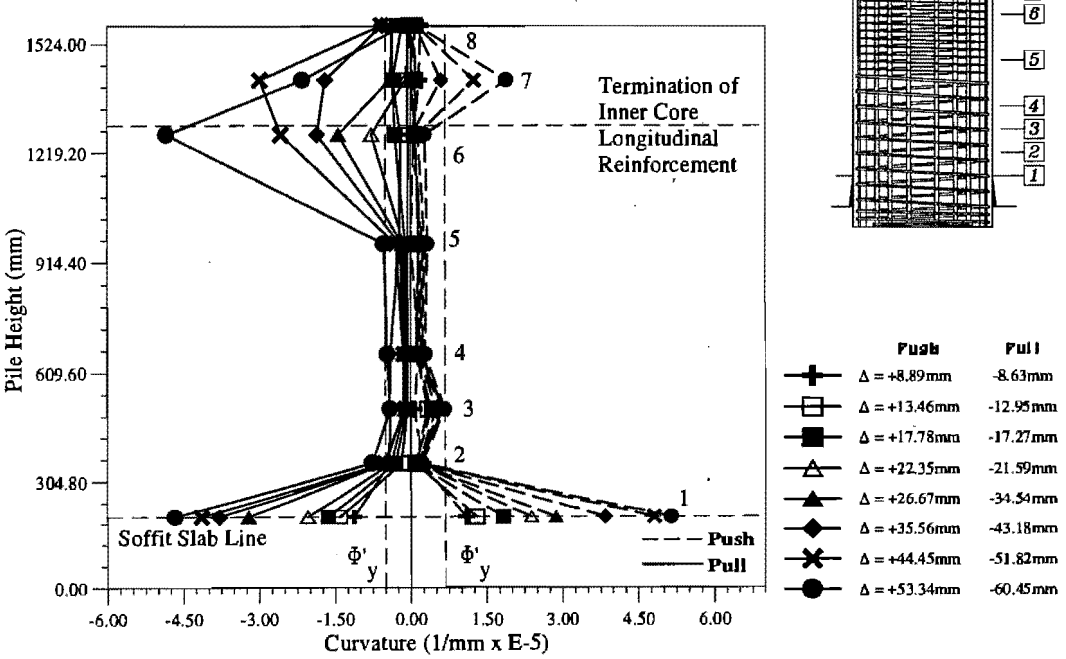

(b) Vertical Strain Profiles - Final Stages of Testing

Fig. 6-22 Curvature Vertical Profiles

6.4 Flexural and Shear Components of Deformation

Flexural components of deformation were calculated from data recorded from linear potentiometers installed on the test specimen to measure curvatures according to the layout presented in **Fig. 3-41** and **Fig. 3-42**. Shear components of deformations were calculated from data recorded from linear potentiometers installed on the test specimen to measure shear panel deformations according to the layout presented in **Fig. 3-43**. Shear deformations were estimated according to the equations presented in **Fig. 3-44**.

Flexural and shear components of deformation are plotted in **Fig. 6-23** and **Fig. 6-24** in terms of the pile top displacement. The curve labeled *Top Deflection* was obtained from the measured pile lateral deflection, the curve labeled *Flexure+Shear* was obtained by adding the *Flexure Component* and *Shear Component* curves, which were determined as previously described, and the curve labeled *Revised Flexure* was obtained by neglecting increase in curvature near the termination of the inner core longitudinal reinforcement.

In these plots, comparison of *Top Deflection* with *Flexure+Shear* suggests a correlation with a minimum error between these two curves. As expected, errors between these two curves are expected because of the nature measured versus calculated data. For example, when computing the shear and flexure components of deformation, it is assumed that the instrumentation devices are rigidly connected to the test specimen and any deformation of the devices is ignored for computational simplicity. However, the presented data depicts a good correlation between these variables.

From the plots depicted in **Fig. 6-23** and **Fig. 6-24**, it is observed that the flexure component of deformation dominates response, indicating a more predominant ductile flexural response of the pile section under the imposed lateral loads. However, as indicated earlier, fracture of the spiral reinforcement along an inclined crack occurred at later stages of the testing procedure without reduction to the lateral load carrying capacity of the section. Referring to **Fig. 2-34**, and based on the UCSD three component shear model, the shear strength of the pile section relies primarily on the shear capacity of the concrete and a more predominant shear response should have occurred after fracture of the spiral reinforcement because of the reduced capacity of the concrete component in relation to the shear demand imposed on the section. This observation suggests that the shear capacity of the precast concrete shell was considerably higher than originally computed and the concrete shell is adequate in confining the cast in place concrete core.

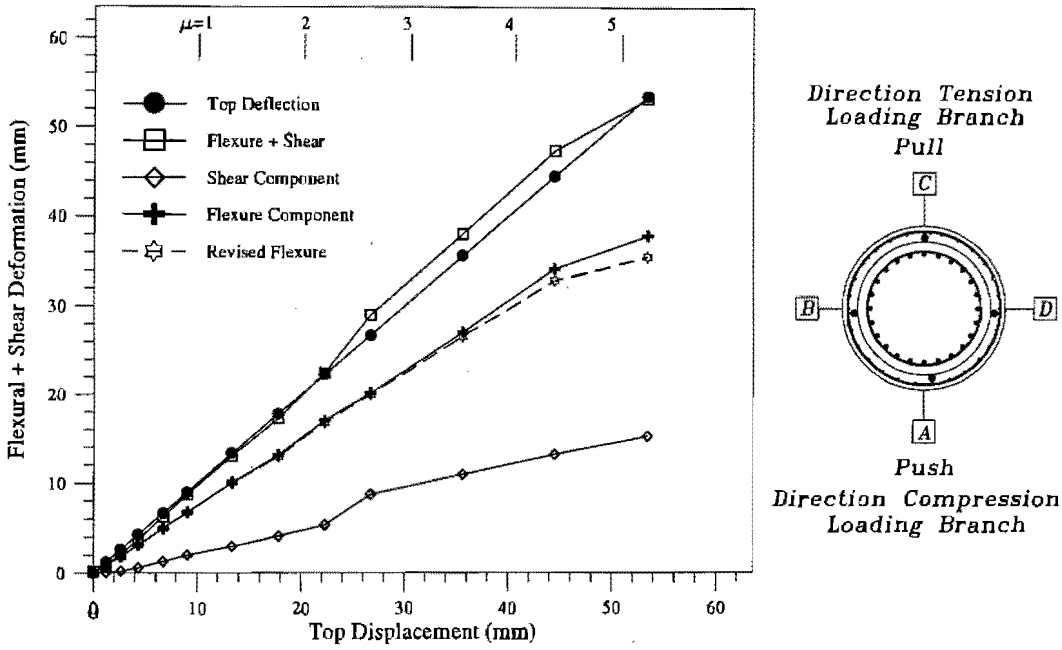

(a) Displacement Components - Compression Loading Branch

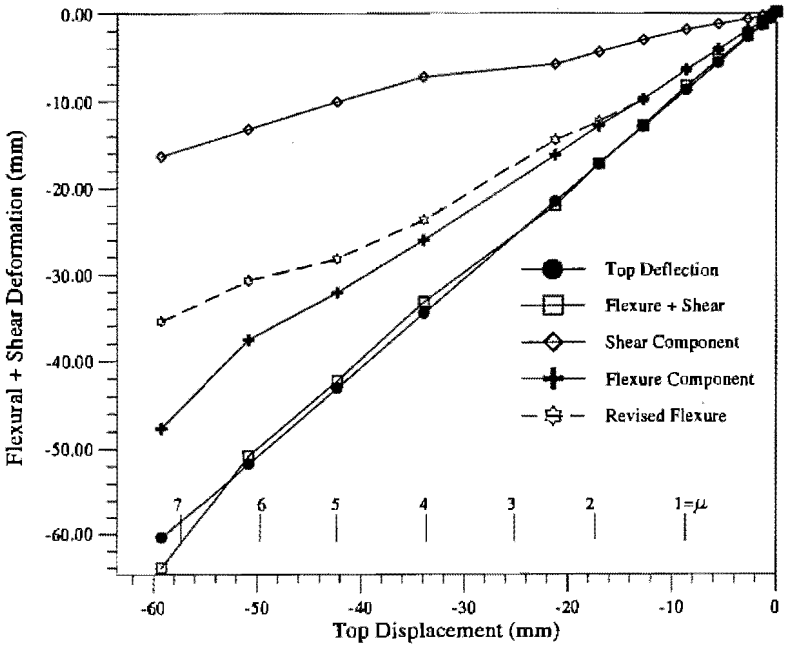

(a) Displacement Components - Tension Loading Branch

Fig. 6-23 Displacement Components versus Pile Lateral Deflection

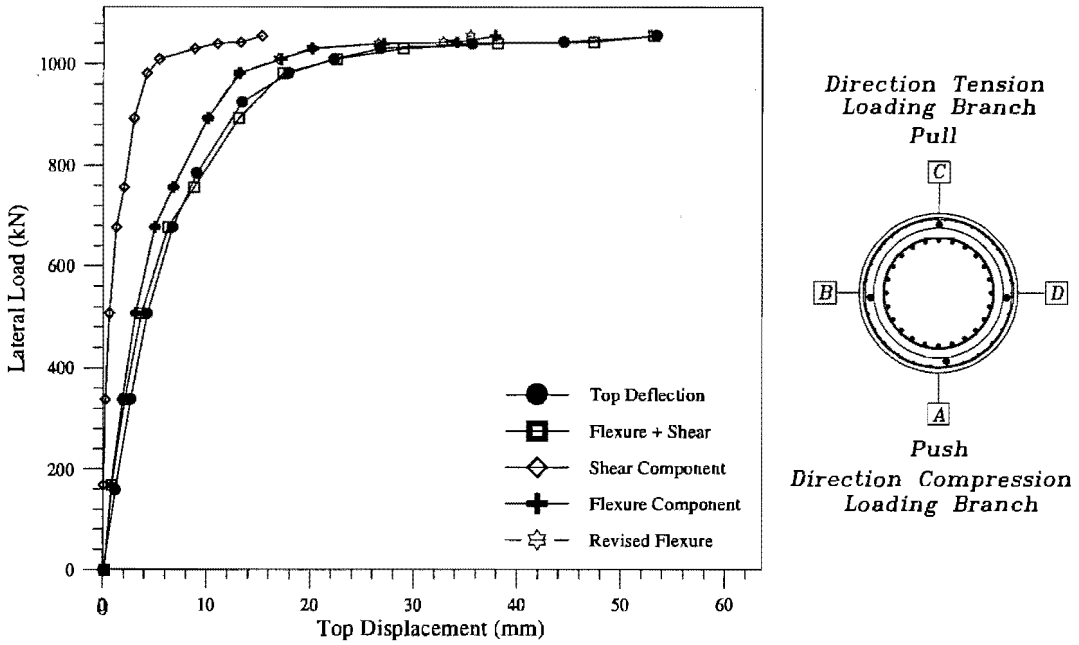

(a) Displacement Components - Compression Loading Branch

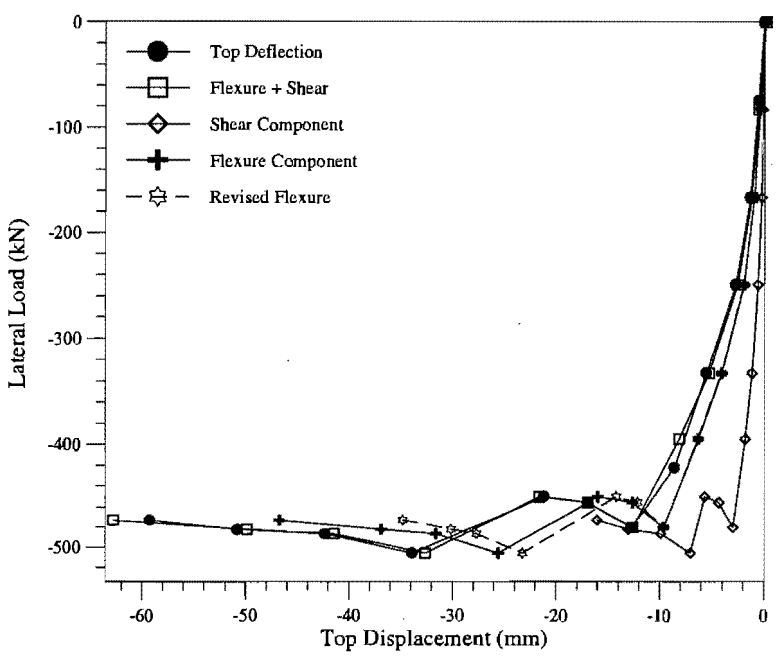

(a) Displacement Components - Tension Loading Branch

Fig. 6-24 Displacement Components versus Lateral Load

6.5 Pile Inner Core Longitudinal Reinforcement Strain Profiles

The inner core reinforcement consists of #7 Grade40 (f_y=276 MPa) steel with a yield strain of approximately 1500$\mu\varepsilon$.

6.5.1 Pile Longitudinal Reinforcement - Vertical Strain Profiles

Vertical strain profiles for the inner core longitudinal reinforcement are presented in **Fig. 6-25** through **Fig. 6-28**.

Strain profiles along inner core bar ***A*** reveal that yielding of this bar in compression occurred at the pile cap interface at μ_Δ=+1.5, and yielded in tension at μ_Δ=−1.5 also at location ***3***. Yield strain penetrations were recorded in this bar to a depth of approximately -304 mm, which indicates a strain penetration of $0.045d_bf_y$. Similar to test unit *COR1*, strain profiles indicate an approximate linear variation of strains from the top of the bar to approximately position ***6***, which suggests a development length of approximately 533 mm.

The profiles for bars ***B*** and ***D***, which are positioned on the sides of the pile, revealed that these bars where always in tension and reached yielding only at later stages of the testing procedure at μ_Δ=+1.5. The vertical profiles for bars ***B*** and ***D*** are similar as a result of the symmetrical position of these two bars with respect to the loading direction.

Strain profiles along inner core bar ***C*** reveal this bar yielded in compression at approximately μ_Δ=-4 and in tension this bar yielded at μ_Δ=+1. Yield strain levels for this bar were not recorded below a depth of approximately -304 mm, which matches the results for bar ***A***.

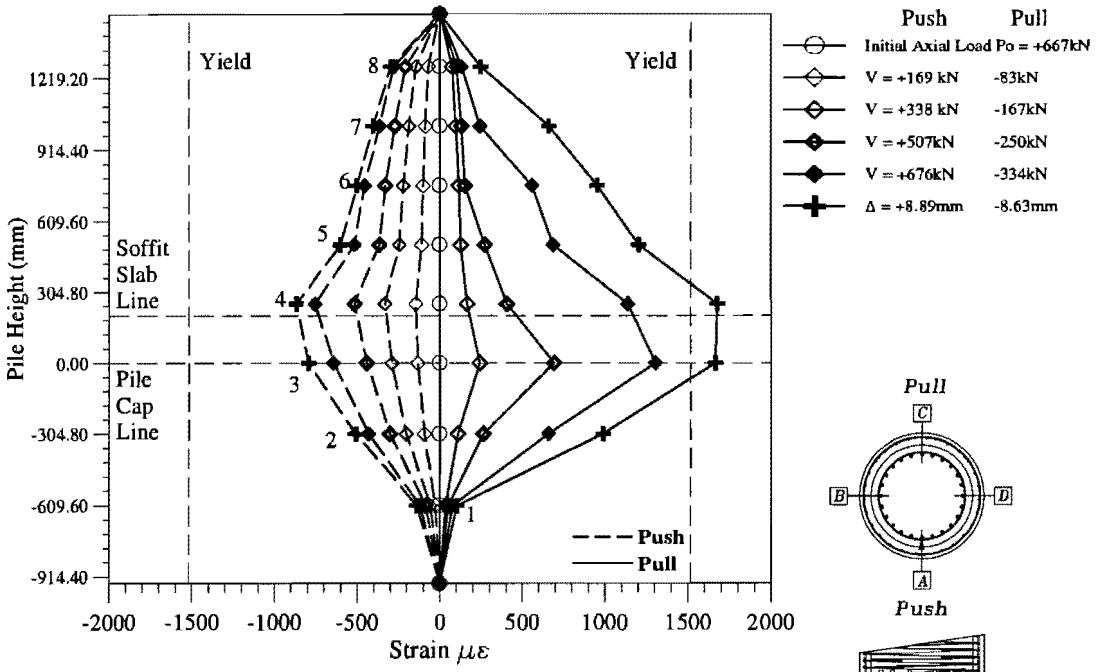

(a) Vertical Strain Profiles - Initial Stages of Testing

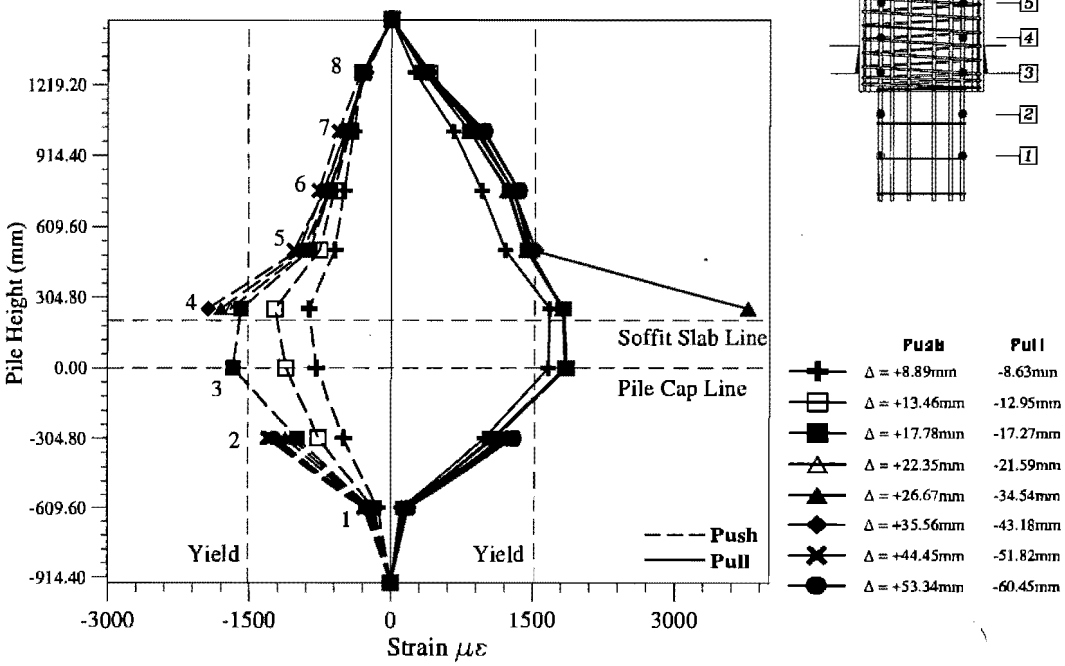

(b) Vertical Strain Profiles - Final Stages of Testing

Fig. 6-25 Vertical Strain Profiles Inner Core Bar *A*

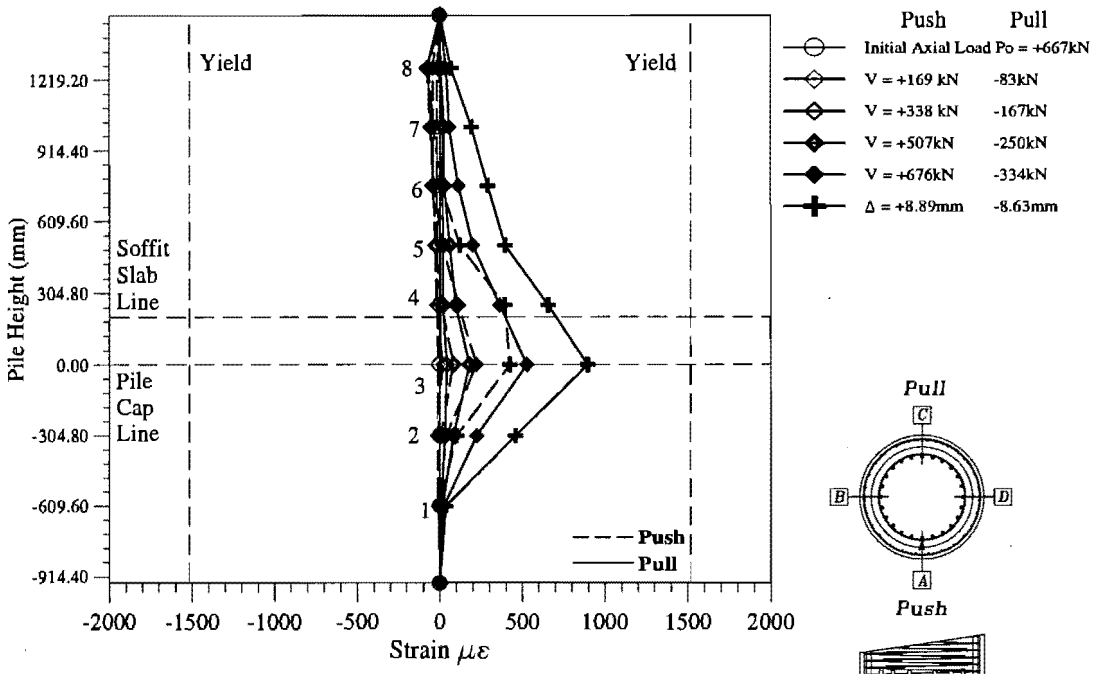

(a) Vertical Strain Profiles - Initial Stages of Testing

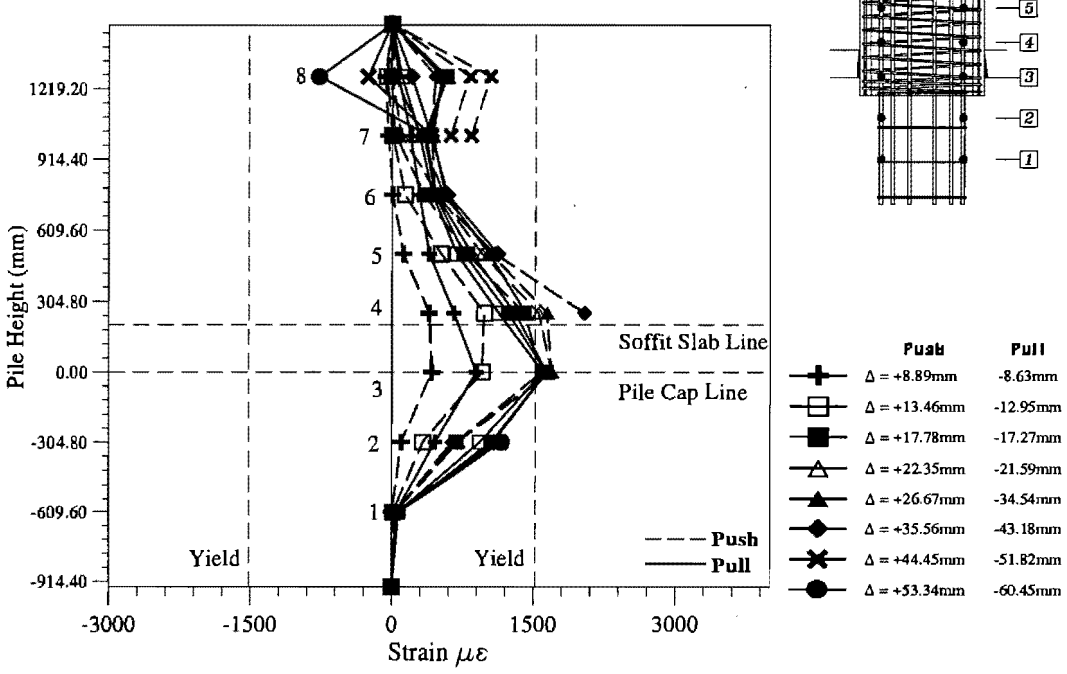

(b) Vertical Strain Profiles - Final Stages of Testing

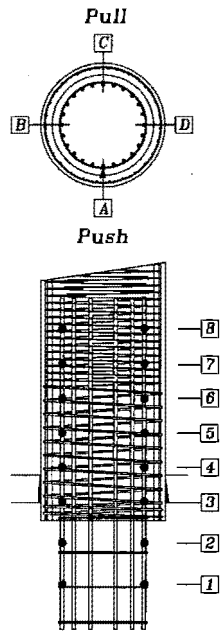

Fig. 6-26 Vertical Strain Profiles Inner Core Bar ***B***

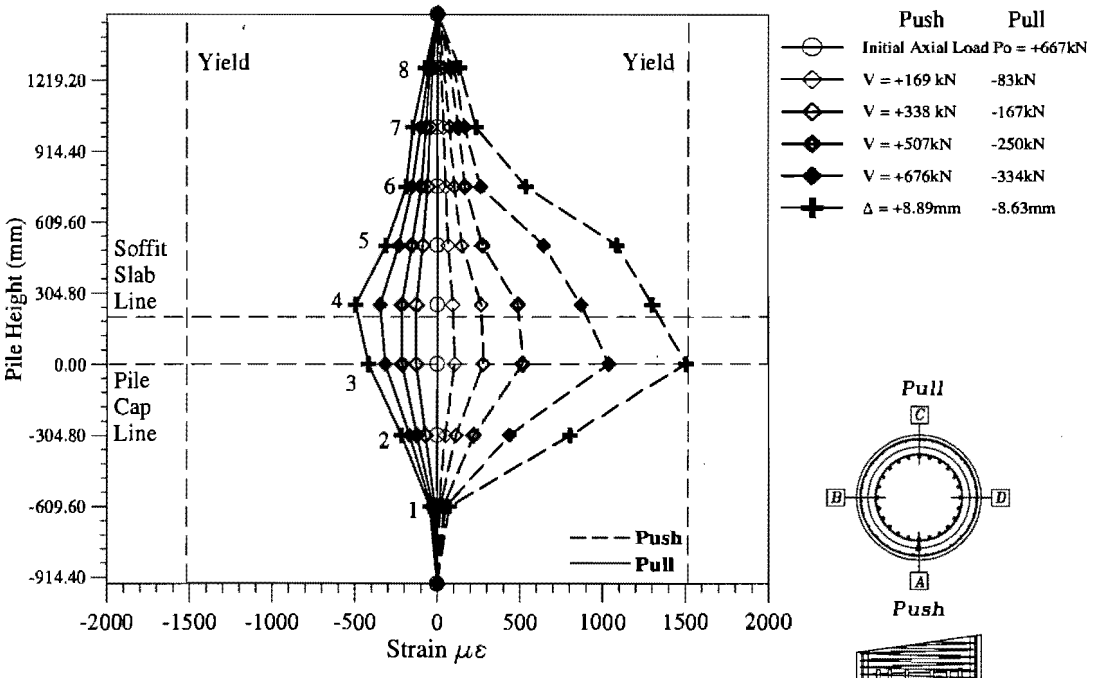

(a) Vertical Strain Profiles - Initial Stages of Testing

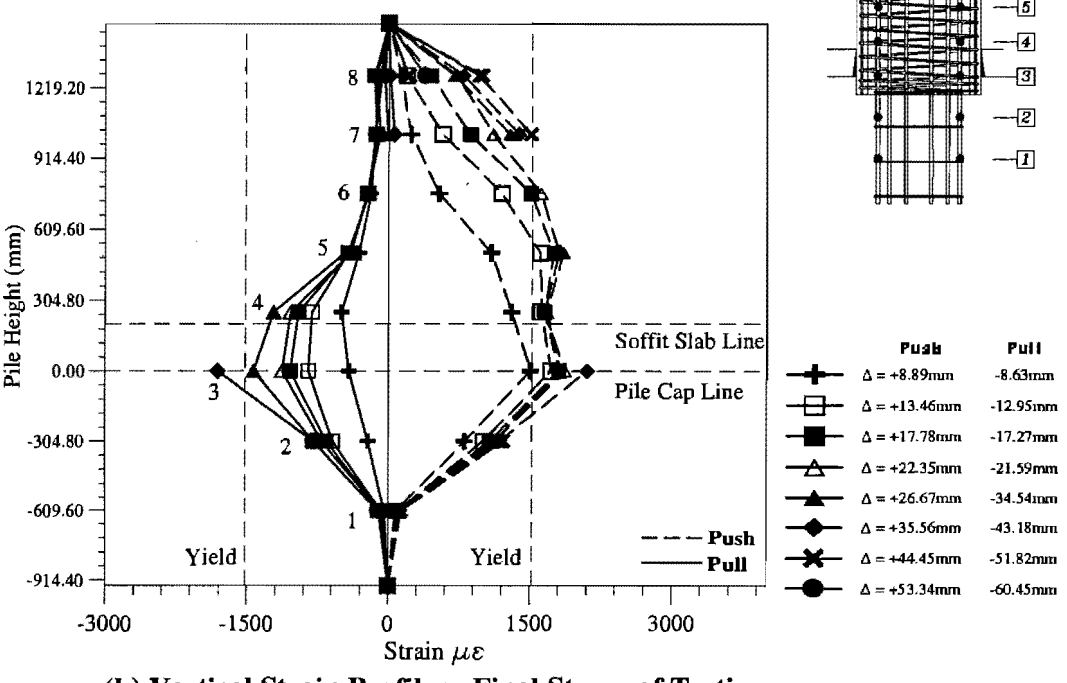

(b) Vertical Strain Profiles - Final Stages of Testing

Fig. 6-27 Vertical Strain Profiles Inner Core Bar *C*

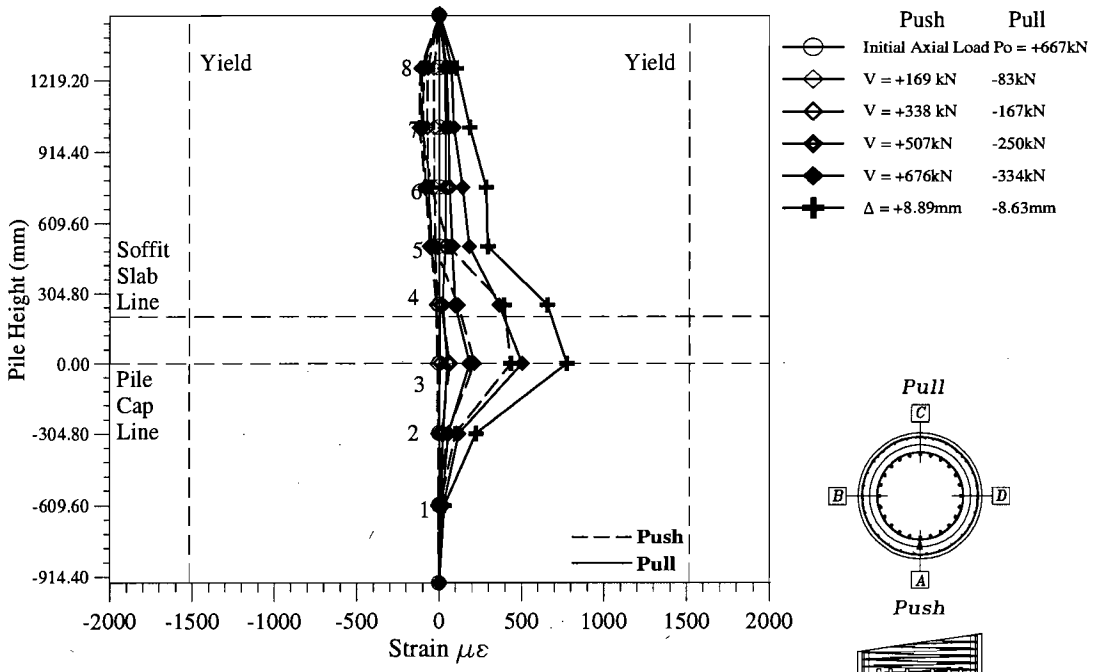

(a) Vertical Strain Profiles - Initial Stages of Testing

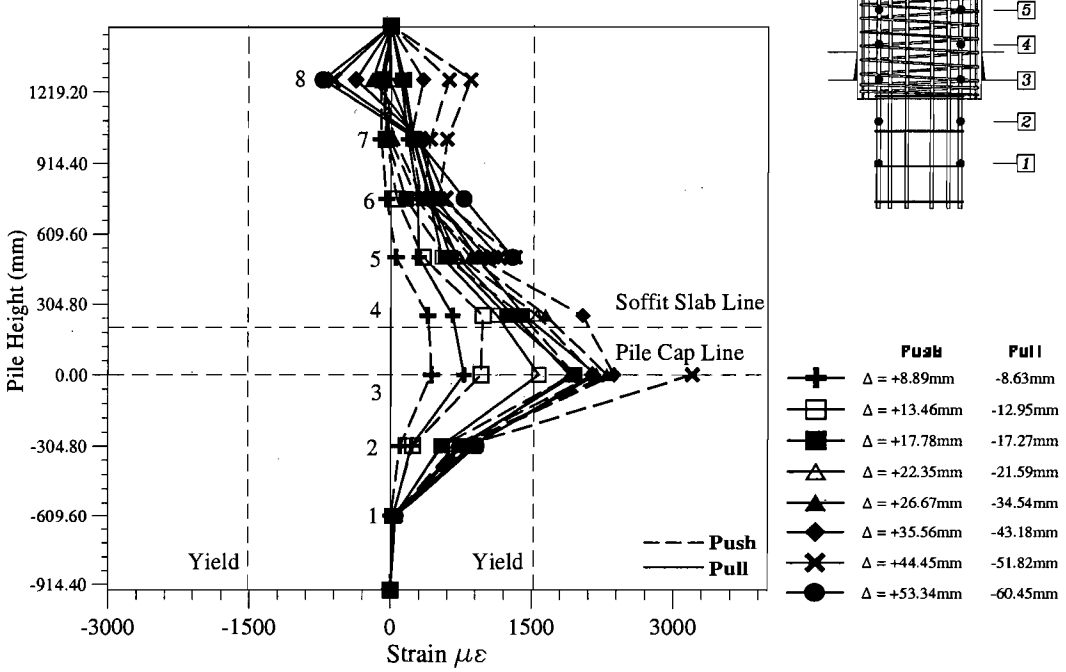

(b) Vertical Strain Profiles - Final Stages of Testing

Fig. 6-28 Vertical Strain Profiles Inner Core Bar ***D***

6.5.2 Pile Longitudinal Reinforcement - Circumferential Strain Profiles

Circumferential strain profiles for the pile inner core longitudinal reinforcement are presented in **Fig. 6-29** through **Fig. 6-32**. The circumferential profiles depicted in these figures indicate that in the initial stages of testing, a linear variation of strain between the longitudinal bars suggests small excursions into yielding strains. Yielding of bars ***A*** and ***C*** occurred mainly between horizontal lines ***2*** and ***7***, with strains significantly higher than yielding only between levels ***3*** and ***4***.

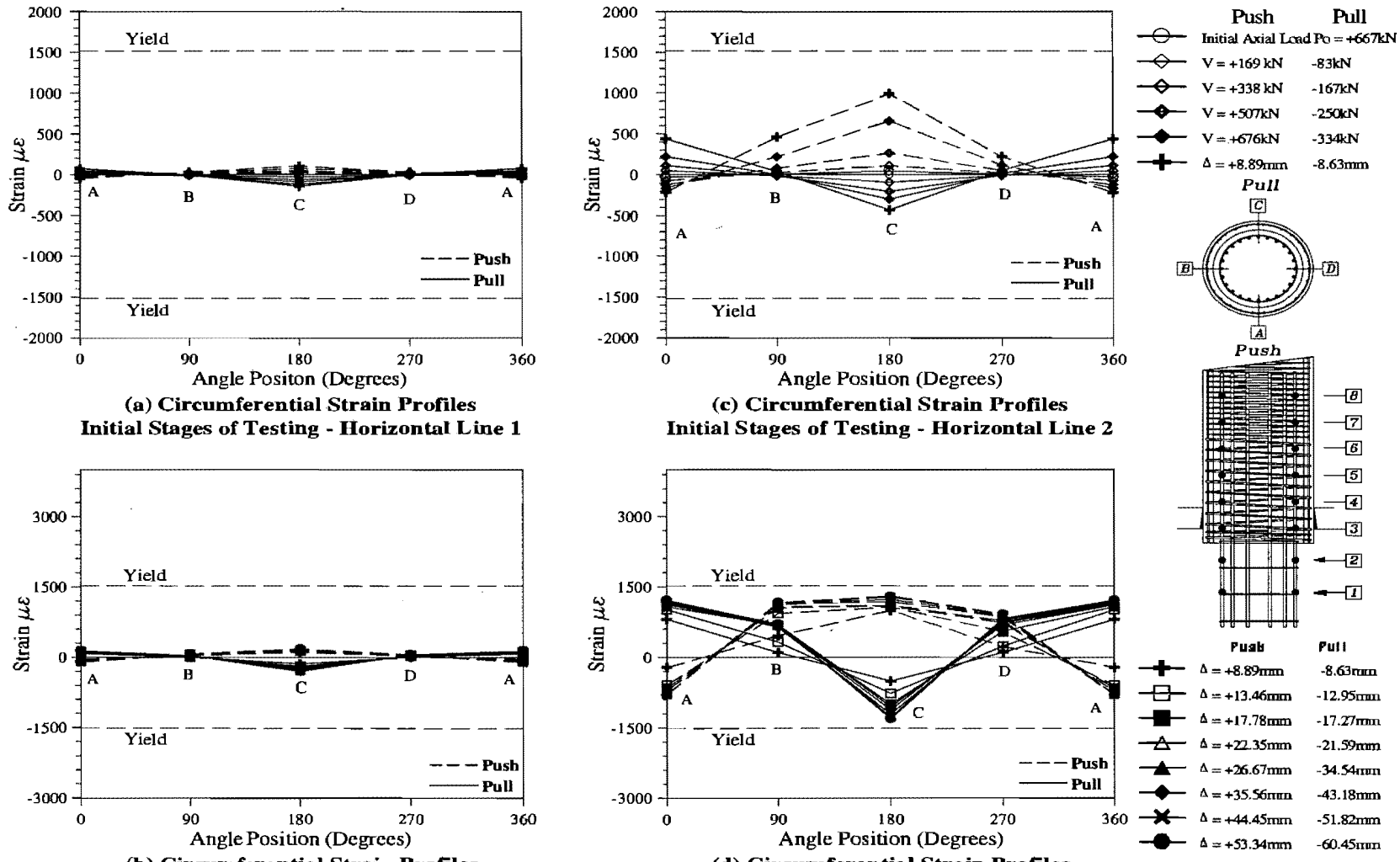

(a) Circumferential Strain Profiles
Initial Stages of Testing - Horizontal Line 1

(c) Circumferential Strain Profiles
Initial Stages of Testing - Horizontal Line 2

(b) Circumferential Strain Profiles
Final Stages of Testing - Horizontal Line 1

(d) Circumferential Strain Profiles
Final Stages of Testing - Horizontal Line 2

Fig. 6-29 Inner Core Reinforcement Strain Profiles Along Horizontal Line *1* and *2*

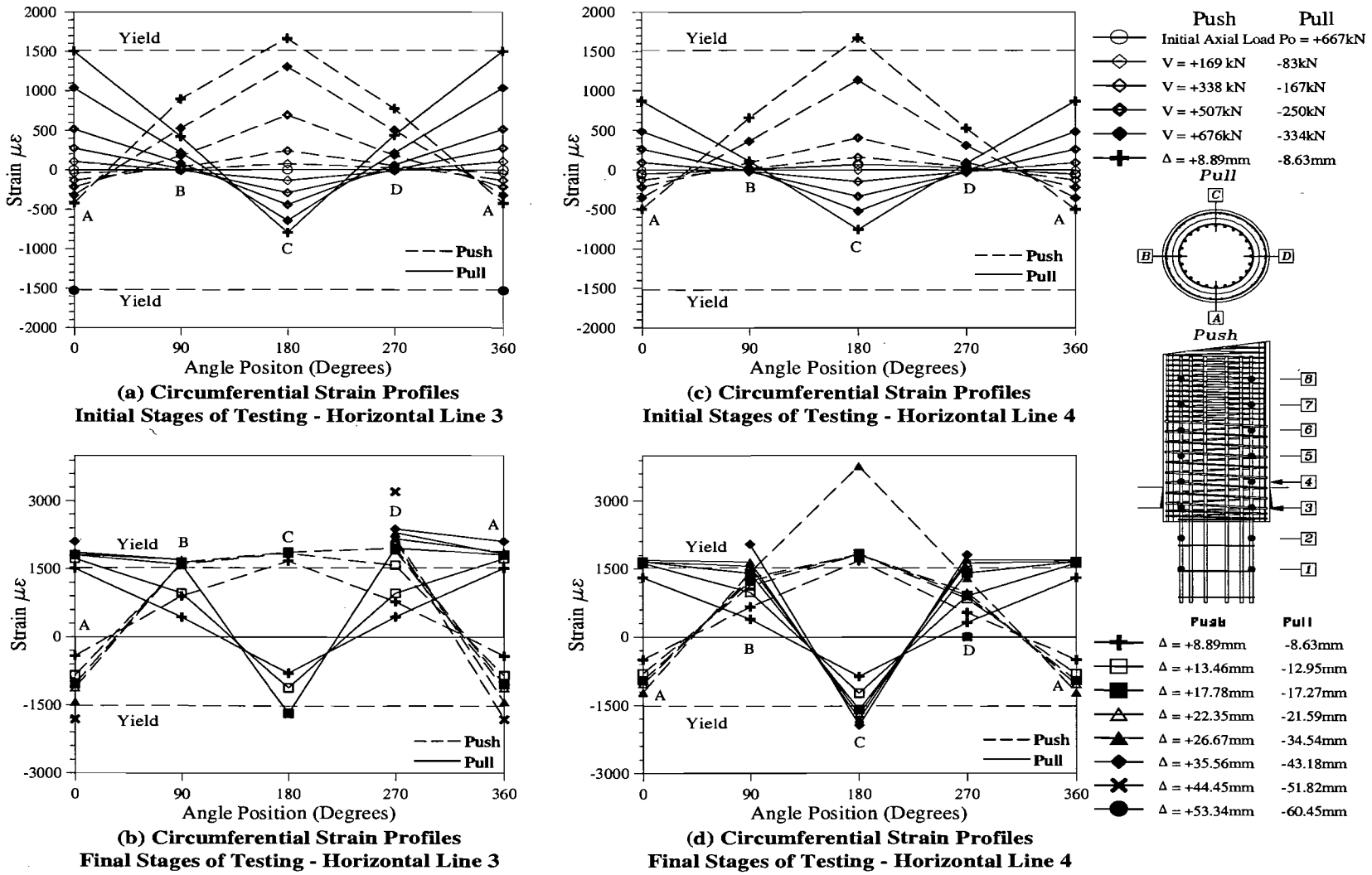

Fig. 6-30 Inner Core Reinforcement Strain Profiles Along Horizontal Line *3* and *4*

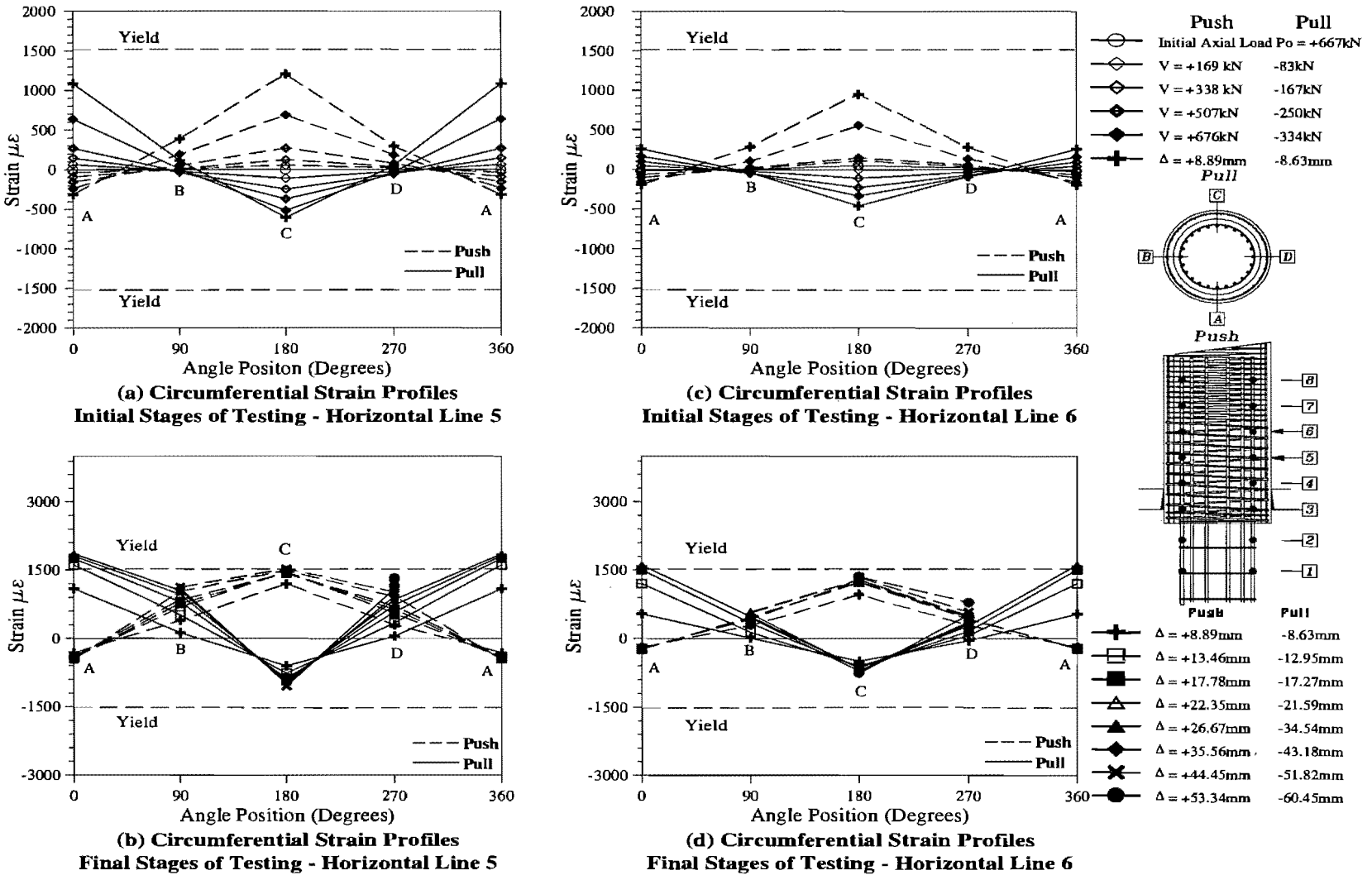

Fig. 6-31 Inner Core Reinforcement Strain Profiles Along Horizontal Line *5* and *6*

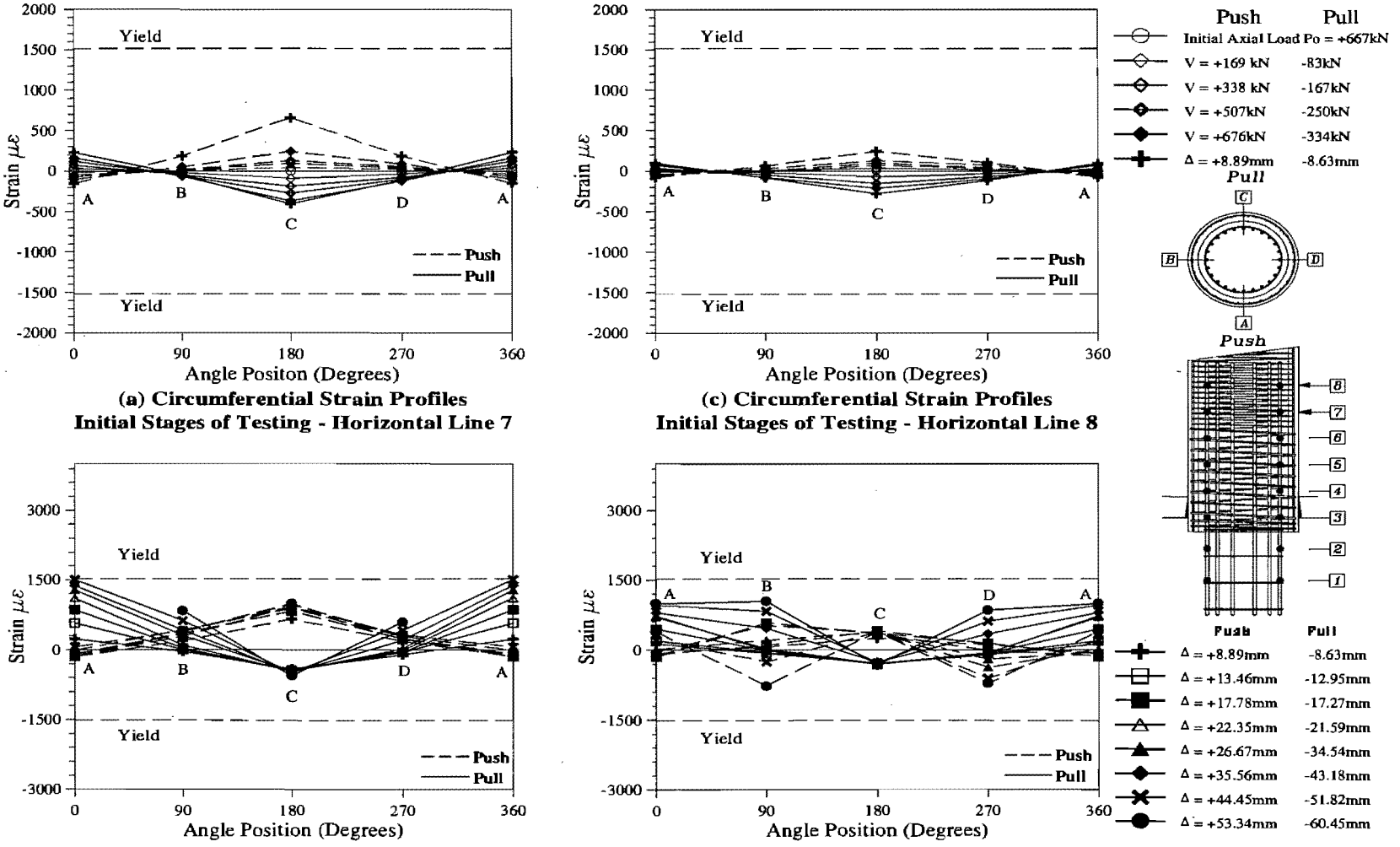

(a) Circumferential Strain Profiles
Initial Stages of Testing - Horizontal Line 7

(c) Circumferential Strain Profiles
Initial Stages of Testing - Horizontal Line 8

(b) Circumferential Strain Profiles
Final Stages of Testing - Horizontal Line 8

(d) Circumferential Strain Profiles
Final Stages of Testing - Horizontal Line 8

Fig. 6-32 Inner Core Reinforcement Strain Profiles Along Horizontal Line *7* and *8*

6.6 Prestressing Strands Vertical Strain Profiles

Strain profiles for the prestressing strands are presented in **Fig. 6-33** through **Fig. 6-36**. Similar to test unit *COR1*, strain readings were obtained during fabrication of the precast prestressed concrete shell while at *Utility Vault* and the gages were disconnected between fabrication and testing at UCSD. Then, before testing, these same gages were reconnected to the data acquisition system and balanced to zero. Then, the final strains recorded during the fabrication process were added to the strains obtained during testing.

In the final stages of the testing procedure, strain profiles presented in these figures indicate that maximum strains were achieved between positions ***6*** and *7*, which is approximately where the inner core longitudinal reinforcement terminates. This indicates that a total development length of approximately 1,524 mm is expected. The code required development length is computed based on equation **(5.4)**. Similar to test unit *COR1*, based on an initial prestressing force of approximately 1,378 MPa and a prestressing diameter of 9.53 mm, one obtains the required development length of 1,302 mm, which is slightly less than extrapolated from experimental test results.

At the pile cap interface flexure cracking is significant and reduces bond strength, increasing the required development length. Development length extrapolated from test results match with those values used in the pre-test analysis and are corroborated by test results in which plastic deformations occurred where longitudinal reinforcement terminates. In addition, recorded strains along the strands were predominantly higher near the ends of the inner core longitudinal reinforcement, which indicates increasing transfer of forces to the strands. In addition, these high levels of recorded strains suggest that minimum slippage of the prestressing strands may have occurred near the load stub interface.

Strain profiles presented in **Fig. 6-33** through **Fig. 6-36** indicate that prestressing forces are always in tension with minimum decrease under compressive loads and increase under tension loads, depending on the position of the strand relative to section compression toe. Along strand ***A***, maximum strains are observed in the pull direction because in this direction, this strand is in tension and, along strand ***C***, maximum strains are observed in the push direction when this strand is in tension.

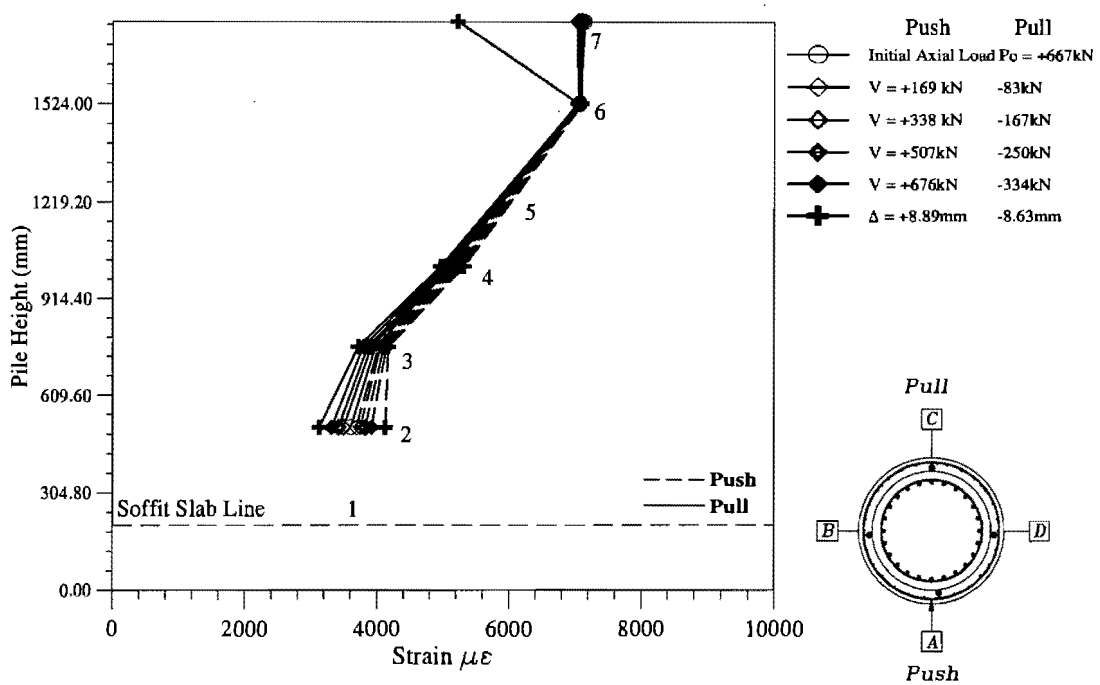

(a) Vertical Strain Profiles - Initial Stages of Testing

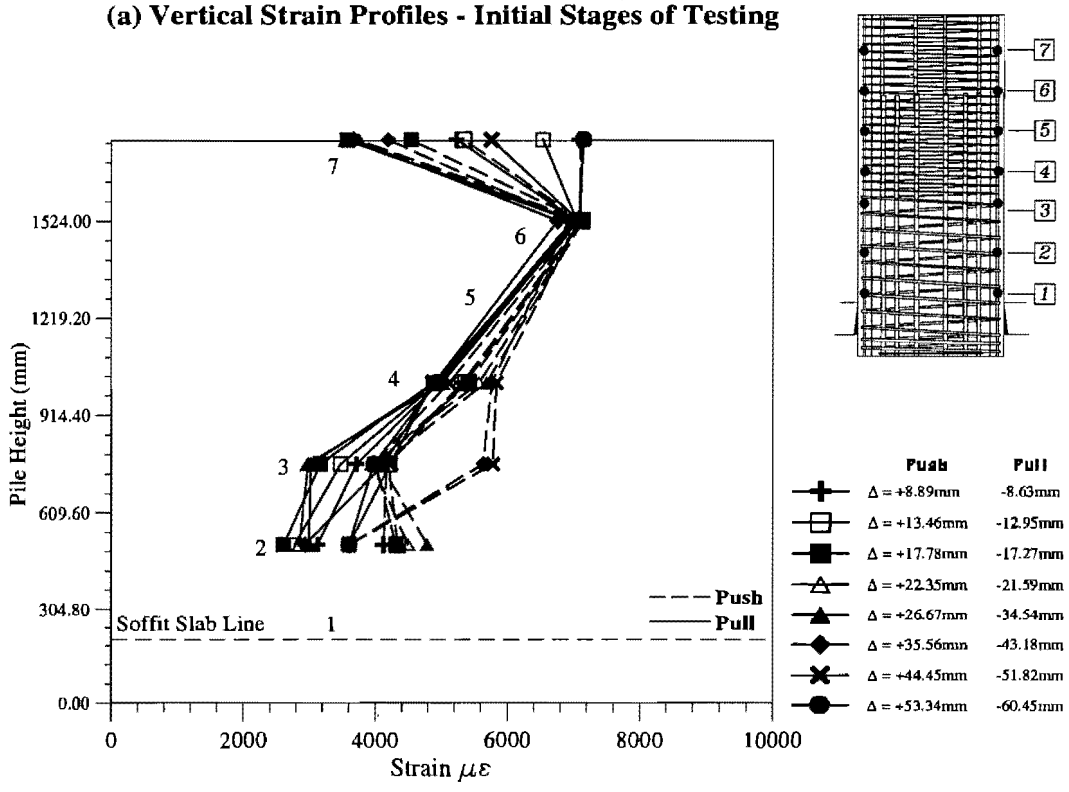

(b) Vertical Strain Profiles - Final Stages of Testing

Fig. 6-33 Vertical Strain Profiles Along Strand *A*

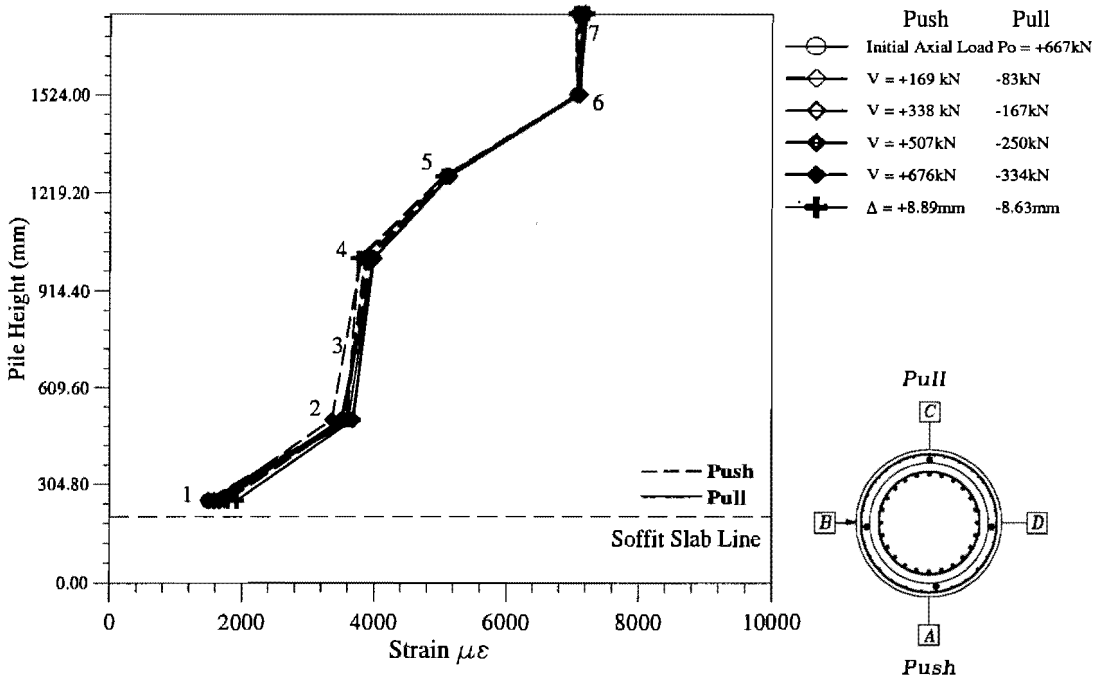

(a) Vertical Strain Profiles - Initial Stages of Testing

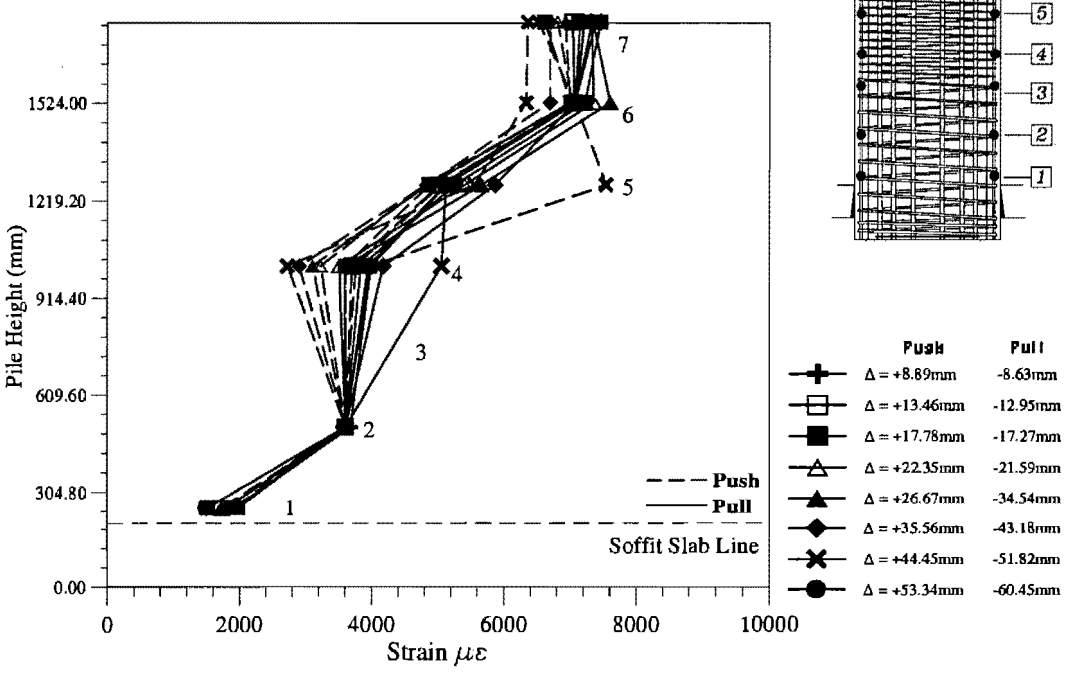

(b) Vertical Strain Profiles - Final Stages of Testing

Fig. 6-34 Vertical Strain Profiles Along Strand ***B***

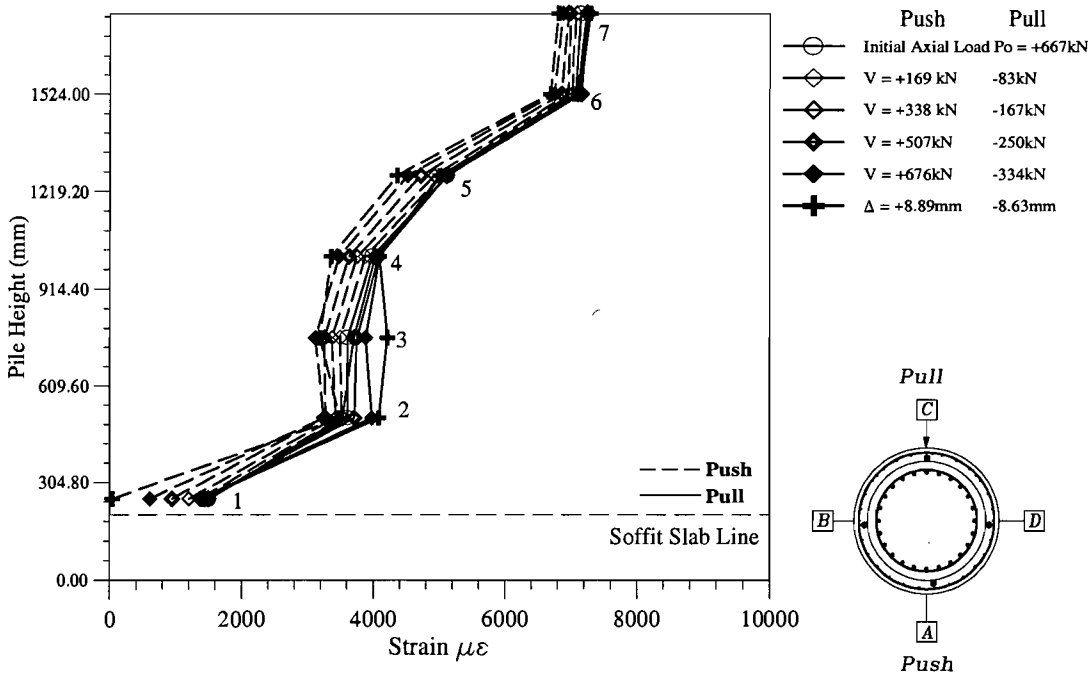

(a) Vertical Strain Profiles - Initial Stages of Testing

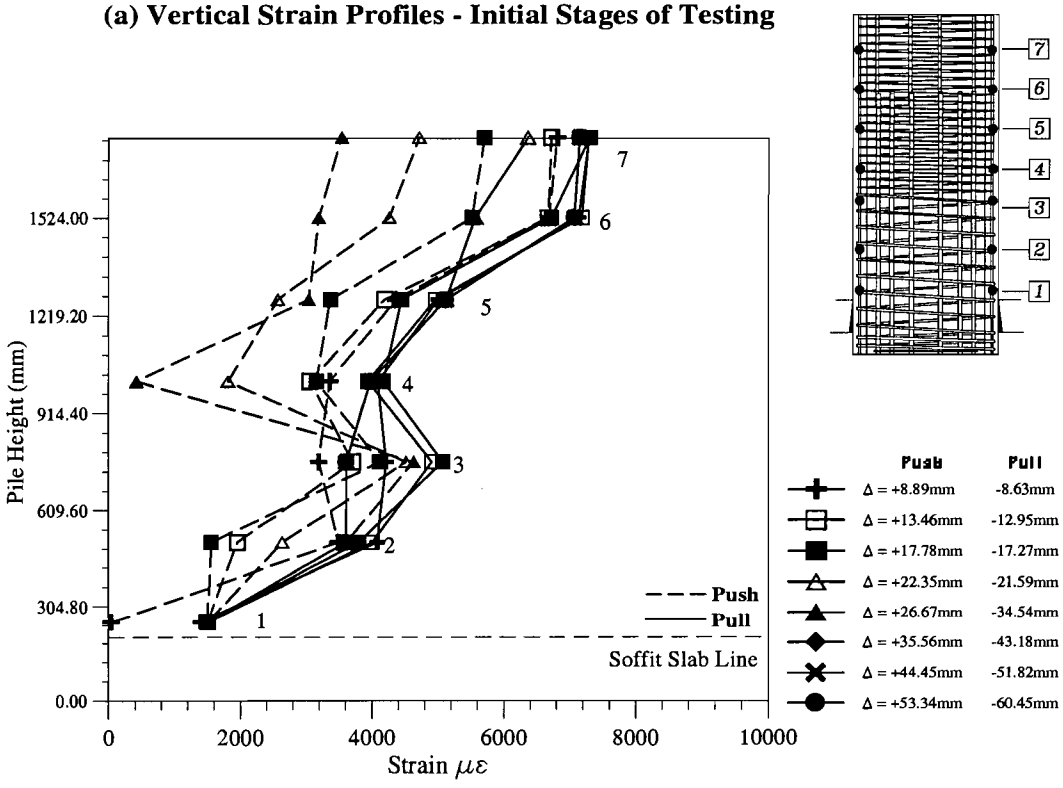

(b) Vertical Strain Profiles - Final Stages of Testing

Fig. 6-35 Vertical Strain Profiles Along Strand *C*

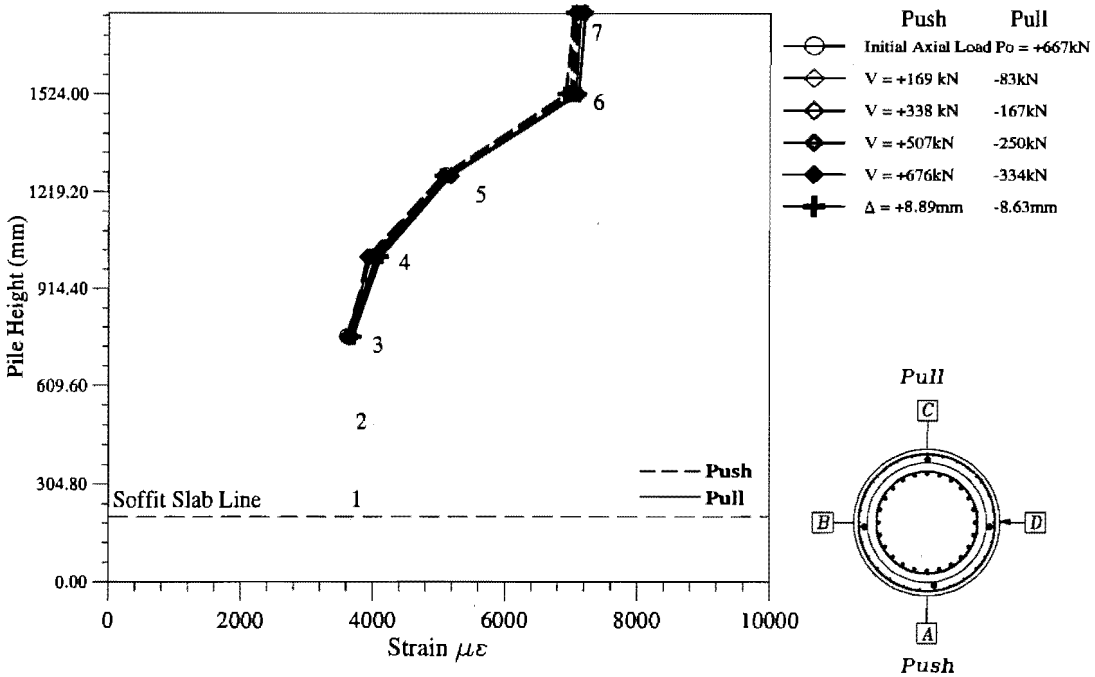

(a) Vertical Strain Profiles - Initial Stages of Testing

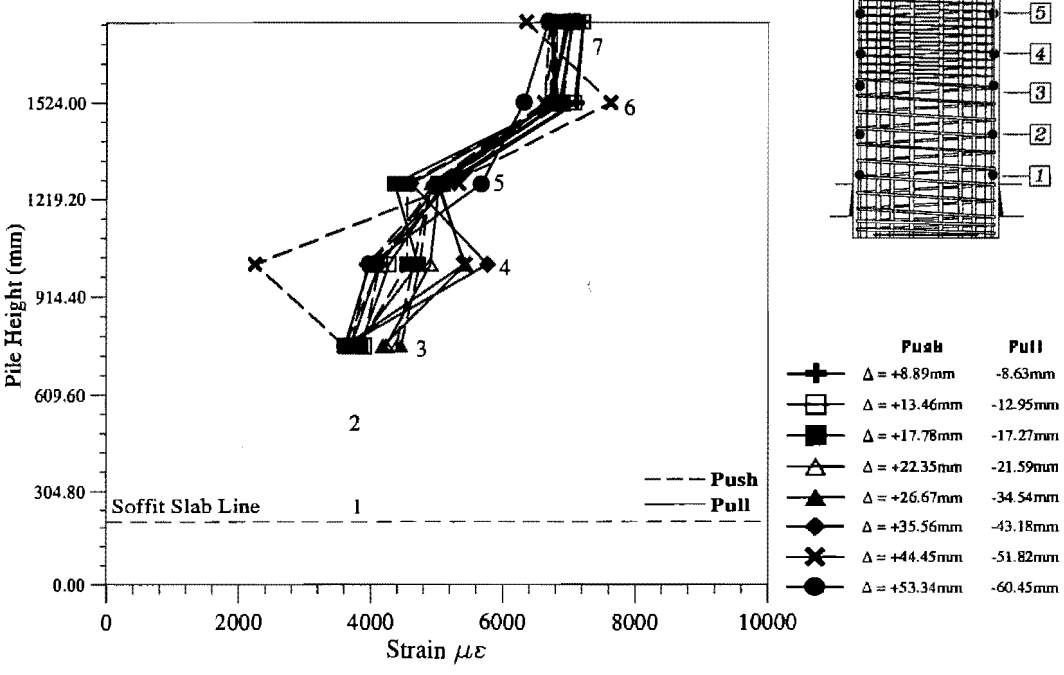

(b) Vertical Strain Profiles - Final Stages of Testing

Fig. 6-36 Vertical Strain Profiles Along Strand ***D***

6.7 Pile Transverse Reinforcement Strain Profiles

The spiral reinforcement used in this test unit varied between #3 on a 84 mm spiral pitch at the pile cap interface to a W3 on a 57 mm spiral pitch above the inner cage longitudinal reinforcement, as illustrated in **Fig. 2-30**.

6.7.1 Pile Transverse Reinforcement - Vertical Strain Profiles

Vertical strain profiles for the pile transverse reinforcement are presented in **Fig. 6-37** through **Fig. 6-40**. The strain profiles along longitudinal line ***A*** (see **Fig. 6-37**) and along longitudinal line ***C*** (see **Fig. 6-39**) indicate the level of confinement strain developed in the pile section as a result of the applied axial load and deformations. As in test unit *COR1,* strains in the spiral cage recorded along these lines indicate higher strains along line ***A*** than along line ***C*** because of higher axial compressive forces that develop in the push direction, which results in higher confinement demands.

Along lines ***A*** and ***C*** in the early stages of the testing procedure, maximum strains were recorded in the vicinity of the pile cap as a result of high confinement demands in this region than in the upper portion of the pile section. However, in the later stages of the testing procedure, strains at position ***8*** are significantly higher than at position ***1*** because of large spalling of the cover concrete where the inner core reinforcement terminates, which imposes higher confinement demands at this location for prevention of buckling of the prestressing strands.

The strain profiles along longitudinal line ***B*** (see **Fig. 6-38**) and along longitudinal line ***D*** (see **Fig. 6-40**) indicate the level of shear-induced strain as a result of the applied lateral load. High strains above position ***5***, and significant loss of strains gages above this location, suggests higher shear demands in this region, which matches extensive cracking of the pile section near the termination of longitudinal reinforcement with cracks at 45° cracks, marked on the sides of the pile section.

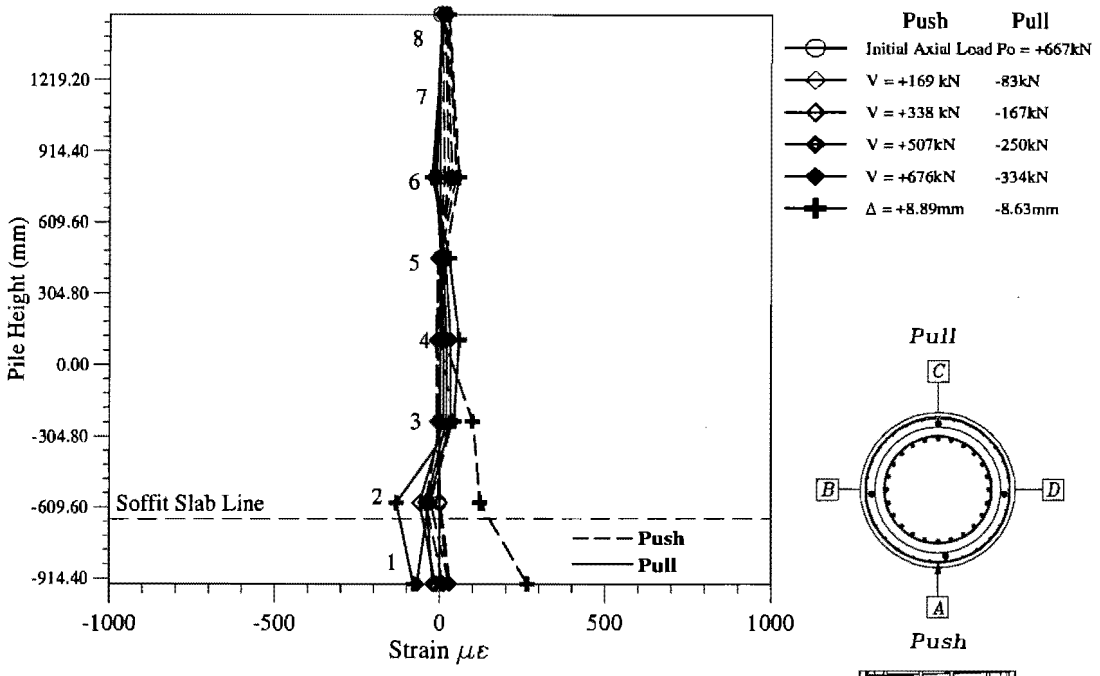

(a) Vertical Strain Profiles - Initial Stages of Testing

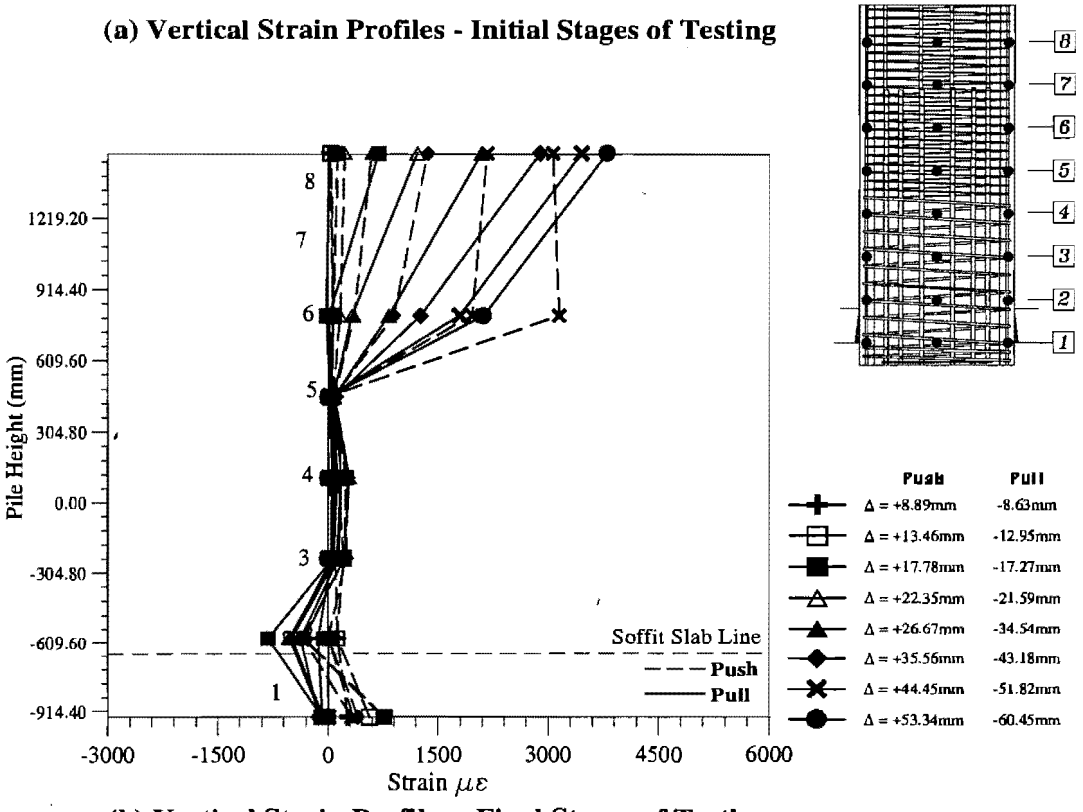

(b) Vertical Strain Profiles - Final Stages of Testing

Fig. 6-37 Pile Transverse Reinforcement Strain Profiles Along Line *A*

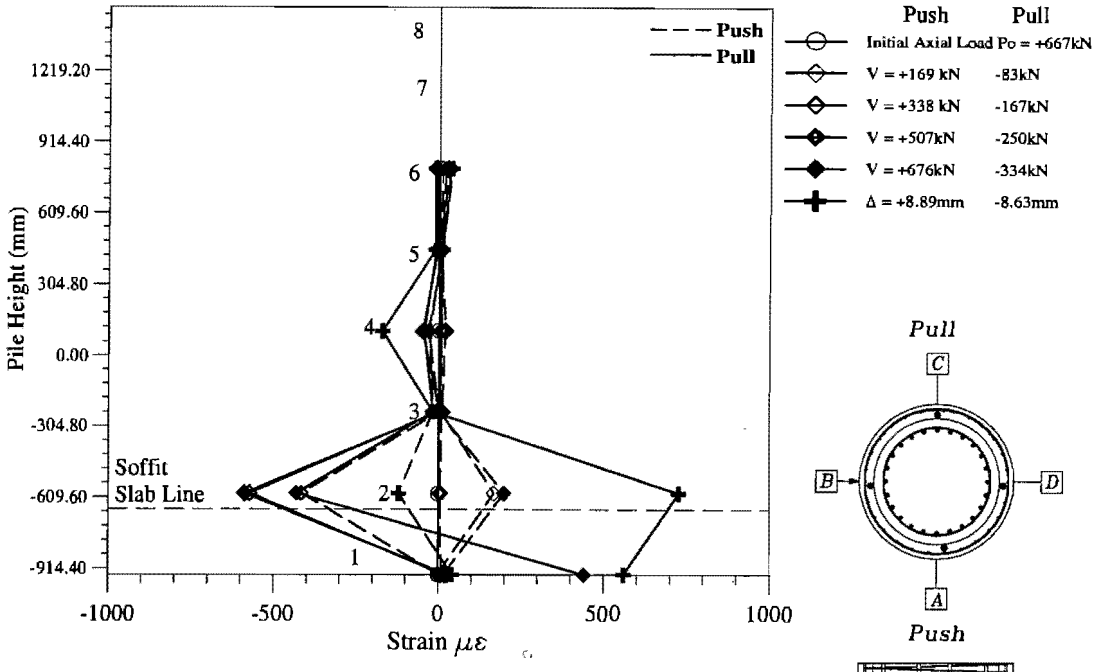

(a) Vertical Strain Profiles - Initial Stages of Testing

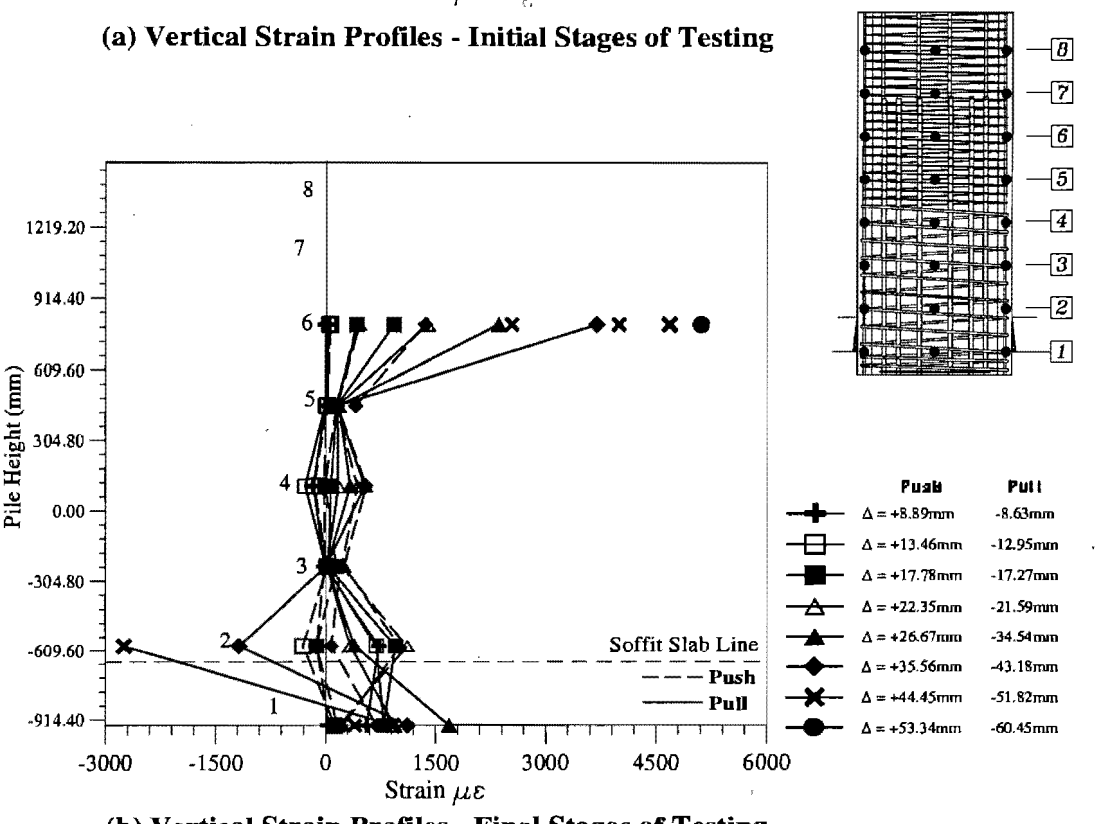

(b) Vertical Strain Profiles - Final Stages of Testing

Fig. 6-38 Pile Transverse Reinforcement Strain Profiles Along Line ***B***

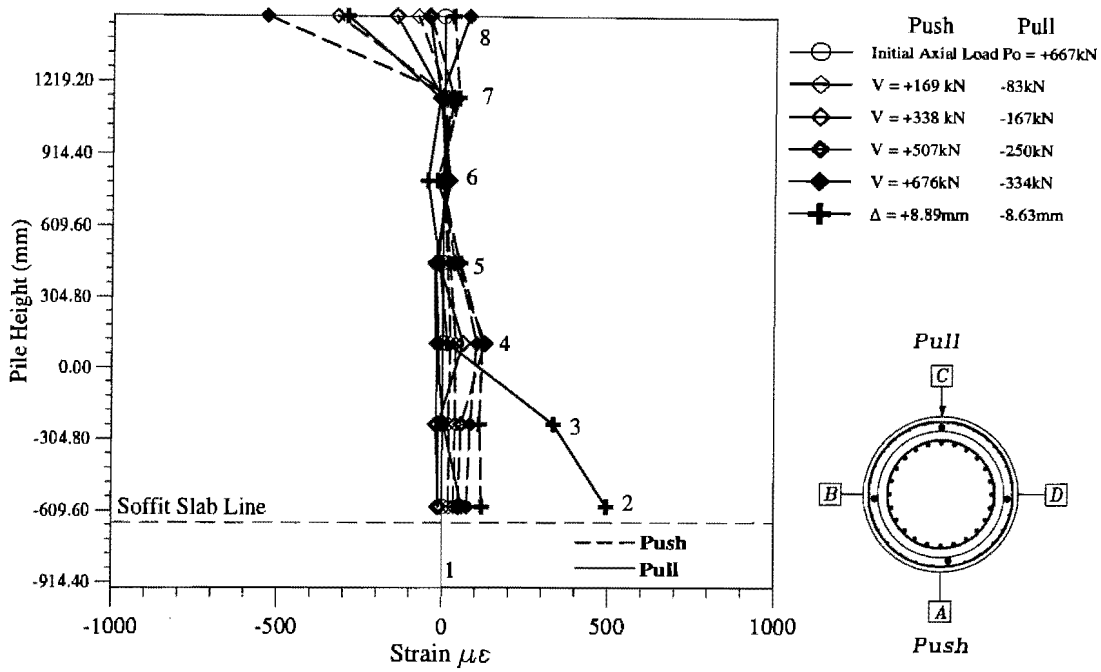

(a) Vertical Strain Profiles - Initial Stages of Testing

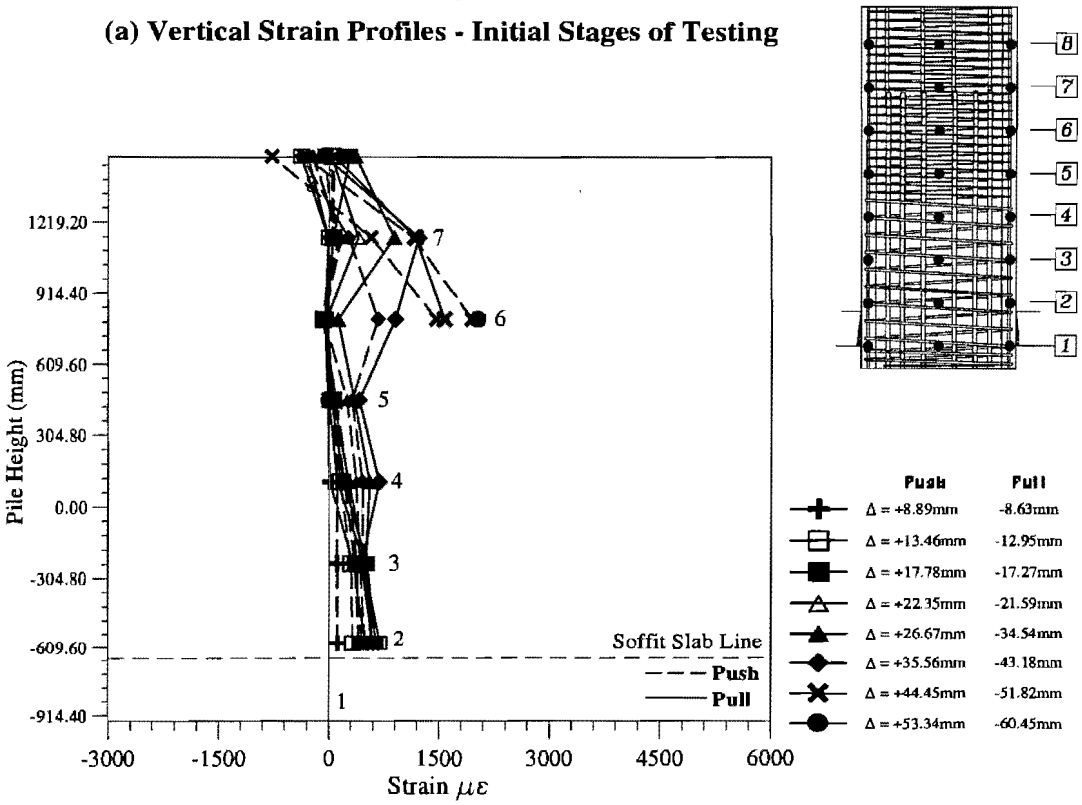

(b) Vertical Strain Profiles - Final Stages of Testing

Fig. 6-39 Pile Transverse Reinforcement Strain Profiles Along Line *C*

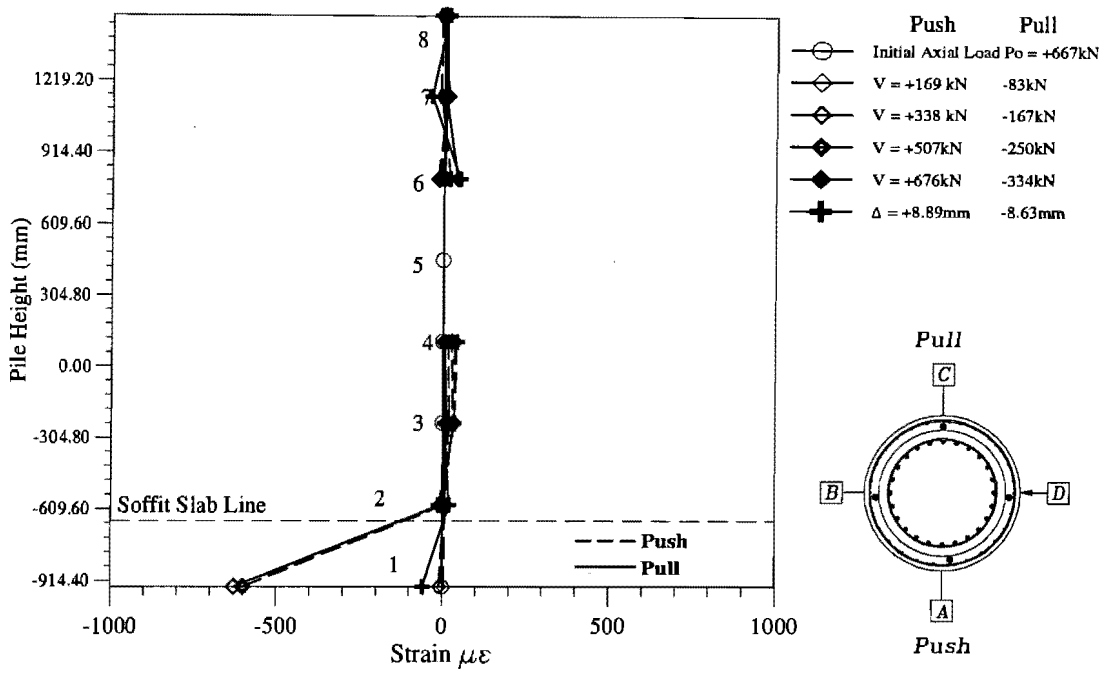

(a) Vertical Strain Profiles - Initial Stages of Testing

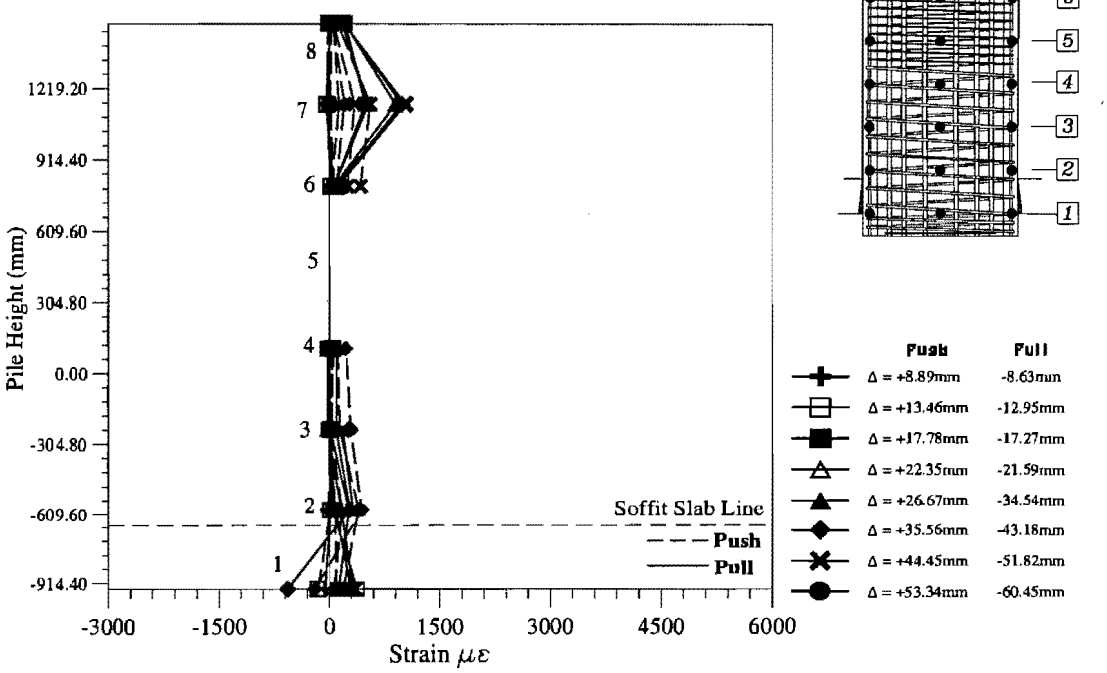

(b) Vertical Strain Profiles - Final Stages of Testing

Fig. 6-40 Pile Transverse Reinforcement Strain Profiles Along Line *D*

6.7.2 Pile Transverse Reinforcement - Circumferential Strain Profiles

Circumferential strain profiles for the pile transverse reinforcement are presented in **Fig. 6-41** through **Fig. 6-43**. Circumferential strain profiles indicate higher strains are always registered at position ***A*** rather than at position ***C*** as a result of confinement induced strains in the early stages of the testing procedure. At later stages of the testing procedure, this increase in strains at position ***A*** are more a result of prevention of strands buckling due to spalling of the cover concrete where longitudinal reinforcement terminates.

Maximum strains are recorded at positions ***B*** and ***D*** at later stages of the testing procedure, which illustrates increase in shear demand in regions where shear-induced inclined cracks were registered.

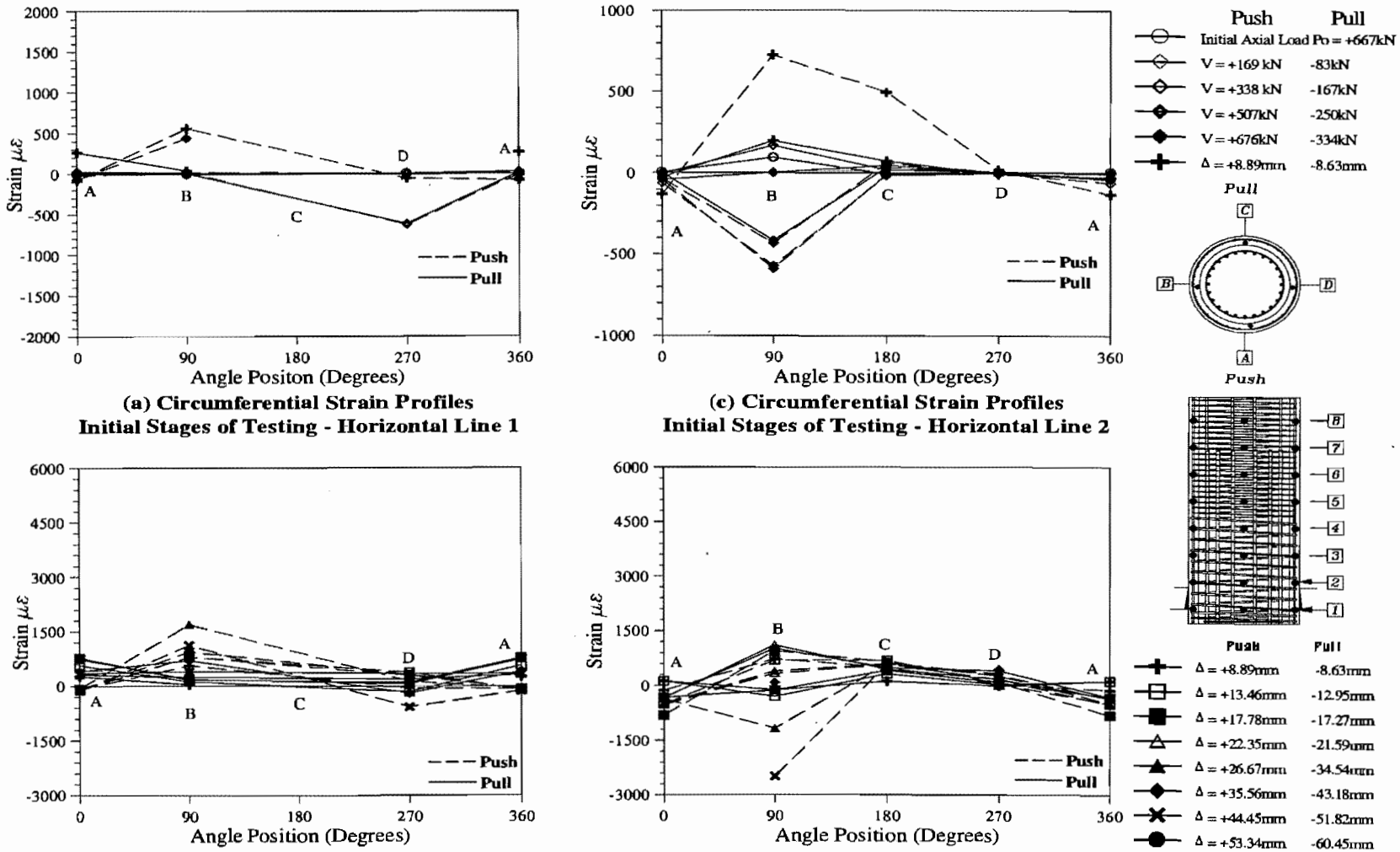

(a) Circumferential Strain Profiles
Initial Stages of Testing - Horizontal Line 1

(c) Circumferential Strain Profiles
Initial Stages of Testing - Horizontal Line 2

(b) Circumferential Strain Profiles
Final Stages of Testing - Horizontal Line 1

(d) Circumferential Strain Profiles
Final Stages of Testing - Horizontal Line 2

Fig. 6-41 Pile Transverse Reinforcement Strain Profiles Along Horizontal Line *1* and *2*

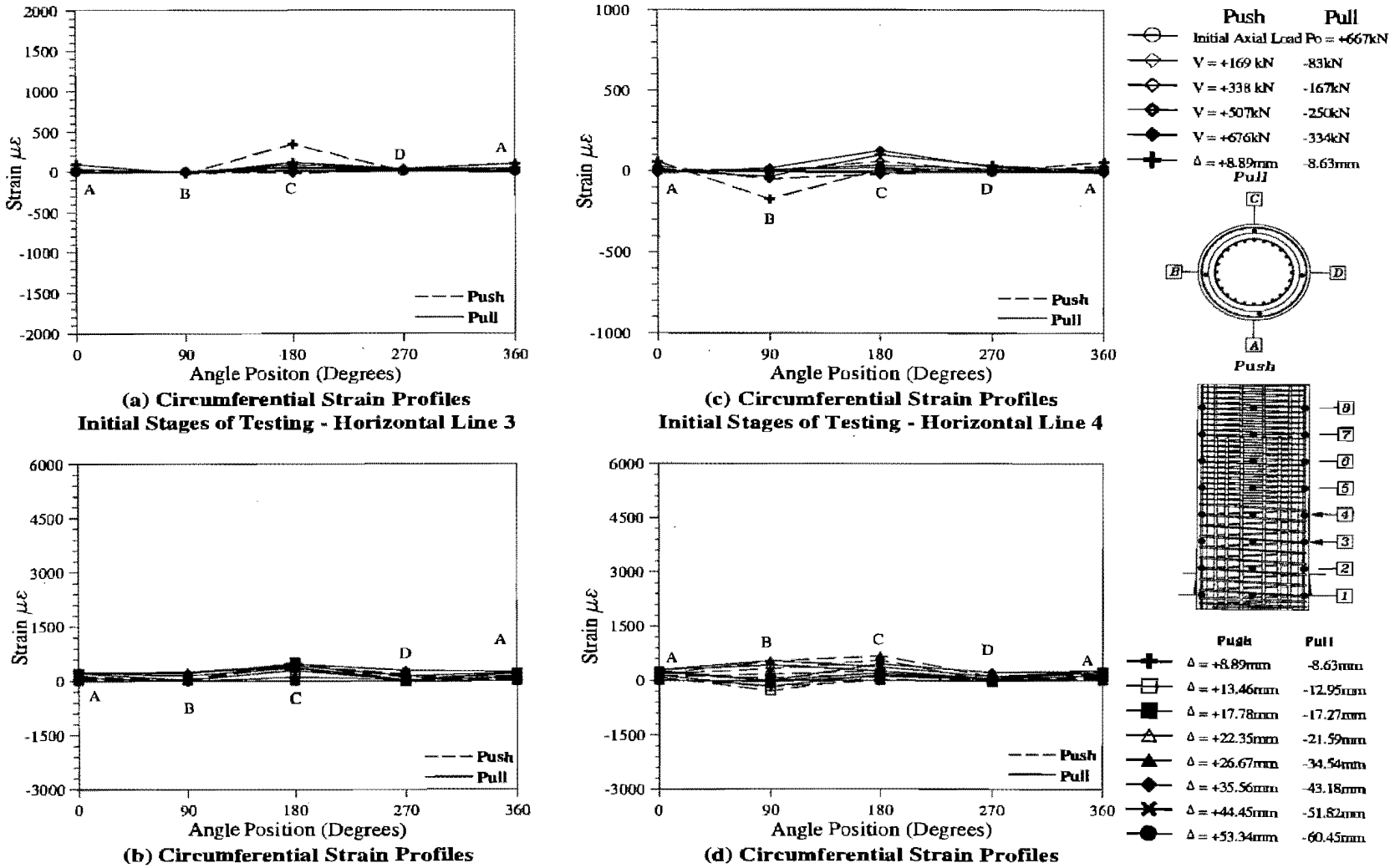

(a) Circumferential Strain Profiles
Initial Stages of Testing - Horizontal Line 3

(c) Circumferential Strain Profiles
Initial Stages of Testing - Horizontal Line 4

(b) Circumferential Strain Profiles
Final Stages of Testing - Horizontal Line 3

(d) Circumferential Strain Profiles
Final Stages of Testing - Horizontal Line 4

Fig. 6-42 Pile Transverse Reinforcement Strain Profiles Along Horizontal Line *3* and *4*

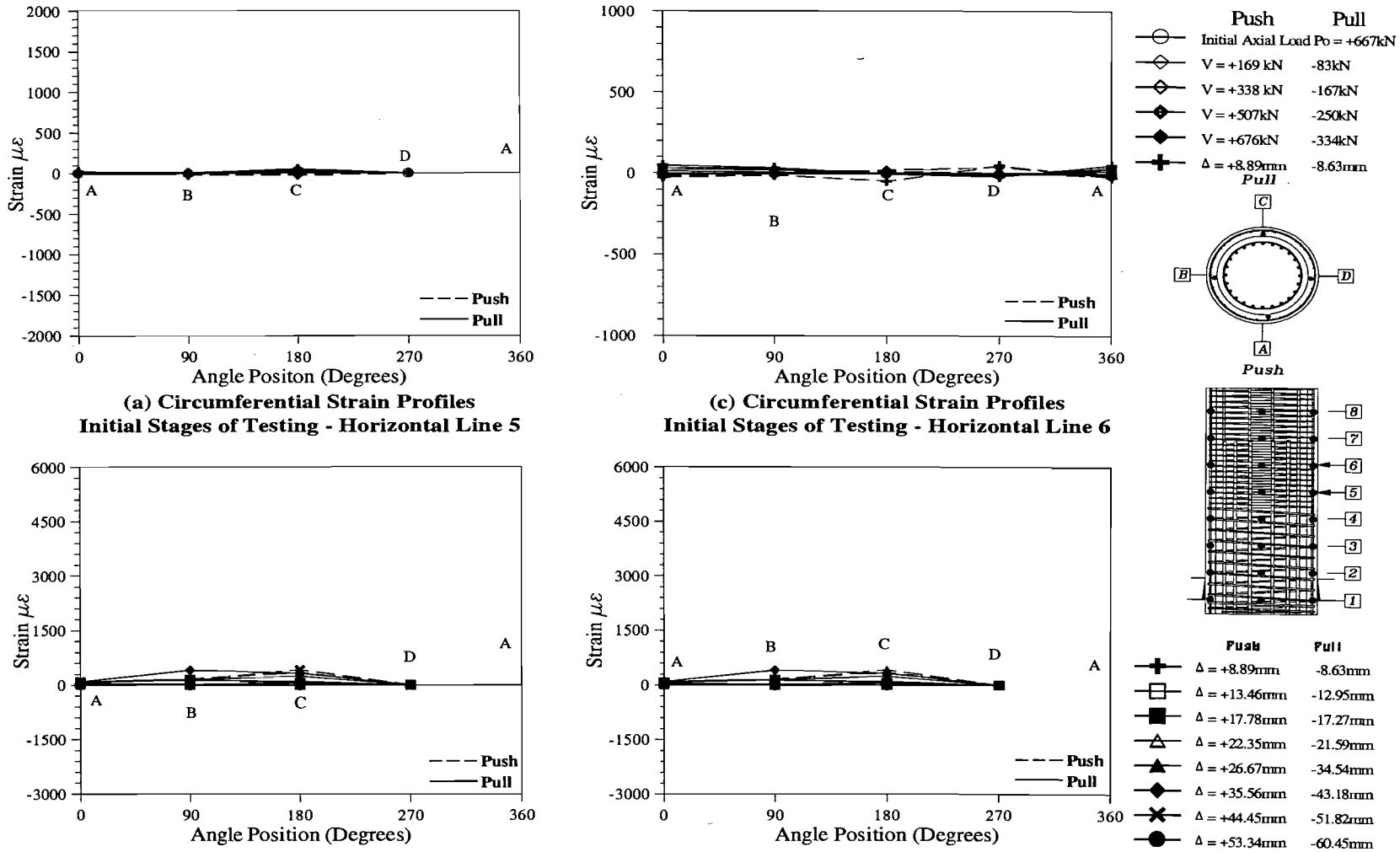

(a) Circumferential Strain Profiles
Initial Stages of Testing - Horizontal Line 5

(c) Circumferential Strain Profiles
Initial Stages of Testing - Horizontal Line 6

(b) Circumferential Strain Profiles
Final Stages of Testing - Horizontal Line 5

(d) Circumferential Strain Profiles
Final Stages of Testing - Horizontal Line 6

Fig. 6-43 Pile Transverse Reinforcement Strain Profiles Along Horizontal Line *5* and *6*

6.8 Pile Cap Reinforcement Strain Profiles

Maximum strains in the pile cap top and bottom reinforcement positioned in the direction of applied lateral load, were registered in the pile cap bottom reinforcement at strain gage ***Bottom 2-B***. Note that bottom reinforcement refers to position of reinforcement as it occurs in the prototype structure. For strain gage location, refer to **Fig. 3-37**. Strain readings illustrated in **Fig. 6-44** indicate minimum strains recorded in this reinforcement. Thus, strain profiles for the pile cap top and bottom reinforcement are not shown since strain levels were always considerably below yielding.

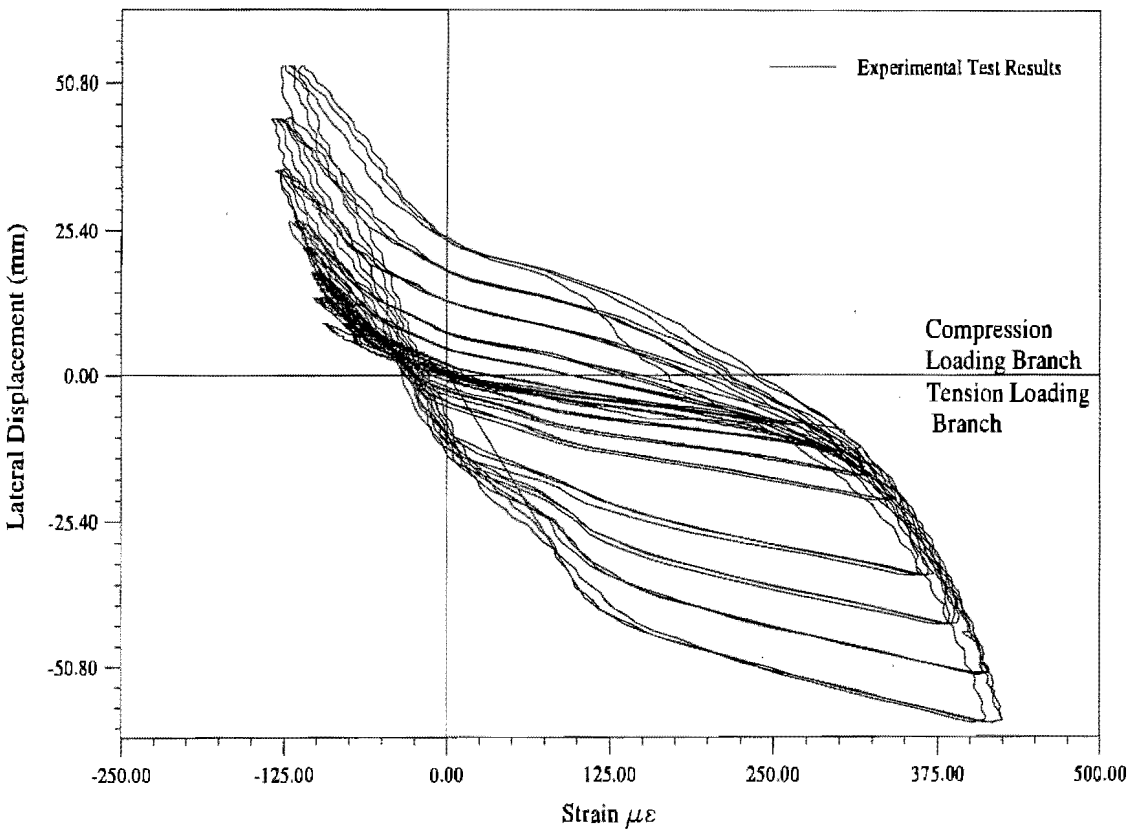

Fig. 6-44 Lateral Deflection versus Strain
Strain Gage Pile Cap Bottom Reinforcement ***Bottom 2-B***

Maximum strains in the pile cap vertical reinforcement were registered at strain gage ***3-B***. For strain gage location, refer to **Fig. 3-39**. As in test unit *COR1*, strain readings illustrated in **Fig. 6-45** indicate minimum strains recorded in this reinforcement. Thus, strain profiles for the pile vertical reinforcement are not shown since strain levels were always considerably below yielding. Strain levels recorded in this reinforcement can be taken as an indication of joint performance. Levels of principal tensile stress computed in Chapter 2 and presented in **Fig. 2-27** indicate that no joint shear failure was expected as a result of minimum level of expected stress in the joint region, which were $0.16\sqrt{f_c'} < 0.29\sqrt{f_c'}$ *[MPa]* and $0.27\sqrt{f_c'} < 0.29\sqrt{f_c'}$ *[MPa]*. These values corroborate observed test results in which negligible strains were recorded in the pile cap vertical reinforcement, indicating that no joint cracking occurred.

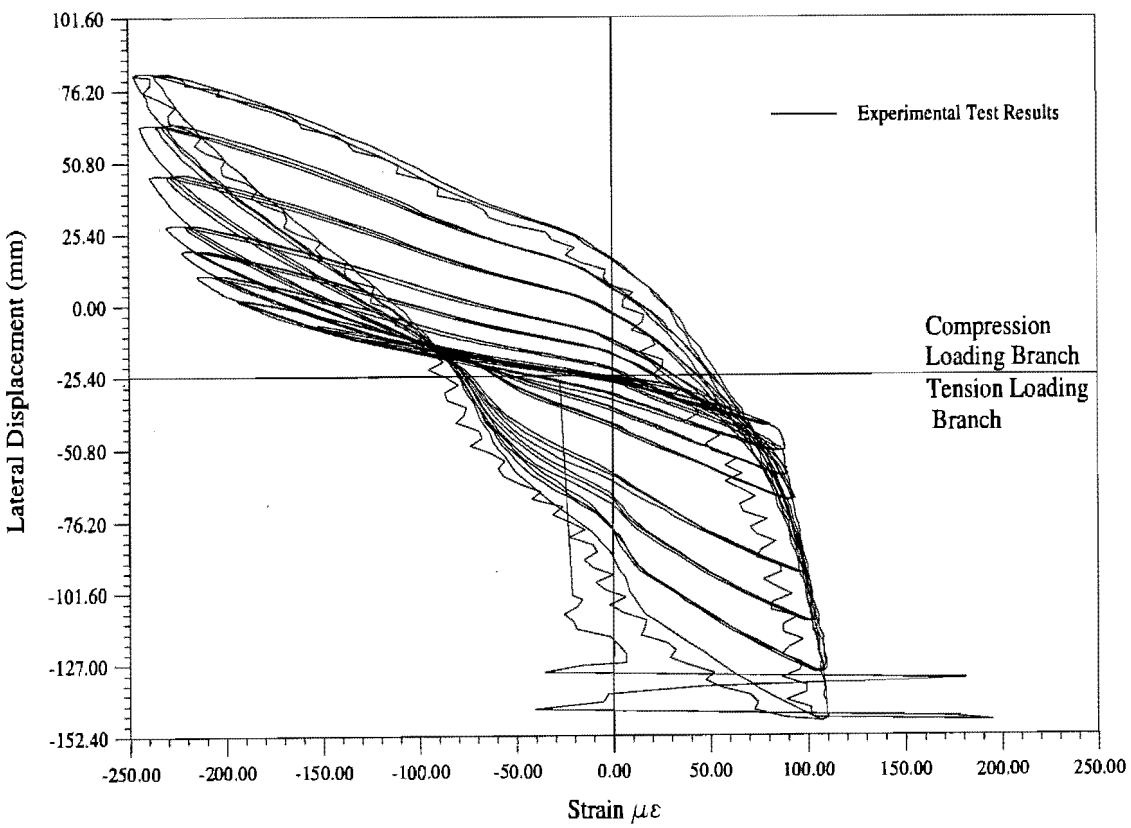

Fig. 6-45 Lateral Deflection versus Strain
Strain Gage Pile Cap Vertical Reinforcement ***3-B***

6.9 Pile Cap Rotation

Similar to test unit *COR1,* uplift of the pile cap from the strong floor was monitored by linear potentiometers positioned at the base of the pile cap, as illustrated in **Fig. 3-41** and **Fig. 3-42**. Rotation of the pile cap was then computed based on equation **(5.5)**. Contribution of pile cap rotation to pile lateral deflection may then be estimated according to equation **(5.6)**. Based on the values presented in **Fig. 6-46**, the maximum pile cap rotation, ψ_{cap}, was 0.000027/rad and was computed when the lateral deflection was +53.34 mm. This rotation of the pile cap will contribute 0.09 mm to the pile lateral deflection at peak response, which is rather small and, as a result no correction to the pile lateral deflection was computed.

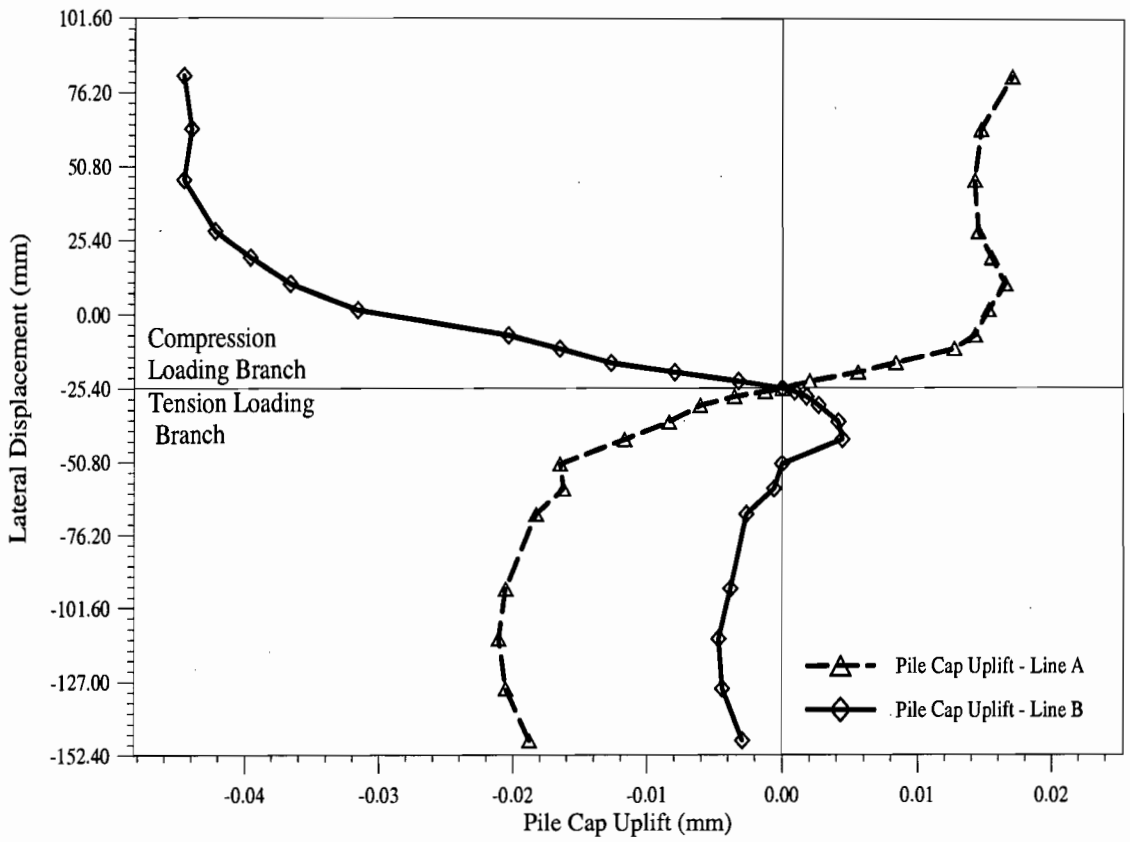

Fig. 6-46 Lateral Deflection versus Pile Cap Uplift

7. Test Unit *COR3* Experimental Test Results

This chapter includes a brief discussion of the general test description, load deformation characteristics, control loading program performance, axial load versus lateral load characteristics, vertical strain profiles longitudinal reinforcement and curvature profiles.

7.1 General Test Observations

Seismic load simulation of the pile specimen required application of fully reversed cycles in both the vertical and lateral actuators. In this section, when in compression, the axial force is designated as positive and, when in tension, the axial force is designated as negative. In addition, when in the compression loading branch, the lateral force is positive and in the tension loading branch, the lateral force is designated as negative. The complete test setup for unit *COR3* is shown in **Fig. 3-19**. Indicated on the test unit 1,295 mm above the pile cap is a horizontal line that marks the end of the inner core longitudinal reinforcement.

General observations recorded during the testing procedure are summarized as follows:

Initial Axial Force Simulation : The first loading stage in the testing procedure consisted of loading the specimen axially to +863 kN while controlling the top lateral displacement to +0.00 mm. At the end of this loading stage the lateral force was registered at approximately +10 kN.

At +82 kN in the compression loading branch: This loading stage corresponds to the specified +25% yielding force level. In this cycle the registered deflection was +1.88 mm and the axial load was +1073 kN.

At -39 kN in the tension loading branch: This loading stage corresponds to the prescribed -25% yielding force level. The lateral deflection and the axial load were -1.23 mm and +700 kN, respectively.

At +161 kN in the compression loading branch: At the prescribed +50% yielding force level, the lateral deflection was +5.29 mm and the axial load was+1,439 kN. At this loading stage, the structure displayed no signs of physical distress as no cracks were observed in the test specimen.

At -83 kN in the tension loading branch: At -50% yielding the lateral deflection and axial load were -3.01 mm and +546 kN, respectively.

At +238 kN in the compression loading branch: In this cycle the structure was loaded to +75% yielding in which the lateral deflection was registered at +10.79 mm and the axial load was+1,846 kN.

At -127 kN in the tension loading branch: At -75% yielding the lateral deflection was -5.30 mm and the axial was +404 kN.

At +317 kN in the compression loading branch: This loading stage corresponds to the theoretical first section yielding (+100% yielding), at which stage the lateral deflection and axial load were, respectively, +18.44 mm and +2,311 kN. Onset of flexural cracking began at this stage with two horizontal cracks at approximately 305 mmn and 1,219 mm from the soffit slab (see **Fig. 7-2**).

At -172 kN in the tension loading branch: This loading stage corresponds to the theoretical first section yielding while in the tension loading branch (-100%yielding). At this stage the lateral deflection and the axial load were registered at approximately -10.83 mm and +202 kN, respectively.

After this cycle the loading pattern was changed from single cycles to three cycles, according to the prescribed displacement ductility levels. The experimental yield displacements, Δ'_y, and the loads corresponding to theoretical first section yield, V'_y, and yield, V_y, that were used in the bilinear approximation calculations are as follows:

1. Lateral deflections at theoretical first section yielding:

   Compression : Δ'_{yC} = +18.44 mm

   Tension : Δ'_{yT} = -10.83 mm

2. Lateral load at theoretical first section yielding:

   Compression : V'_{yC} = +317 kN

   Tension : V'_{yT} = -172 kN

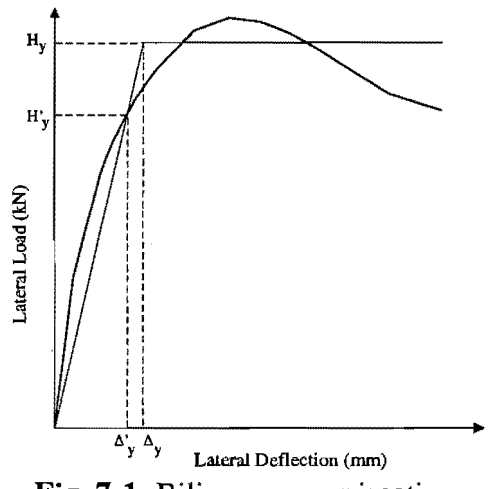

Fig. 7-1 Bilinear approximation

3. Lateral load at theoretical section yielding:

Compression : V_{yC} =+ 454 kN

Tension : V_{yT} = -186 kN

4. Calculation of displacement ductility μ_Δ = +,-1:

$$\textit{Compression}: \frac{V_{yC}}{V'_{yC}} \Delta'_{yC} = +26.42mm \qquad \textit{Tension}: \frac{V_{yT}}{V'_{yT}} \Delta'_{yT} = -11.68mm$$

At Δ = +26.42 mm in the compression loading branch (μ_Δ = +1): This loading stage corresponds to the displacement ductility level of μ_Δ= +1. Extension of the artificial crack along line ***D*** from its lower extremity of approximately 610 mm, long and extension of previous horizontal cracks,was observed (see **Fig. 7-3** and **Fig. 7-4**). During the third cycle, extension of the artificial crack along line ***D*** from its upper extremity to approximately the load stub height was observed, as illustrated in **Fig. 7-5** and **Fig. 7-6**. The peak lateral load was recorded at +375 kN and the axial load at +2645 kN.

At Δ = -11.68 mm in the tension loading branch (μ_Δ = -1): In this cycle the structure was displaced to the theoretical section yielding computed above. Onset of vertical splitting cracks, originating from the artificial crack along line ***A***, was observed (see **Fig. 7-7**). At this displacement ductility level, the lateral load was -170 kN and the axial load was +169 kN.

At Δ = +39.62 mm in the compression loading branch (μ_Δ = +1.5): Horizontal cracks developed in the previous cycles continued to extend around the circumference of the section (see **Fig. 7-8**). Onset of inclined cracks propagating towards the compression toe and vertical splitting cracks were observed, as depicted in **Fig. 7-8** and **Fig. 7-9**. One of these vertical cracks are observed to be oriented along a very steep angle on the side of the pile to almost vertical as a result of the forces present in the prestressing strands, because the component of the prestressing force begins to incline the compression field near these cracks (see **Fig. 7-9**). Peak lateral and axial loads at this displacement ductility level were +425 kN and +2,749 kN, respectively. At this cycle the prescribed maximum axial compressive load that the prototype structure might experience in a seismic event was achieved.

At Δ = -17.53 mm in the tension loading branch (μ_Δ = -1.5): In the tension loading branch, onset of flexural cracking occurred at this cycle with a single horizontal crack forming in the vicinity of the termination of the inner core longitudinal reinforcement, as shown in **Fig. 7-10** and **Fig. 7-11**. Extension of the vertical crack emanating from the artificial crack along line ***A*** is also documented in this figure. Peak lateral and axial loads at this displacement ductility level were -193 kN and +22 kN, respectively.

At Δ = +52.83 mm in the compression loading branch (μ_Δ = +2): Lateral load and axial load at this displacement level were +438 kN and +2,749 kN, respectively.

At Δ = -35.05 mm in the compression loading branch (μ_Δ = -3): At this displacement ductility level, the lateral load was -224 kN and the axial load was -167 kN. At this cycle the axial load was for the first time in tension. Because the structure is expected to display an increased displacement ductility capacity in the tension loading branch compared to ductility levels in the compression loading branch, the loading procedure was effected such that the ratio in increase of the current ductility level to the expected ultimate ductility level was approximately the same in both loading branches to avoid early failure in any one of the loading branches.

At +78.74 mm in the compression loading branch (μ_Δ = +3): An increase in the number of horizontal and vertical cracks were documented in the previous cycles. In this cycle the horizontal crack at the termination of the inner core longitudinal reinforcement wraps around the pile section with its maximum width recorded at 1.60 mm (see **Fig. 7-12**). At this displacement ductility level the lateral load was +495 kN and the axial load was +2749 kN., and at this stage, the specimen achieved its maximum flexural strength under axial compressive loading.

At -52.07 mm in the tension loading branch (μ_Δ = -4.5): Large concentration of cracks emanating from the artificial crack along line ***2*** were observed with the horizontal crack in the vicinity of the limits of the inner core longitudinal reinforcement dominating response (see **Fig. 7-13** and **Fig. 7-14**). Registered lateral load and axial load were -221 kN and -302 kN, respectively. At this cycle, the prescribed maximum axial tensile load that the prototype structure might experience in a seismic event was achieved.

At +92.46 mm in the compression loading branch (μ_Δ = +3.5): Peaks loads at this displacement ductility level were respectively +496 kN and +2,749 kN.

At -82.04 mm in the tension loading branch (μ_Δ = -7): Peaks loads at this displacement ductility level were -241 kN and -302 kN, respectively.

At +105.92 mm in the compression loading branch (μ_Δ = +4): No significant increase in the number of flexural, vertical or inclined cracks was recorded. Sudden crushing and spalling of the cover concrete in an explosive manner near the region where the longitudinal reinforcement terminates was observed, followed by a rapid drop in the axial load carrying capacity of the section for this stipulated ductility level. **Fig. 7-15** documents the distress pattern observed at this displacement ductility cycle, which was very similar to that observed during testing of test unit *COR1*. Peak loads were lateral load +488 kN and axial load +2,749 kN, respectively.

At -116.84 mm in the tension loading branch (μ_Δ = -10): After considerable drop in the axial load observed during the previous cycle, the loading procedure was carried out only in the tension loading branch with small excursions into the compression loading branch up to an axial load of approximately +1334 kN and a lateral deflection of 2.54 mm. Reversed cyclic loading propagated the extension of spalling of the cover concrete, with spalling of the cover concrete occurring in large blocks of concrete characteristics of high strength concrete (see **Fig. 7-16**). Peak loads were lateral load -235 kN and axial load -302 kN, respectively.

At -143.26 mm in the tension loading branch (μ_Δ = -12): At this displacement ductility level, the lateral load was -248 kN and the axial load was -302 kN.

Fig. 7-17 documents the extent of spalling of the cover concrete and unwinding of the prestressing strands in the region were the inner core longitudinal reinforcement terminates. The testing procedure was stopped after the maximum lateral deflection observed during testing of test unit *COR1* was reached.

Fig. 7-3 Cracking Pattern at +26.42 mm

Fig. 7-2 Onset of Flexure Cracking at V=+317 kN

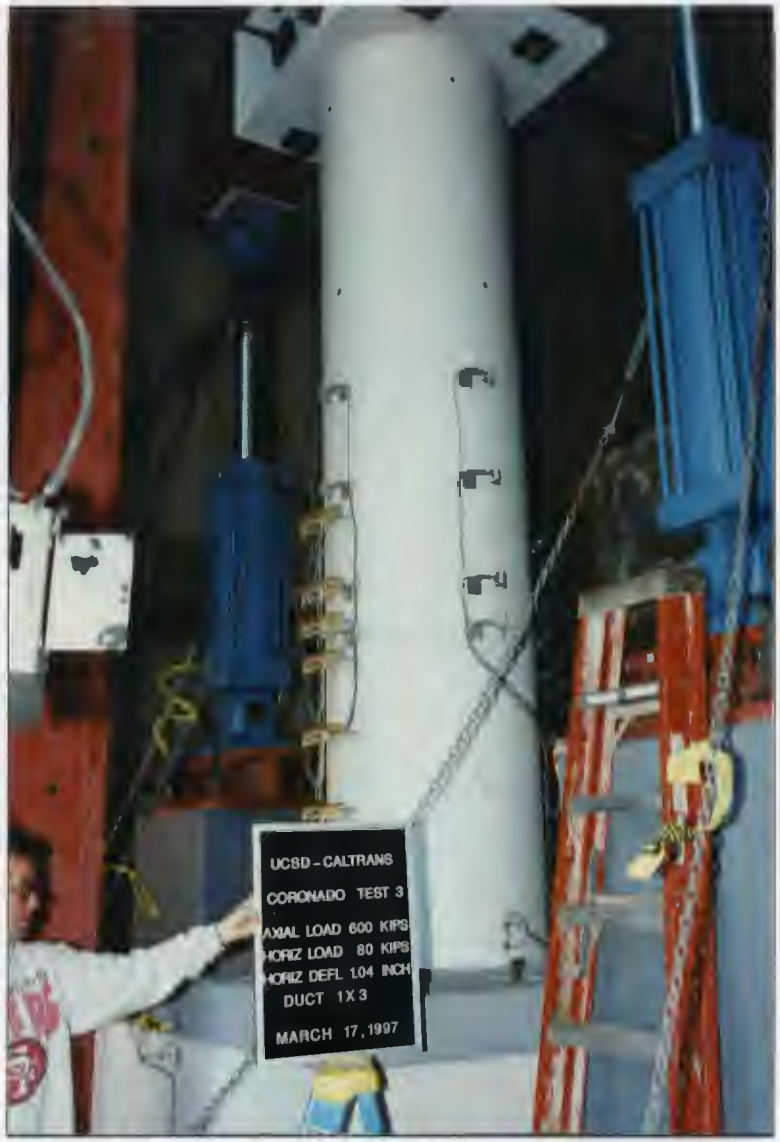

Fig. 7-5 Cracking Pattern at +26.42 mm

Fig. 7-4 Cracking Pattern at +26.42 mm

Fig. 7-7 Cracking Pattern at -11.68 mm

Fig. 7-6 Cracking Pattern at +26.42 mm

Fig. 7-9 Cracking Pattern at +39.62 mm

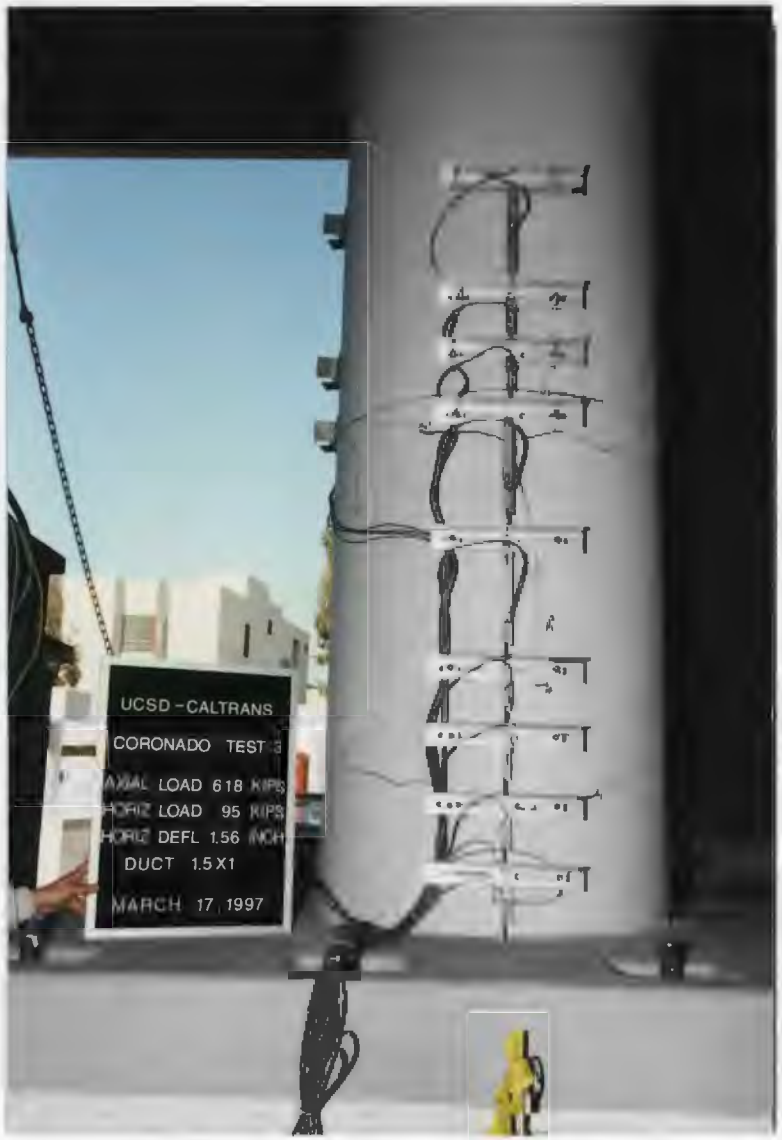

Fig. 7-8 Cracking Pattern at +39.62 mm

Fig. 7-11 Cracking Pattern at -17.53 mm

Fig. 7-10 Cracking Pattern at -17.53 mm

Fig. 7-12 Cracking Pattern at Lateral Deflection of +78.74 mm

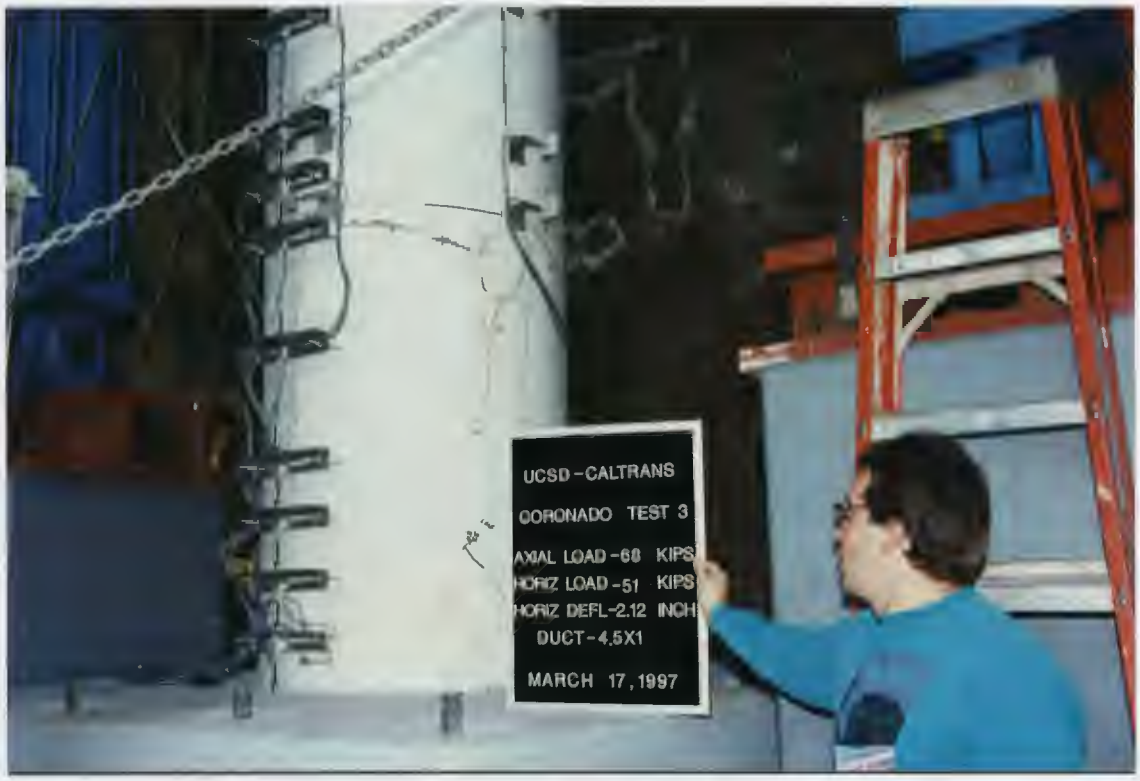

Fig. 7-13 Cracking Pattern at Lateral Deflection of -52.07 mm

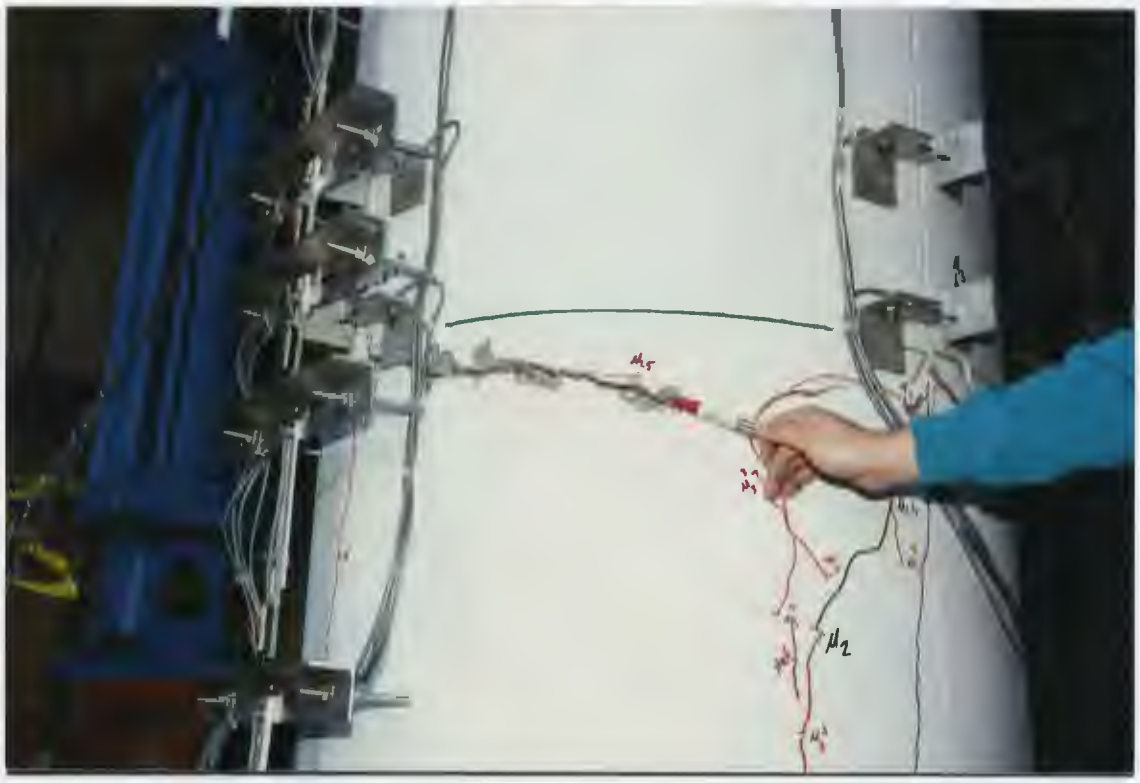

Fig. 7-14 Cracking Pattern at Lateral Deflection of -52.07 mm

Fig. 7-15 Extent of Spalling of Cover Concrete at Lateral Deflection of +105.92 mm

Fig. 7-17 Wide Open Crack

Fig. 7-16 Plastic Hinge Relocation

7.2 Load Deformation Characteristics

Fig. 7-18 shows the measured lateral force versus lateral displacement response of the test unit. The initial response of the pile suggests a good correlation between the expected and the observed stiffness in both loading branches. However, in the compression loading branch, after the lateral load exceeded 50% of the expected first yield lateral load, there was an apparent softening of the structure compared to the expected stiffness of the pile. Post test investigation of the opening width of the artificial cracks reveals that the artificial cracks were opening up at low load level cycles. The opening of these cracks influences the confinement of the inner core cast in place concrete. Thus, a post test analysis was carried out in which the precast concrete shell and the inner core cast in place concrete in the region where these cracks appear was assumed unconfined. The post test moment curvature analysis is also shown in **Fig. 7-18**, and it shows a good correlation with the test results. Thus, post-test analysis shows that confinement of the concrete in the artificial cracked region is indeed affected when the cracks open up.

The confined concrete model used to develop the pre-test analysis for test unit *COR3* was the model proposed by Bjerkeli **[24]**, which is different than the concrete model used to develop the pre-test analysis for test units *COR1* and *COR2*. Pre-test analysis for test units *COR1* and *COR2* was developed using the Mander model **[15]** for confined concrete. Study of the differences between these two models for confined concrete is presented in Chapter 8.

At peak load in the compression loading branch, the predicted maximum load was approximately 12% lower than the measured maximum load. The maximum achieved lateral load of test unit *COR3* was approximately the same as for test unit *COR1*. Peak load in test unit *COR1* was reached at +51.05 mm and, in test unit *COR3*, the peak load was not reached until +78.74 mm, which suggests slight softening of the pile section of test unit *COR3*, as previously indicated. In this loading branch a maximum lateral load of +495 kN was recorded at μ_Δ=+3x1 without excessive degradation in the lateral strength of the pile section during successive cycles.

In the tension loading branch the predicted response of the pile section matches closely the observed test results. A maximum lateral force of -248 kN was recorded during the displacement cycle μ_Δ=-9x1. The testing procedure was stopped at μ_Δ=-9x2 because the section was maintaining constant lateral load and maximum achieved lateral deflection at this cycle match that reached when testing unit *COR1*.

Post test investigation of the test data indicates that a maximum displacement ductility of μ_Δ=+4 was achieved in the compression loading branch and approximately μ_Δ=−12 was achieved in the tension loading branch with minimum degradation in the lateral strength of the section. In the compression loading branch, lateral deflections at maximum displacement and yield were, respectively, Δ_{max}= +105.92 mm and Δ_y= +26.42 mm, while in the tension loading branch these values were Δ_{max} = −143.26 mm and Δ_y = −11.68 mm, respectively.

Fig. 7-19 shows the measured lateral force versus curvatures computed at the pile cap interface. The main characteristics visible in this figure are very similar to those indicated earlier for the pile lateral deflection mainly pinching of the hysteresis loops at the transition from the compression to the tension loading branch and vice versa.

Post test investigation of the test data indicates that a maximum curvature ductility of μ_φ=+7 was achieved in the compression loading branch and approximately μ_φ=-13.5 in the tension loading branch. In the compression loading branch, maximum and yield curvatures are, respectively, φ_{max}=+0.000068 mm^{-1} and φ_y=+0.0000099 mm^{-1}, and φ_{max}=−0.000070 mm^{-1} and φ_y=−0.0000050 mm^{-1} in the tension loading branch. As expected, curvature ductility levels are slightly higher than displacement ductility levels.

Similar to test units *COR1* and *COR2,* curvatures presented in **Fig. 7-19** represent average values and were computed according to equation **(5.1)**. Also, during computations of curvatures at the pile cap interface the height of the linear potentiometer cell, h_{cur}, includes an additional term to account for tensile strain penetration into the pile cap by including the strain penetration length into the curvature cell height, h_{cur}, according to equation **(5.2)**.

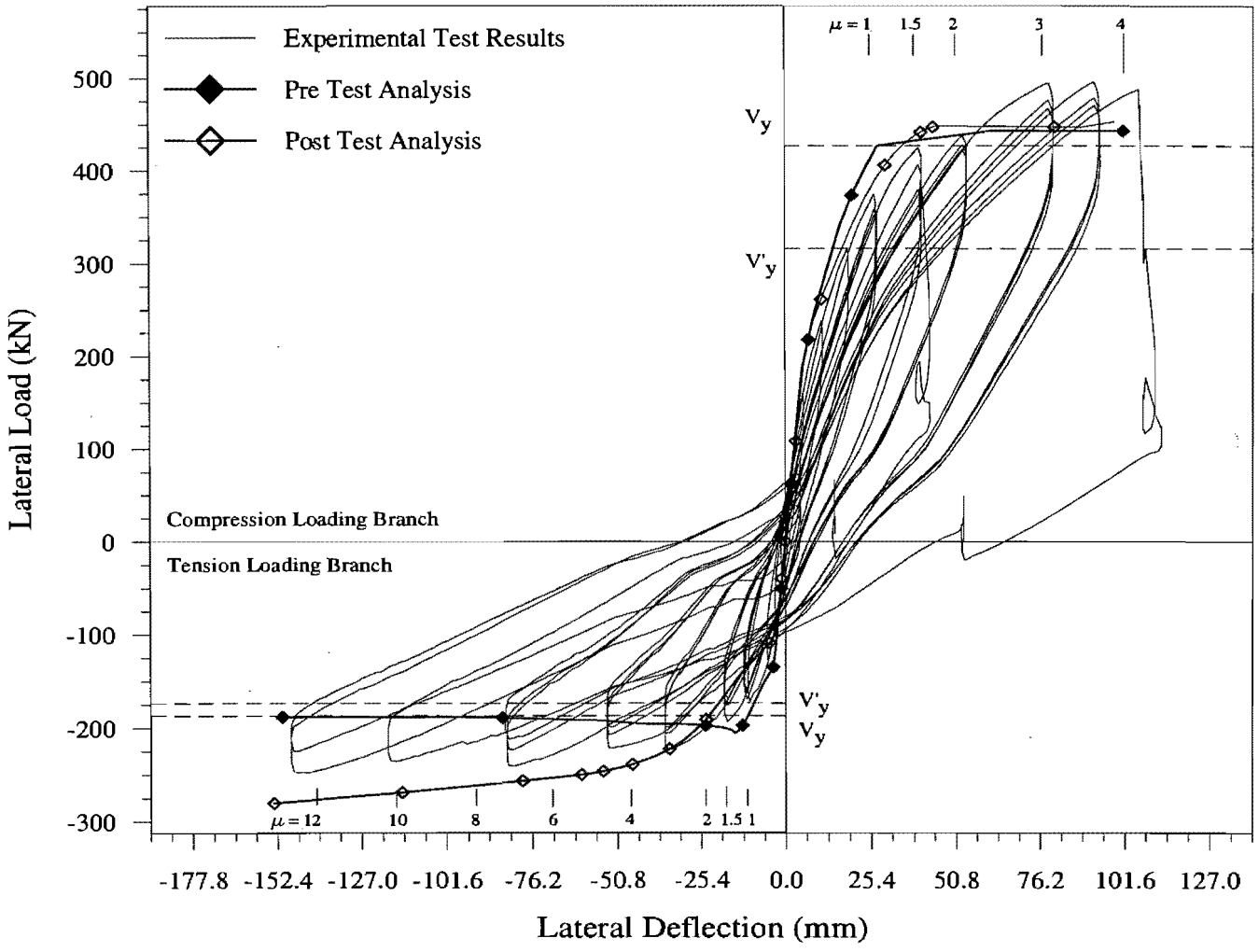

Fig. 7-18 Lateral Load versus Lateral Deflection Characteristics

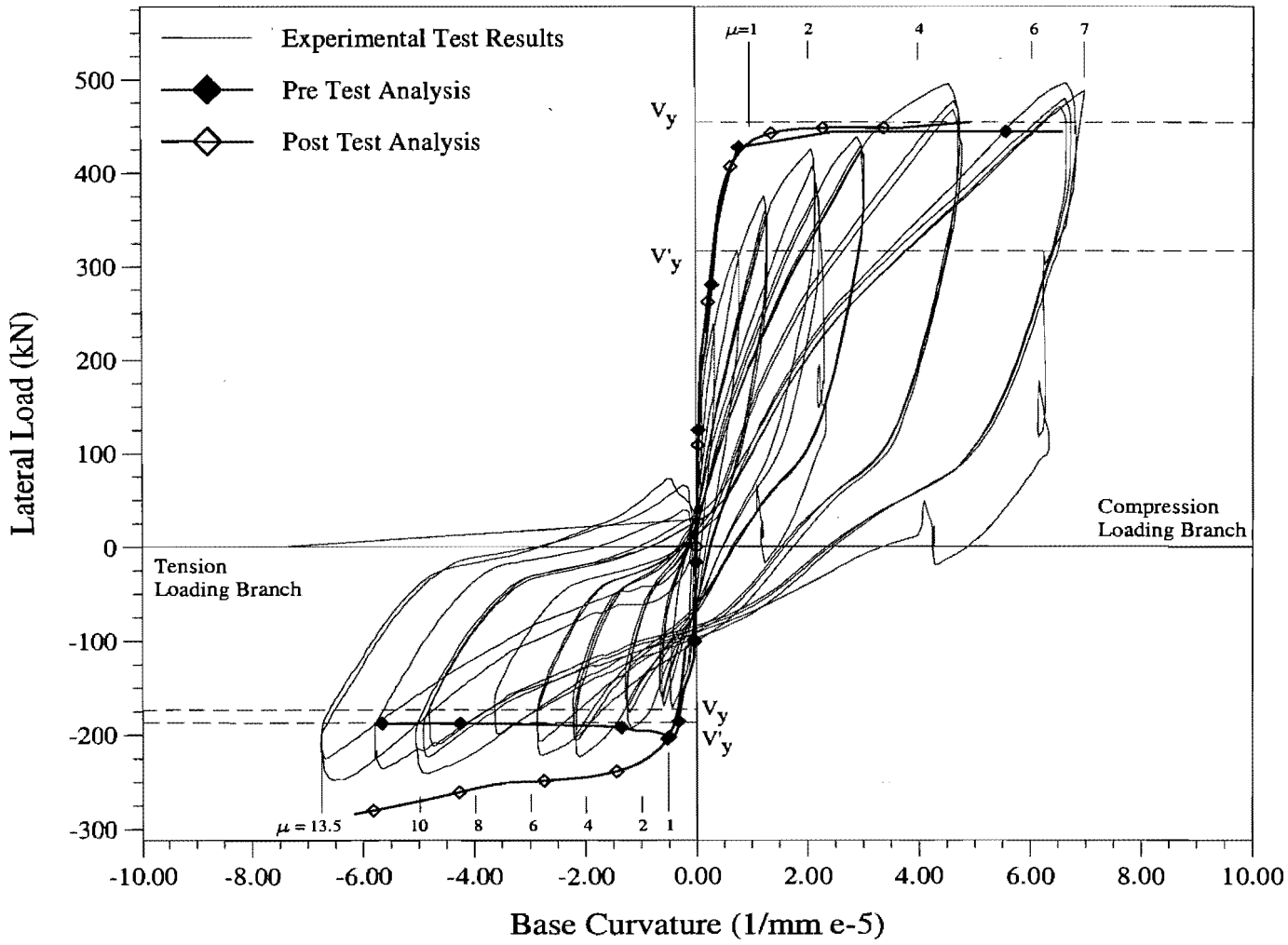

Fig. 7-19 Lateral Load versus Base Curvature Characteristics

Axial load versus lateral deflection characteristics are presented in **Fig. 7-20**. This figure also shows the profile of the loading path that was employed to control the application of the simulated seismic forces. The maximum and minimum axial loads were predefined at +2793 kN in the compression loading branch and -302 kN in the tension loading branch, respectively. These values are identical to test units *COR1* and *COR2*.

Loading curves defined in Chapter 3 for test units *COR1* and *COR3* are also presented in **Fig. 7-20**. In addition, indicated in this figure are the location at which the residual displacements, Δ_i, were obtained when Curve VII and Curve XIV crossed the initial axial load axis and used to define Curve I, Curve II and/or Curve II in **Region 1** and Curve VIII, Curve IX and/or Curve X in **Region 3**, which redirect the loading path towards the control program loading path. Note that not all curves are presented for clarity. Refer to **Fig. 3-53** for additional curves not shown here. As expected, these curves are straight lines which emanate from the residual displacements, Δ_i, and point towards the end points of these curves.

Fig. 7-21 presents the axial load versus the lateral load characteristics for test unit *COR3*. In this figure is also shown the pre-test analysis loading path which was used to develop the control program loading path depicted in **Fig. 7-20**. Pinching in the hysteresis loops at the initial axial load are due to the fact that the control program loading path in the unloading branches is described by a straight line initiating at the peak deformation to the initial load state.

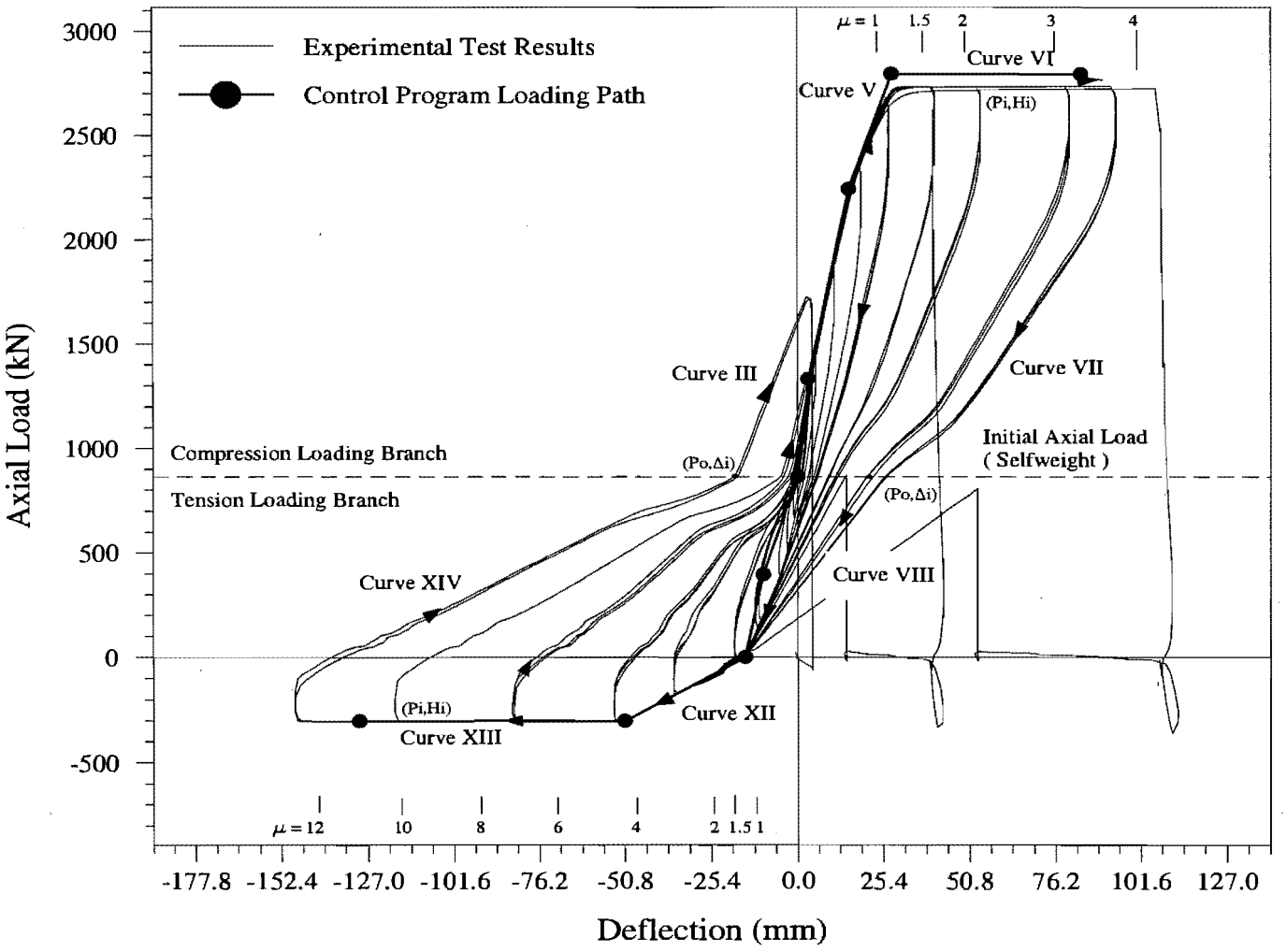

Fig. 7-20 Axial Load versus Lateral Deflection Characteristics

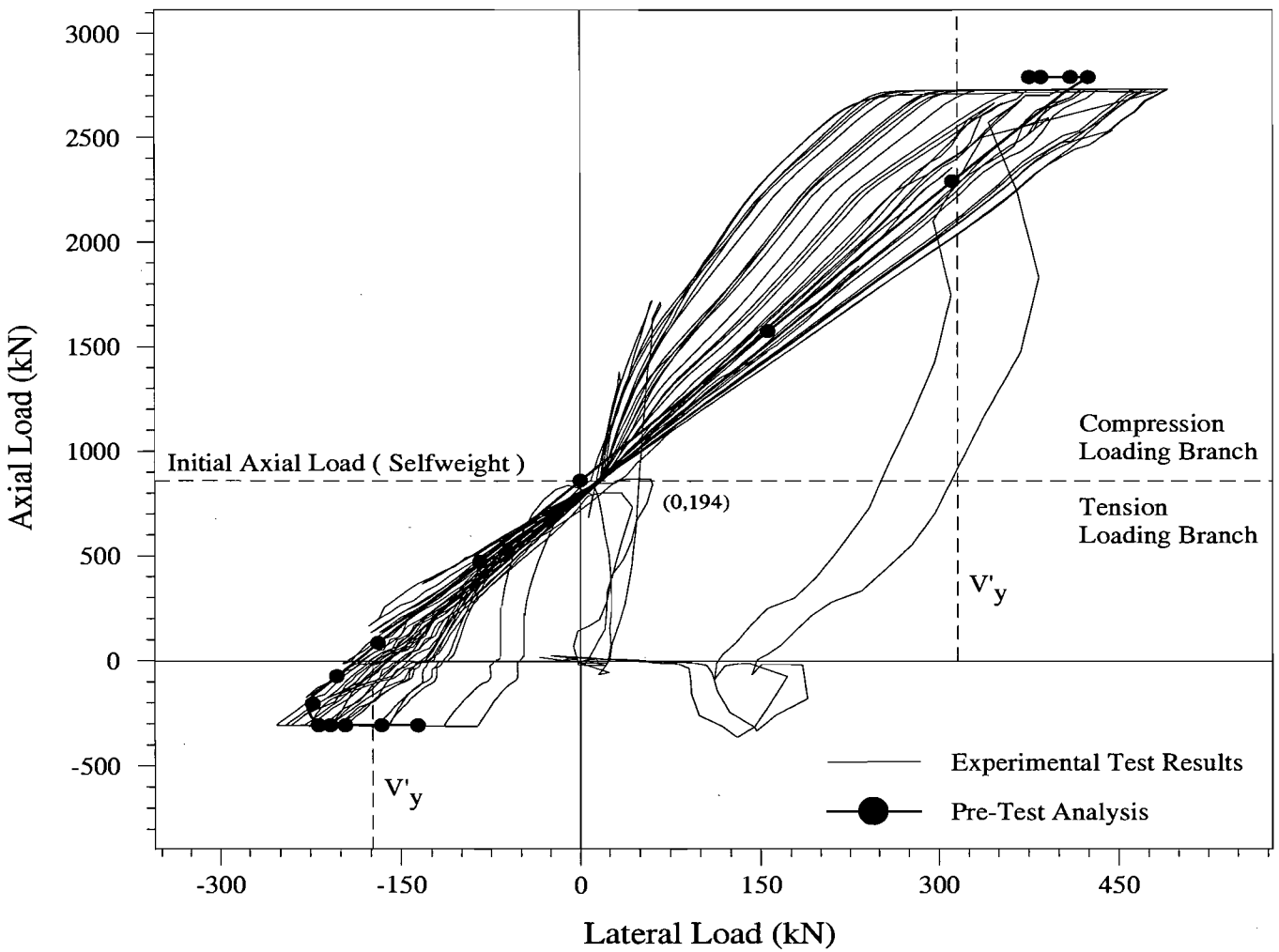

Fig. 7-21 Axial Load versus Lateral Load Characteristics

7.3 Pile Curvature Profiles

In this section and future sections, the plotted values are the first cycle peak values for each cyclic response. Curvature vertical profiles along the height of the pile are presented in **Fig. 7-22(a)** and **Fig. 7-22(b)** for initial and final stages of the testing procedure, respectively.

The curvature profiles depicted in **Fig. 7-22(a)** show that in the initial stages of the testing procedure, region of plastic deformations form at the bottom of the pile section illustrated by a significant increase in curvature a position ***1***. A second region of plastic deformations is well illustrated in **Fig. 7-22(a)**, depicted by a significant increase in curvature near the region where the inner core longitudinal reinforcement terminates. Increase in curvature in this region is more accentuated in the tension loading branch. This second region of plastic deformations began to form when the lateral deflection was $\Delta = -27.43$ mm as a result of wide open cracks at this location, as previously described.

Indicated in these figures are the yield curvature levels obtained from **Fig. 7-22(a)**, which provides a visual indication of regions of plastic deformations achieved in the different loading stages. The length of the plastic hinge reached a maximum height of approximately 423 mm near the soffit slab, which is sightly lower than the theoretical effective plastic hinge length, l_p, of 522 mm, obtained from equation **(5.3)**.

At the location where the longitudinal reinforcement terminates it is not readily perceived what is the exact length of plastic deformations; however, region of plastic deformations are more concentrated between positions ***8*** and ***6*** which leads to a plastic hinge length of approximately 305 mm.

A comparison with the curvature profiles of test unit *COR1* is presented in Chapter 8 while discussing test results.

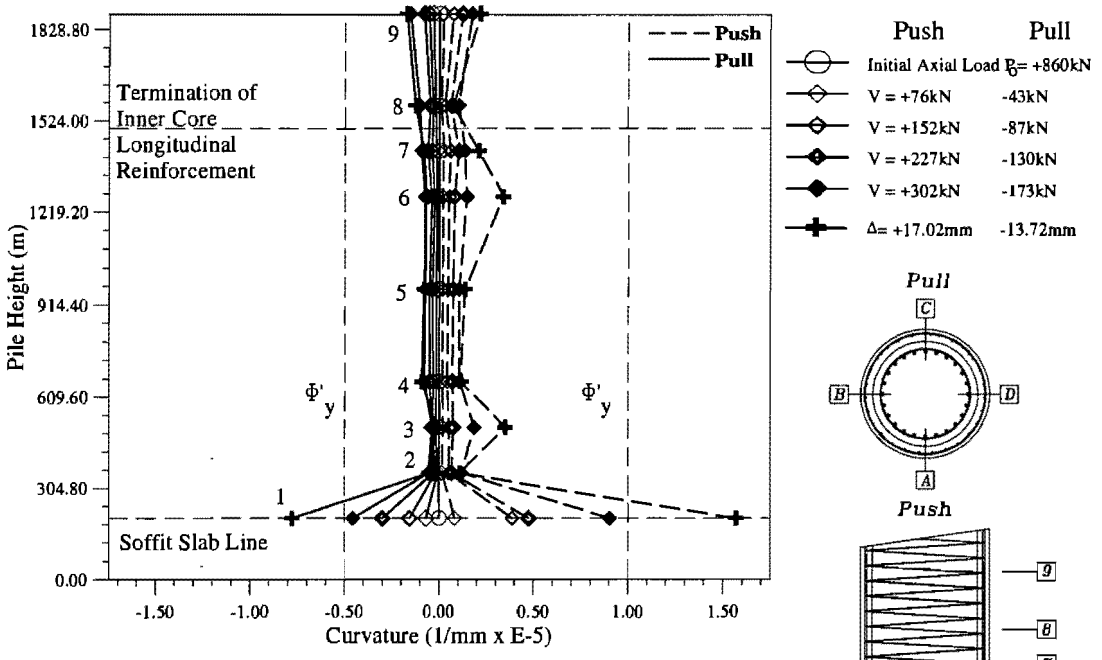

(a) Curvature Vertical Profiles - Initial Stages of Testing

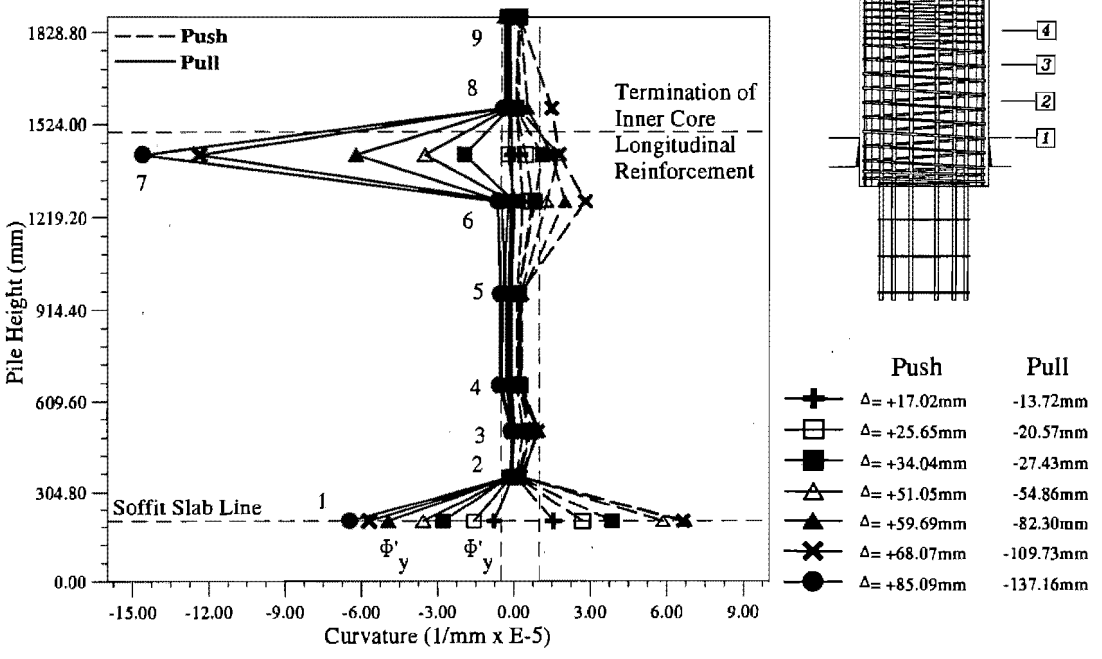

(b) Curvature Vertical Profiles - Final Stages of Testing

Fig. 7-22 Curvature Vertical Profiles

7.4 Vertical Profiles of Artificial Cracks Opening

During the testing procedure the crack width or opening of the artificial cracks was monitored with 8 linear potentiometers positioned along the artificial cracks, as illustrated in **Fig. 3-33**.

Vertical profiles along lines ***A*** and ***D*** are shown in **Fig. 7-23** and **Fig. 7-24**, respectively. Along line ***A*** the artificial crack opening increases from the start of the testing procedure after the initial axial load of +863 kN is applied (see **Fig. 7-23**), which corroborates the loss in confinement of the concrete in this region. Opening of this cut is registered after +50% yielding, which corresponds with the stage at which cracks are seen to emanate from the cut. Moreover, in the early stages, crack width opening is more accentuated at the central positions ***2*** and ***3***. However, in the later stages of the testing procedure, crack width opening is more accentuated at position ***1***. This is so, because in the early stages of the testing procedure, confinement demands are rather small and the tensile strength of the concrete is adequate in preventing crack from opening at its extremities. In the later stages of the testing procedure, confinement demands at the lower extremity are more accentuated as a result of formation of plastic hinge at the lower extremity.

Along line ***D***, opening of the crack is not visible in the early stages of the testing procedure and very small up to 100% yielding. A considerable jump in its opening is visible at approximately μ_Δ=1 and μ_Δ=-1. At these loading stages, the crack width opening is more accentuated at position ***4*** because it was at this position where the first cracks were recorded to emanate from this extremity. However, at later stages of the testing procedure, there is a shift and crack width opening is more accentuated at its lower extremity. During the later stages of the testing procedure, crack width opening along cracks ***A*** and ***D*** at location ***1*** is approximately the same, which suggests constant radial expansion of the concrete shell as a result of confinement demands.

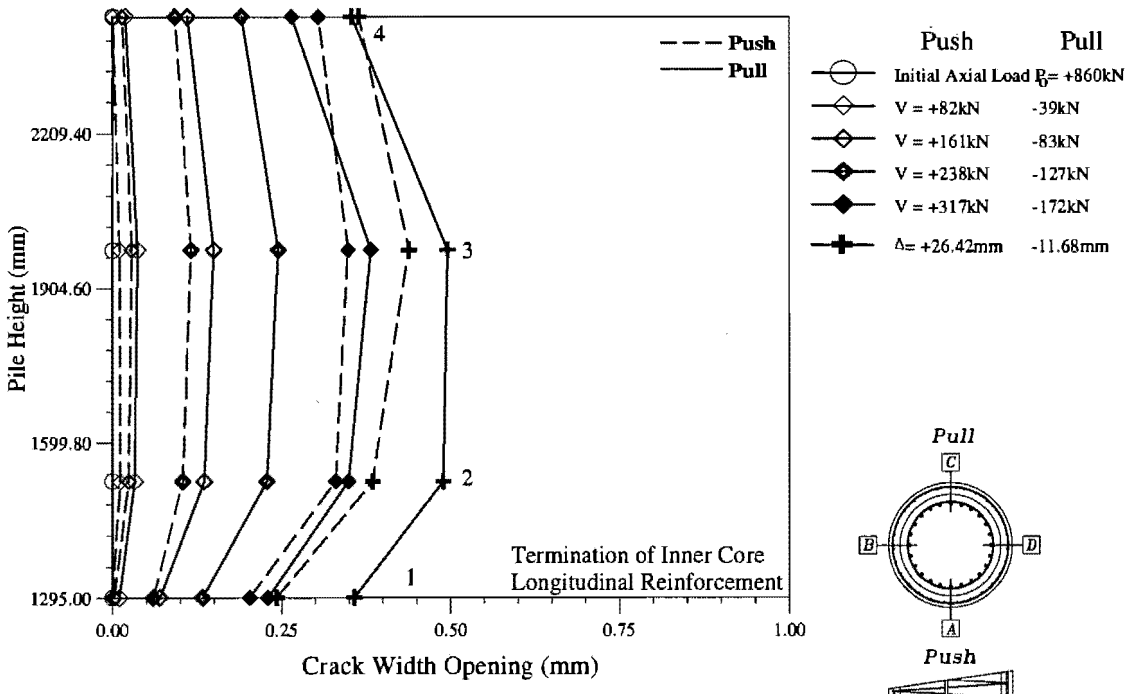

(a) Vertical Profiles - Initial Stages of Testing

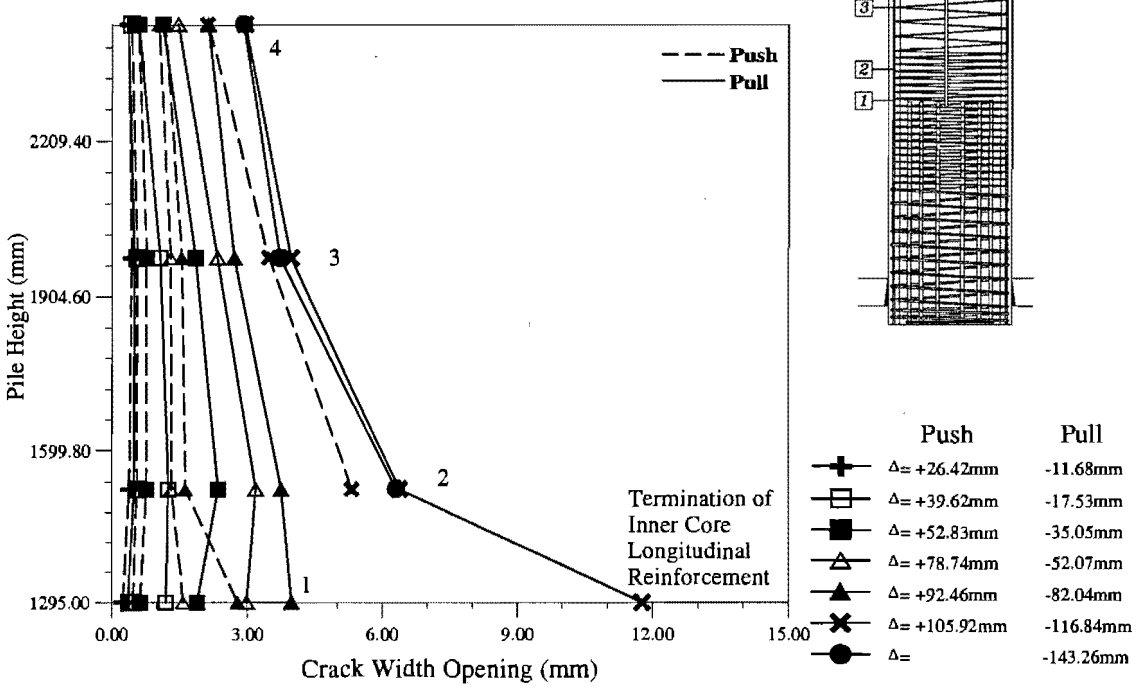

(b) Vertical Profiles - Final Stages of Testing

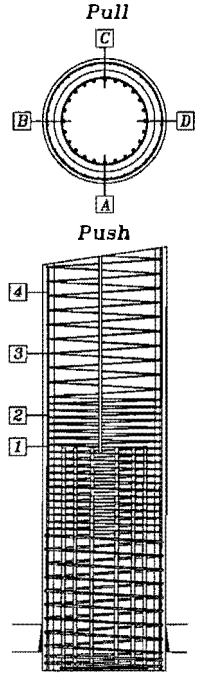

Fig. 7-23 Crack Width Opening Vertical Profiles Along Line *A*

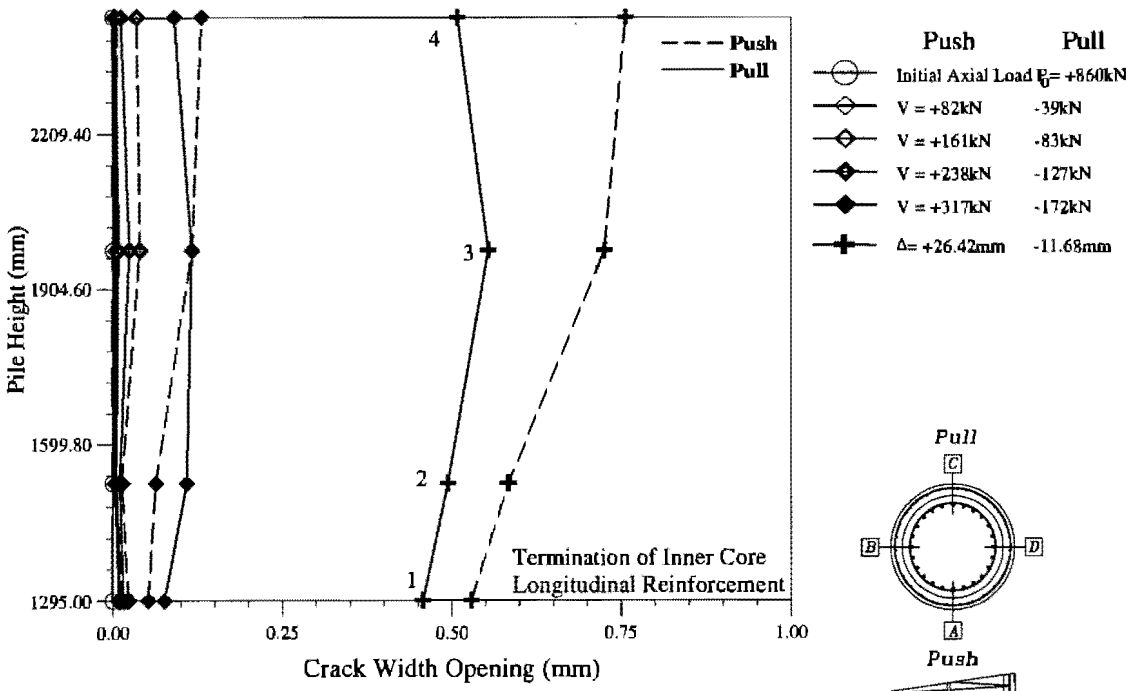

(a) Vertical Profiles - Initial Stages of Testing

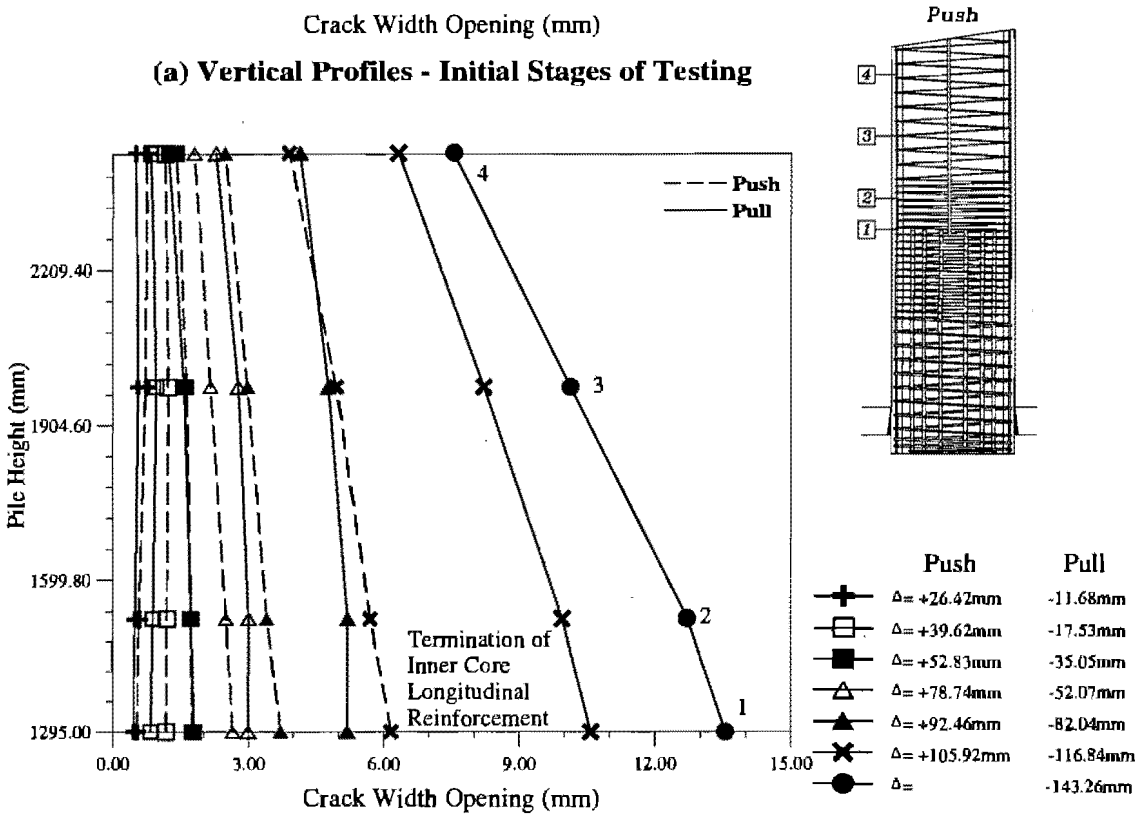

(b) Vertical Profiles - Final Stages of Testing

Fig. 7-24 Crack Width Opening Along Vertical Line ***D***

7.5 Pile Inner Core Longitudinal Reinforcement Strain Profiles

As in test units *COR1* and *COR2*, the inner core reinforcement consists of #7 Grade40 (f_y=276 MPa) steel with a yield strain of approximately 1500$\mu\varepsilon$.

7.5.1 Pile Longitudinal Reinforcement - Vertical Strain Profiles

Vertical strain profiles for the inner core longitudinal reinforcement are presented in **Fig. 7-25** through **Fig. 7-28**.

Strain profiles along inner core bar ***A*** reveal that yielding of this bar in compression occurred above the soffit slab line at μ_Δ=+4.0 and yielded in tension at μ_Δ=−3, also at location ***4***.

The profiles for bars ***B*** and ***D***, which are positioned on the sides of the pile, revealed that these bars where always in tension and below yielding levels. The vertical profiles for bars ***B*** and ***D*** are similar as a result of the symmetrical position of these two bars with respect to the loading direction.

Strain profiles along inner core bar ***C*** reveal that strains in this bar were below yielding levels in compression, and in tension, this bar yielded at μ_Δ=+1.5.

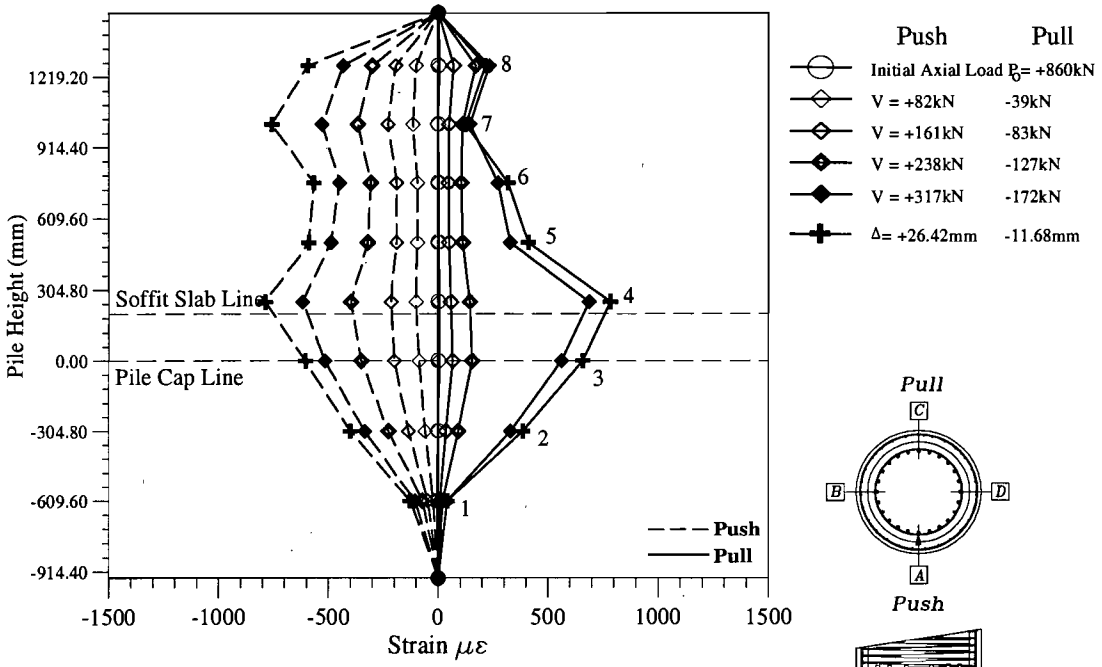

(a) Vertical Strain Profiles - Initial Stages of Testing

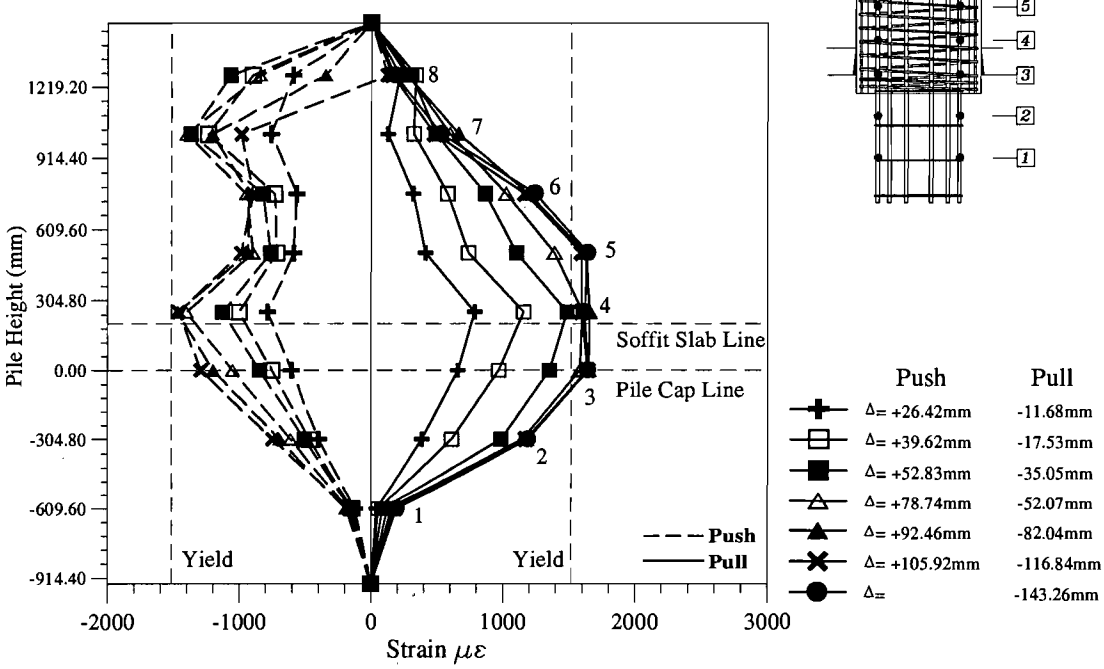

(b) Vertical Strain Profiles - Final Stages of Testing

Fig. 7-25 Vertical Strain Profiles Inner Core Bar *A*

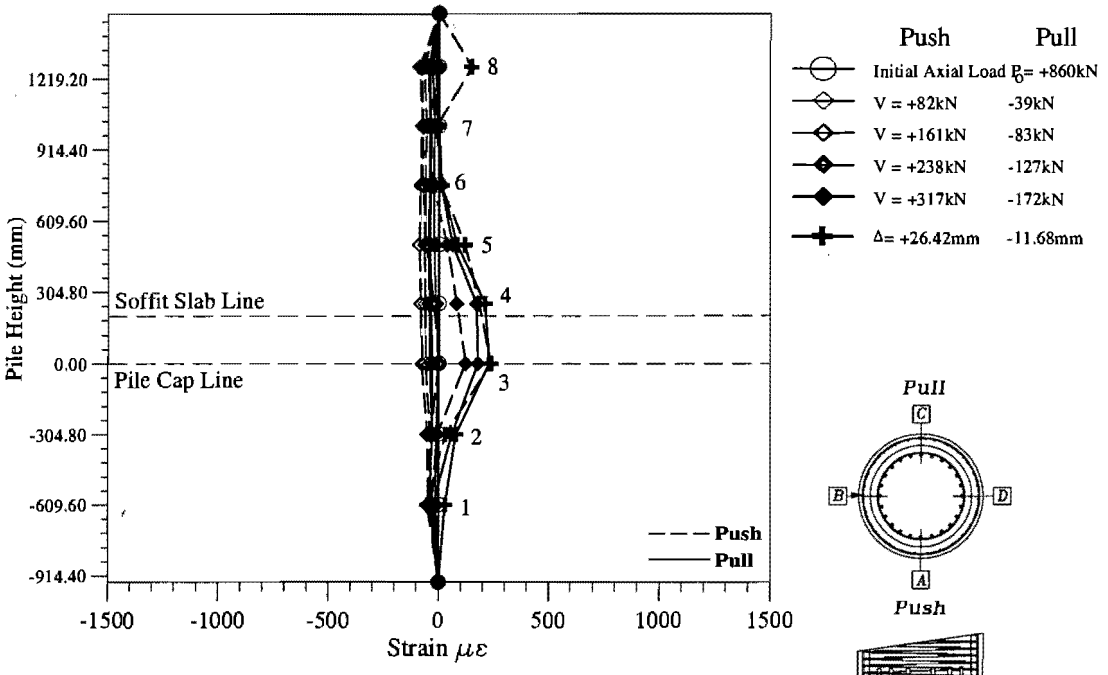

(a) Vertical Strain Profiles - Initial Stages of Testing

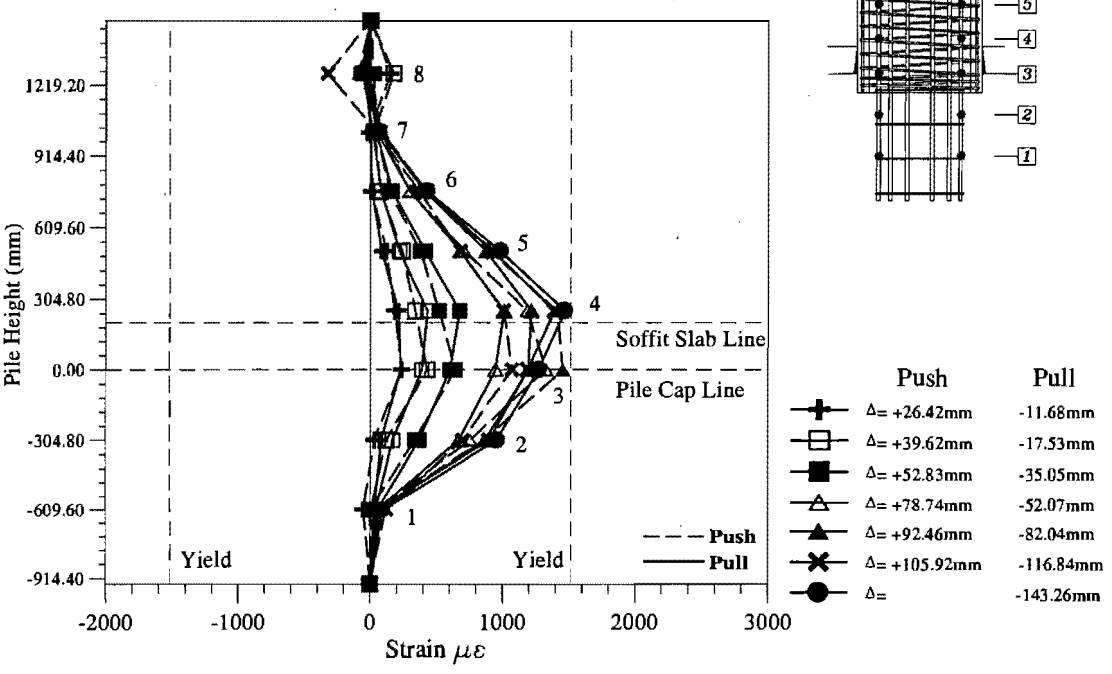

(b) Vertical Strain Profiles - Final Stages of Testing

Fig. 7-26 Vertical Strain Profiles Inner Core Bar ***B***

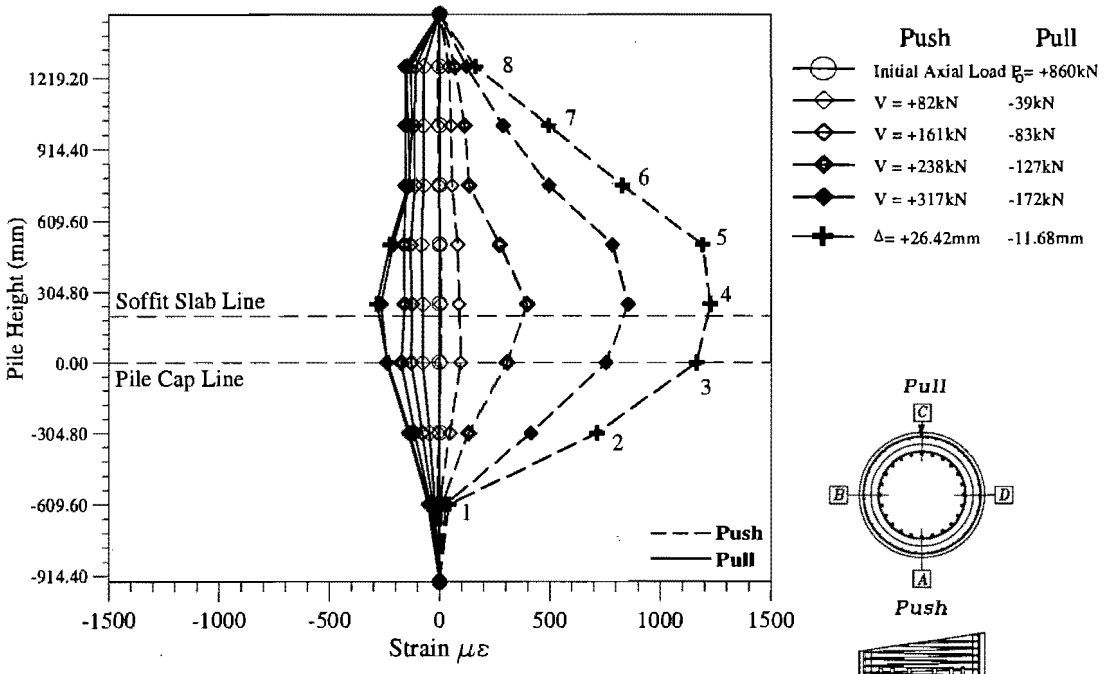

(a) Vertical Strain Profiles - Initial Stages of Testing

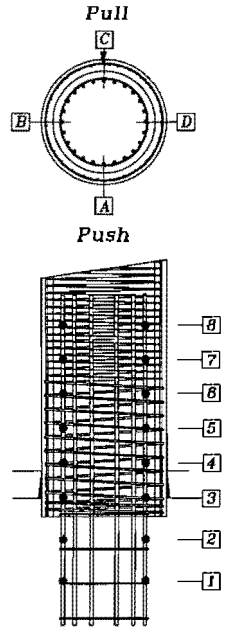

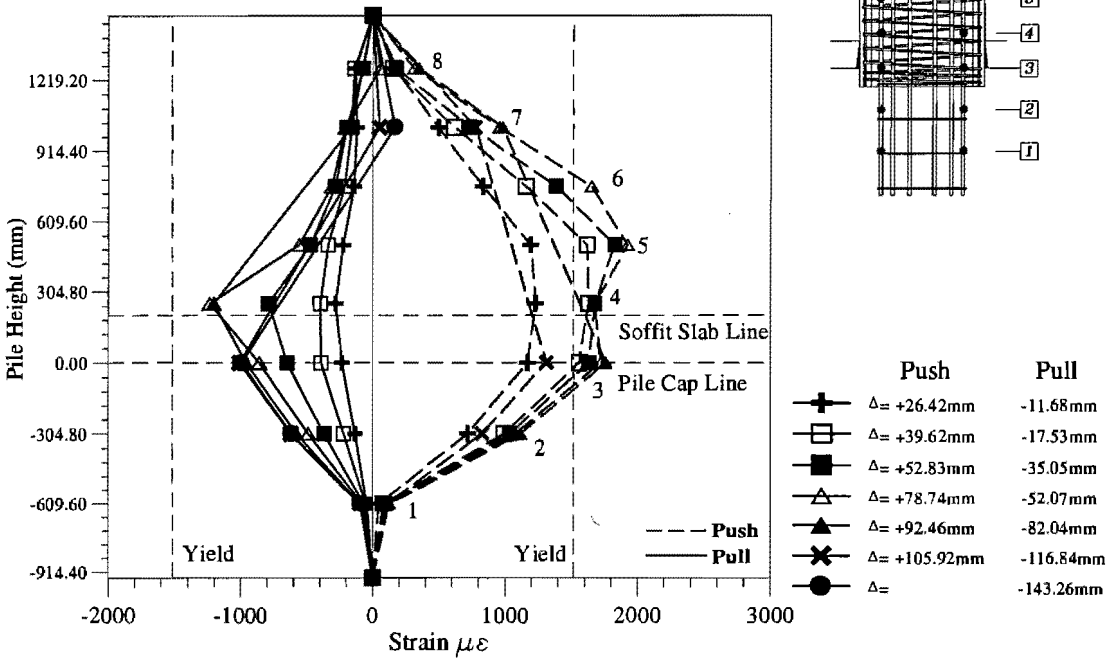

(b) Vertical Strain Profiles - Final Stages of Testing

Fig. 7-27 Vertical Strain Profiles Inner Core Bar *C*

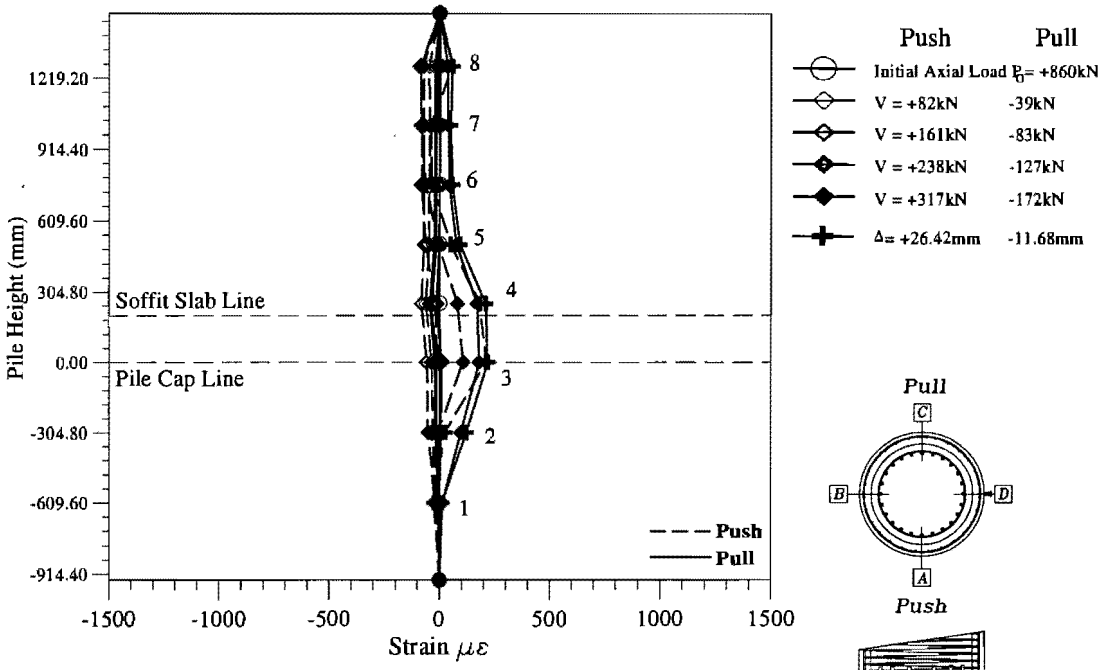

(a) Vertical Strain Profiles - Initial Stages of Testing

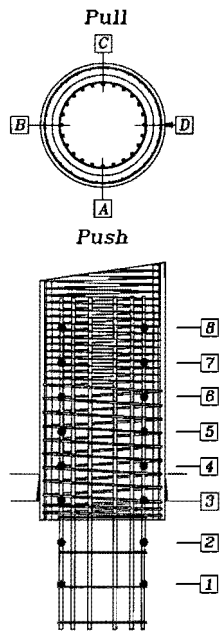

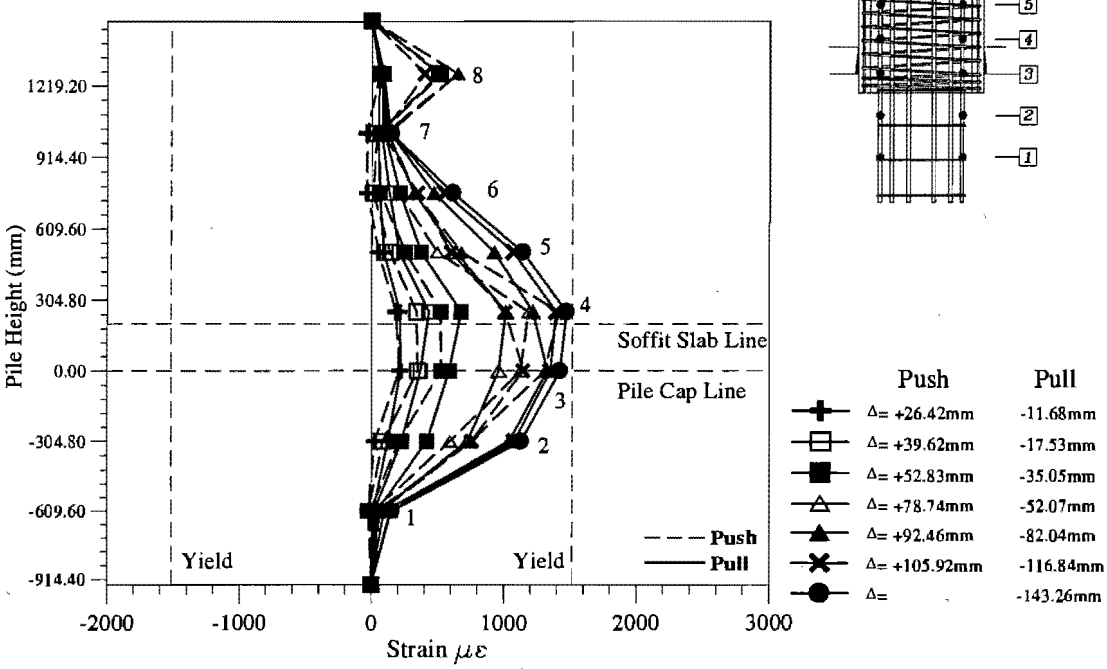

(b) Vertical Strain Profiles - Final Stages of Testing

Fig. 7-28 Vertical Strain Profiles Inner Core Bar ***D***

7.5.2 Pile Longitudinal Reinforcement - Circumferential Strain Profiles

Circumferential strain profiles for the pile inner core longitudinal reinforcement are presented in **Fig. 7-29** through **Fig. 7-32**. The circumferential profiles depicted in these figures indicate in the initial stages of testing a linear variation of strain between the longitudinal bars, which suggests small excursions into yielding strains. Yielding of bars ***A*** and ***C*** occurred mainly between horizontal lines ***2*** and ***7***, with maximum registered strains slightly higher than yielding only between levels ***3*** and ***5***.

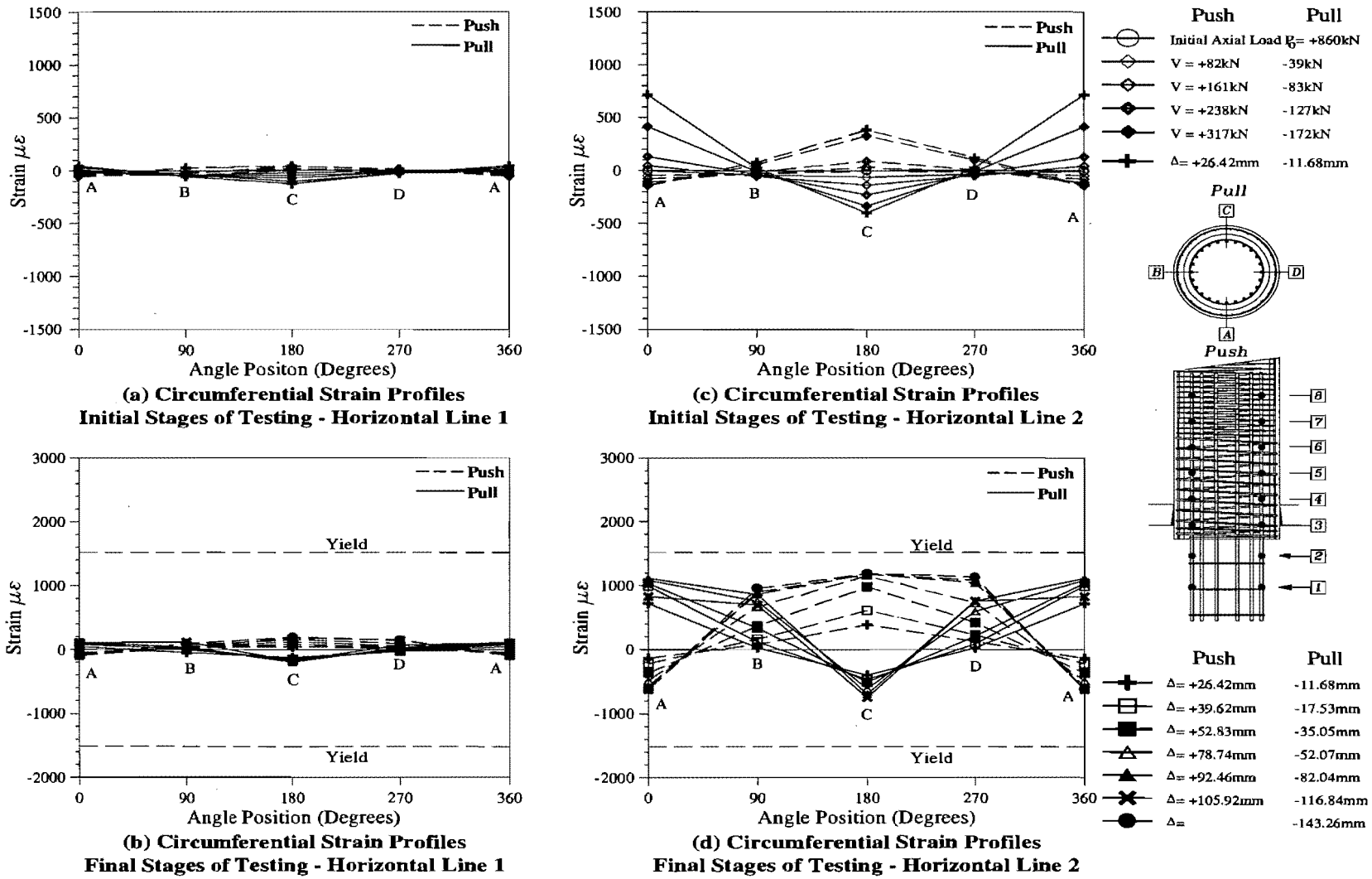

(a) Circumferential Strain Profiles
Initial Stages of Testing - Horizontal Line 1

(c) Circumferential Strain Profiles
Initial Stages of Testing - Horizontal Line 2

(b) Circumferential Strain Profiles
Final Stages of Testing - Horizontal Line 1

(d) Circumferential Strain Profiles
Final Stages of Testing - Horizontal Line 2

Fig. 7-29 Inner Core Reinforcement Strain Profiles Along Horizontal Line *1* and *2*

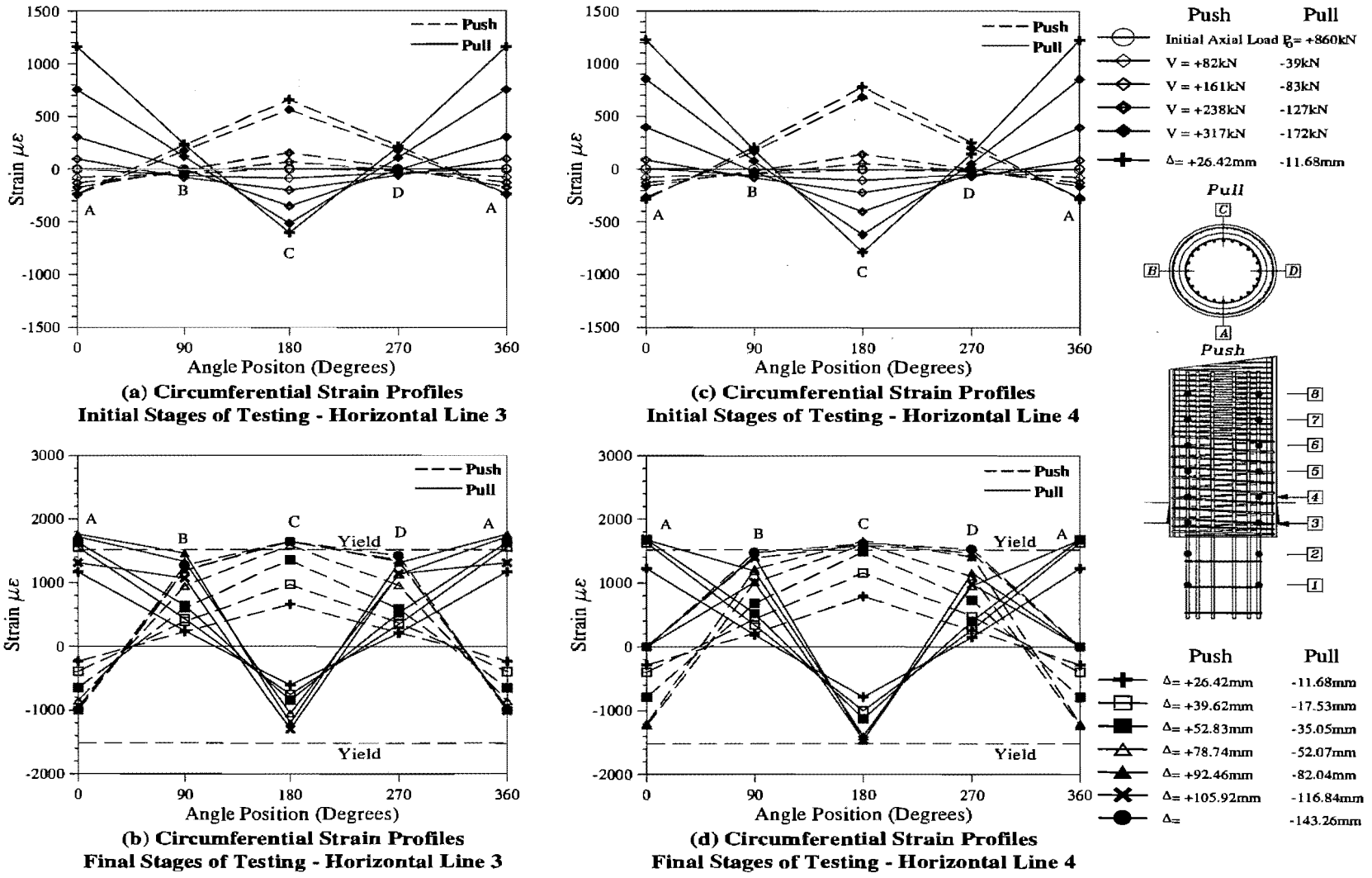

(a) Circumferential Strain Profiles
Initial Stages of Testing - Horizontal Line 3

(c) Circumferential Strain Profiles
Initial Stages of Testing - Horizontal Line 4

(b) Circumferential Strain Profiles
Final Stages of Testing - Horizontal Line 3

(d) Circumferential Strain Profiles
Final Stages of Testing - Horizontal Line 4

Fig. 7-30 Inner Core Reinforcement Strain Profiles Along Horizontal Line *3* and *4*

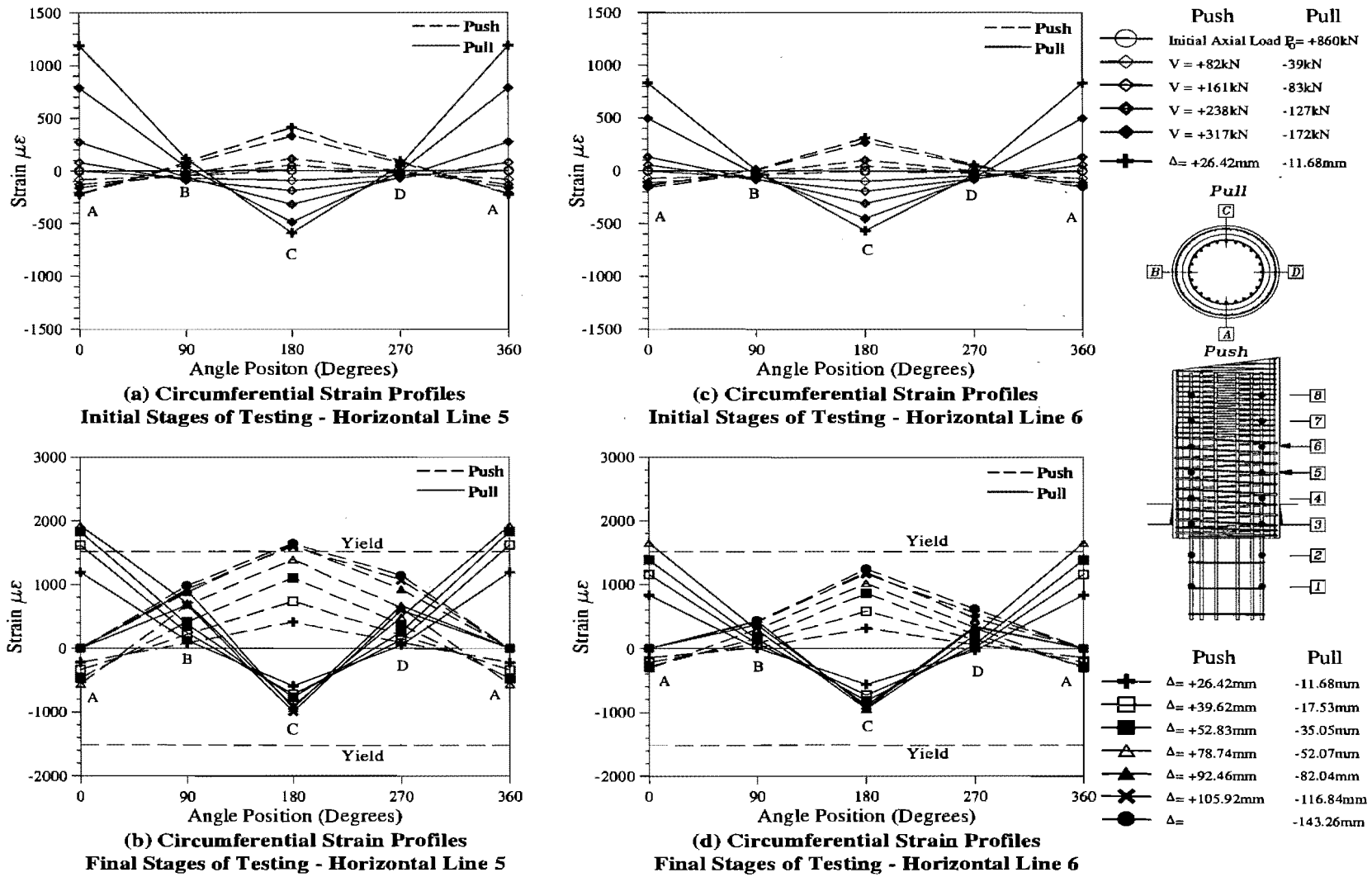

(a) Circumferential Strain Profiles
Initial Stages of Testing - Horizontal Line 5

(c) Circumferential Strain Profiles
Initial Stages of Testing - Horizontal Line 6

(b) Circumferential Strain Profiles
Final Stages of Testing - Horizontal Line 5

(d) Circumferential Strain Profiles
Final Stages of Testing - Horizontal Line 6

Fig. 7-31 Inner Core Reinforcement Strain Profiles Along Horizontal Line *5* and *6*

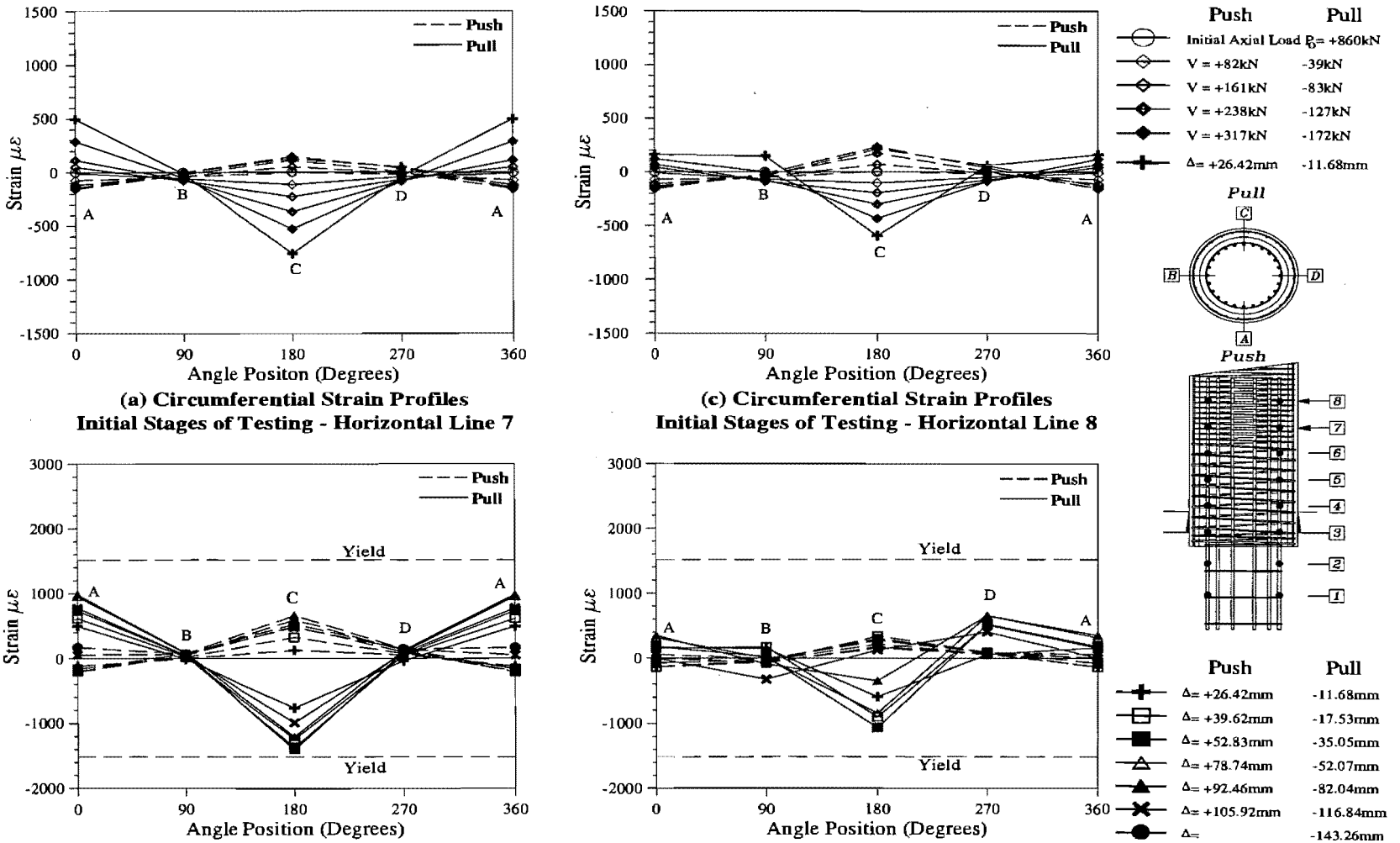

(a) Circumferential Strain Profiles
Initial Stages of Testing - Horizontal Line 7

(c) Circumferential Strain Profiles
Initial Stages of Testing - Horizontal Line 8

(b) Circumferential Strain Profiles
Final Stages of Testing - Horizontal Line 7

(d) Circumferential Strain Profiles
Final Stages of Testing - Horizontal Line 8

Fig. 7-32 Inner Core Reinforcement Strain Profiles Along Horizontal Line *7* and *8*

7.6 Prestressing Strands Vertical Strain Profiles

Strain profiles for the prestressing strands are presented in **Fig. 7-33** through **Fig. 7-36**. Similar to test unit *COR1*, strain readings were obtained during fabrication of the precast prestressed concrete shell while at *Utility Vault*, and the gages were disconnected between fabrication and testing at UCSD. Then, before testing, these same gages were reconnected to the data acquisition system and balanced to zero. Then, the final strains recorded during the fabrication process were added to the strains obtained during testing.

A large number of strain gages were malfunctioning after manufacturing of the concrete shell for test unit *COR3*, and during zeroing of the gages for the testing procedure, many gages were not connected. Along strand ***C*** all strain gages were functioning and vertical profiles along this strand are presented in **Fig. 7-35**. In the final stages of the testing procedure, strain profiles presented in this figure indicate that maximum strains were achieved between positions *3* and *7*. This indicates a much smaller development length for the prestressing strands than that observed for test unit *COR1*. This observation will be discussed in greater detailed in Chapter 8 when comparing behavior of these two test units.

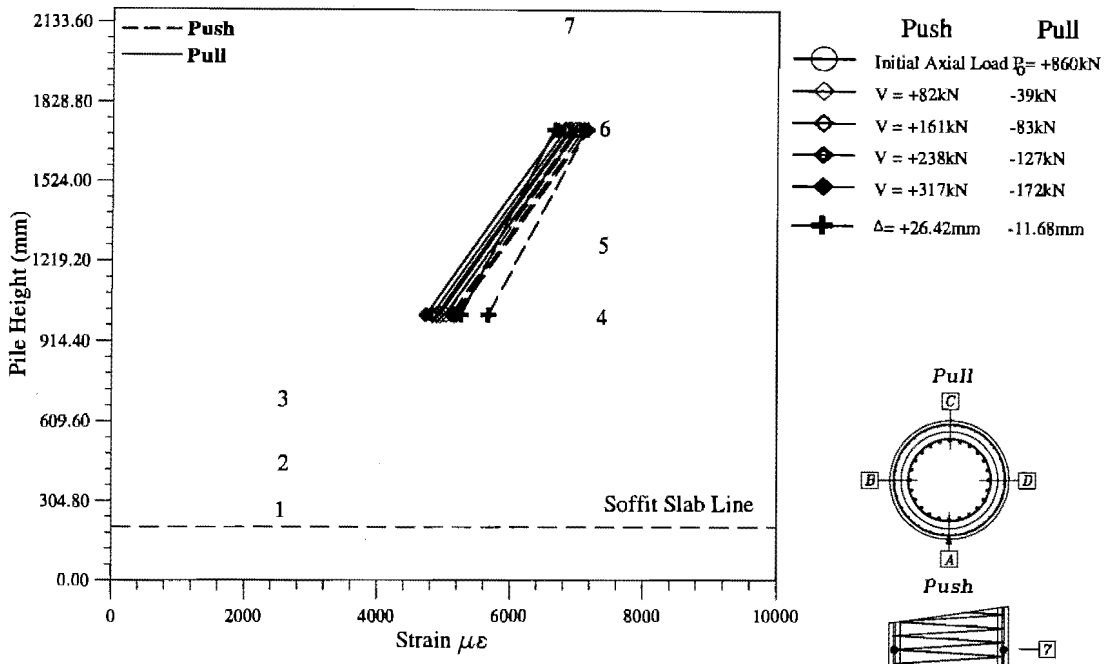

(a) Vertical Strain Profiles - Initial Stages of Testing

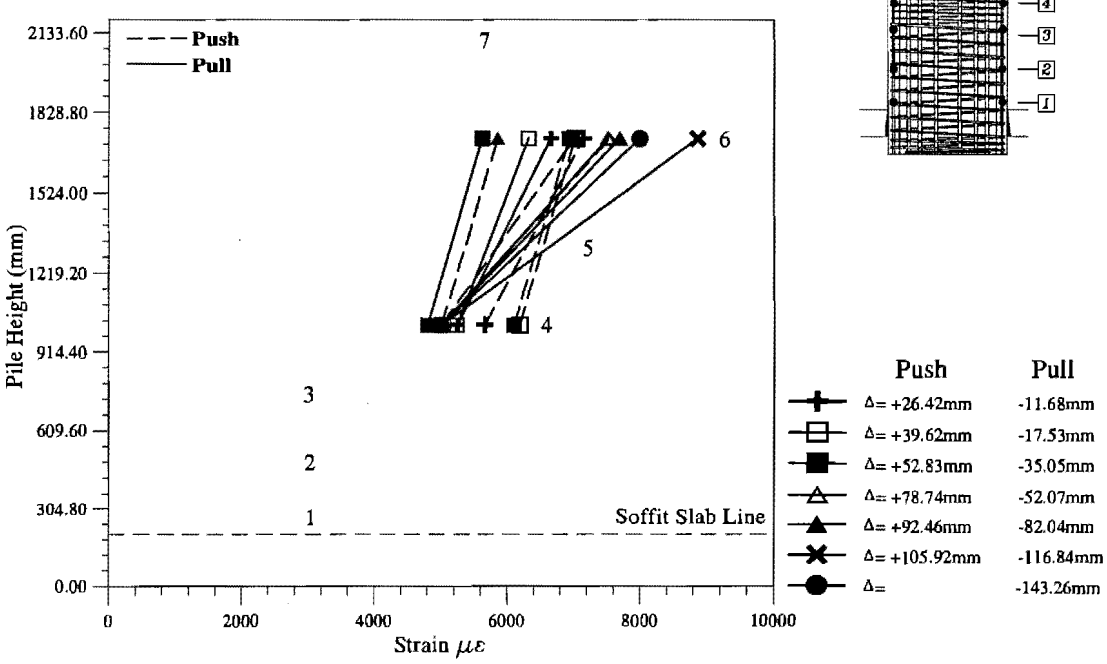

(b) Vertical Strain Profiles - Final Stages of Testing

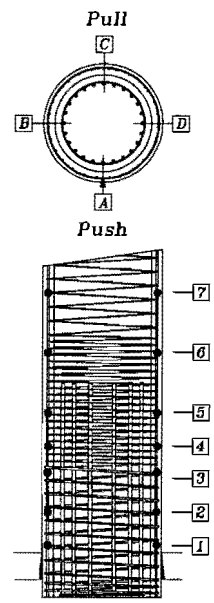

Fig. 7-33 Vertical Strain Profiles Along Strand *A*

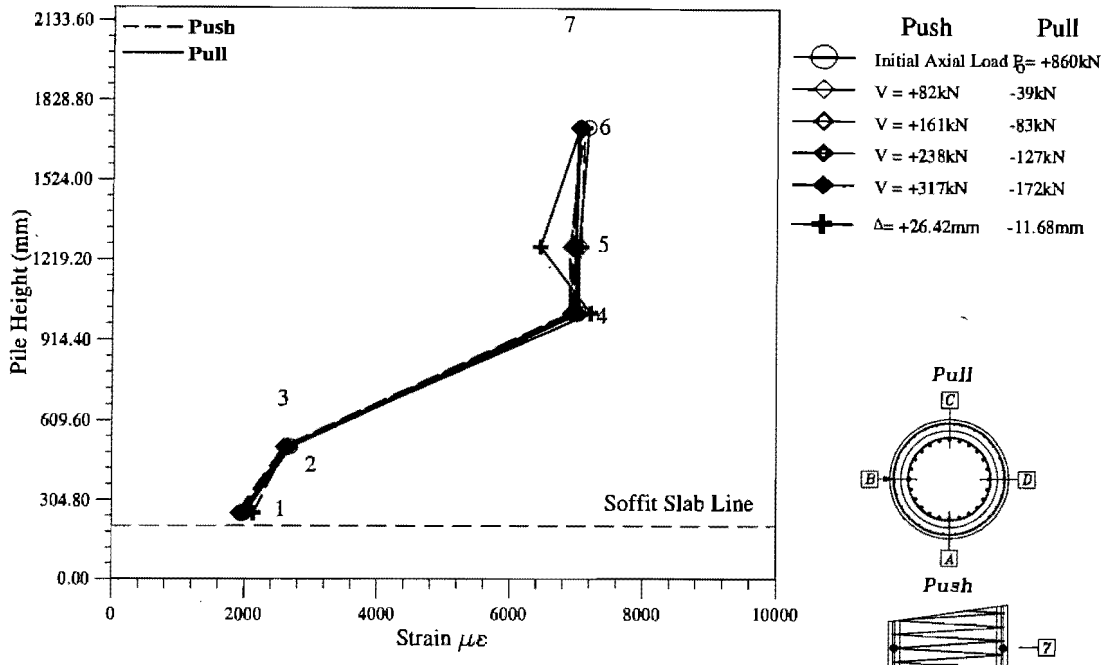

(a) Vertical Strain Profiles - Initial Stages of Testing

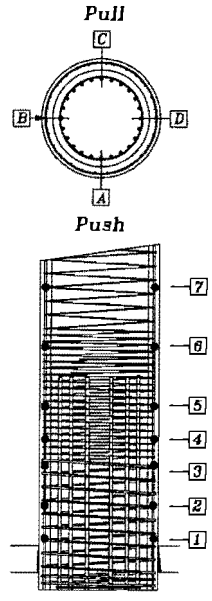

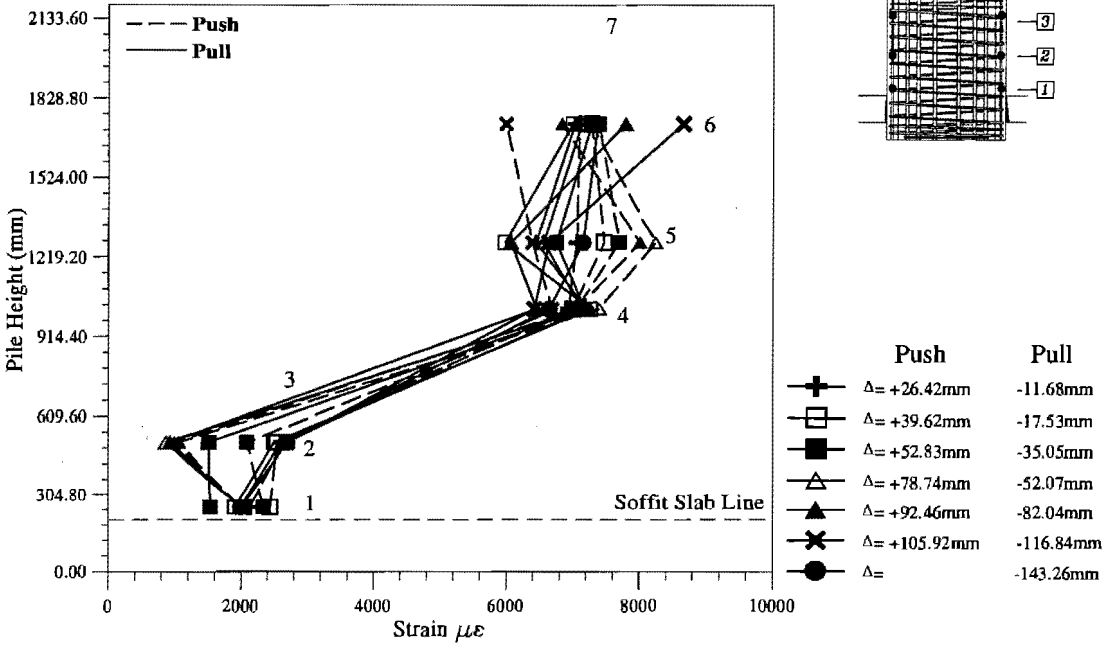

(b) Vertical Strain Profiles - Final Stages of Testing

Fig. 7-34 Vertical Strain Profiles Along Strand ***B***

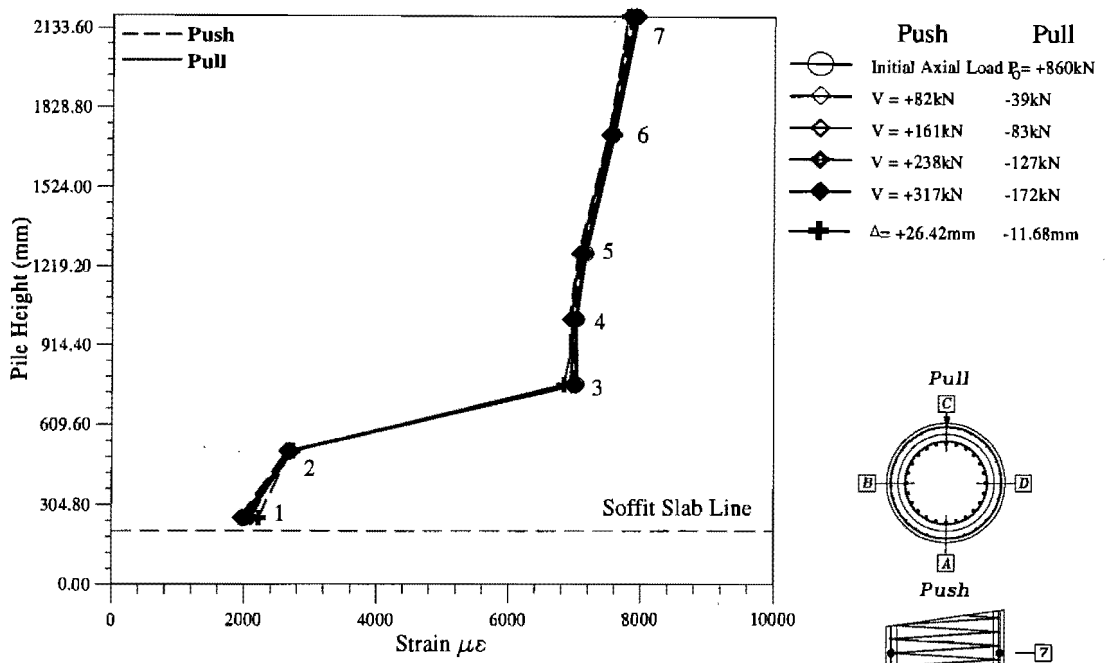

(a) Vertical Strain Profiles - Initial Stages of Testing

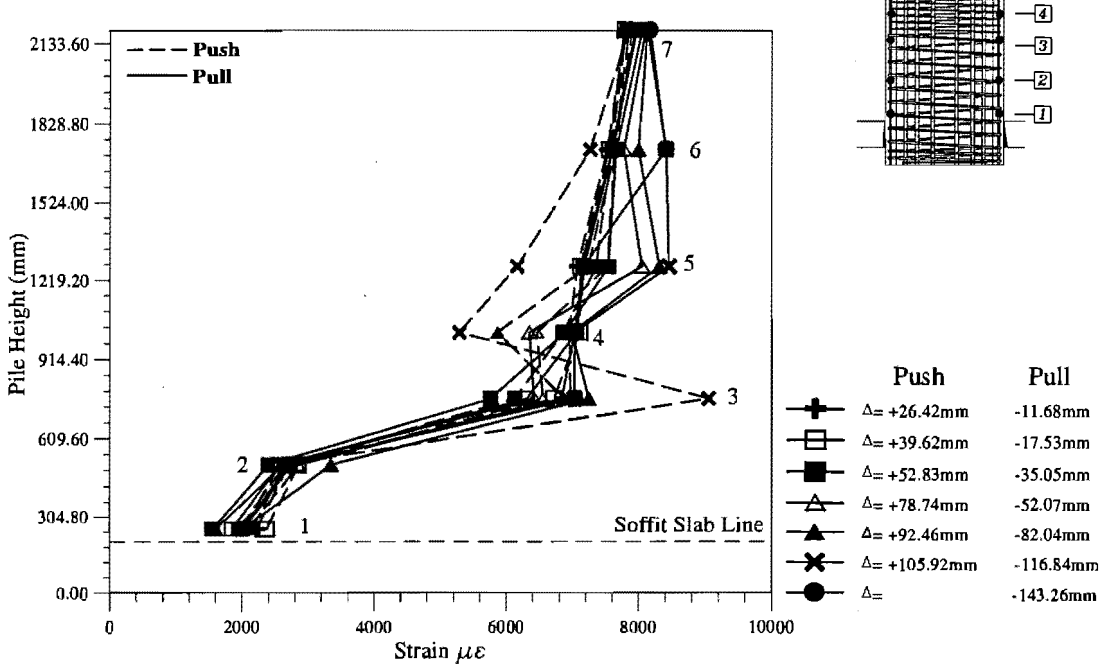

(b) Vertical Strain Profiles - Final Stages of Testing

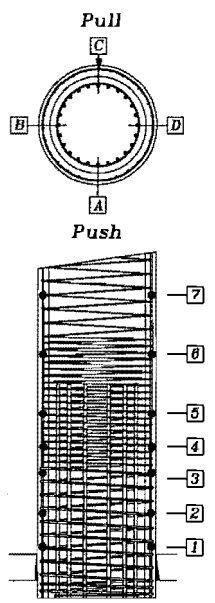

Fig. 7-35 Vertical Strain Profiles Along Strand *C*

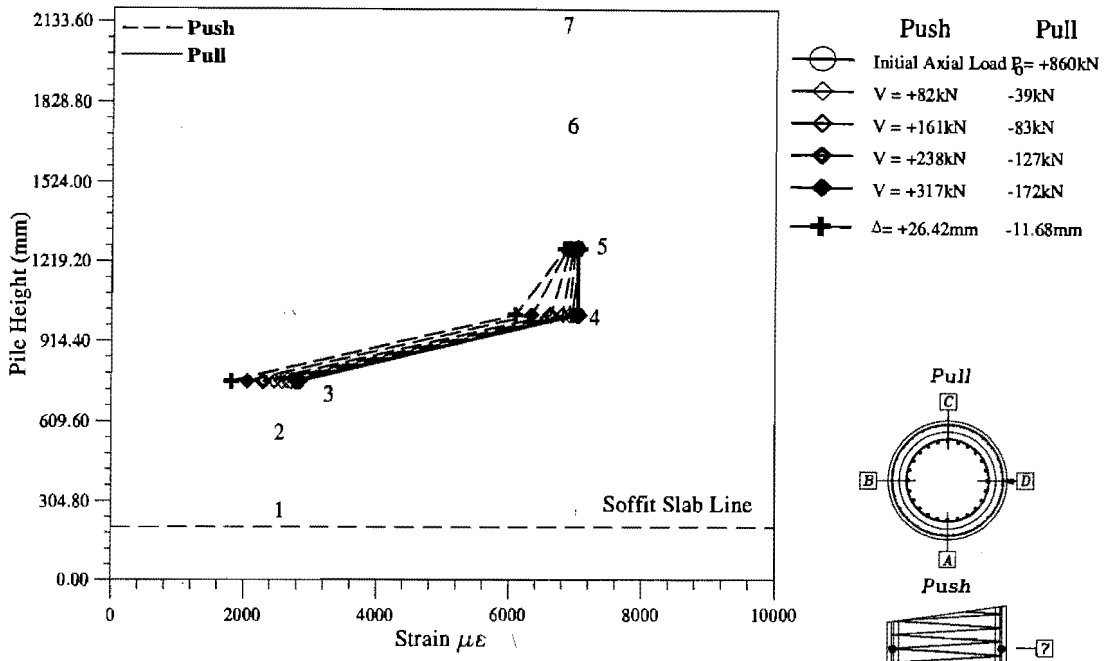

(a) Vertical Strain Profiles - Initial Stages of Testing

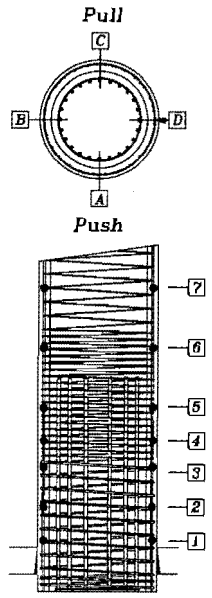

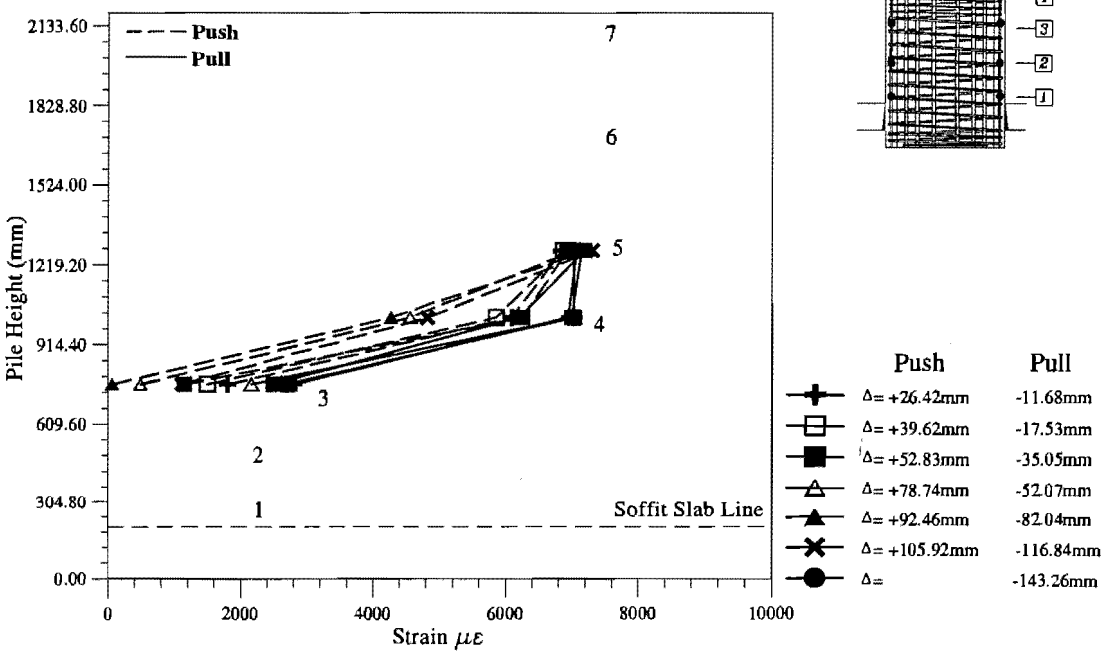

(b) Vertical Strain Profiles - Final Stages of Testing

Fig. 7-36 Vertical Strain Profiles Along Strand ***D***

7.7 Pile Transverse Reinforcement Strain Profiles

The spiral reinforcement used in this test unit varied between #3 on a 84 mm spiral pitch at the pile cap interface to a W3 on a 114 mm spiral pitch above the inner cage longitudinal reinforcement. Strain gages above position *5* for this test unit are not shown because cutting of the artificial cracks through the concrete shell also cut the strain gages cables. For completeness, in this section only, pile transverse reinforcement vertical strain profiles are shown.

7.7.1 Pile Transverse Reinforcement - Vertical Strain Profiles

Vertical strain profiles for the pile transverse reinforcement are presented in **Fig. 7-37** through **Fig. 7-40**. The strain profiles along longitudinal line *A* (see**Fig. 7-37**) and along longitudinal line *C* (see **Fig. 7-39**) indicate the level of confinement strain developed in the pile section as a result of the applied axial load and deformations. Strain profiles along longitudinal line *B* (see **Fig. 7-38**) and along longitudinal line *D* (see **Fig. 7-40**) indicate the level of shear-induced strain as a result of the applied lateral load. Observation of these figures is similar to test unit *COR1*.

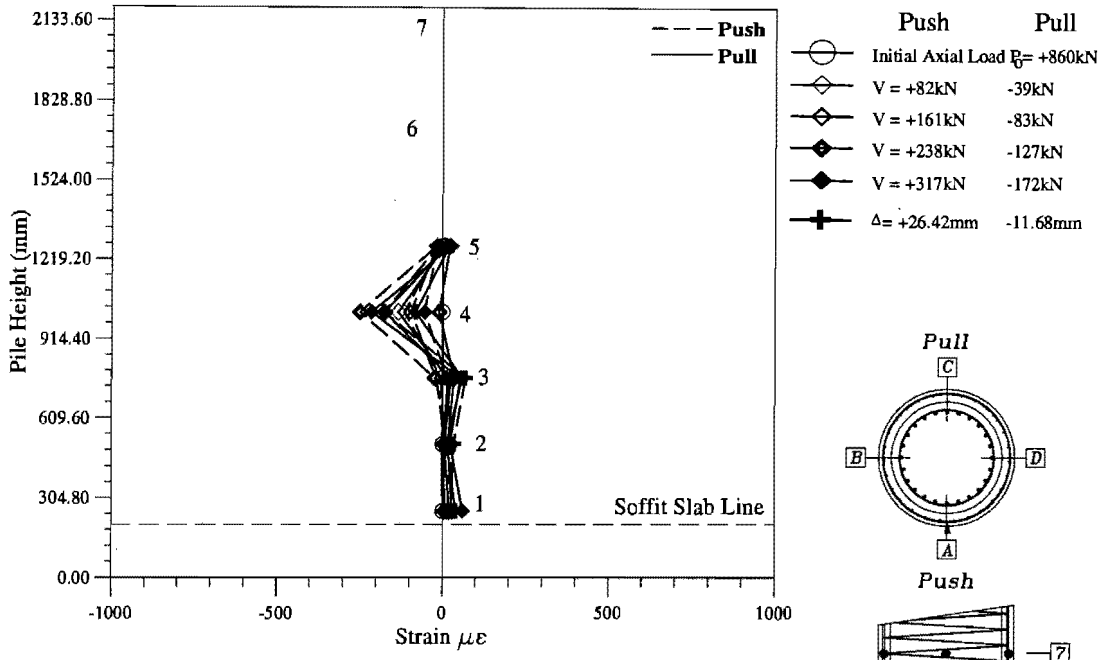

(a) Vertical Strain Profiles - Initial Stages of Testing

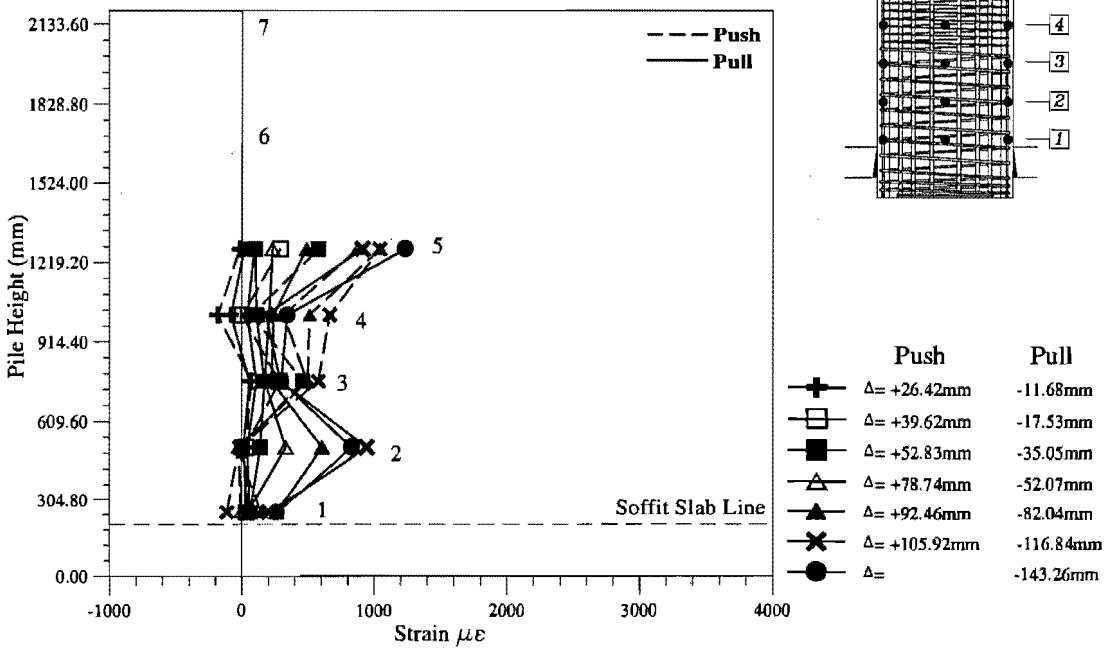

(b) Vertical Strain Profiles - Final Stages of Testing

Fig. 7-37 Pile Transverse Reinforcement Strain Profiles Along Line *A*

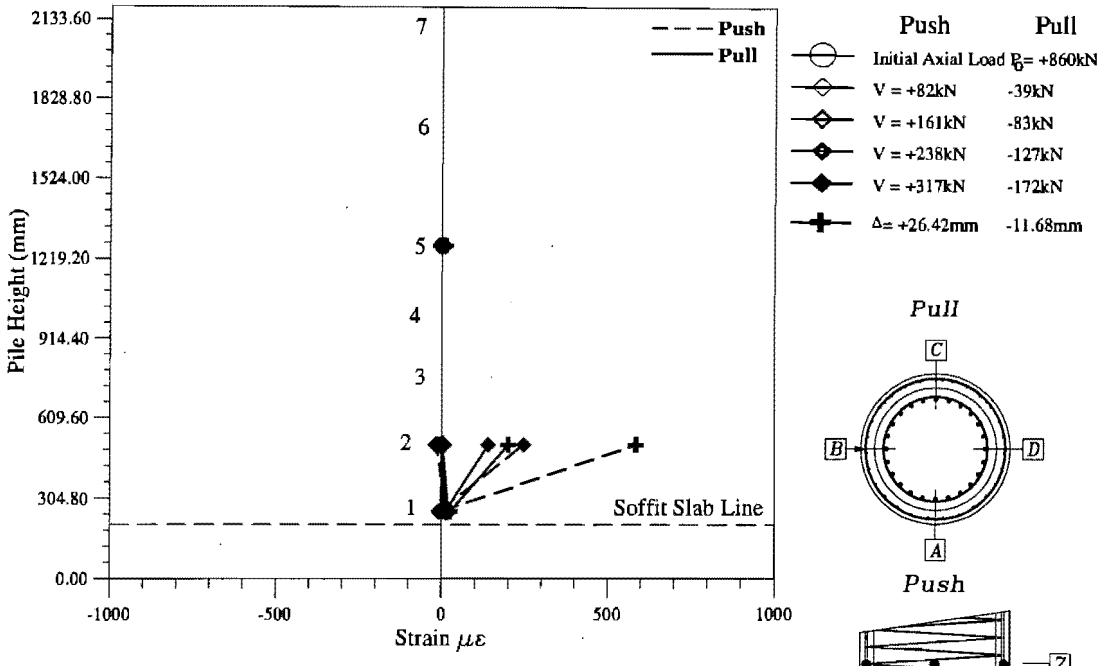

(a) Vertical Strain Profiles - Initial Stages of Testing

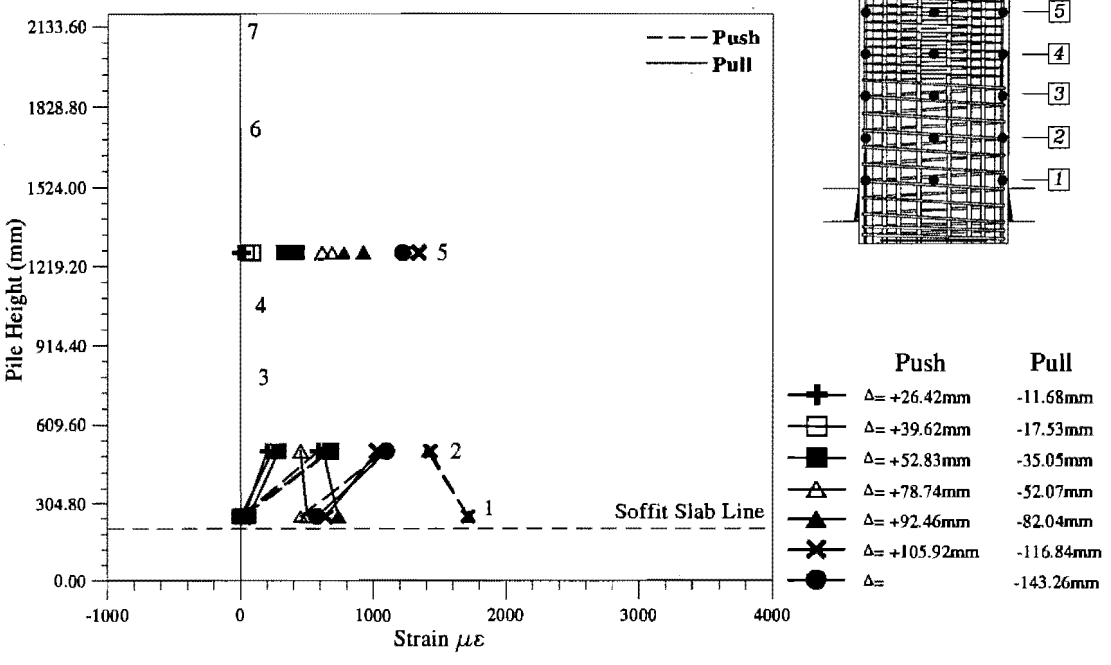

(b) Vertical Strain Profiles - Final Stages of Testing

Fig. 7-38 Pile Transverse Reinforcement Strain Profiles Along Line ***B***

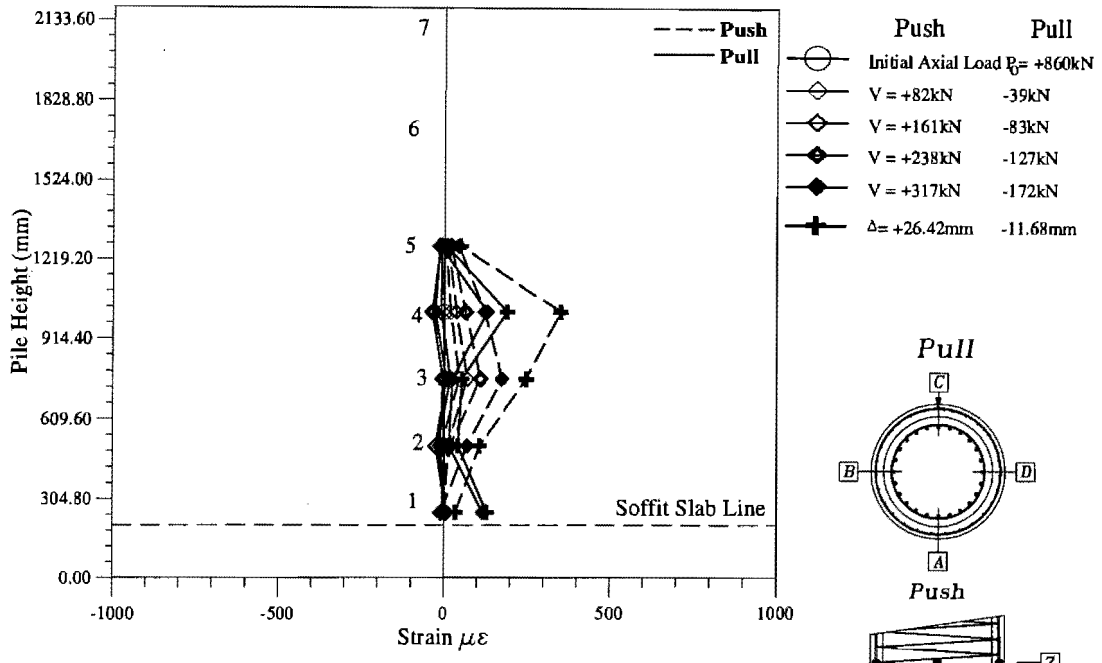

(a) Vertical Strain Profiles - Initial Stages of Testing

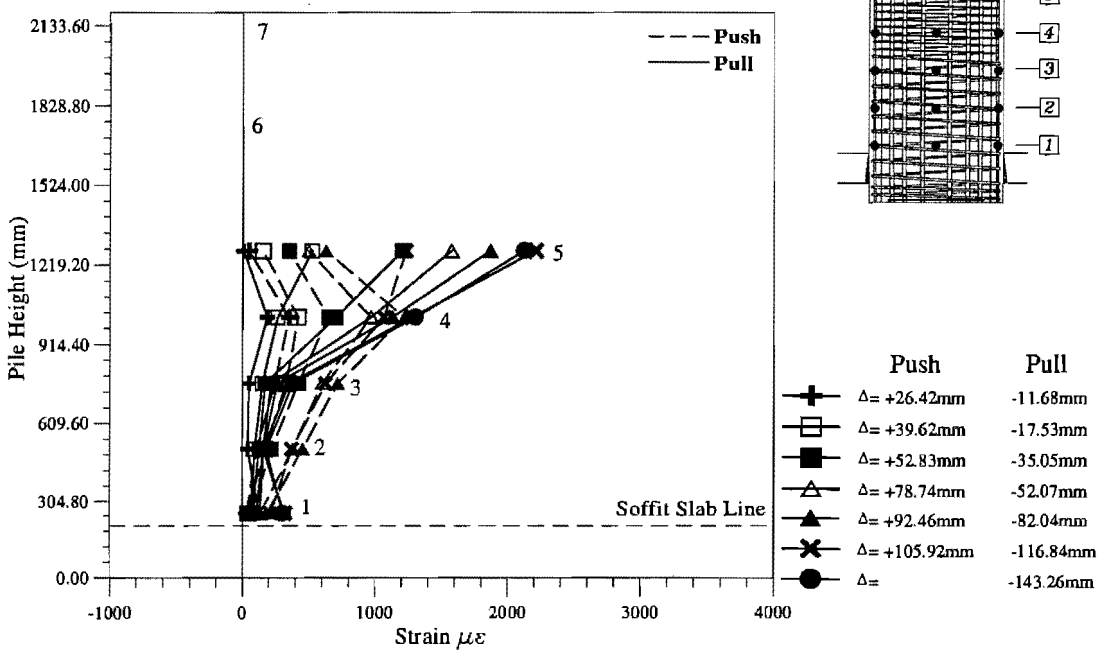

(b) Vertical Strain Profiles - Final Stages of Testing

Fig. 7-39 Pile Transverse Reinforcement Strain Profiles Along Line *C*

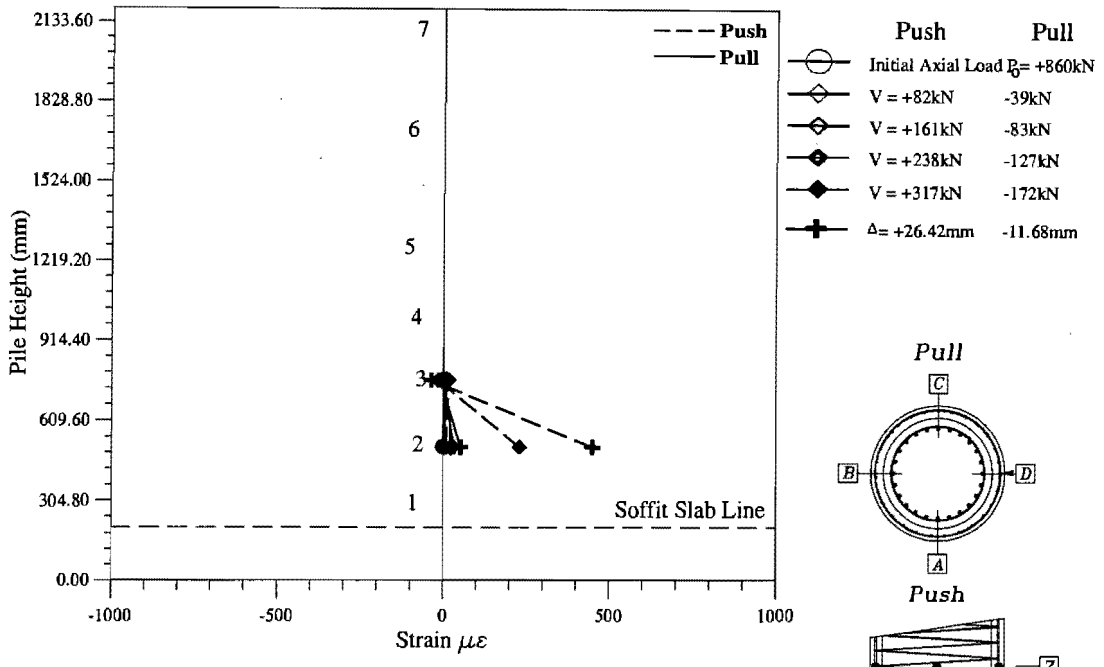

(a) Vertical Strain Profiles - Initial Stages of Testing

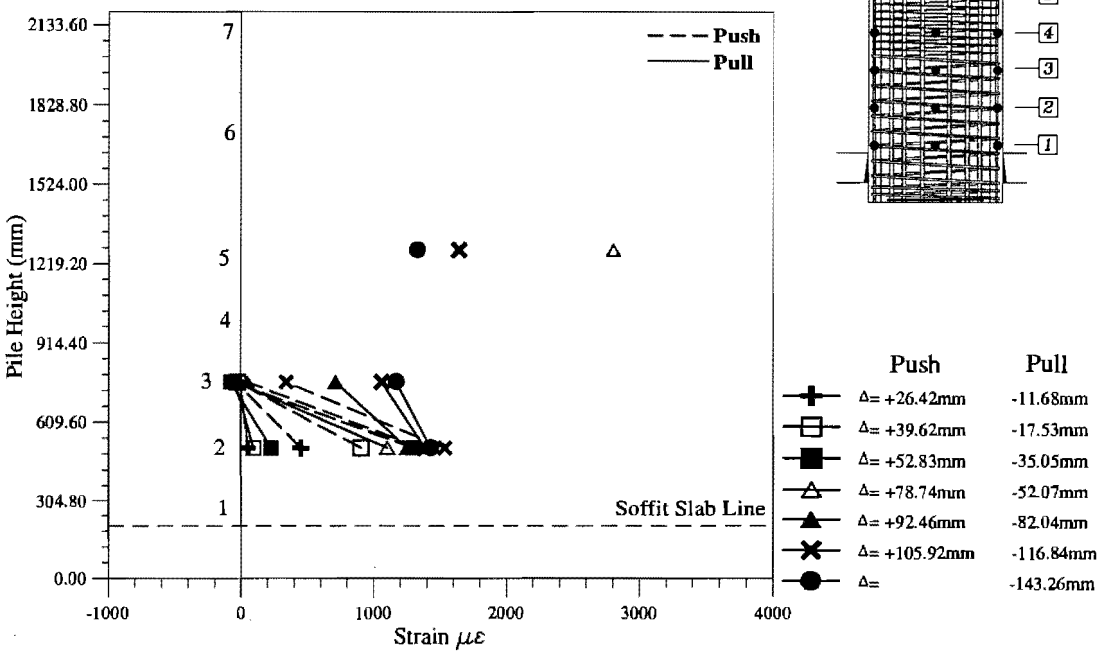

(b) Vertical Strain Profiles - Final Stages of Testing

Fig. 7-40 Pile Transverse Reinforcement Strain Profiles Along Line *D*

7.8 Pile Cap Reinforcement Strain Profiles

Maximum strains in the pile cap top and bottom reinforcement, positioned in the direction of applied lateral load, were registered in the pile cap bottom reinforcement at strain gage ***Bottom 3-C***. Note that bottom reinforcement refers to position of reinforcement as it occurs in the prototype structure. For strain gage location, refer to **Fig. 3-37**. Strain readings illustrated in **Fig. 7-41** indicate minimum strains recorded in this reinforcement. Thus, as in test unit *COR1,* strain profiles for the pile cap top and bottom reinforcement are not shown since strain levels were always considerably below yielding.

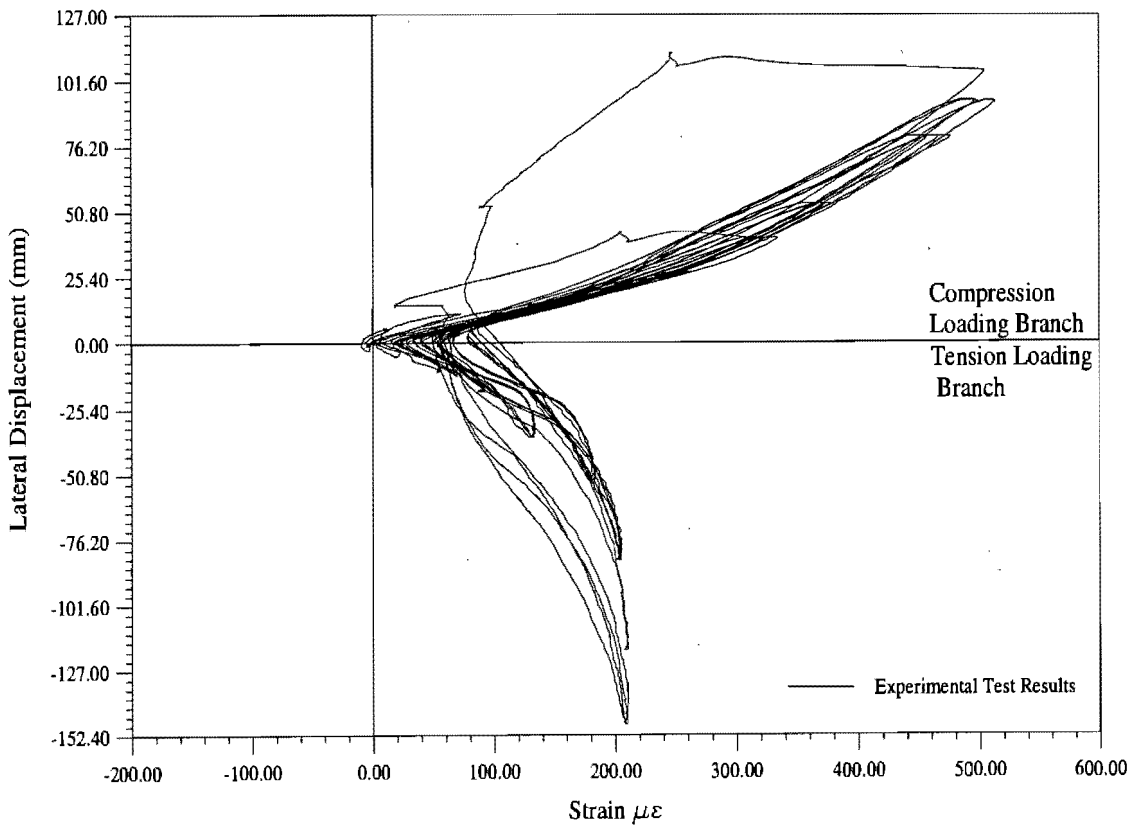

Fig. 7-41 Lateral Deflection versus Strain
Strain Gage Pile Cap Bottom Reinforcement ***Bottom 3-C***

Maximum strains in the pile cap vertical reinforcement were registered at strain gage ***3-B***. For strain gage location, refer to **Fig. 3-39**. As in test unit *COR1,* strain readings illustrated in **Fig. 7-42** indicate minimum strains recorded in this reinforcement. Thus, strain profiles for the pile vertical reinforcement are not shown since strain levels were always considerably below yielding. Strain levels recorded in this reinforcement can be taken as an indication of joint performance. Levels of principal tensile stress computed in Chapter 2 and presented in **Fig. 2-27** indicate that no joint shear failure was expected as a result of minimum level of expected stress in the joint region, which were $0.16\sqrt{f_c'} < 0.29\sqrt{f_c'}$ *[MPa]* and $0.27\sqrt{f_c'} < 0.29\sqrt{f_c'}$ *[MPa]*. These values corroborate observed test results in which negligible strains were recorded in the pile cap vertical reinforcement indicating that no joint cracking occurred. Note, that these values are the same for all the three test units.

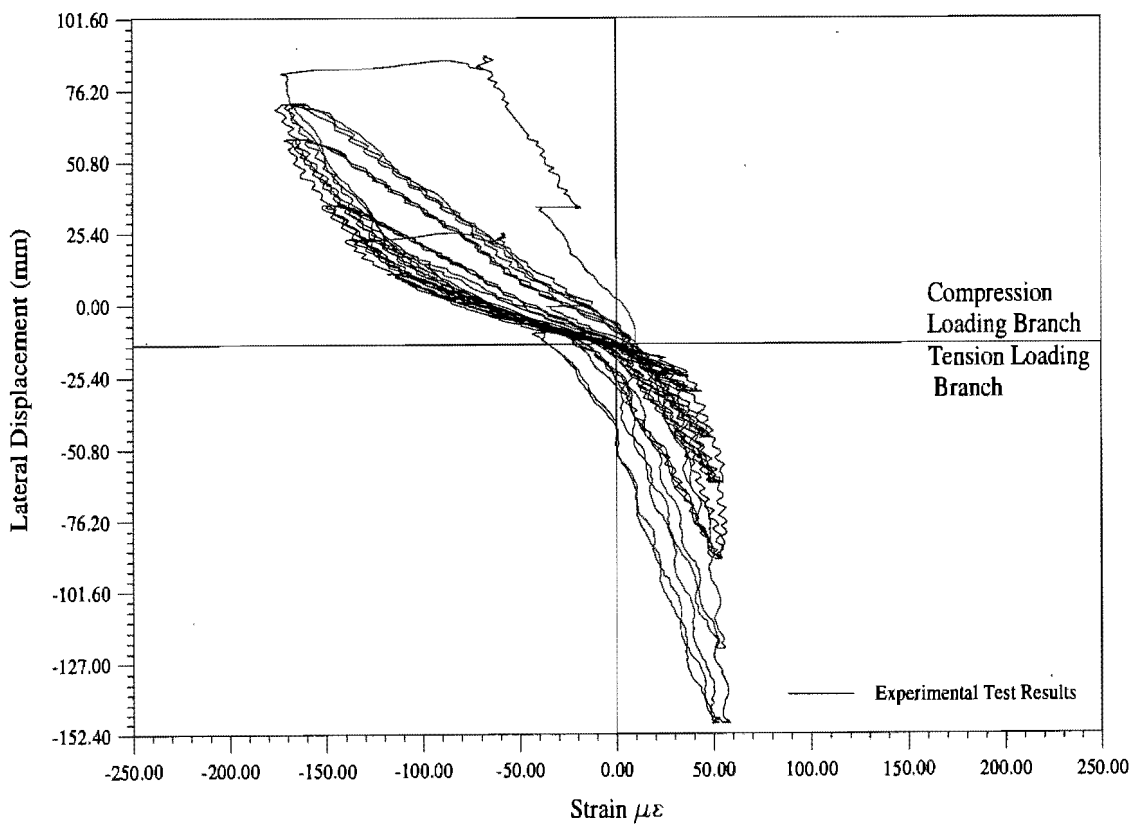

Fig. 7-42 Lateral Deflection versus Strain
Strain Gage Pile Cap Vertical Reinforcement ***3-B***

7.9 Pile Cap Rotation

Similar to test units *COR1* and *COR2*, uplift of the pile cap from the strong floor was monitored by linear potentiometers positioned at the base of the pile cap, as illustrated in **Fig. 3-41** and **Fig. 3-42**. Rotation of the pile cap was then computed based on equation **(5.5)**. Contribution of pile cap rotation to pile lateral deflection may then be estimated according to equation **(5.6)**. Based on the values presented in **Fig. 7-43**, the maximum pile cap rotation, ψ_{cap}, was 0.000024 rad^{-1} and it was computed when the lateral deflection was +78.74 mm. This rotation of the pile cap will contribute 0.14 mm to the pile lateral deflection at peak response, which is rather small and, as a result, no correction to the pile lateral deflection was computed.

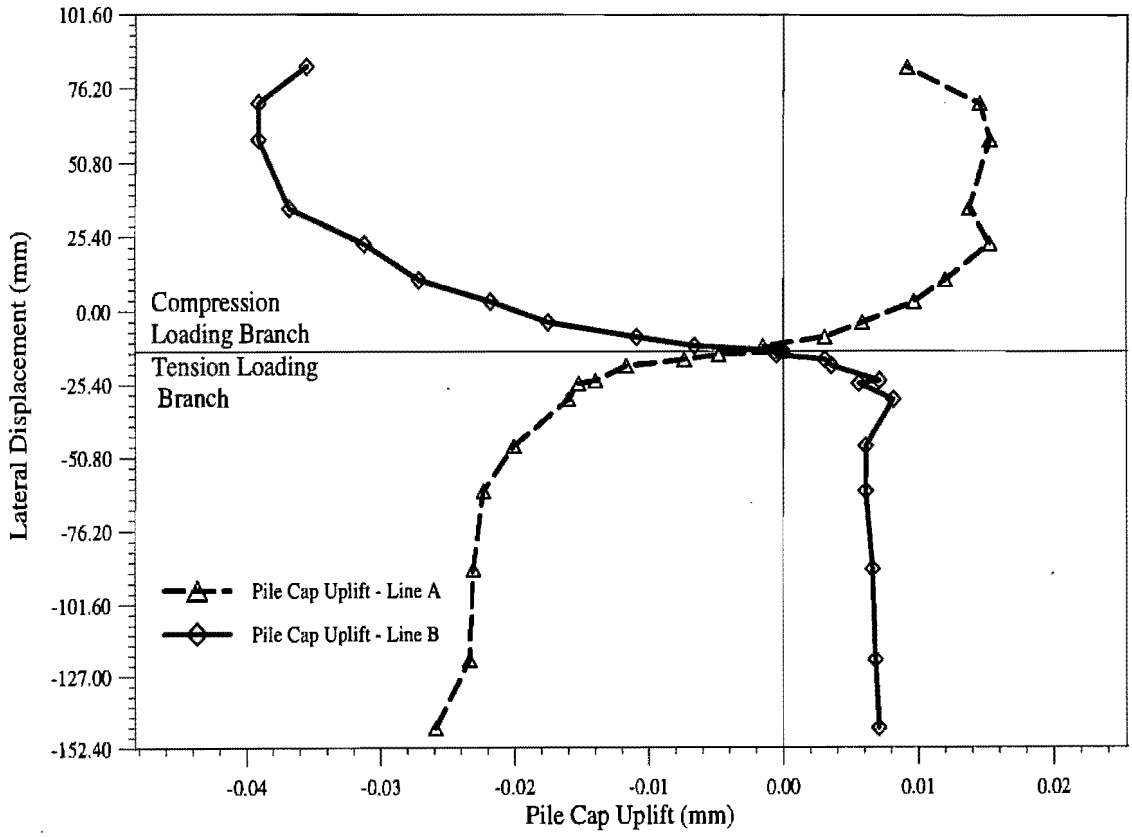

Fig. 7-43 Lateral Deflection versus Pile Cap Uplift

8. Discussion of Experimental Test Results

In this section a brief discussion of key experimental test results and post test analyses investigated for the three test units *COR1, COR2* and *COR3* are presented.

8.1 Test Units *COR1, COR2* and *COR3*

Development of the pre-test analysis for test unit *COR1* and *COR2* force displacement response outlined in Chapter 2 include the contribution of the following terms to the pile lateral deflection:

A. Confined concrete model proposed by Mander **[15]** was employed in the moment curvature analysis to compute forces present in the concrete.

B. The column height, H_{pile}, was used for lateral deflection calculations.

Section 5.2 and 6.2 present the force-deformation characteristics for test units *COR1* and *COR2*. Comparison of the pre-test analysis curve with the experimental test results indicates a lower flexural strength than initially predicted. In lieu of this difference, a post-test analysis was carried out to evaluate the response of test unit *COR1* and *COR2*. Development of the post-test analysis for test unit *COR1* and *COR2* is presented in the next section and the force-displacement response includes the contribution of the following terms to the pile fixed base lateral deflection:

C. Confined concrete model proposed by Bjerkeli **[24]** and modified by Ibrahim **[25]** was employed in the moment curvature analysis to compute forces present in the concrete.

D. The effective column height, H_{eff}, was used for lateral deflection calculations **[26]**.

8.1.1 Test Unit *COR1* and *COR2* - Post-Test Analysis Concrete Models

Pre-test analysis predicted within an acceptable margin of error the behavior of the test unit while in the tension loading branch, as illustrated in **Fig. 5-12**. However, within the compression loading branch, the structure achieved a lower flexural strength than initially predicted. Experimental test results suggest that the concrete model used in the pre-test analysis, which was the Mander model for confined and unconfined concrete, predicts a structure with a lower flexural strength under high levels of axial load.

Nawy **[27]** classifies a concrete with a compressive strength of at least 41MPa as high-strength concrete. Chemical and mineral admixtures are used in the production of concrete to achieve concrete with this level of strength. Values for the high strength concrete compressive strength utilized in casting of the concrete shells are presented in **Table 3-1**, which shows that the minimum concrete compressive strength at 28 days was f'_c=58MPa and, at the day of the test mark, the concrete compressive strength was f'_c=68MPa for test unit *COR2*. This indicates that the concrete utilized in the manufacturing of test units *COR1*, *COR2* and *COR3* may be classified as high-strength concrete. The day of the test concrete compressive strength was utilized in the development of the post-test analysis for all three test units.

Stress-Strain relationships for high-strength concrete proposed by Ibrahim **[24]**, Muguruma **[28]**, and Yong **[29]** were investigated to develop the post-test analysis of test units *COR1* and *COR2*. The Bjerkeli concrete model modified by Ibrahim was implemented into the moment curvature analysis for post-test investigation because it gave the closest agreement with the experimental test results. In this section, a brief description of the Mander and modified-Bjerkeli model are presented.

8.1.1.1 *Mander Model*

The model proposed by Mander was developed for concrete subjected to uniaxial compressive loading and confined by transverse reinforcement. In the Mander model the confined compressive strength is given by the expression:

$$f'_{cc} = f'_{co}\left(-1.254 + 2.254\sqrt{1 + \frac{7.94 f'_l}{f'_{co}} - 2\frac{f'_{cc}}{f'_{co}}}\right) \tag{8.1}$$

where the effective lateral confining pressure, f'_l, is given by the expression:

$$f'_l = k_e f_l \tag{8.2}$$

In equation **(8.2)** f_l is the lateral confining pressure provided by the transverse reinforcement **[8]**, and k_e is the confinement effectiveness coefficient which for a circular section confined with circular spirals is determined according to the following expression:

$$k_e = \frac{1 - \frac{s'}{2 d_s}}{1 - \rho_{cc}} \tag{8.3}$$

where s' is the vertical clear distance between spirals and d_s is the spirals center to center diameter. The peak stress, f'_{cc}, as shown in **Fig. 8-1**, is reached at a strain, ε_{cc}, given by:

$$\varepsilon_{cc} = \varepsilon_{co}\left(1 + 5\left(\frac{f'_{cc}}{f'_{co}} - 1\right)\right) \tag{8.4}$$

where ε_{co} is the strain at the peak unconfined concrete compression stress generally assumed as 0.002. In the Mander model, for any given concrete strain ε the corresponding concrete stress is given by the expression:

$$f_c = \frac{f'_{cc}\, x\, r}{r - 1 + x^r} \tag{8.5}$$

where $x=\varepsilon_c/\varepsilon_{cc}$ and $r=E_c/(E_c-E_{sec})$. The tangent modulus of elasticity of concrete is obtained by the relation:

$$E_c = 5000\sqrt{f'_{co}}\ [MPa] \tag{8.6}$$

and the secant modulus of elasticity of concrete by the relation:

$$E_c = \frac{f'_{cc}}{\varepsilon_{cc}} \tag{8.7}$$

Based on the unconfined concrete compressive strength f'_c=69MPa at the 28 day mark, and the equations presented above, the stress-strain relationships for test unit *COR1* concrete model were determined and are presented in **Fig. 8-1** for a transverse reinforcement ratio of 0.40%, which corresponds to the section above the pile cap interface reinforcement with #3 spirals at 84 mm on centers.

8.1.1.2 Modified Bjerkeli Model

The empirical model developed by Bjerkeli et al. and modified by Ibrahim was used in the development of the post-test analysis moment curvature analysis for test unit *COR1* and *COR2*. Test unit *COR3* pre-test analysis was developed with the modified Bjerkeli concrete model for high strength concrete. The empirical models developed by Bjerkeli were based on test of concentrically loaded circular and rectangular high-strength concrete columns confined with by means of transverse reinforcement. Unlike the Mander model, which is described by a single curve, in this model different curves are defined to fully describe the stress-strain relationships.

The ascending branch in the concrete model is in the form:

$$f_c = \frac{E_c\,\varepsilon_c}{1 + (E_c / E_{sec} - 2)(\varepsilon_c / \varepsilon_{cc})(\varepsilon_c / \varepsilon_{cc})^2}\ ; \quad \varepsilon_c < \varepsilon_{cc} \tag{8.8}$$

where the tangent modulus of elasticity of concrete is obtained by the relation:

$$E_c = 9500\ (f'_{co})^{0.3}\ [MPa] \tag{8.9}$$

which is different than the tangent modulus of elasticity of concrete presented in the Mander model and the secant modulus of elasticity of concrete is defined as in the Mander model. In the Bjerkeli model, the confined compressive strength is given by the expression:

$$f'_{cc} = f'_{co} + 4.0\,K_g f_l\ ; \quad 40MPa < f'_{co} < 80MPa \tag{8.10}$$

where K_g is the section geometry factor and, as the name suggests, is developed based on the section geometry and is similar to k_e in the Mander model. K_g is a modified variable by Ibahim [25] and is given by the following expression :

$$K_g = \left(1 - \frac{s'}{d_s}\right)\left(1 - \frac{c}{5.5\,d_s}\right) \tag{8.11}$$

where c is the distance between laterally supported longitudinal bars.

Similar to the Mander model, the peak stress f'_{cc} as shown in **Fig. 8-2**, is reached at a strain, ε_{cc}, given by:

$$\varepsilon_{cc} = 0.025 + 0.0250\ K_g \frac{f_l}{f'_{co}} \tag{8.12}$$

This variable was modified from the original model according to a similar model proposed by Ibrahim et al **[25]**.

The second curve in the Bjerkeli model describes the unloading branch in the form:

$$f_c = f'_{cc} - 0.15 \frac{f'_{cc}}{\varepsilon_{0.85} - \varepsilon_{cc}} (\varepsilon_c - \varepsilon_{cc}) : \quad \varepsilon_c > \varepsilon_{cc} \tag{8.13}$$

where $\varepsilon_{0.85}$ is given by the equation:

$$\varepsilon_{0.85} = \varepsilon'_{0.85} + 0.040\ K_g \frac{f_l}{f'_{co}(1 - F)} \tag{8.14}$$

and the variables $\varepsilon'_{0.85}$ and F are given by the expressions:

$$\varepsilon'_{0.85} = 0.025 \left[\left(\frac{17.07}{f'_{co}} \right)^2 + 1 \right] \tag{8.15}$$

and the variable F is taken as:

$$F = \frac{1}{1 + \left(\frac{1}{f_l K_g} \right)^{\frac{1}{4}}} \tag{8.16}$$

Similar to the Mander model, the stress-strain relationships for test unit *COR1* concrete model were determined and are presented in **Fig. 8-2** for the pile section bottom layer.

Stress-strain relationships proposed by Mander **[15]** and modified Bjerkeli model **[25]** were investigated. Referring to **Fig. 8-1** and **Fig. 8-2**, it can deduced from the numerical values presented in these figures that the modified Bjerkeli model leads to a model with a higher maximum compressive strength for confined concrete for the levels of confinement used in the construction of the test unit, which explains higher flexural strength obtained in test results.

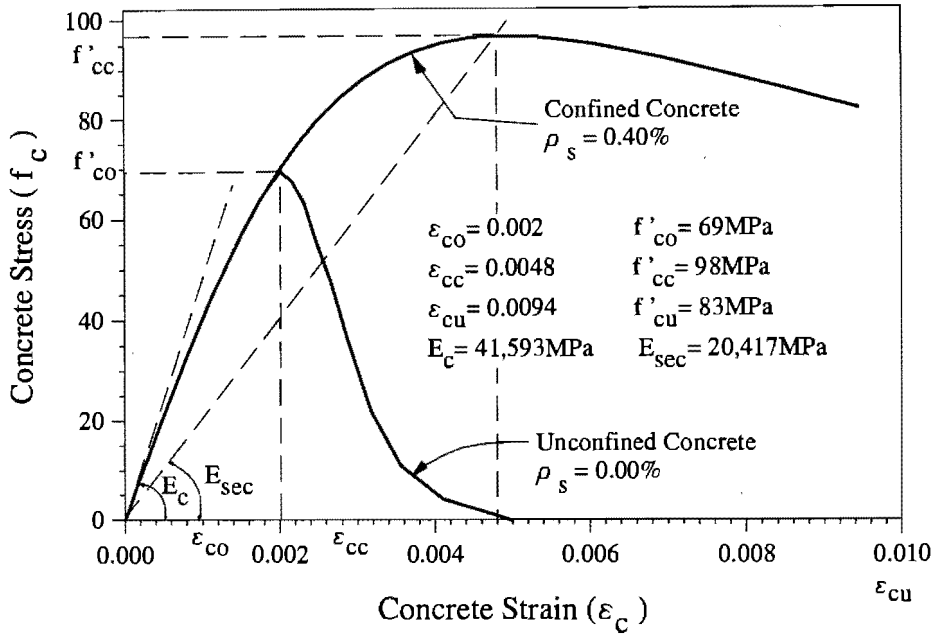

Fig. 8-1 Stress-Strain Curve for Confined and Unconfined Concrete - Mander Model

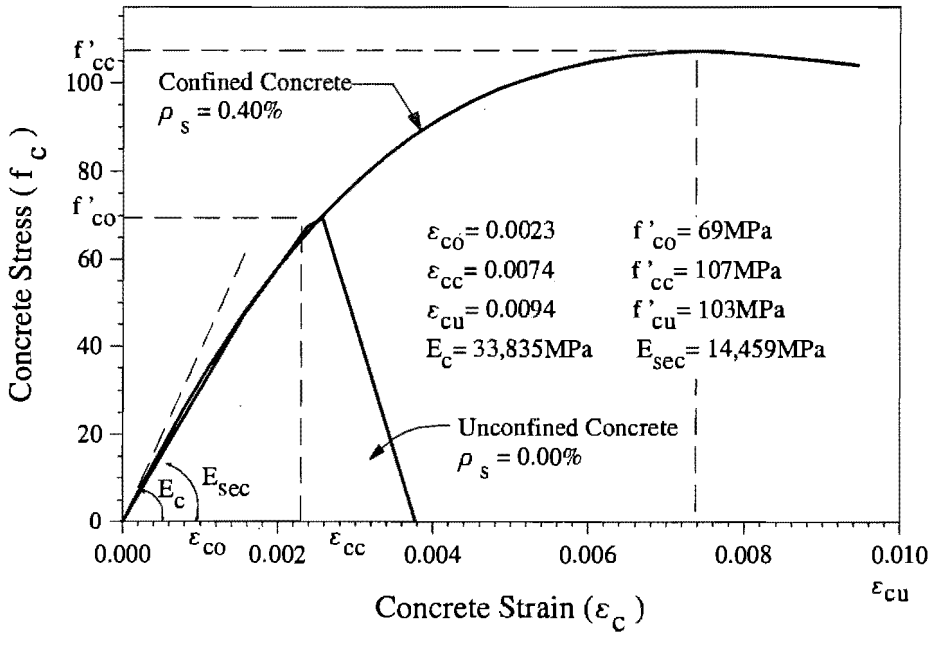

Fig. 8-2 Stress-Strain Curve for Confined and Unconfined Concrete - Modified Bjerkeli Model

For example, for a transverse reinforcement ratio of 0.40%, the maximum confined concrete compressive strength predicted by the Mander model was 98 MPa and 107 MPa for the modified Bjerkeli model, which represents a difference of approximately 10%. For test unit *COR1*, the maximum pre-test analysis predicted lateral load was +425 kN and maximum achieved lateral load was +520 kN, which indicates a difference of approximately 18%. For test unit *COR2*, the maximum pre-test analysis predicted lateral load was +921 kN and maximum achieved lateral load was +1,009 kN, which indicates a difference of approximately 9%. It is important to recognize that a direct comparison between predicted and achieved lateral load is somewhat misleading because at the base of the pile section, the section is confined by the soffit slab, which will lead to a different strength ratio.

The model proposed by Bjerkeli was then implemented into the moment curvature analysis to develop the post-test analysis for test units *COR1* and *COR2*. As previously indicated, the model proposed by Bjerkeli was implemented into the moment curvature analysis to develop the pre-test analysis for test unit *COR3* and *COR2*. **Fig. 8-3** presents these two models for a direct comparison of the tangent modulus of elasticity and maximum achieved confined concrete compressive strength. Stress-Strain relationships based on the Mander model and the modified Bjerkeli model for confined concrete were investigated for different levels of horizontal confinement encountered along the length of the pile and are presented in **Fig. 8-3**. Near the pile cap and in the region confined by the concrete soffit slab, a horizontal volumetric reinforcement ratio of approximately 3.5% was used, which reflects a section with a tie spacing of one tie diameter. It can be seen that for low levels of horizontal confinement the three models yield similar results. However, for large confinement ratios, there is a great difference between the three models.

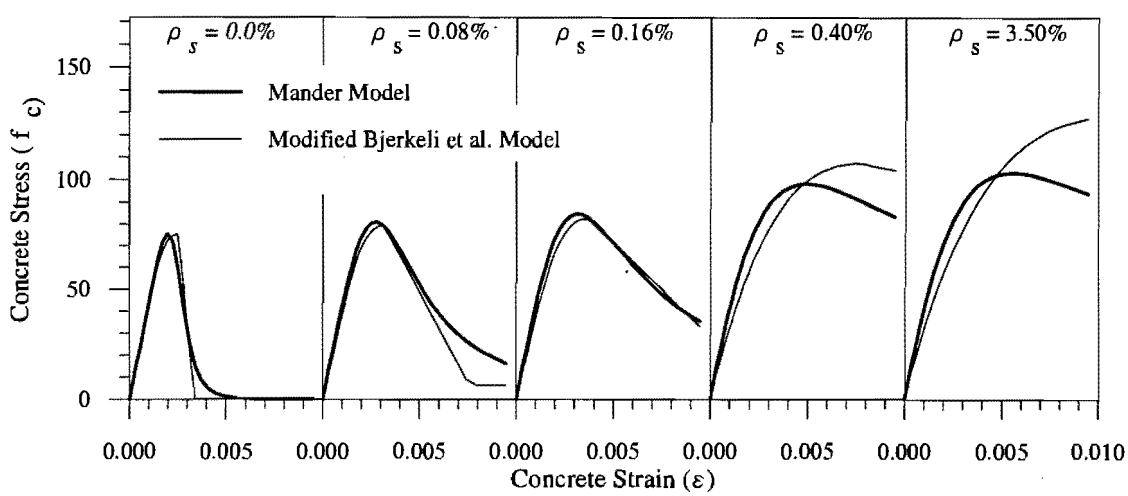

Fig. 8-3 Concrete Models Stress-Strain Characteristics

8.1.2 Test Units *COR1, COR2* and *COR3*- Post-Test Analysis Tensile Strain Penetration Contribution to Pile Lateral Deflection

Contribution of tensile strain penetration to top lateral deflection was effected by considering the pile effective cantilever length for lateral deflection according to the expression:

$$H_{eff} = H_{pile} + 0.022\, d_b f_s \qquad [MPa] \qquad \textbf{(8.17)}$$

where d_b is the pile main bar diameter and f_s is the pile main bar stress obtain from the moment curvature analysis.

Equation **(8.17)** indicates the pile effective cantilever length increases as the extreme bar stress increases. The effective cantilever length was introduced into the computation of the lateral deflection employing the second moment area theorem according to the expression:

$$\Delta = \sum_{X=0}^{H_{eff}} \left((\varphi_i + \varphi_{i-1}) \frac{\Delta_x}{2} X \right) \qquad \textbf{(8.18)}$$

where which φ_i and φ_{i-1} are the curvatures in the pile section within the segment Δ_x and X is the distance from the center of the respective segment to the center of the load stub as shown in **Fig. 8-4**. Curvature profiles along pile height for post-test analysis are presented in **Fig. 8-4**, where L_a is computed according to the second term presented in equation **(8.17)**. Refer to **Fig. 5-12**, **Fig. 6-18** and **Fig. 7-18** for test units *COR1*, *COR2* and *COR3* post-analysis results.

According to equation **(8.18)** contribution of strain penetration into fixed base equation may be computed based on:

$$\varphi_{base}\, L_a \left(H_{pile} + \frac{L_a}{2} \right) \qquad \textbf{(8.19)}$$

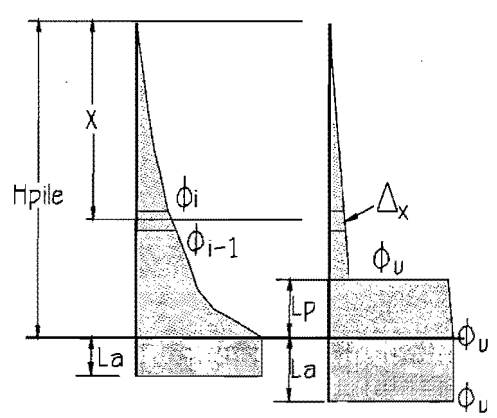

(a) Peak Load Curvature Profile *(b) Ultimate Curvature Profile*

Fig. 8-4 Curvature Profiles

8.2 Comparison of Test Results

In this section a brief comparison between the structural response of test units *COR1*, *COR2* and *COR3* is presented. The performance of these test units may be formulated in terms of load versus deformation characteristics and damage states based on cracking patterns, first yielding of inner core longitudinal reinforcement, peak loads and ultimate state.

8.2.1 Test Units *COR1* and *COR3*

The hysteretic lateral load versus lateral deflection diagrams for test units *COR1* and *COR3* presented in **Fig. 5-12** and **Fig. 7-18**, respectively, suggest a behavior essentially ductile because there is no excessive strength degradation with successive cycling or increasing displacement, and the hysteretic loops are stable with good energy absorption. A slight pinching of the loops in the transition between the compression and tension loading branch is observed for higher levels of displacement because of the variations in the axial load, as previously described in Chapter 5.

The total area inside the hysteretic envelope shown in **Fig. 8-5** is approximately the same for test units *COR1* and *COR3*. The area inside the hysteresis envelope is a measure of the amount of energy that can be dissipated by the section because of plastic deformations in the plastic hinge region. Thus, the amount of energy dissipated by test unit *COR1* pile section was approximately the same as test unit *COR3* pile section.

One of the first damage states that may be formulated from visual observations is the cracking limit state, which corresponds to the onset of cracking of the concrete. In test unit *COR1*, onset of cracking was observed at a displacement ductility of μ_Δ=+1.5x3 in the compression loading branch, accompanied by a vertical splitting crack as recorded in **Fig. 8-6**. At this stage the horizontal peak load was +415 kN, with a corresponding axial load of 2630 kN and a lateral deflection of +25.65 mm. Comparatively, onset of cracking of test unit *COR3* occurred at a lower stage when the lateral load was recorded at +317 kN, which corresponds to first section yielding. The axial load and lateral deflection corresponding to this stage are, respectively, +2,311 kN and +18.44 mm, as shown in **Fig. 8-7**.

Another limit state that may be formulated is the limit in which yielding of the inner core longitudinal reinforcement is first recorded, which corresponds to the reinforcement first yielding state. **Fig. 8-8** suggests that yielding of the longitudinal reinforcement along inner core bar ***A*** was not reached until displacement ductility of μ_Δ=-1.5 (-20.57 mm) for test unit

COR1 and μ_Δ=-3.0 (-35.05 mm) for test unit *COR3*. **Fig. 8-10** suggests that yielding of the longitudinal reinforcement along inner core bar ***C*** was not reached until displacement ductility of μ_Δ=+2.0 (34.04 mm) for test unit *COR1* and μ_Δ=+1.5 (+39.62 mm) for test unit *COR3*. Furthermore, referring to **Fig. 8-8** through **Fig. 8-11**, it is clear that the strain profiles for test unit *COR1* and *COR3* have approximately the same shape.

Previously, it was shown that the energy absorption for test units *COR1* and *COR3* was approximately the same, which suggests that the maximum plastic hinge length for both test units should be approximately the same. Based on the curvature profiles for both test units shown in **Fig. 8-12**, two regions of plastic deformations were observed in both loading branches for each test unit. The plastic hinge reached a maximum height of approximately 356 mm near the pile cap interface and 609 mm in the region near the termination of the longitudinal reinforcement for both test units.

In the compression loading branch, a maximum lateral force of +520 kN was recorded at approximately μ_Δ=3 in test unit *COR1,* and in test unit *COR3*, the peak lateral load was reached at about the same ductility level μ_Δ=3x1 at 495 kN. In the tension loading branch, a maximum lateral force of -227 kN was recorded during cycle μ_Δ=-6x1 for test unit *COR1*, and in test unit *COR3,* the pile section achieved a higher flexural strength than test unit *COR1*. At peak response, the maximum lateral force of -248 kN was recorded in the tension loading branch during cycle μ_Δ=-9x1 for test unit *COR3*.

Fig. 8-13 and **Fig. 8-14** indicate that in both test units a second region of plastic deformations was achieved in the region where the inner core longitudinal reinforcement terminates implied by the extent of spalling of the cover concrete during the final stages of the testing procedure. In addition, test unit *COR1* cracking pattern below this second plastic hinge region exhibits a significantly higher amount of horizontal and vertical splitting cracks than observed in test unit *COR3*. In test unit *COR1,* the cracking pattern shows that at most of the prestressing strands location vertical splitting cracks occurred and in test unit *COR3* fewer and less extensive vertical splitting cracks are visible. This could be a result of the earlier cracking of test unit *COR3* at the termination of the longitudinal reinforcement with a single horizontal cracking at this level dominating the response of the section. Thus, with fewer cracks, bonding of the prestressing strands was more effective in test unit *COR3* than in test unit *COR1*, and higher forces could be developed in the prestressing strands of test unit *COR3* in the development length region, which confirms the higher achieved peak loads in test unit *COR3* in the tension loading branch.

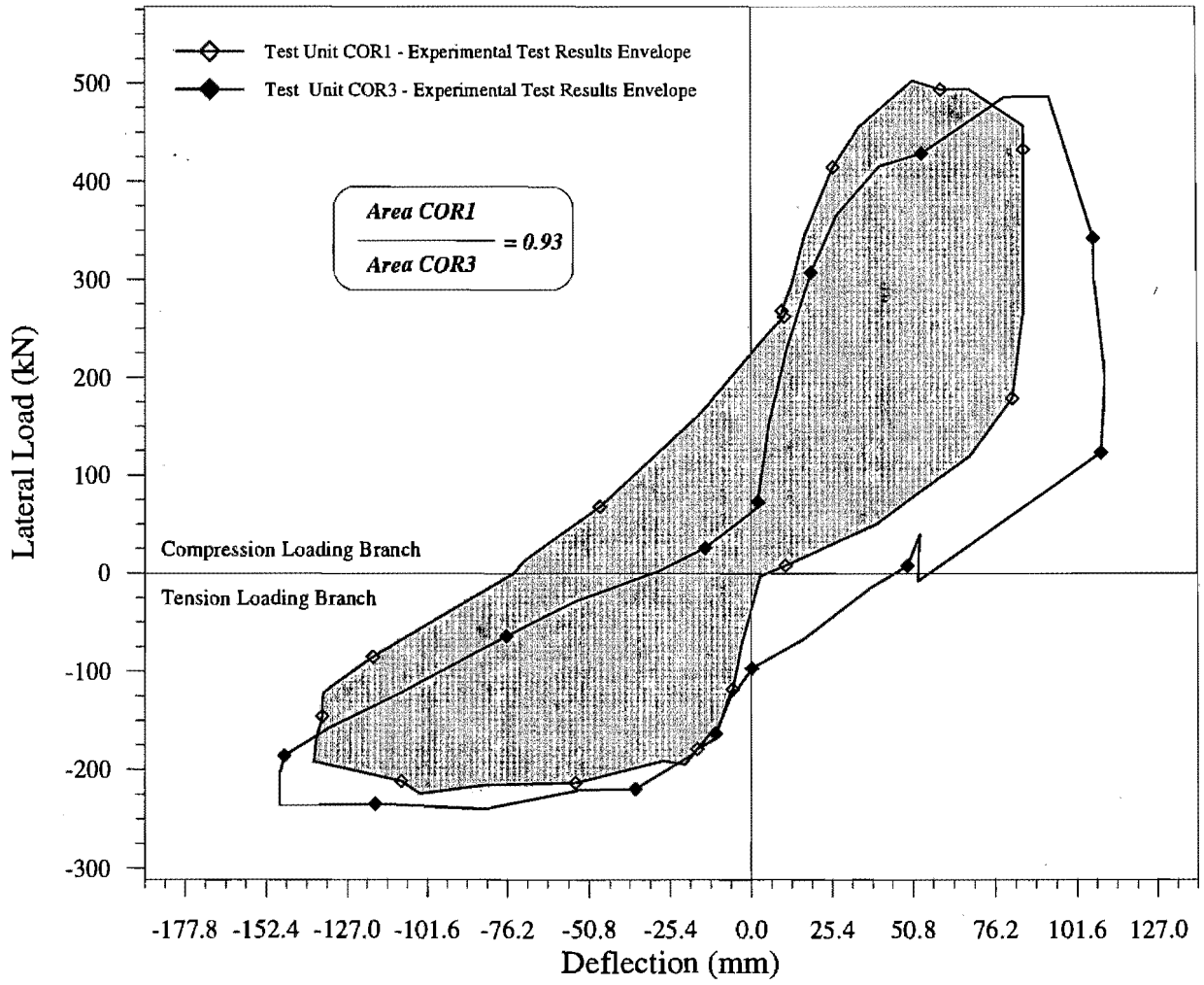

Fig. 8-5 Test Units *COR1* and *COR3* - Lateral Load versus Lateral Deflection Envelope

Fig. 8-6 Onset of Flexural Cracking at μ_Δ 1.5x3 - Test Unit *COR1*

Fig. 8-7 Onset of Flexural Cracking at First Section Yielding - Test Unit *COR3*

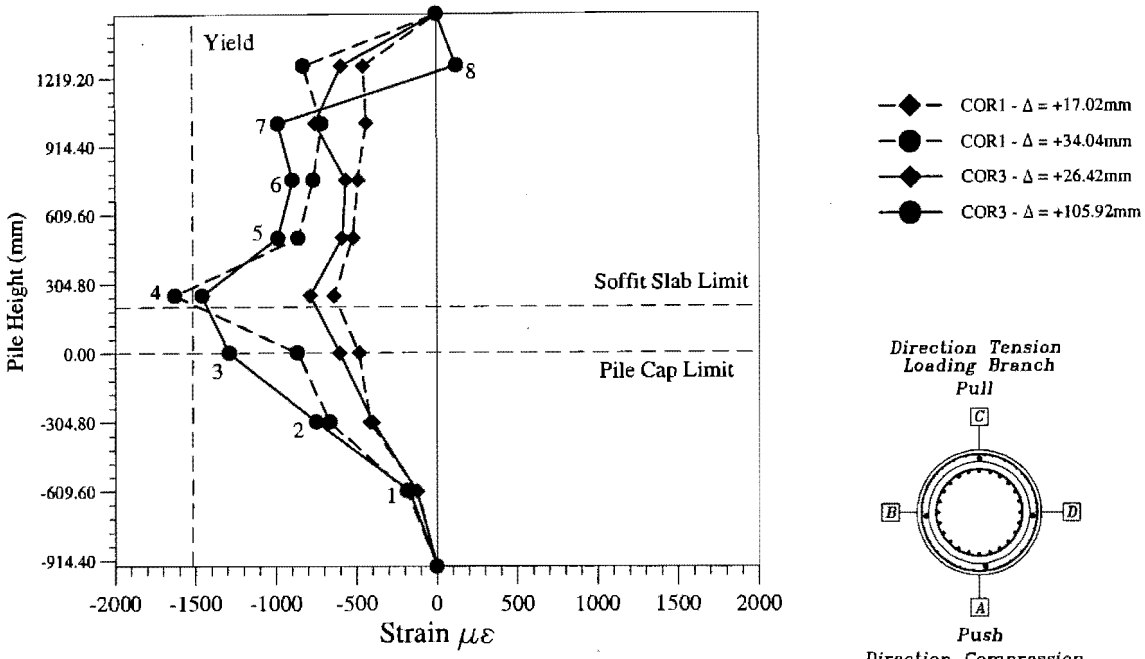

(a) Vertical Strain Profiles - Compression Loading Branch

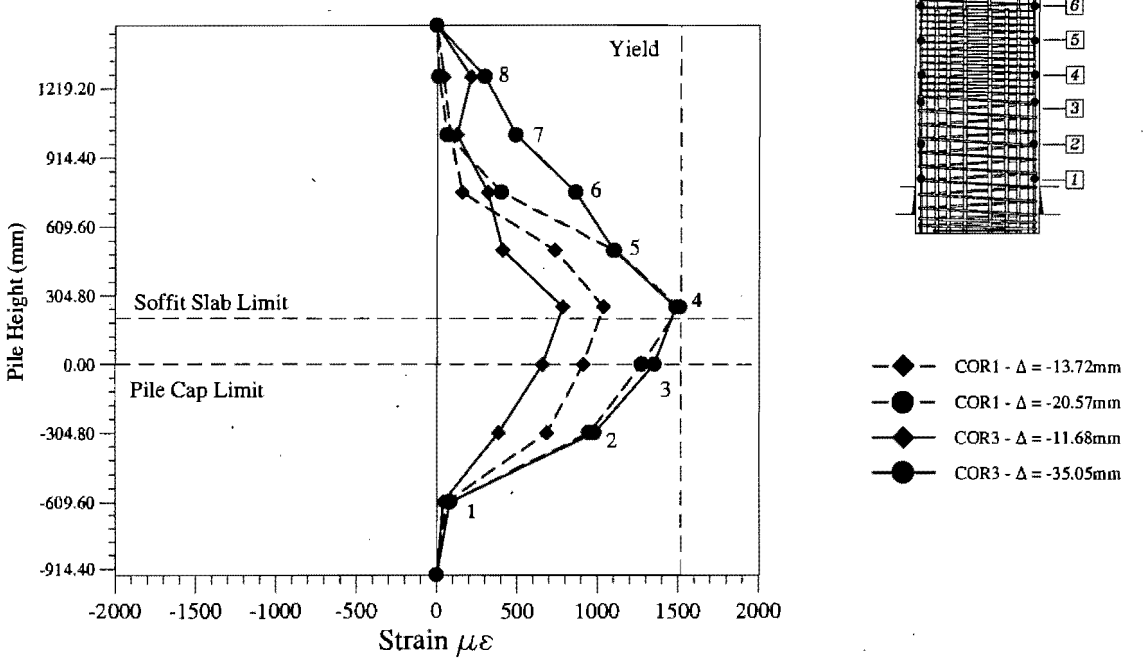

(b) Vertical Strain Profiles - Tension Loading Branch

Fig. 8-8 Vertical Strain Profiles Inner Core Bar *A*

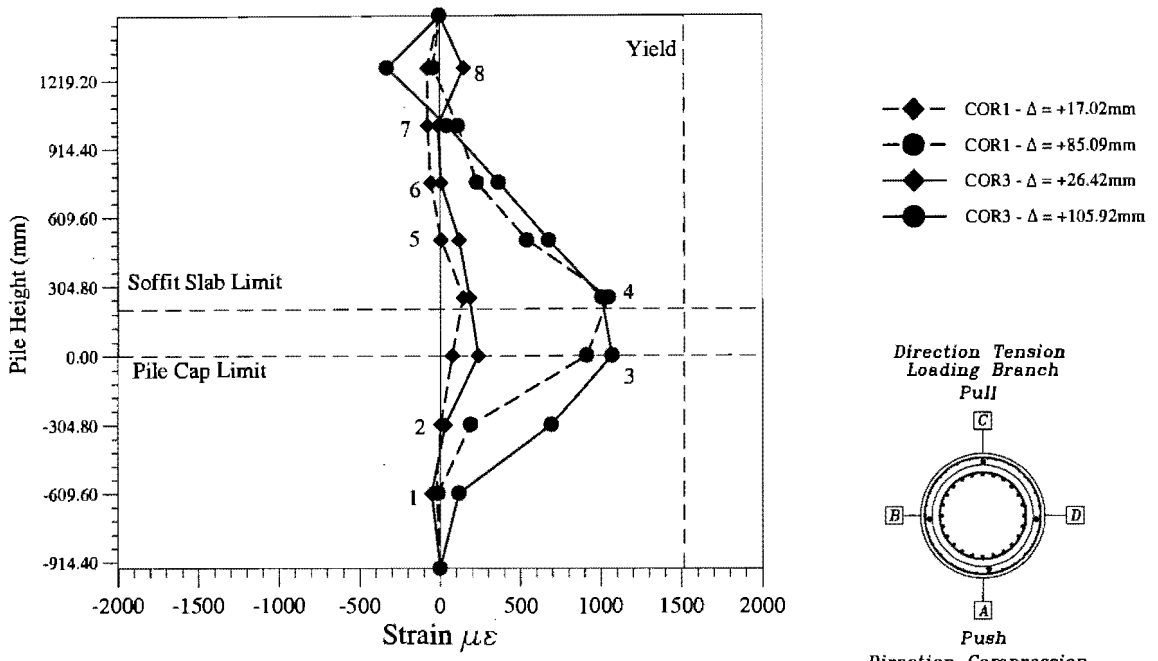

(a) Vertical Strain Profiles - Compression Loading Branch

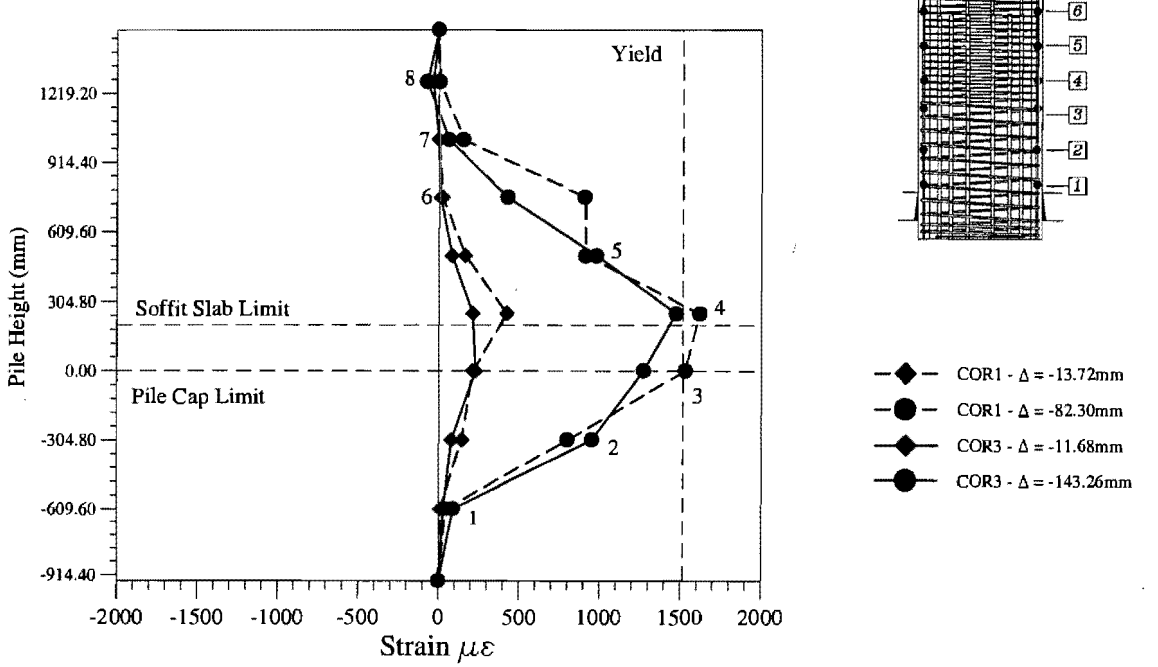

(b) Vertical Strain Profiles - Tension Loading Branch

Fig. 8–9 Vertical Strain Profiles Inner Core Bar ***B***

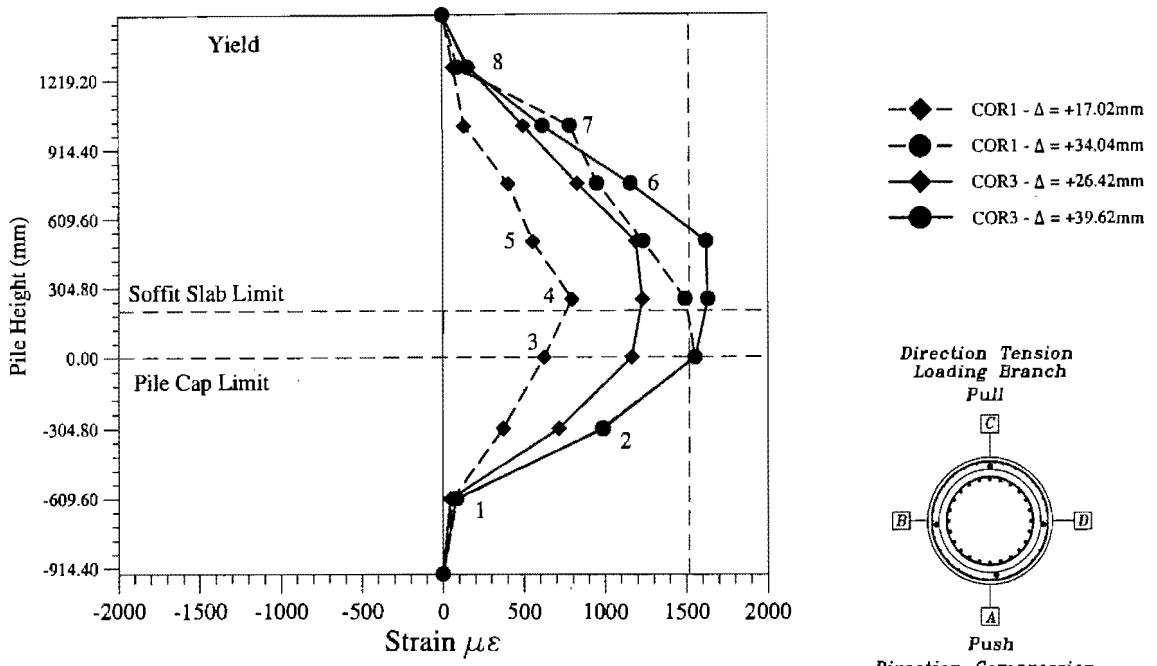

(a) Vertical Strain Profiles - Compression Loading Branch

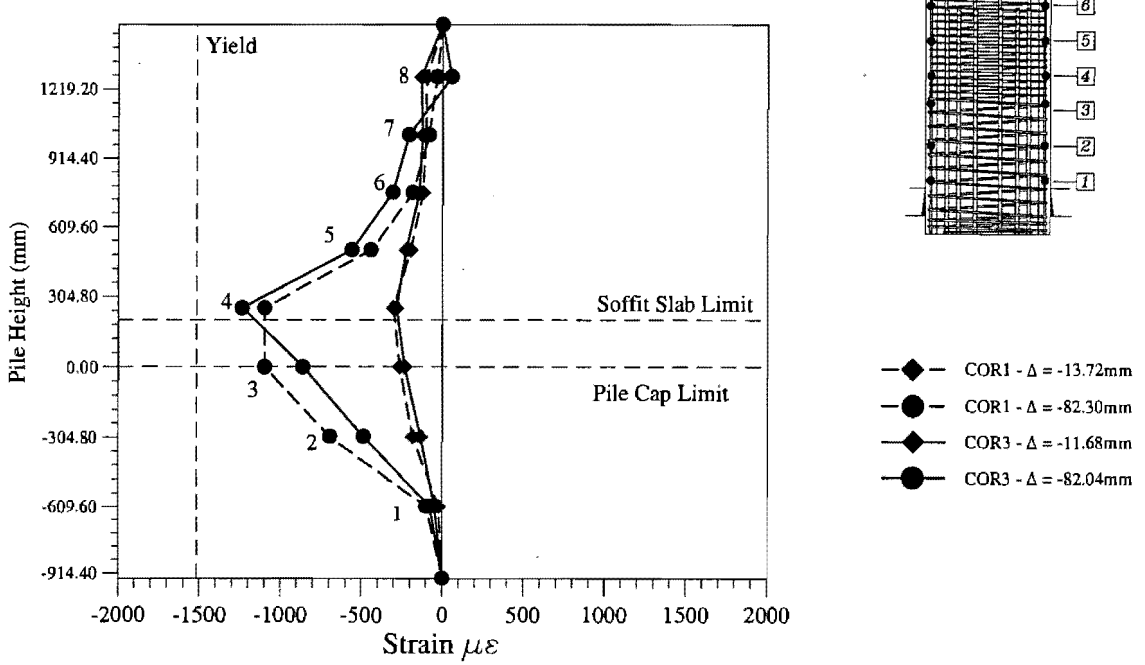

(b) Vertical Strain Profiles - Tension Loading Branch

Fig. 8-10 Vertical Strain Profiles Inner Core Bar *C*

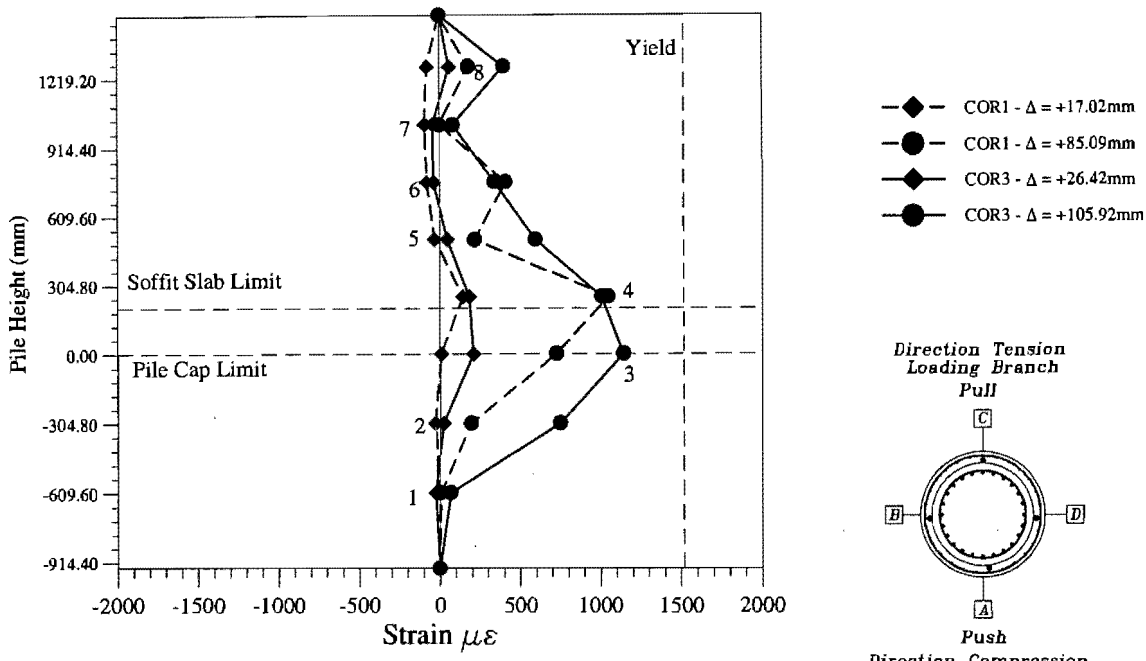

(a) Vertical Strain Profiles - Compression Loading Branch

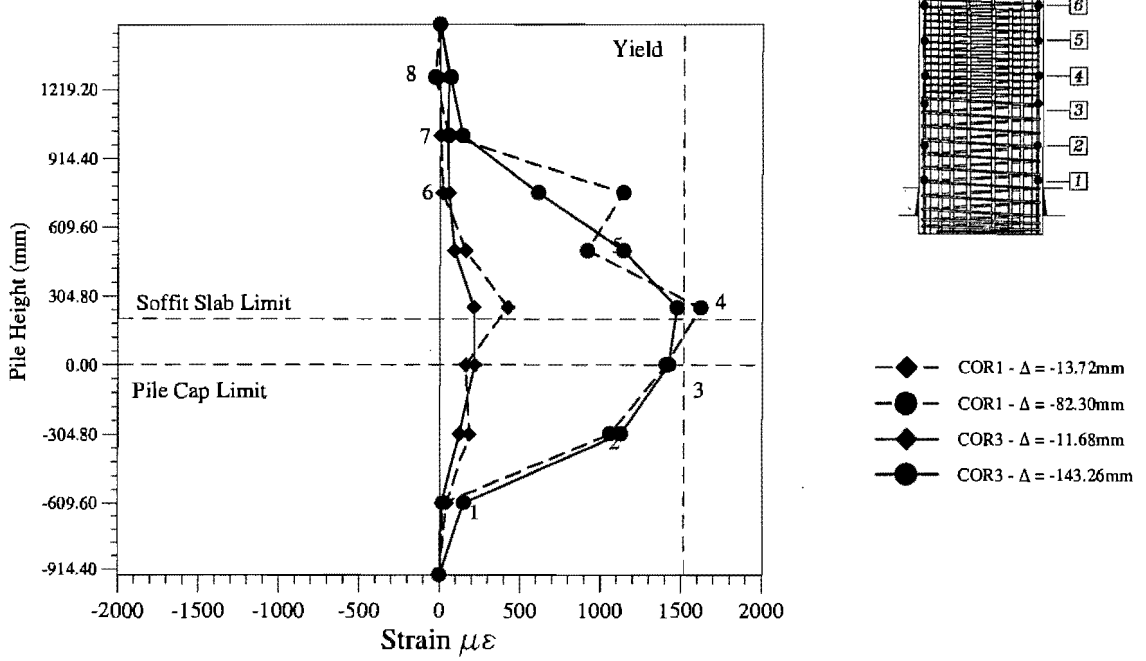

(b) Vertical Strain Profiles - Tension Loading Branch

Fig. 8-11 Vertical Strain Profiles Inner Core Bar ***D***

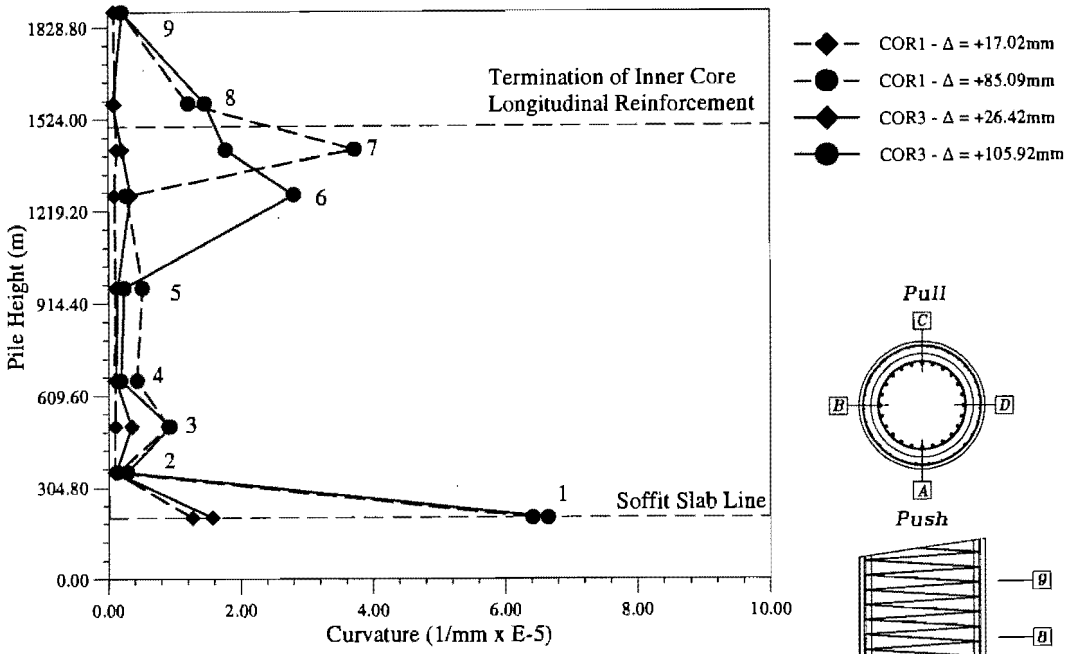

(a) Curvature Vertical Profiles - Compression Loading Branch

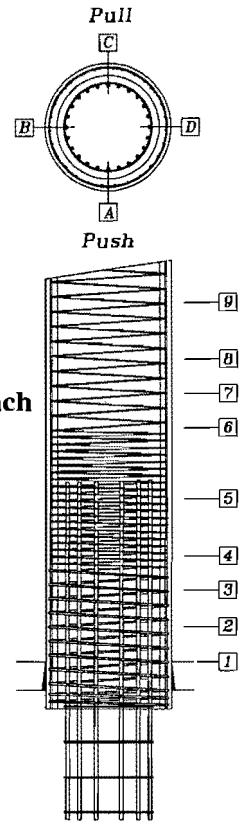

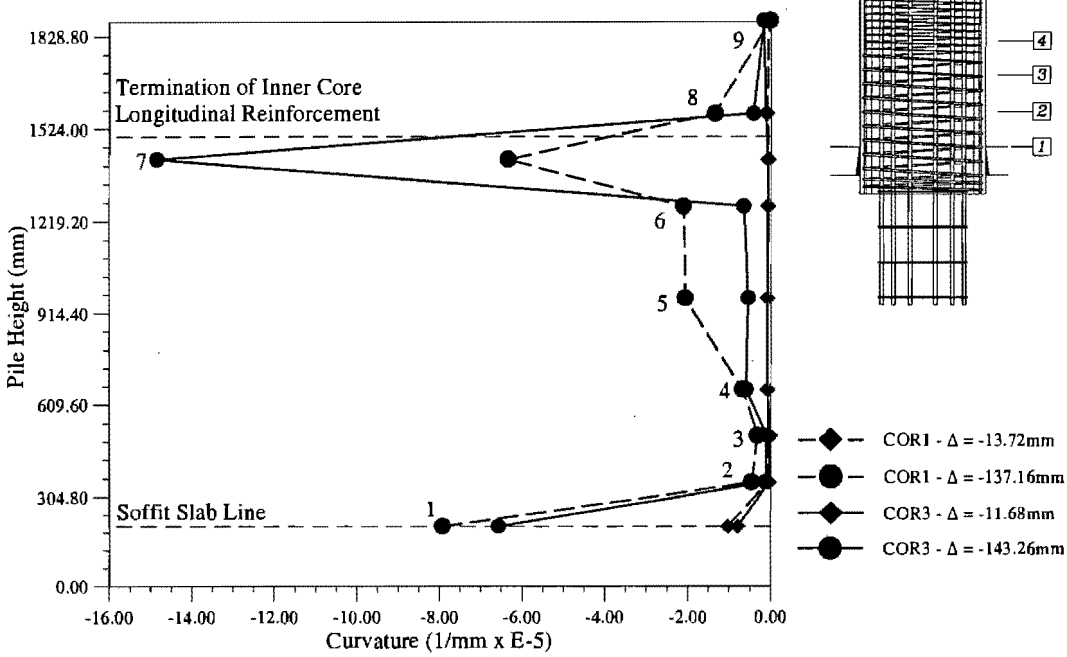

(b) Curvature Vertical Profiles - Tension Loading Branch

Fig. 8-12 Test Units *COR1* and *COR3* - Curvature Vertical Profiles

Fig. 8–13 Extent of Spalling of Cover Concrete - Test Unit *COR1*

Fig. 8–14 Extent of Spalling of Cover Concrete - Test Unit *COR3*

8.2.2 Test Units *COR1, COR2* and *COR3*

In this section a brief comparison between the structural response of test units *COR1*, *COR2* and *COR3* are presented.

The measured Moment versus Curvature envelopes presented in **Fig. 8-15** indicate that all the three test units displayed a ductile response, because there is no excessive strength degradation in succeeding cycles or increasing curvature. The envelopes depicted in **Fig. 8-15** indicate that the structural stiffness of test unit *COR2* was the highest and test unit *COR3* the lowest and, in the tension loading branch, there is a good agreement between the behavior of the three test units.

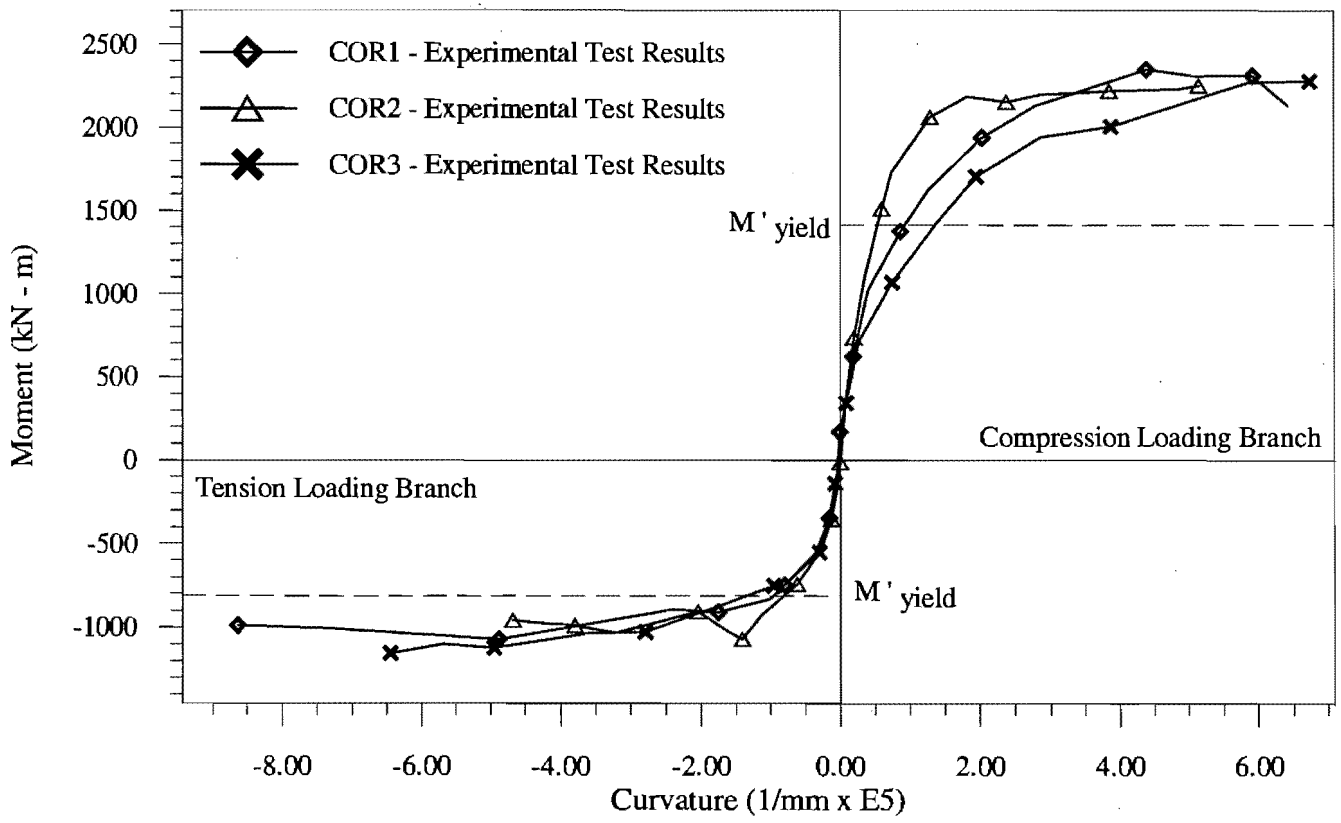

Fig. 8-15 Test Units *COR1*, *COR2* and *COR3* - Moment versus Curvature Envelopes

9. Conclusions

Response of the Coronado Bay Bridge piles and their connection to the pile cap were investigated under simulated seismic loading. Test results indicate test unit *COR1* reached its theoretical flexural capacity under compressive and tensile axial loading. The test unit performed in a very ductile manner in both loading directions and significantly exceeded design assumptions initially used for the retrofit design of the Coronado Bay Bridge. In addition, test results show that in the early stages of the testing procedure, regions of plastic deformations occurred first at the pile cap interface. However, at later stages, as the transfer length of the prestressing steel increased due to damage of the cover concrete and/or slipping of the prestressing strands, a second region of inelastic deformations began to form around the termination of the pile inner core longitudinal reinforcement.

Test unit *COR2* flexural strength under compressive axial loading exceeded the capacity determined during the pre-test analysis. This test unit displayed a more predominant flexural-shear response due to fracture of the spiral cage under large displacements along an inclined crack. Thus, observed fracture of the spiral cage indicates that there is the propensity for a shear failure. Similarly to test unit *COR1*, test unit *COR2* pile significantly exceeded the design displacement ductility capacity.

Investigation of test unit *COR3* test results suggests that the imposed cracks and cutting of the spiral and prestressing reinforcement did not have great influence in the overall response of the structure. In comparison with the test results for test unit *COR1*, test unit *COR3* structure achieved approximately the same flexural strength under axial compressive loads and even exceeded the flexural strength of test unit *COR1* pile under axial tensile loads, as discussed in Chapter 8.

Test unit *COR1* reached a maximum lateral load of +520 kN at a displacement ductility of μ_Δ=+3 in the compression loading branch and achieved a maximum displacement ductility of μ=+5. The lateral load at this stage was +457 kN, a reduction of 13% from the registered peak lateral load. Under tensile axial loads, the maximum lateral load was registered at −229 kN when the displacement ductility was μ_Δ=-4. The maximum displacement ductility μ_Δ=-10 was reached when the lateral load was -192 kN, a reduction of approximately 16%. **Table 9-1** presents a summary of key experimental test results for test unit *COR1*.

Test unit *COR2* maximum lateral loads were registered in the compression and tension loading branches at +1,009 kN and -506 kN when the displacement ductility was μ_Δ=+2.5 and μ_Δ=-4, respectively. In the compression loading branch, the lateral load remained essentially constant up to μ_Δ=+6. In the tension loading branch a decrease of approximately 7% was registered when the lateral load was approximately -473 kN at the maximum displacement ductility of μ_Δ=-7. **Table 9-2** presents a summary of key experimental test results for test unit *COR2*.

Test results presented in Chapter 7 indicate that test unit *COR3* maximum flexural strength in the compression loading branch occurred when the lateral load was +495 kN at μ_Δ=+3. In the tension loading branch, the maximum lateral load was -248 kN when the displacement ductility was μ_Δ=-9. Maximum displacement ductility achieved before conclusion of the testing procedure were μ_Δ=+4 in the compression loading branch and μ_Δ=-12 in the tension loading branch, when the lateral load was respectively +488 kN and -248 kN. **Table 9-3** presents a summary of key experimental test results for test unit *COR3*.

Table 9-1 Test Unit *COR1* - Experimental Test Results

		First Section Yielding	Ideal Yielding	Maximum Lateral Load	Maximum Lateral Deflection
Compression Branch	Lateral Load	+302 kN	+403 kN[1]	+520 kN	+457 kN
	Fixed Base Deflection	+12.75 mm	+17.02 mm	+51.05 mm μ_Δ=+3	+85.09 mm μ_Δ=+5
Tension Branch	Lateral Load	-173 kN	-204 kN[1]	-229 kN	-192 kN
	Fixed Base Deflection	-11.64 mm	-13.72 mm	-54.86 mm μ_Δ=-4	-137.16 mm μ_Δ=-10

[1]Lateral load corresponds to ideal flexural strength at ε_c=0.005.

Table 9-2 Test Unit *COR2* - Experimental Test Results

		First Section Yielding	Ideal Yielding	Maximum Lateral Load	Maximum Lateral Deflection
Compression Branch	Lateral Load	+676 kN	+899 kN[1]	+1009 kN	+1055 kN
	Total Deflection	+6.68 mm	+8.89 mm	+22.35 mm μ_Δ=+2.5	+53.34 mm μ_Δ=+6
Tension Branch	Lateral Load	-334 kN	-511 kN[1]	-506 kN	-473 kN
	Fixed Base Deflection	-5.63 mm	-8.63 mm	-34.54 mm μ_Δ=-4	-60.45 mm μ_Δ=-7

[1]Lateral load corresponds to ideal flexural strength at ε_c=0.005.

Table 9-3 Test Unit *COR3* - Experimental Test Results

		First Section Yielding	Ideal Yielding	Maximum Lateral Load	Maximum Lateral Deflection
Compression Branch	Lateral Load	+317 kN	+454 kN[1]	+495 kN	+488 kN
	Fixed Base Deflection	+18.44 mm	+26.42 mm	+78.74 mm μ_Δ=+3	+105.92 mm μ_Δ=+4
Tension Branch	Lateral Load	-172 kN	-186 kN[1]	-248 kN	-248 kN
	Fixed Base Deflection	-10.83 mm	-11.68 mm	-143.26 mm μ_Δ=-12	-143.26 mm μ_Δ=-12

[1]Lateral load corresponds to ideal flexural strength at ε_c=0.005.

References

[1] R. A. Dameron, R. R. Parker, and L. Zhang, *"Supplemental Capacity Analysis of the San Diego Coronado Bay Bridge"*, Report to Caltrans and McDaniel/JMI, October 1995.

[2] Memorandum to Consultant Contract Management Branch - Caltrans, Condition Survey of the San Diego-Coronado Toll Bridge Seismic Retrofi Project Piles File # 11-021901, December 1996,

[3] McDaniel Engineering / J. Muller International Memorandum *"San-Diego Coronado Bay Bridge Seismic Retrofit,"* File No. 61.05, Excerpt from a Geotechnical Report by Earth Mechanics, September 1995.

[4] American Concrete Institute, *"Building Code Requirements for Structural Concrete,"* ACI318-95, October 1995.

[5] Collins, M. P., and Mitchell, D., *"Prestressed Concrete Structures,"*Response Publications, Canada, 1997, 766pages.

[6] Paulay, T., and Priestley, M. J. N., *"Seismic Design of Reinforced Concrete and Masonry Buildings,"* John Wiley & Sons, Inc., New York, 1992, 744 pages.

[7] Kowalsky, M.J., Priestley, M.J.N., and Seible, Frieder, *"Shear Behavior of Lightweight Concrete Columns Under Seismic Conditions,"* Department of AMES , UCSD, La Jolla, CA, July 1995.

[8] Priestley, M. J. N., Seible, F., and Calvi, M., *"Seismic Design and Retrofit of Bridges,"* John Wiley & Sons, Inc., New York, 1995, 672 pages.

[9] Priestley, M. J. N., *"Assessment and Design of Joints for Single-Level Bridges with Circular Columns,"* Department of AMES, University of California San Diego, La Jolla, California, Report No. SSRP-93/02, February 1993.

[10] Seible, F., Kurkchubasche, A., and Mazzoni, S., *"CALSD Instructional Computer Programs for Structural Engineering,"* University of California San Diego, California, January 1991.

[11] ANATECH Memorandum *"PY Data Used In Coronado Analysis,"* July 1996.

[12] Priestley, M. J. N., Budek, A., and Benzoni, G., *"An Analytical Study of the Inelastic Seismic Response of Reinforced Concrete Pile-Columns in Conhesionless Soil,"* Department of AMES, University of California San Diego, La Jolla, California, Report No. 95/13, December 1995.

[13] McDaniel Engineering / J. Muller International Memorandum *"San-Diego Coronado Bay Bridge Seismic Retrofit Mud Line Elevation Comparison,"* File No. 61.15.25, Excerpt from a Summary Geotechnical Report, November 1995.

[14] Pender, M. J., *"Aseismic Pile Foundation Design Analysis,"* Bulletin of the New Zealand National Society for Earthquake Engineering, Vol. 11, No. 2, June 1978, pp 49-160.

[15] Mander, J.B., Priestley, M.J.N., and Park, R., *"Theoretical Stress-Strain Model for Confining Concrete,"* Journal of Structural Engineering, ASCE, V. 114, No. 8, August 1988, pp. 1804-1826.

[16] Structural Research and Analysis Corporation, *"COSMOS/M Nonlinear Analysis,"* Santa Monica, California, June 1994.

[17] Janney, J. R. , *"Nature of Bond in Pre-Tensioned Prestresses Concrete"*, ACI Structural Journal, V. 25, No. 9, May 1954, pp. 717-736.

[18] Naaman, A. E., *"Prestressed Concrete Analysis and Design Fundamentals,"* McGraw-Hill, Inc., New York, 1982, 672 pages.

[19] Ang, A. H-S. , and Tang, W. H., *"Probability Concepts in Engineering Planning and Design - Volume I - Basic Principles"*, John Wiley & Sons, Inc., New York, 1975, 409 pages.

[20] Ang, A. H-S. , and Tang, W. H., *"Probability Concepts in Engineering Planning and Design - Volume II - Decision Risk and Reliability"*, John Wiley & Sons, Inc., New York, 1990, 562 pages.

[21] Martin, L. D., and Scott, N. L., *"Development of Prestressing Strands in Pretensioned Members "*, ACI Structural Journal, V. 73, No. 8, August 1976, pp. 453-456.

[22] Hanson, N. W., and Kaar, P. H., *"Flexural Bond Tests of Pretensioned Prestressed Beams "*, ACI Structural Journal, V. 55, No. 7, January 1959, pp. 783-803.

[23] Russel, B. W., and Burns, N. H., *"Measurement of Transfer Lengths on Pretensioned Concrete Elements "*, Journal of Structural Engineering, ASCE, V. 123, No. 5, May 1997, pp. 541-549.

[24] Bjerkeli, L., Tomaszewicz, A., and Jensen, J. J., *"Deformation Properties and Ductility of High-Strength Concrete,"* Proceedings of the Second International Symposium on Utilization of High-Strength Concrete, University of California, Berkeley, California, May 1990, pp 215-238.

[25] Ibrahim, H. H. H., and MacGregor, J. G., *"Flexural Behavior of Laterally Reinforced High-Strength Concrete Sections "*, ACI Structural Journal, V. 93, No. 6, December 1996, pp. 674-684.

[26] Benzoni, G., Ohtaki, T., Priestley, M.J.N., and Seible, F., *"Seismic Performance of Circular Reinforced Concrete Columns Under Varying Axial Load,"* Department of AMES, University of California San Diego, La Jolla, California, Report No. SSRP-96/04, August 1996.

[27] Nawy, E., *" Reinforced Concrete - A Fundamental Approach,"* 2nd Edition, Prentice Hall, Englewood Cliffs, New Jersey, 1985.

[28] Muguruma, H., Watanabe, F., and Komuro, T., *"Applicability of High-Strength Concrete to Reinforced Concrete Ductile Column,"* Transactions of the Japan Concrete Institute, V. 11, 1989, pp 309-316.

[29] Yong, Y.K., Nour, M.G., and Nawy, E.G.,*"Behavior of Laterally confined High-Strength Concrete Under Axial Load,"* Journal of Structural Engineering, ASCE, V. 114, No. 2, Feb. 1988, pp. 332-351.

[30] Caltrans *"Bridge Design Specifications / Seismic Design References,"* Sacramento, California, June 1990

[31] King, D.J., Priestley, M.J.N., and Park, R., *"Computer Program for Concrete Column Design,"* Department of Civil Engineering, Report No. 86-12, University of Canterbury, Christchurch, New Zealand, May 1986.

[32] Pyke, R., and Beikae, M., *"A New Solution for the Resistance of Singles Piles to Lateral Loading,"* ASTM Committee D-18 on Soil and Rock, Kansas City, MO, June 1983, pp3-20.

[33] Bowles, J. E., *"Foundation Analysis and Design,"* 5th Edition, McGraw Hill, 1996.

Appendix A - Test Unit *COR3* - Concrete Core Data

A brief summary of the concrete core data from the condition survey of the Coronado Bay Bridge [2] is presented in **Fig. A-1** through **Fig. A-5**. Data presented in these figures indicate that in the plug region, no cracks were detected during the under water surveying of the piles at Pier 19. Chapter 3 presents the modeling of test unit *COR3* based on this condition survey.

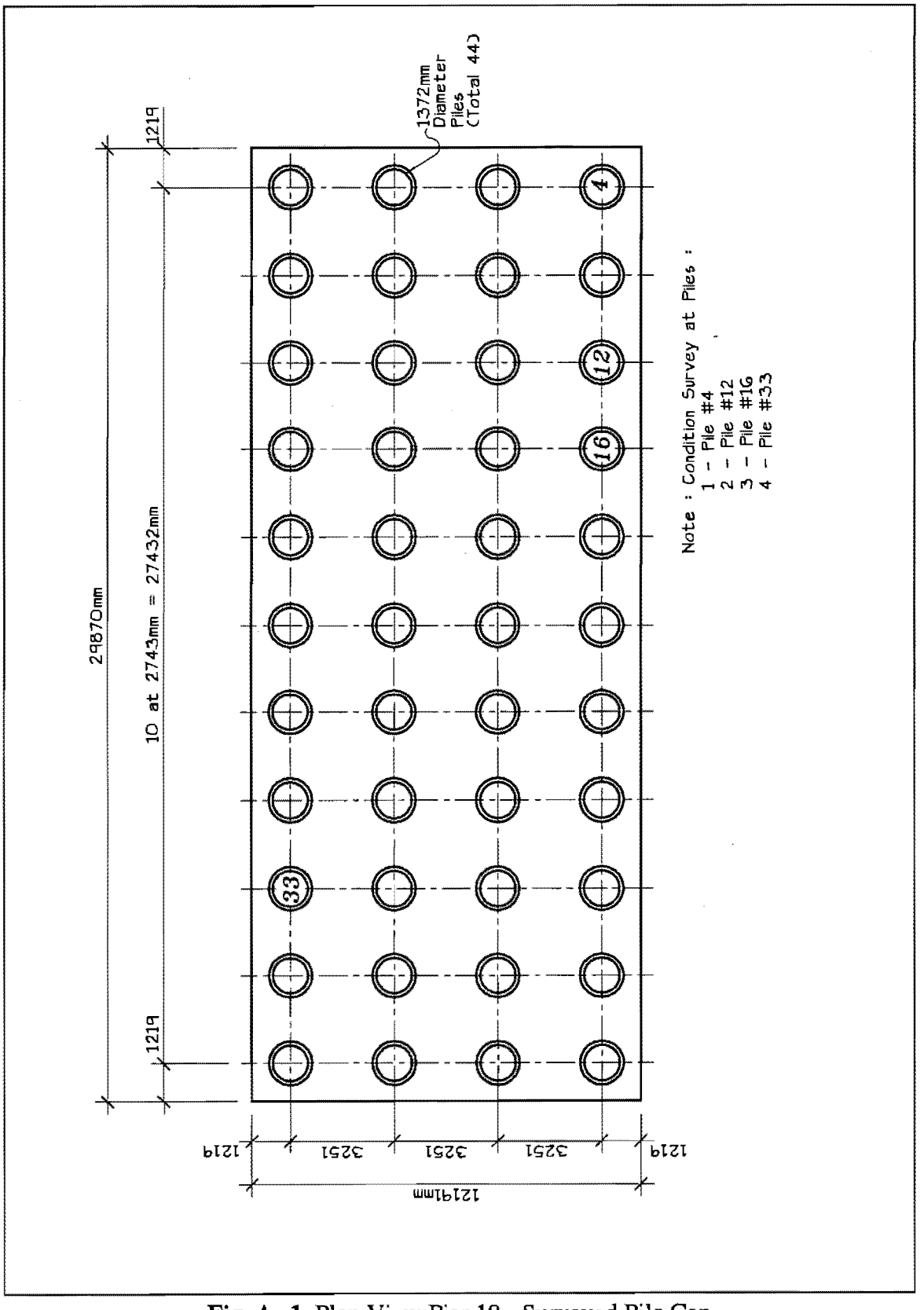

Fig. A-1 Plan View Pier 19 - Surveyed Pile Cap

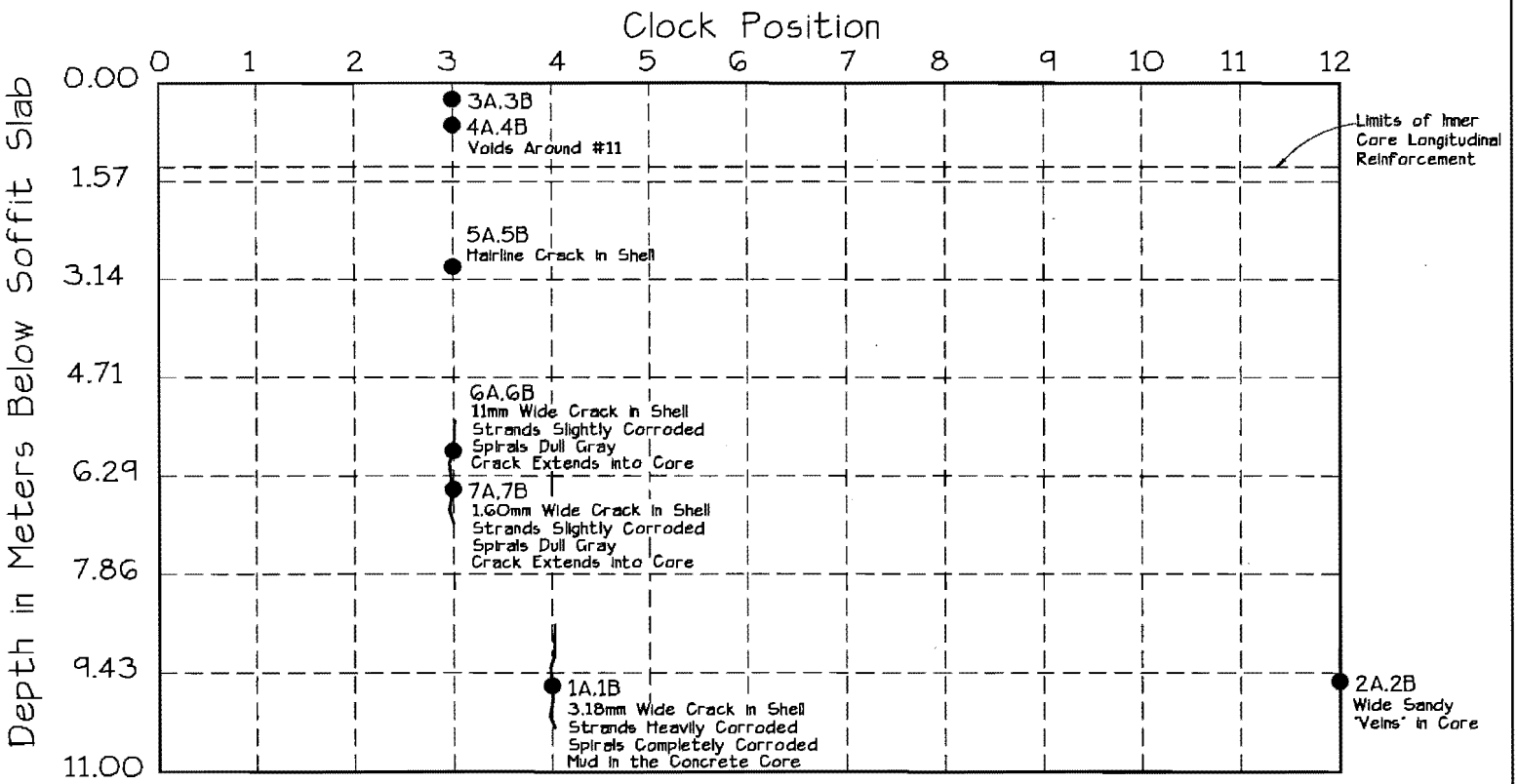

Fig. A-2 Pier 19 - Surveyed Pile Number *4*

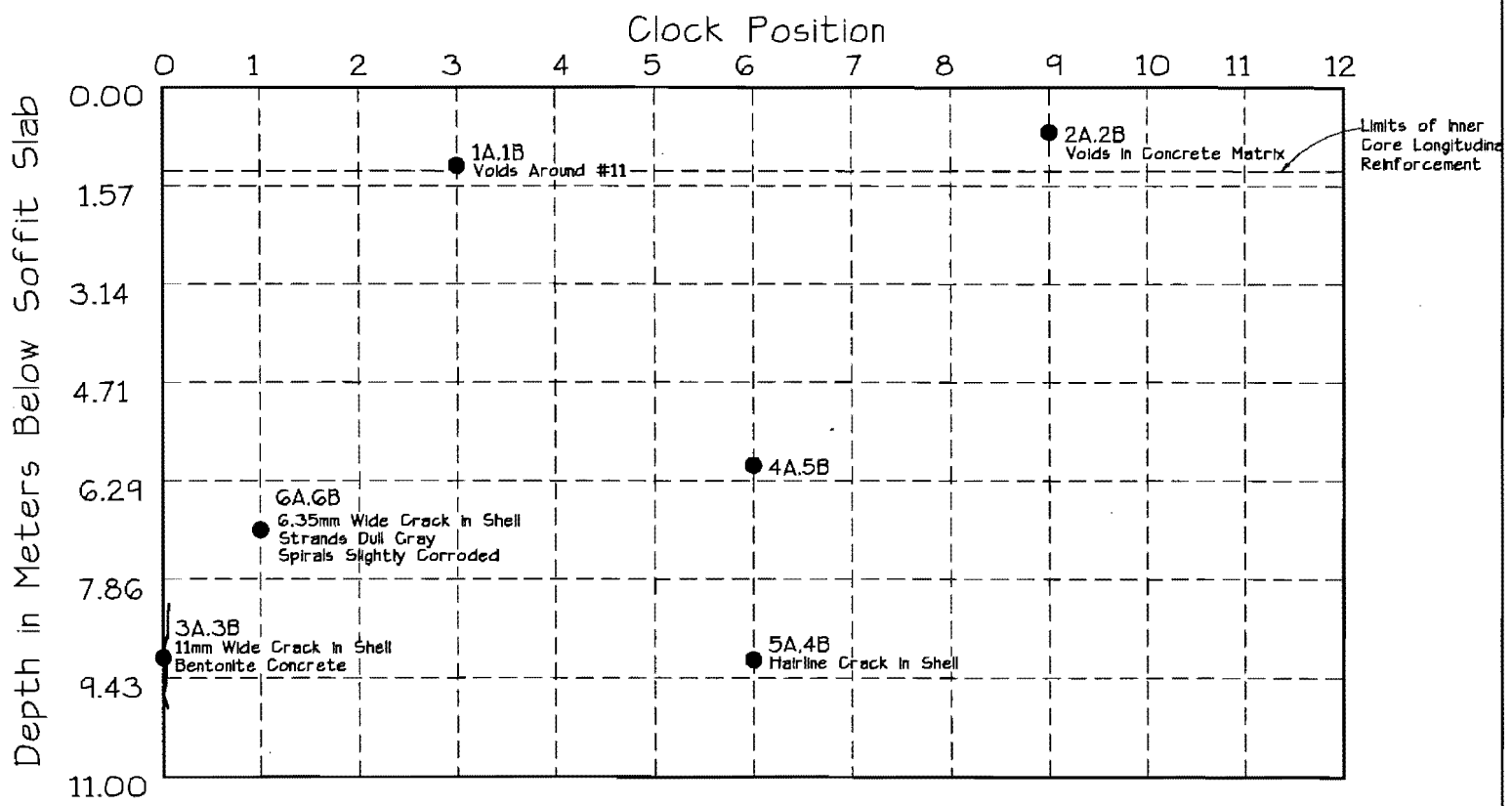

Pile No. 12

Legend

● 1A.1B – Indicates Concrete Core Location and Core Number

Fig. A-3 Pier 19 - Surveyed Pile Number *12*

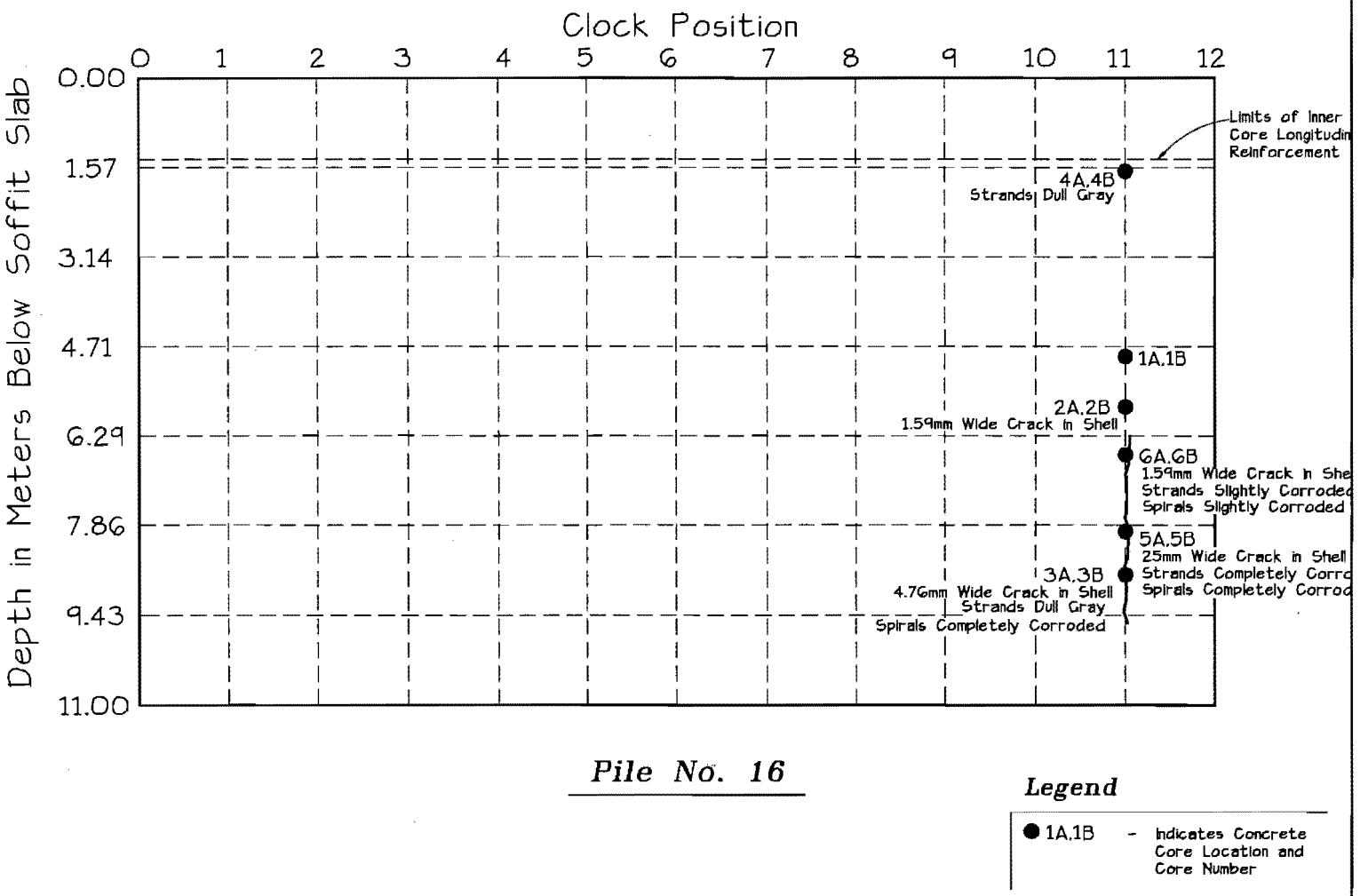

Fig. A-4 Pier 19 - Surveyed Pile Number *16*

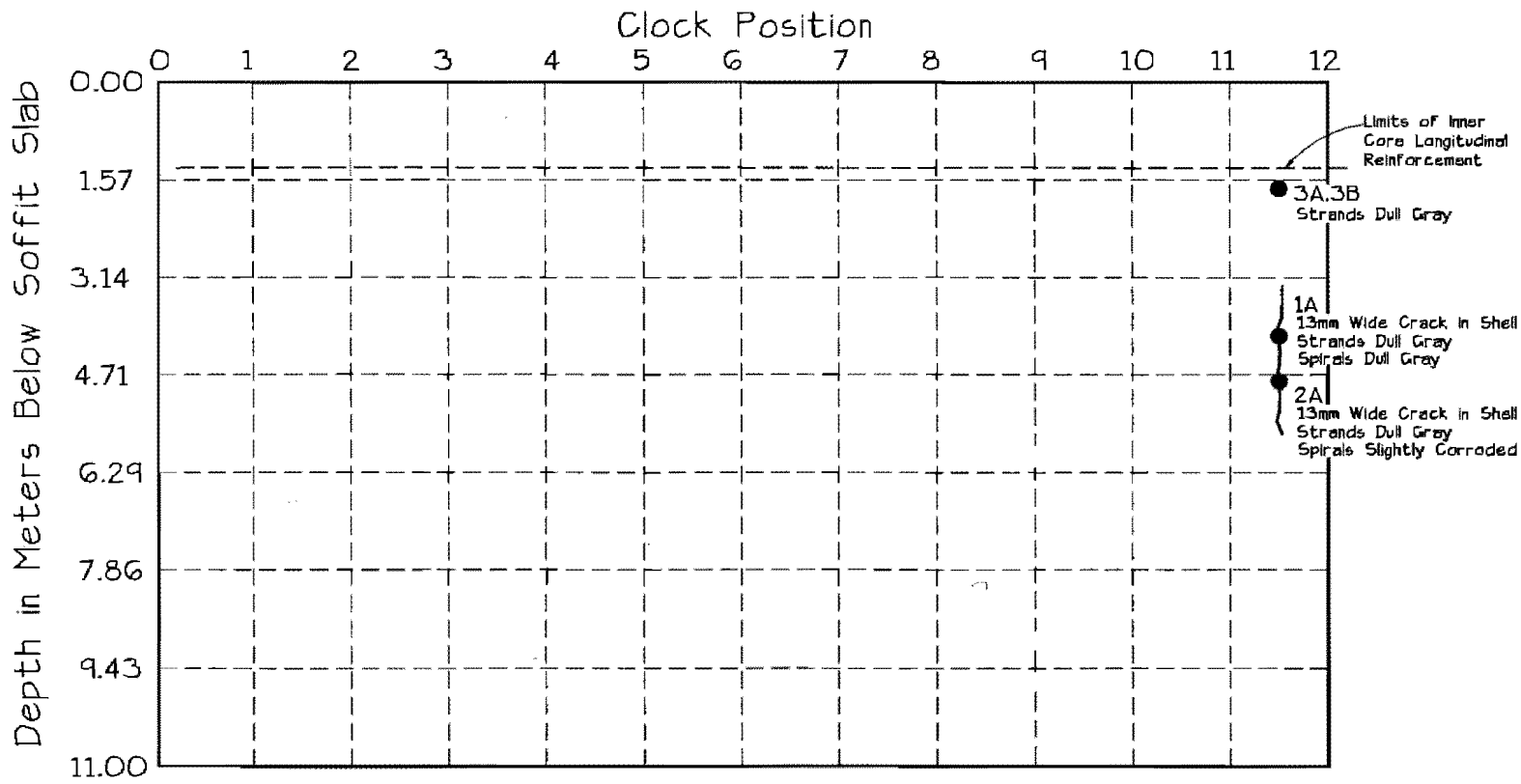

Pile No. 33

Legend

● 1A,1B - Indicates Concrete Core Location and Core Number

Fig. A-5 Pier 19 - Surveyed Pile Number **33**

Appendix B - Control Program Loading Path

B.1 Test Units *COR1* and *COR3* - Flowchart

In Chapter 3 the control program loading path for test units *COR1* and *COR3* was presented. In this appendix, a flowchart is presented to describe schematically the control program . **Fig. B-1** through **Fig. B-4** present the control program loading path for the different regions of the path described in Chapter 3. **Region 1** is defined as the *Compression Loading Branch*, **Region 2** is defined as the *Compression Unloading Branch*, **Region 3** is defined as the *Tension Loading Branch*, and **Region 4** is defined as the *Compression Unloading Branch*

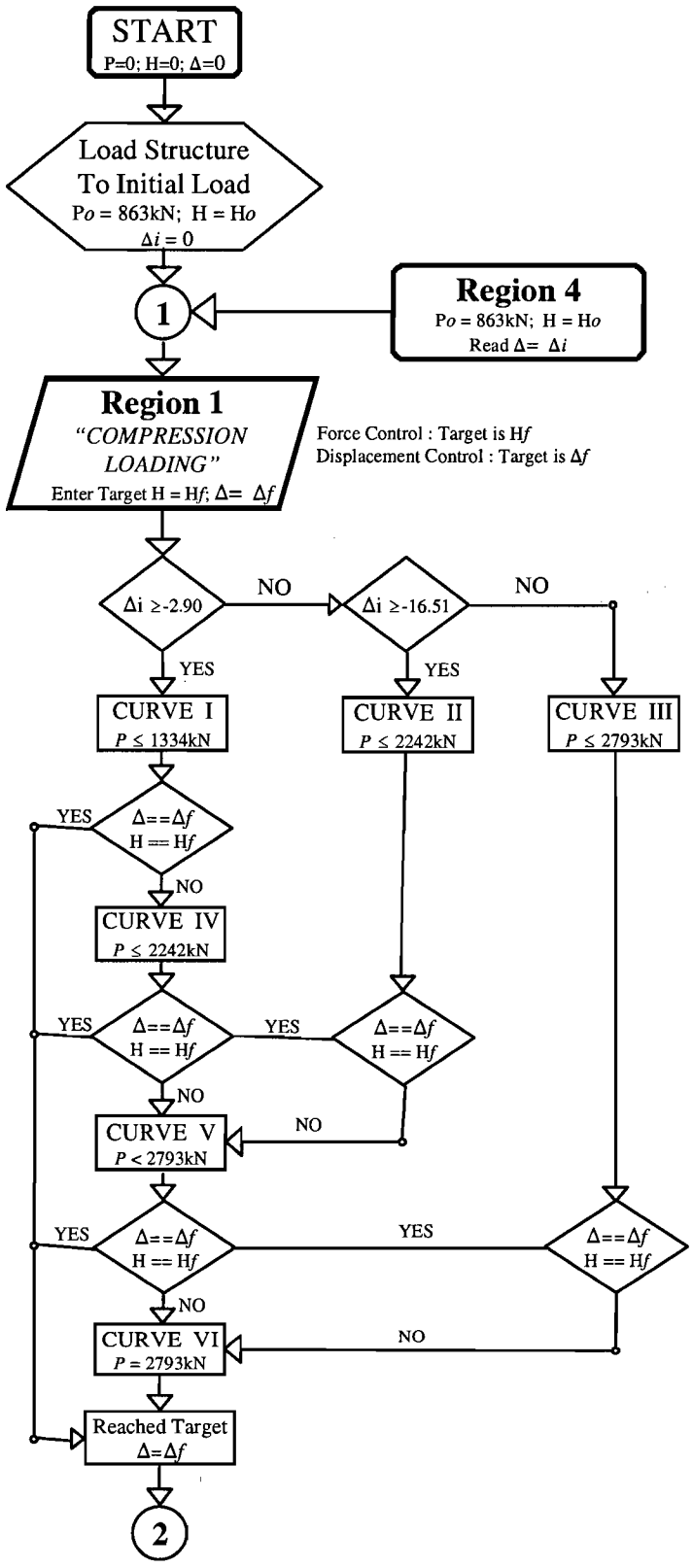

Fig. B-1 Test Units *COR1* and *COR3* - Flowchart **Region 1**

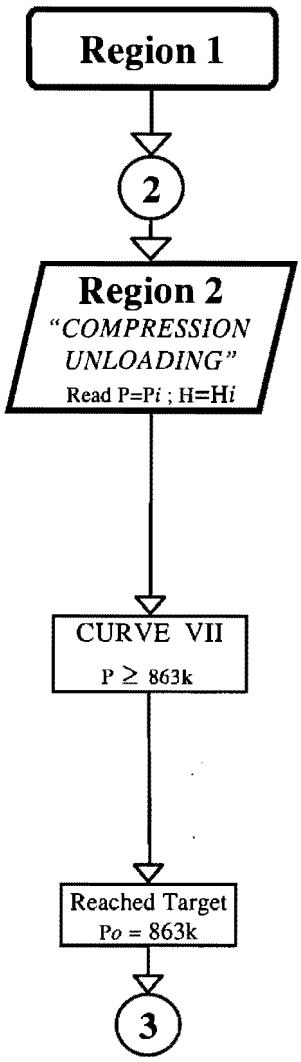

Fig. B-2 Test Units *COR1* and *COR3* - Flowchart **Region 2**

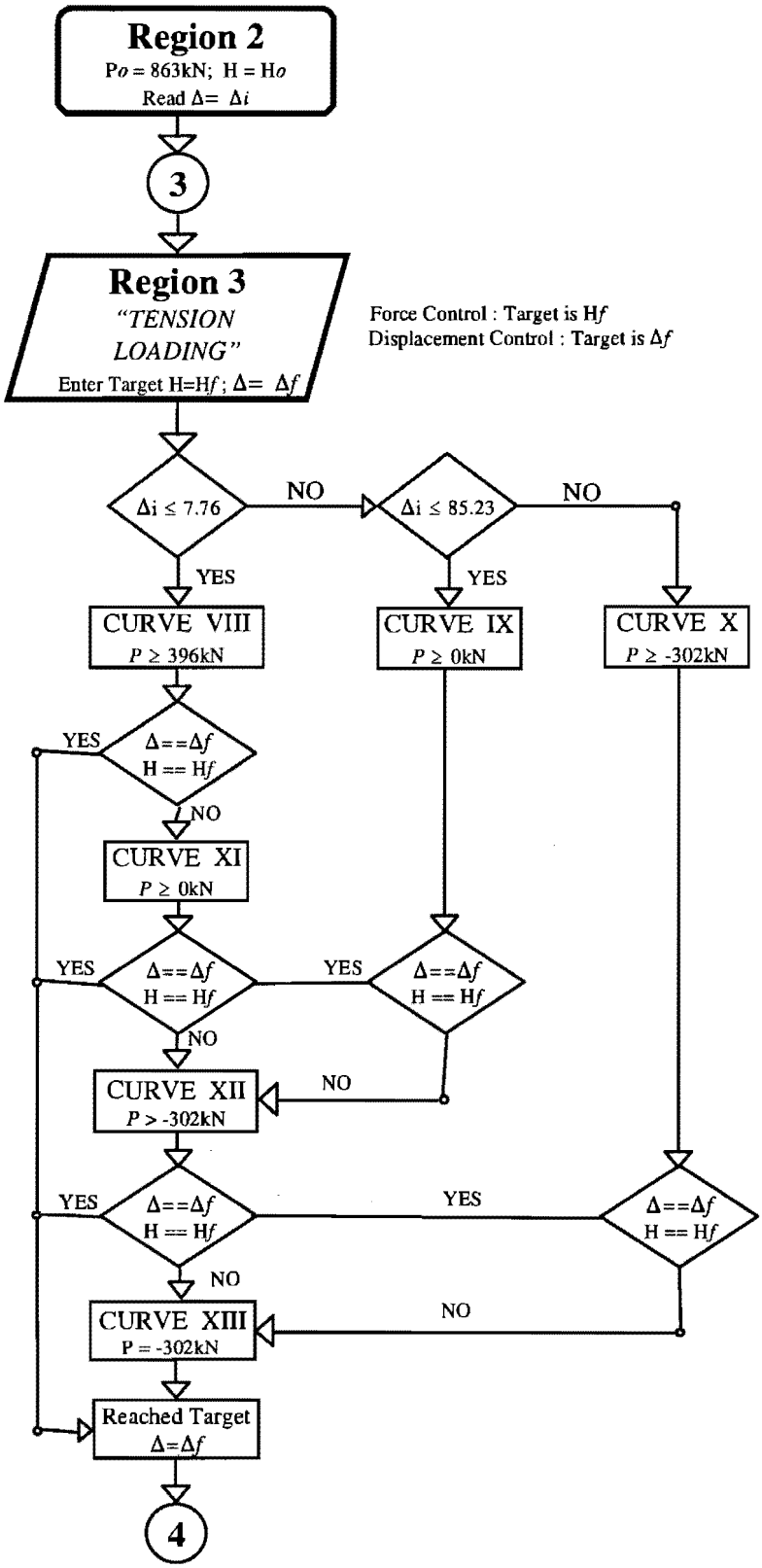

Fig. B-3 Test Units *COR1* and *COR3* - Flowchart **Region 3**

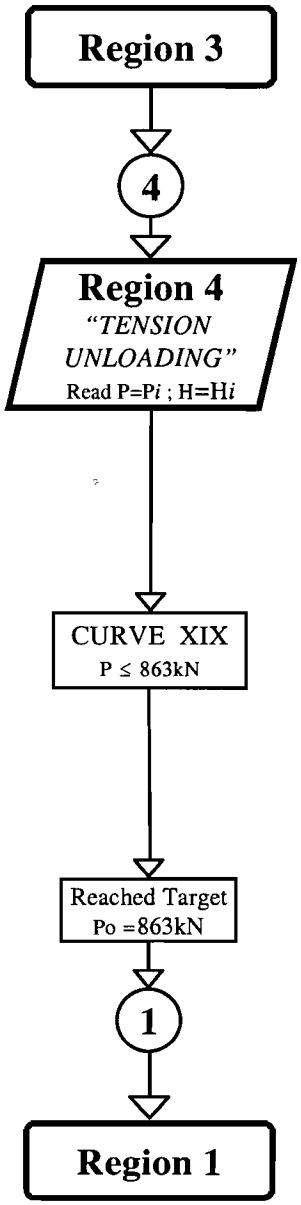

Fig. B-4 Test Units *COR1* and *COR3* - Flowchart **Region 4**

B.2 Test Unit *COR2* - Flowchart

In Chapter 3 the control program loading path for test unit *COR2* was presented, and in this appendix, a flowchart is presented to describe schematically the control program. **Fig. B-5** through **Fig. B-8** present the control program loading path for the different regions of the path described in Chapter 3. As before, **Region 1** is defined as the *Compression Loading Branch*, **Region 2** is defined as the *Compression Unloading Branch*, **Region 3** is defined as the *Tension Loading Branch*, and **Region 4** is defined as the *Compression Unloading Branch*

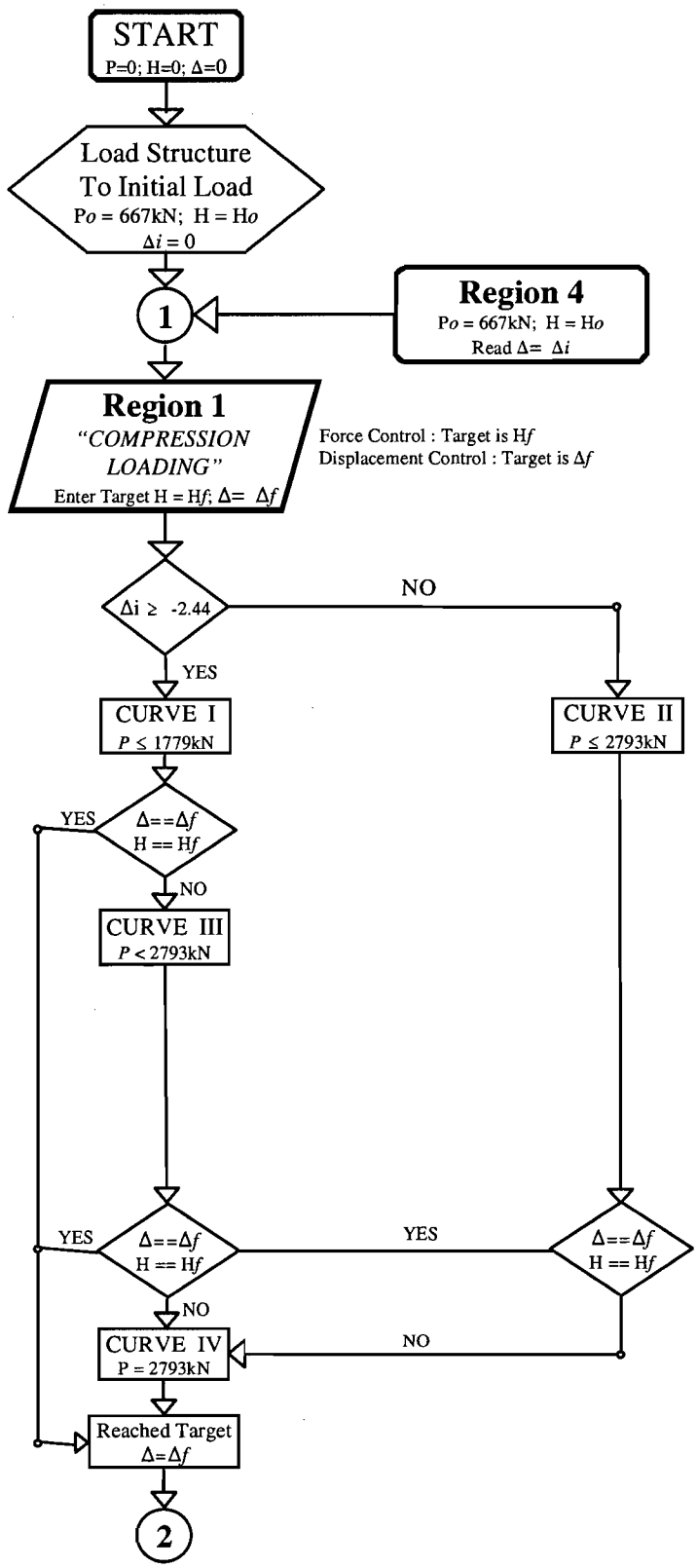

Fig. B-5 Test Unit *COR2* - Flowchart **Region 1**

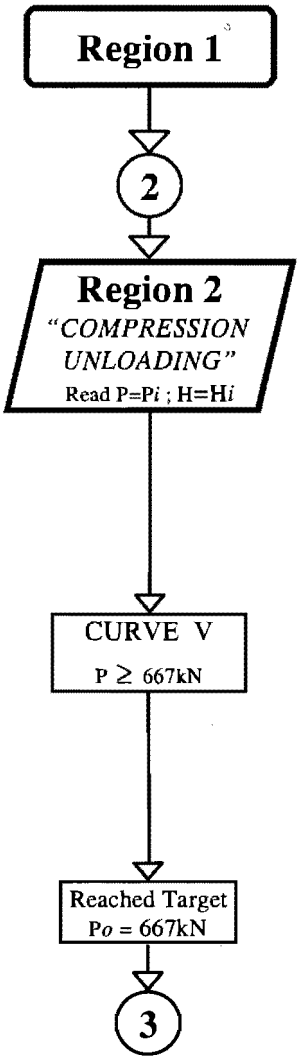

Fig. B-6 Test Unit *COR2* - Flowchart **Region 2**

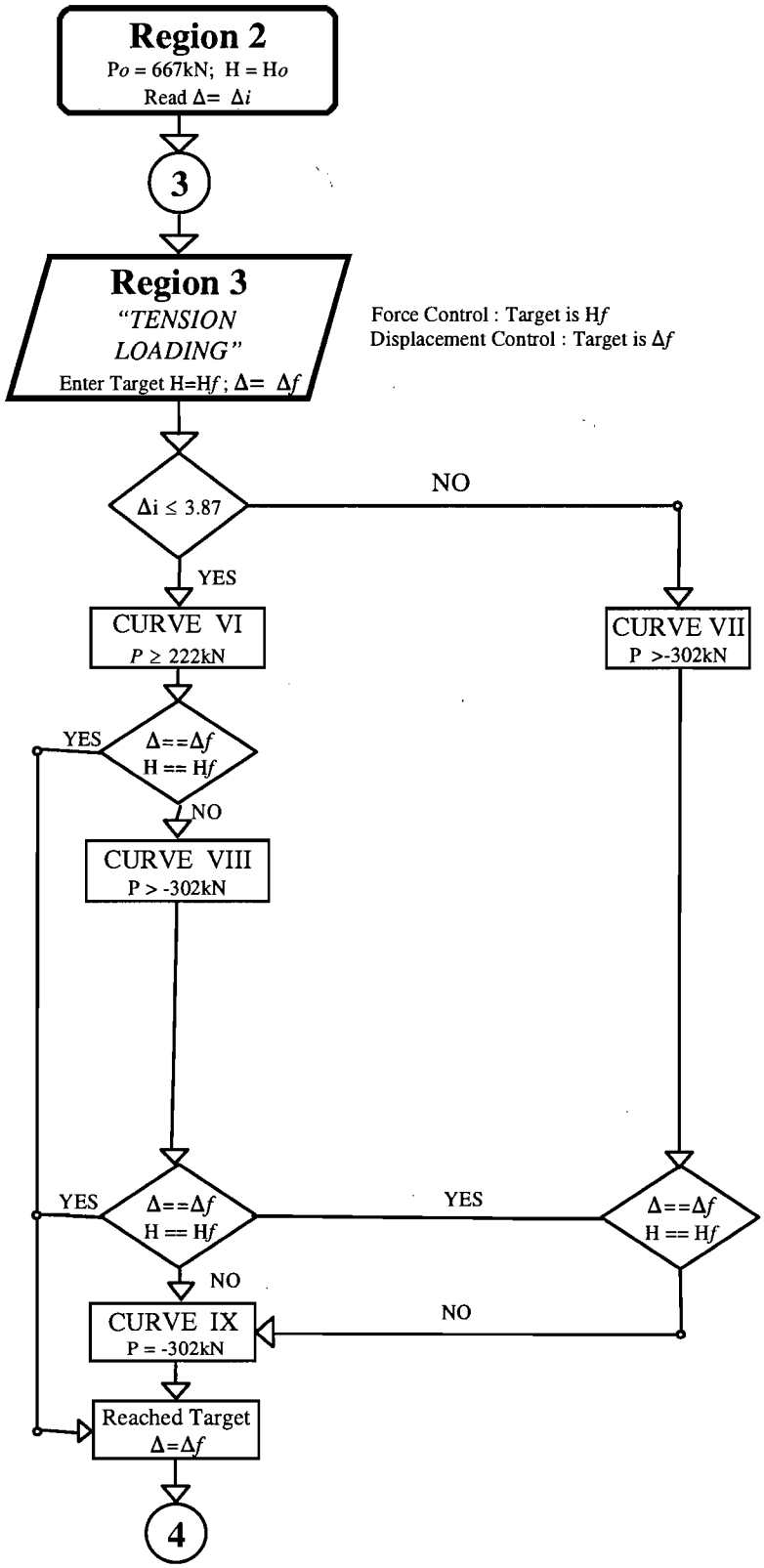

Fig. B-7 Test Unit *COR2* - Flowchart **Region 3**

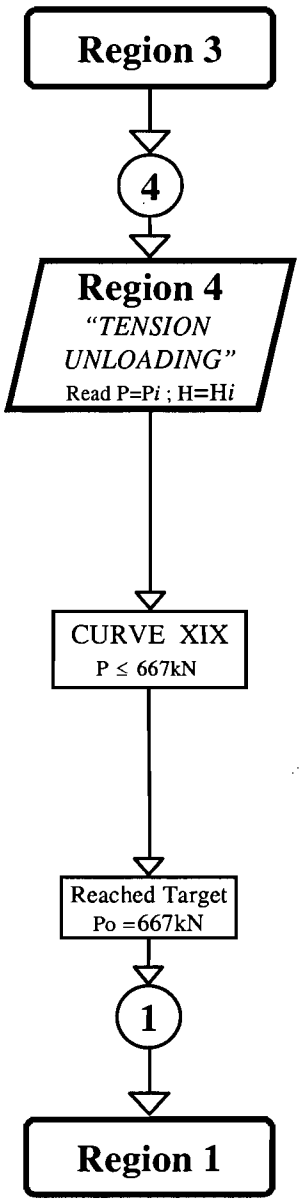

Fig. B-8 Test Unit *COR2* - Flowchart **Region 4**